THE UNIVERSITY of ADELAIDE

Late Paleozoic and Mesozoic thermotectonic evolution of the north-eastern margin of the Tianshan (Kazakhstan, NW China), and investigations of apatite detrital provenance methods

Jack Gillespie

This thesis is submitted in fulfilment of the requirements for the degree of Doctor of Philosophy

School of Physical Sciences
Department of Earth Sciences
University of Adelaide
Australia

June 2019

“实事求是”

Contents

List of Figures

List of Tables

Signed Statement

I certify that this work contains no material which has been accepted for the award of any other degree or diploma in my name, in any university or other tertiary institution and, to the best of my knowledge and belief, contains no material previously published or written by another person, except where due reference has been made in the text. In addition, I certify that no part of this work will, in the future, be used in a submission in my name, for any other degree or diploma in any university or other tertiary institution without the prior approval of the University of Adelaide and where applicable, any partner institution responsible for the joint-award of this degree.

I acknowledge that copyright of published works contained within this thesis resides with the copyright holder(s) of those works.

I also give permission for the digital version of my thesis to be made available on the web, via the University's digital research repository, the Library Search and also through web search engines, unless permission has been granted by the University to restrict access for a period of time.

I acknowledge the support I have received for my research through the provision of an Australian Government Research Training Program Scholarship.

Signed: ..... Date: .....

Acknowledgements

I have many people to thank, not only for the success of this project, but also for their roles in making it such a rewarding and enjoyable experience.

I must thank my primary supervisor, Stijn Glorie, for giving me this opportunity and for his ceaseless drive that pushed me to always do more. The sage advice and encouragement in all aspects of academic life from my secondary supervisor, Alan Collins, was rivalled only in importance by his excellent espresso machine.

The experience of undertaking a PhD would have been radically different if not for the fact I was working on one of two parallel projects on the thermotectonic history of Central Asia. As a result of the camaraderie of Gilby Jepson through the course of our postgraduate studies, it never really felt like I was working on this alone. Morgan Blades took me under her wing when I began to get involved in research during my third year of undergraduate, and has been an endless source of support, advice, and friendship since. I cannot for lack of space name all of the wonderful members of the postgraduate research community at the University of Adelaide who made the past four years so truly excellent. The coffee breaks, nights out, chats in the corridor, and endless other interactions, big and small, always made me feel like I belonged.

I could not have done this without the constant support of my family. Congratulations, Dad, for beating me to the finish line by several months, and submitting your PhD earlier this year.

Mr Paul Hoopman, who taught me in year four at Bellevue Heights Primary School, was an inspirational teacher who encouraged my interest in the natural world, in science, and in the outdoors.

The technical and analytical support from Sarah Gilbert and Ben Wade at Adelaide Microscopy was instrumental to the acquisition of the LA-ICP-MS data in this work. The assistance of colleagues in Kazakhstan and China was invaluable in terms of carrying out field work and providing important insight into the local geology. Thank you to Fedor Zhimulev, Dmitriy Gurevich, Dongfang Song, Zhiyong Zhang, and Yongchen Li for your guidance and advice. I am grateful to Professor Takahiro Tagami for hosting me at Kyoto Unversity during my Endeavour Research Fellowship, and to the friends who made me feel so welcome there.

Abstract

Intracontinental deformation and orogenesis is an understudied but important aspect of the Earth system. The Central Asian Orogenic Belt is a natural laboratory for the study of intracontinental mountain-building, with the major Tianshan and Altai mountain belts as the overwhelming focus of previous thermochronological studies in the area. However, these studies tend to investigate primarily the most recent phase of deformation that occurred in response to the Cenozoic collision of India with Eurasia.

This thesis presents studies of areas in Central Asia that did not experience large amounts of reworking during the Cenozoic, and correspondingly preserve less disturbed thermochronological information about the thermotectonic history of the region prior to the late Cenozoic.

The thermal history of late Paleozoic and early Mesozoic deformation in the Eurasian continental interior is well preserved in the West Junggar and Tarbagatai Mountains, which bridge the gap between the Tianshan and Altai.

The West Junggar Mountains record an episode of rapid cooling in the Early–Middle Permian, followed by an extended period of tectonic quiescence. The Tarbagatai Mountains, to the west of the West Junggar, record a more complex history. Middle–Late Permian rapid cooling is preserved in some regions of the study area, but is largely overprinted by a Late Triassic cooling event. Permian rapid cooling in both these areas is related to the deformation of Central Asia following the amalgamation of Kazakhstan with the Siberian active margin to the north and the collision of the Tarim block to the south. The development of large strike-slip structures during this widespread Permian deformation had an important effect on the subsequent history of these regions.

The spatial extent of Late Triassic exhumation in the Tarbagatai Mountains was controlled by the reactivation of these structures. Limited Jurassic–Cretaceous reactivation was similarly accommodated by the reactivation of late Paleozoic strike-slip structures. The orientation of these structures may be an important control on their later reactivation. Early Cretaceous cooling along the NW–SE striking Chingiz-Tarbagtai Fault is recorded in apatite fission track and (U-Th-Sm)/He data. In constrast, the anomalous NE–SW strike of faults in the West Junggar compared

to other major structures in the Kazkhstan Orocline may explain why this area is tectonically stable relative to its surroundings.

The easternmost Tianshan experienced significant reworking during the late Mesozoic and Cenozoic. The thermal history of this area is more similar to the other ranges of the Tianshan than to the West Junggar or Tarbagatai Mountains. Triassic rapid cooling signals are limited to areas outside the major range-bounding faults, common Jurassic–Cretaceous ages reflect extended residence in the partial annealing zone before rapid cooling in the Late Cretaceous, and no Cenozoic fission track ages were obtained.

The use of single grain apatite U–Pb and trace element analysis to understand the provenance of sediment was also investigated in this thesis, developing capabilities for more representative detrital geochronology studies in the future.

Chapter 1

Introduction

1.1 Aims and thesis motivation

The modern plate tectonic paradigm implies that deformation and mountain building occur at plate margins, where essentially rigid lithospheric plates interact. Classic examples of convergent margin interactions can be seen in the continent-continent collisions of the Himalaya or the European Alps, and an example of convergent continental-oceanic plate interaction can be seen in the Andes. However, this model neglects the case of deformation in supposedly rigid continental interiors, such as the modern example of the mountain belts of Central Asia, where the vast Tianshan and Altai Mountains can be found. The Tianshan stretches laterally in excess of 2500km, with a width of up to 300–500km and peaks over 7000m in elevation. The profound and ongoing intracontinental deformation in Central Asia makes the region a natural laboratory for the study of intracontinental mountain-building. The study of this region can help to develop a better understanding of the occurrence and evolution of these systems in geological history, and clarify their role and effect on global and local climate, sediment budgets and supply, and the implications for paleogeographic reconstruction.

The aim of this thesis is to improve our understanding of the intracontinental tectonic history of the Central Asian Orogenic Belt. Previous studies on the high elevation ranges of the Tianshan and Altai focussed mostly on trying to understand the timing and nature of reactivation and uplift in response to the collision of India with Eurasia. While Mesozoic thermochronological ages in the Tianshan and Altai are widespread and common, the interpretation of these data are hampered by the degree of Cenozoic reworking in the most well-studied areas. The study of the lower elevation (~1000–3000m) ranges between the Tianshan and Altai is necessary to understand the intracontinental tectonic history and spatial distribution of deformation in Central Asia prior to the deformation induced by the Indian collision.

In addition to low-temperature thermochronological analysis of basement rocks in Central Asia, part of this thesis aims to explore the use of apatite U–Pb and trace element analysis as a tool to investigate the provenance of sediment. Apatite grows in a range of igneous and metamorphic rocks, and its sensitive trace element geochemistry allows for discrimination between source rocks. The lower Pb closure temperature in apatite compared to other accessory minerals means it can detect medium temperature geological events that may be difficult to detect otherwise. As a consequence, this type of multi-method apatite analysis has shown great potential for investigating systems with rare or dominantly mafic magmatism, and for detecting medium temperature metamorphism in the detrital geochronology record. Apatite U–Pb and trace element analysis therefore has potential applications in intracontinental systems and other magma-poor orogens.

1.2 Geological Background

The Tianshan and Altai are part of the Central Asian Orogenic Belt (CAOB), which lies between the Eastern European, Siberian, Tarim, and North China cratons (Fig. 1.3), encompassing much of Central Asia and parts of East Asia (Windley et al., 2007). The CAOB is composed of arc terranes, accretionary wedges and microcontinents that were assembled largely over the course of the Paleozoic, with the early stages occurring during the Neoproterozoic. The final amalgamation of the CAOB occurred with the closure of the Paleo-Asian Ocean in either the Carboniferous–Permian or Permian–Early Triassic (Xiao et al., 2010; Charvet et al., 2011).

The Paleo-Asian Ocean can be divided into several sub-oceans from the mid-Paleozoic onwards, following the amalgamation of the Kazakhstan continent as an approximately linear belt (Fig. 1.1; Windley et al., 2007; Xiao et al., 2010; Li et al., 2018). The formation of the Kazakhstan continent was completed by the end of the Silurian, as the result of the amalgamation of early Paleozoic island arcs (Filippova et al., 2001; Degtyarev et al., 2015). During the Early and Middle Devonian, continental arc magmatism along the Kazakhstan margin formed the Devonian (or 'Outer') Volcanic Belt (Degtyarev, 2011; Bazhenov et al., 2012). The initiation of slab rollback in the Late Devonian caused magmatism to shift, forming the Inner Volcanic Belt (i.e. the Balkhash-Yili arc; Levashova et al., 2003a; Windley et al., 2007).

The Ob-Zaisan Ocean was located between Kazakhstan and the Siberian active margin, while the Turkestan Ocean (i.e. South Tianshan Ocean) was located between Kazakhstan and the Tarim Craton (Fig. 1.1). The Ob-Zaisan Ocean contained the Devonian-Carboniferous Zharma-Saur island arc, while on the northern side lay the terranes of the Altai (Fig. 1.1). The Turkestan Ocean contained the various terranes of the western and central Tianshan. Further to the east, the ter-

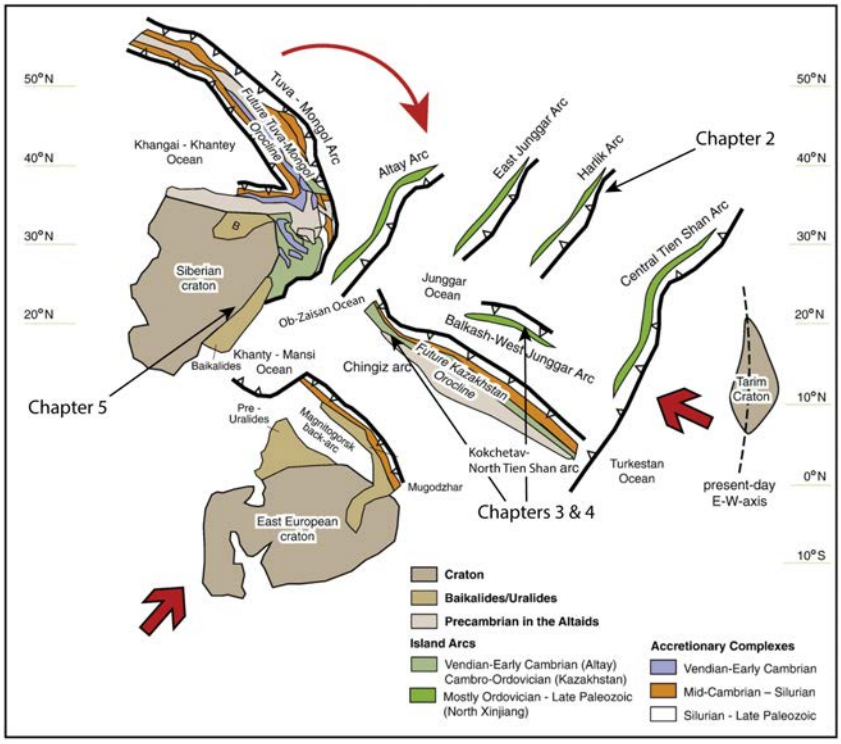

Figure 1.1: Example of a tectonic reconstruction of the Paleo-Asian Ocean in the mid-Paleozoic. Approximate locations of study locations for each chapter labelled. Modified after Xiao et al. (2010).

ranes of the eastern Chinese Tianshan and the East Junggar lay between the Tarim craton and the southern Siberian (Angaran) active margin (Xiao et al., 2004).

The Kazakhstan continent experienced the initial stages of oroclinal bending during the Late Devonian–Early Carboniferous, although the mechanism by which this occurred is still debated (e.g. Fig. 1.2) (Levashova et al., 2003a; Levashova et al., 2012; Li et al., 2018). The northern and southern limbs of the orocline were bent to the east, with the Junggar-Balkhash Ocean in between.

The Ob-Zaisan and Junggar-Balkhash Oceans were mostly closed by the end of the Carboniferous, although a limited oceanic basin in central Kazakhstan existed as a remnant of the Junggar-Balkhash Ocean into the Permian (Windley et al., 2007; Choulet et al., 2011). The closure of the southern Paleo-Asian Ocean in the west (i.e. the Turkestan Ocean) probably occurred in the Late Carboniferous or Early Permian with the northwards movement of the Tarim craton (e.g. Windley et al., 2007; Han and Zhao, 2018). The eastern reaches of the Paleo-Asian Ocean, between the North China Craton and the Mongolian terranes, closed along the Solonker suture perhaps as late as the mid-Triassic, significantly later than along

the Tianshan suture in the west (e.g. Eizenhöfer and Zhao, 2018).

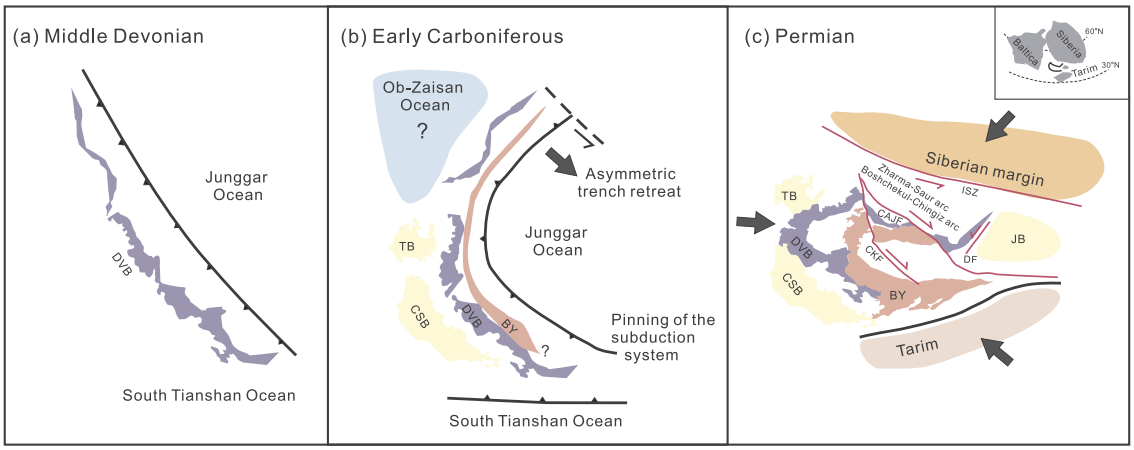

Figure 1.2: Simplified rollback model for Kazakhstan Orocline bending. Modified after Li et al. (2018). DVB = Devonian Volcanic Belt, TB = Teniz basin, CSB = Chu-Sarysu basin, BY = Balkhash-Yili arc, ISZ = Irtysh Shear Zone, CKF = Central Kazakhstan Fault, DF = Dalabute Fault, JB = Junggar block.

The relative motion and rotation of the Tarim and Siberian cratons during the Permian drove large scale strike-slip deformation of the intervening region (Fig. 1.2), with hundred to thousand-kilometre scale offset along reactivated suture zones and new structures that formed during this event (Allen et al., 1995; Shu et al., 1999; Laurent-Charvet et al., 2003; Wang et al., 2007; Choulet et al., 2012a; Li et al., 2018).

Following the Permian closure of the Paleo-Asian Ocean, representing the final accretion and amalgamation of the western CAOB, ongoing tectonic events at the plate margins of the Eurasian continent continued to affect the continental interior (Avouac et al., 1993; De Grave et al., 2007). Stress that propagated from the plate margins drove reactivation and intracontinental deformation in Central Asia throughout the Mesozoic and Cenozoic, leading to the formation of the Tianshan and other Central Asian mountain ranges (e.g. Sobel et al., 2006b; De Grave et al., 2007; Jolivet et al., 2010).

In order to decipher the relationship between plate margin collisions and the intracontinental tectonic response, many studies have focussed on understanding the exhumation and uplift history of the Tianshan, particularly in the high-elevation ranges of the Kyrgyz Tianshan, where late Cenozoic thermochronological ages are common (e.g. Bullen et al., 2001; Macaulay et al., 2014; Glorie and De Grave, 2016). This reflects the degree of exhumation and reworking this area has experienced since

the Oligocene, when uplift in response to the India-Eurasia collision began (Hendrix et al., 1994).

Mesozoic low-temperature thermochronological ages are extremely common throughout the Tianshan, with Jurassic–Cretaceous ages especially abundant (Glorie and De Grave, 2016). The interpretation of Jurassic–Cretaceous ages in terms of the timing, rate, and spatial extent of cooling is problematic, however, due to the fragmented and heterogeneous distribution of the data. Triassic ages from low-temperature thermochronometers, such as the apatite fission track method, are largely restricted to relict landforms both along the margins and within the mountains, although for methods with higher temperature sensitivity these ages are more common (De Grave et al., 2011a; De Grave et al., 2013; Jepson et al., 2018c; Jepson et al., 2018b). The distribution of thermochronological data in Central Asia with respect to major Paleozoic structures suggests that deformation throughout the Mesozoic and Cenozoic in Central Asia was often strongly controlled by the reactivation of the structural architecture inherited from the earlier tectonic evolution of the region (e.g. Jolivet et al., 2010; Glorie et al., 2011).

The relatively low-elevation regions between the Tianshan and Altai, to both the east and west of the Junggar Basin (Fig. 1.3), have been largely neglected in past studies of the thermotectonic history of Central Asia. During the late Cenozoic these marginal regions experienced far less tectonic reworking, and as a result they more clearly record the thermotectonic history of Central Asia prior to the collision of India with Asia. The objective of this thesis is to explore the evolution of the Eurasian continent from the Paleozoic to modern times, focussing on the exhumation histories of the regions on the margins of the Tianshan in order to provide a more complete picture of the intracontinental evolution of the Central Asian Orogenic Belt over the last ~300 million years.

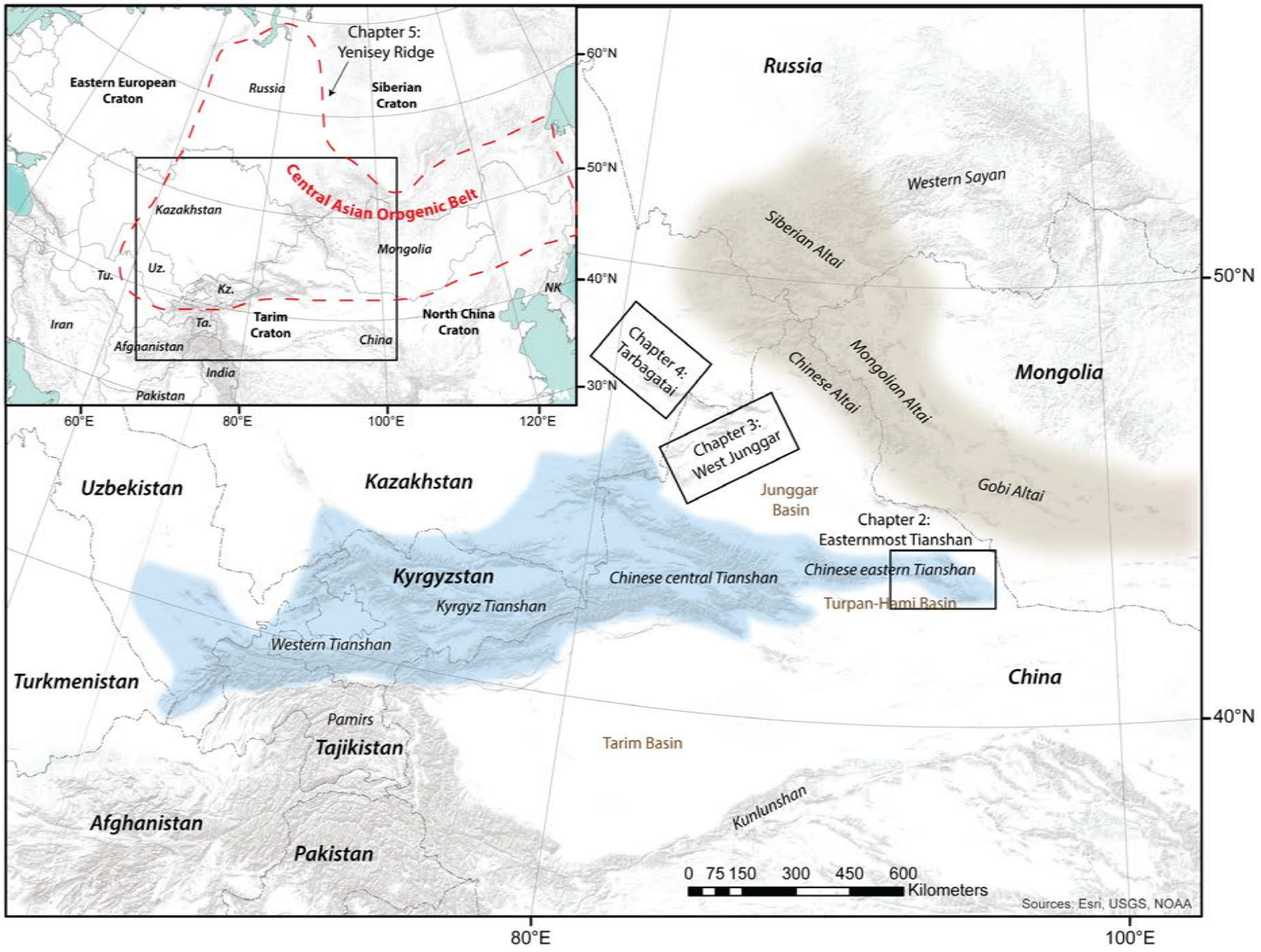

Figure 1.3: Map of Central Asia, showing the Tianshan and Altai mountain belts, and subdivisions thereof as commonly referred to in the scientific literature. Inset shows north-eastern Eurasia, with the extent of the Central Asian Orogenic Belt and surrounding cratonic blocks.

1.3 Methods

The elevated topography of mountain belts is a consequence of *surface uplift*, produced when the rate of *rock uplift* outstrips the rate of *denudation* (England and Molnar, 1990). As rock uplift and denudation compete to control surface uplift, these factors lead to the *exhumation* of rock as it moves closer to the surface from a point deeper within the earth (England and Molnar, 1990). This process also causes the cooling of the rock.

Thermochronological data from areas of active mountain building are therefore usually interpreted in the context of exhumational cooling. This is the case in Central Asia, where thermochronological information about the timing of cooling is generally related either to erosional exhumation of uplifted areas, or to tectonic exhumation via overburden displacement along faults (e.g. Hendrix et al., 1994). However, mechanisms other than exhumation can also cause rocks to cool, such as regionally decreasing geothermal gradient, or local thermal relaxation following heating, such as by magmatic intrusion (Malusà and Fitzgerald, 2019).

The mineral apatite is widely used as a thermochronometer, as it records a variety of information about the thermal history of the host rock as a result of the thermally sensitive retention of the products of the radioactive decay of isotopes such as ^{238}U, ^{235}U, and ^{232}Th (e.g. Chew and Spikings, 2015). The primary investigative tool applied in this thesis is the apatite fission track method, with secondary use of the (U-Th-Sm)/He and U–Pb systems. Additionally, this thesis applied the novel combination of U–Pb isotopic analysis and trace element geochemistry of apatite to investigate the source rock types of detrital grains in sedimentary rocks.

1.3.1 Apatite geochemistry

Apatite ($Ca_5(PO_4)_3(F,Cl,OH)$) is a common accessory mineral that forms in both magmatic and metamorphic rocks under a wide variety of physical and chemical conditions (e.g. Hughes and Rakovan, 2015). A huge range of elements can be substituted into the structure of an apatite crystal, making it a sensitive and powerful geochemical tool for investigating a range of processes from petrogenesis to hydrothermal alteration (e.g. Webster and Piccoli, 2015; Harlov, 2015). The formula for apatite when considering substitutions (Barbarand et al., 2003) can be expressed as:

$$X_{10}YO_4Z_2 \tag{1.1}$$

where X = mainly Ca, Y = P, and Z = F,Cl,OH.

The X site allows for the direct substitution of many divalent cations including

Sr, Ba, Pb, Cd, Mg, Fe, Mn, Co, Ni, Cu, Zn, and Sn, while trivalent cations such as REEs can occupy these sites via coupled substitution. Common coupled substitutions include:

$$Na^{+} + REE^{3+} \leftrightarrow 2Ca^{2+} \tag{1.2}$$

$$Si^{4+} + REE^{3+} \leftrightarrow P^{5+} + Ca^{2+} \tag{1.3}$$

U^{4+} and Th^{4+} are also able to substitute into this site, and are frequently present in concentrations ranging from sub-ppm to hundred-ppm levels.

The characteristic geochemistry of apatite from different source rocks and the processes responsible for the observed differences are the topic of Chapter 5, where this subject is discussed in detail.

1.3.2 Apatite fission track analysis

Fission track thermochronology makes use of the temperature-dependent annealing of radiation damage features in the crystal lattice of a mineral to determine the timing and rate of cooling (Fleischer et al., 1975). These linear zones of damage, or 'fission tracks', are created by the spontaneous fission of ^{238}U (Price and Walker, 1963), which occurs at a rate approximately 1.82 million times less frequently than the α-decay of ^{238}U (Jaffey et al., 1971). Fission tracks in apatite are stable below ~60 °C, and are quickly fully annealed above ~120 °C (Gleadow et al., 1986a). Between these two states of stability and total annealing, fission tracks slowly anneal, becoming progressively shorter until they are totally annealed. The temperature window where this behaviour occurs is known as the apatite partial annealing zone (APAZ) (e.g. Wagner et al., 1989), and the temperature range of this window depends on the chemistry of the apatite grain (Green et al., 1986; O'Sullivan and Parrish, 1995; Carlson et al., 1999; Barbarand et al., 2003).

The Cl content of an apatite is the largest control on fission track annealing when present in concentrations above ~0.4 wt.% (Green et al., 1986). Several other elemental substitutions into the crystal structure of apatite are known to affect the annealing characteristics of apatite to lesser degrees, such as Sr^{2+}, Mn^{2+}, V^{2+}, Fe^{2+}, Na^{+}, and REE^{3+} (Carlson et al., 1999; Barbarand et al., 2003).

Fission tracks are invisible to the naked eye, but may be rendered visible through chemical etching (Price and Walker, 1962). The annealing kinetics of a particular apatite grain can be empirically estimated by measuring the size of the etch pit created by the intersection of the etched fission track path with the polished internal surface of the apatite grain (Burtner et al., 1994; Donelick et al., 2005). The length

of this feature parallel to the C axis of the apatite grain is known as D_{par}.

As a result of the predictable shortening of tracks with respect to their residence time in the APAZ, the distribution of confined track lengths (i.e. those that do not intersect the grain boundary or internal surface) provides information about the thermal history experienced by a sample (Gleadow et al., 1986b; Galbraith, 1990). Measuring the lengths of confined tracks in a sample makes thermal history modelling possible by providing information about the rate of cooling, in addition to the information about the timing of cooling that is provided by the fission track age. Inverse thermal history modelling is commonly used to statistically reconstruct possible thermal histories experienced by a sample, or set of samples (Ketcham et al., 1999; Ketcham et al., 2007; Gallagher, 2012).

Ongoing debate in the apatite fission track community about the potential role of radiation damage as a factor in the annealing of fission tracks continues (e.g. Hendriks and Redfield, 2005; Green et al., 2006; Kohn et al., 2009), and currently no models take this factor into account. Recent work suggests α-radiation damage annealing may have a significant effect on the annealing of fission tracks in apatite over long and slow cooling histories (McDannell et al., 2019).

Age determination

The fundamental age equation that underpins the fission track method is given by Vermeesch (2017) as:

$$t = \frac{1}{\lambda} ln\left(1 + \frac{\lambda}{\lambda_f}\frac{2\rho_s}{[^{238}U]L}\right) \tag{1.4}$$

where λ is the total decay constant of ^{238}U ($1.55125 \times 10^{-10} yr^{-1}$)(Jaffey et al., 1971), λ_f is the spontaneous fission decay constant ($8.52 \times 10^{-17} yr^{-1}$)(Holden and Hoffman, 2000), ρ_s is the density of spontaneous tracks on an internal surface of the apatite, [^{238}U] is the number of ^{238}U atoms per unit volume, and L is the etchable length of the tracks (Galbraith et al., 1988).

In the early days of fission track dating, several approaches for determining a fission track age were experimented with, including the subtraction and population methods (Gleadow, 1981). These methods were largely superseded by the the external detector method (EDM), which was preferred for its practicality, and as it allowed for the determination of individual grain ages (Gleadow, 1981). This approach measures the amount of ^{238}U in the sample via proxy, by inducing spontaneous fission of ^{235}U in a nuclear reactor, and recording these fission events in

a sheet of mica (known as a detector) adjacent to the polished internal surface of the apatite grain. The intensity of the dose received in the reactor is calibrated by the track density that results from the irradiation of a glass standard with a known concentration of ^{235}U. The spontaneous track density in the sample and the induced track density in the detector can be compared to produce an age. By analysing a standard of known age simultaneously to unknown samples, a 'zeta' calibration value could be determined that accounted for uncertainty in a number of factors including neutron fluence, the values of constants (especially λ_f), and variations between individual analysts (Hurford and Green, 1983).

The EDM was the most commonly used fission track dating technique for decades, until work in the early 2000's showed the feasibility of directly measuring the ^{238}U contents of an apatite grain via laser ablation inductively coupled plasma mass spectrometry (LA-ICP-MS) (Hasebe et al., 2004). The fundamental difference between the two techniques is that in contrast to the EDM, where ^{238}U is measured via the proxy of ^{235}U induced tracks in a mica detector, the LA-ICP-MS method directly measures the ^{238}U concentration in the area of the apatite in which tracks were counted. A transition from the well-established EDM to the LA-ICP-MS method is currently occurring in fission track laboratories around the world (e.g. Ketcham et al., 2018).

The LA-ICP-MS approach is advantageous for several reasons, particularly in that it eliminates the need for access to a nuclear reactor. This has obvious health and safety benefits, and also reduces the time necessary to obtain results as the wait time for access to reactors is often long, and samples cannot be handled for a period of time following irradiation. It also eliminates the need for track counting of the external detector and dosimeter. The disadvantages of the LA-ICP-MS method include reduced statistical robustness and elegance compared to the matched-pairs design of the EDM (Galbraith, 2010) and the potential error introduced by U heterogeneity within individual grains and counting areas (e.g. Vermeesch, 2017).

Recent work (e.g. Galbraith, 2010; Vermeesch, 2017) has begun to address several of these problems by re-examining the statistical basis of age calculation using the LA-ICP-MS method and proposing methods to minimise source of uncertainty related to this approach. Strategies such as multiple laser spots per counting area and reduction of counting area to the size of the laser spot may help in the future to increase the accuracy of the method, at the cost of increased analytical time and reduced precision, respectively (Vermeesch, 2017).

As is the case with the EDM, a LA-ICP-MS zeta-calibration factor can be gen-

erated using the measured age of a standard to a known 'true' value (Hasebe et al., 2013; Vermeesch, 2017). This eliminates the need to precisely know the true values of various constants that in the past were not well known, such as λ_f. It can also compensate for factors in LA-ICP-MS analysis such as matrix effects between the SRM NIST glasses typically used as primary standards and the natural apatite secondary standards and unknowns.

The age equation adapted for LA-ICP-MS fission track dating can be expressed as:

$$\hat{t} = \frac{1}{\lambda} ln\left(1 + \lambda \hat{\zeta}_{icp} \frac{N_s}{A_s[^{238}\hat{U}]}\right) \tag{1.5}$$

where the zeta-calibration factor $\hat{\zeta}_{icp}$ can be obtained by measuring an age standard and rearranging Eq. 1.5, λ is the total decay constant of ^{238}U ($1.55125 \times 10^{-10} yr^{-1}$), N_s is the number of counted spontaneous tracks, A_s is the area over which the spontaneous tracks were counted, and $[^{238}\hat{U}]$ is the measured concentration of ^{238}U.

The other components of the LA-ICP-MS age equation that are encapsulated by the zeta-calibration factor can be given as:

$$\xi = \frac{M}{\lambda_f N_A d R k} \tag{1.6}$$

where M is the atomic mass of ^{238}U, λ_f is the fission decay constant, N_A is Avogadro's number, d is the density of apatite, R is the etchable range of one fission fragment (half of 'L' in Eq. 1.4), and k is the detection efficiency of the etched internal apatite surface.

This ξ factor can be considered an absolute calibration factor and can effectively replace $\hat{\zeta}_{icp}$ in Eq. 1.5 if there is sufficient confidence in the constants and $[^{238}\hat{U}]$.

Gleadow et al. (2015) adopts values for Eq. 1.6 that produce $\xi = 2.07 \pm 0.07 \times 10^{-3}$, within uncertainty of the zeta-calibration value (2.010×10^{-3}) calculated for the analysed age standards in that study. That value for ξ is also within uncertainty of the equivalent values in Hasebe et al. (2004). This suggests that the determination of constants and measurement of ^{238}U are well developed enough that an absolute calibration for fission track dating might be possible.

In this thesis the zeta-calibration factor is used in order to minimise risk of inaccurate age determination (Vermeesch, 2017). The Durango apatite (McDowell et al., 2005) is used to calculate zeta-calibration values during LA-ICP-MS apatite

fission track analysis in this work.

1.3.3 Apatite (U-Th-Sm)/He analysis

Apatite (U-Th-Sm)/He thermochronology relies on the production and loss of radiogenic ^{4}He that is created as a result of the radioactive decay of ^{238}U, ^{235}U, and ^{232}Th to stable isotopes of Pb, and ^{147}Sm to stable Nd. The time-dependent ingrowth of ^{4}He is described by the following equation:

$$^{4}He = 8^{238}U[e^{-\lambda 238t} - 1] + 7^{235}U[e^{-\lambda 235t} - 1] + 6^{232}Th[e^{-\lambda 232t} - 1] + ^{147}Sm[e^{-\lambda 147t} - 1] \quad (1.7)$$

where ^{238}U, ^{235}U, ^{232}Th, and ^{147}Sm are the measured amounts of these isotopes, and λ_{238}, λ_{235}, λ_{232}, and λ_{147} are the relevant decay constants.

The amount of ^{4}He present in a crystal depends on the balance over time between production (as above) and loss through alpha-ejection and thermally activated volume diffusion (Zeitler et al., 1987; Farley et al., 1996). The partial retention zone (PRZ) of He in apatite (~30–90 °C)(Flowers et al., 2009) is generally lower than the APAZ (60–120 °C), and varies considerably depending on many factors including, but not limited to, grain size, cooling rate, and degree of radiation damage (Dodson, 1973; Farley, 2000; Flowers et al., 2009).

Increasing recognition of the potentially large dispersion in the single grain ages produced by this method (e.g. Ketcham et al., 2018; Green and Duddy, 2018) due to an array of factors has lead to the publication of explanations for age dispersion (e.g. Fitzgerald et al., 2006; Ault and Flowers, 2012; Gautheron et al., 2012; Brown et al., 2013; Fox et al., 2019), models to correct for these factors (e.g. Flowers et al., 2009; Gautheron et al., 2009), and discussions of the shortcomings of these solutions (e.g. Green and Duddy, 2018).

In summary, the (U-Th-Sm)/He system has the potential to powerfully augment studies of low-temperature geological processes when used in combination with fission track thermochronology. However, further works to better understand the system are still necessary, and this method should be treated with appropriate care and caution in terms of application.

The apatite (U-Th-Sm)/He analysis presented in this thesis was performed at the John de Laeter Center at Curtin University.

1.3.4 Apatite U–Pb analysis

Apatite U–Pb dating uses the complete decay of ^{238}U and ^{235}U to stable ^{206}Pb and ^{207}Pb, respectively, to provide information about the geological history of a sample (e.g. Schoene, 2014). Measuring the abundance of these isotopes via secondary ion mass spectrometry (SIMS), thermal ionization mass spectromety (TIMS), or LA-ICP-MS allows calculation of a U–Pb age that is generally interpreted to reflect the timing of the closure of the mineral to Pb mobility .

The mechanism for the closure or reset of the U–Pb system can be challenging to ascertain in apatite, but the thermally activated volume diffusion of Pb (Dodson, 1973; Cherniak et al., 1991) is often assumed in magmatic apatite (Blackburn et al., 2011), unless there is clear evidence for crystallization or recrystallization of the grain below the assumed or calculated closure temperature (Kirkland et al., 2018). The PRZ of Pb in apatite generally lies in the range ~370–550 °C (Schoene and Bowring, 2007; Blackburn et al., 2011; Cochrane et al., 2014; Smye et al., 2018; Paul et al., 2019).

Non-radiogenic (i.e. common or initial) Pb is ubiquitous in natural apatite, presenting a major analytical challenge. The development of new standards (Thomson et al., 2012) and data reduction schemes (Chew et al., 2014a) for LA-ICP-MS analysis of U–Pb isotopes has made this method much more accessible and practical to apply routinely. The analytical method used to collect apatite U–Pb data in this thesis is largely based on the advances of these publications.

1.4 Thesis outline

The chapters of this thesis are described in brief below.

In addition to this introductory chapter, this thesis comprises three chapters that focus on understanding the late Paleozoic and Mesozoic intracontinental tectonic history of the Central Asian Orogenic Belt, and one chapter that explores the use of multi-method apatite analysis as a tool for provenance studies. A final chapter summarises the results from the earlier chapters and discusses further directions for research in these areas.

Chapters 2 and 5 have been published as journal articles, while Chapter 3 is currently under review, and Chapter 4 has been written as a manuscript for publication.

1.4.1 Chapter 2

This chapter has been published as: Gillespie, J., Glorie, S., Jepson, G., Zhang, Z.Y., Xiao, W.J., Danišík, M., Collins, A.S., 2017. Differential exhumation and crustal tilting in the easternmost Tianshan (Xinjiang, China), revealed by low-temperature thermochronology. Tectonics 36, 2142– 2158. doi: 10.1002/2017TC004574

Chapter 2 consists of a study of the tectonic history of the Harlik and Balikun ranges of the easternmost Tianshan (NW China), which separate the Turpan-Hami and Gobi-Junggar Basins. This study found mostly Jurassic–Cretaceous and some Triassic AFT central ages, with episodes of rapid cooling identified during the Triassic and Late Cretaceous. The rocks of the easternmost Tianshan cooled slowly during the Jurassic–Early Cretaceous, suggesting little tectonic activity and low exhumation rates. Late Cenozoic uplift in response to the India-Asia collision tilted planation surfaces that developed in the early Paleogene following Late Cretaceous exhumation.

1.4.2 Chapter 3

This chapter is in review at JGR: Solid Earth.

Chapter 3 consists of a study of the tectonic history of the West Junggar Mountains, on the western margin of the Junggar Basin in Xinjiang Province of north-west China. The West Junggar was largely exhumed to 1–2km depths in the crust during the Permian, soon after its amalgamation into the Central Asian Orogenic Belt. The region then experienced tectonic stability and little uplift over the course of the Mesozoic and Cenozoic, prior to recent uplift that is too minimal for detection via thermochronology. Permian–Triassic AFT central ages are common in the low-relief parts of the study area, while Jurassic ages were found in areas where later exhumation exposed deeper levels of the crust. These locations include deeply incised valleys in the high-relief parts of the study area, and near regional scale strike-slip faults where local exhumation may have occurred in the late Mesozoic.

1.4.3 Chapter 4

This chapter has been written as a manuscript for publication and is yet to be submitted.

Chapter 4 consists of a study of the tectonic history of the Tarbagatai Mountains in eastern Kazakhstan. The study area lies to the west of the West Junggar Mountains, mid way between the Tianshan and Altai mountain belts. This region experienced Permian exhumation during a phase of strike-slip deformation that occurred throughout Central Asian Orogenic Belt. Large strike-slips structures in the study area were created during the Permian, and continued to be reactivated throughout

the Mesozoic. Late Triassic exhumation affected much of the study area, controlled by the position of sample locations relative to the major Kalba-Chingiz Shear Zone. Younger Jurassic–Early Cretaceous AFT central ages are concentrated around the Chingiz-Tarbagatai Fault, which was the locus of Early Cretaceous reactivation.

1.4.4 Chapter 5

This chapter has been published as: Gillespie, J., Glorie, S., Khudoley, A., Collins, A.S., 2018. Detrital apatite U–Pb and trace element analysis as a provenance tool: Insights from the Yenisey Ridge (Siberia). Lithos 314–315, 140-155. doi: 10.1016/j.lithos.2018.05.026

Chapter 5 consists of a case study exploring the use of simultaneous U–Pb and trace element LA-ICP-MS analysis of detrital apatite to recover information about the provenance of apatite grains. This approach allows for both age and source rock information to be obtained for individual grains. Apatite crystallizes far more readily than zircon from mafic magma, and can therefore provide information about the presence of a greater diversity of source rocks. It can also form under a variety of metamorphic conditions. The sensitive trace element chemistry of apatite can also be used to distinguish between different types of source rocks.

1.4.5 Chapter 6

Chapter 6 is a summary and discussion of the results and outcomes of the work carried out in this thesis.

Chapter 2

Differential exhumation and crustal tilting in the easternmost Tianshan (Xinjiang, China), revealed by low-temperature thermochronology

This chapter is published as:
Gillespie, J., Glorie, S., Jepson, G., Zhang, Z.Y., Xiao, W.J., Danišík, M., Collins, A.S., 2017. Differential exhumation and crustal tilting in the easternmost Tianshan (Xinjiang, China), revealed by low-temperature thermochronology. Tectonics 36, 2142– 2158. doi: 10.1002/2017TC004574

Statement of Authorship

Title of Paper	Differential exhumation and crustal tilting in the easternmost Tianshan (Xinjiang, China), revealed by low-temperature thermochronology.
Publication Status	☑ Published ☐ Accepted for Publication ☐ Submitted for Publication ☐ Unpublished and Unsubmitted w ork w ritten in manuscript style
Publication Details	Published as: Gillespie, J., Glorie, S., Jepson, G., Zhang, Z.Y., Xiao, W.J., Danišík, M., Collins, A.S., 2017. Differential exhumation and crustal tilting in the easternmost Tianshan (Xinjiang, China), revealed by low-temperature thermochronology. Tectonics 36, 2142–2158. doi: 10.1002/2017TC004574

Principal Author

Name of Principal Author (Candidate)	Jack Gillespie		
Contribution to the Paper	Sample preparation, analysis, data reduction, data interpretation, figures, writing		
Overall percentage (%)	70		
Certification:	This paper reports on original research I conducted during the period of my Higher Degree by Research candidature and is not subject to any obligations or contractual agreements with a third party that would constrain its inclusion in this thesis. I am the primary author of this paper.		
Signature		Date	

Co-Author Contributions

By signing the Statement of Authorship, each author certifies that:

i. the candidate's stated contribution to the publication is accurate (as detailed above);

ii. permission is granted for the candidate in include the publication in the thesis; and

iii. the sum of all co-author contributions is equal to 100% less the candidate's stated contribution.

Name of Co-Author	Stijn Glorie		
Contribution to the Paper	Primary supervision, data interpretation		
Signature		Date	
Name of Co-Author	Gilby Jepson		
Contribution to the Paper	Data interpretation		
Signature		Date	

Name of Co-Author	Zhiyong Zhang		
Contribution to the Paper	Sample collection		
Signature		Date	
Name of Co-Author	Wenjiao Xiao		
Contribution to the Paper	Geological background		
Signature		Date	
Name of Co-Author	Martin Danišík		
Contribution to the Paper	Analysis, methods		
Signature		Date	
Name of Co-Author	Alan S. Collins		
Contribution to the Paper	Supervision, data interpretation		
Signature		Date	

2.1 Introduction

The Central Asian Orogenic Belt (CAOB) is the largest intracontinental deformation belt in the world (Xiao et al., 2004; Windley et al., 2007) and is an ideal natural laboratory for the study of intracontinental reactivation. The CAOB has experienced several phases of reactivation in response to tectonic events at the Eurasian plate margin since its amalgamation in the Paleozoic, most notably in response to the ongoing India-Eurasia collision (Molnar and Tapponnier, 1975; De Grave et al., 2007; Jolivet et al., 2010; Glorie and De Grave, 2016). The Tianshan is currently the largest of several intracontinental mountain belts within the CAOB that formed in response to the collision of India and Eurasia, stretching more than 2500 km through the Central Asian republics into north-western China (Windley et al., 1990). The easternmost extent of the mountain belt is located within the Xinjiang Uyghur Autonomous Region of China, terminating just short of the Mongolian border (Fig. 2.1).

A multitude of low temperature thermochronological studies utilizing the apatite fission track (AFT) and/or (U-Th)/He (AHe) systems have attempted to constrain the cooling history of the Tianshan, generally concluding that the onset of modern mountain building occurred at ~25–15 Ma in response to the India-Eurasia convergence (Hendrix et al., 1994; Sobel and Dumitru, 1997; Dumitru et al., 2001; Shen et al., 2006; Sobel et al., 2006a; Wang et al., 2009c; Glorie et al., 2011; De Grave et al., 2013; Macaulay et al., 2013; Macaulay et al., 2014; Glorie and De Grave, 2016; Käßner et al., 2016a; Bande et al., 2017). These Oligocene–Miocene ages were mainly obtained for samples taken in the vicinity of the major fault zones and associated steep topography within the Tianshan in Kyrgyzstan, Tajikistan and western Xinjiang. Away from major reactivated faults and in regions of relatively subdued topography, relict Mesozoic ages have been reported as the amount of exhumation is not sufficient to expose deeper crustal levels with Cenozoic AFT ages (Glorie et al., 2011; De Grave et al., 2013).

Previous work within the easternmost Tianshan, however, revealed Oligocene–Miocene AFT ages (Wang et al., 2008), which were interpreted as recording exhumation related to progressive eastwards reactivation in response to the ongoing India-Eurasia collision. The young, regionally distributed AFT ages found by Wang et al. (2008) spurred this study to further investigate the thermotectonic history of the easternmost Tianshan, particularly due to the apparent value of those young ages in providing insight into the nature and timing of late Cenozoic reactivation in the eastern Tianshan.

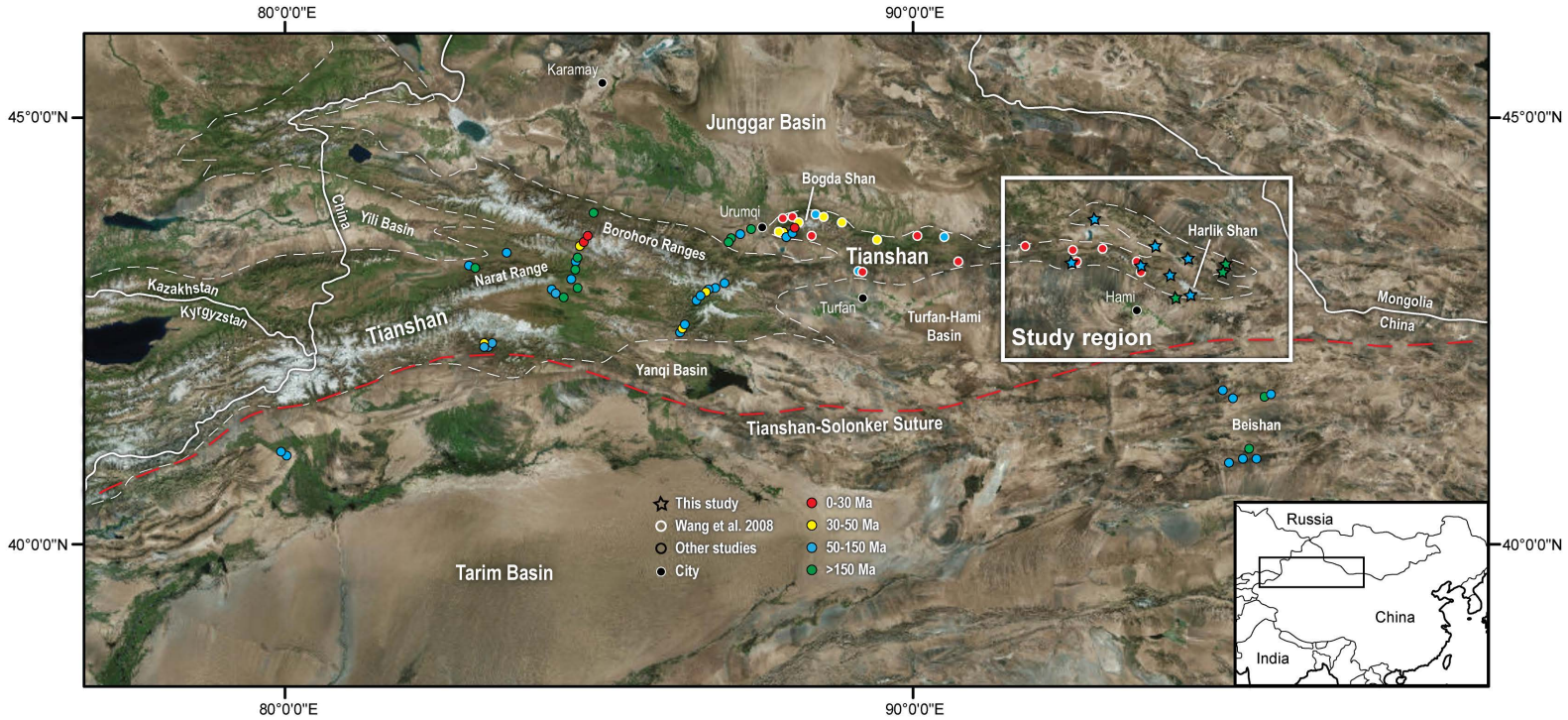

Figure 2.1: Satellite map of the eastern Tianshan and NW China. Published apatite fission track central ages from the Chinese Tianshan and immediate surrounds are indicated by colored dots. White dashed line indicates extent of the Tianshan. Stars are central ages from this study. Data are from (Dumitru et al., 2001; Ma et al., 2006; Shen et al., 2008; Wang et al., 2008; Wang et al., 2009c; Zhang et al., 2009; Jolivet et al., 2010; Lü et al., 2013; Tang et al., 2015; Tian et al., 2016; Gillespie et al., 2017b).

2.2 Background

2.2.1 Structural architecture

The easternmost Tianshan comprises three ranges that strike roughly NW–SE. The Balikun Shan and Harlik Shan (also known as Barkol Tagh and Karlik Tagh) are located to the south of the slightly lower Dahei Shan (Fig. 2.2). The ranges of the easternmost Tianshan are bound by doubly vergent outward directed thrusts, forming asymmetric flower structures that control the exhumation of the study area (Cunningham et al., 2003). Asymmetric drainage patterns and slope profiles in the Balikun and Harlik Ranges suggest that the northern flanks have experienced more extensive uplift and exhumation.

The apparent lack of major faults within the core of the ranges, in conjunction with topographic analysis, led Cunningham et al. (2003) to conclude that both ranges were largely uplifted as single contiguous blocks undergoing southward tilting. Cunningham et al. (2003) furthermore noted the presence of a late Cretaceous – early Cenozoic planation surface preserved in many parts of the study area, prominently on the southern slopes of Harlik Shan and on more spatially limited areas of Balikun Shan. Planation surfaces of this age are also preserved in western Mongolia and in other parts of the Chinese Tianshan (Devyatkin, 1974; Heilbronn et al., 2015). This planation surface provides important constraints on the interpretation of thermochronological data from the study area.

The major bounding faults to the north and south of the ranges experienced ductile deformation from the late Permian to early Triassic and were subsequently reactivated as brittle faults (Cunningham et al., 2003). These faults thrust older rock over Quaternary sediment, offset alluvial fans, and have a historical record of seismicity that attests to their ongoing activity (Cunningham et al., 2003). Brittle reactivation of inherited structural elements is also common elsewhere in the Tianshan (e.g. Glorie et al., 2011; Macaulay et al., 2014).

2.2.2 Basement history

The easternmost Tianshan is tectonically part of the Paleozoic Harlik Arc, which constitutes the northern half of the Harlik-Dananhu arc system. The Harlik Arc was formed during the southwards subduction of the Kelaimeili Ocean, prior to its closure in the Carboniferous (Xiao et al., 2004). The terminal suture resulting from this closure defines the northern margin of the arc system. The Harlik-Dananhu arc system is correlated to the west with the Chinese northern Tianshan (Windley et al., 1990). The Harlik Arc consists of rocks that range from Ordovician to Permian in age. Devonian–Carboniferous arc-related volcanic rocks with a broad range of compositions are abundant, as are Carboniferous flysch sequences (Xiao et al., 2004).

The region also features numerous Devonian–Carboniferous igneous intrusions and late Carboniferous to early Permian post-collisional granites (Fig. 2.2; Ma et al., 2015).

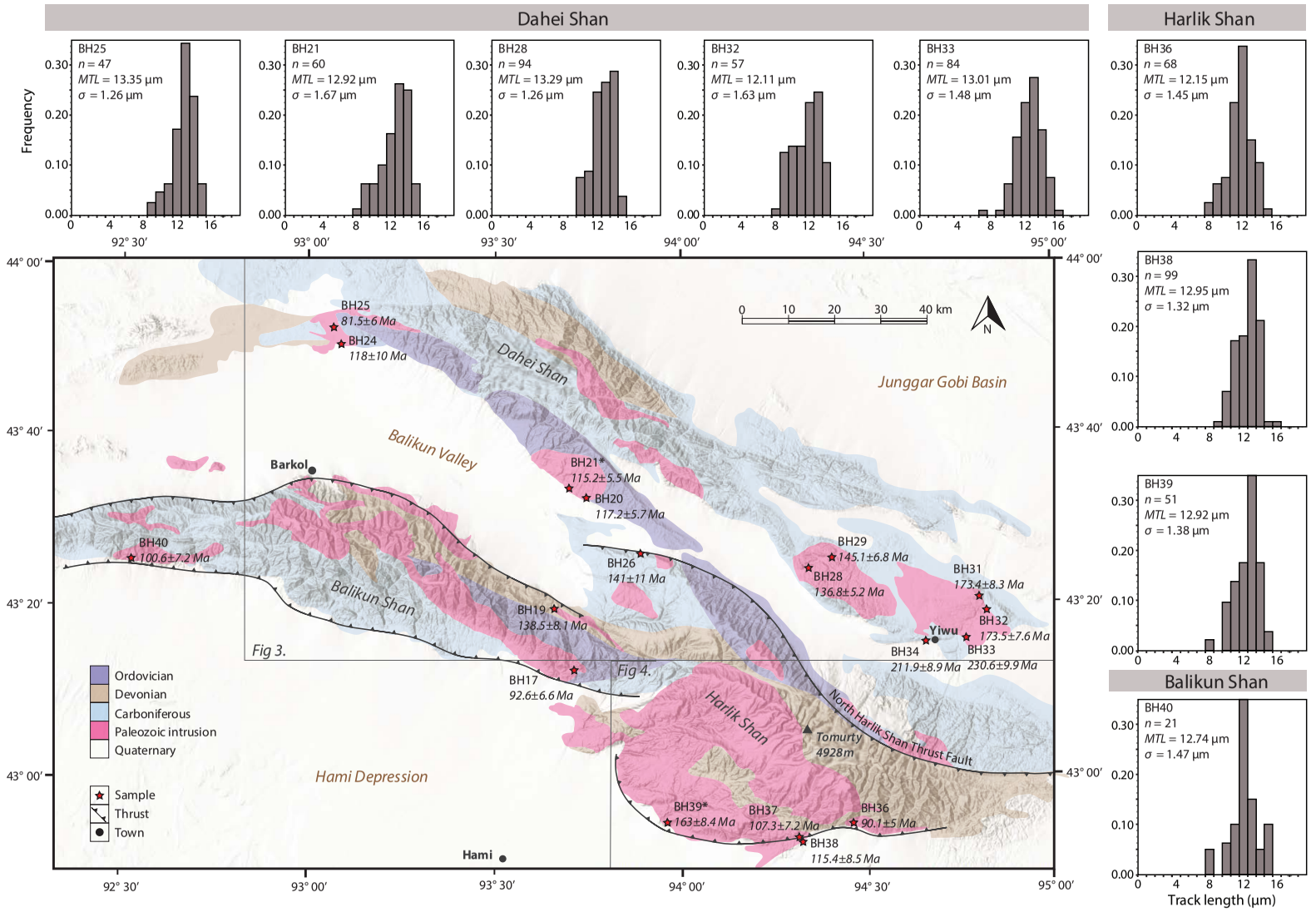

Figure 2.2: Geological map of the easternmost Tianshan featuring sample locations and apatite fission track central ages. Samples marked with asterisk were also analysed with AHe method. Confined track length distribution plots arranged around the map provide information about the rate of cooling through the apatite partial annealing zone. n = number of lengths, MTL = mean track length, σ= standard deviation.

2.3 Samples and Methods

2.3.1 Sample locations

Samples were collected as widely as possible from intrusive igneous bodies throughout the study area. Where practical, structures identified in Cunningham et al. (2003) were targeted for sampling. Eighteen samples were taken from Devonian–Permian granitoids within all three of the ranges of the easternmost Tianshan (Fig. 2.2). Ten samples span the entire length of the southern slopes and eastern extent of Dahei Shan. Five samples were taken from around the margins of Harlik Shan, and three samples were taken from Balikun Shan. Sample descriptions, including geographical locations, can be found in Table 2.1.

Table 2.1: Location and lithological data

Sample	IGSN	Latitude (WGS84)	Longitude (WGS84)	Altitude (m a.s.l.)	Locality	Lithology
Balikun:						
BH17	IEJAG000H	N43°12.042	E93°42.618	1851	S Balikun Shan	Granite
BH19	IEJAG000I	N43°19.467	E93°40.083	2343	N Balikun Shan	Mylonite/ amphibolite
BH40	IEJAG000Y	N43°24.656	E92°30.608	2073	S Balikun Shan	Granite
Dahei:						
BH20	IEJAG000J	N43°31.324	E93°44.982	2088	Dahei Shan	Granite
BH21	IEJAG000K	N43°32.284	E93°42.609	2096	Dahei Shan	Granite
BH24	IEJAG000L	N43°50.119	E93°04.907	1786	NW Dahei Shan	Granodiorite
BH25	IEJAG000M	N43°51.793	E93°03.867	1794	NW Dahei Shan	Granodiorite
BH28	IEJAG000O	N43°23.803	E94°20.759	2353	SE Dahei Shan	Granite
BH29	IEJAG000P	N43°24.843	E94°23.741	1839	SE Dahei Shan	Granite
BH31	IEJAG000Q	N43°19.482	E94°49.066	1423	SE Dahei Shan	Granodiorite
BH32	IEJAG000R	N43°18.261	E94°49.616	1608	SE Dahei Shan	Granite
BH33	IEJAG000S	N43°15.088	E94°46.290	1677	SE Dahei Shan	Granite
BH34	IEJAG000T	N43°14.963	E94°40.458	1741	SE Dahei Shan	Dolerite
Harlik:						
BH26	IEJAG000N	N43°25.329	E93°54.175	2317	N Harlik Shan	Diorite
BH36	IEJAG000U	N42°53.790	E94°28.342	2270	S Harlik Shan	Granodiorite
BH37	IEJAG000V	N42°52.302	E94°20.645	1740	S Harlik Shan	Diorite
BH38	IEJAG000W	N42°51.740	E94°21.019	1656	S Harlik Shan	Granite-gneiss
BH39	IEJAG000X	N42°53.787	E93°56.970	1090	S Harlik Shan	Granite

IGSN = international geosample number

2.3.2 Apatite fission track analysis

The apatite fission track dating method integrates information about the cooling history of apatite crystals in the upper crust in the temperature range of ~60 °C to ~120 °C, known as the apatite partial annealing zone (APAZ) (Gleadow et al., 1986a). The exact temperature range of the APAZ depends on the cooling rate and the chemistry of the individual apatite grains (Ketcham et al., 1999). Typically, chlorine content (Cl wt.%) is considered to be the dominant annealing control in apatite (Green et al., 1986). The c-axis etch pit diameter (Dpar) is often used as a kinetic parameter (Ketcham et al., 1999). Other unquantified parameters may act as controls on the annealing of fission tracks, as Cl wt.% and Dpar often do not adequately explain all the variability in individual AFT grain ages (Barbarand et al., 2003). Some authors have suggested that the concentration of uranium may (by various mechanisms) influence the rate of annealing in apatite (Carpena et al., 1988; Hendriks and Redfield, 2005), although this is not widely accepted.

For this study, spontaneous tracks were etched in 5.0 M HNO3 for 20 ± 1 s at 20.0 ± 0.5 °C (Donelick et al., 1999). Fission track densities and confined track lengths were measured using the FastTracks software after image capture on a Zeiss AXIO Imager M2m Autoscan system at The University of Adelaide (Gleadow et al., 2009). 238U concentrations in apatite grains were measured directly using the NewWave 213 ablation system coupled to the Agilent 7500 mass spectrometer. Ages and uncertainties were calculated as described in Hasebe et al. (2004) using session-specific zeta-calibration calculated against repeated measurements of the Durango apatite age standard (McDowell et al., 2005). Further details can be found in Glorie et al. (2017). Radial plots (Galbraith, 1990) of single grain ages were constructed using the RadialPlotter program (Vermeesch, 2009). Isotopes of uranium and lead were also measured during LA-ICP-MS spot analysis, with data reduction performed in Iolite (Paton et al., 2011) using the DRS "VizualAgeUcomPbine" (Chew et al., 2014a). This data can be found in the appendices for this chapter but is not discussed further here.

2.3.3 Apatite (U-Th-Sm)/He analysis

The apatite (U-Th-Sm)/He (AHe) dating method relies on accumulation and temperature sensitive diffusion of radiogenic He in apatite crystals (Ehlers and Farley, 2003). Partial retention of He occurs between ~40°C and ~85°C (depending on the crystal size and cooling rate), allowing for the refinement of the low temperature thermal history reconstructed from the AFT data (Wolf et al., 1998). Samples for (U-Th-Sm)/He analysis were selected based on the AFT results obtained for the sample, the structural position of the sample within the study area, and the sample quality (Farley, 2002). AHe analysis was performed on two samples (BH21

and BH39) at the John de Laeter Centre at Curtin University following procedure outlined in Evans et al. (2005) and Danišík et al. (2012a) and Danišík et al. (2012c).

Apatite crystals were hand-picked following the recommendation of Farley (2002). For each sample, five apatite crystals of similar size and shape were selected, then photographed, measured for physical dimensions and loaded in platinum tubes. ^{4}He was extracted from single-grain aliquots by heating to ~960°C using a diode laser under ultra-high vacuum, and measured by isotope dilution on a Pfeiffer Prisma QMS-200 mass spectrometer. Following He measurements, the apatites were spiked with ^{235}U and ^{230}Th and dissolved in nitric acid. The solutions were analysed by isotope dilution for U and Th, and by external calibration for Sm on an Agilent 7500 ICP-MS. The total analytical uncertainty (TAU) was calculated as a square root of sum of squares of uncertainty on He and weighted uncertainties on U, Th, and Sm measurements. The raw apatite (U-Th)/He ages were corrected for alpha ejection (Ft correction) after Farley et al. (1996), whereby a homogenous distribution of U, Th, and Sm was assumed for the crystals. Replicate analyses of Durango apatite (n=6) measured over the period of this study as internal standard yielded mean (U-Th-Sm)/He age of 31.8 ± 1.5 Ma, which is good agreement with the reference Durango (U-Th-Sm)/He age of 31.02 ± 1.01 Ma (Farley, 2002; McDowell et al., 2005).

2.3.4 Thermal history modelling

Fission track age, confined length and apatite (U-Th-Sm)/He data were modelled using QTQt v. 5.6.0 to explore the likely low-temperature cooling histories of the study area (Gallagher, 2012). QTQt uses a 'Bayesian transdimensional Markov Chain Monte Carlo (MCMC)' approach to model the thermal history of a sample or set of samples. A thorough explanation of the theory and mathematics is provided in Gallagher (2012). In general, an initial unconstrained run is performed to explore the statistical space, followed by adjustments to the search parameters or the addition of geological constraints where necessary. This approach follows the Bayesian philosophy of the software, which seeks to minimise the complexity of the model by statistical means. Many iterations ($\gg$ 10,000) are run to generate a range of models that create a probability distribution, from which individual models can be selected, including the maximum likelihood and 'expected' (weighted mean) paths. The range of the general prior was set as t=AFT central age ± AFT central age, temperature=70 ± 70°C. Acceptance rates for models were between 0.2 and 0.6 and birth-death ratio was ~1. Spherical geometry and the radiation damage model of Gautheron et al. (2009) were used for modelling AHe data. The annealing model from Ketcham et al. (2007) was used for fission track data with Dpar as kinetic parameter.

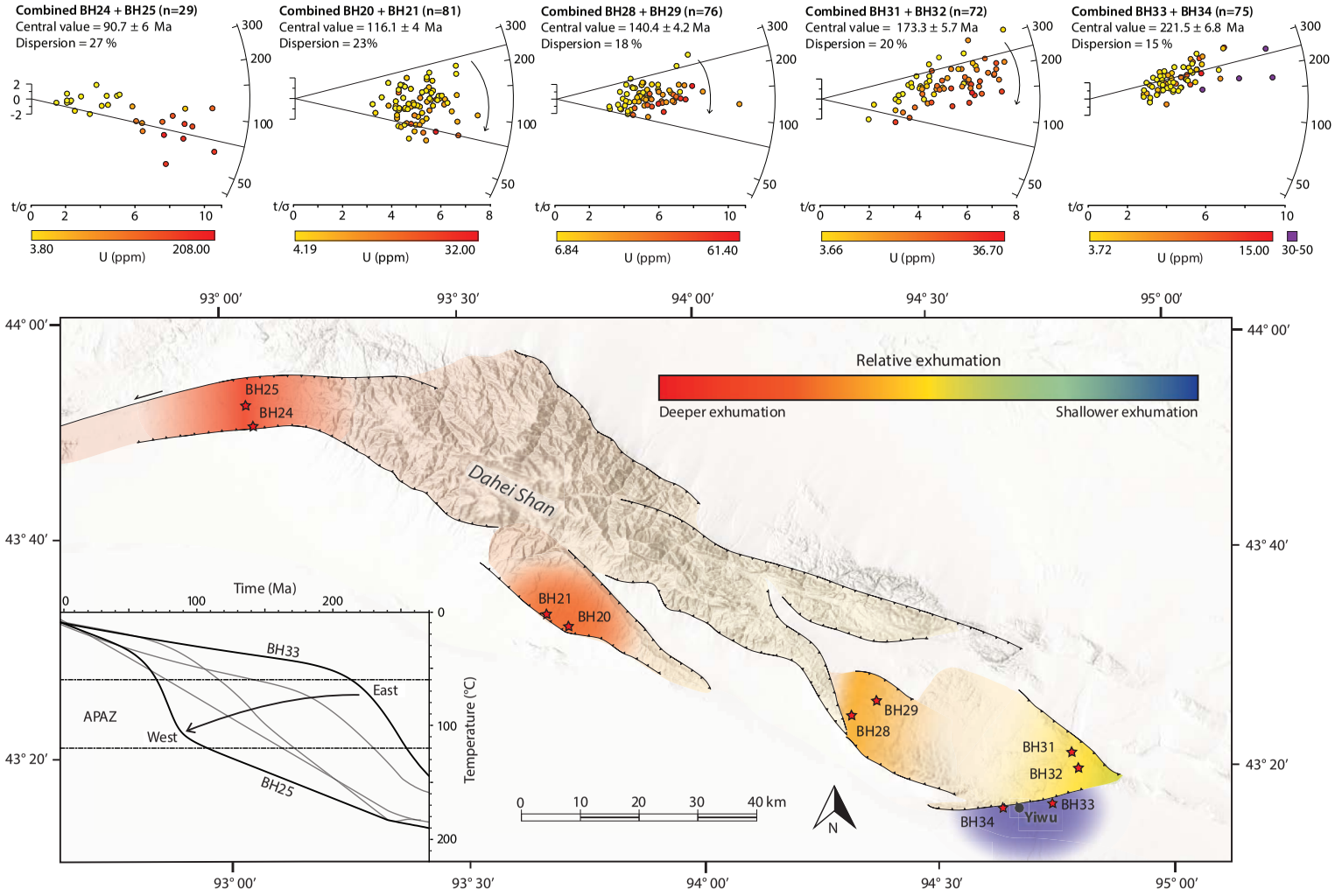

Figure 2.3: Hillshade DEM of Dahei Shan with overlay depicting the amount of relative exhumation. Radial plots of single grain ages at top of figure display 'open jaw' pattern linked to partial reset between thermal events. Modelled timing of enhanced cooling shown by lines on radial plots, with arrows indicating possible reset. Inset simplified thermal history models show weighted mean cooling paths for individual samples. See Figure 5 for full models.

2.4 Results

2.4.1 Apatite fission track

Eighteen samples were analysed using the AFT method, producing exclusively Mesozoic central ages. Central ages were dominantly Cretaceous, with the exception of several samples in the east of the study area that preserved Jurassic or Triassic ages (Table 2.2).

Table 2.2: Apatite fission track data

Sample	n	ρs ($x10^5 cm^{-2}$)	N_s	^{238}U (ppm)	D_{par} (μm)	t (Ma ± 1σ)	MTL (μm)	St.Dev. (μm)	N_{length}
Balikun:									
BH17	37	5.86	409	14.26	1.3	92.6 ± 6.6	-	-	-
BH19	40	3.84	447	6.14	1.8	138.5 ± 8.1	-	-	-
BH40	13	25.17	491	59.15	1.7	100.6 ± 7.2	12.74	1.47	21
Dahei:									
BH20	37	6.40	1075	11.66	1.4	117.2 ± 5.7	-	-	-
BH21	44	4.64	1329	8.56	1.4	115.2 ± 5.5	12.92	1.67	60
BH24	14	9.01	141	15.41	1.5	118.0 ± 10.0	-	-	-
BH25	15	48.13	1223	127.42	2.1	81.5 ± 6.0	13.35	1.26	47
BH28	40	18.25	1595	28.72	2.0	136.8 ± 5.2	13.29	1.26	94
BH29	36	11.22	1203	16.08	1.8	145.1 ± 6.8	-	-	-
BH31	35	18.86	1471	21.92	1.7	173.4 ± 8.3	-	-	-
BH32	37	8.29	1021	11.08	1.1	173.5 ± 7.6	12.11	1.63	57
BH33	36	13.73	1242	14.01	1.8	230.6 ± 9.9	13.01	1.48	84
BH34	39	5.17	795	4.86	2.0	211.9 ± 8.9	-	-	-
Harlik:									
BH26	31	2.66	171	4.03	2.1	141.0 ± 11.0	-	-	-
BH36	36	7.89	1035	22.92	1.8	90.1 ± 5.0	12.15	1.45	68
BH37	24	7.90	377	15.58	1.7	107.3 ± 7.2	-	-	-
BH38	24	12.05	701	23.34	1.4	115.4 ± 8.5	12.95	1.32	99
BH39	34	10.58	1348	13.05	1.4	163.0 ± 8.4	12.92	1.38	51

n is the number of analysed grains. ρs is the density of spontaneous tracks. N_s is the total number of counted spontaneous tracks. ^{238}U (ppm) is the average concentration of ^{238}U. D_{par} is the etch pit length parallel to the c-axis. t is the apatite fission track central age produced by RadialPlotter (Vermeesch, 2009). MTL is the mean length of confined tracks. St.Dev. is the standard deviation of the measured lengths. N_{length} is the number of measured confined tracks. Individual grain data is available in the appendices. $\zeta = 1.96 \pm 0.04 \times 10^{-3}$

Dahei Shan

Traversing from east to west along Dahei Shan, central ages become progressively younger, particularly as major faults are crossed, and the obtained AFT results are therefore discussed accordingly (Fig. 2.3). The ten samples that were analysed for the Dahei Shan can be grouped into five pairs that have similar central ages. The easternmost block of the Dahei Shan is an eastwards closing wedge controlled by a pair of outward directed thrust faults (Cunningham et al., 2003). Four samples were taken in the vicinity of those thrust faults. The two samples closest to the town of Yiwu (Fig. 2.3) lie to the south of an EW trending fault that demarcates the ridge front to the north of the town. This area is the south-easternmost extent of the Dahei Shan range. The central ages of these samples (BH33, BH34) are the oldest for the entire area at 230.6±9.9 Ma and 211.9±8.9 Ma respectively (Table 2.2). Sample BH33 has a mean track length (MTL) of 13.01 μm with a standard deviation of 1.48 μm (Fig. 2.2; Table 2.2).

Just north of BH34 and BH33, over the thrust fault, identical central ages of 173.4±8.3 Ma and 173.5±7.6 Ma were obtained for samples BH31 and BH32, respectively (Fig. 2.3). Sample BH32 has a MTL of 12.11 μm and a standard deviation of 1.63 μm. Further to the west, within the same major structural block of the Dahei Shan, BH28 and BH29 produce ages of 136.8±5.2 Ma and 145.1±6.8 Ma, respectively. A significant elevation difference (BH28 ~500 m higher) potentially contributes to the age disparity (Table 2.1). However, much like the easternmost samples, overlapping uncertainties demonstrate the strong similarity between these two samples. BH28 has a MTL of 13.29 μm and a standard deviation of 1.26 μm. On the southern margin of Dahei Shan, near the centre of the range, BH20 and BH21 yield identical central ages of 117.2±5.7 Ma and 115.2±5.5 Ma. BH21 has a MTL of 12.92 μm and a standard deviation of 1.67 μm. The westernmost and youngest sample from Dahei Shan is BH25, with a central age of 81.5±6 Ma. BH25 has a MTL of 13.35±1.26 μm, the longest of any sample in the study region. It is accompanied by BH24, with an older central age of 118±10 Ma (Table 2.2).

Harlik Shan

Five samples were taken from Harlik Shan, one on the northern margin, and four on the southern margin. The northern flank of Harlik Shan (BH26) recorded a central age of 141±11 Ma. The four samples from the southern margin of the mountain are arrayed west-east, becoming younger to the east. The westernmost sample (BH39) has the oldest central age of 163±8.4 Ma and was taken at the lowest elevation of these samples, near to the planation surface (Fig. 2.4). It has a MTL of 12.92 μm and a standard deviation of 1.38 μm. BH37 and BH38 have similar central ages of 107.3±7.2 Ma and 115.4±8.5 Ma respectively, with sample locations around 1 km

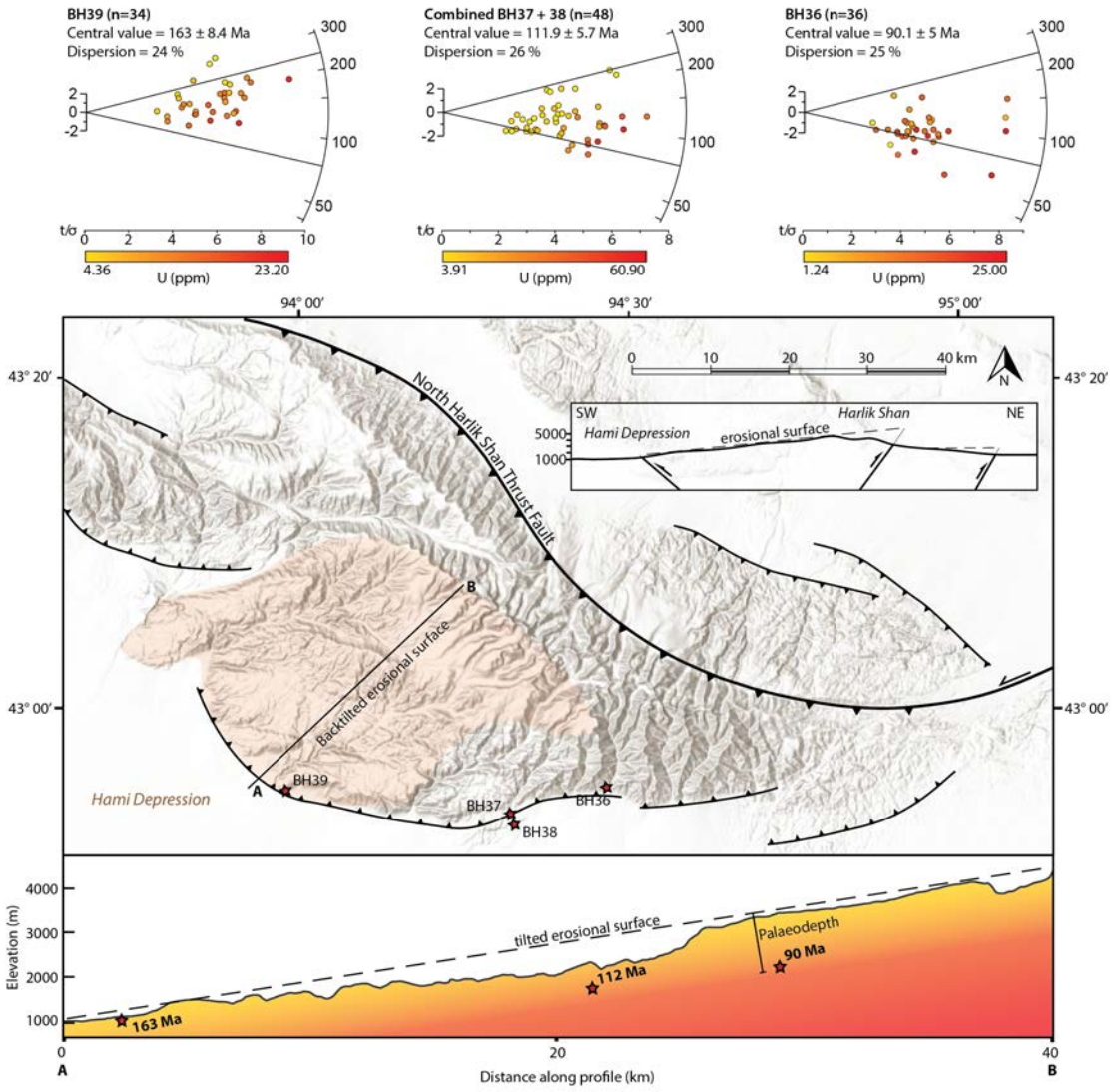

Figure 2.4: Detail of Harlik Shan illustrating the tilted peneplain identified by Cunningham et al. (2003) that composes the southern flank of the mountain. Elevation profile shows planation surface with schematic preserved thermal structure based on AFT ages, represented by the colour gradient. AFT sample locations are projected onto profile based on elevation and location within the tilted peneplain. Modelled timing of enhanced cooling shown by lines on radial plots.

apart and no intervening major structures. BH38 has a MTL of 12.95 μm and a standard deviation of 1.32 μm. Taken from within a deeply incised valley to the east, BH36 has a central age of 90.1±5 Ma and a MTL of 12.15±1.45 μm (Table 2.2).

Balikun Shan

Three samples were taken from Balikun Shan (Fig. 2.2). The samples taken from the southern flank of the range produced central ages of 100.6±7.2 Ma in the west (BH40) and 92.6±6.6 Ma in the east (BH17). These two samples lie in a similar structural position near to the southern bounding fault of the range. On the northern flank, BH19 recorded an older central age of 138.5±8.1 Ma, similar to the central age of BH26 from the northern flank of Harlik Shan (see appendices for further figures). BH19 was also taken from a higher altitude (2343m) than BH17 (1851m) or BH40 (2073m, Table 2.1).

2.4.2 Apatite (U-Th-Sm)/He

Apatite (U-Th-Sm)/He analysis was carried out on five grains from both sample BH21 (Dahei Shan) and BH39 (Harlik Shan). In both cases, highly dispersed individual grain ages were produced, ranging from 46.0±3.1 Ma to 559.8±42.4 Ma (Table 2.3). After discounting the three grains with AHe ages older than zircon U–Pb ages (288 ± 3 Ma, Daliugou Pluton, BH21; 298 ± 2 Ma, Badashi Pluton, BH39) for the sampled intrusions (Wang et al., 2009b; Yuan et al., 2010), the remaining grains (mostly Jurassic–Cretaceous in age) were incorporated individually into the relevant QTQt model (Gallagher, 2012) using the radiation damage model of Gautheron et al. (2009).

2.4.3 Thermal history modelling

Thermal history modelling was conducted for all eight samples that yielded sufficient (>50) confined tracks. Due to poor sample quality (e.g. small grain size, low grain yield, low track density), many samples contained insufficient confined tracks to build an adequate population for modelling.

Dahei Shan

Five samples from Dahei Shan were suitable for modelling. Models were run without constraints, other than a start point based on zircon U–Pb ages of 300–285 Ma for the sampled intrusions (Ma et al., 2015). The zircon U–Pb ages were used to impose initial high temperature boxes from 350–250 Ma at 200±20°C, chosen to

Table 2.3: Apatite (U-Th-Sm)/He data

Sample	Th (ng)	± (%)	U (ng)	± (%)	Sm (ng)	± (%)	He (ncc)	± (%)	TAU (%)	Th/U	Unc. Age (Ma)	±1σ(Ma)	Ft	Cor. Age (Ma)	±1σ(Ma)
21															
a	0.004	5.4	0.007	5.5	0.018	0.4	0.331	3.1	5.7	0.56	349.3	19.9	0.62	559.8	42.4
c	0.011	4.0	0.017	4.0	0.028	0.3	0.468	2.8	4.4	0.62	190.7	8.5	0.66	287.2	19.2
b	0.006	5.4	0.024	5.6	0.028	0.7	0.189	3.6	6.3	0.25	60.5	3.8	0.59	102.7	8.3
d	0.092	3.8	0.063	4.0	0.130	0.2	1.471	2.9	4.2	1.45	140.1	5.9	0.77	182.4	11.9
e	0.030	5.3	0.021	5.5	0.041	0.3	0.291	3.4	5.4	1.43	83.7	4.5	0.59	140.9	10.4
39															
a	0.219	5.3	0.135	5.5	0.023	0.4	0.671	1.9	4.6	1.62	29.6	1.4	0.64	46.0	3.1
b	0.039	3.8	0.009	4.0	0.005	0.4	0.578	2.7	3.8	4.05	251.0	9.6	0.62	404.3	25.5
c	0.211	5.3	0.043	5.5	0.021	0.3	1.206	2.4	4.5	4.85	105.9	4.8	0.64	165.2	11.1
d	0.090	3.8	0.023	4.0	0.012	0.5	0.428	1.9	3.3	3.94	79.6	2.7	0.60	132.3	8.0
e	0.063	5.4	0.028	5.5	0.007	0.6	0.264	2.0	4.5	2.27	50.9	2.3	0.58	88.1	5.9

Th is ^{232}Th, U is ^{238}U, and Sm is ^{147}Sm in ng (nanogram). He is ^{4}He in ncc (nanocubic centimeter). TAU is the total analytical uncertainty. Unc. Age is the uncorrected He age. Ft is the alpha recoil correction factor after Farley et al. (1996). Cor. Age is the corrected He age.

allow maximum freedom for the model and to allow the data to be fully explored by the software. The thermal history model for BH33 suggests a relatively rapid transit through the APAZ during the Triassic, entering at ~250 Ma and cooling below 60°C at ~220 Ma (Fig. 2.5).

Samples BH32, BH28 and BH21 produced models that predict slow cooling through the APAZ during the late Triassic–late Cretaceous. The timing of modelled cooling decreases from east to west, from BH32 at ~230–140 Ma, to BH28 at ~175–115 Ma, and BH21 at ~165–80 Ma. The model obtained for sample BH25 shows a phase of enhanced cooling through the APAZ at ~80 Ma.

Harlik Shan

Three samples from Harlik Shan were suitable for modelling (Fig. 2.5). The thermal history model for Harlik Shan was constrained by a number of geological observations that by necessity introduced significant complexity to the model. Samples BH36 and BH39 from Harlik Shan belong to a monolithic block that was uplifted and tilted without the presence of intervening faults (Fig. 2.4; Cunningham et al., 2003). The low temperature constraint is provided by sample BH39 that was taken in proximity to the preserved planation surface that constitutes the southern flank of Harlik Shan. The proximity of BH39 to the planation surface implies that this sample must have cooled to near surface temperatures by the time the planation

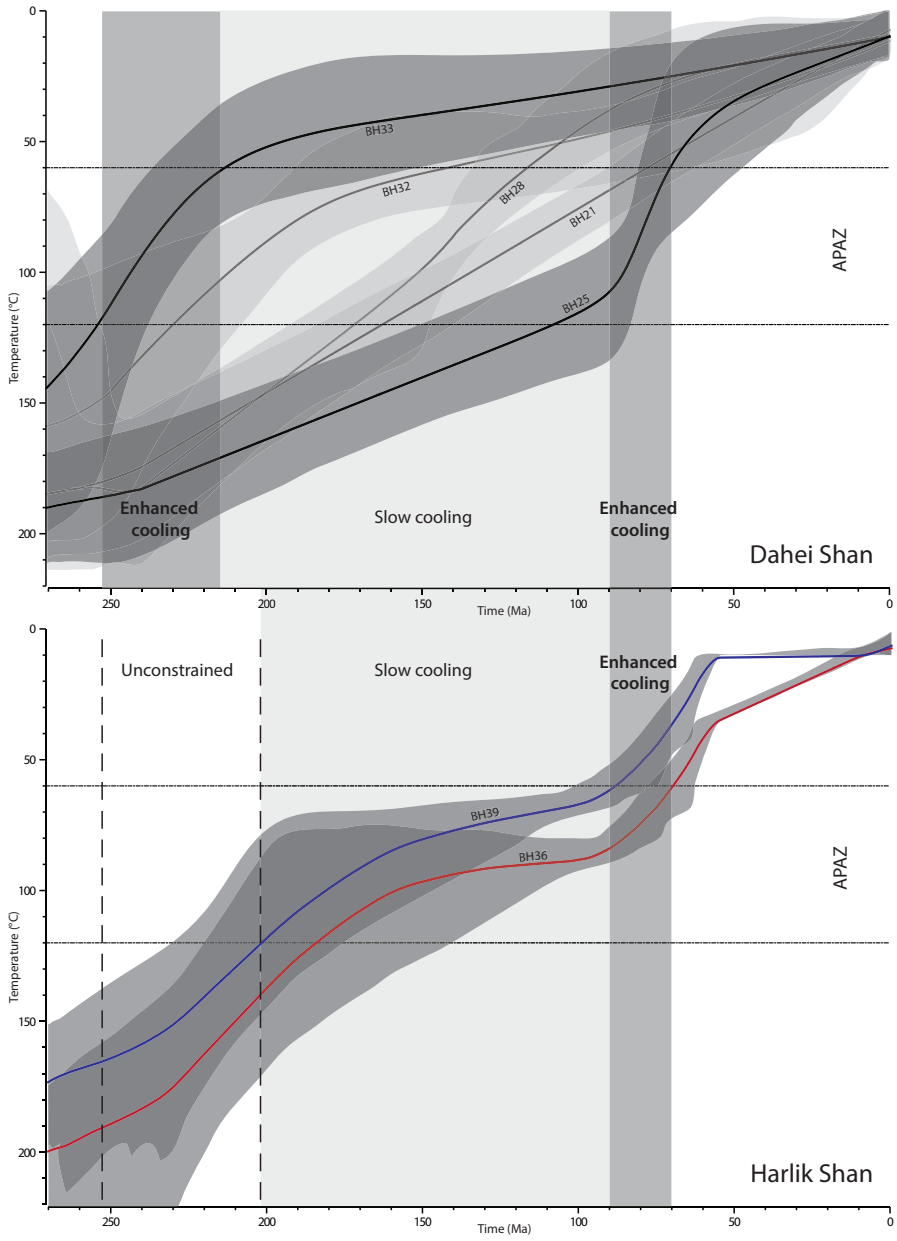

Figure 2.5: Thermal history models generated in QTQt (Gallagher, 2012). All models are based on AFT data, with the additional use of AHe data for BH21 and BH39. For all modelled samples the 'expected' models with 95% credible intervals are displayed. The expected model is effectively the weighted mean of all the sampled thermal histories.

surface was formed during the late Cretaceous–early Paleogene.

As this surface was uplifted and tilted as a single block (Cunningham et al., 2003), we can estimate the pre-tilting vertical depth of samples taken from within the incised valleys of the uplifted section of this block with respect to the planation surface. The sample locations from the southern margin of Harlik Shan were projected onto a cross section through the peneplain defined in Cunningham et al. (2003) (Fig. 2.4), and the relative position of the samples to the surface was calculated by creating a grid of elevation profiles across the southern flank of the mountain to identify the elevation and slope of the peneplain. The resulting age-paleodepth pattern along the cross-section reveals the low-temperature thermal structure of the crust prior to tilting. Knowing the extent of this vertical separation allows us to combine samples to form a pre-tilting 'vertical profile' and model their thermal histories together (Fig. 2.4). High temperature constraints on possible thermal histories (350–250 Ma at 200±20°C) were based on zircon U–Pb crystallization ages of ~300–285 Ma age for the sampled intrusions on Harlik Shan (Ma et al., 2015).

The paleodepth profile thermal history model of Harlik Shan reveals two main pulses of cooling. Initial slow cooling into the APAZ was modelled to take place at ~200–160 Ma, which brought BH36 and BH39 (red and blue lines in Fig. 2.5, respectively) to middle and upper APAZ temperatures, according to their relative paleodepths. A subsequent period of relative quiescence kept the samples at APAZ temperatures until ~100 Ma, followed by a second phase of cooling at ~80 Ma. This late Cretaceous cooling event brought the shallowest sample (BH39) to the surface and is similar in timing and rate to that modelled for BH25. The model predicts a late Cenozoic pulse of cooling that tilted the deeper samples to their present outcrop position, however, the actual timing of tilting cannot be obtained from our data as it is outside the validity zone of the model (below ~60°C). The model is similarly not meaningful prior to ~200 Ma as the samples are below the APAZ until this time.

Modelling samples BH36 and BH39 as a pseudo-vertical profile provides a much more consistent and reasonable thermal history distribution when compared to modelling them separately. Sample BH38 was modelled separately to BH36 and BH39 as there is an intervening fault. The model produced for BH38 was constrained only by a Carboniferous–Permian high temperature box based on published zircon U–Pb ages (Ma et al., 2015) and predicted monotonic cooling from emplacement to surface temperatures.

2.5 Discussion

2.5.1 Thermotectonic history of the easternmost Tianshan

Thermal history

Understanding the regional structure of the easternmost Tianshan is the key to interpreting its thermal history. According to structural analysis in Cunningham et al. (2003), the modern fault-bound ranges of the easternmost Tianshan were uplifted as large contiguous blocks. By applying this concept and attempting to define fault blocks according to previous work and major mapped faults, patterns in the AFT data can be deciphered and reveal a picture of the thermal history of the region.

In the northern range of the easternmost Tianshan (Dahei Shan), AFT age patterns appear to show differential fault-block exhumation, resulting in different exposure levels of the crust (and their preserved thermal structure) with respect to the relative degree of exhumation. Although the whole area probably experienced regional, widespread exhumation during the Triassic as a result of the Paleoasian Ocean closure (Xiao et al., 2009), only the area outside the fault bound range (represented by BH33/34) preserves a Triassic signal. The preservation of this age implies that the area outside the major bounding faults was not reactivated during subsequent periods of exhumation (Fig. 2.3). North across a bounding thrust fault from BH33/34 (Fig. 2.3), the easternmost block of the Dahei Shan records quite different central ages to those outside the ranges.

In contrast to rapid cooling during the Triassic, this block records an AFT signal that suggests a more complex Mesozoic cooling history. Samples within the ranges record progressively younger ages and longer MTLs further west along the range, with this trend culminating in sample BH25 that yields the youngest AFT age and longest MTL of the entire range (Fig. 2.2, 2.3). All of the samples from within the ranges with the exception of those in the far west (BH24/25) record relatively slow cooling during the Jurassic and Cretaceous, with extended periods of residence in the APAZ. The thermal history model based on AFT data from sample BH25, meanwhile, predicts enhanced rates of cooling at ~80 Ma.

All of the samples from Dahei Shan appear to have experienced some degree of partial reset except for BH25, which was cooled relatively rapidly through the APAZ according to thermal history modelling. Radial plots of data from the Dahei Shan samples show a transition from early Jurassic to late Cretaceous ages from east to west, with most samples exhibiting mixed ages reflected in moderate to high levels of dispersion (Fig. 2.3). The mixed samples show to some extent an 'open jaw' pattern (O'Sullivan and Parrish, 1995) in the radial plots (Fig. 2.3), the spread of individual grain ages visually demonstrating the progressive amount of reset each sample has experienced depending on their depth/period of residence in the APAZ (O'Sullivan

and Parrish, 1995). In many samples there is also an apparent correlation (of varying strength) between the age of a grain and its uranium concentration (Fig. 2.3) that may suggest the uranium concentration has some influence on the annealing characteristics of the apatites (e.g. Carpena et al., 1988; Hendriks and Redfield, 2005).

Although some work has attempted to address this issue through annealing experiments (e.g. Carpena and Lacout, 2010), further experiments are clearly needed to properly explore the association. Conversely, there does not appear to be a correlation between Dpar and age in any of the samples (see appendices). The mostly Jurassic–Cretaceous single grain AHe ages from BH21 and BH39 are also highly dispersed. Although the causes of single grain AHe age dispersion are highly complex and remain a topic of much debate (e.g. Farley, 2002; Fitzgerald et al., 2006; Brown et al., 2013), it has been suggested that slow cooling rates may result in highly variable single grain ages (Fitzgerald et al., 2006), as seen in our results. This concept may help to explain the dispersion of our AHe ages and would be consistent with our thermal models, which suggest both BH21 and BH39 experienced extended slow cooling through much of the Jurassic and Cretaceous.

Differences in the central ages preserved at the surface today are probably due to differential exhumation of the rock that preserves this Mesozoic signal. Younger ages in the west of Dahei Shan would then imply deeper exhumation than that experienced in the east. This is consistent with the observation that on the scale of the Tianshan, there is a greater accommodation of strain in the west than in the east, related to the collision of the north-western extent of the Indian plate with Eurasia, and the associated clockwise rotation of the Tarim block (e.g. Avouac et al., 1993).

The backtilted planation surface that constitutes the southern flank of Harlik Shan provides important insight into the thermal structure of the crust prior to the modern uplift of the ranges. The age-paleodepth pattern across the block reveals the low-temperature thermal structure of the crust prior to tilting. Samples taken from progressively more deeply incised valleys record younger AFT ages, reflecting their deeper position below the ancient surface. The model for Harlik Shan (Fig. 2.5) shows that the samples were brought up into the APAZ at some point in the Triassic–Jurassic, remaining there until the top sample was exhumed to near surface by the late Cretaceous, in time for the development of the late Cretaceous–early Paleogene planation surface (Cunningham et al., 2003). This ~80 Ma cooling phase is similar in timing and rate to the major phase of cooling modelled for BH25.

Tectonic context

The results presented in this paper record the Meso-Cenozoic thermal history of the study region. As the tectonic amalgamation of the Harlik-Dananhu Arc was

complete by the late Carboniferous (Xiao et al., 2004), the Meso-Cenozoic events that induced cooling of the easternmost Tianshan must have occurred in an intra-continental setting. Triassic cooling is the oldest signal recorded in the study area, preserved solely on the fringes of the easternmost Tianshan outside the main fault-bound ranges. Thermal modelling of sample BH33 suggests cooling at ~250–230 Ma (Fig. 2.5), coeval with $^{40}Ar/^{39}Ar$ ages attributed to ductile thrusting along the major mylonitic bounding faults of Balikun and Harlik Shan (Cunningham et al., 2003).

Indeed, widespread activity along major shear zones throughout Central Asia occurred during the Permian to early Triassic, related to large scale block rotation and reorganisation (e.g. Laurent-Charvet et al., 2003; Allen et al., 2006). This may play a role in the cooling we see recorded in our thermochronological data. Separation of the Junggar and Turfan-Hami basins at this time (Hendrix, 2000) lends further credence to the idea that early Triassic cooling corresponds to the generation of topography in the Paleo-Tianshan. It is also possible, due to the proximity of the Tianshan-Solonker (Paleoasian) suture to the south of the study area (Fig. 2.1; Xiao et al., 2013), that the closure of the Paleoasian Ocean was the driver of the thermotectonic activity we see recorded at this time. The timing of the closure of the Paleoasian Ocean remains a controversial question. Some authors argue that the final closure of the Paleoasian Ocean and the collision of the Tarim Craton with the southern Siberian active margin occurred during the late Permian–early Triassic (Xiao et al., 2009; Lehmann et al., 2010). Alternate models suggest that final amalgamation occurred significantly earlier, during the Carboniferous or early Permian (Biske and Seltmann, 2010; Charvet et al., 2011).

The cause of late Cretaceous reactivation throughout Central Asia is not clear. In the western Tianshan, Cretaceous ages are sometimes attributed to the accretion of the Kohistan-Dras arc in modern Afghanistan (Hendrix et al., 1992). While this may be a plausible explanation for reactivation in the western Tianshan (e.g. De Grave et al., 2007), this event is unlikely to have caused dramatic tectonic effects as far afield as Mongolia or Siberia. In these locations, the influence of the Mongol-Okhotsk orogeny is generally judged to be more significant (Jolivet et al., 2009), although the final closure of the Mongol-Okhotsk Ocean probably took place during the early Cretaceous, rather than late Cretaceous (Metelkin et al., 2010). Some authors have argued that ongoing tectonic forces associated with the Mongol-Okhotsk orogeny, such as orogenic collapse and extension, continued to have an influence on Central Asia for an extended period following the actual collision (Graham et al., 2001; Fan et al., 2003; Jolivet et al., 2009; Jolivet et al., 2013).

2.5.2 Comparison with neighbouring regions

The results presented in this study are generally in agreement with earlier work in the central Chinese Tianshan. Dumitru et al. (2001) and Jolivet et al. (2010) found that some mountain ranges experienced late Triassic–early Jurassic cooling followed by a period of apparent quiescence in the middle Jurassic–Cretaceous. Initial formation of an extensive planation surface over most of Central Asia began during this period of relative stability (Jolivet et al., 2013). This planation surface is still preserved in various places throughout Central Asia (Allen et al., 2001; Jolivet et al., 2007; Vassallo et al., 2007; Jolivet et al., 2013).

The late Cretaceous reactivation of the easternmost Tianshan bears many similarities to localised late Cretaceous – early Paleogene deformation recorded in the South Borohoro and Narat Ranges of the central Chinese Tianshan (Jolivet et al., 2010). These areas possess similar basement architecture to the easternmost Tianshan, and also experienced uplift associated with the reactivation of older shear zones. The steep, deeply incised northern slopes and tilted southern flank of the South Borohoro Range especially resembles the topography and geomorphology of the easternmost Tianshan (Jolivet et al., 2010). These regions all seem to have experienced similar, localised deformation focussed around reactivated inherited structures in what was probably a transpressive tectonic setting (Jolivet et al., 2013). Sedimentological records from the northern Tarim Basin and the southern Junggar Basin show increased rates of basin subsidence during the late Cretaceous and early Paleogene, accompanied by the deposition of coarse clastic sediments (Hendrix et al., 1992). Following the localised deformation and uplift described above, the area once again experienced erosion and planation, forming a new regional erosional surface in western Mongolia and the Chinese Tianshan (Devyatkin, 1974; Cunningham et al., 2003; Heilbronn et al., 2015).

Late Cenozoic cooling has also been reported from areas within the Chinese Tianshan, generally limited to areas near major faults. Several studies have reported Oligocene–Miocene ages from Bogda Shan (Shen et al., 2006; Shen et al., 2008), to the immediate east of Urumqi, and a wide range of Cenozoic ages from major faults in the ranges of the Tianshan to the west of the city (Hendrix et al., 1994; Dumitru et al., 2001; Wang et al., 2009c; Jolivet et al., 2010; Lü et al., 2013). However, Cenozoic AFT ages were not found in this study, suggesting that in contrast to the ranges further to the west, Cenozoic exhumation in the easternmost Tianshan was not extensive enough to expose rocks that record Cenozoic cooling.

The mountain ranges of the Kyrgyz Tianshan experienced a variety of Mesozoic thermal histories that span most of the Jurassic and Cretaceous. Periods of enhanced cooling have been identified at 230–190 Ma, 150–130 Ma, 110–90 Ma and 75–65 Ma (Sobel et al., 2006b; Glorie et al., 2011; De Grave et al., 2013; Macaulay et al., 2014; Glorie and De Grave, 2016). Since these ranges are located far to the west of the

study region, it is difficult to link the varying histories of the Kyrgyz Tianshan to the easternmost Tianshan in a more precise manner. During the Cenozoic, many of the inherited Paleozoic structures of the Kyrgyz Tianshan were reactivated in response to the India-Eurasia collision, and therefore record Oligocene–Pliocene AFT ages (Sobel et al., 2006b; Glorie et al., 2011; De Grave et al., 2013; Macaulay et al., 2014; Bande et al., 2017).

Work in the Siberian Altai, to the north of the Tianshan, found a phase of rapid cooling during the late Triassic–early Jurassic that was attributed to the initiation of the Mongol-Okhotsk orogeny (Metelkin et al., 2007; Glorie et al., 2012a). This cooling signal is coeval with cooling in the south of the CAOB, where it is more commonly associated with the Qiangtang collision based on geographical proximity (Schwab et al., 2004; Zhai et al., 2011; Glorie and De Grave, 2016). The Siberian Altai furthermore records slower cooling from the late Jurassic to early Cretaceous as a result of slow regional denudation at that time, which was followed by a phase of more rapid cooling during the late Cretaceous and the early Paleogene. The latter rapid cooling phase was interpreted to be the result of the collapse of the Mongol-Okhotsk orogeny and the subsequent transition into the Lake Baikal rifting regime with block reorganisation in the eastern CAOB (Jolivet et al., 2009). The Chinese Altai similarly records a late Cretaceous cooling phase, albeit with an earlier cessation of cooling that was interpreted to have ended prior to the end of the Mesozoic (Yuan et al., 2006).

In contrast to the thermal histories proposed for the Siberian and Chinese Altai, work in the Gobi Altai has uncovered little evidence for a late Cretaceous phase of cooling (Jolivet et al., 2007; Vassallo et al., 2007). The Gobi Altai appears to have experienced early–middle Jurassic cooling followed by an extended period of thermal quiescence prior to very recent reactivation in response to the India-Eurasia collision.

To the immediate southeast of the easternmost Tianshan, the Beishan plateau records evidence for late Triassic–early Jurassic cooling and a later Cretaceous phase of cooling, suggesting that both regions experienced a comparable thermotectonic history during the Mesozoic (Tian et al., 2016; Gillespie et al., 2017b). As in the easternmost Tianshan, no thermochronological evidence was found within the thermal history record of the Beishan to suggest any Cenozoic activity. The Beishan differs from the mountains to the north in that it has very subdued internal topography and presents no structural or topographic evidence for significant late Cenozoic reactivation (Cunningham et al., 2003).

2.5.3 Comparison with existing data in the easternmost Tianshan

Previous AFT work in the easternmost Tianshan found much younger ages than the results of this study. All the central ages for the easternmost Tianshan presented in Wang et al. (2008) were less than 33 Ma in age, with Miocene ages dominating the region. This result is highly unusual for the Tianshan, where Cretaceous and Jurassic ages are most prevalent regionally (Fig. 2.1), while younger ages are typically concentrated in reactivated sutures and other major inherited structures (e.g. Glorie et al., 2011). Miocene ages all throughout the easternmost Tianshan would imply that the area has undergone regional exhumation to an equivalent degree as in the Kyrgyz Tianshan or the Pamir. The presence of low-altitude planation surfaces already raises questions about the conclusions of Wang et al. (2008) as they constrain the amount of uplift that could have occurred during the Cenozoic (Cunningham et al., 2003). Wang et al. (2008) describes the sample preparation and analytical procedure in sufficient detail that a possible explanation for the discrepancy can be found.

Apatite mounts were submerged in a $HN0_3$ concentration of 7% (presumably vol %) at 20°C for 35 s during the spontaneous fission track etching procedure. While these parameters are within the variation in preparation technique used by different laboratories around the world, experiments presented in Seward et al. (2000) found that these etching conditions resulted in the majority of tracks being under-etched. Seward et al. (2000) recommended that a further 20 s of etching at these conditions (i.e. 55 s total) was required for complete etching to occur and for the results to be comparable with the conditions they found to be optimal — that is, at 21°C for 20 s in 5M HNO3. The number of spontaneous tracks counted for each sample is also very low (mostly <200, 50% of samples $\ll$ 100).

Consequently, the unusual distribution of young central ages may be a result of this experimental factor. The lack of GPS coordinates or detailed small-scale maps makes the exact locations of the samples from this study difficult to precisely ascertain, but it appears as though several do overlap closely with samples from this study. Several were seemingly taken along the mountain pass where both BH17 and BH19 were obtained (Fig. 2.1). The Cretaceous central ages of these two samples contrast strongly with the Oligocene–Miocene central ages presented in Wang et al. (2008).

2.6 Conclusions

The easternmost Tianshan experienced three phases of cooling throughout the Mesozoic and Cenozoic, only two of which this study has directly revealed via ther-

mochronological evidence. An initial phase of cooling during the early to middle Triassic was driven by regional exhumation in response to the final closure of the Paleoasian Ocean, with the collision of the Tarim Craton to the immediate south of the modern Tianshan. An extended period of slow cooling lasting until the late Cretaceous was followed by a phase of enhanced cooling at ~80 Ma. Cooling at this time was limited to the area within the bounding faults of the modern mountain range. The thermal structure established during late Cretaceous cooling was preserved in the stable upper few kilometres of the crust until late Cenozoic reactivation, when the ranges were variably uplifted and exhumed, creating the distribution of ages that we see today. Late Cenozoic reactivation of the easternmost Tianshan is evident from structural relationships and topographic analysis, but cannot be constrained by thermochronological data due to the low level of exhumation. The combination of AFT, AHe and structural/topographic data synthesised here is incompatible with the conclusions of Wang et al. (2008).

Chapter 3

Late Paleozoic exhumation of the West Junggar Mountains, NW China

This chapter has been submitted to JGR: Solid Earth with Stijn Glorie, Gilby Jepson, Wenjiao Xiao, and Alan S. Collins as co-authors

Statement of Authorship

Title of Paper	Late Paleozoic exhumation of the West Junggar Mountains, NW China
Publication Status	☐ Published ☐ Accepted for Publication ☑ Submitted for Publication ☐ Unpublished and Unsubmitted work written in manuscript style
Publication Details	Submitted for publication in Journal of Geophysical Research: Solid Earth

Principal Author

Name of Principal Author (Candidate)	Jack Gillespie		
Contribution to the Paper	Sample collection, sample preparation, analysis, data reduction, data interpretation, figures, writing		
Overall percentage (%)	70		
Certification:	This paper reports on original research I conducted during the period of my Higher Degree by Research candidature and is not subject to any obligations or contractual agreements with a third party that would constrain its inclusion in this thesis. I am the primary author of this paper.		
Signature		Date	

Co-Author Contributions

By signing the Statement of Authorship, each author certifies that:

i. the candidate's stated contribution to the publication is accurate (as detailed above);

ii. permission is granted for the candidate in include the publication in the thesis; and

iii. the sum of all co-author contributions is equal to 100% less the candidate's stated contribution.

Name of Co-Author	Stijn Glorie		
Contribution to the Paper	Primary supervision, data interpretation		
Signature		Date	
Name of Co-Author	Gilby Jepson		
Contribution to the Paper	Sample collection, data interpretation		
Signature		Date	

Name of Co-Author	Wenjiao Xiao		
Contribution to the Paper	Geological background		
Signature		Date	
Name of Co-Author	Alan S. Collins		
Contribution to the Paper	Supervision, data interpretation		
Signature		Date	

3.1 Introduction

The West Junggar Mountains lie on the western rim of the Junggar Basin in north-western China (Fig. 3.1; e.g. Feng et al., 1989; Buckman and Aitchison, 2004). The position of these, between the major Tianshan and Altai mountain belts, and in close proximity to the petroleum-rich region of the Junggar Basin, makes the exhumation history of the West Junggar an important aspect of Central Asian geology (Fig. 3.1).

The cooling and exhumation histories of the mountain belts of Central Asia are often linked to the reactivation of structures that are inherited from the amalgamation of the Central Asian Orogenic Belt during the late Paleozoic (e.g. Windley et al., 2007; De Grave et al., 2007; Glorie et al., 2011). Widespread ductile deformation occurred along many such major structures throughout Central Asia, including in the West Junggar, in response to plate reorganisation and the rotation of Siberia during the Permian (e.g. Allen et al., 1995; Laurent-Charvet et al., 2003; Buslov et al., 2004).

Prominent structures in the West Junggar, such as the Dalabute, Toli, and Barleik faults (Fig. 3.2), appear to have been reactivated to some degree in the Mesozoic and Cenozoic, but the extent of this reactivation is unclear (Allen and Vincent, 1997). The unusual NE–SW trend of major structures in the West Junggar may have caused them to respond differently to stresses propagated from the Eurasian plate margin (e.g. Allen and Vincent, 1997; Cunningham, 2013), leading to a record of reactivation that contrasts with surrounding regions.

Regional thermochronological studies across the main structural architecture of the West Junggar are limited. Previous thermochronological studies of the region have focused mainly on mineral deposits in the far south-east and on the magmatic rocks flanking the Dalabute Fault (Li et al., 2014; Yin et al., 2018).

Studying the regions that lie between the well-studied Tianshan and Altai sheds light on the extent and timing of intracontinental deformation in Central Asia in response to the far-field effect of events at the Eurasian plate margin. In this study, new apatite fission track thermochronology on igneous rocks from throughout the West Junggar is integrated with existing thermochronometric data to refine models for the cooling and exhumation history of the area.

3.2 Geological Background

The West Junggar Mountains are located to the south of the Chinese Altai, separated by the >1000km long NW–SE striking Irtysh Shear Zone (ISZ, e.g. Laurent-Charvet et al., 2003; Briggs et al., 2009; Li et al., 2018). The region is bordered to the south by the NW–SE striking Chingiz-Alakol-North Tianshan Fault (CANTF)

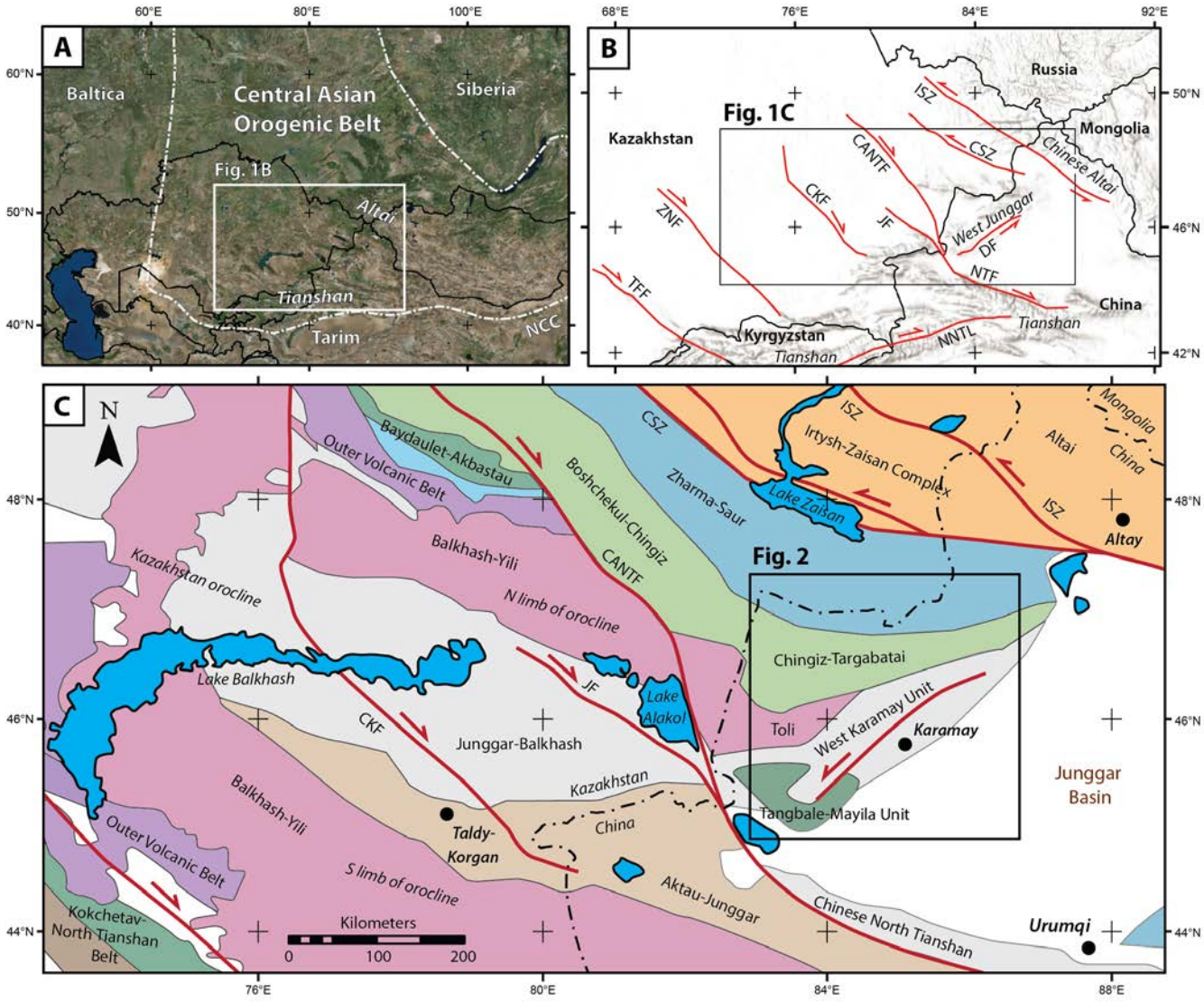

Figure 3.1: Maps of the study area showing A) Location relative to major tectonic divisions (NCC = North China Craton) B) Major structures of the Central Asian Orogenic Belt (ISZ = Irtysh Shear Zone, CSZ = Char Shear Zone, CANTF = Chingiz-Alakol-North-Tianshan-Fault, DF = Dalabute Fault, JF = Junggar Fault, CKF = Central Kazakhstan Fault, NTF = North Tianshan Fault, NNTL = Nikolaev-Natali Tectonic Line, ZNF = Zhalair-Naiman Fault, TFF = Talas-Fergana Fault). C) Tectonic divisions of East Kazakhstan-far NW China after Windley et al. (2007).

and the Junggar Fault (JF) (Fig.3.1). Most of the major faults in the West Junggar strike NE to ENE, and constitute reactivated structures that originated during the late Paleozoic amalgamation of the area (Allen and Vincent, 1997).

The West Junggar represents the easternmost part of the northern limb of the Kazakhstan orocline, part of the Central Asian Orogenic Belt (CAOB) (Fig.3.1C; Windley et al., 2007; Li et al., 2018). Ongoing debate concerning cross-border correlation of the tectonic units is complicated by the relative paucity of recent geochronology work in Eastern Kazakhstan. The Chingiz-Tarbagatai Ordovician–Silurian island arc in the north of the West Junggar is usually correlated with the Boshchekul-Chingiz arc in Kazakhstan, while the Devonian–Carboniferous Saur magmatic arc is correlated over the border with the Zharma arc of the same age (e.g. Buckman and Aitchison, 2004; Choulet et al., 2012a; Choulet et al., 2016). The structures in this area tend to strike ENE-WSW.

In the south of the West Junggar, the Toli Unit is considered to be a Devonian–Carboniferous magmatic arc that corresponds to the Balkhash-Yili arc (i.e. the 'Inner volcanic belt' of the Kazakhstan Orocline), while the West Karamay Unit is a Devonian–Carboniferous accretionary complex that is part of the larger Junggar-Balkhash accretionary complex. The Tangbale-Mayila Unit is an Ordovician–Silurian accretionary complex (e.g. Buckman and Aitchison, 2004). Several major NE–SW trending faults, including the Barliek, Toli, and Dalabute faults, cut through the southern part of the West Junggar (Fig.3.2).

The amalgamation of the units that compose the West Junggar was completed with the closure of the Junggar and Ob-Zaisan Oceans by the end of the Carboniferous (e.g. Windley et al., 2007; Li et al., 2017b). The Permian tectonics of the CAOB was dominated by the rotation of Siberia relative to Baltica and Tarim, which induced complex patterns of deformation along major shear zones throughout Central Asia (e.g. Şengör et al., 1993; Buslov et al., 2004; Wang et al., 2007).

The timing of sinistral-reverse shearing along the Irtysh Shear Zone was found to have occurred between ~290–252 Ma according to $^{40}Ar/^{39}Ar$ dating of shear fabric minerals and the age of cross cutting dykes (Laurent-Charvet et al., 2003; Briggs et al., 2007; Briggs et al., 2009; Li et al., 2015c; Li et al., 2015d; Li et al., 2016a; Li et al., 2016b). This transpressional event was accompanied by regional uplift in the southern Chinese Altai at ~270 Ma as a result of convergence between the Chinese Altai and the East/West Junggar terranes (Li et al., 2015d). Dextral deformation along major structures to the south-west, such as the CANTF, Junggar Fault, and Central Kazakhstan Fault, appears to have occurred simultaneously to sinistral movement recorded in the Irtysh Shear Zone (e.g. Shu et al., 1999; Buslov et al., 2001; Wang et al., 2014). Further to the west, the major Talas-Fergana Fault also experienced dextral movement during the Permian at 290–260 Ma (Rolland et al., 2013). Permian displacement along these structures has been estimated to be in the

range of hundreds to more than one thousand kilometers (Allen et al., 1995; Allen et al., 2001; Buslov et al., 2004; Wang et al., 2007; Alexeiev et al., 2009; Choulet et al., 2011; Li et al., 2018).

The NE-striking Dalabute Fault in the West Junggar was active during the Permian, generating cataclasite and offsetting the West Karamay Unit by $\approx$ 100 km (Allen et al., 1995; Choulet et al., 2012b). Direct evidence for Mesozoic fault activity within the West Junggar is less common than for the Paleozoic. Evidence from seismic profiles in the western Junggar Basin suggest some fault activity during the Jurassic, although this is far more pronounced in the north-eastern and southern Junggar basin than in the west (Yang et al., 2015; Li et al., 2017a). Cenozoic reactivation in the West Junggar has been weak compared to that experienced by the Tianshan (Avouac et al., 1993). Sinistral motion along the Dalabute fault during the latest Cenozoic has generated a sharp but low fault scarp, with Quaternary sediments deposited alongside (Allen and Vincent, 1997).

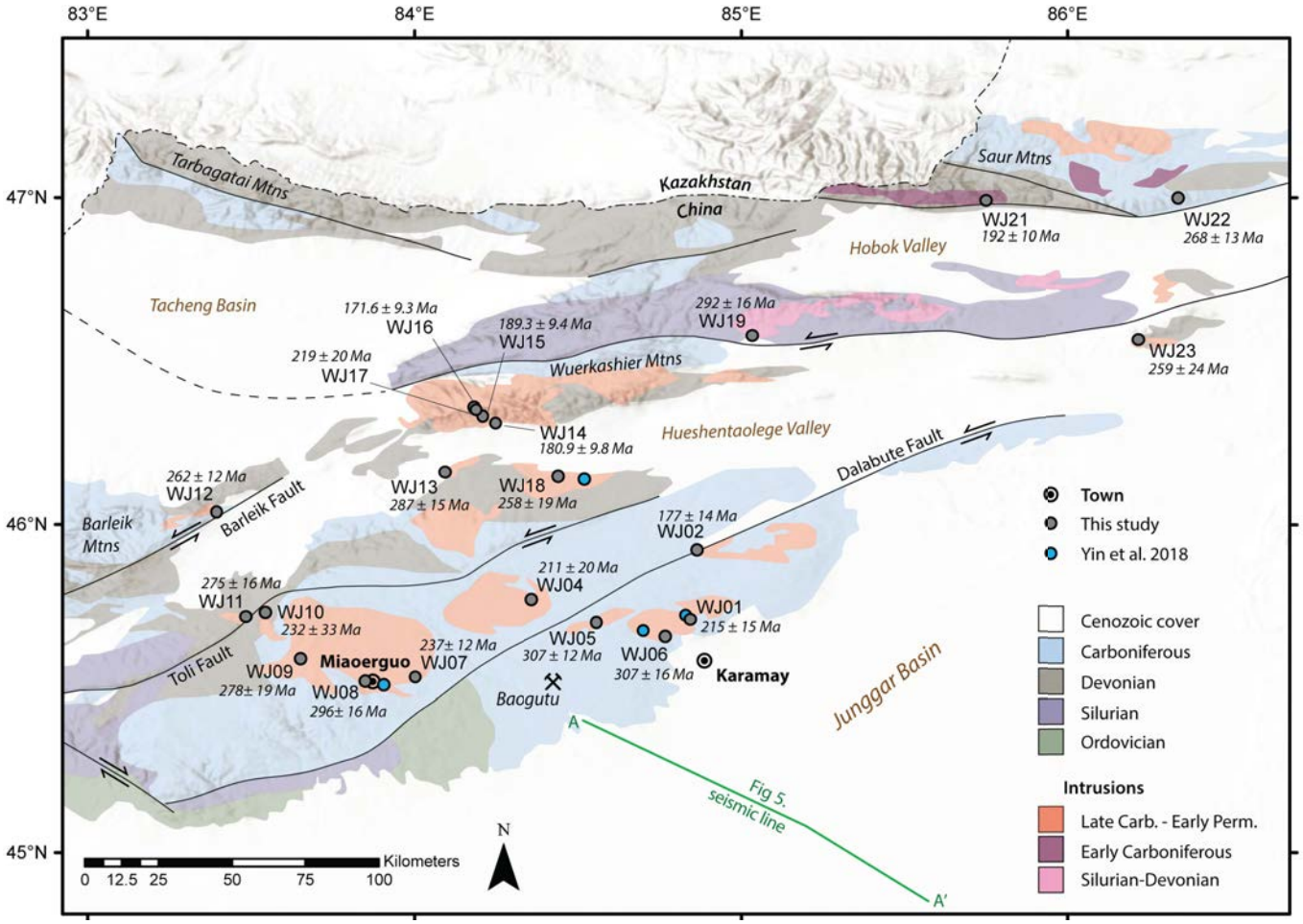

Figure 3.2: Geological map of the West Junggar after Feng et al. (1989) and Yin et al. (2017) overlaid on hillshade relief map generated in ArcMap. Labelled are the location of samples and the apatite fission track central ages from this study. Yin et al. (2018) locations indicate position of (U-Th)/He dates. AA' line indicates location of seismic profile from Li et al. (2017a), as in Fig. 3.5.

3.3 Methods

3.3.1 Samples

Twenty-three igneous rocks from throughout the West Junggar were sampled for this study. Conventional rock crushing and mineral separation procedures were used to separate apatite grains from these rocks. Twenty-one samples produced sufficient quantities of high quality apatite for further analysis, and two samples contained either low quality or too few apatite grains. See Table 1 for location and lithological data.

3.3.2 Apatite U–Pb dating

Apatite U–Pb analysis was conducted at the University of Adelaide using a NewWave UP213 laser ablation unit coupled to an Agilent 7900 mass spectrometer. During analysis the ^{204,206,207,208}Pb, ^{232}Th, and ^{238}U isotopes were measured, with the Madagascar apatite (Thomson et al., 2012) as the primary standard for instrumental drift and downhole fractionation corrections (Chew et al., 2014a). The Mt. McClure apatite (reference age 523.51 ± 2.09 Ma, Schoene and Bowring, 2006, this study, Tera-Wasserburg lower intercept age = 519.3 ± 3.6 Ma, MSWD = 1.2, n = 72) was used as a secondary standard to assess the accuracy of the data (Fig. C.4). Data reduction was performed in Iolite (Paton et al., 2011) using the "VizualAgeUcomPbine" data reduction scheme (DRS) to account for variable common Pb in the standards (Chew et al., 2014a). The apatite U–Pb dates were calculated using linear regression through a population of analyses in Tera-Wasserburg concordia space (Tera and Wasserburg, 1972), with the lower concordia intercept giving the U–Pb age of the apatite population (e.g. Gibson and Ireland, 1996). For further details on the LA-ICP-MS application of this approach see Chew et al. (2011) and Chew et al. (2014a). Isotopic data were plotted and Tera-Wasserburg lower concordia intercept ages (T-W intercept ages) were calculated using the IsoplotR package v.2.3 (Vermeesch, 2018) in R v.3.5.2.

3.3.3 Apatite fission track dating

Apatite fission track dating was conducted at the University of Adelaide. Apatite grains were hand-picked and mounted in epoxy resin, then ground and polished to reveal an internal surface with 4π geometry (Tagami and O'Sullivan, 2005). The mounts were etched in 5.0 M HNO_3 for 20 seconds at 20 ± 1 °C (Barbarand et al., 2003). Mounts were coated in 5nm gold and imaged using Trackworks software and a Zeiss AXIO Imager M2m Autoscan system (Gleadow et al., 2009). Irradiation by ^{252}Cf for 30 minutes at the University of Adelaide was necessary in several cases to

Table 3.1: Location and lithological data

Sample	IGSN	Latitude (WGS84)	Longitude (WGS84)	Altitude (m a.s.l.)	Lithology	Locality
WJ01	IEJAG001J	45.708	84.845	733	Granite	North Karamay
WJ02	IEJAG001K	45.922	84.866	747	Granite	Dalabute Fault
WJ04	IEJAG001M	45.770	84.359	1156	Granite	Akebastao
WJ05	IEJAG001N	45.700	84.558	977	Granodiorite	West Karamay
WJ06	IEJAG001O	45.656	84.769	645	Granite	East Karamay
WJ07	IEJAG001P	45.532	84.003	1310	Granite	Miaoergou
WJ08	IEJAG001Q	45.520	83.849	1509	Granite	Miaoergou
WJ09	IEJAG001R	45.589	83.651	1820	Granite	Miaoergou
WJ10	IEJAG001S	45.730	83.545	1521	Granite	Toli Fault
WJ11	IEJAG001T	45.717	83.485	1548	Granite	Toli Fault
WJ12	IEJAG001U	46.037	83.395	1191	Andesite	Barliek Mtns
WJ13	IEJAG001V	46.159	84.094	975	Granite	Tiechanggou
WJ14	IEJAG001W	46.309	84.248	1210	Granodiorite	Wuerkashier Mtns
WJ15	IEJAG001X	46.332	84.210	1582	Granodiorite	Wuerkashier Mtns
WJ16	IEJAG001Y	46.360	84.181	2532	Granite	Wuerkashier Mtns
WJ17	IEJAG001Z	46.351	84.188	2040	Granodiorite	Wuerkashier Mtns
WJ18	IEJAG0020	46.147	84.442	839	Granite	Tiechanggou
WJ19	IEJAG0021	46.579	85.035	1410	Granodiorite	Shaburt Mtns
WJ21	IEJAG0023	46.989	85.749	2134	Granite	Saur Mtns
WJ22	IEJAG0024	46.997	86.337	1784	Tonalite	Saur Mtns
WJ23	IEJAG0025	46.565	86.217	1132	Monzonite	Shaburt Mtns

Note: IGSN = international geosample number

increase the number of visible confined tracks (Donelick and Miller, 1991). Fission track density and confined track length measurements were conducted manually using the FastTracks software package (Gleadow et al., 2009). The concentration of ^{238}U in the counted area of the apatite grains was determined by LA-ICP-MS analysis with a NewWave UP213 laser ablation unit coupled to an Agilent 7900 mass spectrometer, while U–Pb isotope acquisition occurred simultaneously. NIST SRM 610 was used as the primary standard with ^{43}Ca as the internal elemental standard (Hasebe et al., 2013). Age calculation was performed according to the equations of Vermeesch (2017) using zeta-calibration (Hurford and Green, 1983; Hasebe et al., 2013; Vermeesch, 2017) based on repeated measurements of the Durango apatite (McDowell et al., 2005). AFT analysis of the Durango apatite produced a central age of 31.89 ± 0.94 Ma (dispersion = 0%, $P(\chi^2) = 0.98$, n = 74, Fig. C.1) compared to the reference age of 31.44 ± 0.18 Ma (McDowell et al., 2005).

3.3.4 Inverse thermal history modelling

Inverse thermal history modelling was conducted using QTQt software v.5.6.0 (Gallagher, 2012). This program uses a Bayesian transdimensional Markov Chain Monte Carlo approach to generate a range of thermal histories based on thermochronological data and other geological constraints. The software outputs a variety of models based on the input data that can be evaluated by the comparison of the observed versus predicted values for the relevant model. The expected model (weighted mean of the posterior distribution) and corresponding 95% confidence interval (95% CI) are used in this study as the most representative thermal history model (Gallagher, 2012). Thermal history modelling was conducted for the fifteen samples that produced sufficient numbers (>35) of confined track lengths (Table 3.2). Twelve samples were modelled using AFT data from this study (WJ02, WJ11, WJ12, WJ13, WJ14, WJ15, WJ16, WJ17, WJ19, WJ21, WJ22, and WJ23) and three samples (WJ06, WJ07, and WJ18) were modelled using both AFT data from this study and (U-Th)/He data from Yin et al. (2018). All models were constrained at temperatures above the APAZ at the time of the apatite U–Pb age obtained for the sample and were otherwise unconstrained except by surface temperatures at 0 Ma. D_{par} was used as the kinetic parameter. For a detailed description of the modelling parameters and procedure used to generate the models presented in this study see (Table C.1).

Table 3.2: Apatite fission track data

Sample	n	N_s	ρs ($x10^5 cm^{-2}$)	^{238}U (ppm)	$P(\chi^2)$	t (Ma)	$\pm 1\sigma$	D_{par} (μm)	MTL (μm)	SD	N_L
WJ01	22	522	17.20	4.35	0.13	215	15	1.13	-	-	-
WJ02	17	184	7.35	7.01	0.62	177	14	1.03	12.3	1.4	37*
WJ04	12	129	2.68	1.94	0.36	211	20	1.07	-	-	-
WJ05	25	828	11.36	7.82	0.45	307	12	1.55	-	-	-
WJ06	25	439	6.74	4.12	0.59	307	16	1.93	14.0	1.0	64*
WJ07	35	414	5.39	4.56	0.98	237	12	1.08	12.7	1.3	34*
WJ08	36	361	4.18	2.75	0.97	296	16	1.20	-	-	-
WJ09	27	254	3.86	3.45	0.32	278	19	1.27	-	-	-
WJ10	11	52	3.33	3.39	0.94	232	33	1.14	-	-	-
WJ11	33	308	4.59	3.30	0.69	275	16	1.03	13.0	1.1	44*
WJ12	32	630	8.97	5.84	0.37	262	12	2.21	14.1	1.2	85*
WJ13	40	586	5.20	3.66	0.11	287	15	1.12	13.2	1.2	52*
WJ14	36	608	12.43	9.88	0.08	180.9	9.8	1.29	12.0	1.5	100
WJ15	33	818	18.34	19.20	0.03	189.6	9.4	1.56	12.1	1.4	66
WJ16	24	388	15.56	18.05	0.96	171.6	9.3	0.81	12.4	1.5	57
WJ17	20	395	13.20	4.70	0.00	219	20	1.22	12.2	1.6	47
WJ18	21	306	8.58	5.36	0.09	258	19	1.09	12.4	1.7	86*
WJ19	17	442	16.21	9.32	0.56	292	16	2.58	14.1	1.1	96*
WJ21	39	600	12.17	9.54	0.14	192	10	1.49	12.6	1.3	66
WJ22	30	506	13.82	9.63	0.52	268	13	1.61	12.8	1.3	50
WJ23	24	131	3.11	2.52	0.97	259	24	1.35	12.8	1.4	46*

n = number of grains analysed, N_s = number of spontaneous tracks counted, ρs = spontaneous track density, ^{238}U = average uranium concentration of the analysed grains, $P(\chi^2) = (\chi^2)$ probability after Galbraith (1981), D_{par} = mean track etch pit diameter parallel to the crystallographic c-axis, MTL = mean confined track length, SD = standard deviation of the track length distribution, N_L = number of confined track length measurements. Asterisks mark samples irradiated with ^{252}Cf to increase the number of visible confined tracks.
$\zeta = 2.091 \pm 0.073 \times 10^{-3}$

Table 3.3: Apatite U–Pb summary data and zircon U–Pb crystallization ages

Sample	Apatite U–Pb age (Ma)	0.95 CI	MSWD	n	Zircon U–Pb age ± 2σ (Ma)
WJ01	305.3	8.9	2.1	24	304 ± 3[e]
WJ02	308.9	11.4	2.6	17	301 ± 4[c]
WJ05	335.2	32.9	1.3	27	314 ± 3[e]
WJ06	311.6	22.8	0.78	27	316 ± 3[e]
WJ07	328.1	35.9	1.6	36	308 ± 6[c]
WJ09	288.0	11.0	0.95	29	308 ± 6[c]
WJ11	336.6	34.3	1.8	35	309 ± 2[f]
WJ12	331.8	17.3	1	31	C_2 - P_1[f]
WJ13	290.5	42.4	1.6	39	C_2 - P_1[f]
WJ14	289.3	8.8	0.73	30	302 ± 2[d]
WJ15	301.3	9.0	1.2	32	302 ± 2[d]
WJ16	281.3	33.4	2.3	21	302 ± 2[d]
WJ17	302.0	9.2	2	23	302 ± 2[d]
WJ18	292.4	11.9	1.1	25	308 ± 4[a]
WJ19	408.1	13.7	0.84	17	420 ± 5[d]
WJ21	326.3	10.2	1.3	40	338 ± 4[a]
WJ22	337.8	16.0	0.99	30	324 ± 6[b]

Apatite U–Pb age = T-W lower intercept age, 0.95 CI = 95% confidence interval
[a] Han et al. (2006)
[b] Zhou et al. (2008)
[c] Geng et al. (2009)
[d] Chen et al. (2010)
[e] Tang et al. (2012)
[f] Xu et al. (2012)

3.4 Results

3.4.1 Apatite fission track and U–Pb dating results summary

Apatite U–Pb dating of 21 igneous samples yielded mostly Carboniferous–early Permian T-W lower intercept ages (Fig. C.5). Four samples produced relative uncertainties of >15% and have been excluded from the summary data table (Table 3.3). The uncertainty on the T-W lower intercept ages varied considerably between samples, depending mostly on the level of variation in the $^{238}U/^{206}Pb$ and $^{207}Pb/^{206}Pb$ ratios between individual apatite grains, and on the median U contents of the grains. Samples with high inter-grain variability in terms of common versus radiogenic Pb component produced better constrained regressions with smaller 95% confidence intervals (95% CI), while those with low median U (<3.5 ppm) tended to produce less precise results. See appendices for complete tabulations of individual spot analytical data and T-W plots.

Apatite fission track analysis of 21 igneous samples yielded AFT central ages ranging from latest Carboniferous to Early Jurassic, with a majority of samples producing Permian or Triassic central ages (Table 3.2). Eight of the samples analysed in this study are located in the area of the West Junggar to the north of the E-W oriented Hueshentaolege Valley, and the remaining thirteen are located in the southern part of the region (Fig.3.2). Fifteen samples yielded more than 30 confined track lengths (mostly >50), with mean track length (MTL) values ranging from 14.1–12.0 μm. See appendices for a detailed description of the individual sample data, tables of analytical data, confined track length data, and associated plots.

3.5 Discussion

3.5.1 U–Pb and $^{40}Ar/^{39}Ar$ geochronology

Many of the igneous rocks sampled for apatite thermochronology in this study have previously been dated using zircon U–Pb geochronology (e.g. Han et al., 2006; Zhou et al., 2008; Geng et al., 2009; Chen et al., 2010; Tang et al., 2012; Xu et al., 2012; Yin et al., 2017). The new mostly Carboniferous–early Permian apatite U–Pb dates presented in this study are within uncertainty or slightly younger than the known zircon U–Pb ages (Table 3.3). This suggests rapid cooling of the sampled intrusive rocks to below the apatite U–Pb closure temperature of ~450–550 °C soon after emplacement (e.g. Smye et al., 2018). This is also consistent with the similar ages produced by zircon U–Pb and $^{40}Ar/^{39}Ar$ biotite dating of the North Karamay and Tiechanggou plutons (Yin et al., 2018).

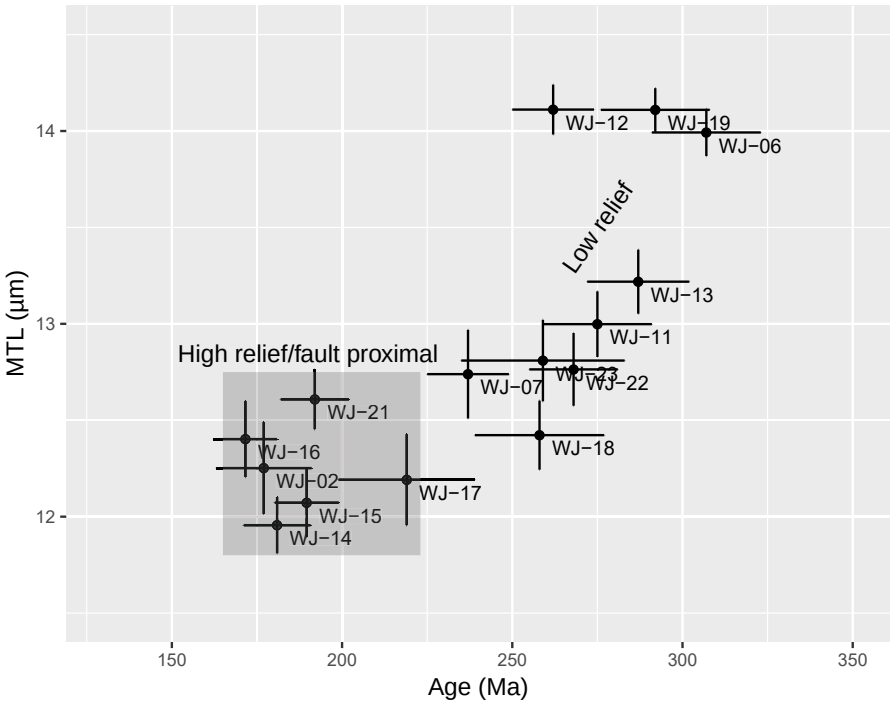

Figure 3.3: AFT Central Age vs MTL 'boomerang' plot

3.5.2 Apatite fission track thermochronology

A clear relationship exists between the AFT central ages and MTLs of the analysed samples, whereby the samples with the oldest central ages have the longest MTLs, and those with younger central ages record progressively shorter track lengths (Fig. 3.3). In addition, a distinct spatial trend can be observed for the AFT central ages. Results from the northern part of the West Junggar record a pattern that is consistent across the different sampled ranges (e.g. Wuerkashier vs. Saur Mountains; Fig. 3.2). Areas of low relief (WJ19, 22, 23) tend to record older ages and longer MTLs that suggest relatively rapid cooling through the APAZ in the early–middle Permian. Samples from areas of high relief, such the face of the escarpment overlooking the Hueshentaolege Valley (WJ14,15,16,17), or deep valleys incised in the western Saur Mountains (WJ21), record younger (mostly Jurassic) ages with shorter MTLs.

In the southern area, the samples with older (latest Carboniferous–Permian) AFT central ages also tend to produce longer MTL distributions, reinforcing the idea that rapid cooling occurred at this time. This is consistent with the small difference between the apatite U–Pb ages and the AFT central ages of these samples (Tables 3.2, 3.3). Due to the generally low relief of the southern West Junggar, a relationship between the AFT central age of a sample and the local modern topography is not

evident for this area. However, the sample that was taken adjacent to the Dalabute fault (WJ02) records the youngest AFT age and shortest MTL of any sample in the southern area. Samples WJ04 and WJ07, the closest samples to the northern side of the Dalabute Fault, similarly record younger AFT ages than surrounding samples (Fig. 3.2).

Plots of fission track age vs. MTL are sometimes called boomerang plots due to the distinctive concave-up shape that can be produced under some circumstances (e.g. Green, 1986; Malusà and Fitzgerald, 2019, Chapter 10). This characteristic distribution of data is usually interpreted to indicate that the samples experienced coeval cooling at a range of paleodepths. The older, long MTL section of the curve is composed of those samples that cooled to above the APAZ at the timing of initial cooling, and have been residing near the surface for an extended period (Hendriks et al., 2007). Samples in the middle of the boomerang have the shortest MTLs and resided in the APAZ for the greatest amount of time before cooling to above the APAZ. The position of the high relief and fault proximal samples in the boomerang plot (Fig. 3.3) is therefore interpreted to mean that these ages (central ages $\lesssim 250$ Ma) are not cooling ages representative of the timing of an event, but rather indicate extended residence in the APAZ (Green, 1986). A full boomerang also includes a younger population of ages with long MTLs, indicating the timing of most recent cooling from below the APAZ.

In this case only a half-boomerang is present, as there is no corresponding population of younger ages with long MTLs (Fig. 3.3). This implies that the West Junggar did not experience significant regional scale exhumation since the initial event during the Permian, and that subsequent events were insufficient to exhume rock from below the APAZ. The samples that record extended residence in the APAZ following Permian exhumation must have cooled and been exhumed to the modern surface at some point following the Middle Jurassic AFT apparent ages recorded by these samples. These samples may have been exhumed to the surface over the course of several small events rather than one major phase of later exhumation. The timing of these phases of later cooling and exhumation cannot be determined by the available thermochronological data.

3.5.3 West Junggar thermochronology

(U-Th)/He dating

Samples from several plutons in the southern West Junggar have previously been analysed using the apatite (U-Th)/He (AHe) and zircon (U-Th)/He (ZHe) thermochronometers (Li et al., 2014; Yin et al., 2018). These methods can provide information about the thermal history of a sample in the range of ~30–90 °C for AHe (Flowers et al., 2009) and <50–210 °C for ZHe (Guenthner et al., 2013; An-

derson et al., 2017; Johnson et al., 2017). Samples from the North Karamay, East Karamay, Miaoerguo, and Tiechangguo plutons were analysed with the AHe and ZHe methods in Yin et al. (2018) and various rocks from the Baogutu porphyry Cu deposit, to the SW of Karamay, were also analysed using these methods in Li et al. (2014) and Yin et al. (2018).

Samples from the East Karamay pluton were dated using the AFT method in this study (WJ06) and by both AHe and ZHe dating in Yin et al. (2018). AFT dating produced a central age of 307 ± 16 Ma, compared to three overdispersed ZHe analyses with corrected dates that range from 312–271 Ma. Three overdispersed AHe corrected dates for the same pluton range from 254–205 Ma. WJ01 from the North Karamay pluton produced an AFT central age of 215 ± 15 Ma, compared to two overdispersed ZHe analyses with corrected dates of 250 ± 10 Ma and 226 ± 9 Ma. WJ07 from the Miaoerguo pluton produced an AFT central age of 237 ± 12 Ma, overlapping with the range of five overdispersed ZHe analyses with corrected dates of 272–216 Ma. WJ18 from the Tiechangguo pluton produced an AFT central age of 258 ± 18 Ma, overlapping with the range of five overdispersed ZHe analyses with corrected dates of 299–259 Ma. Two overdispersed AHe analyses for this pluton produce younger corrected dates of 237 ± 7 Ma and 211 ± 9 Ma.

All of the AHe and ZHe dates from Yin et al. (2018) are overdispersed with respect to their analytical uncertainties of 3–4% for ZHe analyses and 3–8% for AHe analyses (Fig. 3.4). This is a commonly observed phenomenon in (U-Th)/He dating that stems from the many possible sources of uncertainty that can contribute to the variability of (U-Th)/He results (e.g. Wildman et al., 2016; Green and Duddy, 2018; Ketcham et al., 2018). Possible sources of uncertainty include the effect of grain size, radiation damage, grain breakage/fragmentation, zonation of parent isotopes, 'bad neighbour' He implantation, and mineral or fluid inclusions (e.g. Fitzgerald et al., 2006; Vermeesch et al., 2007; Gautheron et al., 2009; Brown et al., 2013; Beucher et al., 2013; Johnson et al., 2017). At present, a variety of strategies are employed to account for some of these factors, but in practice it is essentially impossible to quantify and properly correct for all the different sources of uncertainty (Green and Duddy, 2018). Ketcham et al. (2018) found that even for a 'well-behaved' sample used for inter-laboratory comparison, uncertainties of 17–21% were necessary to account for the dispersion. This is around three times the commonly assigned laboratory uncertainties of 6–8% for He dating based on the reproducibility of standards. Although the use of (U-Th)/He data unsupported by accompanying AFT data is potentially misleading (Danišík et al., 2015), the (U-Th)/He method as part of a multi-methodological approach can be used provide information about the thermal history of a sample over a wider temperature range than the AFT method alone. The (U-Th)/He data from the West Junggar is geologically reasonable and consistent between comparable samples, and so in this study single grain ZHe and

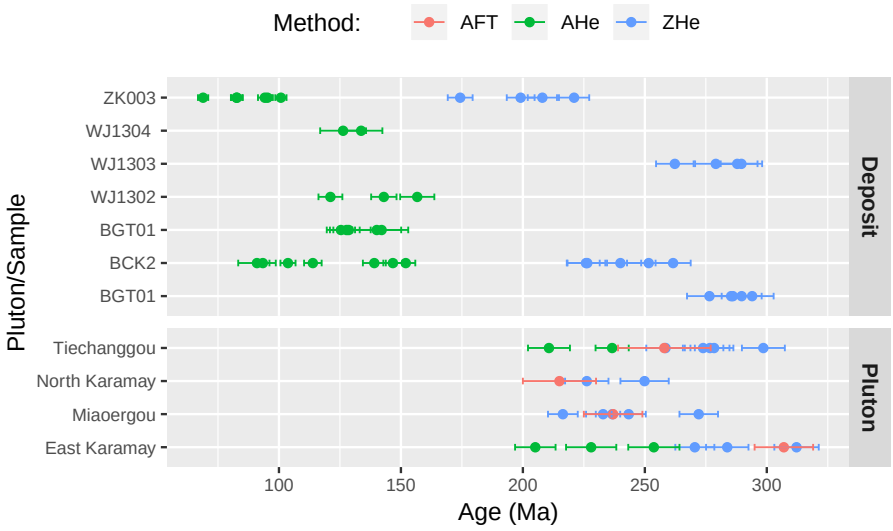

Figure 3.4: Comparison between AFT central ages and single grain AHe and ZHe dates from the Baogutu deposit and from non-mineralised plutons in the West Junggar. Temperature ranges for each method are: ~30–90 °C for AHe (Flowers et al., 2009), 60–110 °C for AFT (Gleadow et al., 2002), <50–210 °C for ZHe (Guenthner et al., 2013; Anderson et al., 2017; Johnson et al., 2017). AFT data from this study, single grain AHe and ZHe data from Li et al. (2014) and Yin et al. (2018). Uncertainty is given as 2σ for AHe/ZHe and 1σ for AFT data. Samples from plutons: Tiechanggou - WJ1306, WJ18; North Karamay - WJ1111, WJ01; Miaoergou - MG01, WJ07; East Karamay - KLMY02, WJ06.

AHe analyses were incorporated into thermal history modelling where available. In order to compensate for the difficulties in assigning appropriate uncertainties to the ZHe and AHe analyses, QTQt was allowed to resample the input uncertainties during thermal history modelling (Table C.1, Fig. C.7).

Baogutu deposit thermochronology

Previous low-temperature thermochronological studies of the West Junggar have focused heavily on the large Baogutu porphyry Cu deposit, and a majority of the published AHe and ZHe data are derived from analysis of the stocks and dikes associated with mineralisation (Li et al., 2014; Yin et al., 2018). Previous interpretations of the regional thermal history of the West Junggar did not draw a clear distinction between data from the deposit and from the more widespread and representative plutonic rocks in the region (Li et al., 2014; Yin et al., 2018). Figure 3.4 shows that the corrected dates of individual AHe analyses from the Baogutu deposit are

significantly younger than the AHe analyses obtained for the plutonic rocks in the West Junggar. Neither of the sampled plutons produced individual corrected AHe dates younger than 200 Ma, compared to a range of 157–69 Ma for the AHe analyses from the Baogutu deposit (Fig. 3.4). In contrast, ZHe dates from the deposit and plutons are reasonably similar, with comparable minimum and maximum corrected dates. The data from ZK003 (sampled from a drill hole in the deposit at 473m depth) is anomalous as it produces somewhat younger ZHe dates.

The difference between the dates obtained for the deposit and those from the plutonic rocks of the West Junggar suggest that data from the deposit do not reflect the regional thermal history of the West Junggar. Given the high degree of overdispersion, the AHe dates are unlikely to represent a particular cooling event and should be interpreted as apparent ages without direct geological meaning, rather than cooling ages linked to a specific event (e.g. Danišík et al., 2015).

This interpretation suggests that data from the Baogutu deposit should not be used to draw general conclusions about the thermal history of the West Junggar region, as they are likely due to local conditions related to the deposit rather than factors that had a widespread influence.

Previous fission track studies

Several published studies have previously applied AFT dating to intrusive igneous rocks in the West Junggar (Guo et al., 2006; Li et al., 2010; Qin et al., 2018). These studies produced mostly conflicting results. Guo et al. (2006) and Li et al. (2010) produced AFT central ages of 163 ± 16 Ma (MEG3) and 67 ± 6 Ma (ZX1) respectively, from immediately adjacent samples in the same pluton near the town of Miaoerguo (Fig. 3.2). Similarly, for neighbouring samples TLC1 and D480/1 near the Toli Fault, central ages of 171 ± 20 Ma and 78 ± 7 Ma were found by Guo et al. (2006) and Li et al. (2010). These significant differences between the ages produced from the same locations make it difficult to assess the data. The ages produced by these studies are both significantly younger than the AHe ages in Yin et al. (2018) and the AFT ages found in this study. The East Karamay pluton has been dated using the ZHe and AHe methods, and was dated using the AFT method in this study and Guo et al. (2006). A thermal history model using only ZHe and AHe data from Yin et al. (2018) and a model that incorporates AFT data from this study reveal that in either case, cooling to above the APAZ is required prior to 200 Ma (Fig. C.6). It is difficult to reconcile the ~160 Ma AFT central ages of Guo et al. (2006) for the East Karamay pluton with these new, well constrained models that incorporate data from a range of a different thermochronometers. Due to these obstacles we have chosen not to include the data from these previous studies in further discussion.

3.5.4 Thermal history modelling

Thermal history modelling was used to explore possible cooling histories for the AFT data in this study, and to integrate the new results with existing low-temperature thermochronological data.

Samples with central ages older than ~250 Ma, interpreted in the age vs track length diagram (Fig. 3.3) to record the timing of a major cooling event, produce thermal history models that suggest a phase of rapid cooling occurred during the early–middle Permian at ~285–260 Ma (Fig.3.5). A common feature of these fast cooling models is an inflection point at ~260–250 Ma, indicating a transition from rapid to slow cooling during the late Permian. Thermal history modelling of younger samples produce a variety of possible paths that show relatively slow cooling, interpreted to reflect variable periods of extended residence in the APAZ.

These models suggest that the rock currently exposed at the surface was exhumed to above the APAZ (~60 °C) during the early–middle Permian. We interpret that samples that produce Triassic–Jurassic AFT central ages were cooled to within the APAZ during this event, where they remained at temperatures between ~120–60 °C for an extended period, before eventually cooling to temperatures at which the fission tracks became stable. These samples that produce Tirassic–Jurassic AFT central ages were collected from locations where deeper levels of the crust are exposed via mechanisms such as the uplift of the Wuerkaishier and Saur Mountains, or localised exhumation along the Dalabute Fault (Fig. 3.1). The timing of this later exhumation cannot be determined from these data as it was not extensive enough to be recorded by the current available thermochronometers.

3.5.5 Regional context

Amalgamation and magmatic history of the West Junggar

The West Junggar experienced a long and complex accretionary history that spanned much of the Paleozoic (e.g. Kwon et al., 1989; Feng et al., 1989). Several ophiolitic melanges have been recognised within the West Junggar with ages of 508 Ma to 332 Ma (Feng et al., 1989; Zhang et al., 1993; Buckman and Aitchison, 2004; Xu et al., 2006; Xu et al., 2012; Yang et al., 2013a), while the arc-related components of the region range from Ordovician to Carboniferous in age (Feng et al., 1989; Buckman and Aitchison, 2004).

During the Carboniferous, the West Junggar was intruded by abundant and diverse magmatic rocks that have inspired equally diverse interpretations by various authors (e.g. Geng et al., 2009; Chen et al., 2010; Tang et al., 2012; Xu et al., 2012; Gao et al., 2014; Yin et al., 2015). The timing of the transition from subduction to a post-collisional environment is still the topic of much disagreement, and a variety of settings have been proposed for the West Junggar during the Carboniferous

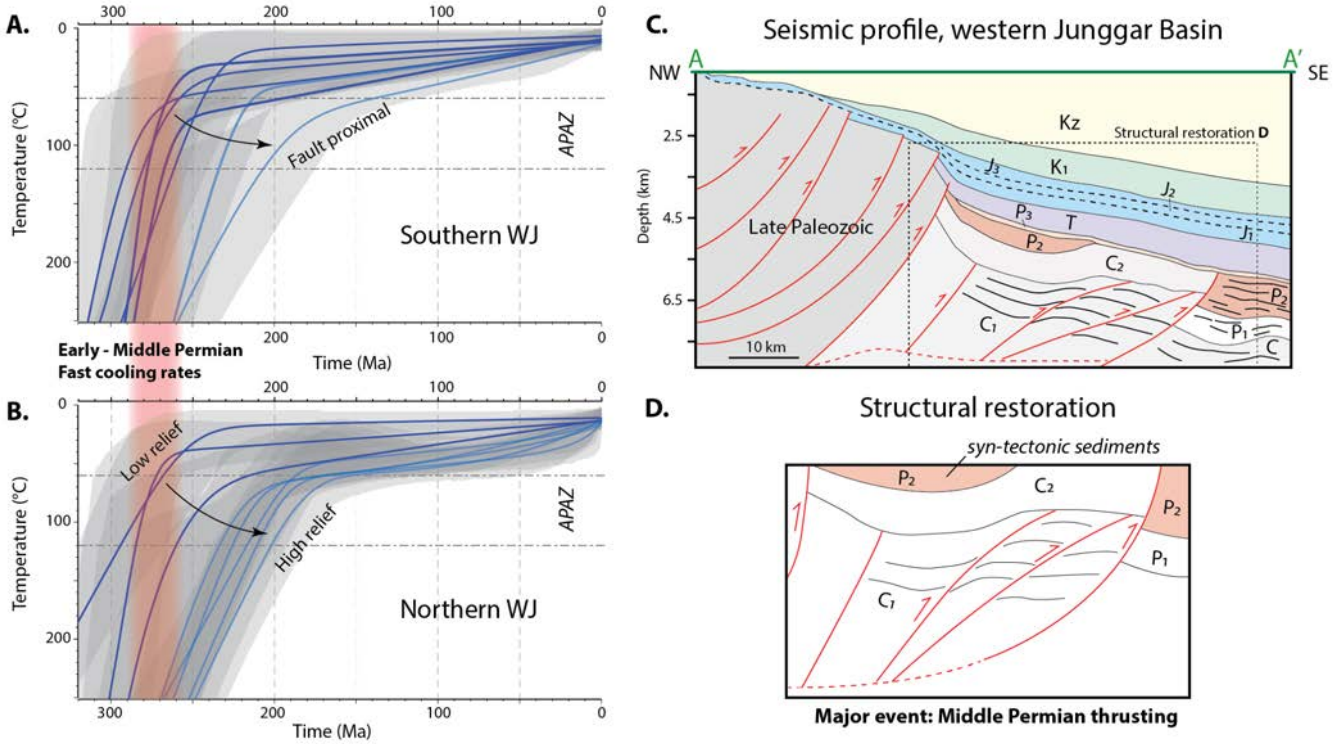

Figure 3.5: Thermal history models for samples from the southern West Junggar (A) and northern West Junggar (B) and seismic interpretation showing main stage of thrusting in the western Junggar Basin, to the east of Karamay (C,D). Thermal history models - blue line is the expected model, grey envelopes are the 95%CI for the expected model. Dark blue = upper part of boomerang, light blue = lower part of boomerang in Fig. 3.3. Seismic profiles and structural restoration from Li et al. (2017a). Red shaded bar indicates timing of rapid cooling phase.

and earliest Permian. Some authors consider the late Carboniferous–early Permian plutons to be post-collisional (e.g. Kwon et al., 1989), linking them to stitching plutons of similar age elsewhere in Central Asia and interpreting them as evidence for amalgamation prior to the intrusion of the late Carboniferous magmatism (Chen et al., 2010). Other models suggest that ridge subduction in the late Carboniferous can provide an explanation for the presence of these plutons, implying that subduction must have continued into the late Carboniferous, and possibly into the earliest Permian (Geng et al., 2009). Choulet et al. (2012b) argues, based on structural relationships, that accretion and subduction in the West Junggar must have ceased during the late Carboniferous, with transition from an accretionary to post-accretionary setting at 305–300 Ma. This interpretation is consistent with the lack of evidence for Permian subduction in the sedimentary or tectonic records (Feng et al., 1989; Buckman and Aitchison, 2004; Choulet et al., 2012b).

Following the transition to a post-accretionary setting at the end of the Carboniferous, the West Junggar experienced a major phase of deformation during the Permian (Allen et al., 1995; Allen and Vincent, 1997; Laurent-Charvet et al., 2003; Choulet et al., 2012b). The $^{40}Ar/^{39}Ar$ dating of major structures across Central Asia produces ages ranging from 290–245Ma, indicating widespread ductile deformation during the Permian and into the Triassic (e.g. Shu et al., 1999; Laurent-Charvet et al., 2003; Briggs et al., 2007; Wang et al., 2009a; Rolland et al., 2013; Li et al., 2015d). This deformation was dominantly strike-slip throughout Central Asia, but was often accompanied by a component of compressional or extensional deformation depending on the location and orientation of the structure.

According to paleomagnetic data, the West Junggar experienced counter-clockwise rotation relative to Siberia during the early Permian (Wang et al., 2007; Choulet et al., 2011), accommodated by sinistral motion along the Irtysh Shear Zone (Laurent-Charvet et al., 2003). Choulet et al. (2011) propose that bending of the West Junggar during counter-clockwise rotation also led to the development of the CANTF, with dextral strike-slip motion along this new structure (Fig. 3.6) coeval to the activation of SE vergent thrusts in the West Junggar (Buslov, 2011). Seismic profiles in the Junggar Basin show that at this time the West Junggar was thrust over the basement rocks of the Junggar Basin (Fig. 3.5; Li et al., 2017a). Since the late Permian, the paleomagnetic poles of West Junggar, North Kazakhstan, and Siberia have been consistent, implying a lack of further significant rotation or translation offset relative to one another. However, South Junggar, Yili, and Tarim have a further counter-clockwise rotational component relative to West Junggar-North Kazakhstan-Siberia during the late Permian–earliest Triassic, probably accommodated by dextral fault movement in the Tianshan (Choulet et al., 2011).

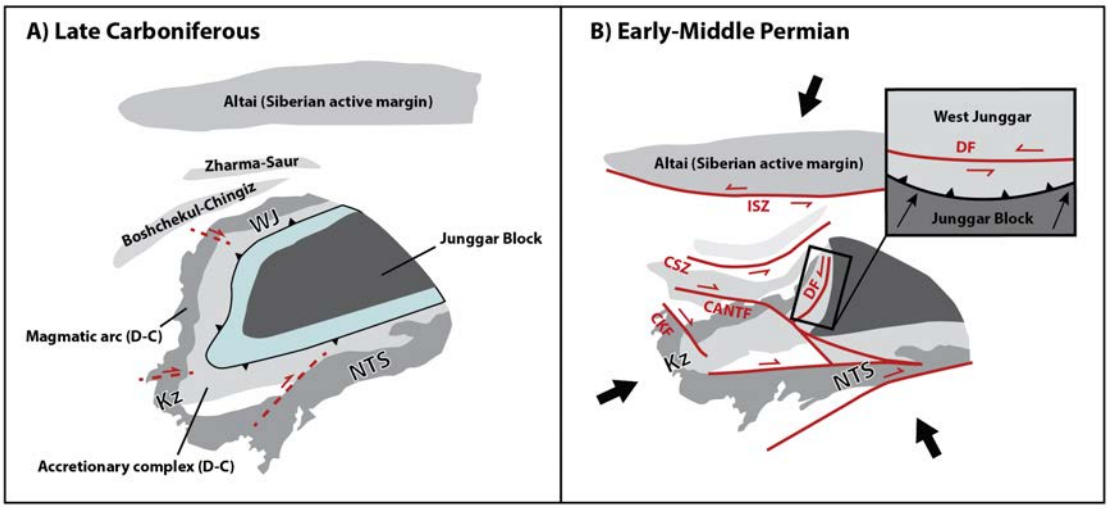

Figure 3.6: Proposed tectonic reconstructions of the West Junggar and surroundings during the late Paleozoic after Choulet et al. (2012b) and Li et al. (2017b). A) Schematic reconstruction for the late Carboniferous showing closure of the Junggar Ocean with oroclinal bending. Initiation of large faults. B) Schematic reconstruction for Early-Middle Permian showing dismemberment of orocline and counter-clockwise rotation of the West Junggar. West Junggar is thrust over the basement rocks of the Junggar Basin. Kz = Kazakhstan, WJ = West Junggar, NTS = North Tianshan, ISZ = Irtysh Shear Zone, CSZ = Char Shear Zone, CANTF = Chingiz-Alakol-North-Tianshan-Fault, DF = Dalabute Fault, CKF = Central Kazakhstan Fault.

Irtysh Shear Zone and Altai Mountains

A study of the Irtysh Shear Zone by Briggs et al. (2007) using a combination of thermobarometry and $^{40}Ar/^{39}Ar$ dating found evidence for rapid exhumation during the early–middle Permian. Monazite Th–Pb dating and $^{40}Ar/^{39}Ar$ amphibole, muscovite, biotite, K-feldspar dating all produced similar ages, indicating rapid cooling at this time. Thermobarometric estimates of the P–T conditions and multi-domain diffusion (MDD) modelling of K-feldspar suggest that from ~280–265 Ma the hanging wall cooled from amphibolite facies to ~150 °C. Slow cooling during the late Permian following this rapid cooling is predicted by K-feldspar MDD modelling. Li et al. (2015d) found evidence for more widespread exhumation in the southern Chinese Altai at ~270 Ma, expanding on the findings of Briggs et al. (2007) and suggesting a regional exhumation event. Further structural studies of the region reinforce the idea that sinistral transpression with a large thrust component led to widespread exhumation in the Chinese Altai and along the Irtysh Shear Zone during the early–middle Permian (Briggs et al., 2009; Li et al., 2016a; Li et al., 2016b). The proposed timing of this exhumation is in agreement with modelled cooling identified in the West Junggar in this study (Fig.3.5).

The thermal history of the region following this phase of activity is revealed by AFT analysis of the Chinese Altai (Yuan et al., 2006) and the Irtysh Shear Zone in NE Kazakhstan (Glorie et al., 2012b) that found mostly Late Cretaceous AFT ages. Fission track studies of the Siberian Altai and Sayan regions further to the north similarly tend to produce Cretaceous ages and generally predict Late Cretaceous cooling (e.g. Glorie et al., 2012a; De Grave et al., 2014; Glorie and De Grave, 2016). Thermal history modelling of samples from the Chinese Altai and Irtysh Shear Zone show temperatures above 120 °C at the beginning of these models in the Late Jurassic or Early Cretaceous and predict cooling through the APAZ during the Late Cretaceous. This implies generally slow and relatively minimal cooling during the early Mesozoic along the Irtysh Shear Zone, between middle Permian exhumation to ~150 °C (Briggs et al., 2009) and the initial time-temperature estimates for the thermal history models. The West Junggar cooled to below the APAZ (~60 °C) by around 260 Ma, and as with the rocks in the hanging wall of the Irtysh Shear Zone (Briggs et al., 2009), experienced tectonic stability throughout the early Mesozoic.

Seismic profiles of the western part of the Junggar Basin are interpreted by Yang et al. (2015) and Li et al. (2017a) to show major reverse fault activity in the Permian, followed by gentle folding in the Late Triassic–Early Jurassic. Yang et al. (2015) found evidence for only minor and localised Early Jurassic reverse faulting in the basin adjacent to the West Junggar, and while the rest of the basin was affected by a major Late Jurassic compressional event, no significant latest Jurassic compressional deformation could be found in the western Junggar Basin (Yang et al., 2015). The West Junggar likely experienced several minor uplift events, perhaps during the

Late Jurassic and Late Cretaceous, but the amount of exhumation was minimal compared to that experienced in the Altai, and was insufficient to expose rock with younger AFT ages. Our results imply less than 1–2 kilometers of exhumation since the end of the Permian, depending on the paleo-geothermal gradient.

Chinese Tianshan

In the Tianshan, the Permian was marked by an episode of major dextral transtension, with significant strike-slip movement along lithospheric-scale faults (e.g. Shu et al., 1999; Wang et al., 2009a; Jolivet et al., 2013). $^{40}Ar/^{39}Ar$ dating of major structures including the North Tianshan Fault, Middle Tianshan Shear Zone and Nikolaev-Natali Tectonic Line show that these structures were active between 285–245 Ma with a dextral shear sense (Shu et al., 1999; Laurent-Charvet et al., 2002; Laurent-Charvet et al., 2003; Wang et al., 2009a; Jong et al., 2009; Wang et al., 2014).

Bedrock AFT evidence of cooling during the latest Paleozoic in the Chinese Tianshan was found by Dumitru et al. (2001) to have been preserved in several areas. To the west of Urumqi, samples from the Erbin Range and 'Domain F' of a N–S transect through the Tianshan recorded cooling through the APAZ at ~270–250 Ma. Zircon (U-Th)/He dating of rocks from the Bayanbulak basin, near the Erbin Range, produced ages of 290–270 Ma (Jolivet et al., 2010). Further to the southwest, at Aksu, AFT thermal history modelling also predicts cooling to above the APAZ by the late Permian (Dumitru et al., 2001). These studies attribute cooling to exhumation as a result of the collision between the Tarim-Central Tianshan and the North Tianshan. Mesozoic and Cenozoic ages are far more prevalent in the Tianshan than late Paleozoic ages due to the large amount of subsequent exhumation experienced by the ranges during repeated reactivation over the last ca. 250 Ma. Many studies cite the far-field effects of tectonic events at the Eurasian margin, such as the collision of the Qiangtang block, Lhasa block, and Kohistan-Dras island arc, the Mongol-Okhotsk ocean closure, and the India-Eurasia collision, as the drivers for Meso-Cenozoic tectonic reactivation in the Tianshan (e.g. Bullen et al., 2001; Dumitru et al., 2001; Sobel et al., 2006b; De Grave et al., 2007; Jolivet et al., 2010; Glorie et al., 2011; Macaulay et al., 2014; Glorie and De Grave, 2016; Gillespie et al., 2017a; Jepson et al., 2018b). As previously described, thermochronological data from the West Junggar records only ambiguous evidence for tectonic reactivation in response to these events.

3.6 Conclusions

Apatite fission track analysis of samples from throughout the West Junggar found clear evidence for fast cooling rates during the early–middle Permian, which we relate to the exhumation of the region during a phase of well-recognised Central Asia-wide deformation. The reorganisation of the cratonic blocks surrounding the Central Asian Orogenic Belt caused widespread strike-slip deformation along lithospheric scale faults, dissecting the Central Asian Orogenic Belt and rotating the major structures of the West Junggar into their present NE–SW orientations. In addition to sinistral fault activity, reverse faulting thrust the West Junggar over the basement of the Junggar Basin. Following the early–middle Permian, the West Junggar was relatively stable. Thermochronometric data near major faults and in high-relief areas suggest a later phase of cooling during the Mesozoic to Cenozoic, but the extent of exhumation was insufficient to expose crust that records the timing of this event with available low-temperature thermochronometers.

Chapter 4

Inherited structure as a control on late Paleozoic and Mesozoic exhumation of the Tarbagatai Mountains, southeastern Kazakhstan

This chapter has been written as a manuscript for publication with Stijn Glorie, Gilby Jepson, Fedor Zhimulev, Dmitriy Gurevich, Martin Danišík, and Alan S. Collins as co-authors.

Statement of Authorship

Title of Paper	Inherited structure as a control on late Paleozoic and Mesozoic exhumation of the Tarbagatai Mountains, southeastern Kazakhstan
Publication Status	☐ Published ☐ Accepted for Publication ☐ Submitted for Publication ☑ Unpublished and Unsubmitted work written in manuscript style
Publication Details	

Principal Author

Name of Principal Author (Candidate)	Jack Gillespie		
Contribution to the Paper	Sample collection, sample preparation, analysis, data reduction, data interpretation, figures, writing		
Overall percentage (%)	70		
Certification:	This paper reports on original research I conducted during the period of my Higher Degree by Research candidature and is not subject to any obligations or contractual agreements with a third party that would constrain its inclusion in this thesis. I am the primary author of this paper.		
Signature		Date	29/05/2019

Co-Author Contributions

By signing the Statement of Authorship, each author certifies that:

i. the candidate's stated contribution to the publication is accurate (as detailed above);

ii. permission is granted for the candidate in include the publication in the thesis; and

iii. the sum of all co-author contributions is equal to 100% less the candidate's stated contribution.

Name of Co-Author	Stijn Glorie		
Contribution to the Paper	Primary supervision, data interpretation		
Signature		Date	29/05/2019
Name of Co-Author	Gilby Jepson		
Contribution to the Paper	Sample collection, data interpretation		
Signature		Date	
Name of Co-Author	Fedor Zhimulev		

Contribution to the Paper	Sample collection, data interpretation, geological background		
Signature		Date	29/05/2019
Name of Co-Author	Dmitriy Gurevich		
Contribution to the Paper	Sample collection, data interpretation, geological background		
Signature		Date	30.05.2019

Name of Co-Author	Martin Danišik		
Contribution to the Paper	Data analysis, data interpretation, methods		
Signature		Date	29/05/2019
Name of Co-Author	Alan S. Collins		
Contribution to the Paper	Data interpretation, secondary supervisor		
Signature		Date	29/05/2019

4.1 Introduction

The Tarbagatai Mountains in eastern Kazakhstan form part of the vast Central Asian Orogenic Belt (CAOB) (Fig. 4.1) (Windley et al., 2007). The Tarbagatai Mountains lie to the north of the Tianshan, the largest intracontinental mountain belt in the world, and a major component of the CAOB. The Tianshan stretches more than 2500km from the China-Mongolia border in the east to Uzbekistan in the west. A multitude of studies have applied low-temperature thermochronology to the Tianshan, particularly in the high-elevation ranges of Kyrgyzstan, attempting to understand the relatively recent episodes of deformation, such as in response to the collision of India with Eurasia (Hendrix et al., 1994; Sobel and Dumitru, 1997; Bullen et al., 2001; Dumitru et al., 2001; Sobel et al., 2006b; De Grave et al., 2007; Jolivet et al., 2010; Glorie et al., 2011; De Grave et al., 2012; De Grave et al., 2013; Macaulay et al., 2014; Käßner et al., 2016a; Bande et al., 2017; Jepson et al., 2018a; Nachtergaele et al., 2018). This ongoing collision is responsible for generating much of the modern topography of the mountain belt (e.g. Tapponnier and Molnar, 1979; Avouac et al., 1993). However, the destruction of the pre-existing landscape through erosion and structural deformation means that evidence of the pre-orogenic history is fragmented and preserved in only certain locations (De Grave et al., 2011a; Jolivet et al., 2013; Glorie and De Grave, 2016; Morin et al., 2019).

This study explores the low-temperature thermochronological record of the Tarbagatai Mountains (maximum elevation 2992m) in order to better understand the development of the landscape and the tectonic history of Central Asia during the late Paleozoic and Mesozoic. The thermotectonic evolution of the ranges centred around the Chingiz-Tarbagatai Fault are reconstructed through inverse thermal history modelling, and the development of the region is compared to other localities throughout the CAOB in order to contextualise the results in the broader tectonic evolution of the Eurasian continent during the late Paleozoic and Mesozoic.

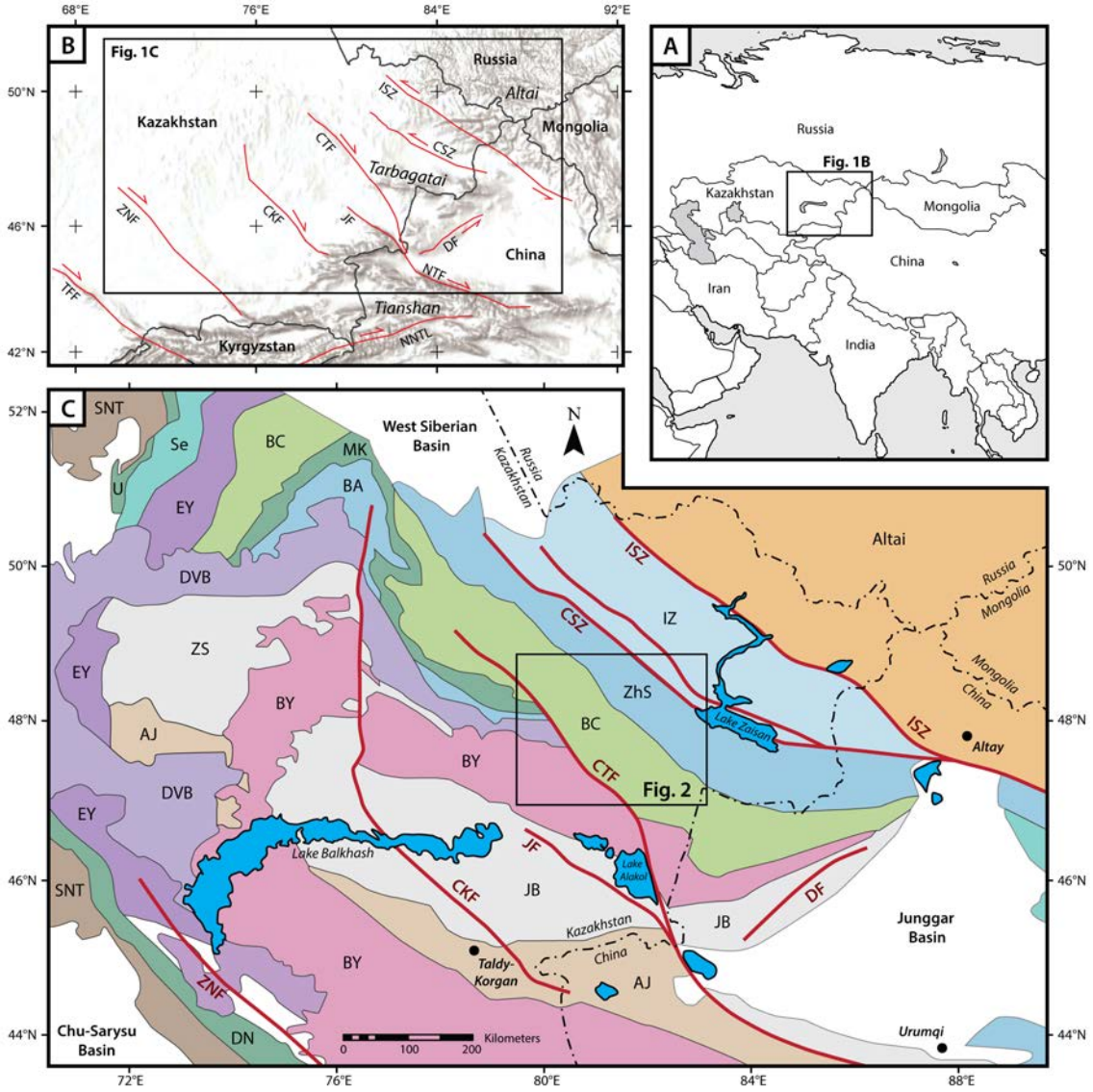

Figure 4.1: Maps showing the location of the study area. A) Location of the study area with respect to international borders. B) Major structures in Central Asia, overlaid on hillshade relief map (Irtysh Shear Zone (ISZ), Char Shear Zone (CSZ), Chingiz-Tarbagatai-Fault (CTF), Dalabute Fault (DF), Junggar Fault (JF), Central Kazakhstan Fault (CKF), North Tianshan Fault (NTF), Nikolaev-Natali Tectonic Line (NNTL), Zhalair-Naiman Fault (ZNF), Talas-Fergana Fault (TFF)). C) Tectonic divisions of the CAOB after Windley et al. (2007) (*Microcontinents*: Aktau-Junggar (AJ), Stepnyak-North Tianshan (SNT); *Volcanic arcs*: Selety (Se), Boshchekul-Chingiz (BC), Baidaulet-Akbastau (BA), Zharma-Saur (ZhS); *Accretionary wedges and suture zones*: Dzalair-Naiman (DN), Urumbai (U), Maikan-Kyzyltas (MK), Erementau-Yili (EY), Zhaman-Sarysu (ZS), Junggar-Balkhash (JB); *Active continental margin arcs*: Devonian Volcanic Belt (DVB), Balkhash-Yili (BY); *Accretionary and collisional belts*: Irtysh-Zaisan (IZ)).

4.2 Background

4.2.1 Paleozoic tectonic history

The Kazakhstan continent, part of the Central Asian Orogenic Belt, developed as a consequence of the progressive closure of the Paleo-Asian Ocean through the accretion and amalgamation of a series of microcontinental fragments and island arcs (Fig. 4.1; Windley et al., 2007). The basement of the Boshchekul-Chingiz arc, which lies in the centre of the study area (Fig. 4.2), is composed of a mixture of oceanic and continental fragments and had a long history of island-arc volcanism spanning the Cambrian–Silurian (Degtyarev et al., 2015). The other, mostly short-lived arcs of the Kazakhstan Orocline also formed during the early Paleozoic and amalgamated by the end of the Silurian (Levashova et al., 2009; Degtyarev et al., 2015).

During the Early Devonian, the Devonian Volcanic Belt (DVB) became the focus of active margin arc magmatism, before it migrated to the Balkhash-Yili arc in the late Devonian (Levashova et al., 2003b; Windley et al., 2007; Degtyarev, 2011). Subduction-related magmatism continued to the south of the Boshchekul-Chingiz arc until the Late Carboniferous. The Devonian–Carboniferous Zharma-Saur island arc, meanwhile, collided with the northern side of the Boshchekul-Chingiz arc during the Late Carboniferous (Chen et al., 2010). Oroclinal bending likely occurred from the Late Devonian through to the Carboniferous–Permian (Levashova et al., 2009; Choulet et al., 2011; Li et al., 2017b; Li et al., 2018). The specifics of this stage of the development of the region are beyond the scope of this paper, and for further details the reader is directed to Li et al. (2018).

Oroclinal bending is strongly implicated in the formation of large NW-SE strike-slip shear zones that experienced a complex pattern of both dextral and sinistral shear during the Permian-earliest Triassic (Choulet et al., 2012a; Li et al., 2018). The Char Shear Zone and the Irtysh Shear Zone experienced synchronous dominantly sinistral deformation during the Permian–earliest Triassic (Fig. 4.1) (Buslov, 2011; Li et al., 2018). In contrast, the Chingiz-Tarbagatai Fault experienced dextral deformation during the Permian, along with other major structures to the south-west (Wang et al., 2007; Choulet et al., 2011). Such structures that experienced Permian dextral deformation include the Central Kazakhstan Fault (CKF), the Junggar Fault (JF), the Zhalair-Naiman Fault (ZNF), and the Karatau-Talas-Ferghana Fault (KTFF). The magnitude of Permian dextral offset along the largest of these structures (e.g. CTF, CKF, KTFF) is estimated to be in the order of several hundred kilometers (Wang et al., 2007; Choulet et al., 2011; Rolland et al., 2013).

4.2.2 Mesozoic–Cenozoic intracontinental deformation

During the Mesozoic-Cenozoic, the Central Asian Orogenic Belt experienced episodic intracontinental reactivation as a result of tectonic events at the Eurasian plate margin (e.g. Sobel et al., 2006b; De Grave et al., 2007; Jolivet et al., 2010). To the south of the Tarbagatai Mountains, in the Tianshan, Late Triassic–Early Jurassic cooling is recorded in areas that did not undergo large amounts of subsequent denudation (e.g. Dumitru et al., 2001; De Grave et al., 2011a). Jurassic and Cretaceous apatite fission track ages are widespread throughout the Tianshan, and record some evidence for episodes of rapid cooling, but the precise timing, and spatial extent of these thermotectonic events varies considerably (Sobel and Dumitru, 1997; Bullen et al., 2001; Dumitru et al., 2001; Sobel et al., 2006b; Glorie et al., 2010; De Grave et al., 2012; Käßner et al., 2016b; Gillespie et al., 2017b; De Pelsmaeker et al., 2018). Localised Early Cretaceous cooling along major NW-SE structures comparable to those in the Tarbagatai Mountains has been detected in geographically widespread locations across western Central Asia (Jepson et al., 2018c; Glorie et al., 2019). Broadly, however, the Tianshan during the Jurassic–Cretaceous was characterised more by slow cooling than any singular and widespread uplift event (Morin et al., 2019).

Beginning in the Oligocene–Miocene, rapid cooling and uplift throughout the Tianshan occurred in response to the India-Eurasia collision (e.g. Hendrix et al., 1994; Sobel and Dumitru, 1997). This phase of uplift is ongoing to the present day and is responsible for the modern topography of the Tianshan.

To the north of the Tarbagatai Mountains (Fig. 4.1), the Altai is dominated by thermochronological evidence for Cretaceous cooling, with Late Triassic–Early Jurassic cooling also recorded in some locations (Yuan et al., 2006; De Grave et al., 2011b; Glorie et al., 2012a). Late Cretaceous rapid cooling occurred in the Chinese Altai (Yuan et al., 2006) and along the Irtysh Shear Zone in NE Kazakhstan (Glorie et al., 2012b). Fault dominated profiles from the Siberian Altai experienced rapid cooling during the Late Cretaceous–Early Paleogene, while the basement distal to major faults records slow cooling throughout the Cretaceous (Glorie et al., 2012a).

4.2.3 Basin records

The Tacheng Basin lies to the immediate south of the Tarbagatai Mountains in westernmost China, along the border with Kazakhstan (Fig. 4.6). Seismic reflection profiles across the basin, and drillhole data in the southern part of the basin, indicate that the basin fill is dominantly Paleozoic, with the top few hundred meters composed of Jurassic and Cenozoic rocks (Li et al., 2015b). Three major unconformities separate the Carboniferous, early Permian, Jurassic, and Cenozoic sequences (Li et al., 2015b). In the northern section of the basin, Cenozoic rocks lie uncon-

Table 4.1: Location and lithological data

Sample	ISGN	Latitude (WGS84)	Longitude (WGS84)	Altitude (m a.s.l)	Locality	Lithology
TA01	IEJAG0026	47.2410	80.8690	688	Balkhash-Yili arc	Granodiorite
TA02	IEJAG0027	47.2824	81.7570	2228	Southern B-C arc	Granite
TA04	IEJAG0029	47.2628	81.7558	1626	Southern B-C arc	Granite
TA05	IEJAG002A	47.2524	81.7497	1356	Southern B-C arc	Granite
TA06	IEJAG002B	47.3006	81.3397	1169	Southern B-C arc	Granite
TA07	IEJAG002C	47.3080	81.1530	1144	Balkhash-Yili arc	Diorite
TA10	IEJAG002F	47.6245	80.8524	921	Southern B-C arc	Granodiorite
TA11	IEJAG002G	47.6303	80.8890	912	Southern B-C arc	Granite
TA14	IEJAG002J	47.7884	81.1836	927	Northern B-C arc	Granite
TA15	IEJAG002K	47.8911	81.2743	1017	Northern B-C arc	Granite
TA16	IEJAG002L	47.6821	81.5452	1175	Southern B-C arc	Granite
TA17	IEJAG002M	47.7897	81.7192	999	Northern B-C arc	Granite
TA18	IEJAG002N	47.6898	82.0928	987	Northern B-C arc	Diorite
TA19	IEJAG002O	47.7277	82.1852	975	Northern B-C arc	Granodiorite
TA20	IEJAG002P	48.2070	81.9542	702	Zharma-Saur arc	Granodiorite
TA22	IEJAG002R	48.6402	82.0473	597	Zharma-Saur arc	Diorite
TA23	IEJAG002S	48.9497	80.9177	593	Zharma-Saur arc	Diorite
TA26	IEJAG002V	48.4082	80.3299	751	Northern B-C arc	Granodiorite
TA27	IEJAG002W	47.9247	80.2717	624	Balkhash-Yili arc	Granodiorite

Note: IGSN = international geosample number, m a.s.l. = meters above sea level, B-C = Boshchekul-Chingiz

formably on what are presumed to be rocks of the Boshchekul-Chingiz arc, as the southern boundary of the arc passes somewhere under the middle of the Tacheng Basin.

The Zaisan Basin, to the north-east of the study area, contains thick Paleozoic sequences like the Tacheng Basin, but also features a more extensive record of Mesozoic and Cenozoic sedimentation (Fig. 4.6). Seismic reflection profiles reveal high-angle thrust faults in the basin and growth strata in the Meso-Cenozoic sequences that are interpreted by Li et al. (2015a) to be reactivated Permian transpressional structures. The Zaisan basin sedimentary record contains four major unconformities. These unconformities occur at the end of the Carboniferous, from the mid-Permian to Early Triassic, during the Late Triassic, and from the Late Jurassic through the Cretaceous (Fig. 4.6).

For this study, igneous samples were collected from the Boshchekul-Chingiz, Balkhash-Yili, and Zharma-Saur arcs for low-temperature thermochronological analysis (Table 4.1).

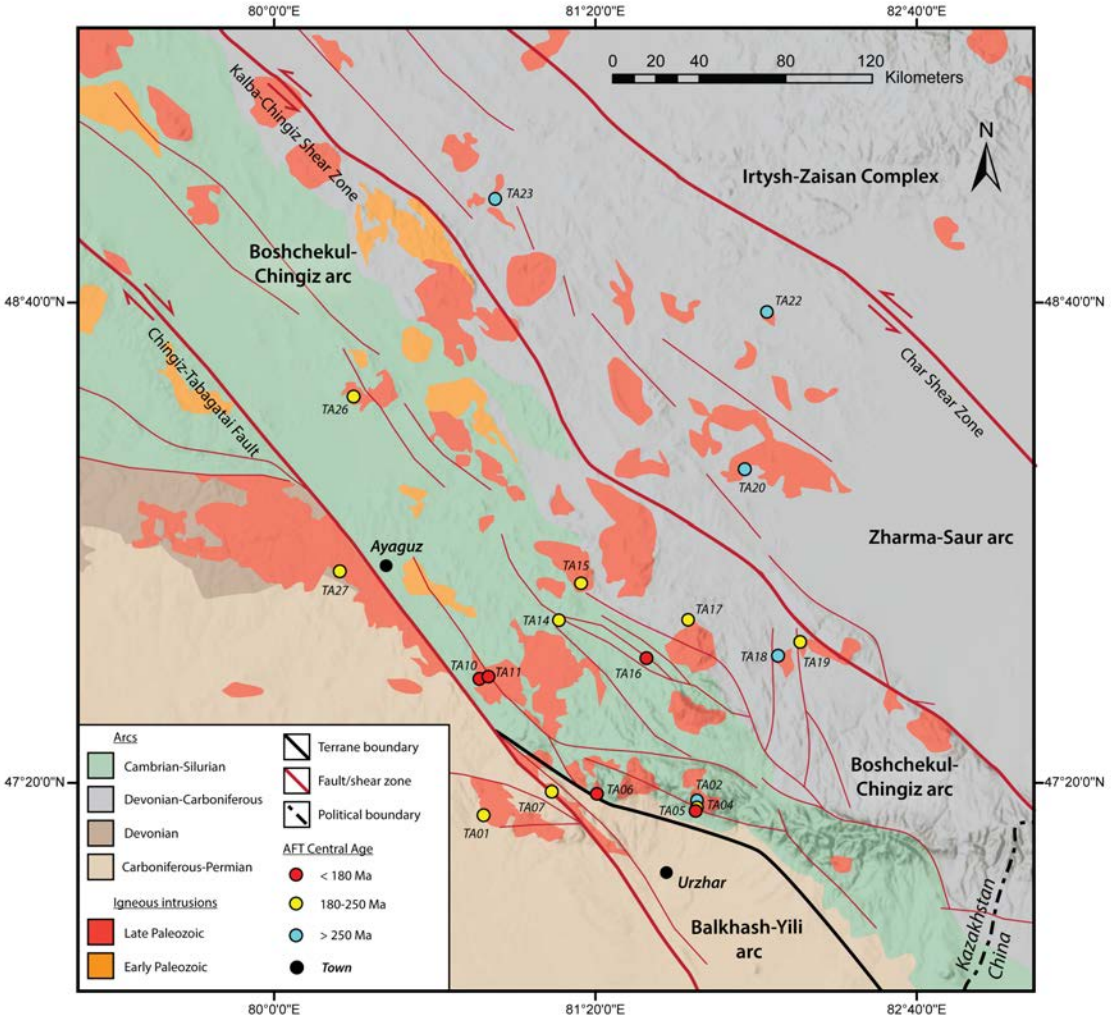

Figure 4.2: Simplified geological map of the study location, showing major tectonic divisions and igneous intrusions.

4.3 Methods

4.3.1 Apatite fission track dating

The apatite fission track (AFT) method provides information about the thermal history of a sample as it passes through the 'apatite partial annealing zone' (APAZ), a temperature window that generally spans the range of ~60-120°C depending on the chemical composition of the apatite (Gleadow et al., 1986a; Green et al., 1986; Barbarand et al., 2003). Apatite fission track analysis was performed at the University of Adelaide. Individual apatite grains were hand picked and mounted in epoxy resin, then ground and polished to obtain an internal surface with 4π geometry (Tagami and O'Sullivan, 2005). Mounts were immersed in 5M HNO_3 at 20°C for 20 seconds to reveal the fission tracks. A 5nm gold coating was applied to the mounts prior to image capture using the Autoscan System (Gleadow et al., 2009). Fission track density and confined track lengths were manually measured using the FastTracks software. The ^{238}U concentration of apatite grains was determined using a 213nm NewWave laser ablation system coupled to an Agilent 7900 mass spectrometer with NIST SRM 610 as the primary standard (e.g. Hasebe et al., 2004; Chew and Donelick, 2012). During LA-ICP-MS analysis, uranium and lead isotopes were also measured in order to determine the U–Pb age of the apatite from each sample. See appendices for details of this process. Data reduction for fission track analysis was performed using the X_Trace_Elements_IS DRS in Iolite (Paton et al., 2011) with ^{43}Ca as the internal elemental standard. Age calculation was performed using a zeta-calibration factor (Hurford and Green, 1983; Hasebe et al., 2013) based on the analysis of the Durango apatite (McDowell et al., 2005) according to the equations of Vermeesch (2017).

4.3.2 Apatite (U-Th-Sm)/He dating

The apatite (U-Th-Sm)/He (AHe) dating method relies on the accumulation of radiogenic helium in apatite crystals (Ehlers and Farley, 2003). The helium generated by the α decay of ^{238}U, ^{235}U, ^{232}Th, and ^{147}Sm is lost from the grain by α ejection and thermally activated volume diffusion. Partial retention of He occurs between ~40°C and ~85°C (depending on the crystal size and cooling rate), allowing for the refinement of the low-temperature thermal history reconstructed from the AFT data (Wolf et al., 1998).

Samples for (U-Th-Sm)/He analysis were selected from the samples that produced the youngest AFT central ages and were of good quality according to the guidelines of Farley (2002). (U-Th-Sm)/He dating was conducted on three samples (TA06, TA10, and TA16) of apatite at the John de Laeter Centre (Curtin University) following the protocols described in Danišík et al. (2012b). Apatite crystals

were hand-picked following the recommendation of Farley (2002) and then photographed, measured for physical dimensions and loaded in Pt microtubes. ^{4}He was extracted at 950°C under ultra-high vacuum using a diode laser and measured by isotope dilution on a Pfeiffer Prisma QMS-200 mass spectrometer. A "re-extract" was run after each sample to verify complete outgassing of the crystals. He gas results were corrected for blank, determined by heating empty microtubes using the same procedure. After the ^{4}He measurements, tubes containing the crystals were retrieved from the laser cell, spiked with ^{235}U and ^{230}Th and dissolved (Evans et al., 2005). Sample, blank, and spiked standard solutions were analysed by isotope dilution for ^{238}U and ^{232}Th, and by external calibration for ^{147}Sm on an Agilent 7500 ICP-MS. The total analytical uncertainty (TAU) was calculated as a square root of sum of squares of uncertainty on He and weighted uncertainties on U, Th, Sm and He measurements, and is typically <5% (1σ). The raw apatite (U-Th-Sm)/He ages were corrected for alpha ejection (Ft correction) after Farley et al. (1996), whereby a homogenous distribution of U, Th and Sm was assumed for the crystals.

Replicates with associated uncertainties were used to calculate the geometric mean and error-weighted standard deviation as representative numbers for each sample.

Replicate analyses of Durango apatite (n = 4) measured over the period of this study as internal standard yielded a mean (U-Th-Sm)/He age of 31.9 ± 1.0 Ma, which is in good agreement with the reference Durango (U-Th-Sm)/He age of 31.02 ± 1.01 Ma (Farley et al., 1996; McDowell et al., 2005).

4.4 Results

4.4.1 Apatite fission track

Apatite fission track dating was performed on nineteen samples. These samples produced AFT central ages ranging from 132.5 ± 6.0 Ma to 301.1 ± 17.3 Ma (Table 4.2). The mean track lengths (MTL) of measured confined tracks in the fourteen samples with >30 lengths vary between 12.1 and 13.8 μm (Fig. 4.3).

The AFT data can be divided into four groups based on geographical location and the similarity of the AFT data recorded by each group of samples.

Samples TA-01, TA-07, and TA-27 were collected from rocks of the Balkhash-Yili arc, in the area to the south-east of the Chingiz-Tabagatai Fault (Fig. 4.2). These samples record AFT central ages of 186.6–213.4 Ma and MTLs of 13.1–13.6 μm. Samples taken from the Boshchekul-Chingiz arc can be divided into two categories based on their geographical location and proximity to NW-SE trending faults. Samples TA-02, TA-04, TA-05, TA-06, TA-10, TA-11, and TA-16 were collected from the southern section of the Boshchekul-Chingiz arc sampling area and are gener-

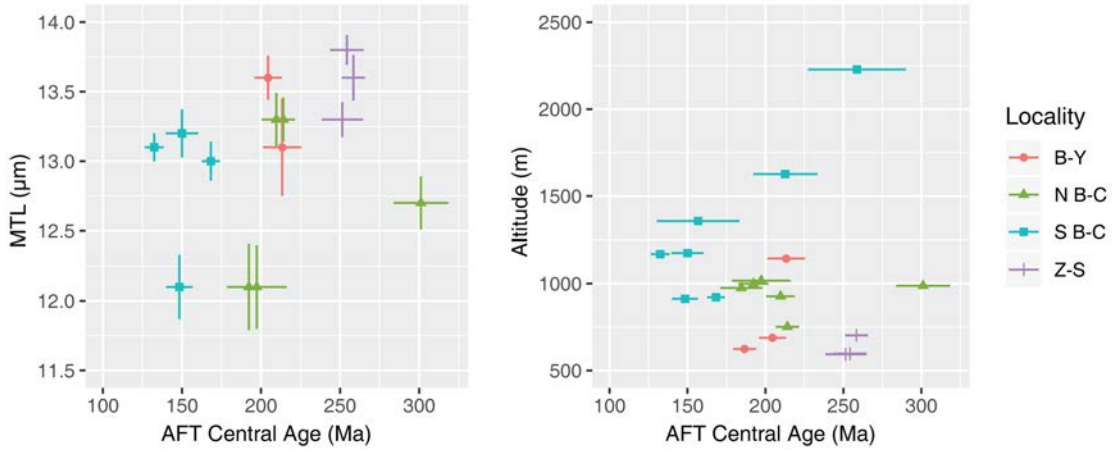

Figure 4.3: AFT central age compared to MTL (left) and altitude (right) of sample. B-Y = Balkhash-Yili, N B-C = northern Boshchekul-Chingiz, S B-C = southern Boshchekul-Chingiz, Z-S = Zharma-Saur. Note that some samples do not have confined track length measurements and are not featured on the left-hand plot.

ally proximal to NW-SE striking faults. These samples record AFT central ages of 132.5–258.7 Ma and MTLs of 12.1–13.2 μm. Samples TA-14, TA-15, TA-17, TA-18, TA-19, and TA-26 were collected in the north of the sampled section of the Boshchekul-Chingiz arc. These samples record AFT central ages of 184.5–301.1 Ma and MTLs of 12.1–13.3 μm. Samples TA-20, TA-22, and TA-23 were taken from rocks of the Zharma-Saur arc, to the north-east of the Boshchekul-Chingiz arc. These samples record AFT central ages of 251.4–258.4 Ma and MTLs of 13.3–13.8 μm.

4.4.2 Apatite (U-Th-Sm)/He

Apatite (U-Th-Sm)/He analysis was carried out on samples TA-06, TA-10, and TA-16, which all produced Middle Jurassic–Early Cretaceous AFT central ages. Four grains were dated from each sample. Intrasample age variability is reasonably low. Across all three samples, there is no clear relationship between raw AHe age and eU (Fig. 4.4). There is a positive relationship between raw AHe age and grain size across the three samples, which is clearer among the analyses from TA06 than in the other samples. These relationships indicate that the age variation that does exist can be explained to a large extent by the effects of grain size. Applying the α-ejection correction (Farley et al., 1996) produces corrected ages that range from 136.3–86.0 Ma (Table 4.3). TA06 has a weighted corrected mean age of 113.9 $\pm$ 10.8 Ma ($p(\chi^2) = 0.71$), and TA16 a weighted corrected mean age of 104.8 $\pm$

Table 4.2: Apatite fission track data

Sample	n	N_s	ρs ($x10^5 cm^{-2}$)	^{238}U (ppm)	$P(\chi^2)$	t (Ma)	± 1σ	D_{par} (μm)	MTL (μm)	SD	N_L
Balkhash-Yili											
TA01	37	925	13.65	13.32	0.14	204.5	8.6	1.89	13.6	1.0	40
TA07	34	354	4.73	4.51	0.29	213.4	12.1	1.51	13.1	1.4	16
TA27	17	944	40.54	45.3	0.65	186.6	7.4	2.63	-	-	-
Boshchekul-Chingiz (S)											
TA02	20	113	4.03	2.80	0.13	258.7	31.3	2.05	-	-	-
TA04	25	121	4.47	4.28	0.40	212.7	20.6	1.78	-	-	-
TA05	4	42	4.34	7.05	0.40	156.8	26.5	1.55	-	-	-
TA06	38	624	6.59	10.22	0.65	132.5	6.0	1.70	13.1	1.1	119
TA10	36	1424	19.03	23.30	0.10	168.3	5.7	2.00	13.0	1.4	100
TA11	27	506	13.16	13.21	0.16	148.4	8.3	1.31	12.1	1.5	42
TA16	32	343	5.74	6.81	0.02	150.0	10.3	1.04	13.2	1.4	65
Boshchekul-Chingiz (N)											
TA14	31	627	11.11	11.95	0.84	209.7	9.2	1.74	13.3	1.1	33
TA15	21	439	15.08	12.75	0.00	197.3	18.8	1.18	12.1	1.7	32
TA17	34	971	8.52	9.63	0.00	192.3	9.7	1.10	12.1	1.7	30
TA18	26	837	11.01	5.73	0.00	301.1	17.3	1.68	12.7	1.4	54
TA19	30	672	8.67	6.57	0.00	184.5	13.5	1.06	-	-	-
TA26	38	1630	10.97	9.90	0.07	214.1	7.4	1.80	13.3	1.2	58
Zharma-Saur											
TA20	40	1536	6.00	4.71	0.90	258.4	7.3	1.46	13.6	1.1	45
TA22	39	791	7.13	5.52	0.21	254.3	10.6	1.88	13.8	0.9	71
TA23	36	1238	16.35	9.45	0.00	251.4	13.0	1.53	13.3	1.2	91

n = number of grains analysed, N_s = number of spontaneous tracks counted, ρs = spontaneous track density, ^{238}U = average uranium concentration of the analysed grains, $P(\chi^2) = (\chi^2)$ probability after Galbraith (1981), D_{par} = mean track etch pit diameter parallel to the crystallographic c-axis, MTL = mean confined track length, SD = standard deviation of the track length distribution, N_L = number of confined track length measurements.
$\zeta = 2.054 \pm 0.112 \times 10^{-3}$

14.2 Ma ($p(\chi^2) = 0.056$). TA10 is slightly overdispersed with a $p(\chi^2)$ value of 0.043. A weighted mean age of 112.1 ± 22.6 Ma can be calculated for TA10 using IsoplotR, taking into account the overdispersion of the analyses when calculating the uncertainty on this age (Vermeesch, 2018). The AHe analyses were incorporated individually into the QTQt software package (Gallagher, 2012), which was used to apply radiation damage and grain size effect corrections during the process of thermal history modelling.

Table 4.3: Apatite (U-Th-Sm)/He data

Sample	Th (ng)	U (ng)	Sm (ng)	He (ncc)	TAU (%)	Th /U	eU (ppm)	Raw age (Ma)	±1σ (Ma)	Ft	r (μm)	Cor. Age (Ma)	±1σ (Ma)
TA06													
1	0.086	0.020	0.936	0.466	3.7	4.23	14.96	79.5	2.9	0.67	48	119.1	7.4
2	0.078	0.017	0.776	0.360	2.8	4.46	16.12	70.0	2.0	0.65	45	108.2	6.2
3	0.070	0.016	0.594	0.342	3.8	4.31	15.29	74.8	2.8	0.65	43	115.0	7.2
4	0.113	0.029	1.091	0.615	2.7	3.82	19.14	77.7	2.1	0.67	49	115.2	6.6
TA10													
1	0.033	0.019	0.138	0.206	4.5	1.78	15.82	61.4	2.8	0.62	41	99.1	6.7
2	0.059	0.034	0.135	0.439	3.4	1.70	44.65	72.8	2.5	0.53	33	136.3	14.4
3	0.028	0.019	0.163	0.228	4.6	1.43	27.09	68.9	3.2	0.54	34	127.2	14.0
5	0.004	0.031	1.817	0.422	3.0	0.14	20.60	73.8	2.3	0.63	41	116.5	6.8
TA16													
1	0.016	0.005	1.043	0.104	2.8	3.13	7.10	49.2	1.4	0.57	37	86.0	8.9
2	0.017	0.007	1.087	0.158	2.3	2.50	7.21	65.3	1.5	0.61	40	107.8	5.9
3	0.036	0.013	0.859	0.202	3.6	2.70	40.00	57.3	2.1	0.44	28	131.8	20.3
4	0.059	0.032	1.600	0.468	2.8	1.81	43.81	65.0	1.8	0.55	35	117.5	12.2

Note: Th is ^{232}Th, U is ^{238}U, and Sm is ^{147}Sm in ng (nanogram). Analytical uncertainty for U, Th, and Sm were in the range of 0.8–6.9%. He is ^{4}He in ncc (nanocubic centimeter). Analytical uncertainty for helium gas analysis ranged from 0.9–1.7%. TAU is the total analytical uncertainty. Raw Age is the uncorrected He age. Ft is the alpha recoil correction factor after Farley et al. (1996). r is the equivalent spherical radius. Cor. Age is the corrected He age. See appendices for full analytical details.

4.4.3 Thermal History Modelling

Inverse thermal history modelling was conducted in QTQt v. 5.7.0 (Gallagher, 2012). Thermal history models were generated for the fourteen samples that produced sufficient (>30) confined tracks. One of the remaining samples (TA07) produced only 16 confined track length measurements, and this sample was modelled but displayed with a dashed line to indicate the low level of certainty associated

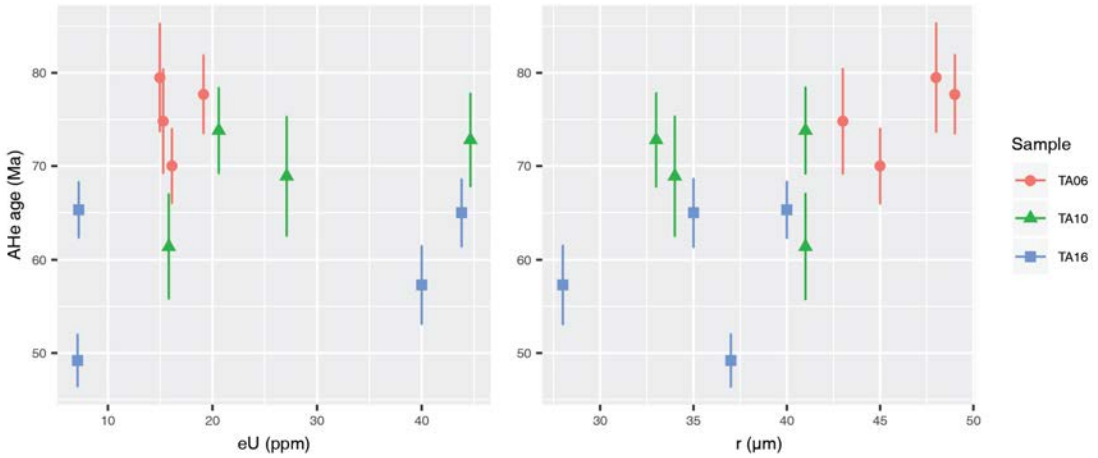

Figure 4.4: Raw AHe age as a function of effective uranium (left) and equivalent spherical radius (right).

with this model. In the case of samples TA06, TA10, and TA16, the AHe data was also incorporated into the models. Apatite U–Pb ages were used to constrain the high-temperature start point for the models.

The reader is referred to the appendices for details of the U–Pb dating, model parameters, and other associated data.

Zharma-Saur samples

The three samples from the Zharma-Saur arc (TA20, TA22, and TA23), to the NW of the Boshchekul-Chingiz arc, all produce thermal history models that predict rapid cooling through the APAZ at 270–245 Ma (Fig. 4.5).

Boshchekul-Chingiz (N) samples

Samples from the northern part of the sampled area of the Boshchekul-Chingiz arc (TA14, TA15, TA17, TA18, and TA26) produce thermal history models that indicate cooling through the APAZ at 230–200 Ma (Fig. 4.5). These models either indicate cooling to below the APAZ by 200 Ma, or indicate a sharp decrease in cooling rates at around this time if they remain in the APAZ . The exception is the model for TA18 that suggests much earlier rapid cooling through the APAZ by 300 Ma based on the AFT central age of this sample.

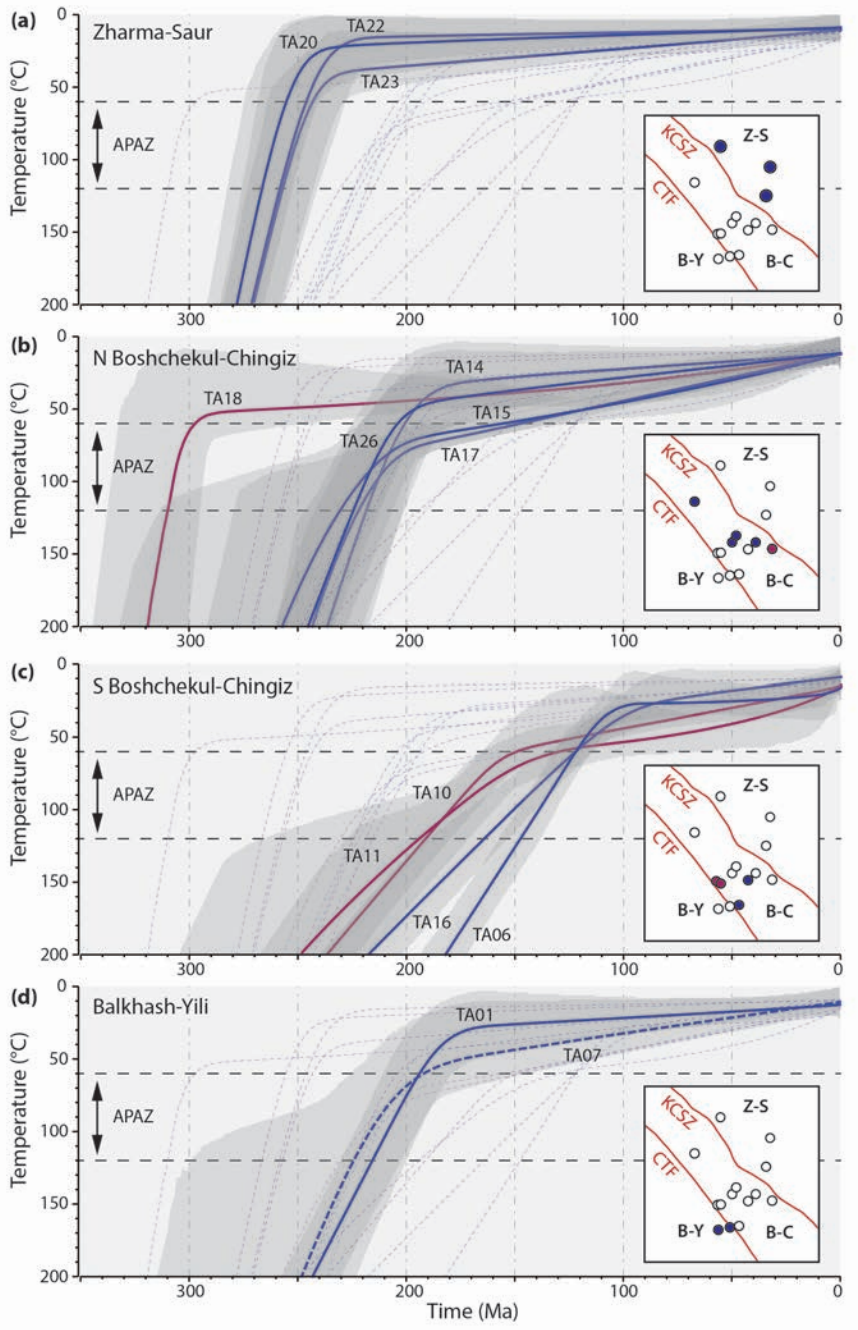

Figure 4.5: Thermal history models produced in QTQt based on the thermochronological data collected for this study. Blue lines indicate expected model, grey envelope denotes 95% confidence interval. Narrow dotted lines show the expected models for other samples to aid comparison. Dashed line for TA07 expected model indicates low confidence due to low number of measured confined tracks. Inset shows schematic map of the study area (Fig. 4.2) with major structures (CTF = Chingiz-Tarbagatai Fault, KCSZ = Kalba-Chingiz Shear Zone) and the highlighted locations of modelled samples in blue. Samples shown in purple are highlighted for ease of identification on the inset map.

Boshchekul-Chingiz (S) samples

Samples from the southern part of Boshchekul-Chingiz arc (TA06, TA10, TA11, and TA16) generally lie close to major structures and record Middle Jurassic to Early Cretaceous AFT central ages (Fig. 4.5). Samples TA06, TA10, and TA16 were also analysed using the AHe method in an attempt to better understand the timing and rates of cooling in these samples.

The thermal history models for the samples from this area are displayed on Fig. 4.5. The adjacent samples TA10 and TA11 (highlighted in purple) produce comparable thermal history models that suggest moderate cooling rates through the APAZ from ~200–150 Ma (Fig. 4.5). Samples TA16 and TA06 produce thermal history models that indicate cooling occurred later than for TA10 and TA11. Models for TA16 and TA06 enter the APAZ at about 165 Ma in the case of TA16, or 145 Ma in the case of TA06 (Fig. 4.5). The cooling rate is more rapid in TA06 than TA16. The model for TA06 predicts cooling to temperatures <40 °C (constrained by AHe data) prior to ~110 Ma. There is an inflection point in the model at this time for TA06 that indicates a change to very slow cooling rates following this phase of rapid cooling.

Balkhash Yili samples

The two modelled samples to the SW of the Chingiz-Tarbagatai Fault (TA01 and TA07) record similar thermal histories to those from the northern part of the Boshchekul-Chingiz sampling area, with moderate cooling rates through the APAZ at 230–195 Ma (Fig. 4.5).

4.5 Discussion

Episodes of enhanced cooling predicted by the inverse thermal history modelling of AFT and AHe data display a clear temporal relationship with two of the unconformities in the basins flanking the study area (Fig. 4.6). This suggests that during several distinct episodes in the late Paleozoic and early Mesozoic, eastern Kazakhstan widely experienced exhumation, and may have been an area of positive relief as a result of regional uplift.

4.5.1 Mid-Permian–Early Triassic

Thermal history models based on AFT data from the Zharma-Saur arc suggest that the area experienced a phase of rapid cooling during the mid Permian to earliest Triassic. At this time both the Tacheng and Zaisan basins record erosional unconformities. This evidence suggests that the cooling recorded by the AFT data was

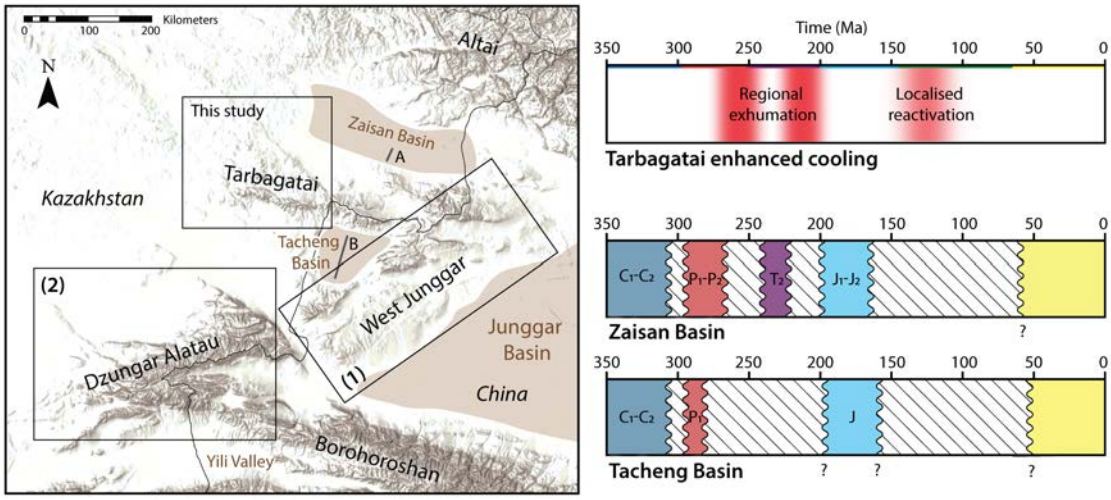

Figure 4.6: Hillshade DEM of study area and surrounding regions. Locations of other low-temperature thermochronological studies indicated by boxes - (1) Chapter Three of this thesis, (2) Glorie et al., 2019. Lines A and B indicate position of seismic reflection profiles in Li et al. (2015a) and Li et al. (2015b) respectively. Top right indicates timing of modelled cooling in the Tarbagatai. Bottom right shows age of sediments in basins and the timing of unconformities.

related to the exhumation of the area, likely during transpressional deformation (e.g. Choulet et al., 2012a; Li et al., 2015d, Chapter 3).

Evidence for strike-slip deformation is found throughout Central Asia for this time period, with $^{40}Ar/^{39}Ar$ dating of many major structures producing Permian–earliest Triassic ages (Shu et al., 1999; Laurent-Charvet et al., 2003; Briggs et al., 2007; Wang et al., 2009a; Rolland et al., 2013; Li et al., 2015d). This Permian deformation is a result of the rotation of Siberia relative to Baltica and Tarim following the final amalgamation of the Central Asian Orogenic Belt and the closure of the Paleoasian Ocean (Allen et al., 1995; Windley et al., 2007). This block rotation caused a complex pattern of deformation across the newly amalgamated CAOB, dissecting the Kazakh Orocline with hundred to thousand-kilometer scale strike-slip structures (Choulet et al., 2011; Buslov, 2011; Li et al., 2018). Structures to the north-east of the Kazakhstan Orocline, such as the North East, Irtysh, Char, and Kalba-Chingiz Shear Zones experienced sinistral offset at this time (Buslov et al., 2004; Briggs et al., 2009; Li et al., 2015d), while in the south and west dextral offset was dominant along the Chingiz-Tarbagatai, Junggar, Central Kazakhstan, and Karatau-Talas-Ferghana faults (Wang et al., 2007; Choulet et al., 2011; Rolland et al., 2013).

Thermochronological and structural data from the Irtysh Shear Zone, Chinese Altai, and West Junggar all record evidence for exhumation during the early–mid Permian. The hanging wall of the Irtysh Shear Zone was exhumed during sinistral transpression south-westwards over the East and West Junggar, while the West Junggar was thrust south-eastwards over the Junggar Basin (e.g. Briggs et al., 2009; Li et al., 2015d; Li et al., 2017a, Gillespie et al., in press).

Permian offset along the well-studied Karatau-Talas-Fergana Fault in the west of Central Asia was dominantly dextral, and this area also experienced substantial deformation and exhumation during the late Permian–early Triassic (Rolland et al., 2013). East–west shortening generated N–S folds in the Karatau Ranges (Burtman, 1980), while zircon fission track thermochronology records cooling at 270–240 Ma (Jepson, 2018). Deformation at this time in the southern part of the Central Asian Orogenic Belt is linked to the collision of the Tarim craton to the south (Jepson et al., 2018c).

In the Tianshan, Permian $^{40}Ar/^{39}Ar$ ages from major shear zones have been found (Shu et al., 1999; Laurent-Charvet et al., 2003; Wang et al., 2009a; Wang et al., 2014), and there is also low-temperature thermochronological evidence for Permian tectonic activity preserved (Dumitru et al., 2001; Jolivet et al., 2010). AFT and zircon (U-Th)/He ages from several locations in the Chinese Tianshan record exhumation during the Permian, although these ages are rare. The thermal history record of Permian exhumation in the Tianshan has mostly been removed via Mesozoic–Cenozoic exhumation and erosion (Glorie and De Grave, 2016).

The low-temperature thermochronological data presented in this study suggests that Permian regional exhumation occurred throughout the areas to the west of the Junggar Basin, including the West Junggar and proximal areas of eastern Kazakhstan. Subsequent Mesozoic exhumation of the Tarbagatai to the SW of the Kalba-Chingiz Shear Zone (Fig. 4.2) erased AFT evidence of this event in most of the study area.

4.5.2 Late Triassic

Evidence for a thermotectonic event during the Late Triassic to earliest Jurassic (230–195 Ma) is widespread in the study area. Thermal history modelling of samples from both the Boshchekul-Chingiz and Balkhash Yili arcs indicate that cooling occurred at this time across most of the study area to the SW of the Kalba-Chingiz Shear Zone. Samples that record cooling at this time tend to have shorter lengths if they have younger (i.e. earliest Jurassic) central ages, as in the case of TA15 and TA17, while samples with slightly older (Late Triassic) central ages have longer lengths, such as TA01, TA14, and TA26. This may indicate that samples with Early Jurassic central ages were not cooled entirely through the APAZ during the Late

Triassic, and instead experienced partial annealing for some time following faster cooling in the Late Triassic. The Zaisan Basin evolved into a contractional basin by the Late Triassic, and short-lived uplift and exhumation in the basin was followed by the deposition of uncomformably overlying Early and Middle Jurassic sedimentary rocks (Li et al., 2015d).

The northern Tarim, southern Junggar, and Turpan-Hami Basins contain coarse Late Triassic sediments interpreted to be related to an episode of deformation and uplift in the Tianshan at this time (Hendrix, 2000). Conglomerates of this age also exist on the eastern Junggar Basin margin (Vincent and Allen, 2001). Corresponding thermochronological evidence for this event is found throughout the Tianshan, often in locations where ancient landforms survive in uplifted plateaus or intramontane basins (Dumitru et al., 2001; De Grave et al., 2011a; Jolivet et al., 2010). Late Triassic deformation in the Tianshan is typically accommodated by the reactivation of Paleozoic structures (e.g. De Grave et al., 2007; Jolivet et al., 2010), and this is also the case in the Tarbagatai, where the Kalba-Chingiz Shear Zone delimits the northern extent of Triassic exhumation (Fig. 4.2).

The evidence for a Late Triassic to earliest Jurassic tectonic event recorded in sedimentary basins and by thermochronometers throughout Central Asia is generally interpreted to indicate that a phase of exhumation occurred at this time, in response to the collision of the Qiangtang terrane at the southern margin of Eurasia (Schwab et al., 2004; Zhai et al., 2011; Glorie and De Grave, 2016; Jepson et al., 2018c).

An alternative possibility is that the Late Triassic cooling recorded in the Tarbatagai Mountains is the result of exhumation due to ongoing erosion of the Permian topography. This interpretation implies that the erosional denudation and general flattening of the Central Asian landscape that characterises the Jurassic could have begun during the Triassic (Jolivet et al., 2013).

4.5.3 Early–Middle Jurassic

Thermochronological results from throughout Central Asia suggest exhumation rates were generally slow in the Early-Middle Jurassic (Dumitru et al., 2001; Jolivet et al., 2010). The development of planation surfaces in many locations from western Mongolia to Kyrgyzstan is thought to have begun during this period, as earlier topography was worn down amid humid conditions (Jolivet et al., 2007; Morin et al., 2018). Arid conditions in Central Asia since the Late Jurassic and generally low denudation rates are identified as key factors in the preservation of these features (Hendrix et al., 1992; Guerit et al., 2016; Morin et al., 2019).

Thermochronological data from the Tarbagatai Mountains suggest that this period was characterised by slow cooling and low exhumation rates, with probably low relief.

4.5.4 Late Jurassic–Cretaceous

The thermotectonic history of Central Asia during the Late Jurassic and Cretaceous is complex and spatially variable. Broadly, however, these periods were characterised by localised tectonic activity and the ongoing development of planation surfaces in many locations away from major structures (Jolivet et al., 2013; Morin et al., 2019).

Late Jurassic–Early Cretaceous

Thermochronological analysis from this study found Late Jurassic–Early Cretaceous AFT and Early Cretaceous AHe ages close to the Chingiz-Tarbagatai Fault. Li et al. (2015d) interpret that Late Jurassic–Cretaceous thrust faults in the Zaisan basin arose mostly from the reactivation of existing structures. Reactivation of the Chingiz-Tarbagatai Fault at a similar time to these structures may imply similar compressional kinematics. The modelled slower cooling of the Jurassic AFT central age samples from the southern Boshchekul-Chingiz area indicates that these samples resided in the APAZ for some time prior to cooling to lower temperatures in the Early Cretaceous, as indicated by the AFT data from TA06 and the Early Cretaceous AHe ages from these samples. Evideince for this episode of cooling is found in a limited area to the north of the Chingiz-Tarbagtai Fault, suggesting that only localised deformation occurred at this time.

Early Cretaceous reactivation in the Dzungarian Alatau to the south of the Tarbagatai Mountains is comparable to the pattern of deformation in the Tarbagatai Mountains (Glorie et al., 2019). In the Dzungarian Alatau, the major Central Kazakhstan Fault is the locus of reactivation, with younger ages found around the fault in comparison to the surrounding area (Glorie et al., 2019). The sample locations proximal to the fault preserve Early Cretaceous AHe and AFT central ages, while the low-topography samples further from the fault record older, often Permian–Triassic ages. Samples from deeper in the high-topography part of the ranges were found to have Late Cretaceous AFT central ages (De Pelsmaeker et al., 2015). The Central Kazakhstan Fault has a similar NW–SE orientation to the Chingiz-Tarbagatai Fault and experienced a comparable Paleozoic history (Li et al., 2018).

The westernmost low-relief Tianshan in Uzbekistan did not experience widespread uplift and exhumation during the Late Jurassic–Early Cretaceous (Jepson et al., 2018c; Jepson et al., 2018b). These regions to the west of the Talas-Ferghana Fault generally record slow cooling during this time, except along suture zones and major structures, where increased cooling rates during the Early Cretaceous are found (Jepson et al., 2018c). Evidence for Early Cretaceous rapid cooling is preserved along the Talas-Ferghana Fault (Nachtergaele et al., 2018) and in the Kyrgyz Tian-

shan to the east of this structure, suggesting that parts of the western Tianshan were tectonically active during the Late Jurassic–Early Cretaceous (De Grave et al., 2007; De Grave et al., 2012; Glorie and De Grave, 2016; De Pelsmaeker et al., 2018).

Further east, low-temperature thermochronology from the Chinese Tianshan more commonly records slow cooling during the Jurassic–Early Cretaceous (Dumitru et al., 2001; Jolivet et al., 2010; Gillespie et al., 2017b). The Late Jurassic–Early Cretaceous saw an increase in coarse sedimentary input into the Junggar and Tarim basins that is often related to uplift and exhumation in Central Asia (e.g. Hendrix et al., 1992) but has also been argued to be the result of climatic changes at this time (Jolivet et al., 2017).

Various drivers for Early Cretaceous cooling have been proposed, including the closure of the Mongol-Okhotsk Ocean in Mongolia and eastern Russia (Zorin, 1999) and the collision of the Cimmerian Lhasa block with Eurasia in modern Tibet (Kapp et al., 2007; Zhu et al., 2016).

North-eastern Asia records extensive evidence for extensional tectonics during the Late Jurassic and Early Cretaceous, attributed to the closure of the Mongol-Okhotsk Ocean and changes in the plate kinematics of the Izanagi oceanic plate in the northern Pacific Ocean (Daoudene et al., 2017). Widespread rift basins, metamorphic core complexes and syn-extensional plutonic emplacement can be found in the area from Transbaikalia, through eastern Mongolia, and into northeast China (Daoudene et al., 2017). Tectonic stability in western Mongolia since the Jurassic (Jolivet et al., 2007) provides a western limit for the extent of this activity, and to the west of this, sedimentological or tectonic evidence for widespread extensional activity during the Late Jurassic–Early Cretaceous is not apparent in the Tianshan and surrounding areas.

It has been suggested that Early Cretaceous cooling along major structures in western Uzbekistan and in the Dzungarian Alatau was due to transtensional reactivation (Jepson et al., 2018c; Glorie et al., 2019). This is based on Early Cretaceous rollback in the Tethys predicted by global plate models (Zahirovic et al., 2016). The Tianshan is, however, generally thought to have experienced compressional deformation during the Early Cretaceous due to evidence for basin inversion in the Zaisan, southern Junggar and northern Tarim basins at this time (Hendrix et al., 1992; Yang et al., 2013b; Li et al., 2015d; Jolivet et al., 2018a).

Late Cretaceous

In the Chinese Tianshan, Late Cretaceous rapid cooling was uncommon, and localised into particular ranges, such as the Narat range in the central Chinese Tianshan and the ranges of the easternmost Tianshan (Jolivet et al., 2010; Gillespie et al., 2017b).

The widespread development of calcrete layers and paleosols in the Tianshan during the latest Cretaceous–early Paleogene indicate an absence of major vertical tectonic movement and mostly flat relief, with either the continuation or re-establishment of erosional surfaces (Cunningham et al., 2003; Heilbronn et al., 2015; Gillespie et al., 2017b; Jolivet et al., 2018a; Jolivet et al., 2018b; Morin et al., 2019).

AFT data suggests the Chinese Altai and samples from the vicinity of the Irtysh Shear Zone in NE Kazakhstan experienced rapid cooling during the Late Cretaceous (Yuan et al., 2006; Glorie et al., 2012b). Likewise, in the Siberian Altai and the Tuva region of Russia, AFT ages are dominated by a Late Cretaceous signal (Glorie et al., 2012a; De Grave et al., 2014). Although this post-dates the Mongol-Okhotsk ocean closure, possible continuity between the Mongol-Okhotsk event and the initiation of the Baikal rift (Jolivet et al., 2009) has led some to ascribe Late Cretaceous reactivation in the Altai to the ongoing influence of the Mongol-Okhotsk ocean closure or tectonic activity in the West Siberian Basin (Glorie et al., 2012a).

4.5.5 Cenozoic

Major uplift occurred throughout Central Asia during the late Cenozoic in response to the collision of India with Eurasia. Thermochronological and sedimentological evidence point to the initiation of this ongoing phase of Central Asia's tectonic history at ~30 Ma (e.g. Hendrix et al., 1994; Sobel and Dumitru, 1997; Bullen et al., 2001; Dumitru et al., 2001; Sobel et al., 2006b; De Grave et al., 2007; Jolivet et al., 2010; Glorie et al., 2011; Macaulay et al., 2014; Käßner et al., 2016a; Bande et al., 2017; Jepson et al., 2018a; Nachtergaele et al., 2018). The results from this study show no evidence for this episode of uplift in the Tarbagatai Mountains, as insufficient exhumation has occurred in the sampled locations to reveal the thermochronological record of this event. Never the less, modern relief in the area was likely enhanced by uplift during the late Cenozoic.

4.6 Conclusion

Apatite fission track and apatite (U-Th)/He dating of samples from the Tarbagatai Mountains in eastern Kazakhstan found evidence for three episodes of increased cooling rates. These cooling events are related to the exhumation of the region, which was controlled by the reactivation of Paleozoic structures. The area experiencing exhumation became more focussed around major structures over time as progressively more spatially limited reactivation occurred. During the Permian, exhumation was probably widespread, reflected in the thermal history modelling of samples from the Zharma-Saur arc in the north of the study area. During the late Triassic, exhumation of the area to the south-west of the Kalba-Chingiz Shear

Zone can be seen in the thermal histories recorded in the Boshchekul-Chingiz and Balkhash-Yili arcs. The final stage of the thermotectonic evolution of the region that was recorded by the available thermochronometers shows Early Cretaceous reactivation in a relatively restricted area around the Chingiz-Tarbagatai Fault. This pattern of reactivation also implies that most of the region did not experience significant post-Triassic exhumation until presumably recent uplift in response to the India-Eurasia collision. Similar regional thermal histories have also been revealed elsewhere in low-topography areas of Central Asia, such as western Uzbekistan and southern Kazakhstan, suggesting that this may be a reflection of the broader state of Central Asian tectonics prior to the collision of India. An alternative explanation is that the relatively stronger lithosphere of the Kazakhstan continent may record a different Mesozoic history compared to the terranes of the Tianshan. In this scenario, limited deformation in the Cretaceous is accommodated by pre-existing structures in the Kazakhstan continent in contrast to regional exhumation as in parts of the Tianshan.

Chapter 5

Detrital apatite U–Pb and trace element analysis as a provenance tool: insights from the Yenisey Ridge (Siberia)

This chapter is published as:
Gillespie, J., Glorie, S., Khudoley, A., Collins, A.S., 2018. Detrital apatite U–Pb and trace element analysis as a provenance tool: Insights from the Yenisey Ridge (Siberia). Lithos 314–315, 140-155. doi: 10.1016/j.lithos.2018.05.026

Statement of Authorship

Title of Paper	Detrital apatite U-Pb and trace element analysis as a provenance tool: Insights from the Yenisey Ridge (Siberia).
Publication Status	☑ Published ☐ Accepted for Publication ☐ Submitted for Publication ☐ Unpublished and Unsubmitted w ork w ritten in manuscript style
Publication Details	Published as: Gillespie, J., Glorie, S., Khudoley, A., Collins, A.S., 2018. Detrital apatite U-Pb and trace element analysis as a provenance tool: Insights from the Yenisey Ridge (Siberia). Lithos 314–315, 140-155.

Principal Author

Name of Principal Author (Candidate)	Jack Gillespie		
Contribution to the Paper	Sample preparation, analysis, data reduction, data interpretation, figures, writing		
Overall percentage (%)	70		
Certification:	This paper reports on original research I conducted during the period of my Higher Degree by Research candidature and is not subject to any obligations or contractual agreements with a third party that would constrain its inclusion in this thesis. I am the primary author of this paper.		
Signature		Date	

Co-Author Contributions

By signing the Statement of Authorship, each author certifies that:

i. the candidate's stated contribution to the publication is accurate (as detailed above);

ii. permission is granted for the candidate in include the publication in the thesis; and

iii. the sum of all co-author contributions is equal to 100% less the candidate's stated contribution.

Name of Co-Author	Stijn Glorie		
Contribution to the Paper	Primary supervision, data interpretation		
Signature		Date	

Name of Co-Author	Andrei Khudoley		
Contribution to the Paper	Samples, geological background, geological interpretation		
Signature		Date	23/05/2019

Name of Co-Author	Alan S. Collins		
Contribution to the Paper	Supervision, data interpretation		
Signature		Date	

5.1 Introduction

Sedimentary basins provide an archive of the tectonic history of their surroundings, making them an invaluable source of information for palaeogeographic and palaeotectonic studies. Studies concerning sedimentary provenance frequently rely on the distribution of zircon U–Pb ages and Hf isotopic composition to understand the sources of sediment, drawing conclusions about the geological history of the basin by comparing detrital age distributions to those found in other basins or in potential source regions (e.g. Bruguier et al., 1997; Cawood et al., 2003; Dickinson and Gehrels, 2003; LaMaskin, 2012; Schoene, 2014). Advances in the statistical methods for displaying and understanding zircon U–Pb data (e.g. KDE and MDS plots; Vermeesch, 2012; Vermeesch, 2013) have improved our ability to effectively interpret and communicate these results (e.g. Armistead et al., 2017; Yang et al., 2018).

However, fundamental sources of biases in the detrital zircon record remain, such as the limited range of magmatic compositions that readily produce zircon and the high preservation potential of this mineral (e.g. Andersen et al., 2016; Malusà et al., 2016; Spencer et al., 2018). The zircon fertility of rocks with similar lithologies can differ by as much as half an order of magnitude (Dickinson, 2008; Moecher and Samson, 2006), while different source regions in the European Alps were found to vary in zircon fertility by five orders of magnitude (Malusà et al., 2016). The typically low zircon fertility of mafic rocks means that sources dominantly composed of mafic rocks are at risk of being under-represented or rendered invisible in the detrital zircon record (Moecher and Samson, 2006). The consequence of these limitations is that detrital zircon age distributions usually do not accurately reflect the proportional contribution of source rocks to the sediment.

In contrast to zircon, apatite grows in both felsic and mafic rocks (Piccoli and Candela, 2002). Furthermore, because the trace element and rare earth element (REE) chemistry of magmatic apatite is sensitive to the composition of the host rock, the analysis of these elements via LA-ICP-MS can be used to understand the source of detrital apatite grains(e.g. Belousova et al., 2002; Morton and Yaxley, 2007). The ability to geochemically characterise detrital apatites as being mafic in origin (Belousova et al., 2002; Bruand et al., 2017; Jennings et al., 2011; Morton and Yaxley, 2007) is important, because this means that apatite analysis can be used to help address fundamental issues in relation to biases in the detrital record. As apatite is more susceptible to chemical and physical weathering than zircon (Morton and Hallsworth, 1999), detrital apatite is more likely to be representative of first-cycle sediment, but also faces an increased risk of destruction between the time of formation and the present. Apatite is very stable during burial and diagenesis but is less stable under some weathering conditions, such as during acidic soil formation, where it is relatively easily dissolved (Morton and Hallsworth, 1999).

U–Pb dating of apatite is complicated by typically low U concentrations and the

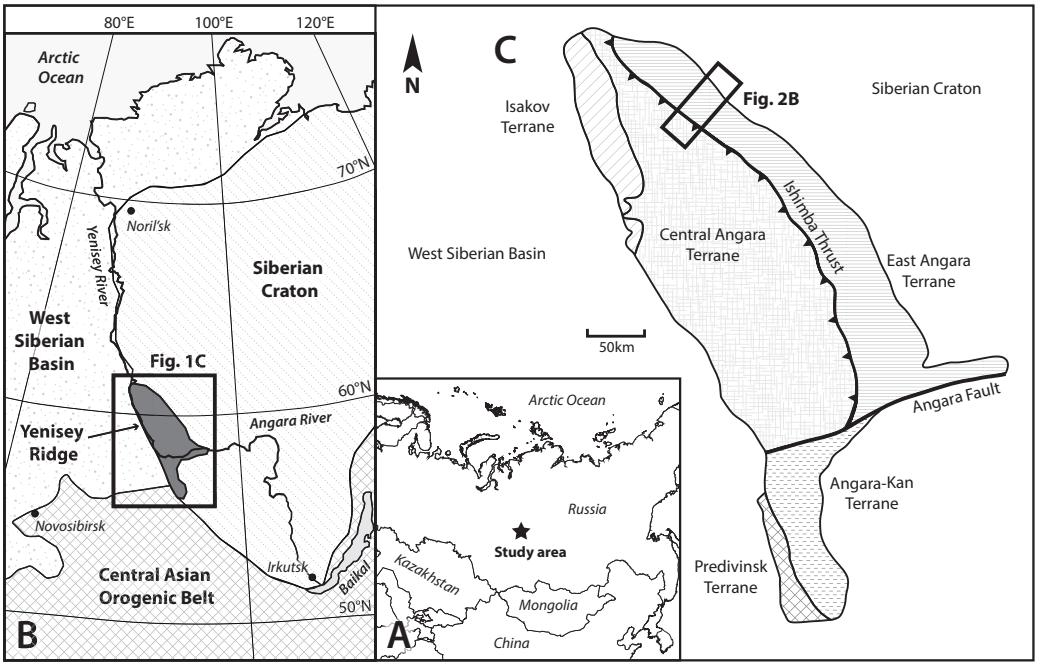

Figure 5.1: A) The location of the study area within Eurasia, B) the position of the Yenisey Ridge with respect to the major geological features of Siberia (modified from Kuzmichev and Sklyarov (2016)), and C) terrane map of the Yenisey Ridge (Vernikovsky et al., 2016).

variable incorporation of non-radiogenic (common) Pb, although the development of new standards and data reduction protocol specifically for apatite U–Pb dating has helped address this problem (e.g. Chew et al., 2014a; Thomson et al., 2012).

Although some published studies have applied detrital apatite geochemistry (Abdullin et al., 2016; Jafarzadeh et al., 2014; Morton and Yaxley, 2007), or U–Pb geochronology (Carrapa et al., 2009; Mark et al., 2016; Painter et al., 2014; Zattin et al., 2012) as a provenance tool, this study presents the novel combination of U–Pb and trace element LA-ICP-MS analysis on individual apatite grains to investigate the provenance of ancient sedimentary rocks. We apply this approach to investigate the provenance of sedimentary and metasedimentary rocks from the Yenisey Ridge, Russia. This case study demonstrates that the combination of multi-method apatite and zircon U–Pb analyses mitigates the drawbacks of either approach in isolation, and illustrates how these methods provide complementary and intersecting information about the provenance of the original sediment.

5.2 Geological setting

5.2.1 Study area: Yenisey Ridge

The Yenisey Ridge is a fold and thrust belt stretching more than 700km NW–SE along the western margin of the Siberian Craton (Fig. 5.1; Likhanov and Santosh, 2017). This contentious and poorly understood area is important for understanding the palaeogeography of Siberia during the Neoproterozoic and Mesoproterozoic, as different tectonic models have implications for the position of Siberia with relation to other continents in the supercontinent Rodinia (Kuzmichev and Sklyarov, 2016; Likhanov et al., 2015; Merdith et al., 2017; Vernikovsky et al., 2016).

The ENE striking strike-slip Angara Fault divides the Yenisey Ridge into two regions. The northern region (Transangaria) comprises the Isakov, Central Angara, and East Angara terranes, while the southern region is composed of the Angara-Kan and Predivinsk terranes (Fig. 5.1; Kuzmichev and Sklyarov, 2016). To the north of the Angara fault, Transangaria is composed primarily of Meso-Neoproterozoic rock, while the southern region includes both the Palaeoproterozoic Angara-Kan and the Neoproterozoic Predivinsk terranes (Vernikovsky et al., 2016). Most of the major structures in the belt strike NW, including the Ishimba thrust that separates the East and Central Angara terranes (Kuzmichev and Sklyarov, 2016).

Both the Central Angara and East Angara terranes are characterised by variably metamorphosed rocks reaching amphibolite facies in the Central Angara terrane and decreasing eastward (Mel'nikov et al., 2005). The East Angara terrane experienced no Neoproterozoic magmatism, while in contrast the Central Angara terrane was intruded by several phases of Tonian magmatism (880–720 Ma) (Vernikovsky et al., 2003; Vernikovsky et al., 2016). The Isakov terrane is mostly composed of volcanogenic-sedimentary and ophiolitic units that are thought to be the remains of an island arc thrust onto the western margin of the Central Angara terrane at ~630 Ma (Vernikovsky et al., 2003).

The East Angara terrane contains rocks of the deformed passive margin of the Siberian Craton, dating to the Meso- and Neoproterozoic (Nozhkin et al., 2009; Vernikovsky et al., 2003; Vernikovsky et al., 2016). The main topic of discussion in the published literature concerning the tectonic evolution of the Yenisey Ridge is the origin and position of the Central Angara terrane (Vernikovsky et al., 2003; Vernikovsky et al., 2016). Vernikovsky et al. (2016) consider the Central Angara terrane to have been an independent block until it collided with Siberia during the late Tonian (~760–720 Ma), while Likhanov et al. (2015) propose that the Central and Eastern Angara terranes were already part of the Siberian margin and experienced 'Grenvillian' orogenesis at ~1050–850 Ma. Kuzmichev and Sklyarov (2016) suggest a model where Central Angara was already a part of Siberia during the Neoproterozoic, and experienced the collision of an unidentified terrane at ~900–855 Ma. This

model interprets the ~800–720 Ma magmatism as rift-related, in agreement with some of the other studies published in the area (e.g. Likhanov et al., 2014; Nozhkin et al., 2011).

5.2.2 Stratigraphy and samples

The Precambrian rocks that compose the Central and East Angara terranes in the north-eastern Yenisey Ridge can be divided into two categories: the metamorphosed Teya and Sukhopit Groups, and the essentially unmetamorphosed Cryogenian–Ediacaran Chingasan and Chapa Groups (Vernikovsky et al., 2016). Seven samples taken from throughout the stratigraphy were analysed in this study (Fig. 5.2). Priyatkina et al. (2016) published detrital zircon U–Pb data for four (YP1, 6, 8, and 21) of the seven samples that were analysed in this study. Note that samples YP1, 6, 8, and 21 in this study are named CHP1, 6, 8, and 21 in Priyatkina et al. (2016).

Two of the studied samples (YP1, 4) are from the Central Angara terrane, whereas the remaining samples are from the East Angara terrane. The Meso- to Neoproterozoic stratigraphy is well studied in the East Angara terrane, where the sedimentary rocks are mildly deformed, unmetamorphosed to slightly metamorphosed, and are not intruded by granites (Mel'nikov et al., 2005; Pokrovsky et al., 2012). The relationships between local formations in the East Angara terrane are well documented. In contrast, the rocks of the Central Angara terrane are highly deformed and variably metamorphosed, with unclear correlations to the East Angara sedimentary succession (Vernikovsky et al., 2016, and references therein).

The Teya Group is exposed in the Central Angara terrane, where is it intruded by granites and has experienced greenschist to most typically amphibolite/epidote–amphibolite facies regional metamorphism (Nozhkin et al., 2012). It is composed of a variety of metamorphic rocks including gneisses, schists, quartzites, amphibolites, and marbles that are interpreted to have sedimentary protoliths (Nozhkin et al., 2012). The Palaeoproterozoic Penchenga Formation of the Teya Group consists mostly of gneisses and crystalline schists, with some marbles and quartzites (Nozhkin et al., 2012). The Penchenga Formation is unconformably overlain by the Korda Formation of the Sukhopit Group (Nozhkin et al., 2012). Sample YP1 was taken from a paragneiss of the Penchenga Formation.

Rock units assigned to the Sukhopit Group are exposed in both the Central And East Angara terranes, but the correlation of these rocks are questionable (Vernikovsky et al., 2016, and references therein). The Sukhopit Group is composed of sandstones, conglomerates, and shales, with some carbonate layers alternating with clastic sedimentary rocks in the central and upper part of the group (Vernikovsky et al., 2016). The basal conglomerate in the Korda Formation of the Sukhopit Group includes pebbles of the underlying Teya Group gneisses and schists (Nozhkin et al., 2012). The rocks of the Sukhopit Group experienced mostly

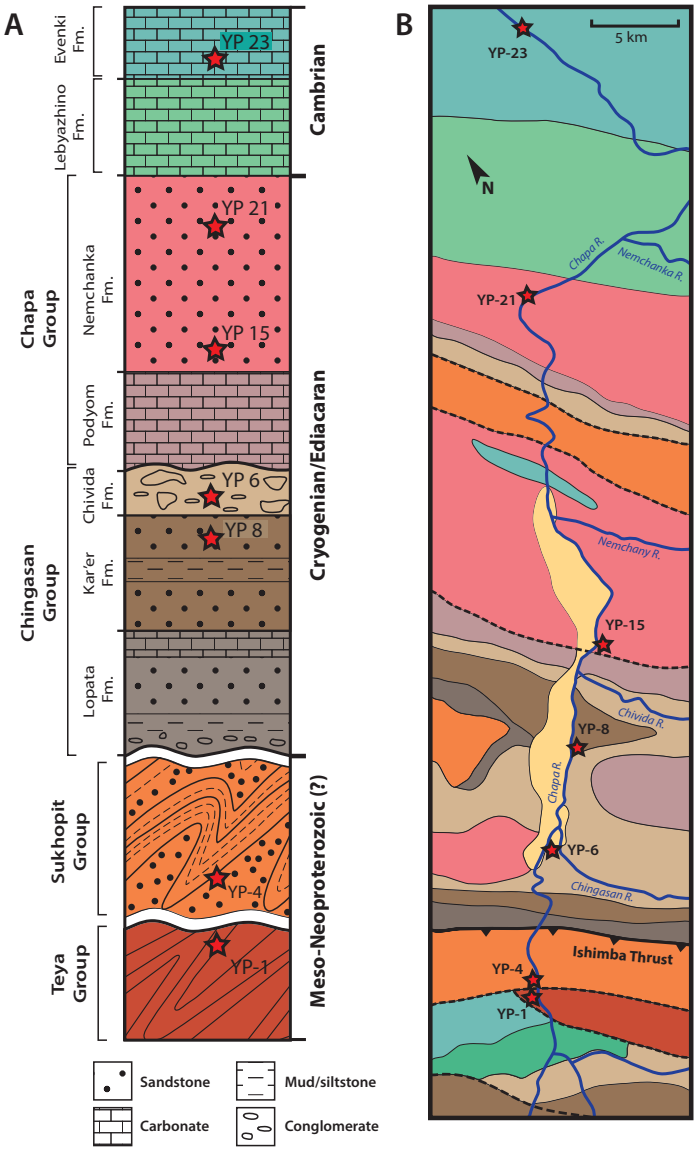

Figure 5.2: A) Stratigraphy of the study area. Pattern corresponds to dominant lithology of unit. Stars represent approximate stratigraphic position of sample. Stratigraphic column modified after Priyatkina et al. (2016). B) Geological map of study area. Colours correspond to stratigraphic units in part A. Dashed lines are undifferentiated faults. Stars represent sample locations. Map modified after Pokrovsky et al. (2012).

Table 5.1: Location and lithological data

Sample	IGSN	Lat.	Long.	Lithology	Formation	Stratigraphic age
YP1	IEJAG0012	60.6826	91.8209	Paragneiss	Penchenga Formation, Teya Group	Paleoproterozoic
YP4	IEJAG0013	60.6839	91.8258	Quartzite	Korda Formation, Sukhopit Group (?)	Meso-Neoproterozoic (?)
YP6	IEJAG0014	60.7463	91.9246	Lithic sandstone	Chivida Formation, Chingasan Group	Cryogenian
YP8	IEJAG0015	60.7732	91.9966	Quartz sandstone	Kar'er Formation, Chingasan Group	Cryogenian
YP15	IEJAG0016	60.8111	92.0884	Red sandstone	Nemchan Formation, Chapa Group	Ediaracan
YP21	IEJAG0017	60.9876	92.2264	Red sandstone	Nemchan Formation, Chapa Group	Ediaracan
YP23	IEJAG0018	61.1080	92.3982	Lithic sandstone	Evenka Formation	Middle-upper Cambrian

Note: IGSN = international geosample number

greenschist facies regional metamorphism, with localised instances of amphibolite facies metamorphism in the lower parts of the group (Likhanov et al., 2007). The metamorphic grade in the lower Sukhopit Group increases with proximity to major thrusts, and this increase in grade is associated with changes in the style and intensity of deformation (Likhanov et al., 2007). In the Korda Formation, the local increase in metamorphic grade is characterised by the obliteration of widespread D1 isoclinal folds (Likhanov and Reverdatto, 2007). Furthermore, the lower part of the Korda Formation is marked by discontinuous volcanic bodies (Nozhkin et al., 2011), conglomerates, and quartzites (Nozhkin et al., 2009).

Previous studies of the chemical and Sm-Nd isotopic composition of the fine-grained rocks from the Sukhopit Group and overlying units found that felsic rocks were the predominant source (Nozhkin et al., 2009; Nozhkin et al., 2008). Nozhkin et al. (2011) found that there was some contribution of juvenile material to the bottom and middle of the Sukhopit Group. $^{40}Ar/^{39}Ar$ biotite ages of 823–826 Ma from metapelitic sections of the Korda Formation are interpreted, by Likhanov et al. (2007), to represent the maximum age of greenschist metamorphism for this unit. Sample YP4 is from a fault-bound unit composed of isoclinally folded quartzite described as belonging to the Korda Formation.

The metamorphosed sedimentary rocks of the Central Angara terrane discussed above are intruded by several phases of granitic magmatism. The earliest of these granites intrudes the Teya Group and lower Sukhopit Group rocks, and provides the only firm age constraint on these sequences at ~880–860 Ma (Vernikovsky et al., 2016). The granitic Kalami pluton (875 ± 7 Ma; Vernikovsky et al., 2007) intrudes rocks of the Korda Formation in the central part of the Yenisey Ridge (Varganov et al., 2010). Subsequent phases of magmatism in the Central Angara terrane occurred until around ~720 Ma (Vernikovsky et al., 2003). In the northern part of the Yenisey Ridge, the Cryogenian–Ediacaran Chingasan and Chapa Group sedimentary rocks unconformably overlie the igneous intrusions and earlier metamorphic rocks (Vernikovsky et al., 2016). These rocks fill the Teya-Chapa sedimentary basin, and consist of unmetamorphosed sedimentary rocks with widely distributed red beds and locally distributed felsic and mafic volcanic rocks described by various authors as either a foreland or rift-related basin (e.g. Nozhkin et al., 2007).

The Chingasan Group is divided into three units: the Lopata, Kar'er and Chivida Formations. The oldest formation in the Chingasan Group, the Lopata Formation, unconformably overlies the metamorphosed rocks of the Sukhopit Group and is mostly composed of fluvial conglomerates and sandstones, capped with stromatolitic dolomite (Nozhkin et al., 2007; Pokrovsky et al., 2012). The Kar'er Formation overlies the Lopata Formation and is composed of quartzose sandstone interbedded with some thin siltstone and mudstone layers. In the upper parts of the formation, some dolomite is also present (Pokrovsky et al., 2012). Sample YP8 was taken from

a quartzose sandstone in the Kar'er Formation. The Chivida Formation contains a diamictite that has been interpreted by some as a Sturtian tillite (Pokrovsky et al., 2012), but is mostly composed of sandstone and siltstone with evidence of turbidite deposition (Nozhkin et al., 2007). Sample YP6 was taken from a sandstone in the Chivida Formation.

The sedimentary rocks of the Chapa Group unconformably overlie the Chingasan Group. The lower part of the Chapa Group, the Podyom Formation, is mostly composed of dolomites and limestones with some thin sandstone and siltstones (Pokrovsky et al., 2012). The Nemchanka Formation conformably overlies the Podyom Formation and is largely composed of clastic sedimentary rock (Pokrovsky et al., 2012). The lower sections are mostly finer sediments including mudstones and siltstones, while the middle is composed of red and pink sandstones with carbonate cement. The upper part is composed of coarse sandstones (Pokrovsky et al., 2012). Sample YP15 is taken from a sandstone in the lower part of the Nemchanka Formation, while YP21 is taken from a sandstone in the upper part up of the formation.

Conformably overlying the Chapa Group sedimentary rocks are Cambrian carbonates including the Lebyazhino and Evenki Formations. The base of the Lebyazhino Formation corresponds to the beginning of the Cambrian, according to palaeontological and isotopic data (Pokrovsky et al., 2012). The Evenki Formation is composed of various limestones and marls that are dated to the Middle–Upper Cambrian based on trilobite palaeontology (Pokrovsky et al., 2012). Sample YP23 is taken from a sandstone in the Evenki Formation.

Table 5.2: Analytical parameters for LA-ICP-MS

	1st round analysis	Trace element/REE reanalysis
Laser parameters		
Instrument	NewWave UP213	NewWave UP213
Washout	20s	20s
Background	30s	30s
Analysis duration	30s	30s
Laser repetition rate	5Hz	5Hz
Spot size	30μm	30μm
Energy	3.5 J/cm^2	3.5 J/cm^2
Carrier gas	700 mL/min He	700 mL/min He
Mass spectrometer		
Instrument	Agilent 7500	Agilent 7900
Isotopic and sample information		
Number of isotopes measured	11	30
Isotopes measured	^{29}Si, ^{35}Cl, ^{43}Ca, ^{44}Ca, ^{91}Zr, ^{204,206,207,208}Pb, ^{232}Th, ^{238}U	^{29}Si, ^{35}Cl, ^{43}Ca, ^{44}Ca, ^{51}V, ^{55}Mn, ^{88}Sr, ^{90}Zr, ^{139}La, ^{140}Ce, ^{141}Pr, ^{146}Nd, ^{147}Sm, ^{153}Eu, ^{157}Gd, ^{159}Tb, ^{163}Dy, ^{165}Ho, ^{166}Er, ^{169}Tm, ^{172}Yb, ^{175}Lu, ^{202}Hg, ^{204,206,207,208}Pb, ^{232}Th, ^{238}U

5.3 Methods

Seven samples were taken in a linear transect across the north-eastern margin of the Yenisey Ridge, from the Central Angara terrane to the south-west of the Ishimba thrust, traversing the East Angara terrane, and ending with a final sample from the Evenki Formation on the Siberian platform (Fig. 5.2, Table 5.1). Apatite mineral separates from these samples were initially analysed for U and Pb isotopes on a NewWave UP213 ablation system coupled to an Agilent 7500 mass spectrometer as in (Jepson et al., 2018a). All samples were further investigated by reanalysis for 30 masses (Table 5.2), including U and Pb isotopes, trace elements and REEs guided by initial U–Pb results. The second round of analysis was carried out on a NewWave UP213 ablation system coupled to an Agilent 7900 mass spectrometer. Analytical parameters and isotopes measured can be found in Table 5.2. The analytical sequence in all cases consisted of two analyses of both the NIST SRM 610 glass (NIST610 hereafter; Hinton, 1999) and the Madagascar apatite (Thomson et al., 2012), plus a single analysis each of the Durango (McDowell et al., 2005) and Mt. McClure (Schoene and Bowring, 2006) apatites.

5.3.1 Apatite U–Pb

The apatite U–Pb method relies on the thermally activated volume diffusion of Pb within the crystal lattice of an apatite grain to provide information about its thermal history (Blackburn et al., 2011). Estimates of the closure temperature of the apatite U–Pb system range from 370°C to more than 550°C (Cochrane et al., 2014), although figures of 450–550°C are more typical (e.g. Blackburn et al., 2011; Schoene and Bowring, 2007). Apatite U–Pb analysis was performed following the method described in Chew et al. (2014a). During apatite U–Pb analysis the Madagascar apatite primary reference material (Thomson et al., 2012) was measured repeatedly throughout the session to correct for instrumental drift and downhole fractionation, and the Mt. McClure (Schoene and Bowring, 2006) and Durango (McDowell et al., 2005) secondary reference materials were analysed as an accuracy check. Data reduction was performed using the 'VizualAge_ UcomPbine' DRS in Iolite (Chew et al., 2014a; Paton et al., 2011).

The often large amount of common (i.e. initial or non-radiogenic) Pb found in apatite necessitates the application of a correction to yield meaningful ages. Here we apply a ^{207}Pb based correction that depends on a known, or assumed, initial $^{207}Pb/^{206}Pb$ ratio (Gibson and Ireland, 1996), and apply this correction to the standards according to the method described in Chew et al. (2014a). For the Mt McClure apatite secondary standard, a weighted mean ^{207}Pb corrected $^{206}Pb/^{238}U$ age of 518.3 ± 6.1 Ma (MSWD = 1.4) was obtained, which is within uncertainty of the reference age of 523.51 ± 1.53 Ma (Schoene and Bowring, 2006).

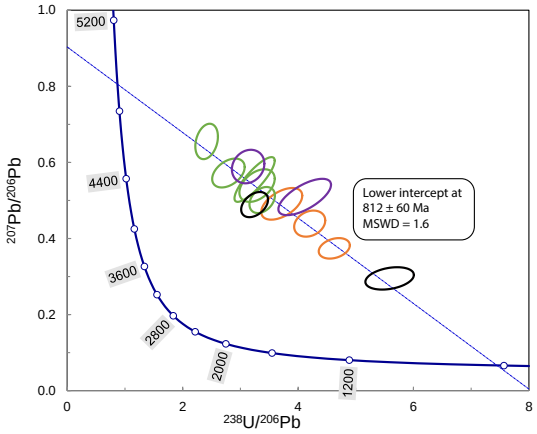

Figure 5.3: Example from Sample YP8 of multiple U–Pb analyses of single apatite grains displayed on a Tera-Wasserburg diagram. Analyses of the same grain are identified by shared colour. Ellipses are plotted at 2σ. Concordia age values expressed in Ma.

Linear arrays of apatite U–Pb analyses in Tera-Wasserburg space were used to infer the initial $^{207}Pb/^{206}Pb$ ratio based on the $^{207}Pb/^{206}Pb$ (y-axis) intercept value for the array, which was subsequently used to perform the ^{207}Pb correction (Gibson and Ireland, 1996). Linear arrays of apatite U–Pb analyses on a Tera-Wasserburg plot are expected for cogenetic populations of apatites from a magmatic rock (e.g. Chew et al., 2014a; Gibson and Ireland, 1996). In the case of detrital apatite grains from a sedimentary rock, a population of analyses that produce a linear array in Tera-Wasserburg space is consistent with the existence of an age population. Multiple populations may be present and thus more complex distributions in Tera-Wasserburg space should be expected (e.g. Mark et al., 2016).

In order to further investigate these populations, we performed further analysis of each grain to determine the trace element and REE composition. Cogenetic apatite grains have similar REE and trace element compositions, which can be used to discriminate between populations and define arrays in Tera-Wasserburg space. In addition, and where possible, multiple apatite U–Pb analyses of single grains were carried out. When the apatite grain has a variable amount of non-radiogenic Pb, multiple analyses define a linear array and further validate the use of a particular initial $^{207}Pb/^{206}Pb$ ratio (Fig. 5.3).

When no clear linear array can be defined from the apatite data, the initial $^{207}Pb/^{206}Pb$ ratio predicted by the Stacey and Kramers (1975) Pb evolution model for the age of detrital zircon peaks was used as a substitute. This is described with reference to individual samples in section 4.1. Repeated analyses of single grains are not included in the Kernel Density Estimator plots (KDE) (Vermeesch, 2012) used

to display the relative abundance of different grain ages. Likewise, plots displaying the trace element and REE characteristics of particular samples only include the subset of analyses for which these elements were recorded. The tables that contain the subsets used in each of the plots can be found in the appendices.

5.3.2 Trace element and REE data

A selection of trace elements and REE were measured simultaneously to the acquisition of U and Pb isotopes with the LA-ICP-MS in order to geochemically characterise the apatite grains (Table 5.2). These elements were chosen based on their potential to provide information about the source rock from which a detrital apatite grain was derived (e.g. Belousova et al., 2002; Bruand et al., 2017; Dill, 1994; Fleischer and Altschuler, 1986; Henrichs et al., 2018; Morton and Yaxley, 2007).

Trace element and REE data reduction were performed using the 'X_ Trace_ Elements_ IS' DRS in Iolite (Paton et al., 2011) as in (Chew et al., 2016). Instrumental drift was corrected using NIST610 as the primary standard and 43Ca was used as the internal elemental standard (Chew et al., 2014b). REE plots and discrimination diagrams were produced using an in-house R script.

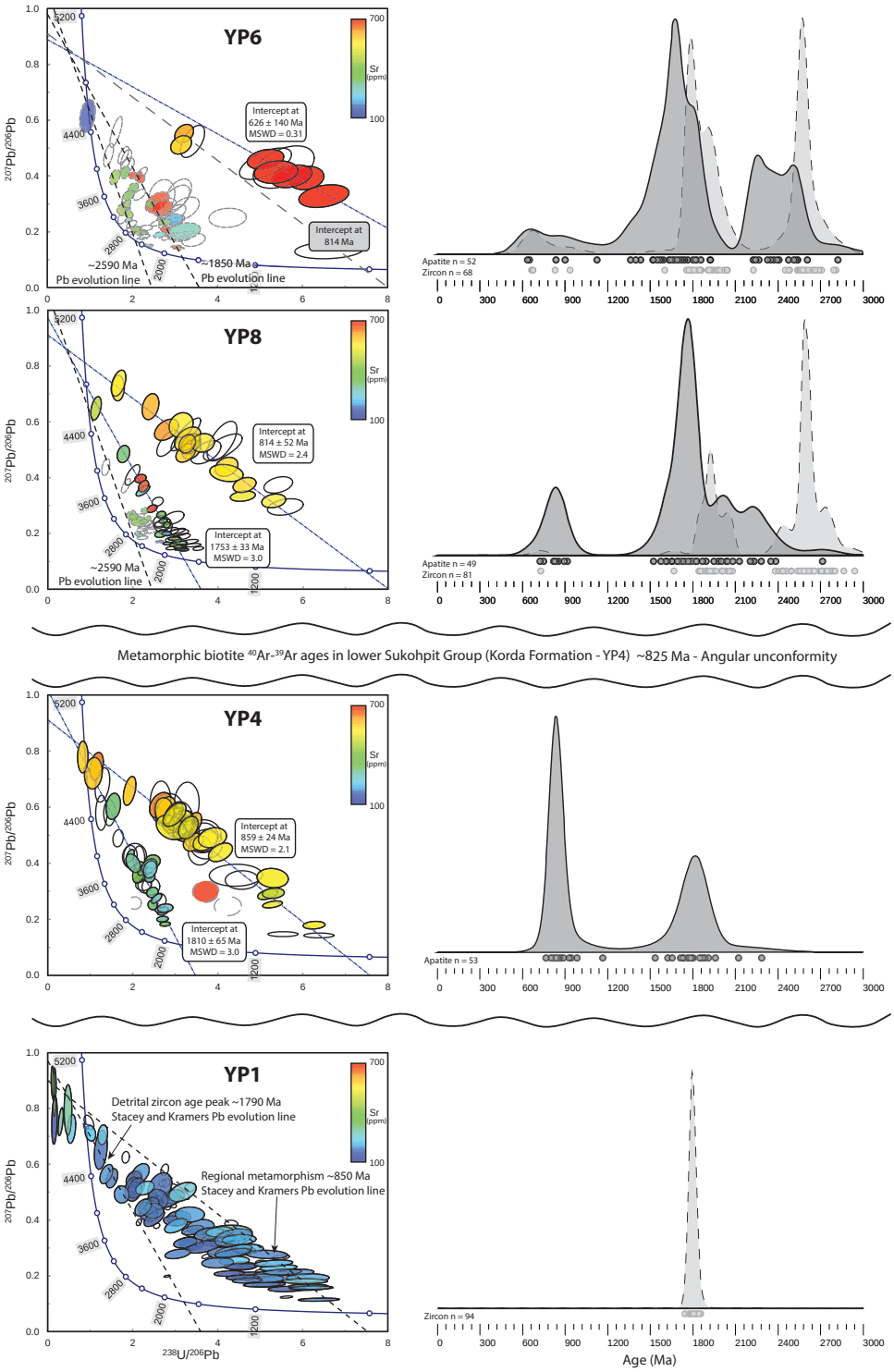

Figure 5.4: See following page for caption.

Figure 5.4: Tera-Wasserburg (T-W) concordia diagrams and Kernel Density Estimator (KDE) plots of apatite U–Pb data from samples YP1,4, 8, and 6 in stratigraphic order. Apatite U–Pb analyses for which trace element data were obtained are coloured according to their Sr contents on the T-W diagrams ellipses are plotted at 2σ. On the T-W diagrams, the narrow-spaced dashed lines correspond to linear regressions through the apatite U–Pb data that were used to obtain an estimate of the initial $^{207}Pb/^{206}Pb$ ratio. The medium dashed lines are common Pb evolution lines defined by the Stacey and Kramers (1975) model for the age of detrital zircon U–Pb age peaks for that sample. The KDE plots show the distribution of zircon U–Pb ages from Priyatkina et al. (2016) in dashed outlines and pale grey fill, and the distribution of the ^{207}Pb corrected apatite U–Pb ages in solid outline and dark grey fill.

5.4 Results

5.4.1 Apatite U–Pb

Sample YP1, taken from a paragneiss of the Penchenga Formation (Teya Group; Fig. 5.2) yielded 111 apatite U–Pb analyses that do not form clear linear arrays in Tera-Wasserburg concordia space (Fig. 5.4). For all analysed apatites, the Sr concentration is relatively low and consistent (~100–300 ppm). The significant data scatter without clear evidence for linear arrays impedes the calculation of common Pb regression lines. Therefore, for this sample, only a maximum and minimum apatite U–Pb age could be estimated at ~1790 Ma and ~850 Ma, respectively (Fig. 5.4). These ages are based on known geological constraints, explained in further detail in section 5.2.1. The majority of U–Pb analyses lie between the arrays in Tera-Wasserburg defined by the Stacey and Kramers (1975) Pb evolution models for the aforementioned ages (Fig. 5.4). The continuous spread of data between those two arrays suggests open system behaviour of Pb, possibly as a result of a thermal perturbation.

Sample YP4, taken from a quartzite in the lower part of the Sukhopit Group (Fig. 5.2), yielded 78 apatite U–Pb analyses that form two distinct linear arrays on a Tera-Wasserburg plot (Fig. 5.4). A Palaeoproterozoic array of apatite analyses has a lower intercept age of 1810 ± 65 Ma (MSWD = 3.0) and is characterised by consistently elevated Sr concentrations (~500–650 ppm). A younger, Neoproterozoic array has a lower intercept age of 859 ± 24 Ma (MSWD = 2.1) and is characterised by apatites with significantly lower Sr concentrations (~250–350 ppm) compared to the Palaeoproterozoic array. The difference in Sr concentrations between the two apatite populations suggests that they are likely derived from sources with different lithologies (likely more mafic for the younger population (e.g. Jennings

et al., 2011). Three analyses (5% of the data) did not fall onto either array. After excluding analyses that represented multiple analyses of the sample grain, 53 unique apatite U–Pb ages were calculated following a ^{207}Pb correction based on the upper (^{207}Pb/^{206}Pb) intercept of the relevant common Pb regression line. A KDE plot (Fig. 5.4) of the corrected age data shows two peaks at the ages of the two lower intercept ages (~860 and ~1810 Ma).

Sample YP8, taken from a quartzose sandstone in the Kar'er Formation, yielded in total 79 apatite U–Pb analyses that form two linear arrays on a Tera-Wasserburg plot in addition to a number of other analyses that do not clearly form arrays. The older linear array has a lower intercept age of 1753 ± 33 Ma (MSWD = 3.0) and the apatites in this array are mostly characterised by low Sr concentrations (<450 ppm; three analyses from a single apatite grain yield anomalously high ~700 ppm Sr values). The younger linear array has a lower intercept age of 814 ± 59 Ma (MSWD = 2.4) and yields apatites with consistently higher Sr concentrations (>500 ppm). Hence, the two defined apatite populations are similar to those in sample YP4, likely reflecting different source lithologies. A cluster of analyses with apparently older ages than the oldest linear array are poorly defined in terms of initial ^{207}Pb/^{206}Pb. These analyses were corrected using an initial ^{207}Pb/^{206}Pb ratio calculated from the Stacey and Kramers (1975) Pb evolution model for the age of the older zircon peak (~2590 Ma) from this sample. These analyses therefore produce ages of low accuracy and should be treated with caution. These apparent >1.8 Ga ages are absent in sample YP4. A KDE plot of the 49 unique apatite U–Pb ages from this sample shows two main peaks with ages similar to the two lower intercept ages, in addition to a tail of older ages from the ~1750 Ma peak (Fig. 5.4). This Palaeoproterozoic apatite peak is younger than the similar zircon U–Pb age peak, while the Neoproterozoic apatite and zircon peaks overlap closely.

Sample YP6 from the Chivida Formation yielded 79 apatite U–Pb analyses that are highly scattered and do not form any clear linear arrays. Repeated analyses of the two youngest grains produced seven analyses that form a linear array with consistently high Sr concentrations (>700 ppm) and a lower intercept age of 629 ± 140 Ma (MSWD = 0.31). Four analyses (with slightly lower Sr concentrations of ~500 ppm) are consistent with the Neoproterozoic linear arrays from YP4 and YP8. The remaining analyses appear to be significantly older (mostly Palaeoproterozoic) and do not form clear linear arrays. The apparently older apatite analyses were corrected using an initial ^{207}Pb/^{206}Pb ratio calculated from the Stacey and Kramers (1975) Pb evolution model for the age of the Palaeoproterozoic–Neoarchaean zircon age peak from this sample. As in YP8, the grains corrected using this approach should be treated with caution. This approach yielded 52 unique apatite U–Pb ages that resemble in terms of proportions of ages the zircon U–Pb age distribution when displayed on a KDE plot (Fig. 5.4). The apatite U–Pb age peaks tend to be slightly

younger than the zircon age peaks.

Two samples were taken from the Nemchanka Formation. YP15 yielded 67 apatite U–Pb analyses that form two linear arrays (Fig. 5.5). The older (Palaeoproterozoic) array has a lower intercept age of 1828 ± 110 Ma (MSWD = 2.4). The younger (Neoproterozoic) array has a lower intercept age of 730 ± 45 Ma (MSWD = 6.5). Sr concentrations for the apatites in the younger array are highly variable, while for the older array, they are rather consistent at ~200–450 ppm. The 47 unique apatite U–Pb ages from this sample form two peaks at ~730 Ma and ~1830 Ma on a KDE plot.

YP21 yielded 60 apatite U–Pb analyses that form two distinct Tera-Wasserburg linear arrays with lower intercepts at 1761 ± 50 Ma (MSWD = 4.6) and 839 ± 32 Ma (MSWD = 4.4). Sr concentrations are rather variable in both populations. Ten analyses did not belong to either array and were corrected as in previous samples using an initial $^{207}Pb/^{206}Pb$ ratio calculated from the age of the oldest detrital zircon peak from this sample. The 43 unique apatite U–Pb ages from this sample form three peaks at ~840 Ma, ~1850 Ma, and ~2500 Ma, similar to the ages of the zircon U–Pb peaks.

The Evenka Formation (YP23) yielded 57 apatite U–Pb analyses that form a linear array on a Tera-Wasserburg plot with a lower intercept of 745 ± 37 Ma (MSWD = 8.6). The Sr contents of these grains are generally low with only one high Sr (>500 ppm) apatite grain. The 48 unique apatite U–Pb ages from this sample form a peak at ~760 Ma on a KDE plot.

5.4.2 Trace element and REE data

Chondrite-normalised REE plots

The chondrite-normalised REE plots for sample YP1 show identical patterns for all grains, suggesting that all analysed apatites define a single trace element population. The apatites from this sample yield a strong negative Eu anomaly, and a fairly flat REE profile, with slight depletion of HREE relative to LREE and MREE (Fig. 5.6).

In contrast, three apatite populations can be defined in sample YP4, based on the differences in their REE patterns. The first apatite population is comprised of all analysed young (Neoproterozoic) U–Pb ages and is characterised by moderate enrichment in LREEs without significant or systematic Eu anomalies. The second population is defined by three old (Palaeoproterozoic) apatites. Their REE patterns are similar to those for the apatites in population one (enriched LREEs) but show an additional negative Eu anomaly. All other Palaeoproterozoic apatites belong to population three, and are moderately to strongly depleted in LREEs (depleted = (Ce/Yb)cn <1) with generally positive Eu anomalies.

Samples YP6 and YP8 are similar to one another in that the majority of the

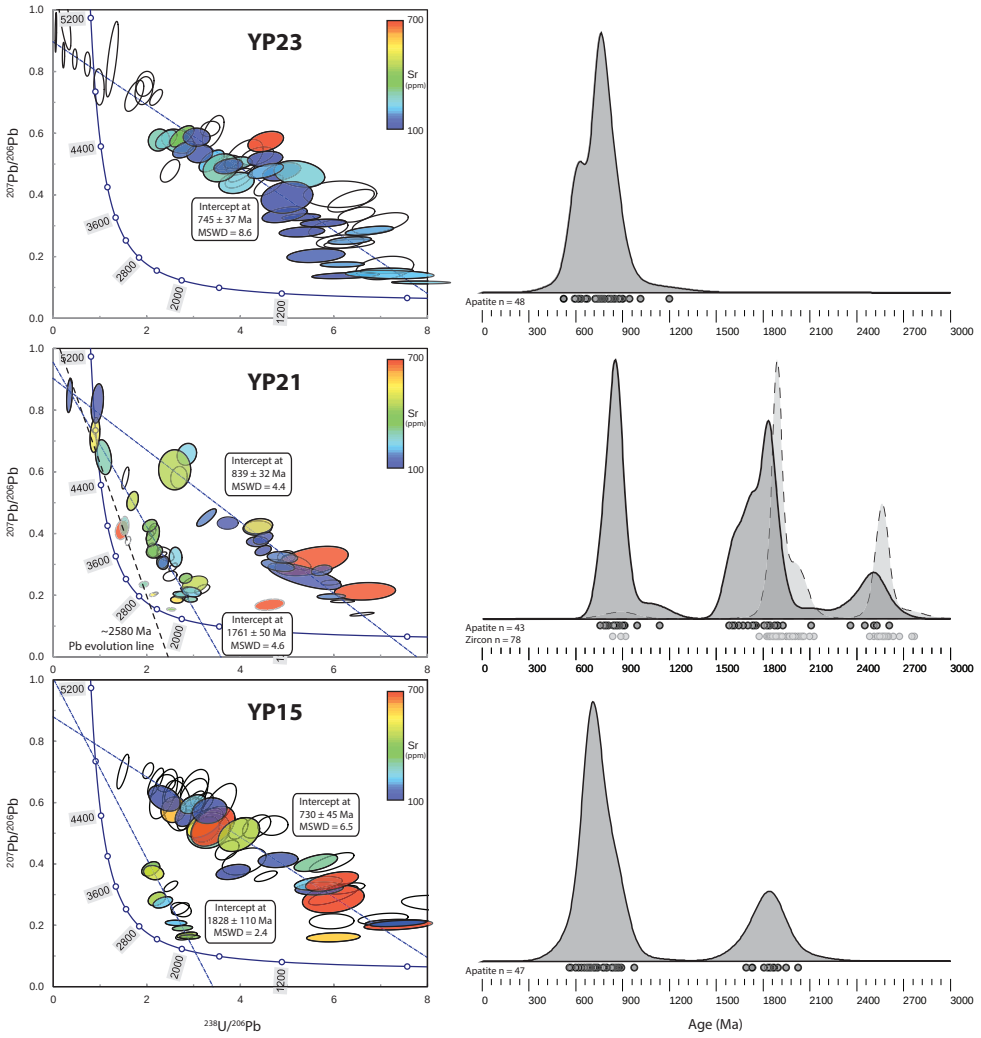

Figure 5.5: Tera-Wasserburg (T-W) concordia diagrams and Kernel Density Estimator (KDE) plots of apatite U–Pb data from samples YP15, 21, and 23 in stratigraphic order. Apatite U–Pb analyses for which trace element data were obtained are coloured according to their Sr contents on the T-W diagrams. Ellipses are plotted at 2σ. On the T-W diagrams, the narrow-spaced dashed lines correspond to linear regressions through the apatite U–Pb data that were used to obtain an estimate of the initial $^{207}Pb/^{206}Pb$ ratio. The medium dashed lines are the common Pb evolution lines defined by the Stacey and Kramers (1975) model for the age of detrital zircon U–Pb age peaks for that sample. The KDE plots show the distribution of zircon U–Pb ages from Priyatkina et al. (2016) in dashed outlines and pale grey fill, and the distribution of the ^{207}Pb corrected apatite U–Pb ages in solid outline and dark grey fill.

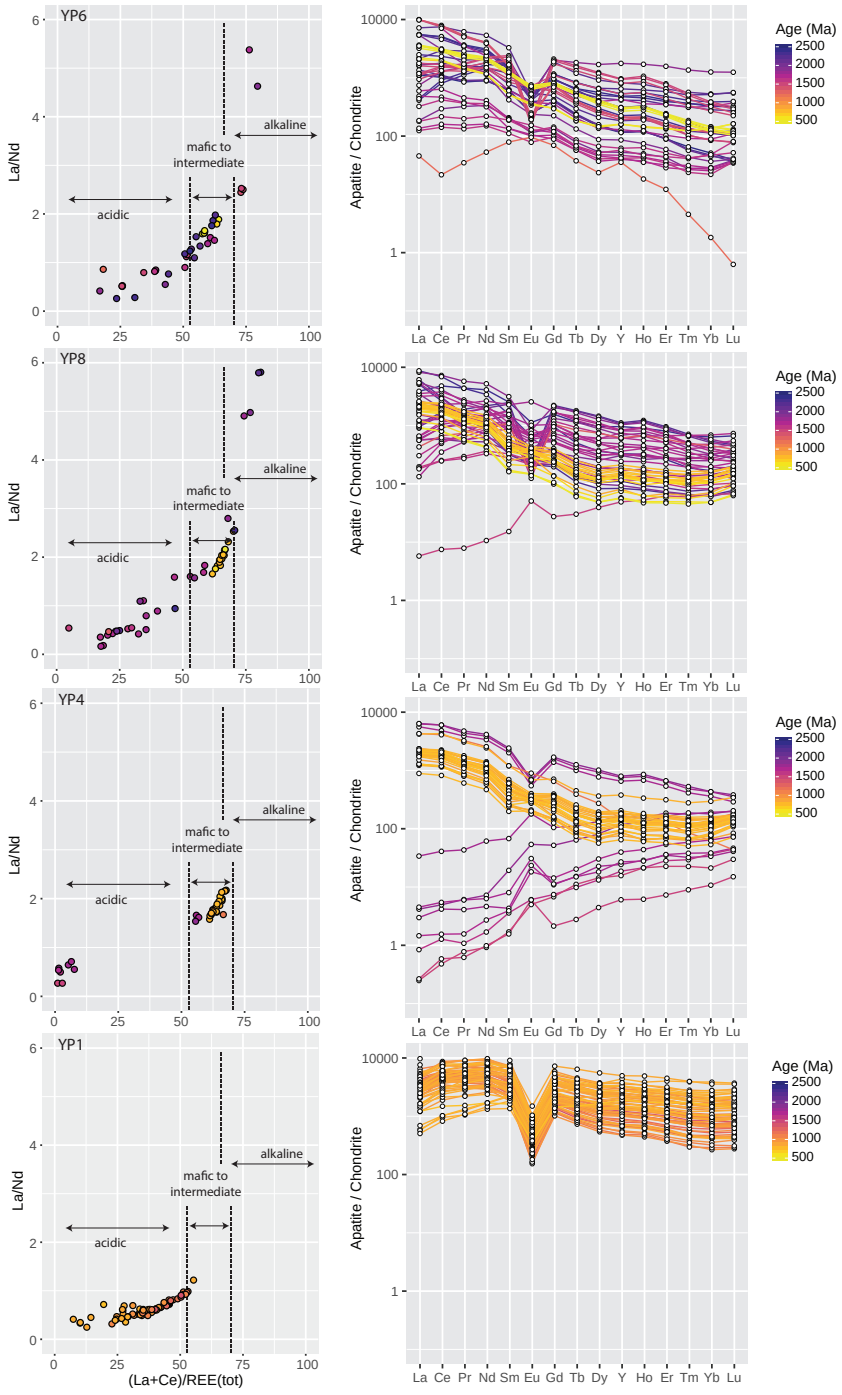

Figure 5.6: La/Nd vs La+Ce/ΣREE diagrams from Fleischer and Altschuler (1986) and chondrite normalised REE profile plots of samples YP1, 4, 8, and 6. Cl chondrite values from Sun and McDonough (1989). Analyses are coloured according to their ^{207}Pb corrected apatite U–Pb age. Note that not all grains were able to be reanalysed for trace elements and REEs so the proportions of each age population are not the same as on KDE plots.

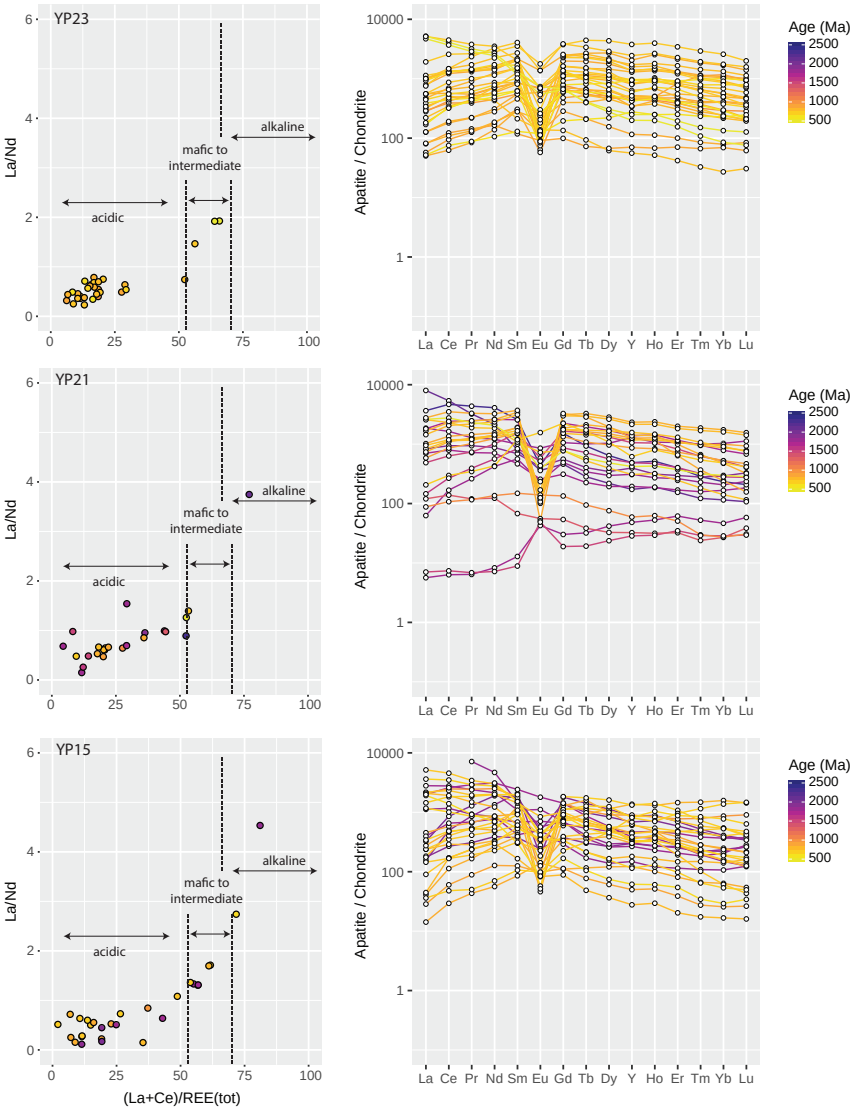

Figure 5.7: La/Nd vs La+Ce/ΣREE diagrams from Fleischer and Altschuler (1986) and chondrite normalised REE profile plots of samples YP15, 21, and 23. Cl chondrite values from Sun and McDonough (1989). Analyses are coloured according to their ^{207}Pb corrected apatite U–Pb age.

grains (with the exception of one analysed old grain from YP8) are moderately enriched in LREEs. Generally, there is a fair amount of diversity in the REE profiles of older grains, with some preserving significant Eu anomalies. In contrast, younger grains have quite uniform REE profiles across all three samples and do not record major positive or negative Eu anomalies.

The REE profiles of samples YP15, YP21, and YP23 are markedly different from those collected below the unconformity defining the base of the Chapa Group (Fig. 5.2, Fig. 5.7). The majority of grains in the youngest three samples have flat REE profiles, while some populations are slightly enriched in LREE or MREE. Older grains tend to have no Eu anomaly, or only minor positive or negative anomalies. A large proportion of younger grains have large negative Eu anomalies.

La/Nd vs La+Ce/ΣREE discrimination diagrams

The analysed apatites from YP1 fall into the acidic field on the La/Nd vs La+Ce/ΣREE plot (Fig. 5.6). In contrast, the young grains from YP4, YP8, and YP6 all have high La/Nd and La+Ce/ΣREE ratios, plotting in the mafic to intermediate field. Older grains from YP4 are mostly very acidic, while the older grains from YP8 and YP6 have a wider range of values (mostly plotting between acidic and intermediate compositions). Only a few grains from each sample fall into the alkaline field. The majority of apatites from YP15, YP21, and YP23 fall into the acidic field, while a few grains with higher La/Nd and La+Ce/ΣREE ratios fall into either the intermediate–mafic or alkaline fields (Fig. 5.6).

Th-U plots

All of the apatites analysed for sample YP1 have higher Th concentrations than U concentrations, and fall between the 1:1 and 10:1 Th-U lines (Fig. 5.8). The apatites tend to have high to very high values of both Th and U (4–150 ppm U, 20–500 ppm Th). The young (Neoproterozoic) apatites from YP4 tend to have Th>U and fall between the 1:1 and 10:1 Th-U ratio lines. In contrast, the older analysed apatites from sample YP4 generally plot on the Th depleted side of the 1:1 or even 1:10 Th-U lines. In samples YP6 and YP8, young grains consistently have Th>U, while older grains fall on both sides of the 1:1 line, and have highly variable Th and U concentrations (<1ppm to >100ppm).

Samples from above the Chingasan–Chapa unconformity (i.e. YP15, YP21, and YP23) have less clear patterns in terms of the distributions of age populations. Both young and old grains in all samples fall on both sides of the 1:1 line, but in general, apatites from these samples more often have Th<U and are sometimes extremely depleted in Th.

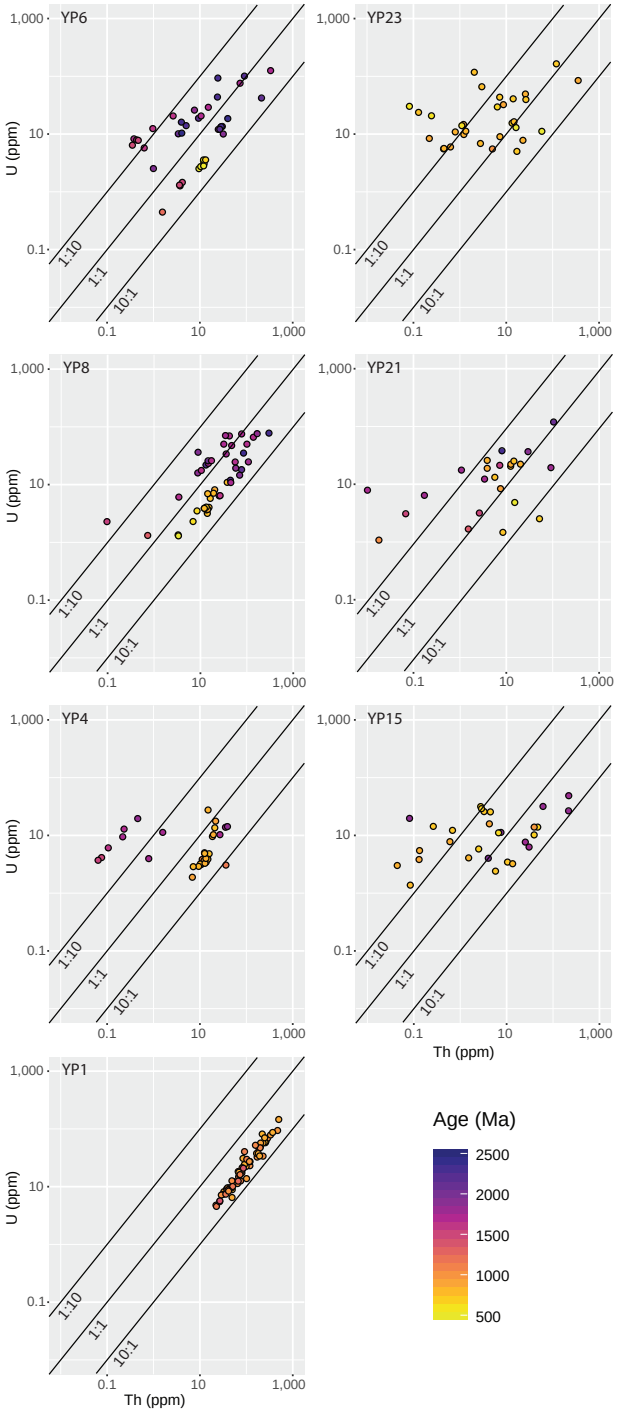

Figure 5.8: Th-U binary plots (Dill, 1994) of grains from all analysed samples, coloured according to ^{207}Pb corrected apatite U–Pb age. Diagonal lines show Th-U ratios of 1:10, 1:1, and 10:1.

5.5 Discussion

The trace element and REE data obtained in this study provide evidence for a significant change in the character of the source rocks at the time of the Chingasan Group (YP6, 8) – Chapa Group (YP15, 21) unconformity. This is seen most obviously in the Neoproterozoic populations, which have similar ages on both sides of the unconformity, but differ significantly in REE and trace element composition (Fig. 5.9).

Studies of apatite geochemistry in terms of provenance discrimination (e.g. Belousova et al., 2002; Bruand et al., 2017; Dill, 1994; Fleischer and Altschuler, 1986; Morton and Yaxley, 2007) have produced many recommendations regarding the categorisation of detrital apatite grains. In this study we have adopted a number of strategies from the literature, described below, in order to understand the geochemical signatures recorded in the analysed apatite grains.

5.5.1 Geochemical provenance discrimination of detrital apatite grains

The La/Nd vs La+Ce/ΣREE plot was proposed by Fleischer and Altschuler (1986) as a tool to categorise detrital apatites. This discrimination diagram has three fields that are defined by host rocks with acidic, intermediate–mafic, or alkaline chemistries. The behaviour of REEs in apatite is controlled by both the host rock composition and the degree of fractionation (Belousova et al., 2002; Morton and Yaxley, 2007). Alkaline rocks and less fractionated mafic rocks tend to be enriched in LREEs (Morton and Yaxley, 2007), while flat to LREE depleted REE profiles are characteristic of S-type and felsic I-type peraluminous granites (Sha and Chappell, 1999). LREE depletion is frequently attributed to the growth of monazite prior to the crystallization of apatite in these magmas. Extreme LREE depletion (extending to Gd) is found in apatite from strongly fractionated granites and in apatite grown under metamorphic conditions, as the result of competition for these elements by minerals such as allanite, epidote and feldspar (Chu et al., 2009; Henrichs et al., 2018).

The presence of a negative Eu anomaly (Eu/Eu*) in apatite is normally interpreted as the result of competition for Eu^{2+} by the crystallisation of feldspar (Belousova et al., 2002) and so is associated with relatively fractionated rocks. The lack of significant Eu anomalies, either positive or negative, is a common feature of apatites from less fractionated mafic rocks (Chu et al., 2009). Positive Eu anomalies in apatite cannot be created by fractionation and so are diagnostic of a pre-existing positive Eu anomaly in the parent magma (Chu et al., 2009).

The negative correlation between the Sr content of a magmatic apatite and the SiO_2 content of the rock in which it formed (Bruand et al., 2016; Bruand et al., 2017;

Jennings et al., 2011) can be used to estimate the whole rock SiO_2 of the source rock for a detrital grain (e.g. Bruand et al., 2017). Apatites from intermediate–mafic rocks tend to have higher Sr contents (~>400 ppm) than those from felsic rocks.

The Th-U binary plot was first used by Dill (1994) as a detrital apatite discrimination plot. The depletion of Th relative to U is usually attributed to the crystallisation of monazite, which has a strong affinity for Th (Spear and Pyle, 2002). Th depletion may be seen in apatite from strongly fractionated rocks where monazite crystallizes before apatite, or in metamorphic apatite from pelitic rocks that may also face competition with monazite or epidote in a similar fashion (Spear and Pyle, 2002). In general, grains on the Th<U side of the line may indicate a more highly evolved source or a metamorphic origin (Sha and Chappell, 1999; Spear and Pyle, 2002). Henrichs et al. (2018) found that Th depletion in low- to medium-grade metamorphic apatite from a variety of protoliths was nearly ubiquitous, and also observed Th depleted metamorphic overgrowths around high Th cores interpreted to be of detrital igneous origin.

In general, metamorphic apatite from low- to medium-grade metapelites and metabasites can be identified by very low Th and LREE concentrations, and are often also low in U (Henrichs et al., 2018; Spear and Pyle, 2002). In addition to having distinct trace element and REE characteristics, Henrichs et al. (2018) found that low-grade metamorphic apatites from a wide range of protoliths and terranes were typically so poor in U that they were undateable using the U–Pb LA-ICP-MS method.

5.5.2 Interpretation of apatite U–Pb data in terms of detrital populations

Below the Chingasan–Chapa unconformity

The oldest unit sampled in this study, the Penchenga Formation (YP1), was found in previous work to have a single, well-defined population of zircons (n = 94 <5% discordant ages) with a peak at ~1790 Ma (Priyatkina et al., 2016). The youngest single grain (YSG) age is 1743 ± 22 Ma. This is consistent with previous late Palaeoproterozoic estimates of the timing of deposition based on 1660–1680 Ma K-Ar mica ages from microschists (Volobuev et al., 1976, as cited in Nozhkin et al., 2012). Our new apatite U–Pb data for this sample do not record a clear linear array but rather a wide band of analyses in Tera-Wasserburg space, with apparent scatter along the $^{238}U/^{206}Pb$ axis of the concordia plot (Fig. 5.4).

Sr and REE patterns are consistent for all grains in sample YP1, suggesting a single apatite population (in terms of trace element geochemistry) with felsic source rock characteristics (Fig. 5.6). The lack of well-defined linear arrays shown by the apatite U–Pb analyses probably does not relate to different detrital sources but

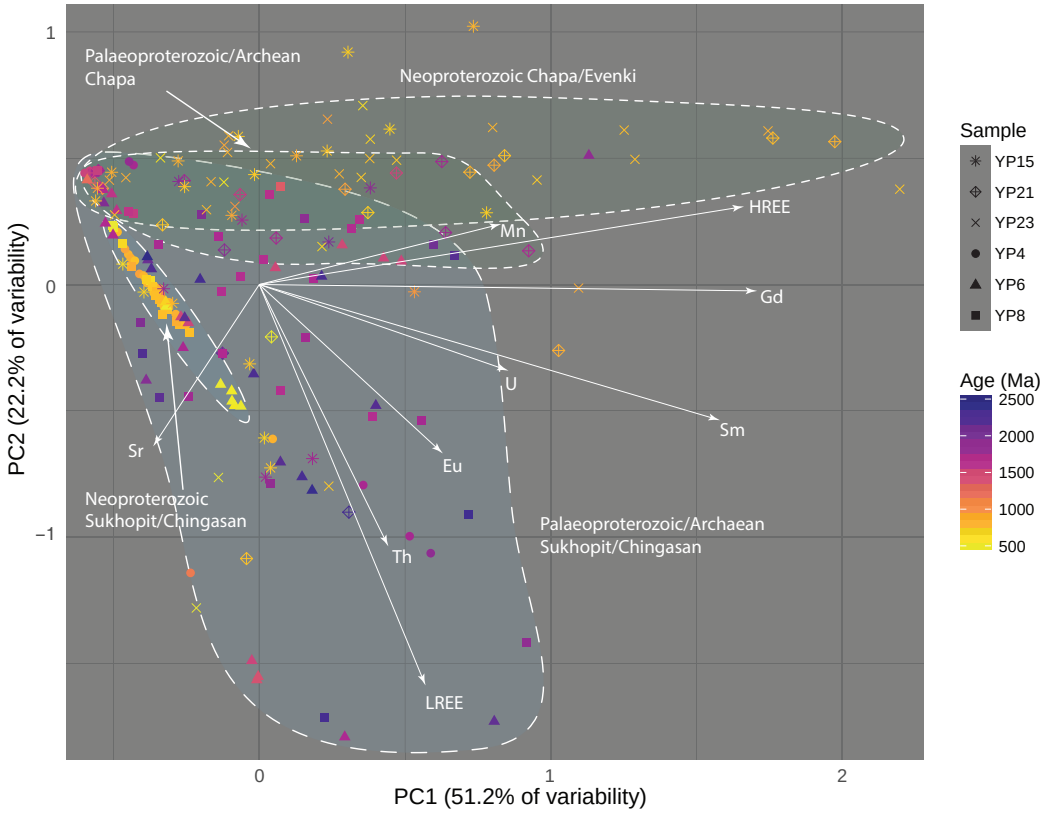

Figure 5.9: Biplot of the results of (scaled) Principal Component Analysis (Oksanen et al., 2017) of geochemical data (19 elements) obtained for detrital apatite grains from six samples in the Yenisey Ridge. Principal Component 1 (PC1) plotted against PC2 explains N73% of the variability in the data. Elemental vectors (white arrows) point in the direction most similar to the variability in elemental concentration. For clarity, many of the REEs with similar vectors are depicted with a representative vector in the case of LREE (La, Ce, Pr, Nd) and HREE (Tb, Dy, Y, Ho, Er, Tm, Yb, Lu). The green zones are the areas interpreted to contain most of the grains from samples YP15, 21, and 23. The blue zones are those that are interpreted to contain most of the grains from YP4, 8, and 6. These zones are further subdivided into the Neoproterozoic and Palaeoproterozoic/Archaean age populations. YP1 was not included as this sample is interpreted to have been significantly affected by metamorphism and may not reflect a detrital signature.

likely reflects open system Pb behaviour partially to completely resetting the U–Pb system, probably by reheating at temperatures of at least ~450–550°C (Blackburn et al., 2011). A maximum age of ~1790 Ma and minimum age of ~850 Ma was estimated based on the spread of apatite U–Pb analyses and the geological history of the sample. We interpret the maximum and minimum apatite U–Pb ages to represent the timing of the original detrital age of the population prior to partial reset (based on zircon U–Pb age of ~1790 Ma) and the time of regional metamorphism in the Yenisey Ridge at ~850 Ma, respectively (Likhanov et al., 2008).

Partial to complete resetting of the apatite U–Pb system via thermally activated volume diffusion of Pb is consistent with the epidote–amphibolite to amphibolite facies metamorphic conditions that the Penchenga Formation is thought to have experienced at ~850 Ma (Likhanov et al., 2008). The high Th values (Fig. 5.8) suggest that the apatite is unlikely to have formed under metamorphic conditions (henrichs2018; spear2002), and consequently the spread of old to young apatite ages are interpreted as the result of the thermally activated volume diffusion of Pb rather than recrystallization or new growth.

Sample YP4 yielded no dateable zircons. The apatites analysed from this sample produced two well-defined age populations. The younger, Neoproterozoic, age population contains 53% of the apatite grains and has an age of 859 ± 24 Ma (MSWD = 2.1). The Palaeoproterozoic age component contains 43% of grains and has an age of 1810 ± 65 Ma (MSWD = 3.0). The remaining three grains do not fall onto either array and are treated as outliers and not discussed further. The two populations are clearly distinguished by their Sr contents (Fig. 5.4) and REE profiles (Fig. 5.6). These different geochemical signatures suggest that the two apatite U–Pb populations reflect different sources rather than partial resetting (discussed further in section 5.1.2).

The relatively high Sr (>500 ppm) content of the young apatites from sample YP4 suggest that it is more likely that the source of these grains had an intermediate–mafic composition (Bruand et al., 2017). These grains are also characterised by a lack of significant Eu anomalies, either positive or negative, a common feature of apatites from less fractionated rocks (Chu et al., 2009). This interpretation is also consistent with the classification of the source of young grains as intermediate–mafic by the La/Nd vs La+Ce/ΣREE discrimination diagram (Fig. 5.6). These Neoproterozoic grains are broadly characterised by an enrichment in LREE and Th, high Sr, and a lack of significant Eu anomalies.

The Palaeoproterozoic age component in YP4 is dominated by apatites that are strongly depleted in LREE and have a positive Eu anomaly (Fig. 5.6). This level of LREE depletion is associated with strongly fractionated granitic source rocks or growth under metamorphic conditions (Chu et al., 2009; Henrichs et al., 2018; Spear and Pyle, 2002). Their relatively low (<350 ppm) Sr concentrations are consistent

with a felsic source. The positive Eu anomaly in apatite cannot be created by fractionation so must be the result of a pre-existing positive Eu anomaly in the parent magma (Chu et al., 2009).

A minor component of the Palaeoproterozoic population is enriched in LREE (including a negative Eu anomaly) and has an intermediate–mafic La/Nd vs La+Ce/ΣREE signature. Both samples from the Chingasan Group (YP8 and YP6) have apatite and zircon U–Pb data. Apatite and zircon record quite different U–Pb age distributions in YP8. Sample YP8 yielded 81 <5% discordant zircon U–Pb ages that range between 728 ± 18 Ma and 2941 ± 14 Ma, with major peaks at ~1870 and ~2580 Ma (Priyatkina et al., 2016). The YSG age is 728 ± 18 Ma. Tonian ages are found in both sets of data, but while this population represents 16% of the apatite data, only a single zircon of this age was found.

The majority of the apatite U–Pb data (~65–75%) falls into a late Palaeoproterozoic (~1700–1800 Ma) population. The remaining 10–20% of the apatite U–Pb data belongs to a poorly defined group that do not clearly belong to a linear array but are clearly older than ~1800Ma. In contrast, the largest population of zircon ages (65%) is early Palaeoproterozoic to Neoarchaean in age (>2400 Ma). The relative lack of old apatite ages in comparison to the proportion of old zircon ages may reflect the increasing chance that old source rocks will have experienced subsequent heating and metamorphism that would reset the apatite U–Pb ages. Alternatively, the relatively high abundance of older zircon ages could also represent the recycling and concentration of old zircons through several sedimentary cycles rather than being a reflection of primary provenance (e.g. Andersen et al., 2016).

The geochemical signatures of the Neoproterozoic populations in YP6 and YP8 are similar to YP4, characterised by elevated Sr concentrations (>500 ppm) in combination with La/Nd ratios and REE patterns that suggest a mafic to intermediate source (Fig. 5.6). This magmatic composition is less likely to produce zircon and may explain the discrepancy between the abundance of Neoproterozoic apatite and zircon ages in YP8.

Older (Palaeoproterozoic or Archaean) apatite grains from YP6 and YP8 have a broad range of trace element and REE characteristics, and do not form such clear populations as those grains discussed thus far. They are variably enriched in LREE and Th, with a significant proportion of analyses falling on either side of the Th/U 1:1 line, and a similarly wide distribution in terms of LREE enrichment as seen on the REE plots and the La/Nd vs La+Ce/ΣREE discrimination diagram. Large negative Eu anomalies are present in a minority of older grains, but small or non-existent anomalies are most common. The Sr contents of most of these grains are low (<400 ppm), with only a few grains that have high (>700 ppm) concentrations.

Sample YP6 yielded 68 <5% discordant zircon U–Pb ages that range from 663 ± 13 to 2807 ± 27 Ma, with a major population at 1800–2000 Ma and an older

peak at ~2590 Ma (Priyatkina et al., 2016). The YSG age is 663 ± 13 Ma. The apatite U–Pb data from YP6 are difficult to interpret due to the highly scattered analyses that do not neatly fall into linear arrays. Trace element characteristics in the different populations are similar to those in YP8, particularly in terms of the high Sr of the younger population and the broadly similar REE profiles. The apatite U–Pb age distribution produces peaks somewhat younger than the zircon age distribution, but the proportion of apatite and zircon grains in each age group is much more similar than for other samples. This is indicative of a broad trend from YP4 through YP8 and YP6, where the proportion of Neoproterozoic apatites decreases as the proportion of >2000 Ma apatites increases. This trend may reflect either the depletion of the young apatite source or an increase in the volume of sediment from a source of older apatites over time.

Implications for the depositional age of the Sukhopit Group

Previous work has generally assumed that the sedimentary rocks of the Sukhopit Group were deposited during the Mesoproterozoic (e.g. Likhanov et al., 2007). The presence of a significant population of apatites with a lower intercept age of ~860 Ma in sample YP4 calls into doubt the correlation of the metamorphic rock unit that this sample was taken from, as this result implies the unit is younger than the Kalami pluton (875 ± 7 Ma; Vernikovsky et al., 2007) that cuts rocks of the Korda Formation elsewhere in the Yenisey Ridge (Varganov et al., 2010). The combination of multiple data sets in our study lends strong evidence to the interpretation of a Neoproterozoic depositional age for sample YP4. The grains that appear to belong to this population all have very similar trace element and REE chemistry, plotting in a tight grouping on the discrimination diagrams and on the REE plot (Fig. 5.6, Fig. 5.8).

This is also seen in the Sr concentrations plotted on the concordia plot for YP4 in Figure 4, with a clear contrast between the Neoproterozoic and Palaeoproterozoic age populations. Metamorphic apatites are commonly characterised by depletion of Th and LREE, particularly in metapelitic samples where the apatite coexists with monazite or epidote (Henrichs et al., 2018; Spear and Pyle, 2002). Figures 6 and 8 show that apatites belonging to the Neoproterozoic age population in YP4 are enriched in LREE and have Th-U ratios greater than 1:1. Based on these criteria, it seems unlikely that the younger apatite population is composed of apatites grown under metamorphic conditions.

The closure temperature of the U–Pb system in apatite is dependent on a number of factors, including the cooling rate, the size of the diffusion domain, and the presence of the conceptual “infinite reservoir” into which Pb can be lost (Blackburn et al., 2011). There is no systematic difference in the grain size or shape of apatites from each of the age populations in YP4, and given that these grains were separated

from a quartzite it seems unlikely that they belonged to different chemical domains within the rock that may have inhibited diffusion of Pb (e.g. Blackburn et al., 2011) or were protected by grain armouring (e.g. Krenn and Finger, 2004).

The greenschist facies metamorphism and corresponding temperatures experienced by the sample means that it is plausible that very slow cooling rates could induce resetting of the apatite U–Pb ages (Blackburn et al., 2011). However, the clear and well defined populations with no continuum of ages representing partially reset grains (Fig. 5.4) suggests that it is unlikely that the different age populations reflect resetting via thermally activated volume diffusion of radiogenic Pb. The distinct trace element and REE profiles that characterise each population further lends evidence to the argument that these are detrital populations. The closure temperatures of Sr and REEs in apatite are significantly higher than Pb (>550°C; Cherniak, 2000), so it is unlikely that the observed geochemical differences between the populations reflect resetting via thermally activated volume diffusion under the temperature conditions this rock is thought to have experienced, suggesting a detrital origin for these geochemical populations.

In light of these consistent results from independent methods of classification, it seems most likely that the Neoproterozoic age apatite grains in YP4 were sourced from a Neoproterozoic magmatic rock of intermediate–mafic composition.

Above the Chingasan–Chapa unconformity

Apatites from three samples (YP15, 21, and 23) from above the Chingasan–Chapa unconformity were analysed, but only one (YP21) possesses zircon U–Pb data. The sample from the lower part of the Nemchanka Formation of the Chapa Group, YP15, has two apatite age populations. An older, Palaeoproterozoic population contains ~26% of the grains, while the younger, rather scattered Neoproterozoic age population comprises the remaining ~74% of the grains.

Sample YP21, from the upper part of the Nemchanka Formation, records three peaks in both apatite and zircon data. Sample YP21 yielded 78 <5% discordant zircon U–Pb ages that range from 834 ± 19 Ma to 2769 ± 15 Ma, with major peaks at ~1880 Ma and ~2580 Ma (Priyatkina et al., 2016). The YSG age is 834 ± 19 Ma. The youngest (Tonian) apatite age peak at 839 ±39 Ma compares well with the zircon age peak at 834 ± 19 Ma (Priyatkina et al., 2016). The populations are similar in terms of age, but vary in the proportion of data that they represent. The youngest zircon population consists of only three grains, constituting only a very small proportion (4%) of the total zircon population, while this population in the apatite data contains 40% of all grains in the sample. This disparity may stem from biases in the generation or preservation of zircon relative to apatite.

The large population of very old zircons is probably due to the persistence of these grains through several sedimentary, metamorphic or magmatic cycles, and

does not accurately reflect the primary magmatic signature of the source (e.g. Andersen et al., 2016). The relative abundance of young apatites compared to zircon may suggest that a more mafic magmatic rock contributed significant amounts of sediment, or that a rock that experienced moderate–high grade metamorphism was a major source. The geochemical signatures for the apatite populations are similar to those for sample YP15 and are summarised below.

For the sample from the Cambrian Evenki Formation (YP23), only a single, highly scattered Neoproterozoic apatite age population was defined. The analyses are rather scattered in Tera-Wasserburg space, but have quite consistent REE profiles. The Neoproterozoic age component of the Chapa Group and Evenki Formation rocks (above the unconformity) is significantly more abundant than the equivalent age population in the Chingasan and Sukhopit Group rocks (below the unconformity). Post-unconformity younger grains are relatively consistent between the samples in terms of REE characteristics, and notably different as a group from the young component below the Chingasan–Chapa unconformity (Fig. 5.9). These grains have mostly flat to LREE depleted REE profiles and strong negative Eu anomalies. This signature is characteristic of S-type and felsic I-type peraluminous granites (Sha and Chappell, 1999). The depletion of Th in most of these grains supports this interpretation as the expected crystallization of monazite prior to apatite in these rocks would also take up Th preferentially (Sha and Chappell, 1999).

The Palaeoproterozoic age component from the Chapa Group rocks is relatively small and does not have any strong defining characteristics. They tend to be flat to moderately enriched in LREE, have low Sr concentrations, low La/Nd ratios, and a range of Eu characteristics, from moderately negative to moderately positive anomalies, possibly indicating a felsic source (Figs. 5,7,8). In YP15 they tend to be enriched in Th, while in YP21 they are more often depleted in Th.

5.5.3 Sediment sources

The Palaeoproterozoic and Archaean age component throughout all the samples is derived from a mixture of sources, with no unifying geochemical characteristics within or between samples. This is expected, as this age component in the detrital zircon record is interpreted to represent material derived from the basement of the Siberian Craton (Priyatkina et al., 2016). In most samples, the population of zircons that records the oldest (>2000 Ma) ages represents a large proportion of all zircons, while in apatite these ages represent a much smaller proportion of the total population. This probably represents the decreased preservation potential of ancient apatite grains in terms of both chemical or mechanical destruction and U–Pb reset. These >2000 Ma grains in the apatite record do not form clear linear arrays in Tera-Wasserburg space and so the ages are poorly defined in addition to being relatively rare. The zircons of this age are interpreted in priyatkina2016 to be

derived from the granites and high-grade metamorphic rocks of the Tungus block (e.g. Rosen et al., 1994; Turkina et al., 2012).

The late Palaeoproterozoic age component at 2000–1750 Ma is characteristic of sediments derived from the Siberian Craton due to extensive magmatism at this time related to the amalgamation of Siberia (e.g. Gladkochub et al., 2013; Glorie et al., 2014; Powerman et al., 2015; Safonova et al., 2010). This population is well defined in some apatite samples, although in other instances (e.g. YP6) it is difficult to distinguish between grains from an older source and the main (~1850 Ma) Palaeoproterozoic peak. The geochemical signatures of these grains are again quite mixed due to the range of sources, including a wide range of magmatism and high-grade metamorphic rocks of this age, that are common on the western margin of the Siberian Craton. The abundance of the 'Siberian' population changes throughout the stratigraphy. The relative increase in the numbers of older apatite grains from YP4 through YP8 up to YP6 is reversed across the Chingasan–Chapa unconformity, after which Palaeoproterozoic or older apatite are relatively rare. A more in-depth discussion of the provenance of the Archaean and Palaeoproterozoic zircons in these samples can be found in Priyatkina et al. (2016).

The source of the Neoproterozoic age component shows systematic changes throughout the stratigraphy (Fig. 5.9). There is a strong geochemical similarity between the Neoproterozoic age component of the deformed and metamorphosed rock from which YP4 was sampled and the unconformably overlying Chingasan rocks (YP6,8). The source of this population is most likely the mafic–intermediate volcanic equivalents of the Teya granite (880–860 Ma; Vernikovsky et al., 2007). In this interpretation, the early phases of the widespread 880–840 Ma magmatism in the Yenisey Ridge contribute material to the rock unit from which YP4 was sampled, which was subsequently deformed and metamorphosed.

The Chingasan Group rocks were then unconformably deposited onto the older metamorphosed rock. The samples from Chingasan rocks (YP6, 8) have a Neoproterozoic source similar to YP4, but the 'Siberian' age component is markedly different in terms of geochemistry. The Neoproterozoic component is also smaller in the Chingasan Group than in the older YP4, and decreases further in relative abundance in the upper part of the sequence (from YP8 to YP6), indicating the depletion of this source over time. The abundance of the Archaean component of the apatite and zircon populations also increases in the upper part of the Chingasan Group, suggesting an increase in sediment sourced from the Tungus block that is characterised by rocks of this age (e.g. Turkina et al., 2014).

The unconformity that demarcates the boundary between the Chingasan and Chapa Group rocks heralds a major change in the source and relative abundance of the Neoproterozoic age component. Apatites from the Chapa Group rocks are dominated by the Neoproterozoic age component, which has a geochemical signature

that can be interpreted as deriving either from an evolved I or S type granite or from a metamorphic rock. Many of the intrusive igneous rocks in the Yenisey Ridge with ages of 880–840 Ma, such as the Teya, Kalami, and Yeruda plutons, are considered to be I to S type (e.g. Nozhkin et al., 2015; Vernikovsky et al., 2007). There are also abundant metamorphic rocks in the area, particularly the Teya Group, which experienced peak metamorphism at ~825 Ma (Likhanov et al., 2012). Thus, it is likely that the Chapa Group rocks were sourced mostly from the Yenisey Ridge, with perhaps some input from the Siberian Craton. This is consistent with palaeocurrent measurements from the Nemchanka Formation in the vicinity of YP21, indicating a NNE direction of flow from the core of the Yenisey Ridge outward onto the craton (Priyatkina et al., 2016).

5.6 Conclusions

In this study, we show how the analysis of detrital apatite can provide important and useful information about the source of sedimentary material, and how this information can be combined with zircon U–Pb data to take advantage of the complementary and intersecting archives of information these minerals contain. In particular, this approach can detect the presence of mafic source rocks that may go undetected through purely the use of detrital zircon analysis.

The trace element data presented in this study complement the apatite U–Pb data, providing information that explicitly ties the age of an apatite grain to the source rock. As such, this method is an improvement on approaches that rely on different materials to provide age (e.g. zircon U–Pb) and source rock information (e.g. whole rock geochemistry or heavy mineral analysis). When used in conjunction with detrital zircon analysis, the relative age abundance of detrital apatites can also provide further insight into the source of sediment and highlights biases in an interpretation based only on zircon U–Pb data.

The change in source detected in this study by the combination of apatite U–Pb and trace element analysis provides insight into the tectonic evolution of the region that could not be detected by either of these methods performed in isolation. We therefore recommend the use of multi-method apatite analysis as a new tool that can be applied to understand the source of sediment.

Chapter 6

Summary and conclusions

This chapter contains a summary of the results of the preceding chapters, and discusses future directions for research. As each chapter integrates and discusses the new results in the context of the intracontinental evolution of Central Asia, this chapter will not duplicate these points, but will instead provide an broad summary, highlighting the key outcomes of the work presented here and exploring their significance in terms of our understanding of the tectonic evolution of Central Asia over the last ~300 million years.

6.1 Summary

In this thesis, the thermotectonic history of three areas to the north-east and east of the Tianshan were studied through fission track and (U-Th-Sm)/He analysis, in an attempt to better understand the pre-Cenozoic distribution of reactivation and exhumation in Central Asia, and to help interpret thermochronological data from elsewhere in the Central Asian Orogenic Belt.

Chapter 2 found that the easternmost ranges of the Tianshan, the Harlik (or Karlik) and Balikun (or Barkol) ranges experienced a thermotectonic history comparable to the other ranges of the Tianshan to the west (e.g. Jolivet et al., 2010; Glorie and De Grave, 2016). Jurassic to Cretaceous AFT central ages are by far the most common, whereas some older Triassic ages were also found in the areas outside the modern fault-bound ranges that were not significantly reactivated during subsequent Mesozoic and Cenozoic tectonic deformation. A key difference is that in this study (Chapter 2) no Cenozoic cooling was detected. In comparison, evidence for late Cenozoic rapid cooling has been found in the Chinese central Tianshan and Kyrgyz Tianshan proximal to major structures that accommodate recent deformation in response to the India-Eurasia collision (Sobel et al., 2006b; Jolivet et al., 2010; Glorie et al., 2011). The lack of very young cooling ages reflects the lesser amount

of denudation and exhumation experienced by the easternmost Tianshan relative to areas further west, as a consequence of the position of the western syntaxis of the Himalayas in the Pamirs, where the most intense deformation has occurred (Avouac et al., 1993).

This history contrasts with the West Junggar (Chapter 3) and Tarbagatai Mountains (Chapter 4), which lie to the north-east of the Tianshan (Fig. 6.1). These areas record evidence for widespread late Paleozoic or early Mesozoic rapid cooling. Fission track ages are mostly from the Permian, Triassic, or earliest Jurassic. Some localised zones produce younger Jurassic–Cretaceous ages, and these are focussed mainly around structures inherited from the Permian–earliest Triassic strike-slip deformation of the Central Asian Orogenic Belt, following its amalgamation.

Permian and Triassic AFT central ages are rarely preserved in the high altitude Tianshan due to subsequent exhumation that destroyed the rock containing this thermochronological signal. However, higher temperature $^{40}Ar/^{39}Ar$, titanite fission track, and zircon (U-Th)/He dating record these older Permian–Triassic ages more widely (Jolivet et al., 2010; De Grave et al., 2011a; De Grave et al., 2013). Apatite and titanite fission track ages from the Late Triassic–Early Jurassic are preserved in ancient landscapes within the Tianshan, such as the Song-Kul basin, which was protected from subsequent phases of deformation by the surrounding structures (De Grave et al., 2011a). In the Altai, similar Late Triassic–Early Jurassic titanite fission track ages are preserved in fault-dominated profiles (Glorie et al., 2012a).

In Uzbekistan, Triassic apatite fission track ages are found along the margins of uplifted areas, where they were preserved due to the lesser amount of subsequent uplift (Fig. 6.2B). These relict landscapes in Uzbekistan are comparable to the Tarbagatai Mountains in that they are ~2000–3000m lower in elevation than the areas in Kyrgyzstan discussed above. Lower temperature methods such as AFT still preserve old ages, without the unusual circumstances necessary for preservation such as in the Song-Kul intramontane basin.

Much of Uzbekistan also appears to have not experienced the major phases of deformation that the central Tianshan was subjected to, seemingly due to the Talas-Ferghana Fault partitioning stress along its length. As a result of this, regional Jurassic–Cretaceous deformation occurred in the Kyrgyz Tianshan to the east of the TFF (Nachtergaele et al., 2018), whereas the deformation experienced the westernmost Tianshan was focussed along reactivated structures (De Pelsmaeker et al., 2018; Jepson et al., 2018c).

The prevalence of older fission track ages in the West Junggar and Tarbagatai Mountains, to the north of the Tianshan, could be interpreted in several ways. The older fission track ages could reflect mostly that they were not reactivated during the late Cenozoic to a significant extent, and so record a thermochronological signal that reflects the state of the Central Asian upper crust prior to late Cenozoic exhumation.

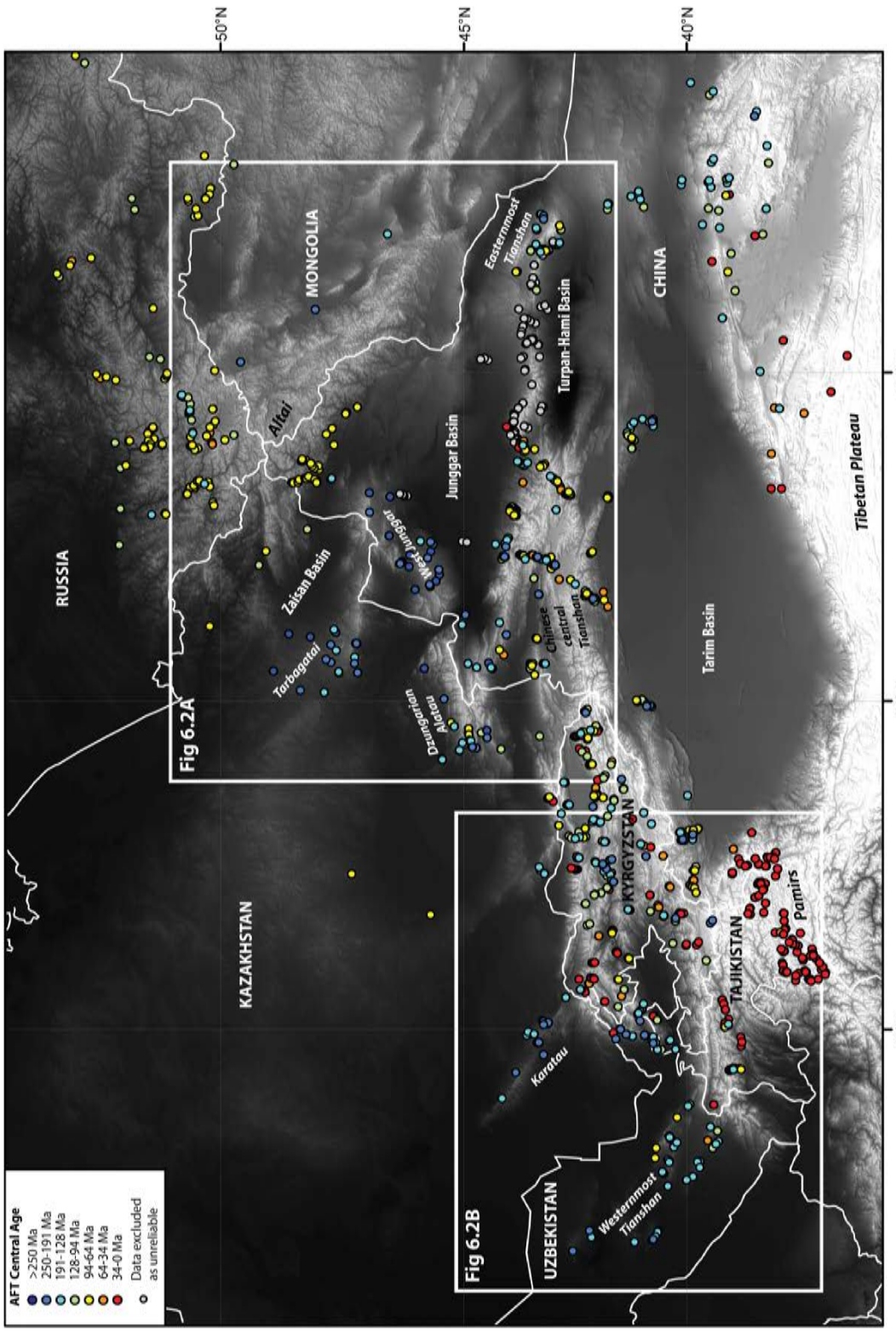

Figure 6.1: Topographic map of Central Asia, displaying a compilation of AFT data in the region.

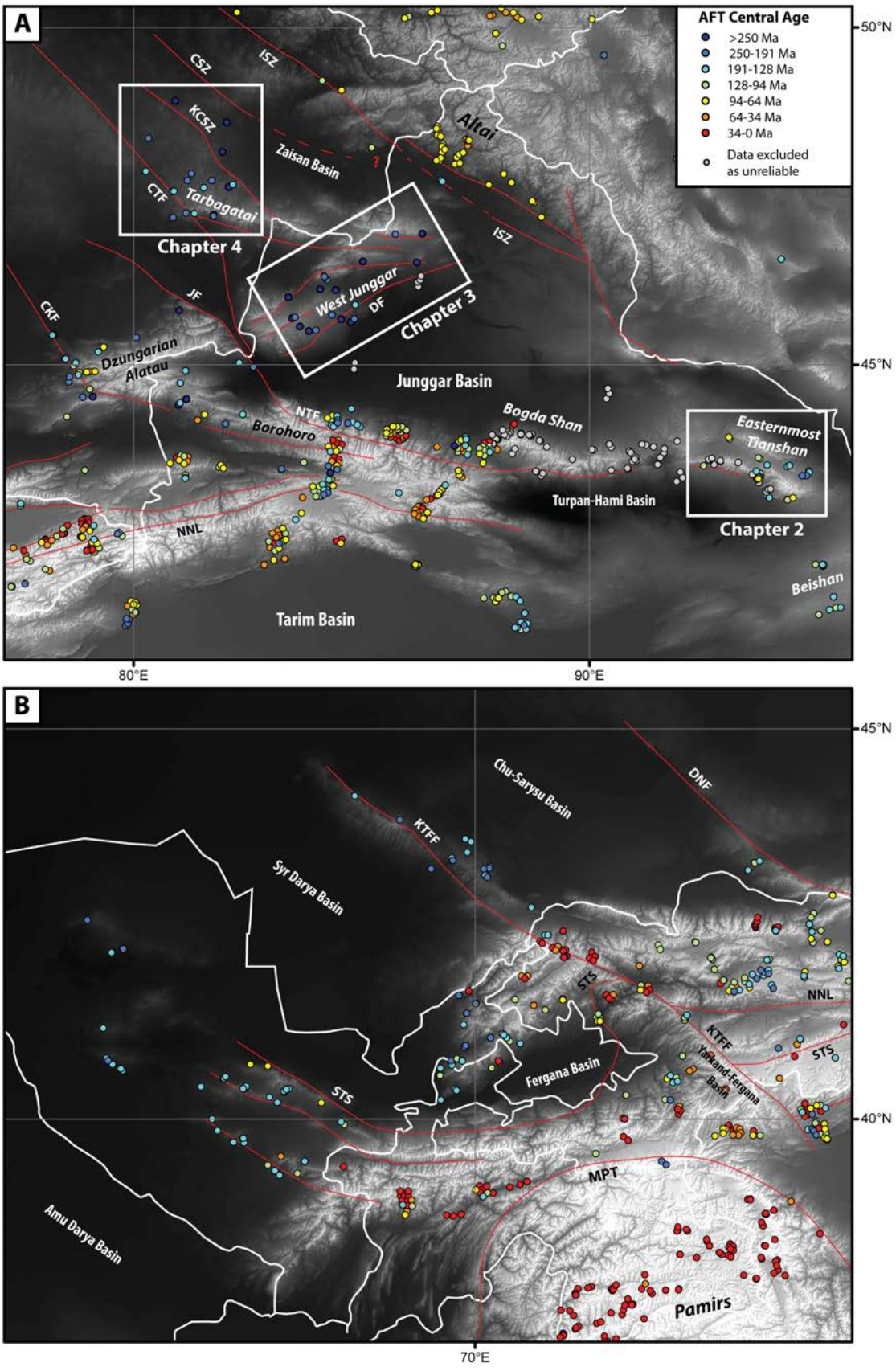

Figure 6.2: See following page for caption.

Figure 6.2: A) Topographic map of the eastern Tianshan, Junggar Basin, and southern Altai. B) Topographic map of the western Tianshan and Pamirs. Acronyms for labelled structures: ISZ = Irtysh Shear Zone, CSZ = Char Shear Zone, KCSZ = Kalba-Chingiz Shear Zone, CTF = Chingiz-Tarbagatai Fault, JF = Junggar Fault, DF = Dalabute Fault, CKF = Central Kazakhstan Fault, NTF = North Tianshan Fault, NNL = Natali-Nikolaev Line, DNF = Dzalair-Naiman Fault, KTFF = Karatau-Talas-Fergana Fault, STS = South Tianshan Suture, MPT = Main Pamir Thrust.

This interpretation implies that the record of cooling revealed in Chapters 3 and 4 is representative more broadly of Central Asia and that Jurassic–Cretaceous cooling was mostly focussed around reactivated structures. An alternate hypothesis is that the lithosphere of these regions to the north of the Tianshan is relatively stronger and so was not reactivated to the same extent throughout the intracontinental evolution of the CAOB.

Comparing the thermotectonic history of the northern and southern limbs of the Kazakhstan Orocline (Windley et al., 2007; Li et al., 2018) shows that the different parts of the Baslkhash-Yili arc, in the vicinity of the Tarbagatai Mountains and in the central Chinese Tianshan, respectively, record very different thermal histories (Fig. 6.1; Chapter 4; Dumitru et al., 2001; Jolivet et al., 2010). Most striking perhaps is the contrasting history of equivalent rocks of the Junggar-Balkhash accretionary complex in the West Junggar (Fig. 6.2A; Chapter 3), on the northern side of the Borohoro Mountains (Jolivet et al., 2010), and in eastern Kazkahstan between the Dzungarian Alatau and the Tarbagatai Mountains. The part of the Borohoro Mountains to the north of the North Tianshan Fault, on the southern margin of the Junggar Basin, has been significantly uplifted in response to the India-Eurasia collision and is an area of high elevation and relief. In contrast, the parts of eastern Kazakhstan where the basement is composed of equivalent rocks from the Devonian-Carboniferous accretionary complex is a regional low that contains Lake Balkhash and Lake Alakol. The same rocks on the western margin of the Junggar Basin form a low range of mountains that have very low internal relief and preserve old AFT and AHe ages that suggest that this area has been tectonically stable since the Permian (Chapter 3). The anomalous trend of the major structures in this area may explain why this is the case, as NE–SW trend of the major structures (Fig. 6.2A) was probably not oriented favourably with regard to the principle stresses that caused later reactivation in Central Asia (Cunningham, 2013). Given these examples, variations in the lithospheric strength does not seem like a satisfactory explanation for the patterns of thermochronological data and deformation that are recorded across the region.

The location of these areas adjacent to the Junggar Basin may be significant. Al-

though the nature of the basement below the Junggar Basin is unclear, the strength of the lithosphere in this location rather than in the adjacent regions could be more important in terms of controlling the distribution of strain. Stress propagating through the basement of the Junggar Basin would drive deformation at the northern and southern margins, as has occurred during the late Cenozoic, protecting regions like the West Junggar and Tarbagtai, which lie to the west. If this is responsible for the differences in the thermal histories, it would further imply that the orientation of the principle stress during past deformation was comparable to the modern orientation.

In addition to the generally lesser amount of reworking experienced by the regions to the north-east of the Tianshan, a pattern of localised reactivation along major inherited structures has emerged in this thesis and other recent studies. However, the nature of localised fault reactivation along the northern margin of the Tianshan is still ambiguous. Thermochronological data from the vicinity of major NW–SE striking faults such as the Chingiz-Tarbagatai Fault in the Tarbagatai Mountains (Chapter 4) and the Central Kazakhstan Fault in the Dzungarian Alatau (Glorie et al., 2019) are younger than samples taken at a greater distance from these faults. Thermal history modelling indicates a distinctly different thermal history for fault proximal versus fault distal samples. Apatite fission track ages from fault proximal samples are generally Middle Jurassic–Early Cretaceous in age and have a range of MTLs. Mostly Early Cretaceous AHe ages from these areas are also evidence for cooling at this time. However, the precise timing, spatial extent, and magnitude of this cooling is not yet clear. The range of MTLs indicates that many of the samples recording younger fission track apparent ages probably resided in the APAZ for some time.

A lack of structural studies focussed on the Mesozoic evolution of these structures, and the general challenges associated with directly dating brittle fault movement make determining the nature of reactivation difficult. Glorie et al. (2019) interprets localised Early Cretaceous cooling to be the result of transtensional fault reactivation in response to slab rollback in the Tethys predicted by global plate reconstructions (Zahirovic et al., 2016). However, the southern Junggar and northern Tarim basins are thought to have experienced basin inversion during the Early Cretaceous, and in the Zaisan basin, Paleozoic transpressional structures were reactivated as high-angle thrusts in the Late Jurassic–Cretaceous (Hendrix et al., 1992; Yang et al., 2013b; Li et al., 2015a).

Jurassic transtensional deformation along the Talas-Fergana fault is reflected in the basins along the fault created as a result of this fault activity (Burtman, 1980; Allen et al., 2001). Morin et al. (2018) suggests that the Early–Middle Jurassic opening of the Yarkand-Fergana Basin was due to this transtensional deformation, which was driven by extension associated with back-arc development in the Neo-

Tethys (Brunet et al., 2017). The Yarkand–Fergana Basin was inverted in the Late Jurassic–Early Cretaceous (Morin et al., 2018) in conjunction with spatially restricted relief building in the adjacent Kyrgyz Tianshan (Nachtergaele et al., 2018), perhaps in response to the collision of the Helmand Block or the Lhasa terrane (Brunet et al., 2017; Morin et al., 2018). Uplift of parts of the Amu Darya Basin and basin inversion in southern Afghanistan during the Late Jurassic–Early Cretaceous supports this interpretation (Brunet et al., 2017).

Compressional or transpressional reactivation of these structures seems more likely than extensional or transtensional reactivation given the evidence, although the driver of this phase of activity is still unclear. The collision of the Lhasa block with the southern Eurasian margin (Kapp et al., 2007; Zhu et al., 2016; Kapp and DeCelles, 2019) and the closure of the Mongol-Okhotsk Ocean (Zorin, 1999; Van der Voo et al., 2015) have been variously suggested as the explanation for Central Asian deformation during the Cretaceous (De Grave et al., 2007; Jolivet et al., 2010), but no clear consensus has emerged.

Following the Mesozoic, no thermochronological evidence for Cenozoic cooling was found in the areas studied in this thesis. The low elevation of the West Junggar and Tarbagtai Mountains, relative to other ranges in Central Asia, make this result unsurprising. Samples from the easternmost Tianshan also did not record late Cenozoic ages, although it is possible that the sampling was not dense enough to detect the potentially narrow zones that might be expected to record late Cenozoic ages, as in the Chinese central Tianshan. Evidence for Quaternary activity along structures such as the Junggar Fault, Dalabute Fault, and the bounding faults of the easternmost Tianshan attest to their recent reactivation (Allen and Vincent, 1997; Cunningham et al., 2003; Campbell et al., 2013), and the role of modern deformation in generating the uplift that is visible today.

6.2 Future directions

6.2.1 Central Asian Tectonics

Future work on understanding the intracontinental tectonics of Central Asia during the late Paleozoic, Mesozoic, and Cenozoic should build on the large body of fission track and other low-temperature thermochronology. Additional basement and detrital thermochronology of understudied regions would be beneficial, with the vast scale and political sensitivity of the area in question being a constant challenge to workers.

A key weakness of low-temperature thermochronology as a tool for studying mountain-building and uplift is the difficulty in linking cooling to surface uplift (e.g. England and Molnar, 1990). Well-constrained elevation or down-hole profiles

can reliably reconstruct the timing and amount of exhumation, but the array of assumptions and uncertainties concerning the rate of erosion over time is a major limitation on the translation of low-temperature thermochronology to models of surface uplift and topography. Further paleoclimatological and paleoenvironmental studies of sites in Central Asia could improve our understanding of the climatic conditions during the Mesozoic. Increasing the temporal and spatial resolution of climate reconstructions are critical to improving estimates of the rate of erosion in the past. More extensive stable isotope studies of sedimentary sequences over key intervals could be used to understand variation in the local climate (e.g. Jolivet et al., 2018b). Clumped isotope studies could potentially help understand the paleoelevation of sites if appropriate study locations are identified (e.g. Quade et al., 2011).

In general, more detailed studies of the Mesozoic sequences in basins throughout Central Asia would be hugely beneficial to our understanding of the timing and magnitude of uplift and erosional events.

Another significant gap in our understanding of Central Asian geology is the timing of fault reactivation. Direct $^{40}Ar/^{39}Ar$ dating of ductile deformation in the Permian–earliest Triassic along structures throughout Central Asia is convincingly linked to large scale strike-slip deformation via the dissection of Paleozoic island arc terranes, and the relative rotation of continental units with respect to one another seen in paleomagnetic data (Shu et al., 1999; Laurent-Charvet et al., 2003; Levashova et al., 2003a; Wang et al., 2007; Choulet et al., 2012a; Li et al., 2018). Quaternary reactivation is also widely documented through observations of the offset or cutting of recent alluvial fans, river channels and terraces, and other modern sedimentological features (e.g. Tapponnier and Molnar, 1979; Avouac et al., 1993; Cunningham, 2013). The Mesozoic and pre-Quaternary Cenozoic brittle deformational history is by comparison extremely poorly understood, and although some major structures are inferred to have been reactivated due to the thermochronological data in their vicinity, direct dates for Mesozoic reactivation are rare. This stems from the difficulty in directly dating brittle deformation. Recent advances in the LA-ICP-MS U–Pb dating of fault-vein hosted calcite provides a means to do so, and this has been successfully applied in several locations throughout the world (Roberts and Walker, 2016; Nuriel et al., 2017; Hansman et al., 2018). This approach could be applied to understand the distribution and timing of brittle deformation through direct dating, complementing the information about the timing of cooling in the surrounding rock gleaned from low-temperature thermochronology.

6.2.2 Apatite provenance studies

Interest in the application of apatite U–Pb and trace element analysis to the problem of detrital provenance has recently increased. While previous publications applied either apatite U–Pb or trace element geochemistry separately to understand the source of detrital apatite grains, in the last few years a number of publications have combined these tools. Advances in LA-ICP-MS U–Pb dating of apatite in the last decade addressed some of the analytical challenges related to the U–Pb isotopic analysis and made routine acquisition of these data practical. Meanwhile, although it is analytically more straightforward to determine apatite trace element concentrations via LA-ICP-MS, our understanding of the trace element signature (e.g. concentrations of Sr, Mn, Y, REEs, etc) of different source rocks is highly variable. Many studies concerning the trace element concentrations of apatite from different igneous rocks allow for reasonably good discrimination of these rock types (Sha and Chappell, 1999; Morton and Yaxley, 2007; Chu et al., 2009), but until recent publications by Henrichs et al. (2018) and O'Sullivan et al. (2018), the trace element geochemistry of metamorphic apatite was poorly understood, especially in terms of the REEs. These publications improved our ability to detect in particular low-medium grade apatite from metapelitic and metabasic rocks. However, the huge variety of possible protoliths and the diversity of pressure-temperature (P-T) paths and conditions that a metamorphic rock could experience make generalisation difficult. The behaviour of apatite in medium-high grade metamorphic rocks of all protoliths, and in low-medium grade low-reactivity rocks (e.g. some igneous or quartz-rich sedimentary rocks) are important subjects for further study. These studies would improve our ability to further discriminate between sources of detrital apatite, with addition benefits in terms of our interpretation of U–Pb data from these grains. The geochemistry of apatite from well-studied metamorphic rocks would also be useful for the integration of apatite into metamorphic PT modelling. Incorporating phosphate accessory minerals (such as apatite and monazite) into PT modelling would enable more advanced petrochronological investigation and feedback into our understanding of apatite trace element geochemistry.

The O, Sr, and Nd isotopic composition of apatite provides information about the conditions under which it formed, particularly the nature of the parent magma in the case of igneous apatite (e.g. Bruand et al., 2017). These isotopic systems could provide information about the contribution of recycled material, degree of crustal assimilation, or fractionation of the melt from which an apatite grew. The analytical advances that made acquisition of these data possible are relatively new, and consequently the behaviour of these isotopes in inorganic apatite is not well understood. Detailed studies of isotopic behaviour in apatite and ongoing method development to improve analytical procedures are needed.

The low resistance of apatite to chemical dissolution in acidic groundwater (Morton and Hallsworth, 1999), and the relative ease of geochemical and isotopic reset under low-medium grade metamorphic conditions (Henrichs et al., 2018) means that apatite can eliminated from the geological record more easily than some other accessory minerals, potentially limiting the applicability of these techniques when considering very ancient rocks (e.g. Bell et al., 2018). Studying apatite inclusions in more robust mineral phases such as zircon is a promising direction, as it has been demonstrated that primary apatite occurring as inclusions (e.g. in zircon) and in the matrix of an igneous rock are geochemically identical and thus grew simultaneously, recording equivalent petrogenetic information (Jennings et al., 2011). The trace element and isotopic composition of the apatite inclusions within zircon or titanite may therefore be capsules of valuable information, as they faithfully record the composition of the melt from which the enclosing grain crystallised. These armoured grains may prove to be a critical source of information about the nature of ancient tectonics or the evolution of the early Earth.

Appendix A

Differential exhumation and crustal tilting in the easternmost Tianshan (Xinjiang, China), revealed by low-temperature thermochronology: Appendix Part 1

A.1 Introduction

The supporting information presented here contains individual radial plots of the AFT data discussed in the paper. It also contains all of the individually generated thermal history models and associated statistical information.

A.2 Radial plots

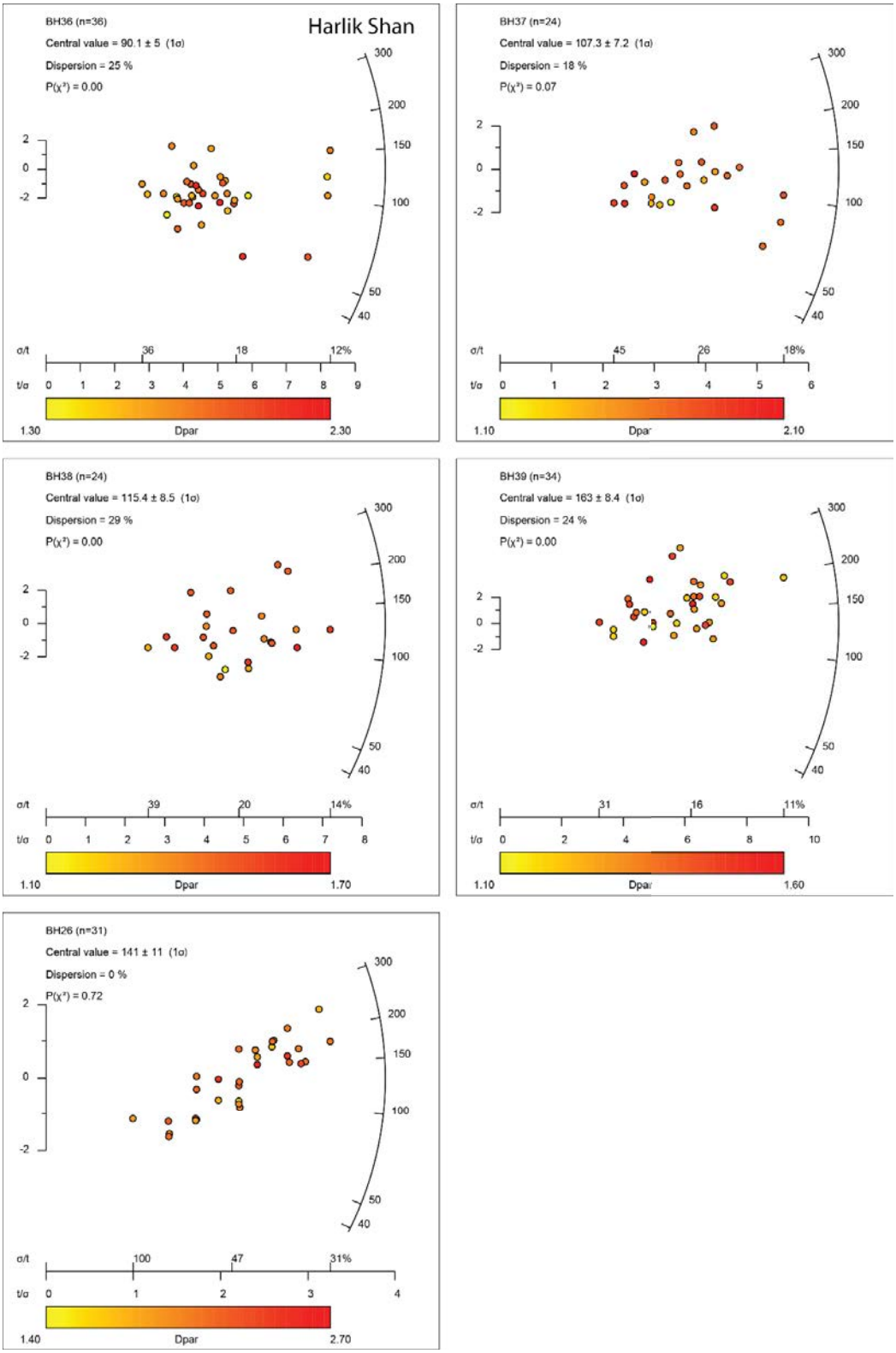

(a) Apatite fission track radial plots for samples from Harlik Shan.

Figure A.1: Apatite fission track radial plots

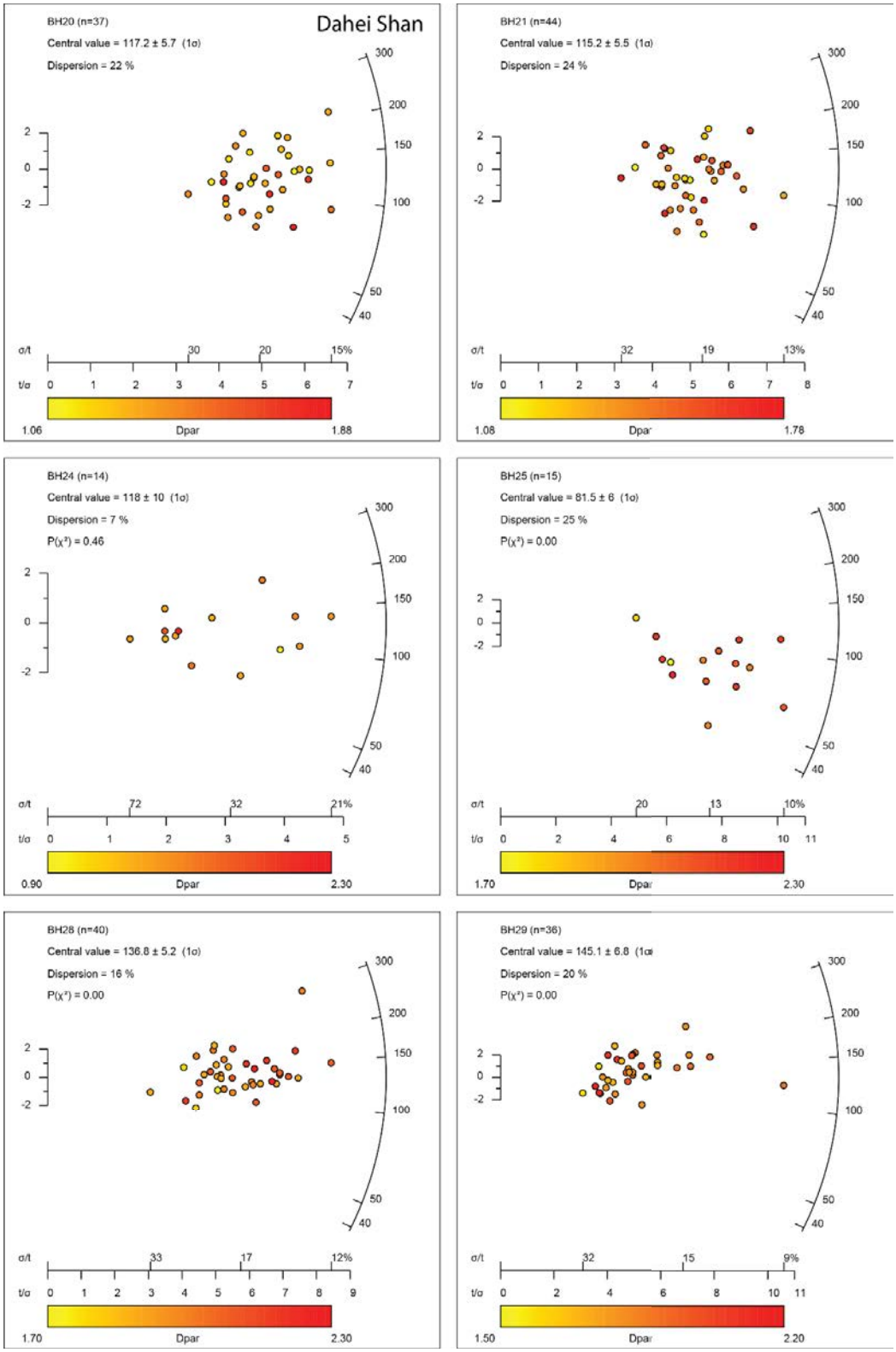

(b) Apatite fission track radial plots for samples from Dahei Shan.

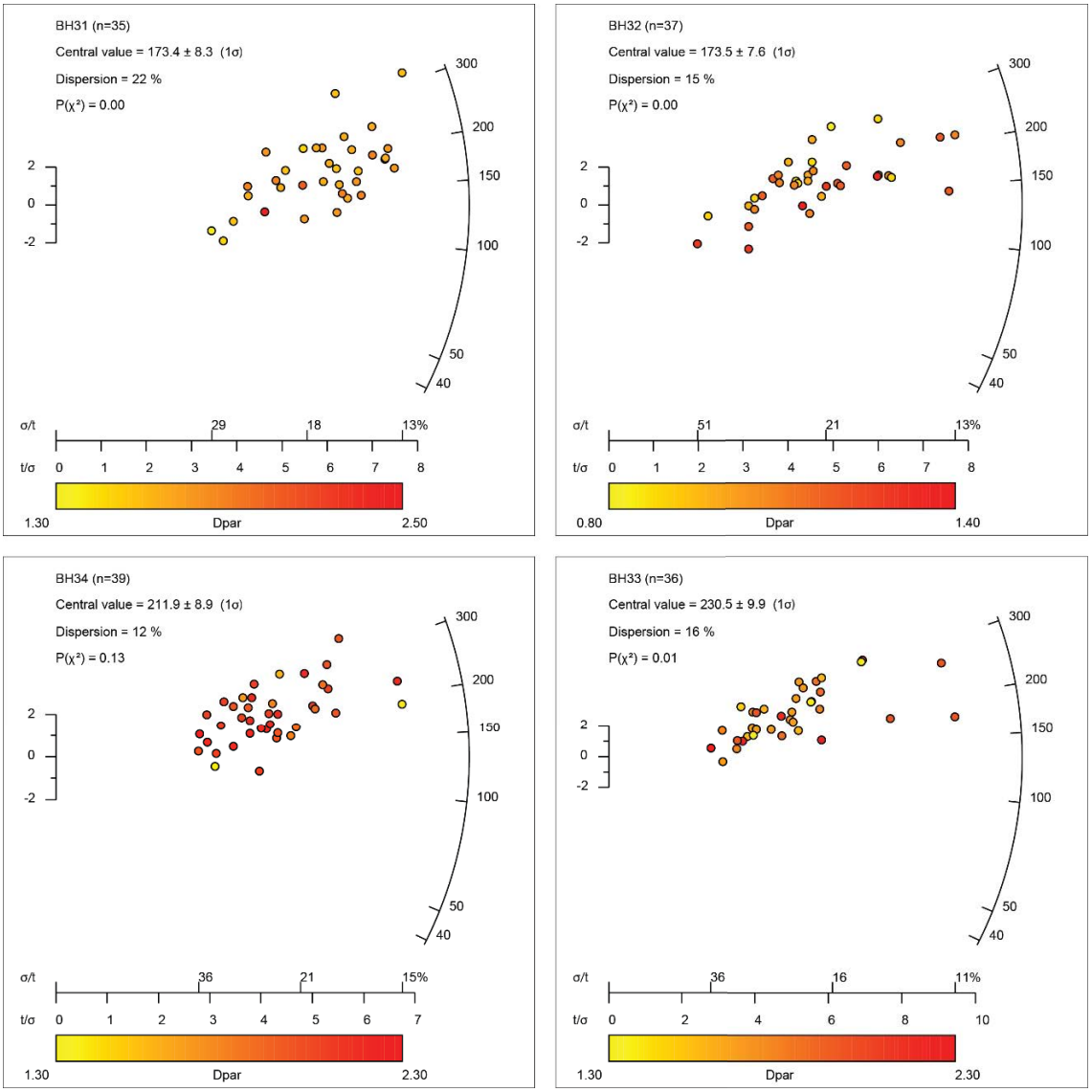

(c) Apatite fission track radial plots for samples from Dahei Shan.

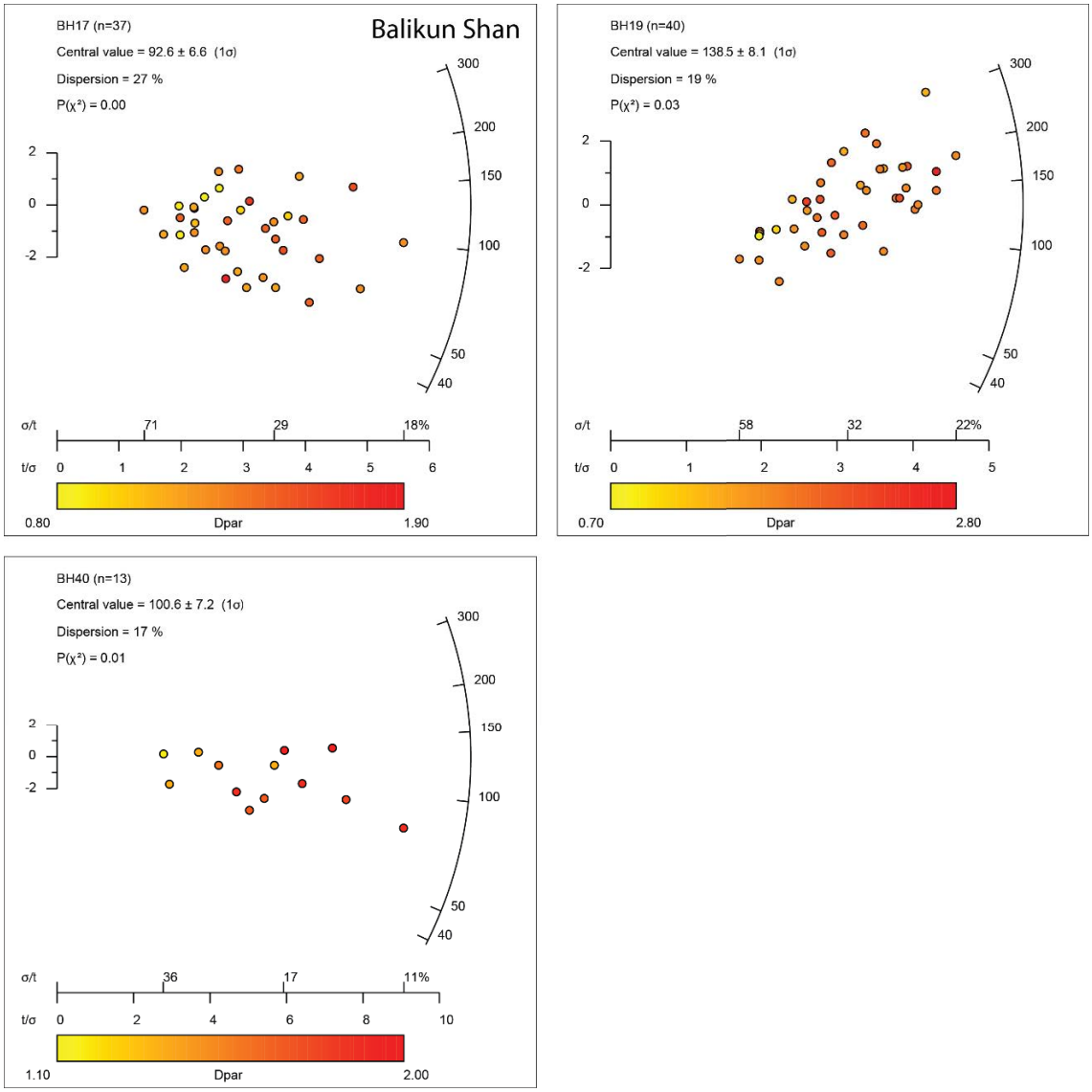

(d) Apatite fission track radial plots for samples from Balikun Shan.

A.3 Thermal history models

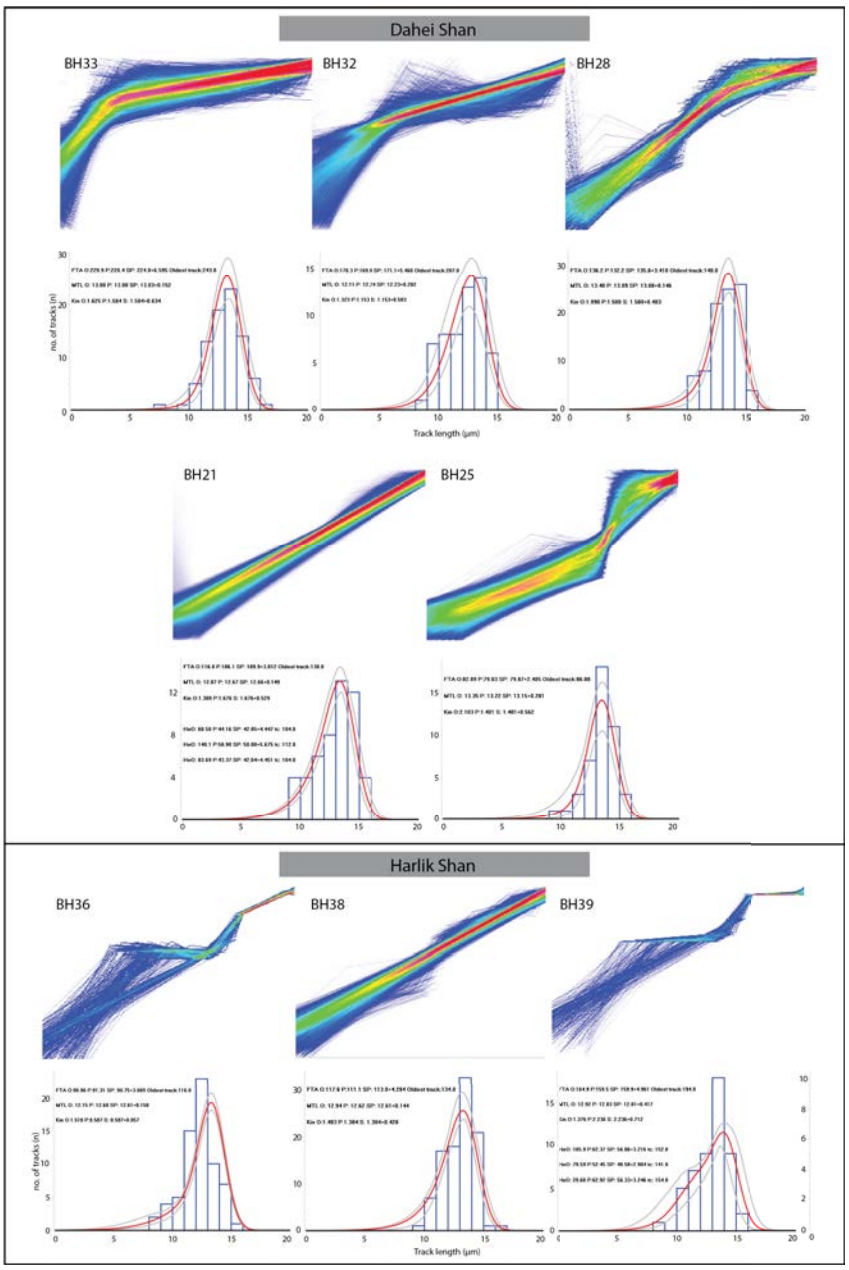

Figure A.2: Probability distributions of the sampled thermal histories for each model illustrated by coloured lines. The actual numbers attached to these probabilities are relative to the model and frequently misunderstood, so accordingly the numbered scale has been removed from the most recent version of QTQt (5.6.0) and is not included here. Histograms provide details of statistical fits between observed and predicted data generated by QTQt.

Appendix B

Differential exhumation and crustal tilting in the easternmost Tianshan (Xinjiang, China), revealed by low-temperature thermochronology: Appendix Part 2

The supporting information presented here consists of the tabulated individual grain/confined track length/analytical spot data for this chapter.

B.1 Apatite fission track individual grain data

Table B.1: Apatite fission track individual grain data

Name	^{238}U (ppm)	2σ	N_s	ρ_s	t (Ma)	1σ	D_{par}
17_1.D	8.6	2.3	6	1.78E+05	40.7	19.8	1.2
17_2.D	23.4	2.7	13	6.74E+05	56.5	17.0	1.3
17_3.D	9.9	0.6	9	6.18E+05	122.4	41.4	1.0
17_4.D	3.5	0.2	4	1.29E+05	73.1	36.7	0.9
17_5.D	9.9	1.0	18	8.78E+05	172.5	44.2	1.2
17_6.D	17.3	1.6	21	7.09E+05	80.3	19.0	1.5
17_7.D	23.1	2.0	10	5.42E+05	46.1	15.1	1.2

Continued on next page

Continued from previous page

Name	^{238}U (ppm)	2σ	N_s	ρ_s	t (Ma)	1σ	D_{par}
17_9.D	10.1	0.7	17	5.87E+05	113.1	28.5	1.5
17_10.D	2.1	0.1	7	2.32E+05	213.7	81.9	1.3
17_11.D	15.9	1.3	27	1.23E+06	150.4	31.5	1.6
17_12.D	19.0	1.1	13	5.12E+05	52.9	15.0	1.2
17_13.D	5.4	1.0	7	4.11E+05	148.3	62.4	0.8
17_14.D	10.7	0.8	15	6.39E+05	116.2	31.2	1.0
17_15.D	18.9	1.2	14	7.81E+05	81.0	22.2	1.6
17_16.D	4.7	0.3	4	2.43E+05	101.9	51.3	1.5
17_17.D	51.9	3.5	27	1.79E+06	67.5	13.8	1.3
17_18.D	4.5	0.3	5	2.84E+05	123.6	55.8	1.5
17_19.D	31.3	2.1	36	1.61E+06	100.5	18.0	1.3
17_20.D	9.8	0.5	7	3.59E+05	71.6	27.3	1.3
17_21.D	25.3	2.2	9	6.97E+05	54.1	18.6	1.2
17_22.D	2.4	0.2	2	1.40E+05	115.0	81.7	1.3
17_23.D	27.2	2.0	12	1.39E+06	99.8	29.7	1.5
17_24.D	10.9	0.9	8	5.80E+05	104.5	38.0	1.5
17_25.D	47.6	4.1	19	1.26E+06	52.1	12.8	1.5
17_26.D	14.8	1.4	14	6.79E+05	89.8	25.5	1.5
17_27.D	14.9	1.7	11	1.04E+06	136.7	44.1	1.7
17_28.D	4.0	0.3	9	4.24E+05	208.2	71.0	1.4
17_29.D	16.9	1.2	13	9.39E+05	108.6	31.1	1.3
17_30.D	18.1	2.8	9	6.29E+05	68.2	25.1	1.3
17_31.D	7.0	0.3	5	3.42E+05	95.3	42.8	1.1
17_32.D	7.2	0.4	5	2.96E+05	81.2	36.6	1.3
17_34.D	16.6	1.7	8	3.89E+05	46.0	16.9	1.9
17_36.D	16.0	1.4	6	5.19E+05	63.6	26.5	1.3
17_37.D	4.3	0.3	5	2.75E+05	125.8	57.1	1.2
17_39.D	4.1	0.3	3	1.43E+05	67.8	39.4	1.2
17_40.D	5.7	0.3	7	4.87E+05	167.8	64.2	0.8
17_41.D	5.0	0.5	4	3.25E+05	128.1	65.1	0.9
19_1.D	7.7	0.5	7	4.82E+05	121.5	46.5	1.6
19_2.D	4.1	0.2	22	3.87E+05	182.8	40.0	1.7
19_4.D	4.1	0.3	8	2.93E+05	138.5	49.8	2.2
19_6.D	7.1	0.6	3	1.77E+05	48.6	28.3	1.7
19_7.D	4.4	0.3	9	1.76E+05	77.8	26.6	2.1
19_8.D	7.1	0.5	4	3.11E+05	86.1	43.4	2.0
19_9.D	4.0	0.2	12	3.08E+05	149.0	43.9	1.7
19_11.D	4.7	0.3	7	3.30E+05	135.9	52.2	2.4
19_12.D	6.9	0.4	20	5.88E+05	165.8	38.4	2.8
19_13.D	21.0	5.0	7	4.74E+05	44.4	19.8	1.7
19_14.D	3.5	0.2	4	1.47E+05	82.7	41.6	1.5
19_15.D	6.4	0.7	13	8.44E+05	254.7	75.4	1.9
19_16.D	6.3	0.6	12	5.11E+05	157.2	47.4	1.5
19_17.D	3.6	0.3	20	5.73E+05	304.0	72.8	1.4

Continued on next page

Continued from previous page

Name	^{238}U (ppm)	2σ	N_s	ρ_s	t (Ma)	1σ	D_{par}
19_18.D	6.1	0.3	6	2.99E+05	96.0	39.4	1.6
19_19.D	6.1	0.3	8	5.25E+05	167.8	60.1	1.8
19_20.D	4.0	0.3	10	4.60E+05	224.3	72.4	1.4
19_21.D	7.4	0.5	5	3.50E+05	92.2	41.8	1.1
19_22.D	6.1	0.4	14	5.64E+05	178.6	49.3	1.4
19_23.D	5.6	0.5	14	5.18E+05	178.4	49.9	1.8
19_24.D	4.3	0.3	9	4.54E+05	205.4	70.1	2.0
19_25.D	6.1	0.3	17	3.94E+05	125.9	31.2	1.8
19_26.D	7.0	0.6	8	4.06E+05	113.0	41.2	1.9
19_27.D	4.2	0.3	10	2.05E+05	96.3	31.1	1.8
19_30.D	5.3	0.4	12	2.91E+05	107.3	32.1	2.0
19_31.D	6.4	0.4	6	4.63E+05	140.5	58.1	1.4
19_32.D	8.2	0.6	17	7.47E+05	177.8	45.2	2.1
19_33.D	6.1	0.4	18	4.07E+05	130.8	32.1	1.7
19_34.D	9.0	0.7	7	3.62E+05	79.3	30.7	1.7
19_35.D	5.0	0.3	16	4.50E+05	176.4	45.6	1.6
19_36.D	4.0	0.2	13	4.68E+05	225.3	63.9	1.9
19_37.D	7.0	0.5	4	2.82E+05	79.6	40.2	0.7
19_38.D	6.5	0.6	15	2.90E+05	86.8	24.0	1.7
19_40.D	6.4	0.5	21	4.71E+05	144.5	33.5	1.9
19_41.D	3.5	0.2	4	9.66E+04	54.5	27.5	1.7
19_42.D	7.0	0.3	9	4.18E+05	116.8	39.2	2.1
19_43.D	6.7	0.6	16	4.77E+05	138.0	36.5	1.8
19_44.D	5.0	0.3	16	3.83E+05	149.1	38.1	1.7
19_45.D	5.1	0.2	8	2.50E+05	95.8	34.1	2.1
19_46.D	6.5	0.5	16	4.62E+05	137.9	36.0	2.2
20_1.D	7.4	0.4	24	5.99E+05	158.5	33.5	1.2
20_2.D	10.0	0.5	22	1.04E+06	201.6	44.2	1.3
20_3.D	13.4	0.9	25	7.56E+05	110.2	23.2	1.2
20_4.D	6.6	0.3	46	7.19E+05	211.1	32.2	1.4
20_5.D	11.5	0.7	34	9.41E+05	158.8	29.1	1.3
20_6.D	14.6	0.7	41	8.81E+05	118.2	19.4	1.7
20_7.D	11.3	0.6	29	4.90E+05	84.9	16.3	1.3
20_8.D	13.0	0.6	40	8.61E+05	129.0	21.1	1.1
20_9.D	12.4	0.9	19	5.22E+05	82.2	19.7	1.2
20_10.D	10.3	0.7	19	4.63E+05	88.2	21.1	1.6
20_11.D	8.8	0.4	21	4.66E+05	104.0	23.2	1.1
20_12.D	11.0	0.9	28	3.82E+05	67.8	13.9	1.5
20_14.D	6.5	0.4	21	5.88E+05	174.8	39.8	1.4
20_15.D	9.0	0.4	37	5.98E+05	130.2	22.1	1.3
20_16.D	8.6	0.5	25	5.15E+05	117.2	24.4	1.4
20_17.D	8.6	0.3	28	4.38E+05	99.6	19.2	1.8
20_18.D	22.5	1.5	39	1.47E+06	127.7	22.2	1.1
20_19.D	11.1	0.8	55	7.80E+05	136.8	20.7	1.3

Continued on next page

Continued from previous page

Name	^{238}U (ppm)	2σ	N_s	ρ_s	t (Ma)	1σ	D_{par}
20_20.D	7.3	0.4	19	2.55E+05	69.1	16.4	1.4
20_21.D	20.6	2.1	22	1.57E+06	148.7	35.1	1.2
20_22.D	7.3	0.4	35	5.54E+05	148.4	26.4	1.2
20_23.D	13.2	0.6	48	6.27E+05	92.8	14.0	1.5
20_24.D	12.7	1.0	35	7.98E+05	122.9	22.8	1.6
20_25.D	32.0	2.2	39	1.21E+06	74.3	12.9	1.9
20_26.D	16.1	1.1	23	6.33E+05	77.1	16.9	1.6
20_27.D	11.1	0.7	27	4.37E+05	77.3	15.7	1.4
20_28.D	9.0	0.6	29	5.14E+05	111.2	21.8	1.3
20_29.D	6.9	0.4	18	4.32E+05	121.6	29.5	1.5
20_30.D	7.4	0.3	21	4.00E+05	106.3	23.7	1.3
20_31.D	10.6	0.6	18	5.93E+05	109.3	26.6	1.8
20_32.D	12.2	0.5	15	6.77E+05	108.1	28.3	1.2
20_34.D	8.5	0.5	36	7.77E+05	177.3	31.6	1.4
20_35.D	9.0	0.4	31	8.54E+05	183.7	34.2	1.2
20_36.D	15.4	1.2	31	1.04E+06	131.2	25.7	1.6
20_37.D	10.4	0.6	25	6.36E+05	119.8	24.9	1.3
20_38.D	16.1	1.4	39	8.70E+05	105.6	19.2	1.3
20_39.D	8.9	0.4	11	3.90E+05	85.3	26.0	1.4
21_1.D	6.7	0.4	33	6.57E+05	191.2	35.6	1.2
21_2.D	6.3	0.5	21	5.65E+05	174.8	40.3	1.5
21_3.D	5.7	0.3	25	3.30E+05	113.6	23.3	1.3
21_4.D	5.1	0.3	38	3.52E+05	135.3	23.1	1.4
21_5.D	6.9	0.5	36	5.07E+05	143.1	25.7	1.6
21_6.D	8.1	0.4	34	4.78E+05	114.8	20.4	1.3
21_7.D	12.2	0.6	65	6.52E+05	104.5	14.0	1.3
21_8.D	6.4	0.4	44	3.96E+05	121.5	19.6	1.6
21_9.D	14.1	1.3	33	5.68E+05	78.9	15.5	1.5
21_10.D	7.7	0.7	20	4.03E+05	103.0	25.0	1.4
21_11.D	4.2	0.2	33	4.45E+05	206.0	37.6	1.2
21_12.D	4.9	0.4	16	4.91E+05	193.4	50.8	1.5
21_13.D	6.1	0.6	11	3.43E+05	109.4	34.5	1.8
21_14.D	7.4	0.5	41	4.81E+05	126.8	21.9	1.5
21_15.D	20.1	1.1	51	7.79E+05	75.9	11.4	1.7
21_16.D	5.3	0.5	21	4.30E+05	158.3	37.4	1.5
21_17.D	9.6	0.6	35	6.25E+05	126.9	22.9	1.4
21_18.D	7.7	0.7	31	4.51E+05	113.9	22.8	1.2
21_19.D	6.7	0.4	23	3.53E+05	103.6	22.5	1.4
21_20.D	8.5	0.7	47	5.94E+05	135.9	22.7	1.4
21_21.D	7.0	0.4	32	5.40E+05	149.5	28.0	1.3
21_22.D	7.8	0.5	42	5.41E+05	135.9	22.7	1.6
21_23.D	4.7	0.3	13	3.26E+05	134.8	38.1	1.1
21_24.D	6.2	0.3	47	5.96E+05	187.4	28.5	1.6
21_25.D	5.8	0.3	19	2.97E+05	100.2	23.6	1.7

Continued on next page

Continued from previous page

Name	^{238}U (ppm)	2σ	N_s	ρ_s	t (Ma)	1σ	D_{par}
21_26.D	22.8	1.2	24	9.00E+05	77.3	16.3	1.4
21_27.D	5.3	0.3	21	3.56E+05	132.0	29.8	1.4
21_28.D	5.6	0.3	21	4.88E+05	168.5	37.6	1.2
21_29.D	5.0	0.3	20	4.58E+05	177.3	41.2	1.6
21_30.D	5.8	0.4	18	3.05E+05	103.0	25.1	1.3
21_31.D	6.8	0.5	37	4.51E+05	130.2	23.7	1.5
21_32.D	10.6	0.7	28	4.99E+05	91.8	18.3	1.2
21_33.D	11.5	0.7	20	4.02E+05	68.5	15.8	1.8
21_34.D	7.8	0.7	26	2.24E+05	56.3	12.1	1.5
21_35.D	18.6	1.2	31	6.56E+05	69.1	13.2	1.5
21_36.D	5.3	0.4	23	1.98E+05	73.5	16.5	1.4
21_37.D	13.5	1.2	37	4.18E+05	60.7	11.4	1.1
21_38.D	9.1	0.5	32	4.21E+05	90.4	16.8	1.8
21_39.D	11.8	0.9	53	6.46E+05	107.1	16.7	1.4
21_40.D	8.3	0.6	27	4.90E+05	115.2	23.7	1.2
21_41.D	5.2	0.3	29	3.93E+05	146.0	28.1	1.7
21_42.D	7.6	0.6	25	4.53E+05	116.6	25.1	1.2
21_43.D	8.1	0.6	20	4.30E+05	104.4	24.5	1.3
21_44.D	16.9	1.0	26	8.02E+05	93.1	19.1	1.5
24_1.D	27.3	1.2	6	8.99E+05	64.6	26.5	1.7
24_2.D	9.6	1.1	5	5.05E+05	102.9	47.5	1.4
24_3.D	11.1	0.8	14	1.21E+06	210.1	57.9	1.6
24_4.D	8.1	0.4	4	3.93E+05	95.1	47.8	1.3
24_5.D	18.3	0.8	24	1.29E+06	137.5	28.7	1.5
24_7.D	6.5	0.4	5	3.76E+05	112.6	50.9	2.3
24_8.D	27.0	1.3	19	1.45E+06	104.9	24.6	1.5
24_9.D	6.6	0.4	4	3.75E+05	110.7	55.7	1.9
24_11.D	27.3	1.3	16	1.39E+06	99.5	25.3	0.9
24_12.D	19.5	1.3	8	1.41E+06	140.5	50.6	1.3
24_13.D	8.0	0.5	4	7.18E+05	175.1	88.1	1.4
24_14.D	3.8	0.5	2	1.61E+05	83.1	59.7	1.4
24_15.D	22.5	1.3	11	7.83E+05	68.2	20.9	1.4
24_17.D	20.2	1.3	19	1.44E+06	138.7	33.1	1.6
25_1.D	174.9	7.9	132	5.75E+06	64.4	6.3	2.1
25_2.D	73.5	6.9	44	4.00E+06	106.3	18.9	2.2
25_3.D	146.0	12.0	107	7.19E+06	96.3	12.2	2.1
25_4.D	90.0	3.9	41	3.48E+06	75.8	12.3	1.7
25_5.D	111.5	7.3	40	4.37E+06	76.7	13.1	2.2
25_6.D	151.9	8.4	107	6.63E+06	85.5	9.5	2.0
25_7.D	174.8	8.5	65	3.60E+06	40.5	5.4	2.0
25_8.D	106.4	5.5	43	3.48E+06	64.1	10.3	2.3
25_9.D	48.7	1.8	82	2.75E+06	110.3	12.8	2.2
25_10.D	185.0	10.0	91	6.50E+06	68.9	8.1	2.2
25_11.D	11.3	0.6	26	8.30E+05	142.7	29.1	1.8

Continued on next page

Continued from previous page

Name	^{238}U (ppm)	2σ	N_s	ρ_s	t (Ma)	1σ	D_{par}
25_12.D	208.0	17.0	86	7.10E+06	66.9	9.0	2.1
25_14.D	129.4	8.9	196	7.51E+06	113.4	11.2	2.2
25_16.D	172.0	11.0	104	7.62E+06	86.7	10.2	2.1
25_17.D	127.8	5.4	59	5.49E+06	84.2	11.5	2.0
26_1.D	4.3	0.3	8	3.33E+05	152.1	54.5	2.2
26_2.D	3.8	0.2	10	4.61E+05	237.5	75.9	1.8
26_3.D	3.9	0.2	3	1.31E+05	66.6	38.6	2.5
26_4.D	3.9	0.3	5	2.36E+05	118.6	53.7	2.3
26_5.D	3.8	0.2	6	3.21E+05	165.3	68.2	1.9
26_6.D	3.9	0.3	3	1.35E+05	67.3	39.2	2.4
26_7.D	4.5	0.3	5	2.09E+05	90.6	40.8	2.1
26_8.D	3.5	0.2	2	7.84E+04	43.8	31.0	2.0
26_9.D	3.6	0.3	4	2.36E+05	127.8	64.6	2.5
26_10.D	4.7	0.4	8	5.13E+05	212.6	76.9	2.1
26_11.D	4.0	0.2	11	3.66E+05	177.4	54.5	2.1
26_12.D	4.1	0.2	9	3.16E+05	151.5	51.0	2.1
26_13.D	3.9	0.2	5	2.51E+05	124.5	56.2	2.2
26_14.D	5.2	0.4	7	4.80E+05	180.8	69.8	1.7
26_15.D	4.3	0.3	6	3.37E+05	151.3	62.5	2.7
26_16.D	4.5	0.3	4	2.20E+05	96.2	48.6	1.8
26_17.D	4.0	0.3	5	2.00E+05	97.8	44.2	1.4
26_18.D	3.8	0.3	5	1.85E+05	94.5	42.7	2.0
26_19.D	4.8	0.4	9	4.26E+05	172.0	59.4	2.1
26_20.D	4.0	0.2	3	2.25E+05	109.1	63.2	2.2
26_21.D	4.8	0.3	5	4.64E+05	186.7	84.4	2.2
26_22.D	3.7	0.2	7	3.64E+05	192.8	73.9	2.1
26_23.D	4.0	0.3	7	3.96E+05	192.1	74.1	2.2
26_24.D	3.9	0.3	2	8.26E+04	41.2	29.2	2.2
26_25.D	3.8	0.3	3	1.27E+05	65.3	38.1	1.9
26_26.D	3.6	0.2	1	7.66E+04	41.9	42.0	1.9
26_27.D	3.8	0.3	8	3.18E+05	161.7	58.4	2.5
26_28.D	3.7	0.3	9	2.82E+05	149.0	51.0	2.4
26_29.D	3.8	0.2	3	2.61E+05	134.1	77.8	2.1
26_30.D	3.5	0.3	2	9.81E+04	55.5	39.5	2.3
26_31.D	3.7	0.3	6	3.39E+05	179.1	74.7	2.0
28_1.D	7.0	0.3	17	5.55E+05	154.6	38.1	1.8
28_2.D	32.4	2.2	35	2.14E+06	129.1	23.5	2.1
28_3.D	28.4	1.3	84	2.14E+06	146.8	17.4	2.1
28_4.D	17.8	0.9	25	1.28E+06	141.0	29.1	2.1
28_5.D	34.7	1.4	50	2.17E+06	122.0	17.9	1.9
28_6.D	53.9	3.2	69	3.57E+06	129.1	17.3	1.9
28_7.D	28.3	1.6	43	2.08E+06	143.5	23.3	2.3
28_8.D	25.7	2.1	31	1.43E+06	109.0	21.5	1.7
28_9.D	13.6	1.3	20	6.03E+05	86.8	21.1	2.2

Continued on next page

Continued from previous page

Name	^{238}U (ppm)	2σ	N_s	ρ_s	t (Ma)	1σ	D_{par}
28_10.D	17.3	0.9	23	1.20E+06	136.0	29.2	1.9
28_11.D	53.2	3.3	45	2.66E+06	98.0	15.8	2.1
28_12.D	9.3	0.5	27	7.38E+05	155.0	30.9	1.9
28_13.D	28.9	1.4	50	1.85E+06	124.8	18.7	2.3
28_14.D	20.8	1.9	34	1.44E+06	134.6	26.1	2.0
28_15.D	34.6	1.7	54	2.38E+06	134.0	19.4	2.1
28_16.D	22.4	1.7	30	1.51E+06	131.4	26.0	1.9
28_17.D	30.0	1.8	40	2.36E+06	153.1	25.9	2.2
28_18.D	30.7	1.4	40	1.94E+06	123.3	20.3	2.0
28_19.D	39.2	2.4	55	2.87E+06	142.5	21.1	2.1
28_20.D	23.7	1.3	29	1.56E+06	128.2	24.8	1.9
28_21.D	9.1	0.5	67	1.37E+06	291.1	38.4	2.0
28_22.D	30.1	1.4	62	2.59E+06	167.5	22.7	2.2
28_23.D	16.6	0.9	26	1.64E+06	191.5	38.8	2.0
28_24.D	20.2	1.2	50	1.62E+06	156.0	23.9	2.2
28_25.D	38.2	2.7	63	2.68E+06	136.8	19.8	2.1
28_26.D	14.8	1.2	38	1.43E+06	187.4	34.0	2.1
28_27.D	39.0	1.6	40	2.38E+06	119.4	19.5	2.0
28_28.D	45.6	3.5	37	2.51E+06	107.4	19.5	2.0
28_29.D	12.2	1.0	10	5.80E+05	93.0	30.4	1.9
28_30.D	56.2	4.4	44	3.34E+06	116.1	19.7	1.9
28_31.D	40.7	2.4	21	1.65E+06	79.5	18.0	1.8
28_32.D	19.6	1.4	32	1.67E+06	165.9	31.6	2.0
28_33.D	40.7	2.4	22	2.06E+06	99.0	21.9	2.0
28_34.D	40.7	2.9	34	3.12E+06	149.2	27.7	1.9
28_35.D	54.0	4.7	84	3.63E+06	131.3	18.3	2.1
28_36.D	20.1	1.2	22	1.23E+06	119.9	26.5	2.1
28_37.D	41.6	4.0	37	2.36E+06	110.8	21.1	2.0
28_38.D	10.5	0.6	21	9.86E+05	182.4	41.2	2.0
28_39.D	28.0	2.4	57	1.74E+06	121.0	19.1	1.9
28_40.D	19.0	1.1	27	2.01E+06	204.8	41.2	1.9
29_1.D	7.4	0.4	14	6.40E+05	169.4	46.1	1.6
29_2.D	11.4	0.7	40	9.61E+05	163.6	27.8	1.8
29_3.D	6.8	0.7	22	8.87E+05	250.7	58.7	1.7
29_4.D	11.2	0.6	27	1.17E+06	201.8	40.1	1.9
29_5.D	24.1	1.4	60	2.14E+06	172.4	24.4	1.8
29_6.D	11.1	0.8	68	8.49E+05	149.6	21.0	1.9
29_7.D	8.9	0.6	27	8.93E+05	195.6	39.6	1.8
29_8.D	14.0	0.9	40	1.31E+06	182.1	31.0	1.8
29_9.D	26.6	1.3	152	1.66E+06	121.8	11.5	1.9
29_10.D	9.1	0.6	60	1.17E+06	250.2	36.1	1.8
29_12.D	18.0	1.6	28	1.42E+06	153.5	32.1	1.8
29_13.D	14.7	1.1	43	1.17E+06	155.6	26.4	1.7
29_14.D	28.5	2.0	15	1.29E+06	88.9	23.8	1.5

Continued on next page

Continued from previous page

Name	^{238}U (ppm)	2σ	N_s	ρ_s	t (Ma)	1σ	D_{par}
29_15.D	8.1	0.5	19	4.86E+05	117.4	27.9	1.7
29_16.D	11.0	0.5	14	5.09E+05	90.9	24.6	2.2
29_17.D	19.0	0.9	48	1.44E+06	148.0	22.4	1.9
29_19.D	61.4	4.3	88	5.17E+06	163.8	20.9	1.9
29_20.D	22.4	1.1	26	1.55E+06	135.2	27.3	1.9
29_21.D	18.4	1.9	24	1.78E+06	187.9	43.0	2.1
29_23.D	15.1	0.9	31	1.22E+06	157.5	29.9	2.0
29_24.D	8.5	0.7	26	6.25E+05	142.9	30.3	1.9
29_25.D	11.3	0.4	15	7.59E+05	131.7	34.4	1.8
29_26.D	21.5	1.7	29	1.58E+06	143.6	29.0	1.8
29_27.D	14.8	1.2	18	9.19E+05	121.3	30.2	1.7
29_28.D	27.0	2.7	39	1.13E+06	82.1	15.5	1.8
29_29.D	9.6	0.5	13	5.12E+05	104.3	29.4	2.2
29_30.D	15.3	0.9	22	1.42E+06	180.3	39.8	1.7
29_31.D	21.7	1.4	25	1.34E+06	120.5	25.3	2.0
29_32.D	13.0	1.0	28	1.29E+06	193.2	39.3	2.0
29_33.D	11.9	0.8	10	5.01E+05	82.8	26.8	1.6
29_34.D	16.9	1.0	33	1.13E+06	130.6	24.0	1.7
29_35.D	17.6	1.2	26	1.30E+06	143.9	29.9	1.8
29_36.D	6.9	0.4	17	7.59E+05	211.9	52.7	2.1
29_37.D	12.4	1.0	19	4.99E+05	78.8	19.2	2.0
29_38.D	12.3	0.9	17	6.50E+05	103.2	26.1	1.8
29_39.D	11.0	0.7	20	5.20E+05	92.4	21.5	1.8
31_1.D	19.9	1.1	63	1.86E+06	181.3	24.9	1.8
31_2.D	8.4	0.5	73	1.42E+06	323.1	42.2	1.6
31_3.D	24.0	1.3	28	2.30E+06	186.5	36.7	1.6
31_4.D	22.2	2.2	22	1.67E+06	146.3	34.4	1.7
31_5.D	22.9	1.5	62	2.78E+06	234.9	33.6	1.7
31_6.D	23.4	1.6	44	2.25E+06	186.9	30.9	1.7
31_7.D	19.1	0.8	37	2.13E+06	216.9	36.8	1.8
31_8.D	12.2	0.7	47	1.44E+06	228.8	35.9	1.7
31_9.D	20.6	1.8	13	9.25E+05	87.9	25.5	1.3
31_10.D	18.2	0.9	38	1.50E+06	160.4	27.1	1.7
31_11.D	23.2	1.4	26	2.03E+06	170.0	34.9	1.9
31_12.D	25.2	1.3	52	1.82E+06	140.5	20.8	1.9
31_13.D	30.0	1.9	50	2.12E+06	137.6	21.3	1.7
31_14.D	22.3	1.1	61	2.10E+06	183.2	25.1	1.7
31_15.D	18.5	1.2	46	1.69E+06	177.5	28.6	1.6
31_16.D	28.7	1.7	45	1.80E+06	122.6	19.7	1.8
31_17.D	19.9	1.2	46	1.58E+06	154.4	24.6	1.7
31_18.D	20.2	1.4	56	1.63E+06	156.9	23.6	1.8
31_19.D	29.6	1.5	33	1.73E+06	113.9	20.7	1.8
31_20.D	20.1	1.0	65	1.74E+06	168.6	22.5	1.8
31_21.D	11.3	0.4	35	1.27E+06	219.2	38.0	1.7

Continued on next page

Continued from previous page

Name	^{238}U (ppm)	2σ	N_s	ρ_s	t (Ma)	1σ	D_{par}
31_22.D	26.1	1.7	55	2.28E+06	169.9	25.4	1.6
31_23.D	21.0	1.1	57	2.05E+06	189.3	27.0	1.9
31_24.D	17.3	1.4	51	3.04E+06	337.5	54.6	1.6
31_25.D	21.9	1.0	16	1.17E+06	104.6	26.6	1.6
31_26.D	19.0	1.2	34	2.20E+06	224.8	41.1	1.5
31_27.D	27.6	2.7	27	1.70E+06	120.3	26.0	2.5
31_28.D	23.9	1.8	15	9.55E+05	78.3	21.1	1.5
31_29.D	24.9	1.7	24	3.06E+06	237.9	51.2	1.8
31_30.D	19.5	1.3	53	2.05E+06	203.6	31.1	1.7
31_31.D	22.6	1.9	30	1.82E+06	156.7	31.5	1.7
31_32.D	16.7	0.9	19	1.41E+06	164.5	38.8	1.9
31_34.D	36.7	2.2	47	2.69E+06	143.1	22.6	1.9
31_35.D	21.9	1.3	67	2.21E+06	195.5	26.6	1.8
31_36.D	28.1	1.8	34	2.28E+06	157.9	28.9	2.1
32_1.D	6.1	0.3	39	8.87E+05	278.5	46.5	0.9
32_2.D	5.4	0.2	18	4.88E+05	176.6	42.3	0.9
32_3.D	7.1	0.5	23	1.03E+06	280.4	61.9	1.0
32_4.D	6.3	0.4	17	7.49E+05	229.3	57.2	1.0
32_5.D	11.9	0.6	10	5.47E+05	90.3	28.9	1.2
32_6.D	29.9	1.4	66	2.20E+06	143.3	18.9	1.2
32_7.D	5.4	0.4	23	5.98E+05	215.5	47.5	0.9
32_8.D	17.3	1.1	26	1.42E+06	159.9	33.0	1.3
32_10.D	5.4	0.3	20	3.55E+05	128.7	29.8	1.4
32_11.D	6.0	0.4	42	5.27E+05	170.0	28.3	0.9
32_12.D	3.7	0.2	12	2.82E+05	150.1	43.8	1.2
32_13.D	8.1	0.4	24	5.97E+05	143.8	30.3	1.0
32_14.D	9.7	0.6	50	1.08E+06	216.5	33.3	1.1
32_15.D	5.9	0.5	31	4.95E+05	163.3	32.0	1.2
32_16.D	7.7	0.5	5	3.97E+05	100.8	45.6	0.9
32_17.D	7.4	0.4	21	7.04E+05	185.7	41.8	1.0
32_18.D	4.5	0.3	28	7.06E+05	301.2	60.8	0.8
32_19.D	7.5	0.8	22	6.58E+05	171.4	40.6	0.9
32_20.D	19.1	1.4	87	2.08E+06	211.1	27.4	1.1
32_21.D	5.6	0.3	40	4.82E+05	168.0	28.1	1.4
32_22.D	27.3	2.1	80	2.98E+06	211.7	28.7	1.2
32_23.D	6.7	0.4	14	6.62E+05	191.8	52.4	1.2
32_24.D	5.8	0.4	4	1.37E+05	46.3	23.4	1.3
32_25.D	30.7	1.5	10	9.69E+05	61.9	19.8	1.3
32_26.D	17.6	2.4	32	1.06E+06	118.2	26.4	1.1
32_27.D	9.7	0.5	21	8.59E+05	173.1	39.0	1.0
32_28.D	3.8	0.2	10	2.49E+05	128.2	41.0	1.0
32_29.D	7.6	0.4	15	7.80E+05	198.2	52.4	1.1
32_30.D	18.7	1.2	30	1.53E+06	159.2	30.8	1.2
32_31.D	4.0	0.2	15	3.65E+05	178.1	46.8	1.1

Continued on next page

Continued from previous page

Name	^{238}U (ppm)	2σ	N_s	ρ_s	t (Ma)	1σ	D_{par}
32_32.D	25.4	1.1	42	2.19E+06	167.5	26.9	1.1
32_33.D	8.9	0.7	19	7.68E+05	167.7	40.5	1.1
32_34.D	6.3	0.4	23	6.32E+05	193.8	42.5	1.1
32_35.D	5.9	0.3	11	4.39E+05	145.3	44.6	0.9
32_36.D	29.4	1.6	45	2.48E+06	164.4	26.1	0.9
32_37.D	7.9	0.5	11	4.92E+05	120.9	37.2	1.1
32_38.D	14.4	1.2	35	1.43E+06	192.9	36.4	1.2
33_1.D	35.4	8.5	22	2.14E+06	117.8	37.8	1.7
33_2.D	8.1	0.5	34	1.06E+06	251.8	45.5	2.0
33_3.D	7.5	0.4	30	1.29E+06	333.3	64.0	1.7
33_4.D	9.3	0.5	31	1.47E+06	305.3	57.4	1.7
33_5.D	5.7	1.4	62	9.58E+05	323.1	89.3	1.5
33_6.D	6.3	0.3	32	8.14E+05	249.4	45.2	1.4
33_7.D	10.1	0.8	17	1.45E+06	276.4	70.2	1.8
33_8.D	7.2	0.6	16	6.90E+05	186.6	49.1	1.6
33_9.D	9.9	0.5	21	1.01E+06	197.5	44.4	1.7
33_10.D	14.8	0.9	57	2.50E+06	324.2	46.8	2.1
33_11.D	6.0	0.4	40	8.47E+05	272.1	47.0	1.9
33_12.D	31.2	1.7	72	2.90E+06	180.8	23.5	2.0
33_13.D	14.9	1.5	50	1.73E+06	224.9	39.0	1.8
33_14.D	52.6	5.1	32	5.80E+06	213.6	43.1	1.7
33_15.D	6.3	0.4	58	1.06E+06	320.8	46.5	1.4
33_16.D	8.4	0.4	14	7.57E+05	174.9	47.6	2.3
33_17.D	11.7	1.0	42	1.90E+06	312.4	55.1	1.9
33_18.D	36.6	2.0	121	3.24E+06	171.9	18.2	2.0
33_19.D	7.9	0.5	25	7.14E+05	175.3	37.0	1.9
33_20.D	6.2	0.5	20	8.73E+05	274.0	64.5	1.6
33_21.D	5.5	0.3	28	7.80E+05	275.6	53.8	1.7
33_22.D	42.0	2.4	113	5.57E+06	256.1	28.2	2.0
33_23.D	7.2	0.4	8	5.88E+05	159.9	57.3	2.3
33_24.D	11.2	0.9	32	1.05E+06	182.6	35.2	1.6
33_25.D	7.9	0.6	41	1.31E+06	318.0	54.7	1.6
33_27.D	6.6	0.4	13	6.10E+05	178.9	50.8	2.0
33_28.D	11.2	0.6	27	1.36E+06	234.2	46.7	1.7
33_30.D	9.6	0.5	16	1.05E+06	211.4	53.9	1.7
33_31.D	6.3	0.5	18	6.64E+05	205.1	50.8	1.7
33_32.D	7.6	0.4	17	1.06E+06	268.5	66.4	2.0
33_33.D	11.2	0.9	30	1.19E+06	205.5	40.7	1.7
33_34.D	6.0	0.4	10	6.99E+05	226.4	73.0	1.8
33_35.D	14.2	1.0	17	1.37E+06	187.5	47.4	1.3
33_36.D	45.1	2.8	39	3.68E+06	158.8	27.3	2.3
33_37.D	7.3	0.5	13	5.73E+05	153.2	43.7	1.8
33_38.D	9.5	0.6	24	1.12E+06	229.5	48.7	2.2
34_1	4.4	0.2	23	3.97E+05	175.1	37.4	1.9

Continued on next page

Continued from previous page

Name	^{238}U (ppm)	2σ	N_s	ρ_s	t (Ma)	1σ	D_{par}
34_2	4.5	0.2	11	6.67E+05	288.7	88.0	2.1
34_3	8.5	0.5	54	8.24E+05	188.3	27.9	1.4
34_4	5.0	0.4	11	5.29E+05	206.3	64.0	2.1
34_5	7.2	0.4	9	6.06E+05	164.1	55.5	2.2
34_6	4.7	0.3	23	3.89E+05	161.0	35.1	1.8
34_7	4.4	0.3	10	2.52E+05	113.2	36.4	1.3
34_8	4.7	0.2	15	6.56E+05	271.0	71.0	2.2
34_9	4.3	0.3	16	7.09E+05	316.1	81.8	2.1
34_10	4.2	0.2	30	6.47E+05	294.8	55.8	2.0
34_11	4.1	0.3	13	5.43E+05	258.9	74.7	2.0
34_12	4.2	0.3	9	5.56E+05	257.1	87.4	2.1
34_13	4.5	0.2	20	7.42E+05	317.2	72.6	1.6
34_14	4.9	0.3	8	3.61E+05	142.7	51.2	2.0
34_16	4.7	0.3	14	5.31E+05	218.2	60.1	2.1
34_17	8.6	0.6	17	4.86E+05	110.3	27.8	2.1
34_18	4.7	0.3	18	4.28E+05	178.5	43.4	2.2
34_19	4.7	0.3	14	6.81E+05	280.0	76.8	1.7
34_20	4.3	0.2	18	4.73E+05	213.9	51.5	2.1
34_21	5.5	0.3	27	5.91E+05	210.4	42.0	2.1
34_22	4.0	0.3	26	6.11E+05	292.2	60.3	2.2
34_23	4.6	0.3	28	4.87E+05	203.8	40.3	1.9
34_24	4.5	0.3	17	4.17E+05	182.2	45.5	2.2
34_25	4.3	0.2	31	5.25E+05	238.4	44.9	2.1
34_26	4.7	0.4	21	3.83E+05	159.5	37.0	2.0
34_27	4.8	0.3	15	6.02E+05	241.5	64.4	2.0
34_28	5.4	0.3	33	5.27E+05	190.4	34.9	2.0
34_29	5.1	0.4	32	6.57E+05	250.4	48.1	1.9
34_30	4.5	0.3	20	3.87E+05	168.7	39.0	2.0
34_31	4.2	0.3	57	4.87E+05	222.4	33.4	2.2
34_32	3.7	0.2	15	3.31E+05	173.2	45.7	2.2
34_33	3.9	0.3	36	7.30E+05	356.0	64.5	2.0
34_34	4.7	0.3	19	4.49E+05	187.4	44.8	2.2
34_35	6.2	0.4	19	7.52E+05	236.3	55.9	1.8
34_36	4.6	0.3	15	4.87E+05	205.0	54.2	2.2
34_37	4.1	0.2	8	4.02E+05	189.8	67.7	2.3
34_38	4.6	0.3	20	4.98E+05	208.2	48.1	2.2
34_39	5.0	0.4	13	3.81E+05	149.5	43.1	2.2
34_40	4.9	0.2	10	3.46E+05	136.8	43.7	2.1
36_1.D	58.6	2.1	74	3.13E+06	104.3	12.7	1.7
36_2.D	18.3	1.0	33	7.88E+05	84.4	15.4	2.0
36_3.D	17.3	1.0	25	1.57E+06	175.9	36.5	1.7
36_4.D	13.6	0.9	34	6.15E+05	88.4	16.1	1.7
36_5.D	84.0	5.2	91	5.25E+06	122.1	14.9	1.5
36_6.D	15.3	0.7	15	6.20E+05	79.2	20.8	1.4

Continued on next page

Continued from previous page

Name	^{238}U (ppm)	2σ	N_s	ρ_s	t (Ma)	1σ	D_{par}
36_7.D	15.8	0.7	80	1.23E+06	152.3	18.4	1.8
36_8.D	17.6	1.0	30	1.01E+06	112.4	21.5	1.6
36_9.D	7.6	0.5	20	3.22E+05	83.0	19.4	1.7
36_10.D	24.6	1.1	22	1.13E+06	90.2	19.7	2.1
36_11.D	13.7	0.7	21	6.62E+05	94.8	21.3	1.9
36_12.D	11.2	0.7	19	5.87E+05	102.4	24.3	2.0
36_13.D	8.4	0.5	14	8.73E+05	202.7	55.3	1.8
36_14.D	15.2	0.8	26	6.95E+05	89.7	18.2	1.7
36_15.D	21.4	1.2	39	1.04E+06	95.3	16.2	1.4
36_16.D	13.5	0.7	21	5.09E+05	73.9	16.6	2.3
36_17.D	16.9	1.0	18	9.11E+05	105.7	25.7	1.9
36_18.D	19.6	2.5	22	7.31E+05	73.1	18.2	2.0
36_19.D	73.0	7.0	17	1.65E+06	44.5	11.6	1.9
36_20.D	10.7	0.6	19	4.61E+05	84.5	19.9	1.6
36_21.D	20.8	0.8	15	8.07E+05	75.9	19.8	1.7
36_22.D	14.1	0.7	18	5.39E+05	74.7	17.9	2.0
36_23.D	9.9	0.7	21	5.12E+05	101.2	23.1	2.3
36_24.D	16.7	1.0	9	6.22E+05	73.0	24.7	1.6
36_25.D	13.0	0.5	29	5.02E+05	75.7	14.3	1.6
36_26.D	10.0	0.7	30	5.51E+05	108.2	21.0	2.0
36_27.D	37.4	2.8	23	1.06E+06	55.7	12.3	1.7
36_28.D	14.9	0.6	27	8.96E+05	117.5	23.1	1.7
36_29.D	11.2	0.9	21	7.97E+05	138.4	32.2	1.7
36_30.D	102.1	5.0	68	3.05E+06	58.7	7.7	2.0
36_31.D	1.2	0.1	8	5.72E+04	90.3	32.2	1.7
36_32.D	14.5	0.6	12	5.88E+05	79.5	23.2	1.8
36_33.D	25.1	2.4	14	6.80E+05	53.2	15.1	1.3
36_34.D	23.8	2.1	32	1.00E+06	82.6	16.3	2.3
36_35.D	15.6	0.9	31	7.55E+05	94.5	17.9	1.8
36_36.D	18.7	1.1	37	4.31E+05	45.3	7.9	2.2
37_1.D	10.2	0.7	17	6.00E+05	114.8	28.9	1.4
37_3.D	5.7	0.3	8	3.05E+05	105.2	37.5	1.5
37_4.D	13.0	0.8	14	7.04E+05	105.6	29.0	1.7
37_6.D	19.4	2.7	22	1.41E+06	141.3	36.0	1.8
37_7.D	12.4	0.9	19	1.34E+06	209.6	50.3	1.8
37_8.D	13.0	0.8	21	8.10E+05	121.6	27.5	1.7
37_9.D	19.2	1.3	19	8.36E+05	85.2	20.4	1.9
37_10.D	8.3	0.6	9	3.24E+05	76.3	25.9	1.4
37_11.D	37.4	2.3	29	1.24E+06	64.9	12.7	1.7
37_12.D	19.6	1.0	23	1.33E+06	132.3	28.4	1.7
37_13.D	9.0	0.5	15	9.57E+05	205.9	54.6	1.6
37_15.D	7.0	0.6	11	4.01E+05	111.4	34.7	1.8
37_17.D	13.2	1.0	13	9.64E+05	142.0	40.8	1.7
37_19.D	10.5	0.6	10	4.10E+05	76.8	24.7	1.4

Continued on next page

Continued from previous page

Name	^{238}U (ppm)	2σ	N_s	ρ_s	t (Ma)	1σ	D_{par}
37_21.D	21.3	1.1	33	1.14E+06	104.7	19.0	1.8
37_22.D	10.6	0.9	20	6.90E+05	126.8	30.3	1.5
37_30.D	12.2	0.8	13	7.58E+05	121.6	34.7	1.7
37_31.D	56.8	4.3	36	2.40E+06	82.9	15.2	1.7
37_33.D	10.7	0.8	6	5.26E+05	96.0	39.8	1.8
37_34.D	17.1	1.4	12	7.19E+05	82.3	24.7	1.1
37_35.D	9.0	0.6	5	2.97E+05	64.8	29.3	1.9
37_36.D	9.9	0.6	6	3.41E+05	67.9	28.0	2.0
37_37.D	13.1	0.9	7	8.09E+05	120.3	46.1	2.1
37_40.D	15.2	1.0	9	6.55E+05	84.3	28.6	1.6
38_1.D	19.9	0.8	34	1.09E+06	107.1	18.8	1.5
38_2.D	35.5	2.3	66	2.25E+06	123.7	17.2	1.6
38_3.D	28.9	2.2	37	1.63E+06	110.4	20.0	1.4
38_4.D	25.0	1.3	19	1.22E+06	95.2	22.4	1.5
38_7.D	8.7	0.8	10	4.45E+05	100.5	32.9	1.6
38_8.D	9.9	0.7	18	7.63E+05	149.7	36.8	1.5
38_9.D	14.0	1.1	19	5.77E+05	80.7	19.6	1.3
38_10.D	60.9	5.8	64	3.23E+06	103.6	16.3	1.7
38_11.D	18.6	1.4	36	1.35E+06	141.6	25.9	1.4
38_12.D	12.2	1.0	7	4.67E+05	75.0	29.0	1.3
38_14.D	43.8	2.7	47	2.75E+06	122.8	19.4	1.4
38_16.D	9.1	0.6	46	1.02E+06	217.4	35.5	1.5
38_17.D	7.5	0.5	24	7.66E+05	198.9	42.6	1.5
38_18.D	19.3	2.0	12	8.23E+05	83.5	25.6	1.6
38_19.D	3.9	0.2	14	4.36E+05	216.0	58.9	1.5
38_21.D	35.3	2.5	30	1.49E+06	82.9	16.2	1.6
38_22.D	11.6	1.0	45	1.42E+06	237.2	40.4	1.5
38_23.D	9.4	0.4	17	6.04E+05	125.7	31.0	1.4
38_26.D	33.4	2.2	25	2.04E+06	119.5	25.2	1.5
38_29.D	29.6	2.6	23	9.52E+05	63.1	14.3	1.4
38_30.D	46.1	2.3	28	1.81E+06	77.0	15.0	1.3
38_31.D	24.2	1.7	23	8.74E+05	70.8	15.6	1.1
38_34.D	41.0	2.9	39	2.22E+06	105.9	18.5	1.5
38_35.D	12.6	1.1	18	6.80E+05	105.5	26.5	1.5
39_1.D	7.5	0.9	12	5.13E+05	133.9	41.6	1.5
39_2.D	13.8	0.6	14	7.06E+05	99.9	27.1	1.2
39_3.D	9.7	0.5	25	1.32E+06	262.5	54.1	1.6
39_5.D	15.6	0.7	63	1.61E+06	200.0	26.8	1.5
39_6.D	13.4	0.6	40	1.24E+06	180.3	29.7	1.2
39_7.D	15.3	0.9	46	1.43E+06	181.2	28.8	1.4
39_8.D	13.5	1.0	65	1.21E+06	174.2	24.9	1.2
39_9.D	17.5	1.0	54	1.19E+06	132.3	19.5	1.3
39_10.D	16.3	0.9	23	7.97E+05	95.9	20.6	1.6
39_11.D	22.5	1.2	112	2.22E+06	191.2	20.8	1.2

Continued on next page

Continued from previous page

Name	^{238}U (ppm)	2σ	N_s	ρ_s	t (Ma)	1σ	D_{par}
39_12.D	14.2	0.7	58	1.18E+06	161.6	22.5	1.3
39_13.D	6.9	0.4	47	7.79E+05	217.7	34.6	1.4
39_14.D	17.4	1.0	34	1.34E+06	149.8	27.1	1.4
39_15.D	13.9	0.7	44	1.19E+06	166.0	26.5	1.6
39_16.D	16.2	0.8	36	1.09E+06	130.9	22.8	1.2
39_17.D	11.0	0.5	50	7.22E+05	128.0	19.2	1.5
39_18.D	7.2	0.4	47	7.64E+05	205.7	31.6	1.3
39_19.D	11.1	0.5	23	8.99E+05	157.2	33.5	1.2
39_22.D	11.4	0.7	46	9.04E+05	155.2	24.6	1.3
39_23.D	4.4	0.3	39	8.02E+05	352.8	60.3	1.3
39_25.D	15.0	0.9	27	9.59E+05	124.5	25.2	1.4
39_26.D	13.0	0.7	62	1.45E+06	216.0	29.7	1.2
39_27.D	10.7	0.5	26	7.21E+05	131.5	26.5	1.5
39_28.D	9.1	0.6	50	8.46E+05	180.1	27.8	1.5
39_29.D	11.5	0.6	14	6.76E+05	115.0	31.3	1.2
39_30.D	7.8	0.6	19	8.24E+05	205.7	49.5	1.4
39_31.D	14.9	0.6	44	9.36E+05	122.5	19.2	1.3
39_32.D	21.0	1.4	37	1.19E+06	111.1	19.7	1.3
39_33.D	13.7	0.8	20	1.03E+06	147.0	33.9	1.5
39_34.D	16.6	0.7	26	1.06E+06	124.4	25.0	1.1
39_35.D	5.1	0.5	42	8.78E+05	328.7	58.7	1.5
39_37.D	23.2	1.6	62	1.31E+06	110.1	15.9	1.3
39_38.D	14.3	1.1	22	1.16E+06	158.1	35.8	1.4
39_40.D	8.8	0.6	19	8.45E+05	186.1	44.3	1.5
40_1.D	46.8	2.2	59	3.38E+06	140.6	19.5	2.0
40_2.D	122.3	7.6	49	6.26E+06	100.2	15.6	1.9
40_9.D	67.2	3.6	32	2.77E+06	80.8	14.9	1.7
40_10.D	106.6	6.1	71	4.99E+06	91.6	12.1	1.8
40_11.D	26.7	1.8	38	1.62E+06	118.3	20.8	1.4
40_12.D	6.2	0.4	8	4.42E+05	139.6	50.1	1.1
40_13.D	119.1	7.1	28	4.07E+06	67.0	13.3	1.7
40_14.D	23.6	1.5	9	8.83E+05	73.3	24.9	1.4
40_15.D	26.1	1.5	24	1.09E+06	81.8	17.4	1.9
40_16.D	21.2	1.2	40	1.51E+06	138.7	23.3	2.0
40_17.D	148.2	6.8	98	6.03E+06	79.8	8.8	1.9
40_18.D	25.0	1.9	20	1.47E+06	114.8	27.1	1.6
40_20.D	30.0	2.3	15	2.15E+06	140.0	37.7	1.4

B.2 Apatite confined track length measurements

Table B.2: Apatite confined track length measurements

Length no.	Confined track length (μm)	Angle to C Axis	Average DPar (μm)
BH20_1	13.78	76.74	1.08
BH20_2	12.35	65.21	1.08
BH20_3	14.33	75.61	1.08
BH20_4	13.56	71.07	1.08
BH20_5	14.17	70.41	1.08
BH20_6	14.26	63.34	0.79
BH20_7	14.04	45.91	1.2
BH20_8	12.53	69.48	0.99
BH20_9	14.11	71.15	0.98
BH20_10	14.31	36.89	1.11
BH20_11	13.31	75.01	1.11
BH20_12	9.94	34.65	1.11
BH20_13	11.43	19.34	1.11
BH20_14	15.66	68.42	1.08
BH20_15	14.63	72.97	1.13
BH20_16	12.77	5.27	1.13
BH20_17	14.19	37.36	1.24
BH20_18	15.75	34.59	1.19
BH20_19	14.38	32.1	1.03
BH20_20	13.62	42.12	1.03
BH20_21	10.1	55.32	1.03
BH20_22	14.04	17.45	1.03
BH20_23	12.11	27.39	0.84
BH20_24	12.05	68.67	0.84
BH20_25	13.22	61.41	0.84
BH20_26	12.64	41.85	1.1
BH20_27	15.3	39.19	1.1
BH20_28	12.13	76.77	1.03
BH20_29	13.37	78.79	1.24
BH20_30	15.4	65.02	1.11
BH20_31	13.85	65.12	1.11
BH20_32	13.24	58.56	1.11
BH20_33	10.57	19.44	1.51
BH20_34	11.52	70.02	1.51
BH20_35	13.69	73.26	1.53
BH20_36	13.05	55.18	1.53
BH20_37	11.47	63.21	1.53
BH20_38	13.94	74.71	1.69
BH20_39	10.83	64.84	1.16
BH20_40	13.2	31.48	1.35
BH20_41	11.78	72.79	1.55

Continued on next page

Continued from previous page

Length no.	Confined track length (μm)	Angle to C Axis	Average DPar (μm)
BH20_42	14.05	31.28	1.55
BH20_43	11.21	42.62	1.62
BH20_44	9.59	19.04	1.69
BH20_45	9.59	27.46	1.24
BH20_46	12.61	79.11	1.63
BH20_47	10.24	70.11	1.52
BH20_48	11.6	25.18	1.08
BH20_49	9.17	71.68	1.38
BH20_50	14.04	26.96	1.19
BH20_51	13.57	59.71	1.28
BH20_52	14.32	37.65	1.34
BH20_53	14.43	51.21	1.35
BH20_54	12.89	78.12	1.79
BH20_55	13.72	45.6	1.15
BH20_56	13.01	57.07	1.61
BH20_57	12.94	81.13	1.24
BH20_58	8.74	34.34	1.24
BH20_59	13.83	46.76	1.62
BH20_60	14.74	68.65	1.43
BH25_1	12.54	21.39	2.05
BH25_2	12.98	46.18	2.05
BH25_3	14.22	44.36	2.05
BH25_4	14.37	58.77	2.05
BH25_5	13.08	40.76	2.05
BH25_6	14.7	83.1	2.24
BH25_7	14.74	52.02	2.07
BH25_8	14.02	81.66	2.07
BH25_9	14.54	38.78	2.07
BH25_10	13.3	72.57	2.07
BH25_11	13.05	24.8	1.68
BH25_12	14	6.71	2.02
BH25_13	9.67	52.91	2.02
BH25_14	13.12	45.88	2.02
BH25_15	13.21	25.94	2.27
BH25_16	12.22	69.61	2.27
BH25_17	12.48	67.95	2.27
BH25_18	13.96	77.6	2.16
BH25_19	13.71	52.24	2.16
BH25_20	12.55	20.07	2.16
BH25_21	11.1	52.67	2.16
BH25_22	13.51	76.22	2.17
BH25_23	13.47	32.63	2.17

Continued on next page

Continued from previous page

Length no.	Confined track length (μm)	Angle to C Axis	Average DPar (μm)
BH25_24	15.48	38.6	2.17
BH25_25	13.38	22.65	2.14
BH25_26	15.29	53.88	2.14
BH25_27	15.07	77.16	2.2
BH25_28	13.76	68.21	2.2
BH25_29	14.58	15.01	2.2
BH25_30	10.47	61.65	2.2
BH25_31	13.02	75.36	2.2
BH25_32	13.75	49.79	2.2
BH25_33	13.37	38.82	2.2
BH25_34	14.12	53.97	2.2
BH25_35	13.13	78.4	2.2
BH25_36	11.6	61.53	2.2
BH25_37	14.35	20.18	2.2
BH25_38	12.19	74.36	2.14
BH25_39	12.46	59.51	2.14
BH25_40	14.97	66.32	1.95
BH25_41	13.41	50.56	1.95
BH25_42	13.12	84.38	1.95
BH25_43	13.25	38	1.95
BH25_44	11.97	17.27	1.95
BH25_45	13.86	52.8	1.45
BH25_46	12.83	59.37	1.45
BH25_47	10.25	39.65	0.94
BH28_1	12.9	51.54	1.9
BH28_2	14.91	41.34	2.02
BH28_3	11.87	85.64	2.04
BH28_4	11.55	82.71	1.86
BH28_5	12.79	73.51	1.89
BH28_6	13.04	71.17	2.12
BH28_7	14.59	44.85	1.91
BH28_8	15.24	88.27	1.94
BH28_9	13.47	29.38	2.07
BH28_10	14.36	47.64	1.96
BH28_11	12.94	66.4	2
BH28_12	14.92	67.78	1.91
BH28_13	11.06	46.94	2.05
BH28_14	12.87	79.6	2.01
BH28_15	14.43	56.75	1.97
BH28_16	11.59	45.7	1.88
BH28_17	14.52	13.2	2.04
BH28_18	14.19	59.23	2.02

Continued on next page

Continued from previous page

Length no.	Confined track length (μm)	Angle to C Axis	Average DPar (μm)
BH28_19	13.55	51.21	1.99
BH28_20	12.27	89.32	1.89
BH28_21	13.75	17.14	2.06
BH28_22	12.95	65.54	1.94
BH28_23	12.86	39.25	1.99
BH28_24	12.1	54.93	2.1
BH28_25	12.87	88.8	2.05
BH28_26	14.41	21.56	2.07
BH28_27	13.01	53.05	1.94
BH28_28	14.15	33.92	2.2
BH28_29	13.08	71.86	2.04
BH28_30	13.62	45.47	1.95
BH28_31	12.84	54.29	2.02
BH28_32	13.74	88.35	1.88
BH28_33	14.35	49.42	2.02
BH28_34	10.84	47.9	1.9
BH28_35	13.25	83.43	2.03
BH28_36	10.66	78.17	2.11
BH28_37	14.08	12.93	1.95
BH28_38	14.6	39.18	2.09
BH28_39	14.07	20.32	2.12
BH28_40	13.75	52.5	1.89
BH28_41	15.21	72.33	2.02
BH28_42	13.46	35.22	2.08
BH28_43	12.76	56.91	1.95
BH28_44	14.52	41.5	2
BH28_45	12.1	58.23	2.01
BH28_46	13.84	61.5	2.09
BH28_47	13.25	88.92	2.18
BH28_48	13.56	21.21	2.12
BH28_49	14.8	21.67	1.96
BH28_50	12.84	31.03	2.11
BH28_51	11.85	81.82	1.98
BH28_52	12.79	49.1	1.85
BH28_53	14.94	12.83	2.02
BH28_54	14.66	60.45	1.95
BH28_55	12.56	61.28	2.11
BH28_56	14.37	56.39	1.91
BH28_57	10.62	68.72	2.05
BH28_58	13.91	46.95	2
BH28_59	13.54	62.67	2.05
BH28_60	12.24	69.18	1.99
BH28_61	14.79	61.59	2.08

Continued on next page

Continued from previous page

Length no.	Confined track length (μm)	Angle to C Axis	Average DPar (μm)
BH28_62	13.97	45.74	2.06
BH28_63	10.64	60.15	2.13
BH28_64	14.35	73.4	1.92
BH28_65	10.14	59.84	1.85
BH28_66	10.72	31.13	1.94
BH28_67	13.95	74.54	2.06
BH28_68	14.31	79	1.98
BH28_69	13.49	42.94	2.04
BH28_70	14.32	29.18	2.17
BH28_71	13.9	44.48	2.18
BH28_72	13.68	66.85	1.88
BH28_73	14.53	11.14	2.01
BH28_74	14.13	68.95	2.11
BH28_75	12.63	68.93	1.96
BH28_76	11.87	23.82	1.93
BH28_77	12.5	57.92	2.06
BH28_78	11.1	49.33	2.07
BH28_79	14.26	9.91	1.85
BH28_80	13.97	50.87	1.85
BH28_81	13.83	54.14	1.85
BH28_82	15.53	18.59	1.91
BH28_83	12.67	57.4	2.11
BH28_84	10.13	62.15	1.82
BH28_85	12.92	40.34	1.89
BH28_86	11.96	66.9	1.89
BH28_87	14.07	0	1.67
BH28_88	13.09	26.83	1.78
BH28_89	12.99	78.56	2
BH28_90	15.37	31.14	1.59
BH28_91	14.32	66.02	1.7
BH28_92	13.98	50.74	1.8
BH28_93	12.18	72.61	1.8
BH32_1	13.63	59.91	1.03
BH32_2	11.4	15.62	1.04
BH32_3	12.46	44.81	1.04
BH32_4	13.86	54.69	1.04
BH32_5	12.46	46.84	1.16
BH32_6	10.6	48.03	0.89
BH32_7	11.94	27.16	0.89
BH32_8	11.36	74.19	1.31
BH32_9	10.87	65.45	1.31
BH32_10	9.69	84.12	1.31

Continued on next page

Continued from previous page

Length no.	Confined track length (μm)	Angle to C Axis	Average DPar (μm)
BH32_11	13.57	0	1.38
BH32_12	10.11	55.43	1.24
BH32_13	9.32	0	0.94
BH32_14	13.31	42.76	1.11
BH32_15	12.04	42.51	1.24
BH32_16	9.25	60.22	1.24
BH32_17	13.47	71.35	1.07
BH32_18	13.08	51.07	0.96
BH32_19	12.67	68.68	0.96
BH32_20	9.78	83.58	1.12
BH32_21	13.83	65.42	1.12
BH32_22	12.37	69.15	0.89
BH32_23	13.3	35.7	0.89
BH32_24	12.66	74.55	1.23
BH32_25	9.06	74.55	1.23
BH32_26	10.94	65.15	1.7
BH32_27	11.99	4.14	1.68
BH32_28	11.68	45.12	1.75
BH32_29	9.93	79.59	1.75
BH32_30	12.32	43.93	1.7
BH32_31	10.77	39.54	1.72
BH32_32	12.55	17.72	1.72
BH32_33	14.74	47.61	1.72
BH32_34	12.48	55.89	1.9
BH32_35	10.21	67.74	1.91
BH32_36	10.51	78.89	1.91
BH32_37	11.94	62.94	1.91
BH32_38	14.7	75.17	1.8
BH32_39	13.04	53.26	1.81
BH32_40	12.4	66.88	1.68
BH32_41	13.05	52.19	1.68
BH32_42	13.62	63.15	1.68
BH32_43	12.8	14.43	1.68
BH32_44	12.31	67.67	1.64
BH32_45	11	42.71	1.61
BH32_46	14.85	64.24	1.61
BH32_47	9.1	54.96	1.5
BH32_48	13.04	24.69	1.82
BH32_49	11.64	49.35	1.82
BH32_50	8.89	71.92	1.69
BH32_51	13.58	84.48	1.69
BH32_52	14.37	47.07	1.69
BH32_53	14.94	17.19	1.86

Continued on next page

Continued from previous page

Length no.	Confined track length (μm)	Angle to C Axis	Average DPar (μm)
BH32_54	12.2	78.55	1.71
BH32_55	13.03	69.52	2.12
BH32_56	10.79	73.27	2.12
BH32_57	14.69	84.27	2.12
BH33_1	11.59	67.43	1.43
BH33_2	14.85	51.5	1.51
BH33_3	13.75	43.49	1.45
BH33_4	10.99	65.89	1.54
BH33_5	12.08	85.65	1.56
BH33_6	13.55	71.55	1.59
BH33_7	11.76	65.9	1.43
BH33_8	14.41	41.36	1.49
BH33_9	12	83.13	1.49
BH33_10	13.23	71.12	1.37
BH33_11	13.82	76.47	1.37
BH33_12	12.44	59.31	1.37
BH33_13	15.44	86.48	1.37
BH33_14	13.24	83.02	1.42
BH33_15	7.11	50.49	1.42
BH33_16	15.18	54.52	1.47
BH33_17	14.21	68.15	1.69
BH33_18	12.05	62.75	1.3
BH33_19	13.46	80.61	1.3
BH33_20	13.76	78.51	1.61
BH33_21	13.78	38.44	1.38
BH33_22	12.62	46.65	1.45
BH33_23	11.29	22.43	1.63
BH33_24	11.53	87.11	1.58
BH33_25	11.28	62.66	1.58
BH33_26	10.98	59.47	1.56
BH33_27	11.9	48.98	1.56
BH33_28	12.2	35.28	1.51
BH33_29	14.69	64.94	1.54
BH33_30	13.58	66.09	1.28
BH33_31	12.92	59.03	1.31
BH33_32	14.57	47.3	1.31
BH33_33	13.51	84.22	1.51
BH33_34	13.95	67.51	1.53
BH33_35	15.06	37.2	1.47
BH33_36	11.97	87.7	1.47
BH33_37	16	42.94	1.17
BH33_38	11.75	46.64	1.3

Continued on next page

Continued from previous page

Length no.	Confined track length (μm)	Angle to C Axis	Average DPar (μm)
BH33_39	13.17	67.21	1.69
BH33_40	13.36	61.29	1.6
BH33_41	12.23	63.19	1.6
BH33_42	13.26	27.91	1.6
BH33_43	13.77	47.88	1.6
BH33_44	13.28	67.86	1.51
BH33_45	13.52	47.21	1.33
BH33_46	15.19	37.88	1.35
BH33_47	11.95	63.84	1.28
BH33_48	14.54	49.25	1.43
BH33_49	12.93	41.44	1.42
BH33_50	9.08	67.38	1.42
BH33_51	11.98	55.08	1.45
BH33_52	14.37	74.91	1.45
BH33_53	14.08	58.66	1.32
BH33_54	12.29	87.35	1.32
BH33_55	15.16	44.14	1.3
BH33_56	15.13	85.42	1.31
BH33_57	14.35	61.65	1.22
BH33_58	14.11	75.19	1.3
BH33_59	12.42	61.63	1.99
BH33_60	14.25	36.56	1.95
BH33_61	13.5	72.58	1.95
BH33_62	13.63	63.57	1.95
BH33_63	13.31	50.36	1.81
BH33_64	11.74	45.39	1.68
BH33_65	12.45	76.75	1.68
BH33_66	12.6	49.72	1.68
BH33_67	12.63	64.98	1.68
BH33_68	13.47	69.9	1.38
BH33_69	10.87	78.44	2.31
BH33_70	12.43	48.27	1.87
BH33_71	13.5	66.51	1.68
BH33_72	12.84	53.18	1.68
BH33_73	10.63	56.54	1.68
BH33_74	13.74	57.78	2.02
BH33_75	10.52	19.34	2.02
BH33_76	14.76	13.28	1.95
BH33_77	14.63	53.82	1.69
BH33_78	14.19	59.3	1.67
BH33_79	11.99	75.04	1.67
BH33_80	12.31	41.13	1.67
BH33_81	11.36	67.96	1.76

Continued on next page

Continued from previous page

Length no.	Confined track length (μm)	Angle to C Axis	Average DPar (μm)
BH33_82	12.82	54.17	1.76
BH33_83	12.7	47.56	1.76
BH36_1	13.41	68.4	1.35
BH36_2	12.43	82.41	1.3
BH36_3	11.35	54.11	1.3
BH36_4	11.78	78.11	1.3
BH36_5	12.56	28.29	1.3
BH36_6	14.06	83.87	1.29
BH36_7	11.87	76.95	1.14
BH36_8	9.53	69.61	1.2
BH36_9	12.94	7.36	1.45
BH36_10	12.03	82.32	1.36
BH36_11	12.57	78	1.36
BH36_12	11.95	32.01	1.37
BH36_13	14.31	33.21	1.4
BH36_14	10.39	72.79	1.36
BH36_15	8.51	77.74	1.45
BH36_16	10.61	49.15	1.45
BH36_17	12.43	36.1	1.45
BH36_18	12.14	53.76	1.47
BH36_19	11.78	65.69	1.47
BH36_20	11.32	62.97	1.45
BH36_21	10.24	26.25	1.34
BH36_22	8.42	35.87	1.43
BH36_23	9.37	15.5	1.45
BH36_24	13.23	72.67	1.35
BH36_25	10.17	44.54	1.3
BH36_26	13.08	10.45	1.3
BH36_27	11.14	41.1	1.3
BH36_28	12.25	87.89	1.3
BH36_29	12.36	63.17	1.29
BH36_30	9.06	25.74	1.14
BH36_31	10.59	89.86	1.2
BH36_32	14.13	49.11	1.45
BH36_33	12.22	57.5	1.36
BH36_34	12.77	38.83	1.36
BH36_35	12.36	10.54	1.37
BH36_36	11.23	52.11	1.4
BH36_37	14.01	82.65	1.36
BH36_38	12.92	46.35	1.45
BH36_39	12.05	44.7	1.45
BH36_40	11.21	61.99	1.45

Continued on next page

Continued from previous page

Length no.	Confined track length (μm)	Angle to C Axis	Average DPar (μm)
BH36_41	14.49	20.78	1.47
BH36_42	12.68	69.33	1.47
BH36_43	11.48	45.29	1.45
BH36_44	11.59	78.12	1.34
BH36_45	13.02	75.37	1.43
BH36_46	12.14	37.9	1.45
BH36_47	12.81	87.03	1.3
BH36_48	15.91	62.91	1.3
BH36_49	13.03	38.75	1.3
BH36_50	11.86	82.31	1.29
BH36_51	13.41	76.03	1.14
BH36_52	11.31	72.22	1.2
BH36_53	12.54	63.33	1.45
BH36_54	9.85	50.03	1.36
BH36_55	13.11	56.45	1.36
BH36_56	13.68	27.72	1.37
BH36_57	12.06	54.39	1.4
BH36_58	12.42	22.59	1.36
BH36_59	12.56	76.63	1.45
BH36_60	11.67	18.21	1.45
BH36_61	12.51	72.32	1.45
BH36_62	12.17	56.56	1.47
BH36_63	13.45	38.16	1.47
BH36_64	13.78	12.66	1.45
BH36_65	11.55	75.99	1.34
BH36_66	14	54.8	1.43
BH36_67	14.16	71.62	1.45
BH38_1	13.74	60.15	1.58
BH38_2	12.45	51.24	1.49
BH38_3	12.68	75.88	1.49
BH38_4	13.95	74.52	1.62
BH38_5	11.24	71.1	1.61
BH38_6	11.01	54.17	1.61
BH38_7	13.89	49.99	1.61
BH38_8	14.38	49.33	1.57
BH38_9	13.11	48.25	1.68
BH38_10	11.74	82.63	1.68
BH38_11	11.45	33.34	1.56
BH38_12	14.46	26.62	1.48
BH38_13	13.62	81.75	1.4
BH38_14	11.26	61.12	1.43
BH38_15	12.27	72.39	1.43

Continued on next page

Continued from previous page

Length no.	Confined track length (μm)	Angle to C Axis	Average DPar (μm)
BH38_16	14.27	83.83	1.35
BH38_17	13.47	3.93	1.35
BH38_18	13.9	49.57	1.58
BH38_19	11.93	75.5	1.58
BH38_20	13.41	42.42	1.66
BH38_21	13.54	52.73	1.52
BH38_22	14.49	58.34	1.52
BH38_23	13.9	58.42	1.62
BH38_24	13.02	69.56	1.46
BH38_25	11.67	54.09	1.46
BH38_26	14.68	51.86	1.49
BH38_27	13.27	74.49	1.49
BH38_28	13.05	80	1.49
BH38_29	13.24	87.63	1.4
BH38_30	16.04	79.78	1.62
BH38_31	10.66	49.28	1.62
BH38_32	13.43	49.73	1.48
BH38_33	13.93	68.69	1.48
BH38_34	13.1	63.05	1.37
BH38_35	13.01	85.9	1.37
BH38_36	14.74	43.31	1.52
BH38_37	15.03	73.48	1.49
BH38_38	14.45	45.27	1.49
BH38_39	10.14	62.36	1.49
BH38_40	10.7	83.35	1.49
BH38_41	13.04	77.93	1.51
BH38_42	13.47	45.7	1.3
BH38_43	14.63	46.68	1.38
BH38_44	14.81	72.71	1.38
BH38_45	13.82	54.7	1.46
BH38_46	14.09	51.56	1.55
BH38_47	12.9	41.66	1.5
BH38_48	14.36	78.44	1.56
BH38_49	14.72	82.49	1.57
BH38_50	14.24	75.14	1.61
BH38_51	12.65	58.86	1.37
BH38_52	9.48	11.79	1.56
BH38_53	14.39	46.49	1.53
BH38_54	14.09	60.31	1.36
BH38_55	14.64	85.59	1.52
BH38_56	12.64	40.44	1.52
BH38_57	11.81	71.63	1.4
BH38_58	14.15	34.47	1.6

Continued on next page

Continued from previous page

Length no.	Confined track length (μm)	Angle to C Axis	Average DPar (μm)
BH38_59	10.52	61.33	1.6
BH38_60	13.46	28.81	1.6
BH38_61	11.6	89.12	1.7
BH38_62	13.41	63.96	1.28
BH38_63	13.3	85.13	1.28
BH38_64	13.35	83.27	1.28
BH38_65	13.4	61.29	1.27
BH38_66	12.5	80.78	1.61
BH38_67	14.94	66.17	1.52
BH38_68	13.19	53.56	1.56
BH38_69	14.63	38.3	1.56
BH38_70	12.22	23.78	1.65
BH38_71	11.09	67.18	1.37
BH38_72	12.13	83.36	1.37
BH38_73	13.1	48.81	1.37
BH38_74	12.63	42.26	1.37
BH38_75	10.11	72.44	1.43
BH38_76	12.73	53.61	1.22
BH38_77	14.69	20.28	1.47
BH38_78	11.87	63.66	1.59
BH38_79	10.45	25.41	1.59
BH38_80	13.11	61.74	1.59
BH38_81	14.5	41.49	1.59
BH38_82	13.1	39.5	1.59
BH38_83	11.21	84.36	1.53
BH38_84	12.37	64.55	1.4
BH38_85	12.62	54.03	1.61
BH38_86	13.51	46.24	1.48
BH38_87	11.57	44.3	1.7
BH38_88	11.9	60.88	1.59
BH38_89	12.06	56.85	1.59
BH38_90	12.79	86.87	1.35
BH38_91	13.45	70.42	1.31
BH38_92	11.51	35.96	1.31
BH38_93	12	83.02	1.14
BH38_94	13.47	89.65	1.53
BH38_95	12.67	79.09	1.5
BH38_96	11.62	68.07	1.47
BH38_97	12.81	87.66	1.43
BH38_98	11.45	67.73	1.45
BH38_99	10.55	57.97	1.53
BH39_1	8.91	77.49	1.36

Continued on next page

Continued from previous page

Length no.	Confined track length (μm)	Angle to C Axis	Average DPar (μm)
BH39_2	14.17	16.34	1.43
BH39_3	15.41	18.04	1.42
BH39_4	12.26	46.9	1.42
BH39_5	13.62	80.73	1.31
BH39_6	13.81	28.92	1.41
BH39_7	12.32	70.43	1.43
BH39_8	13.18	6.57	1.45
BH39_9	10.83	49.17	1.33
BH39_10	13.84	45.27	1.18
BH39_11	12.38	78.46	1.41
BH39_12	13.13	54.46	1.29
BH39_13	12.2	56.77	1.29
BH39_14	14.01	53.8	1.49
BH39_15	13.89	41.1	1.41
BH39_16	10.66	69.82	1.59
BH39_17	11.2	59.12	1.3
BH39_18	12.72	59.36	1.58
BH39_19	13.34	65.83	1.44
BH39_20	14.35	78.81	1.41
BH39_21	13.26	57.14	1.33
BH39_22	11.38	77.43	1.41
BH39_23	13.67	60.13	1.5
BH39_24	11.75	10.88	1.5
BH39_25	13.97	62.95	1.46
BH39_26	13.33	46.27	1.46
BH39_27	11.74	63.41	1.46
BH39_28	13.29	38.53	1.37
BH39_29	10.67	33.24	1.37
BH39_30	14.13	70	0.86
BH39_31	14	15.11	1.25
BH39_32	14.15	39.5	1.47
BH39_33	12.37	71.93	1.47
BH39_34	14.8	42.02	1.5
BH39_35	13.5	56.42	1.31
BH39_36	15.19	75.84	1.56
BH39_37	13.85	71.87	1.56
BH39_38	14.88	57.55	1.56
BH39_39	12.83	30.26	1.56
BH39_40	10.77	61.63	1.49
BH39_41	11.48	69.27	1.26
BH39_42	13.77	3.47	1.24
BH39_43	13.41	87.23	1.33
BH39_44	12.94	53.62	1.38

Continued on next page

Continued from previous page

Length no.	Confined track length (μm)	Angle to C Axis	Average DPar (μm)
BH39_45	14.47	16.88	1.63
BH39_46	11.98	61.79	1.2
BH39_47	13.42	48.04	1.28
BH39_48	12.29	47.74	1.28
BH39_49	11.87	44.06	1.21
BH39_50	13.24	16.07	1.48
BH39_51	10.2	46.2	1.11
BH40_1	11.43	18.35	2.01
BH40_2	12.2	18.03	1.89
BH40_3	15.54	63.98	1.7
BH40_4	13.36	63.33	1.7
BH40_5	11.9	22.37	1.7
BH40_6	13.42	33.88	1.7
BH40_7	12.87	49.24	1.7
BH40_8	12.7	17.43	1.7
BH40_9	8.68	55.75	1.72
BH40_10	12.84	67.16	1.84
BH40_11	13.87	70.62	1.84
BH40_12	12.54	43.83	1.84
BH40_13	10.89	37.86	1.84
BH40_14	12.63	44.52	1.41
BH40_15	12.38	47.37	1.41
BH40_16	12.88	37.6	1.91
BH40_17	14.01	49.37	1.91
BH40_18	15.3	29.74	1.91
BH40_19	12.27	4.04	1.64
BH40_20	12.91	73.34	1.7

B.3 Apatite U–Pb analytical spot data

This data was collected simultaneously to the apatite fission track data, but was not published in the paper associated with this chapter.

Table B.3: Apatite U–Pb analytical spot data

Sample name	Spot number	^{238}U/ ^{206}Pb	2σ	^{207}Pb/ ^{206}Pb	2σ	ρ
17	3	9.354	0.682	0.454	0.038	0.16

Continued on next page

Continued from previous page

Sample name	Spot number	$^{238}U/^{206}Pb$	2σ	$^{207}Pb/^{206}Pb$	2σ	ρ
17	4	5.076	0.412	0.62	0.081	0.51
17	6	11.587	0.953	0.401	0.032	-0.11
17	9	8.695	1.134	0.52	0.052	0.43
17	10	3.205	0.441	0.712	0.084	0.31
17	11	10.626	1.027	0.454	0.04	0.08
17	15	12.987	3.879	0.353	0.032	0.53
17	17	15.649	1.444	0.232	0.025	0.56
17	18	5.347	0.343	0.666	0.065	0.64
17	19	14.513	1.053	0.276	0.031	0.07
17	20	8.968	0.563	0.501	0.047	0.63
17	21	11.904	1.417	0.34	0.026	0.33
17	23	10.638	0.905	0.405	0.034	-0.05
17	25	14.992	1.078	0.248	0.017	0.22
17	27	9.041	0.776	0.481	0.047	0.65
17	28	5.291	0.531	0.667	0.093	0.65
17	31	5.319	0.594	0.605	0.065	0.3
17	34	12.547	0.897	0.355	0.036	0.42
17	37	4.629	0.342	0.65	0.059	0.33
17	41	4.694	0.969	0.638	0.086	0.36
19	1	4.761	0.317	0.536	0.034	0.09
19	2	3.46	0.215	0.671	0.056	0.63
19	4	3.968	0.299	0.624	0.053	0.77
19	6	4.975	0.346	0.545	0.033	0.49
19	7	3.389	0.183	0.622	0.046	0.75
19	8	5.128	0.473	0.561	0.053	0.72
19	9	3.3	0.228	0.679	0.055	0.79
19	11	4.291	0.349	0.609	0.052	0.8
19	12	5.78	0.4	0.552	0.051	0.7
19	14	2.941	0.224	0.669	0.065	0.86
19	16	3.731	0.278	0.612	0.061	0.64
19	17	3.012	0.244	0.684	0.06	0.42
19	18	4.385	0.25	0.613	0.048	0.65
19	19	4.739	0.381	0.599	0.042	0.64
19	20	3.597	0.245	0.727	0.067	0.68
19	21	5.05	0.484	0.562	0.059	0.73
19	22	5.291	0.419	0.594	0.056	0.56
19	23	4.566	0.312	0.598	0.058	0.62
19	24	3.436	0.283	0.588	0.051	0.6
19	25	5.025	0.454	0.622	0.059	0.8
19	26	4.608	0.254	0.513	0.042	-0.01
19	27	3.194	0.306	0.659	0.059	0.65
19	30	4.385	0.365	0.647	0.064	0.67
19	31	5.181	0.322	0.613	0.052	0.69
19	32	5.813	0.439	0.531	0.041	0.56

Continued on next page

Continued from previous page

Sample name	Spot number	$^{238}U/^{206}Pb$	2σ	$^{207}Pb/^{206}Pb$	2σ	ρ
19	33	4.901	0.336	0.685	0.058	0.72
19	34	5.78	0.467	0.536	0.06	0.74
19	35	3.787	0.272	0.575	0.044	0.06
19	36	3.69	0.217	0.68	0.051	0.31
19	37	4.484	0.301	0.63	0.046	0.57
19	38	5.434	0.324	0.539	0.045	0.8
19	40	5.128	0.447	0.564	0.051	0.46
19	42	5.181	0.322	0.578	0.035	0.67
19	44	4.464	0.338	0.617	0.052	0.67
19	45	4.31	0.278	0.675	0.053	0.5
19	46	5.291	0.447	0.682	0.054	0.73
20	1	3.412	0.163	0.7	0.042	0.46
20	2	4.385	0.269	0.678	0.047	0.81
20	3	5.257	0.248	0.643	0.03	0.29
20	4	2.832	0.144	0.688	0.048	0.81
20	5	4.716	0.289	0.644	0.04	0.31
20	6	5.813	0.405	0.618	0.024	0.54
20	7	4.444	0.256	0.697	0.049	0.8
20	8	5.347	0.343	0.681	0.043	0.64
20	11	3.921	0.292	0.715	0.05	0.82
20	12	4.545	0.268	0.656	0.042	0.74
20	14	2.949	0.165	0.732	0.043	0.68
20	15	4.048	0.229	0.677	0.044	0.65
20	16	3.968	0.22	0.724	0.042	0.43
20	17	3.663	0.187	0.695	0.036	0.54
20	18	8.68	0.429	0.544	0.027	0.47
20	19	4.629	0.321	0.692	0.046	0.49
20	20	3.154	0.248	0.725	0.045	0.51
20	22	3.105	0.202	0.687	0.04	0.83
20	23	5.473	0.278	0.66	0.047	0.67
20	24	5.319	0.311	0.661	0.046	0.62
20	26	7.812	0.793	0.537	0.044	0.45
20	27	4.31	0.241	0.675	0.049	0.7
20	28	3.663	0.201	0.694	0.042	0.7
20	29	3.236	0.209	0.776	0.068	0.77
20	30	3.46	0.191	0.704	0.052	0.56
20	31	4.237	0.197	0.662	0.034	0.51
20	32	5.076	0.257	0.619	0.04	0.52
20	36	5.42	0.287	0.636	0.04	0.6
20	37	4.629	0.235	0.711	0.064	0.56
21	1	3.61	0.208	0.699	0.044	0.54
21	2	3.533	0.237	0.663	0.05	0.72
21	3	3.378	0.273	0.724	0.064	0.65
21	4	3.058	0.224	0.74	0.059	0.52

Continued on next page

Continued from previous page

Sample name	Spot number	$^{238}U/^{206}Pb$	2σ	$^{207}Pb/^{206}Pb$	2σ	ρ
21	5	3.773	0.227	0.672	0.042	0.56
21	6	4.237	0.269	0.716	0.056	0.63
21	7	5.847	0.341	0.649	0.053	0.63
21	8	3.649	0.226	0.709	0.039	0.64
21	10	4.405	0.31	0.689	0.071	0.7
21	11	2.666	0.227	0.736	0.055	0.66
21	12	3.115	0.223	0.696	0.061	0.7
21	13	3.496	0.293	0.745	0.06	0.77
21	15	8.264	0.751	0.568	0.049	0.78
21	16	2.624	0.261	0.715	0.063	0.8
21	17	4.901	0.288	0.707	0.05	0.57
21	18	3.831	0.337	0.695	0.048	0.86
21	19	3.703	0.329	0.693	0.066	0.74
21	20	4.524	0.266	0.706	0.046	0.38
21	21	3.846	0.266	0.712	0.063	0.72
21	22	4.405	0.31	0.698	0.073	0.65
21	23	3.058	0.28	0.772	0.077	0.88
21	25	4.132	0.358	0.72	0.074	0.78
21	26	9.025	0.57	0.582	0.037	0.72
21	27	3.03	0.211	0.708	0.059	0.44
21	28	3.424	0.246	0.731	0.065	0.64
21	29	3.039	0.267	0.771	0.082	0.85
21	30	3.134	0.196	0.683	0.058	0.7
21	31	3.649	0.253	0.745	0.053	0.66
21	32	5.434	0.443	0.656	0.062	0.6
21	33	5.813	0.507	0.639	0.075	0.73
21	35	8.123	0.468	0.541	0.034	0.63
21	36	2.89	0.25	0.769	0.071	0.64
21	38	4.975	0.297	0.667	0.056	0.45
21	39	5.847	0.41	0.603	0.043	0.73
21	40	4.149	0.241	0.674	0.045	0.58
21	41	2.849	0.194	0.789	0.076	0.83
21	42	3.571	0.267	0.705	0.074	0.68
21	44	6.743	0.422	0.599	0.054	0.74
24	1	9.92	0.472	0.416	0.023	0.43
24	2	10.309	1.062	0.444	0.056	0.41
24	3	5.617	0.441	0.644	0.047	0.67
24	4	4.784	0.251	0.619	0.048	0.58
24	5	8.156	0.425	0.489	0.033	0.62
24	6	9.661	0.504	0.47	0.031	0.27
24	7	3.597	0.232	0.668	0.044	0.59
24	8	10.57	0.614	0.437	0.028	0.53
24	9	4.166	0.243	0.674	0.048	0.41
24	11	11.976	0.702	0.412	0.027	0.45

Continued on next page

Continued from previous page

Sample name	Spot number	$^{238}U/^{206}Pb$	2σ	$^{207}Pb/^{206}Pb$	2σ	ρ
24	12	8.203	0.639	0.505	0.039	0.34
24	13	4.739	0.404	0.654	0.046	0.08
24	15	9.216	0.671	0.45	0.029	0.5
24	17	8.771	0.684	0.532	0.047	0.42
28	1	5.319	0.339	0.655	0.051	0.79
28	2	12.738	0.665	0.403	0.028	0.39
28	3	11.627	0.824	0.433	0.033	0.76
28	4	9.017	0.398	0.526	0.035	0.61
28	5	13.262	0.65	0.39	0.019	0.39
28	6	15.797	0.673	0.325	0.016	0.4
28	7	12.87	0.828	0.4	0.03	0.64
28	10	8.936	0.527	0.493	0.032	0.46
28	11	13.679	0.617	0.354	0.022	0.51
28	12	5.524	0.335	0.589	0.046	0.75
28	13	11.89	0.593	0.429	0.025	0.53
28	15	13.422	0.63	0.389	0.022	0.48
28	17	10.857	0.589	0.42	0.022	0.42
28	18	11.037	0.462	0.44	0.029	0.23
28	19	12.5	0.75	0.373	0.02	0.39
28	20	10.672	0.489	0.503	0.038	0.46
28	21	5.376	0.375	0.661	0.06	0.77
28	22	10.869	0.708	0.459	0.035	0.3
28	23	8.912	0.603	0.513	0.037	0.28
28	24	9.756	0.561	0.507	0.039	0.59
28	27	12.437	0.495	0.38	0.021	0.43
28	28	12.15	0.693	0.367	0.017	0.63
28	29	5.882	0.346	0.628	0.048	0.69
28	30	14.326	0.615	0.325	0.023	0.46
28	31	12.36	0.534	0.364	0.017	0.69
28	32	8.635	0.604	0.501	0.031	0.72
28	33	13.054	0.681	0.349	0.024	0.57
28	35	14.577	0.871	0.326	0.024	0.49
28	38	5.938	0.299	0.618	0.041	0.66
28	40	9.14	0.526	0.548	0.039	0.57
29	2	6.671	0.422	0.626	0.038	0.59
29	3	4.716	0.378	0.724	0.049	0.68
29	4	6.666	0.288	0.634	0.027	0.4
29	5	10.604	0.562	0.482	0.029	0.61
29	6	6.472	0.272	0.66	0.038	0.47
29	7	5.128	0.368	0.68	0.057	0.69
29	8	7.698	0.397	0.599	0.036	0.62
29	9	10.976	0.602	0.472	0.026	0.54
29	10	5.78	0.434	0.624	0.044	0.52
29	12	7.547	0.444	0.54	0.028	0.6

Continued on next page

Continued from previous page

Sample name	Spot number	$^{238}U/^{206}Pb$	2σ	$^{207}Pb/^{206}Pb$	2σ	ρ
29	13	7.042	0.495	0.579	0.035	0.52
29	14	11.52	0.584	0.493	0.031	0.57
29	15	5.586	0.374	0.709	0.064	0.71
29	16	7.739	0.437	0.571	0.039	0.54
29	17	9.784	0.641	0.553	0.039	0.28
29	21	6.756	0.502	0.572	0.029	0.63
29	23	7.704	0.445	0.604	0.034	0.56
29	24	4.975	0.42	0.663	0.059	0.71
29	25	6.51	0.275	0.609	0.033	0.59
29	26	9.107	0.58	0.575	0.047	0.68
29	27	8.149	0.557	0.595	0.038	0.59
29	29	5.555	0.401	0.684	0.055	0.73
29	30	7.194	0.517	0.608	0.039	0.72
29	31	8.718	0.478	0.502	0.033	0.42
29	32	6.451	0.457	0.568	0.038	0.32
29	33	6.587	0.429	0.583	0.04	0.62
29	34	7.692	0.402	0.563	0.038	0.55
29	35	7.716	0.494	0.558	0.049	0.58
29	36	4.424	0.274	0.705	0.052	0.62
29	37	6.389	0.363	0.654	0.045	0.42
29	38	6.666	0.444	0.637	0.049	0.69
29	39	5.837	0.289	0.663	0.037	0.43
31	3	10.362	0.569	0.435	0.024	0.47
31	5	12.269	0.662	0.369	0.02	0.63
31	6	11.876	0.789	0.374	0.026	0.53
31	7	10.526	0.653	0.453	0.033	0.53
31	8	7.704	0.546	0.504	0.041	0.48
31	10	10.08	0.579	0.486	0.034	0.41
31	14	10.06	0.607	0.46	0.039	0.49
31	15	8.474	0.861	0.506	0.045	0
31	17	8.196	0.403	0.532	0.028	0.41
31	18	10.928	0.644	0.451	0.039	0.32
31	19	13.831	0.688	0.336	0.023	0.47
31	20	8.084	0.522	0.549	0.023	0.84
31	21	8.305	0.462	0.522	0.042	0.79
31	22	10.08	0.904	0.407	0.028	0.79
31	23	8.431	0.568	0.478	0.037	0.59
31	25	10.989	0.507	0.406	0.029	0.45
31	26	10.928	0.597	0.385	0.019	0.38
31	27	10.214	0.74	0.452	0.027	0.07
31	29	12.771	0.946	0.398	0.033	0.72
31	30	8.904	0.666	0.499	0.043	0.45
31	31	10.917	0.631	0.413	0.028	0.38
31	32	9.372	0.641	0.476	0.026	0.53

Continued on next page

Continued from previous page

Sample name	Spot number	$^{238}U/^{206}Pb$	2σ	$^{207}Pb/^{206}Pb$	2σ	ρ
31	35	9.319	0.495	0.477	0.025	0.28
31	36	10.235	0.66	0.473	0.028	0.27
32	3	3.095	0.22	0.719	0.05	0.56
32	4	2.77	0.176	0.717	0.058	0.48
32	7	2.645	0.174	0.803	0.077	0.71
32	10	2.762	0.167	0.756	0.06	0.28
32	11	4.098	0.268	0.735	0.062	0.31
32	12	2.45	0.162	0.755	0.058	0.61
32	13	4.444	0.237	0.707	0.054	0.59
32	14	4.878	0.285	0.672	0.048	0.41
32	15	3.558	0.227	0.782	0.069	0.64
32	17	4.098	0.302	0.715	0.061	0.73
32	18	2.531	0.173	0.709	0.06	0.5
32	21	3.03	0.165	0.75	0.033	0.61
32	23	3.401	0.219	0.724	0.06	0.62
32	24	3.436	0.224	0.772	0.063	0.58
32	25	10.81	0.467	0.479	0.026	0.37
32	26	9.587	0.698	0.536	0.048	0.6
32	27	5.555	0.339	0.671	0.051	0.23
32	28	2.857	0.179	0.813	0.062	0.45
32	30	8.375	0.483	0.567	0.041	0.35
32	31	2.331	0.152	0.774	0.052	0.39
32	32	9.433	0.382	0.495	0.037	0.42
32	33	3.802	0.202	0.717	0.056	0.37
32	34	3.3	0.196	0.71	0.047	0.36
32	35	3.021	0.173	0.768	0.058	0.69
32	37	3.937	0.263	0.725	0.047	0.58
32	38	5.813	0.439	0.66	0.048	0.65
33	3	5.434	0.472	0.61	0.064	0.8
33	6	6.06	0.404	0.574	0.043	0.54
33	9	6.493	0.463	0.6	0.047	0.81
33	10	7.751	0.6	0.526	0.045	0.56
33	11	5.464	0.418	0.645	0.059	0.64
33	12	11.363	0.568	0.431	0.024	0.68
33	13	7.49	0.544	0.596	0.05	0.79
33	14	14.471	1.068	0.308	0.022	0.54
33	15	4.761	0.272	0.663	0.044	0.41
33	16	5.319	0.339	0.655	0.057	0.66
33	17	7.407	0.603	0.633	0.058	0.63
33	18	12.18	0.608	0.38	0.023	0.45
33	19	5.405	0.438	0.711	0.074	0.65
33	20	4.854	0.329	0.662	0.057	0.58
33	21	4.166	0.26	0.712	0.056	0.41
33	22	13.262	0.756	0.345	0.026	0.54

Continued on next page

Continued from previous page

Sample name	Spot number	$^{238}U/^{206}Pb$	2σ	$^{207}Pb/^{206}Pb$	2σ	ρ
33	23	5.302	0.272	0.62	0.051	0.39
33	24	12.87	1.176	0.441	0.053	0.74
33	27	4.464	0.239	0.701	0.05	0.78
33	30	5.617	0.378	0.643	0.063	0.61
33	31	2.941	0.441	0.748	0.055	0.16
33	32	4.95	0.318	0.665	0.052	0.79
33	34	5.291	0.391	0.692	0.068	0.68
33	36	12.953	0.721	0.364	0.016	0.51
33	37	9.009	0.973	0.459	0.065	0.72
33	38	7.168	0.431	0.594	0.053	0.12
34	1	5.347	0.371	0.649	0.046	0.35
34	2	6.06	0.477	0.649	0.054	0.5
34	3	8.368	0.574	0.56	0.048	0.69
34	4	6.451	0.499	0.642	0.061	0.61
34	5	7.204	0.467	0.594	0.048	0.68
34	6	7.462	0.556	0.599	0.064	0.56
34	7	6.666	0.488	0.603	0.05	0.79
34	8	6.493	0.505	0.631	0.054	0.61
34	9	4.95	0.343	0.661	0.05	0.55
34	10	5.813	0.439	0.65	0.049	0.8
34	11	5.347	0.4	0.679	0.048	0.44
34	12	5.714	0.326	0.645	0.053	0.33
34	13	6.756	0.502	0.658	0.075	0.69
34	14	6.993	0.635	0.539	0.062	0.54
34	15	5.813	0.439	0.643	0.069	0.52
34	16	6.097	0.52	0.638	0.055	0.78
34	17	8.865	0.652	0.547	0.05	0.78
34	18	6.097	0.371	0.647	0.054	0.48
34	19	6.849	0.656	0.685	0.095	0.68
34	20	5.681	0.419	0.672	0.06	0.65
34	21	7.326	0.456	0.556	0.036	0.49
34	22	5.747	0.495	0.63	0.057	0.74
34	23	5.847	0.444	0.63	0.051	0.74
34	24	6.329	0.56	0.648	0.066	0.73
34	25	5.586	0.53	0.639	0.069	0.74
34	26	6.172	0.571	0.69	0.065	0.74
34	27	6.172	0.495	0.594	0.053	0.58
34	28	6.896	0.475	0.608	0.071	0.57
34	29	5.988	0.466	0.589	0.048	0.78
34	30	5.617	0.473	0.611	0.064	0.71
34	31	4.854	0.377	0.743	0.06	0.72
34	32	5.05	0.408	0.688	0.075	0.61
34	33	6.25	0.39	0.645	0.04	0.53
34	34	4.273	0.365	0.658	0.055	0.63

Continued on next page

Continued from previous page

Sample name	Spot number	$^{238}U/^{206}Pb$	2σ	$^{207}Pb/^{206}Pb$	2σ	ρ
34	35	6.527	0.383	0.56	0.045	0.39
34	37	5.988	0.537	0.589	0.062	0.64
34	38	4.587	0.357	0.702	0.057	0.56
34	39	6.097	0.557	0.581	0.051	0.37
34	40	6.756	0.593	0.617	0.043	0.76
BH35	3	3.875	0.375	0.577	0.043	0.49
BH35	4	2.336	0.169	0.703	0.05	0.54
BH35	6	3.333	0.222	0.638	0.059	0.51
BH35	7	3.289	0.248	0.678	0.054	0.49
BH35	8	5.347	0.4	0.556	0.041	0.18
BH35	11	3.003	0.207	0.723	0.049	0.76
BH35	12	1.76	0.216	0.713	0.048	0.23
BH35	13	2.873	0.181	0.673	0.063	0.02
36	2	10.649	0.646	0.423	0.037	0.57
36	5	18.903	1	0.142	0.007	0.22
36	6	12.062	0.858	0.449	0.04	0.38
36	7	11.21	0.955	0.435	0.034	0.72
36	8	10.964	0.541	0.417	0.035	0.17
36	9	6.622	0.57	0.557	0.068	0.56
36	11	9.803	0.682	0.448	0.045	0.6
36	12	9.596	0.635	0.468	0.05	0.48
36	13	8.554	0.49	0.541	0.039	0.41
36	14	10.834	0.809	0.464	0.045	0.41
36	16	9.363	0.561	0.513	0.039	0.57
36	17	10.427	0.717	0.449	0.036	0.71
36	22	9.302	0.614	0.477	0.041	0.65
36	24	10.493	0.638	0.435	0.034	0.54
36	25	9.487	0.486	0.466	0.039	0.44
36	26	8.771	0.63	0.523	0.059	0.57
36	28	10.298	0.774	0.476	0.044	0.61
36	31	1.851	0.181	0.77	0.11	0.48
36	36	10.952	0.875	0.441	0.051	0.61
38	1	9.469	0.466	0.441	0.024	0.51
38	3	11.534	0.545	0.432	0.034	0.38
38	4	11.682	0.723	0.377	0.033	0.64
38	7	5.847	0.82	0.66	0.048	0
38	8	6.793	0.443	0.579	0.044	0.38
38	9	7.936	0.478	0.53	0.046	0.57
38	14	14.084	0.793	0.287	0.019	0.59
38	16	5.464	0.388	0.586	0.044	0.53
38	17	5.649	0.446	0.647	0.079	0.7
38	18	9.38	0.563	0.442	0.039	0.53
38	19	3.436	0.295	0.722	0.071	0.81
38	21	14.184	0.925	0.344	0.029	0.67

Continued on next page

Continued from previous page

Sample name	Spot number	$^{238}U/^{206}Pb$	2σ	$^{207}Pb/^{206}Pb$	2σ	ρ
38	22	6.756	0.776	0.573	0.076	0.72
38	23	6.891	0.446	0.63	0.063	0.8
38	26	12.121	0.675	0.351	0.021	0.46
38	29	12.853	0.925	0.39	0.03	0.51
38	30	14.347	0.658	0.294	0.018	0.23
38	31	12.658	0.576	0.364	0.03	0.43
38	34	14.104	0.676	0.326	0.027	0.4
38	35	8.285	0.597	0.531	0.039	0.1
39	3	7.142	0.51	0.549	0.049	0.78
39	5	9.671	0.514	0.488	0.034	0.75
39	6	9.157	0.519	0.518	0.036	0.64
39	7	9.97	0.755	0.485	0.038	0.7
39	8	9.285	0.741	0.508	0.044	0.63
39	9	10.729	0.759	0.484	0.039	0.49
39	10	10.141	0.771	0.496	0.047	0.63
39	12	9.652	0.605	0.537	0.043	0.56
39	13	5.376	0.404	0.619	0.051	0.61
39	14	9.97	0.596	0.484	0.035	0.74
39	15	9.505	0.506	0.486	0.042	0.37
39	16	9.727	0.615	0.469	0.041	0.61
39	18	6.369	0.608	0.645	0.056	0.76
39	19	8.09	0.425	0.59	0.04	0.47
39	22	8.237	0.508	0.577	0.048	0.61
39	23	3.773	0.313	0.673	0.055	0.4
39	25	9.337	0.549	0.529	0.04	0.71
39	26	8.71	0.607	0.486	0.038	0.65
39	27	7.861	0.494	0.609	0.057	0.7
39	28	7.541	0.409	0.588	0.05	0.12
39	29	8.688	0.739	0.567	0.059	0.67
39	30	6.25	0.468	0.628	0.07	0.5
39	31	9.107	0.522	0.492	0.046	0.66
39	32	10.706	0.745	0.463	0.031	0.52
39	33	8.992	0.679	0.545	0.053	0.61
39	34	9.606	0.562	0.483	0.034	0.76
39	35	4.366	0.362	0.608	0.042	0.28
39	37	12.953	0.838	0.458	0.044	0.52
39	38	9.302	0.553	0.531	0.042	0.61
39	40	6.666	0.577	0.585	0.046	0.71
40	2	17.064	0.873	0.199	0.013	0.13
40	9	15.974	1.454	0.259	0.021	-0.24
40	10	18.939	0.968	0.195	0.015	0.57
40	11	11.325	0.692	0.41	0.04	0.65
40	12	4.065	0.264	0.694	0.064	0.51
40	13	18.281	1.102	0.212	0.016	0.08

Continued on next page

Continued from previous page

Sample name	Spot number	$^{238}U/^{206}Pb$	2σ	$^{207}Pb/^{206}Pb$	2σ	ρ
40	14	7.974	0.616	0.57	0.041	0.63
40	15	9.98	0.647	0.461	0.038	0.62
40	16	9.56	0.52	0.513	0.03	0.58
40	20	8	1.152	0.548	0.066	0.53

Appendix C

Late Paleozoic exhumation of the West Junggar Mountains, NW China: Appendix Part 1

The supporting information presented here is divided into three sections, consisting of the supporting summary data and plots for the apatite fission track analysis, apatite U–Pb dating, and the thermal history modelling. For individual grain/spot analytical data and tables of confined track lengths, see the separate attached supplementary data tables.

C.1 Apatite fission track supporting information

This section includes a full textual description of the apatite fission track data summarized in the results section and Table 2 of the main text, in addition to radial plots and confined track length histograms of the data.

C.1.1 Southern area

Samples WJ01, 05, and 06 were collected from the area to the SE of the Dalabute fault, near the city of Karamay. WJ01 was taken from the North Karamay pluton and produced an AFT central age of 215 ± 15 Ma ($P(\chi^2) = 0.13$, n = 22). WJ05 was taken from the West Karamay pluton and produced an AFT central age of 307 ± 12 Ma ($P(\chi^2) = 0.45$, n = 25). WJ06 was taken from the East Karamay pluton and produced an AFT central age of 307 ± 16 Ma ($P(\chi^2) = 0.59$, n = 25) with a MTL of 14.0 ± 1.0 μm (n=64). Sample WJ02 was collected from the north-west facing fault scarp of the Dalabute fault. WJ02 produced an AFT central age of 177 ± 14 Ma ($P(\chi^2) = 0.62$, n = 17) with a MTL of 12.3 ± 1.4 μm (n=37).

Samples WJ04, 07, 08, and 09 were collected in the area west of Karamay, to the NW of the Dalabute fault and to the SE of the Toli fault. WJ04 was taken from the Akebastao pluton and produced an AFT central age of 211 ± 20 Ma ($P(\chi^2) = 0.36$, n = 12). WJ07, WJ08, and WJ09 were all taken from the Miaoerguo pluton. WJ07 produced an AFT central age of 237 ± 12 Ma ($P(\chi^2) = 0.98$, n = 35) with a MTL of 12.7 ± 1.3 μm (n=34). WJ08 produced an AFT central

age of 296 ± 16 Ma ($P(\chi^2) = 0.97$, n = 36). WJ09 produced an AFT central age of 278 ± 19 Ma ($P(\chi^2) = 0.32$, n = 27).

Sample WJ10 was collected immediately to the SE of the Toli fault. It produced an AFT central age of 232 ± 33 Ma ($P(\chi^2) = 0.94$, n = 11). WJ11 was collected immediately to the NW of the Toli fault, across from WJ10. WJ11 produced an AFT central age of 275 ± 16 Ma ($P(\chi^2) = 0.69$, n = 33) with a MTL of 13.0 ± 1.1 μm (n=44).

WJ12 was collected from the SE flank of the Barleik Mountains, to the SE of the Barleik fault. It produced an AFT central age of 262 ± 12 Ma ($P(\chi^2) = 0.37$, n = 32) with a MTL of 14.1 ± 1.2 μm (n=85).

WJ13 and WJ18 were collected from the area to the east of the Toli fault, along the southern edge of the Hueshentaolege Valley near the town of Tiechangguo. WJ13 produced an AFT central age of 287 ± 15 Ma ($P(\chi^2) = 0.11$, n = 40) with a MTL of 13.2 ± 1.2 μm (n=52). WJ18 was taken from the Tiechangguo pluton and produced an AFT central age of 258 ± 19 Ma ($P(\chi^2) = 0.09$, n = 21) with a MTL of 12.4 ± 1.7 μm (n=86).

C.1.2 Northern area

Samples WJ14, 15, 16, and 17 were sampled over a range of elevations from 1210–2533 m on the escarpment on the northern side of the Hueshentaolege Valley, near the town of Tiechanggou. In order of elevation, from lowest to highest, WJ14 (1210 m a.s.l.) produced an AFT central age of 180.9 ± 9.8 Ma ($P(\chi^2) = 0.08$, n = 36) with a confined mean track length (MTL) of 12.0 ± 1.5 μm (n=100), WJ15 (1582 m a.s.l.) produced an AFT central age of 189.6 ± 9.4 Ma ($P(\chi^2) = 0.03$, n = 33) with a MTL of 12.1 ± 1.4 μm (n=66), WJ17 (2041 m a.s.l.) produced an AFT central age of 219 ± 20 Ma ($P(\chi^2) = 0.00$, n = 20) with a MTL of 12.2 ± 1.6 μm (n=47), and WJ16 (2533 m a.s.l.) produced an AFT central age of 171.6 ± 9.3 Ma ($P(\chi^2) = 0.96$, n = 24) with a MTL of 12.4 ± 1.5 μm (n=57).

Samples WJ19 and WJ23 were taken from the Shaburt Mountains, on the northern side of the eastern extent of the Hueshentaolege Valley. WJ19, located in the west of the range, produced an AFT central age of 292 ± 16 Ma ($P(\chi^2) = 0.56$, n = 17) with a MTL of 14.1 ± 1.1 μm (n=96). WJ23, at the eastern extremity of the range, produced an AFT central age of 259 ± 24 Ma ($P(\chi^2) = 0.97$, n = 24) with a MTL of 12.8 ± 1.4 μm (n=46).

In the northernmost part of the study area, across the EW trending Hobok Valley from the Shaburt Mountains, samples WJ21 and WJ22 were taken from the southern margin of the Saur Mountains. WJ21 was collected from a deeply incised valley in the high relief western part of the range, near the Kazakhstan border. WJ21 produced an AFT central age of 192 ± 10 Ma ($P(\chi^2) = 0.14$, n = 39) with a MTL of 12.6 ± 1.3 μm (n=66). WJ22 was collected from the low relief eastern extremity of the Saur Mountains, and produced an AFT central age of 268 ± 13 Ma ($P(\chi^2) = 0.52$, n = 30) with a MTL of 12.8 ± 1.3 μm (n=50).

C.1.3 Apatite fission track figures

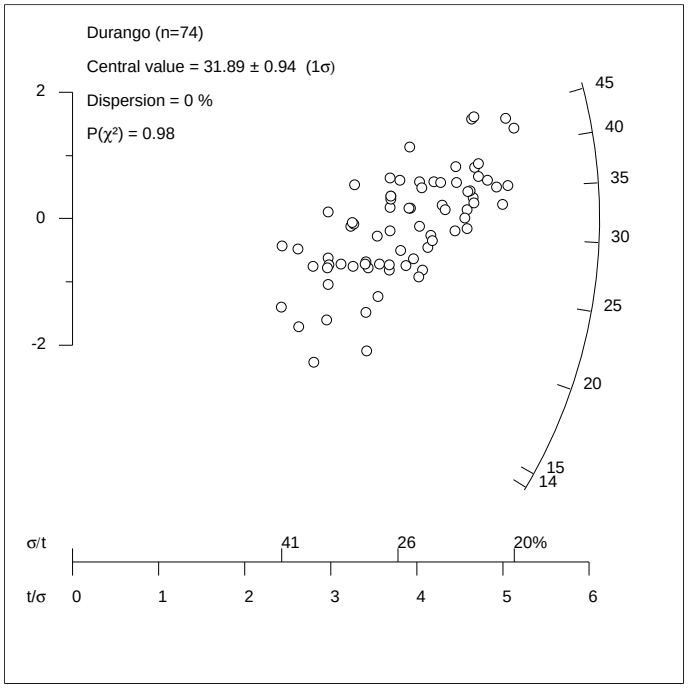

Figure C.1: Radial plot of individual spot data for the Durango secondary AFT standard (reference age 31.44 ± 0.18 Ma; McDowell et al. (2005)) that was used to derive the zeta-calibration factor.

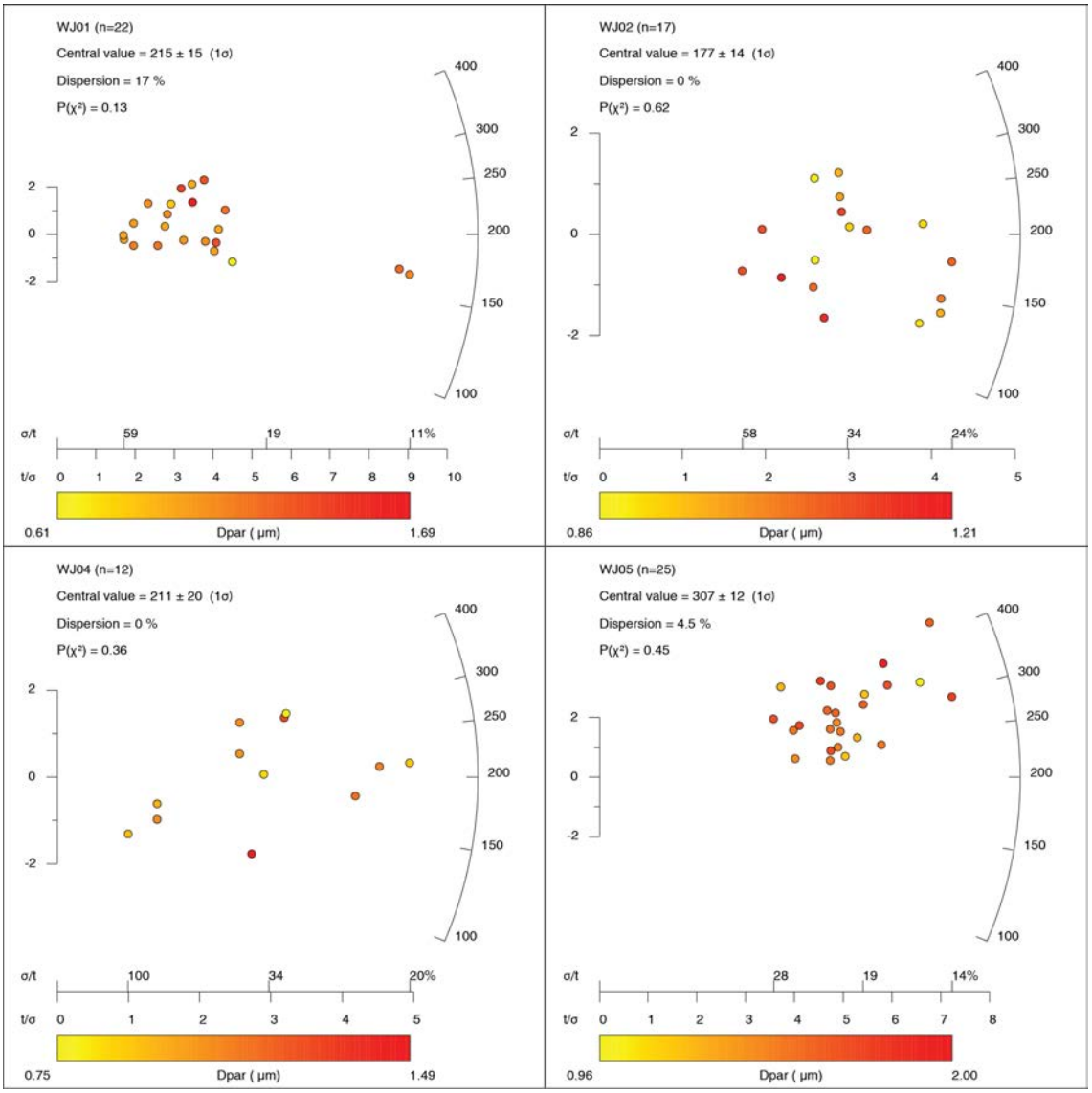

(a) WJ01, WJ02, WJ04, WJ05 radial plots

Figure C.2: Apatite fission track radial plots

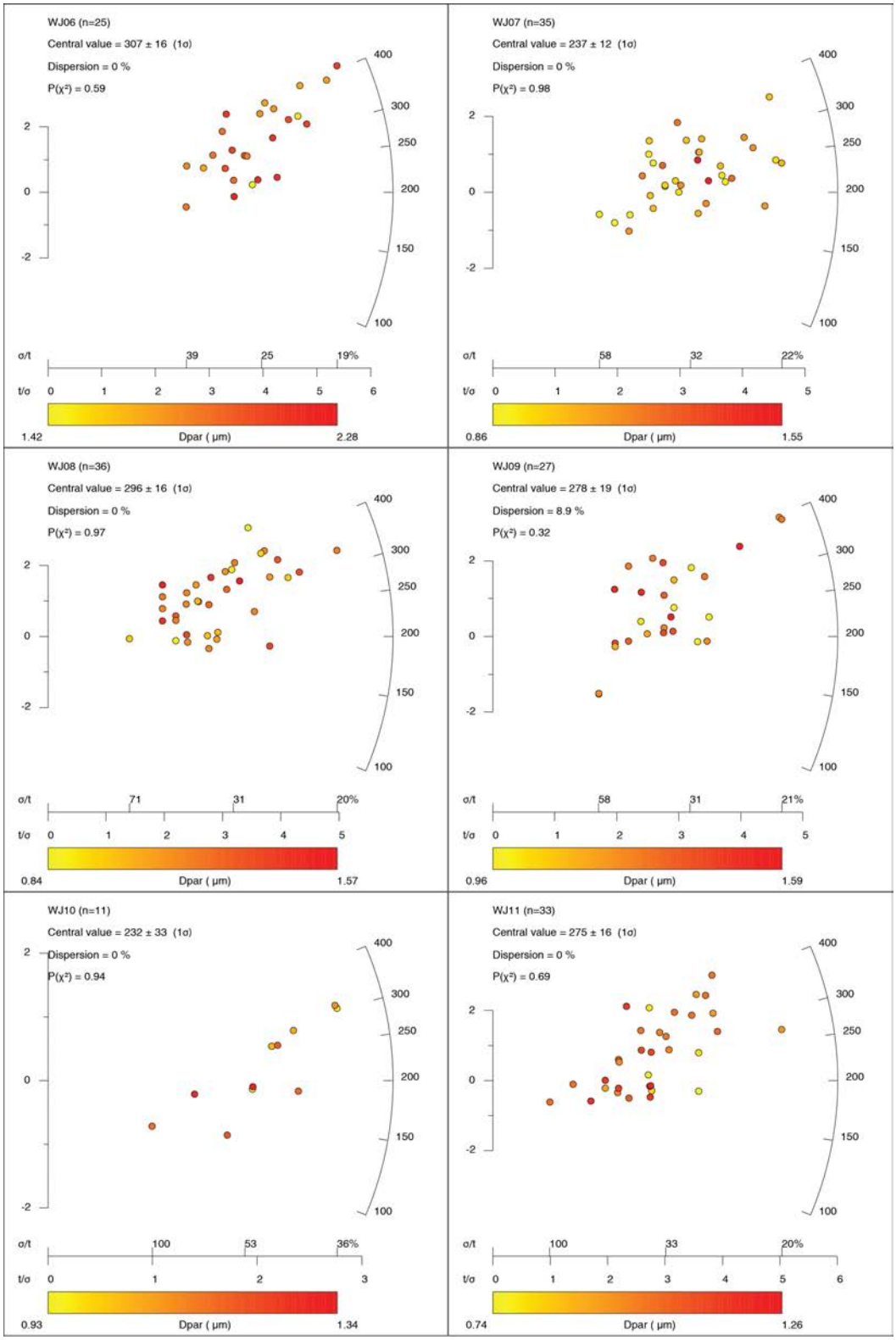

(b) WJ06, WJ07, WJ08, WJ09, WJ10, WJ11 radial plots

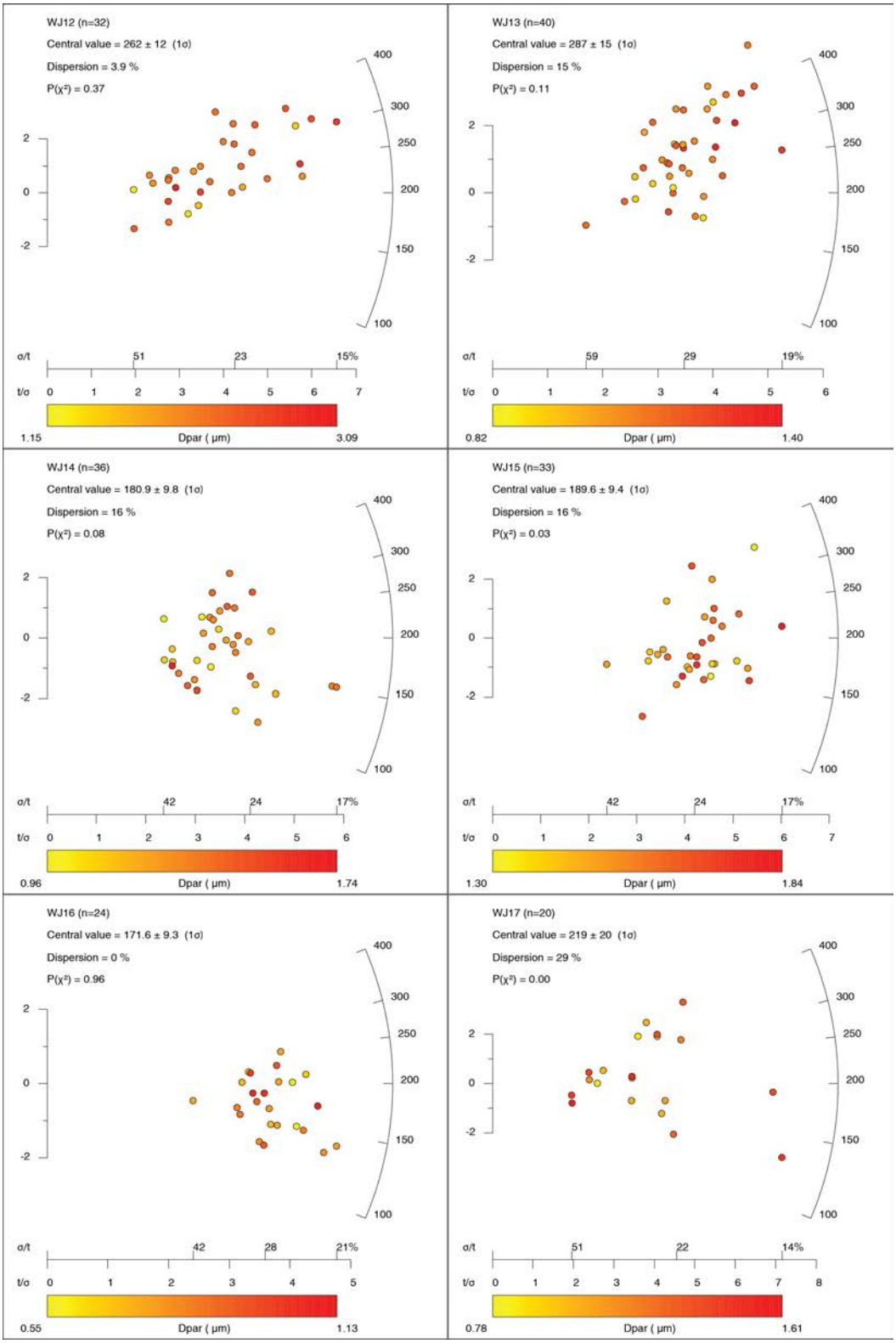

(c) WJ12, WJ13, WJ14, WJ15, WJ16, WJ17 radial plots

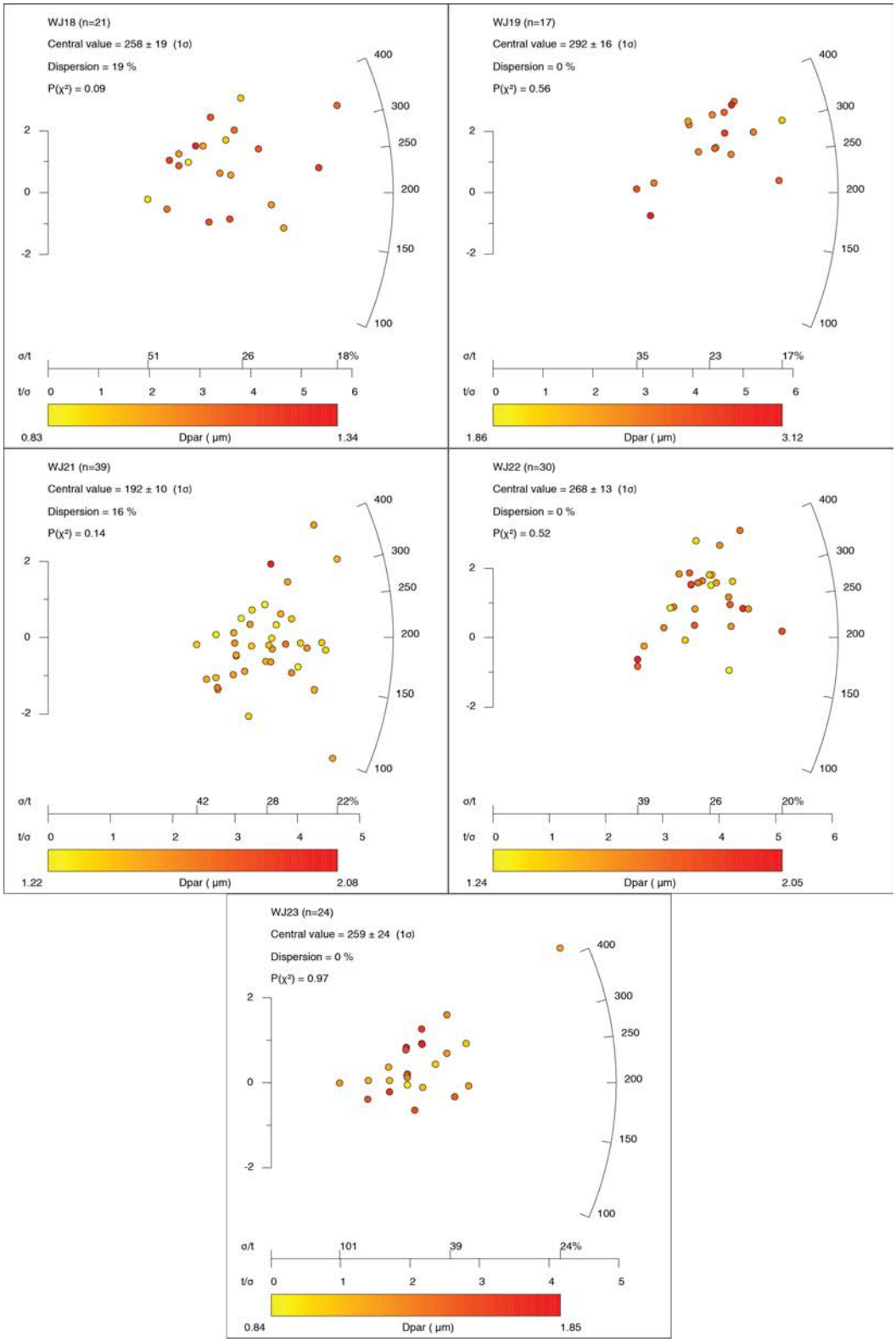

(d) WJ18, WJ19, WJ21, WJ22, WJ23, radial plots

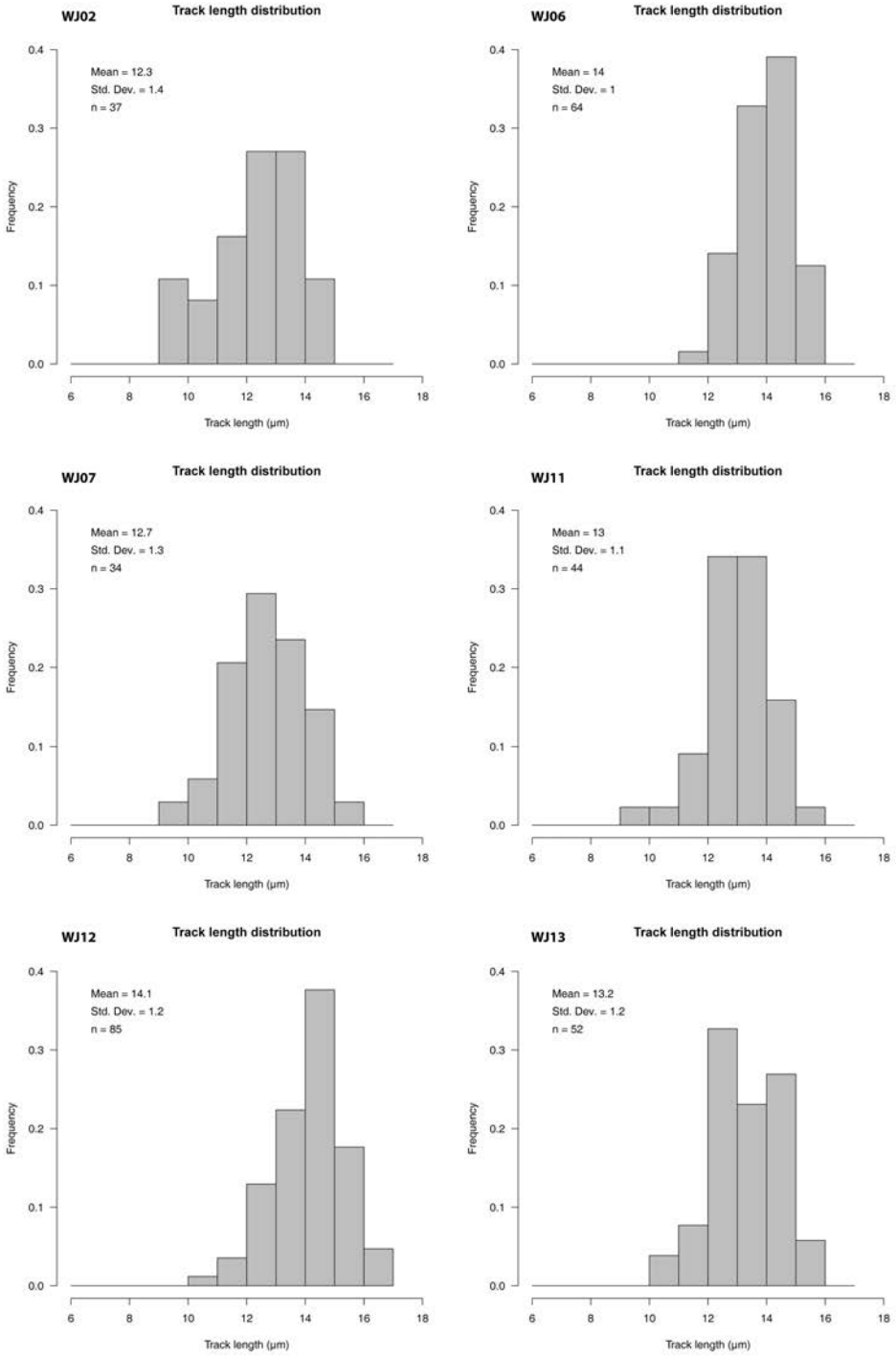

(a) WJ02, WJ06, WJ07, WJ11, WJ12, WJ13 confined track length histograms

Figure C.3: Apatite confined track length histograms

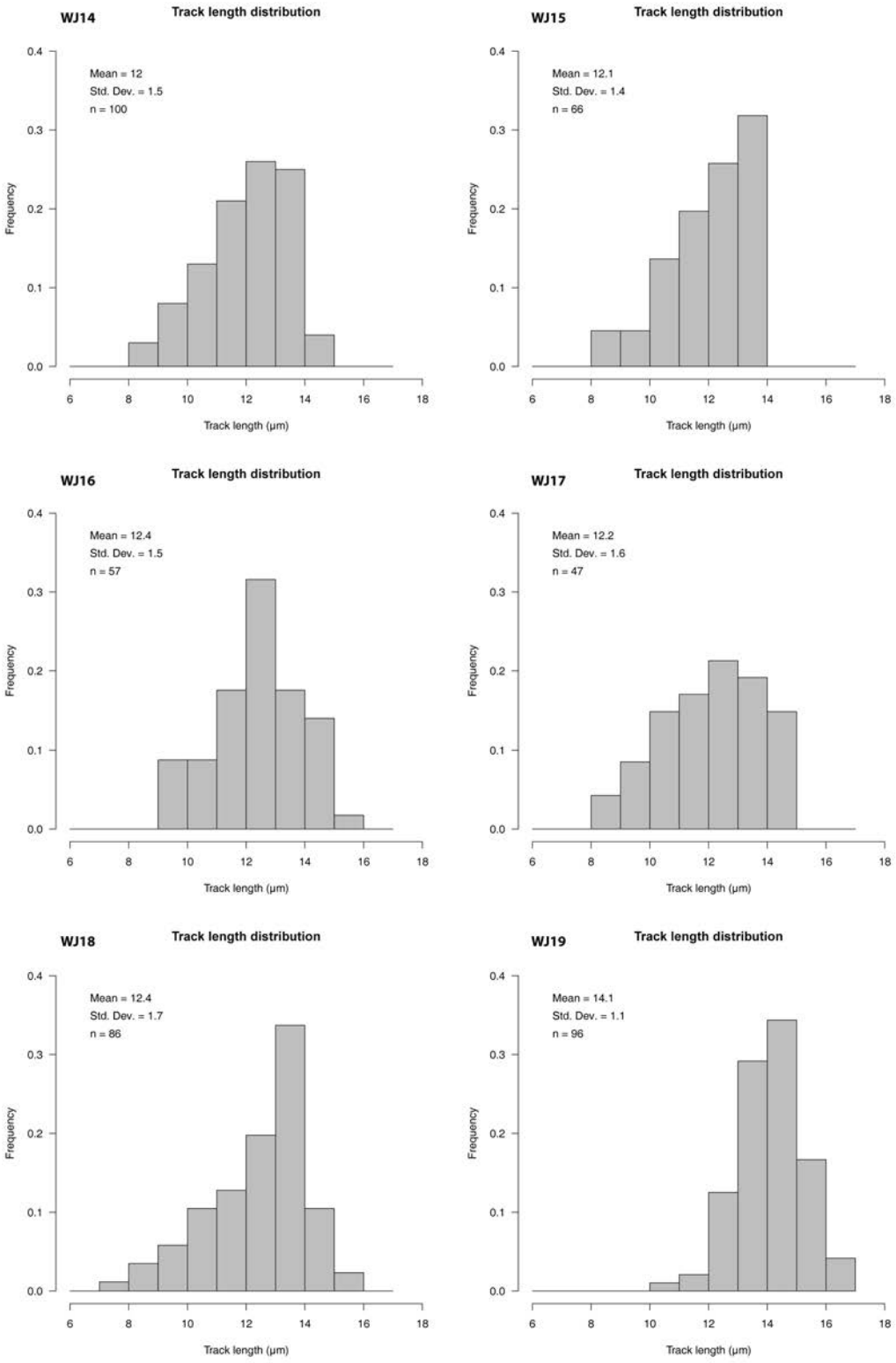

(b) WJ14, WJ15, WJ16, WJ17, WJ18, WJ19 confined track length histograms

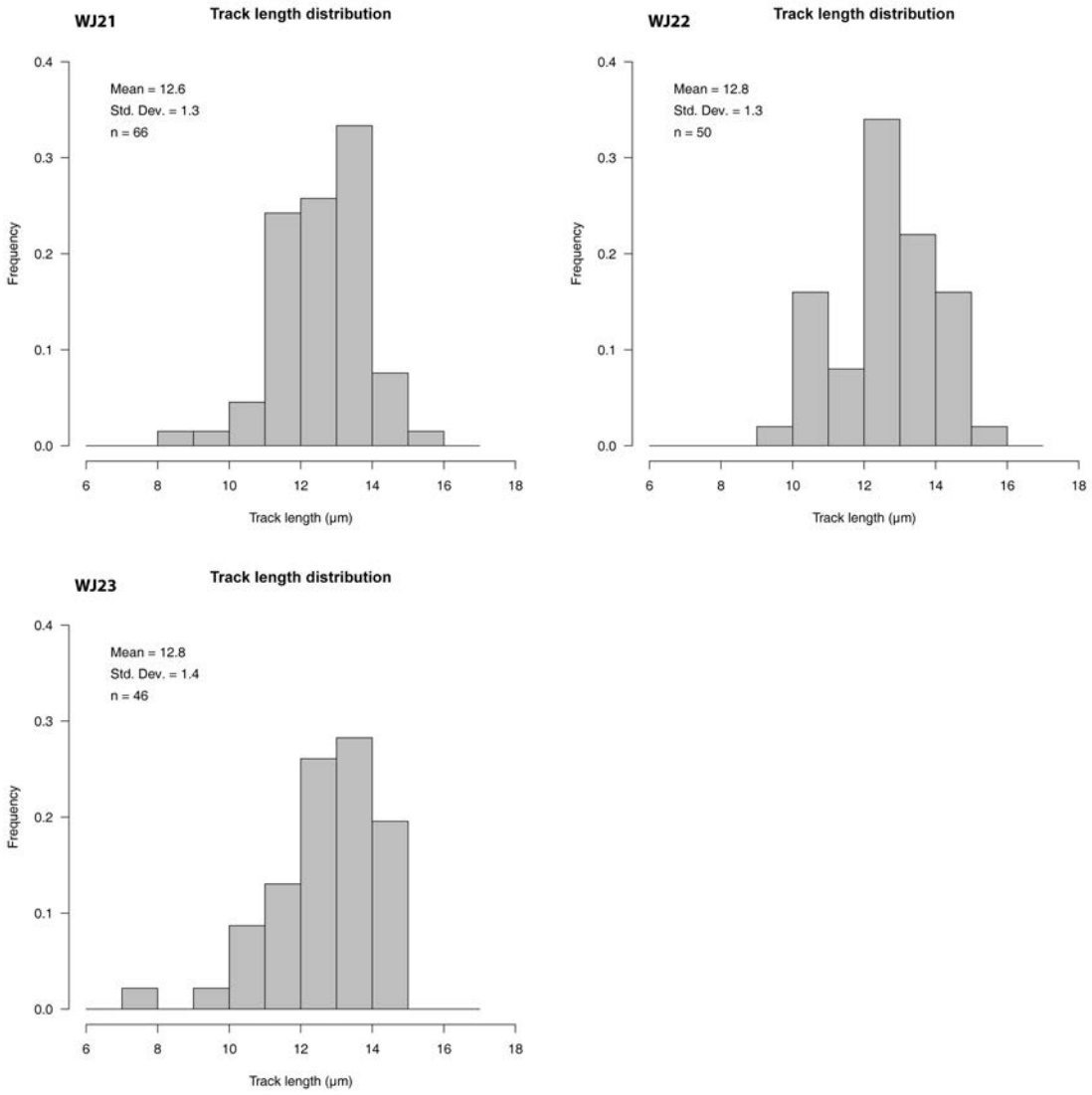

(c) WJ21, WJ22, WJ23 confined track length histograms

C.2 Apatite U–Pb supporting information

This section contains the apatite U–Pb Tera-Wasserburg inverse concordia diagrams for the Mt. McClure secondary U–Pb standard, and for each dated sample.

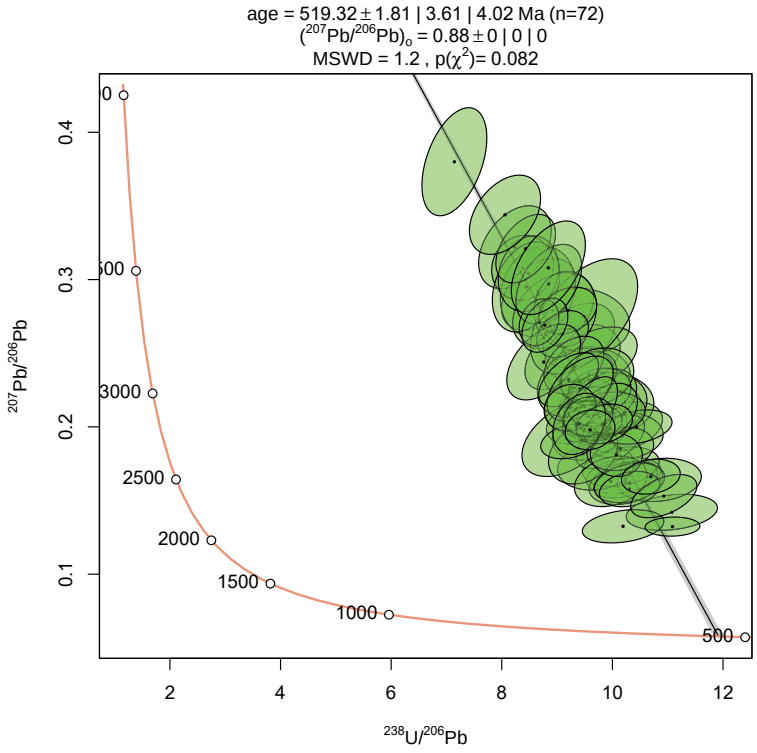

Figure C.4: Tera-Wasserburg inverse concordia diagram of analyses of the Mt. McClure apatite U–Pb secondary standard (reference age 523.51 ± 2.09 Ma), using a fixed upper intercept of 0.8820 based on known initial $^{207}Pb/^{206}Pb$ composition (Schoene and Bowring, 2006). IsoplotR produces several uncertainty values for the lower intercept age and common Pb composition of the regression. In this study we refer to and use the second given value in all further discussions and in the text. This value is the 95% confidence interval for the age, which is the equivalent of 2σ. See Vermeesch (2018) for further details concerning IsoplotR.

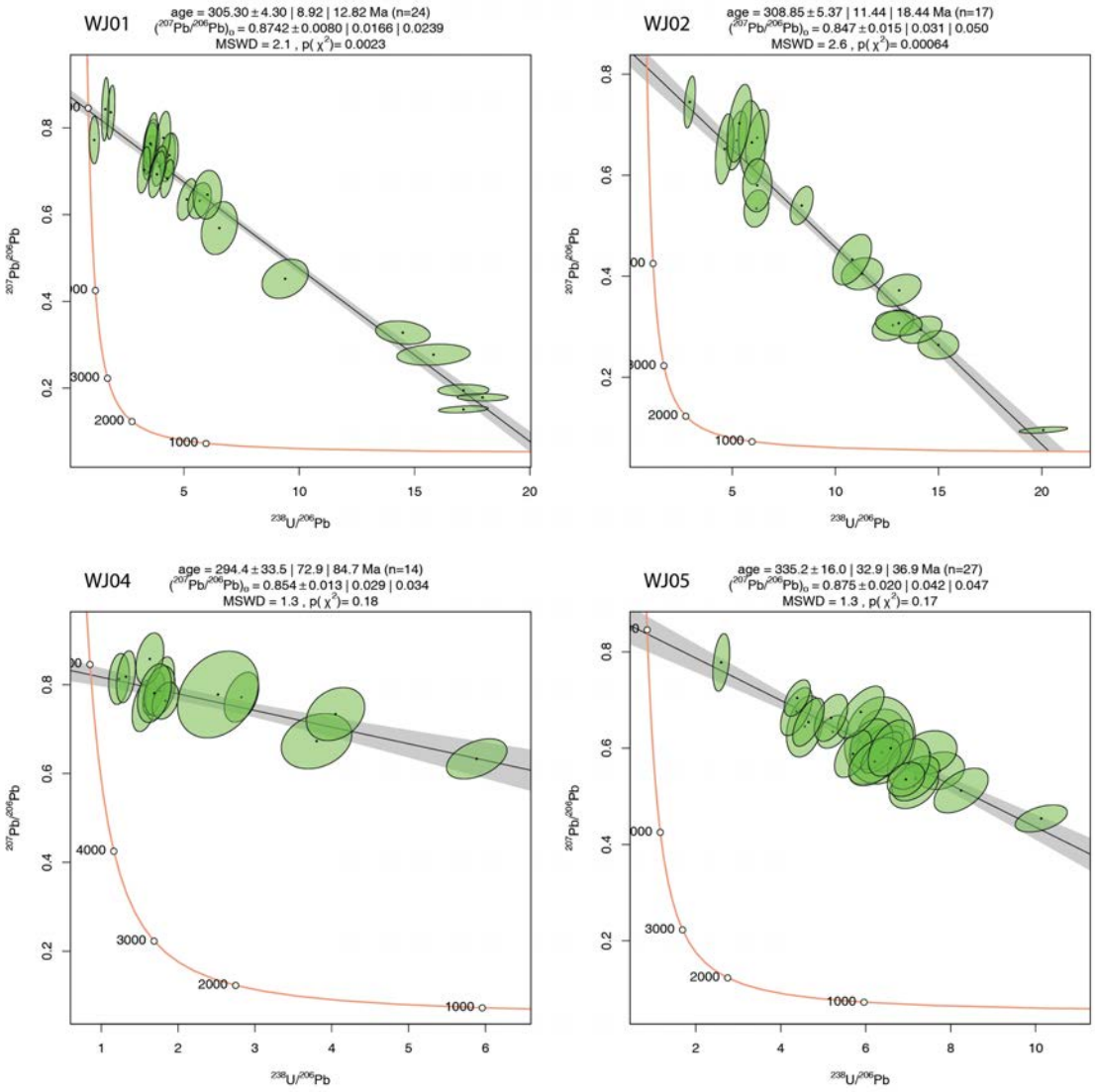

(a) WJ01, WJ02, WJ04, WJ05 T-W diagrams

Figure C.5: Tera-Wasserburg inverse concordia diagrams of apatite U–Pb data

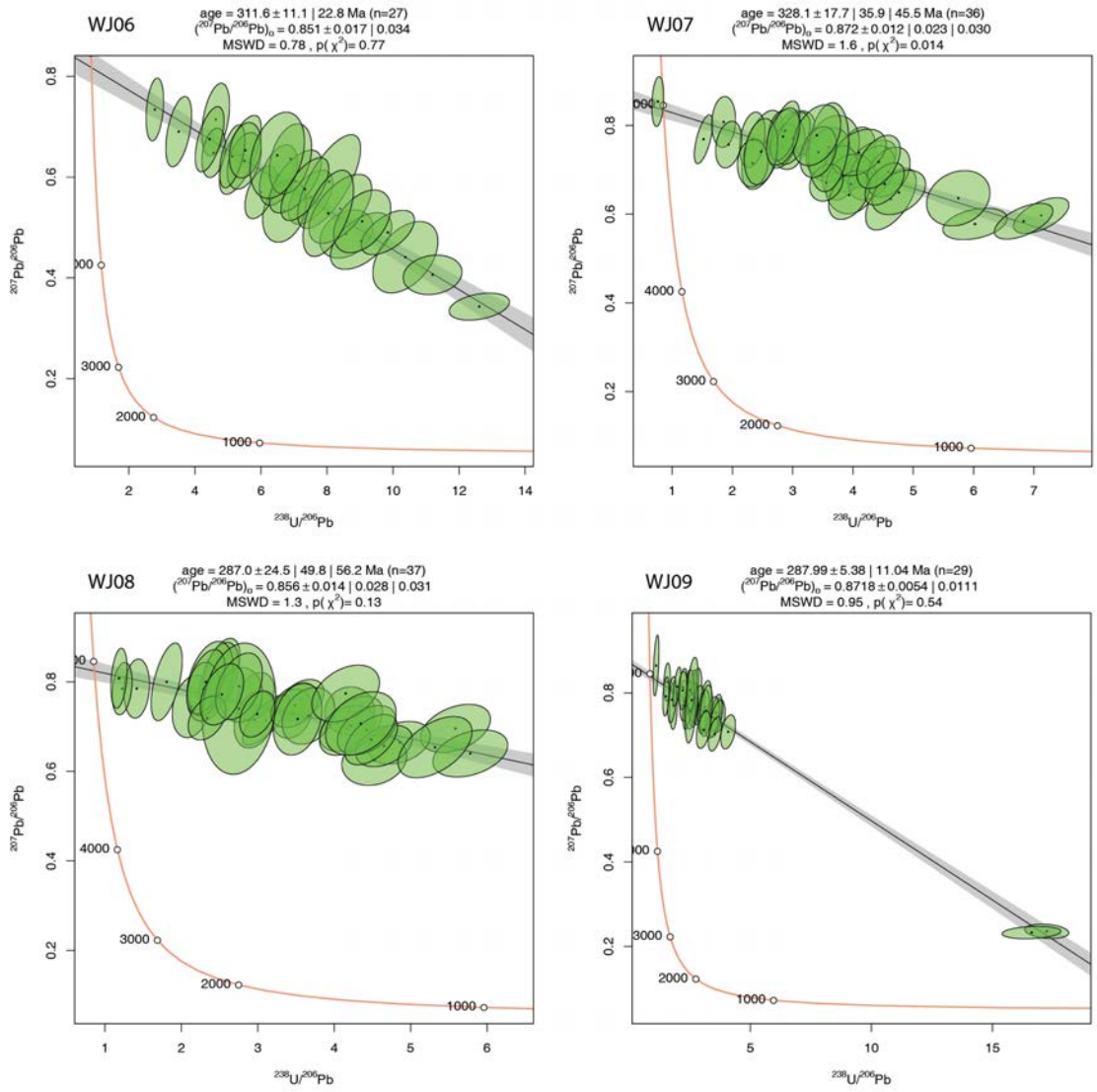

(b) WJ06, WJ07, WJ08, WJ09 T-W diagrams

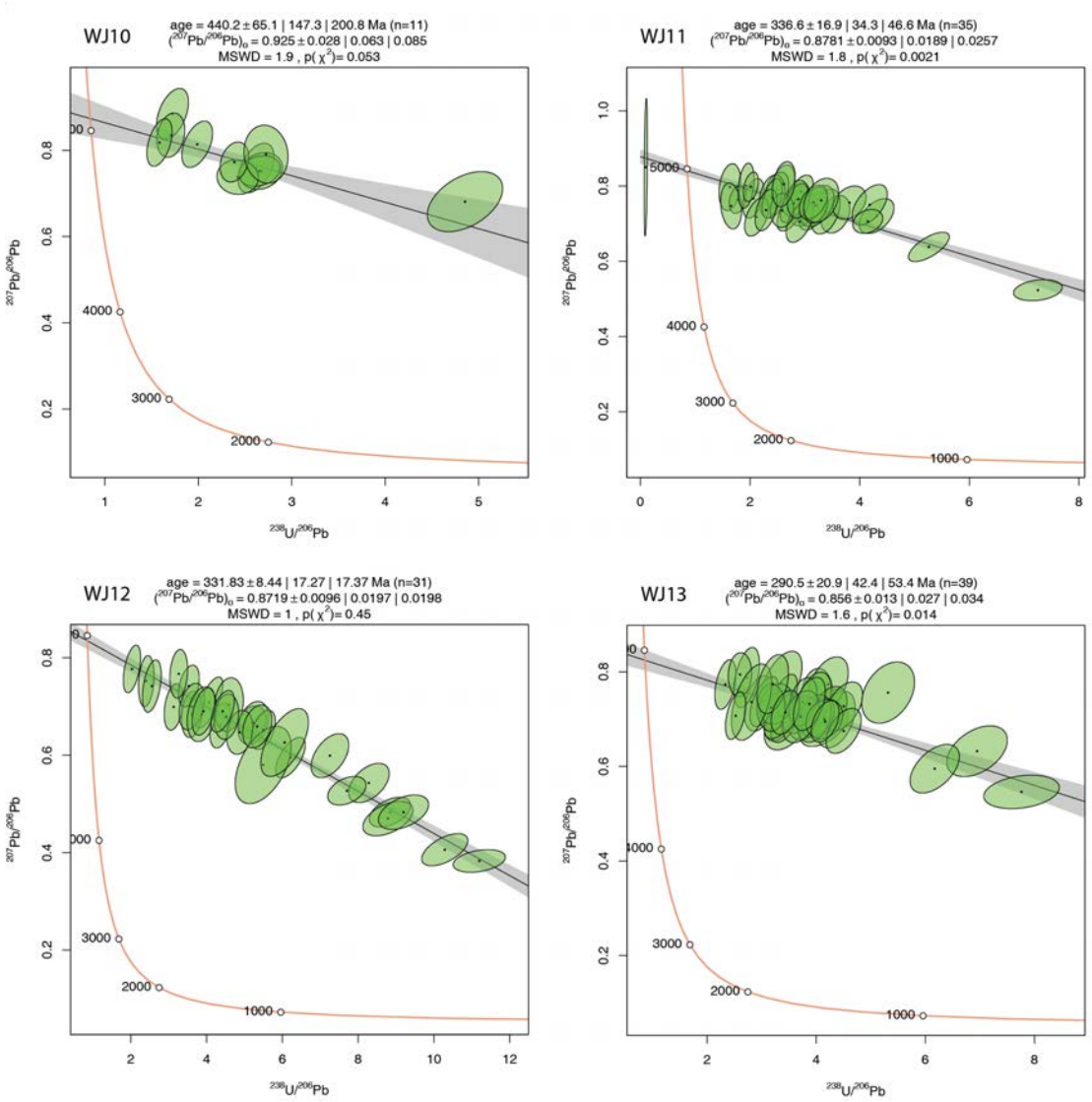

(c) WJ10, WJ11, WJ12, WJ13 T-W diagrams

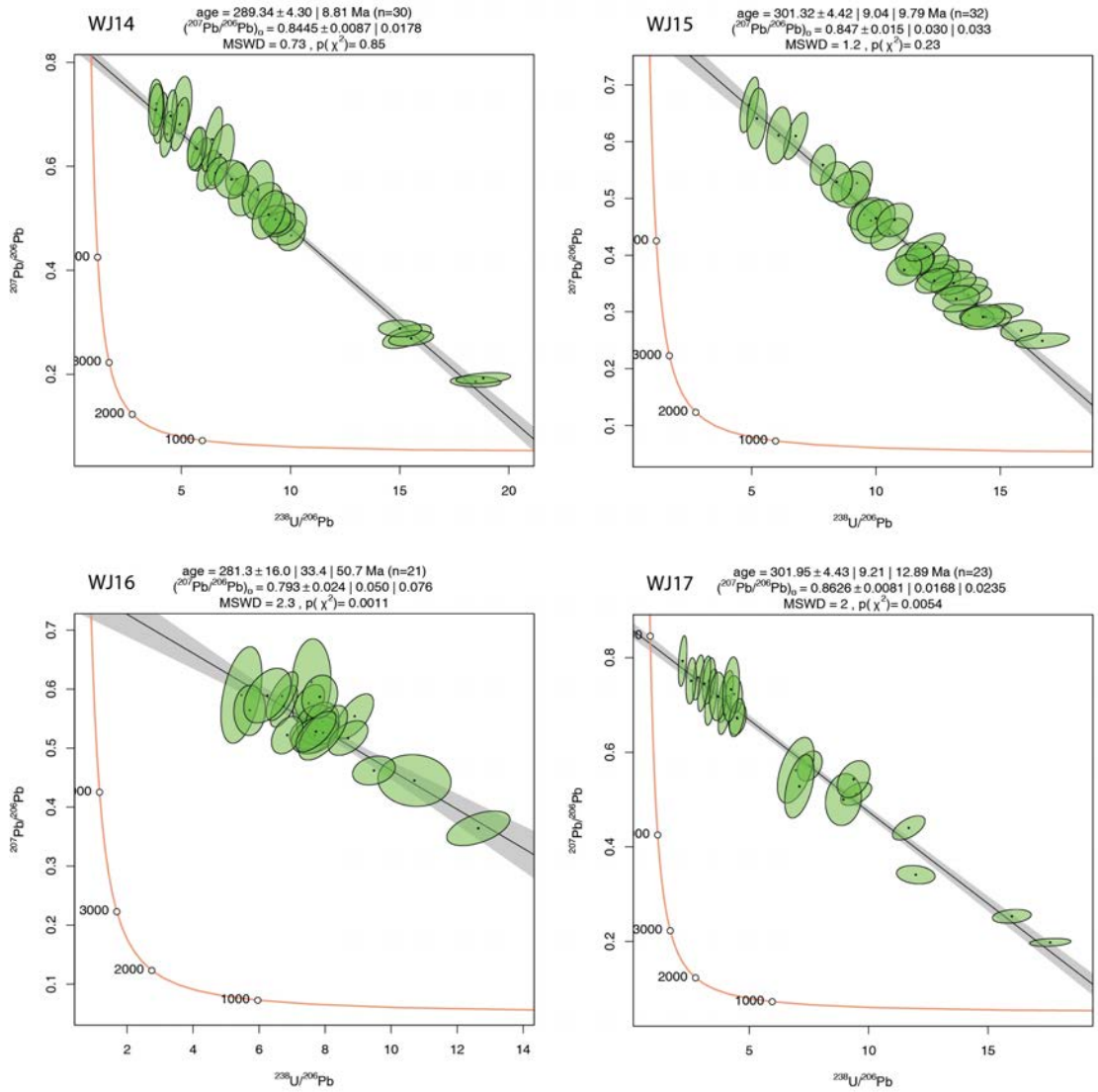

(d) WJ14, WJ15, WJ16, WJ17 T-W diagrams

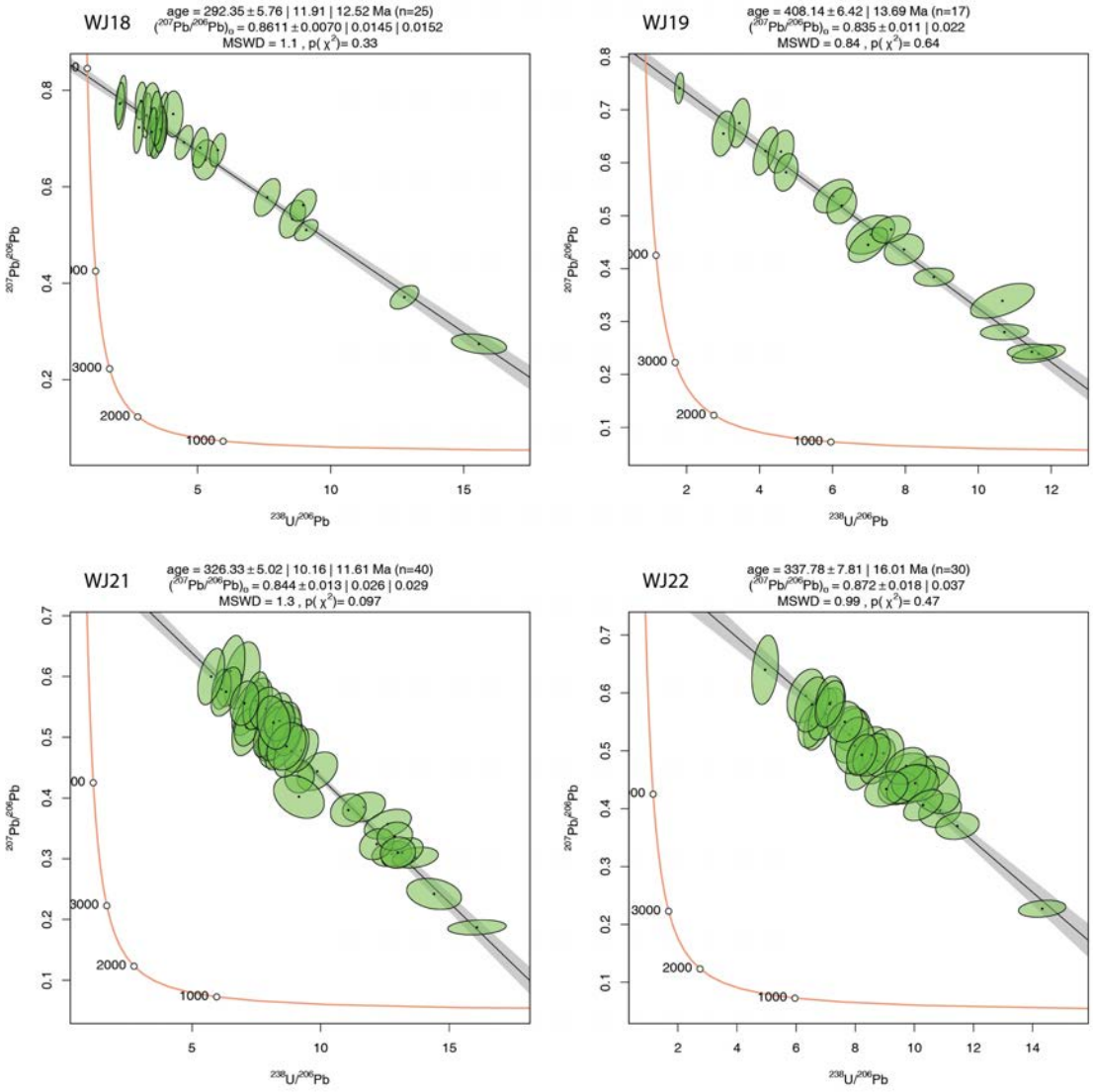

(e) WJ18, WJ19, WJ21, WJ22 T-W diagrams

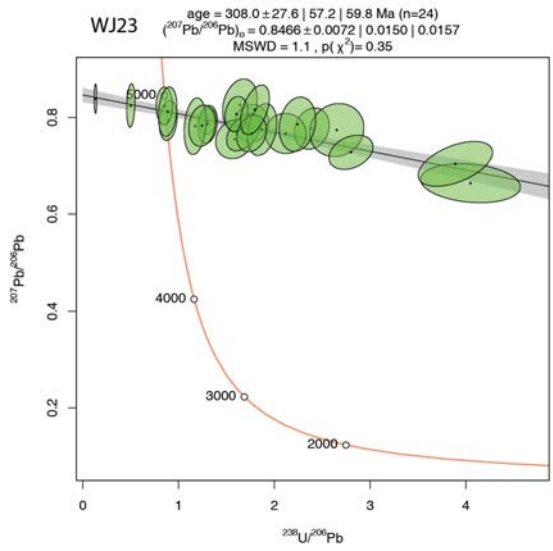

(f) WJ23 T-W diagram

C.3 Thermal history modelling supporting information

This section contains data and plots that summarize the thermal history modelling carried out as part of this study, as well as a selection of other models.

C.3.1 Thermal history modelling parameters

Table C.1: Thermal history modelling inputs, assumptions, and parameters

1. Thermochronological data

	Model input data			Data Source	Published data?
Sample Region	AHe	AFT	ZHe		
Southern West Junggar					
WJ01		x		(1)	Y
WJ02		x		(1)	Y
WJ04		x		(1)	Y
WJ05		x		(1)	Y
WJ06	x	x	x	(1), (2)	Y
WJ07		x	x	(1), (2)	Y
WJ08		x		(1)	Y
WJ09		x		(1)	Y
WJ10		x		(1)	Y
WJ11		x		(1)	Y
WJ12		x		(1)	Y
WJ13		x		(1)	Y
WJ18	x	x	x	(1), (2)	Y
Northern West Junggar					
WJ14		x		(1)	Y
WJ15		x		(1)	Y
WJ16		x		(1)	Y
WJ17		x		(1)	Y
WJ19		x		(1)	Y
WJ21		x		(1)	Y
WJ22		x		(1)	Y
WJ23		x		(1)	Y

Data treatment, uncertainties, and other relevant constraints

He data

Treatment: Each individual analysis input separately into QTQt

Dates (Ma): Uncorrected He date input, α-ejection correction applied in QTQt after (Farley et al., 1996)

Uncertainties (Ma): Analytical uncertainties (1σ) input and resampled with MCMC procedure to account for overdispersion of dates due to sources of uncertainty in He dating that are difficult to quantify

r (μm): Mean equivalent spherical radius of each sample

AFT data

Initial mean track length (μm): 16.3

Track length reduction standard: 0.893

Etchant: 5.0M

Compositional parameter (μm): D_{par}

2. Additional geological information

Assumption	Explanation and data source
Initial high temperature constraints at 400 ± 50 °C at apatite U–Pb age for each sample	Igneous samples. Apatite U–Pb ages from this study
Final constraint at surface conditions, 10 ± 10 °C at 0 Ma	Samples collected from surface

3. System and model specific parameters

AHe radiation damage model: Flowers et al. (2009)
FT annealing model: Ketcham et al. (2007)
FT c-axis projection: no
Modelling code: QTQt 5.6.0 Windows
Iterations: Initial exploratory runs with 10,000 burn-in and 10,000 post burn-in. Final run 100,000 each burn-in and 100,000 post burn-in.
tT path characteristics: Reheating allowed
Acceptance rates: 0.2-0.8. Birth/death 1
Fitting criteria: Model specific observed vs. predicted values comparison below
Range of general prior: t=AFT central age ± AFT central age, T = 70 °C ± 70 °C (AFT only), 100 °C ± 100 °C (AFT + He).
Data source:
(1) - This study, Tables D.1, D.2
(2) - Yin et al. (2018), Supplementary table 2,3

C.3.2 Thermal history modelling figures

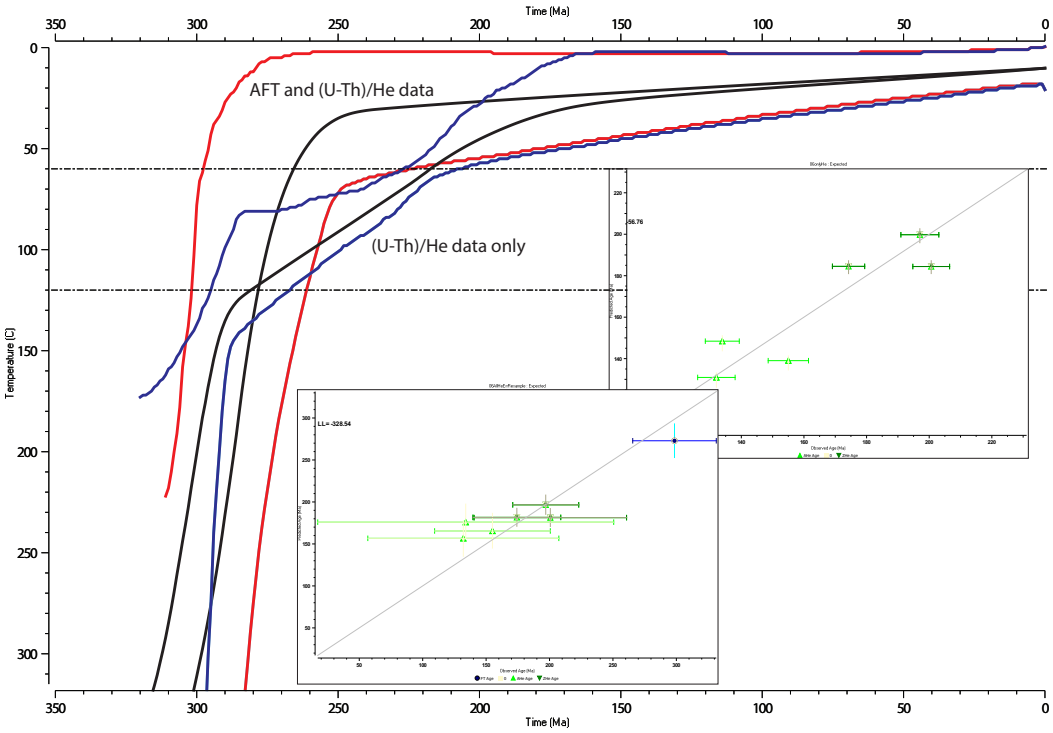

Figure C.6: Models for the thermal history of the East Karamay pluton using both AFT (WJ06) and (U-Th)/He data compared to only using (U-Th)/He data. Both models show cooling to above the APAZ during the Triassic despite differences due to lack of AFT data in the blue model. This shows that existing (U-Th)/He data from Yin et al. (2018) is consistent with the AFT data from this study, in comparison to the AFT data obtained by previous studies that obtained AFT ages 200-100 Ma younger than the timing of cooling through the APAZ shown here. Insets show comparison of the observed vs predicted values for each model, illustrating that observed values are within uncertainty of the predicted values.

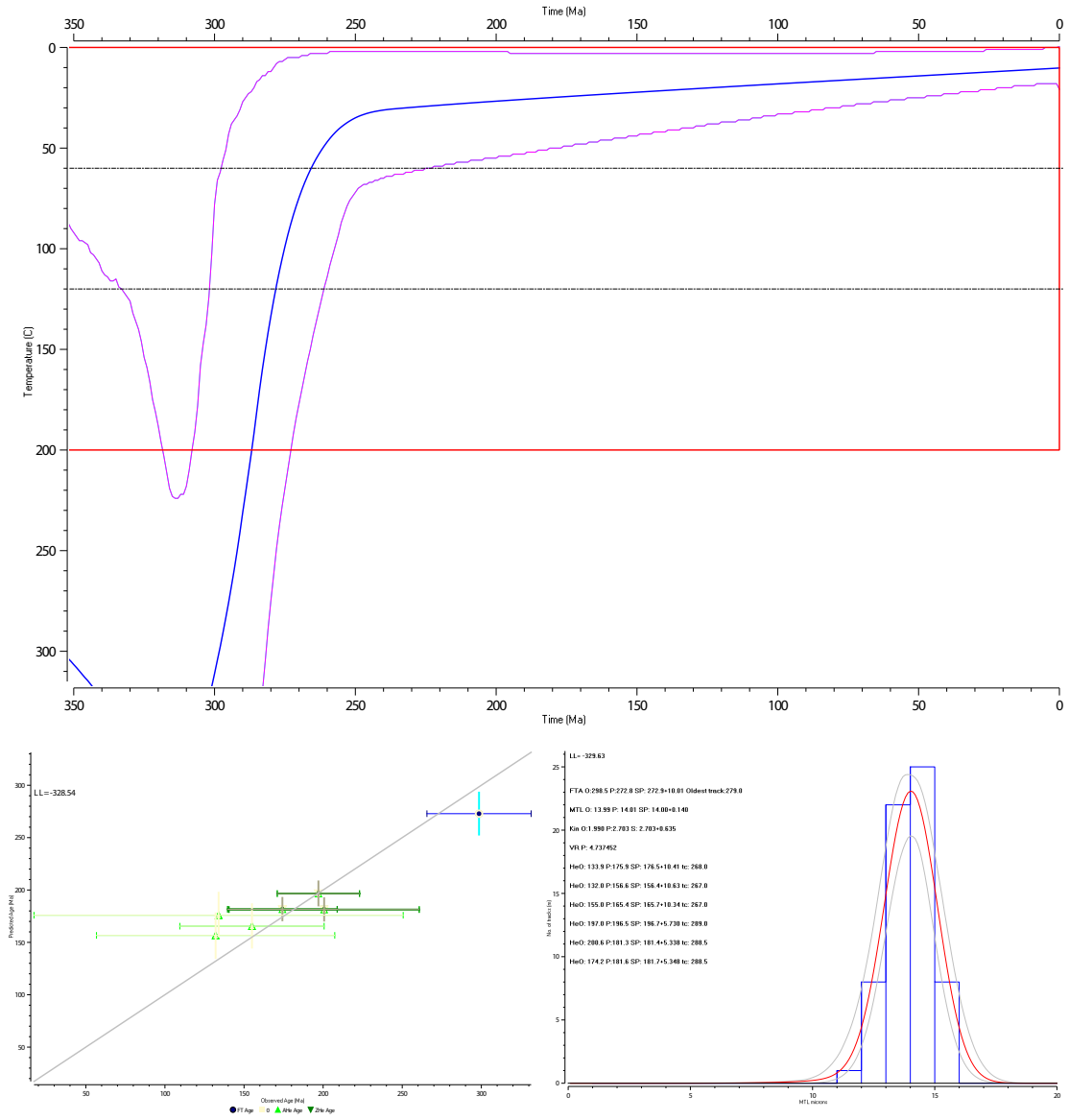

(a) WJ06 modelling report

Figure C.7: Thermal history modelling output from QTQt for models including both AFT and He data (i.e. WJ06, WJ07, WJ18). Expected tT model is shown in the top panel of each subfigure, blue line is expected model, pink envelope is 95% CI. Bottom left is observed vs predicted values for AFT, AHe, and ZHe ages. Bottom right is observed vs predicted summary table showing AFT age, MTL, kinetic parameter (Dpar), and He ages. O = observed, P = predicted, SP = sampled values of the predicted value. For further reading about the interpretation and meaning of the outputs see Gallagher (2012).

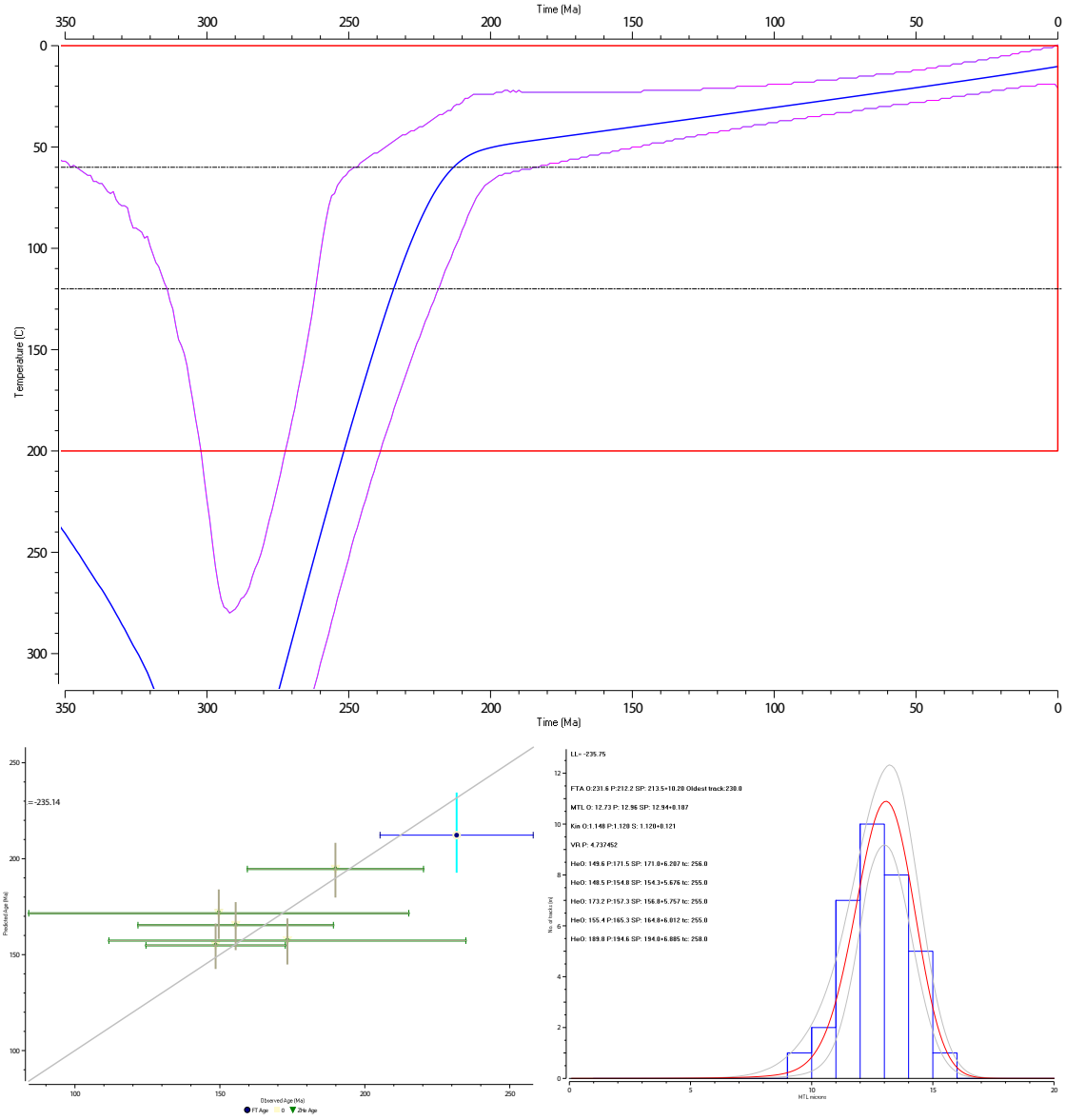

(b) WJ07 modelling report

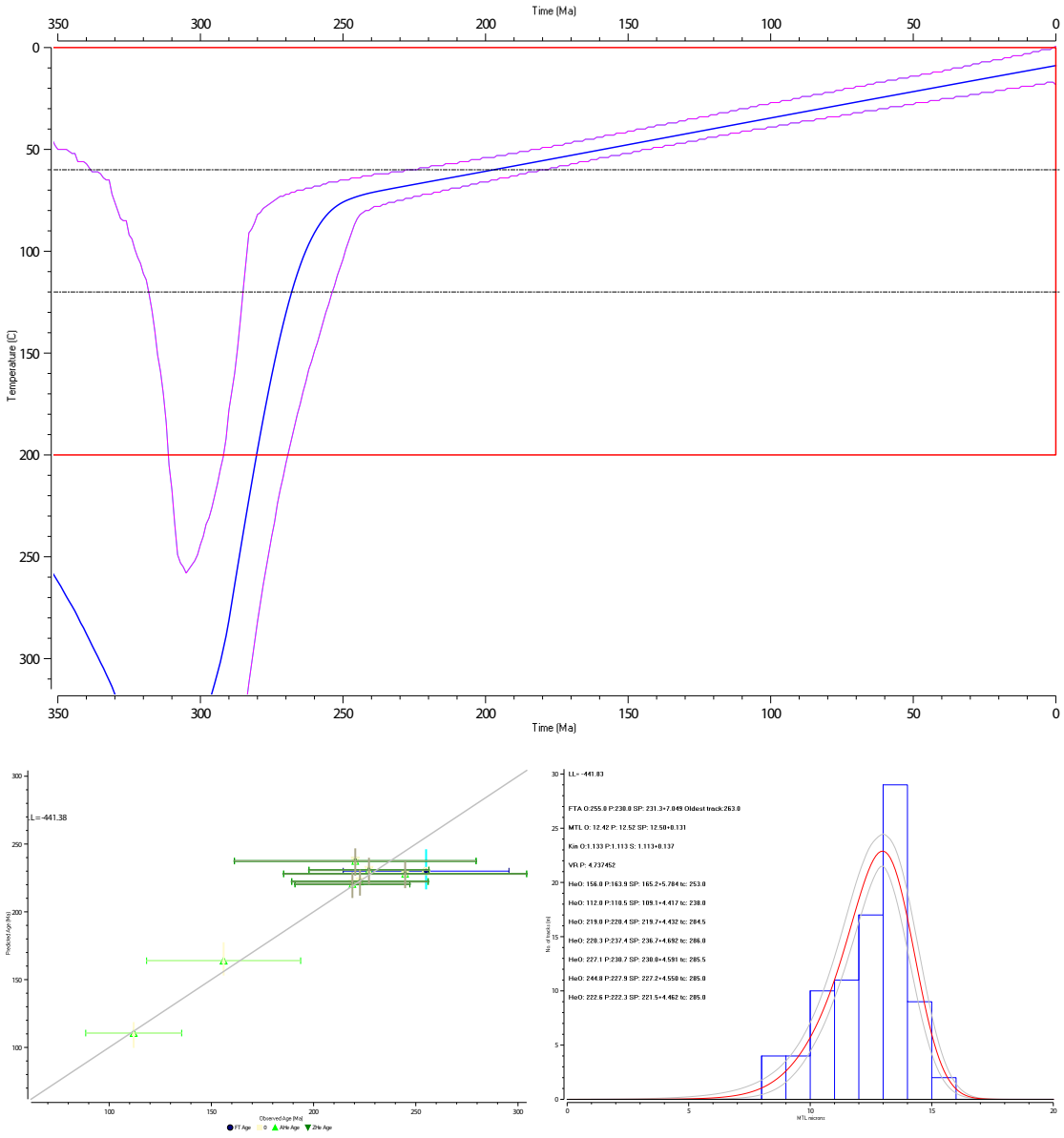

(c) WJ18 modelling report

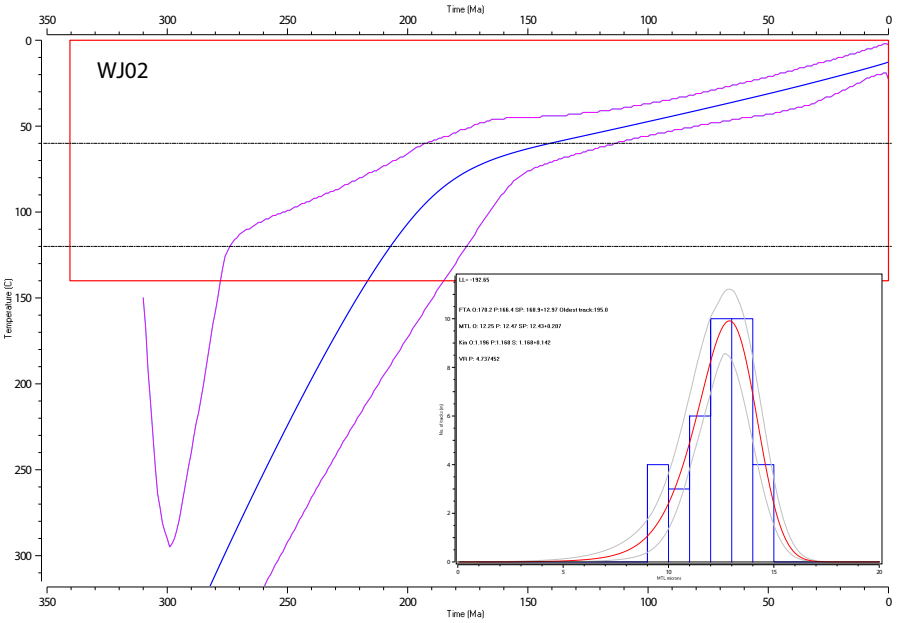

(a) WJ02 modelling report

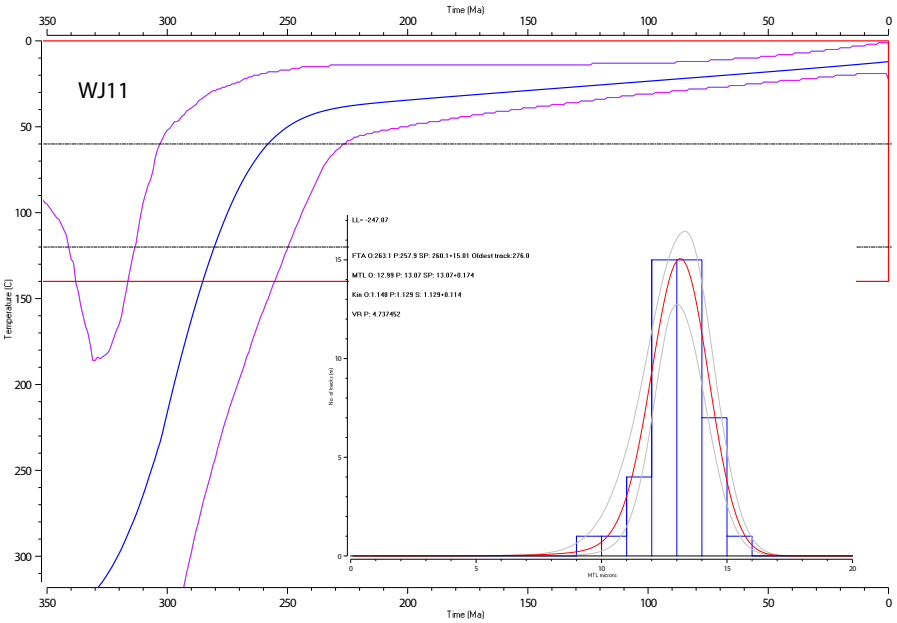

(b) WJ11 modelling report

Figure C.8: Thermal history modelling output from QTQt for models based on AFT data. Expected tT model is shown, blue line is expected model, pink envelope is 95% CI. Inset is observed vs predicted summary table showing AFT age, MTL, kinetic parameter (Dpar). O = observed, P = predicted, SP = sampled values of the predicted value. For further reading about the interpretation and meaning of the outputs see Gallagher (2012).

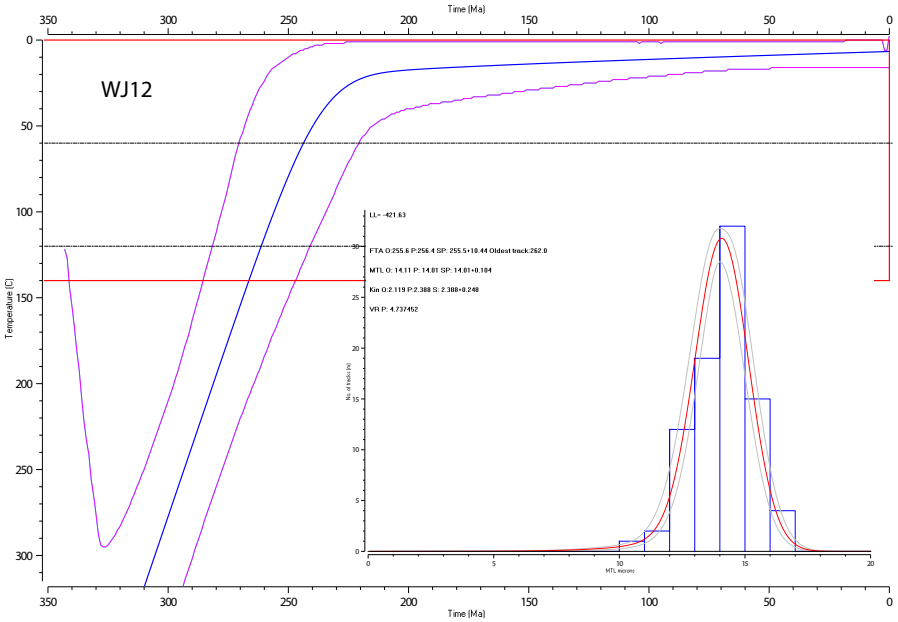

(c) WJ12 modelling report

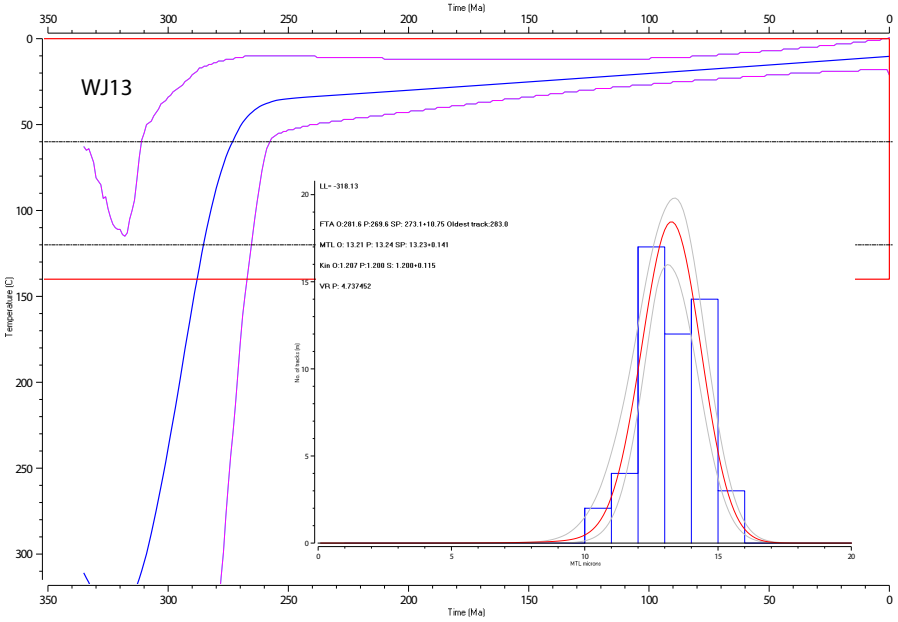

(d) WJ13 modelling report

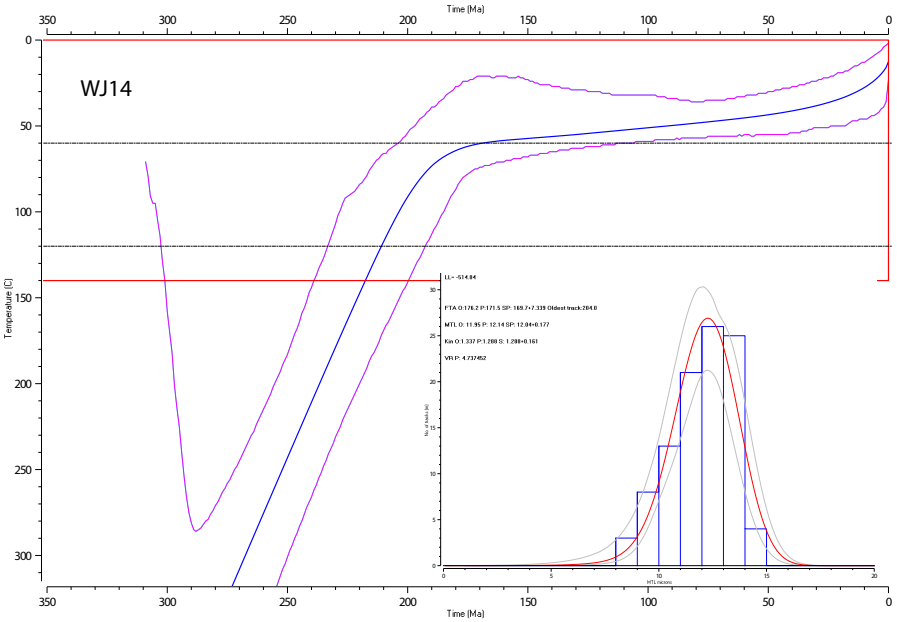

(e) WJ14 modelling report

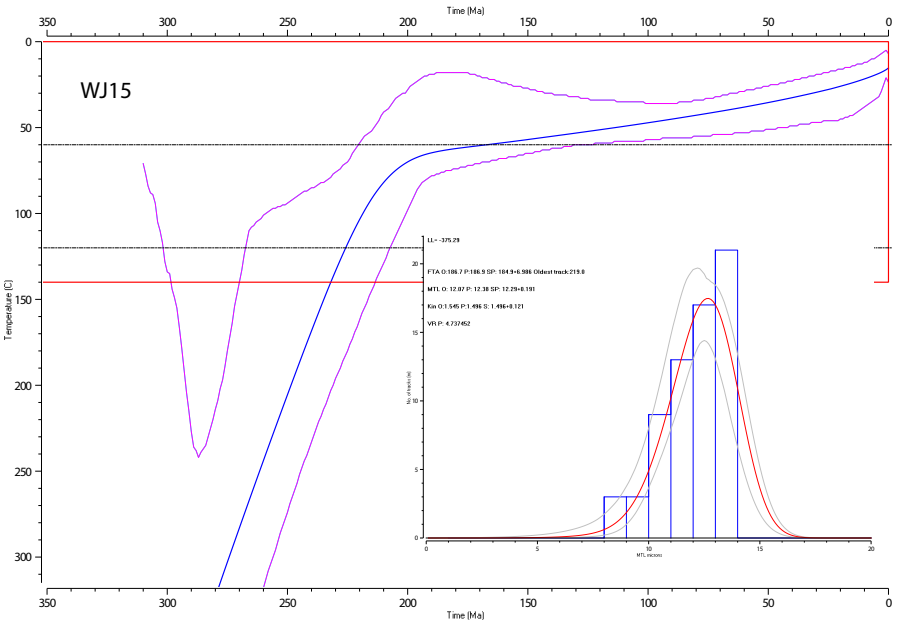

(f) WJ15 modelling report

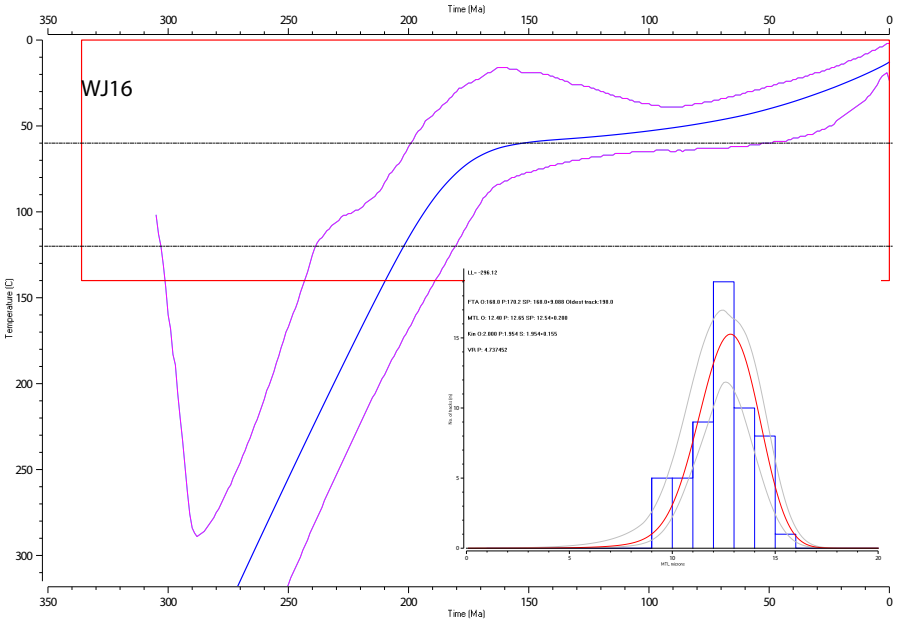

(g) WJ16 modelling report

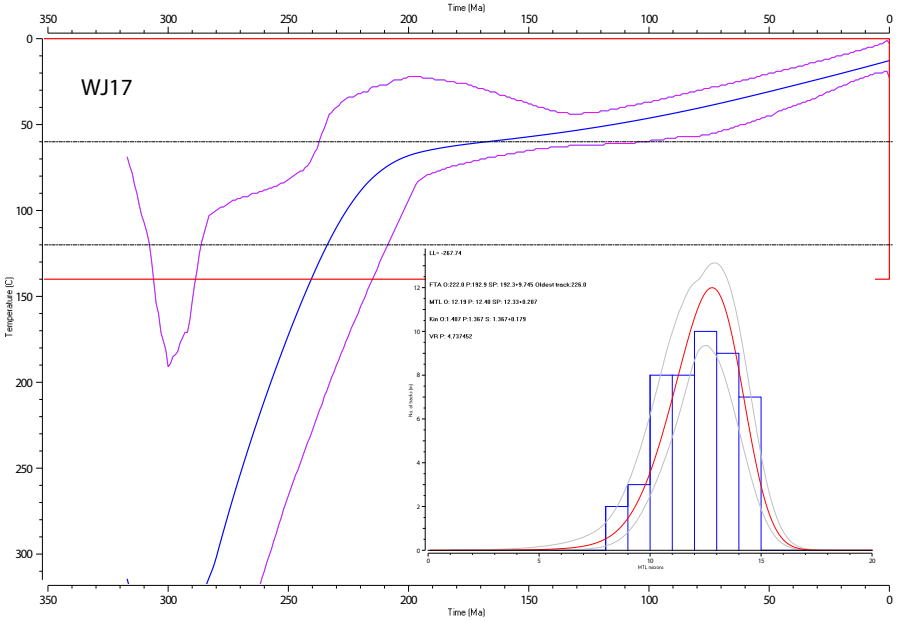

(h) WJ17 modelling report

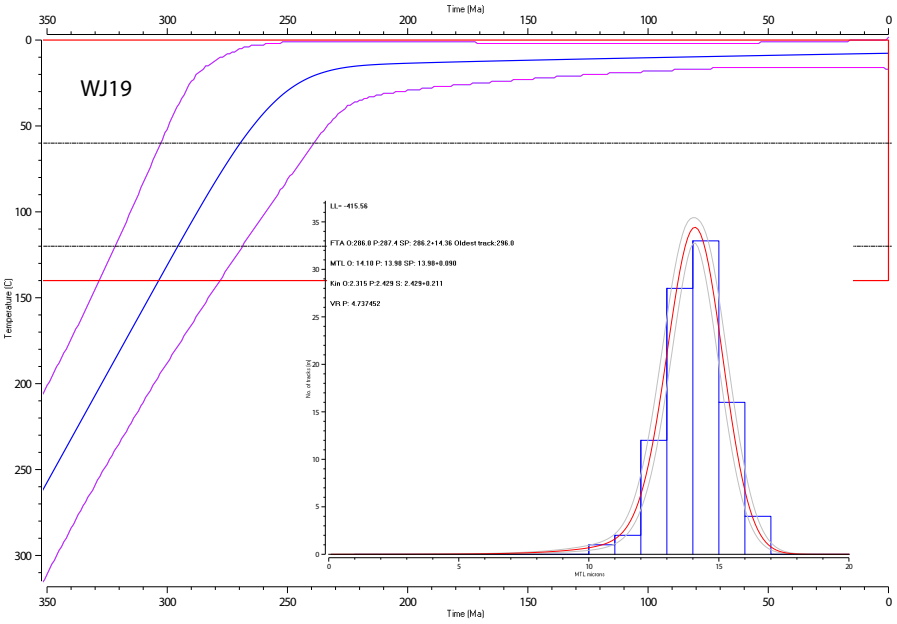

(i) WJ19 modelling report

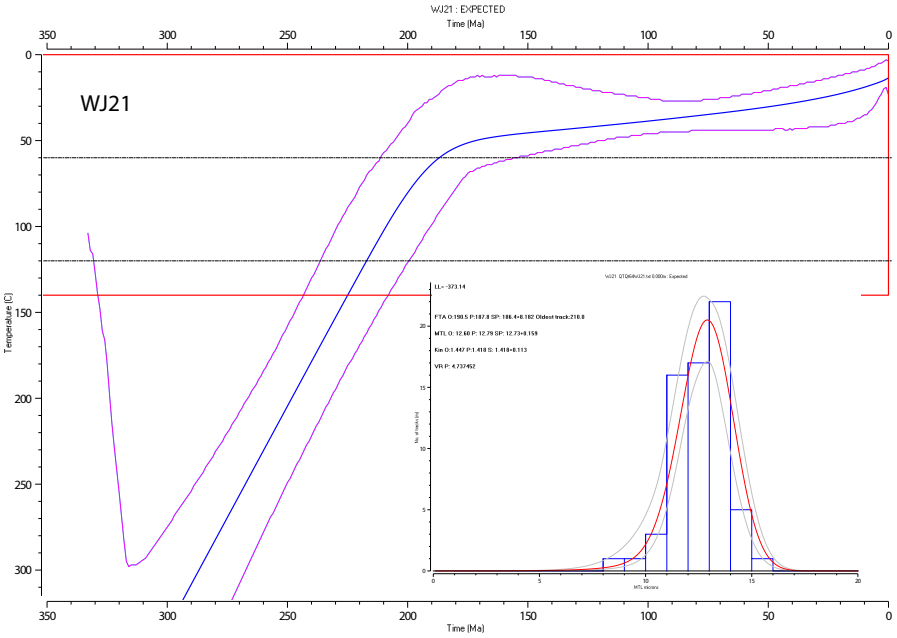

(j) WJ21 modelling report

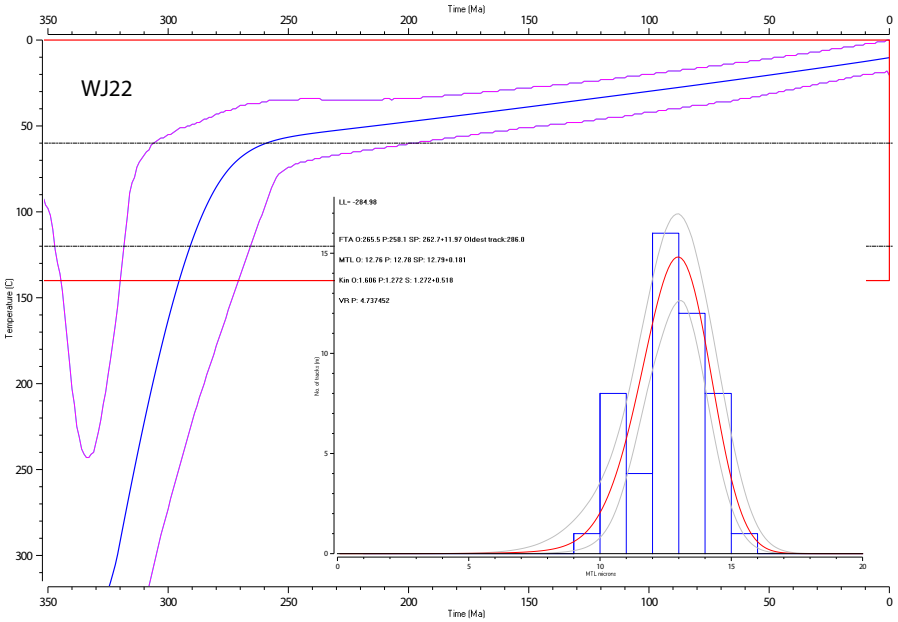

(k) WJ22 modelling report

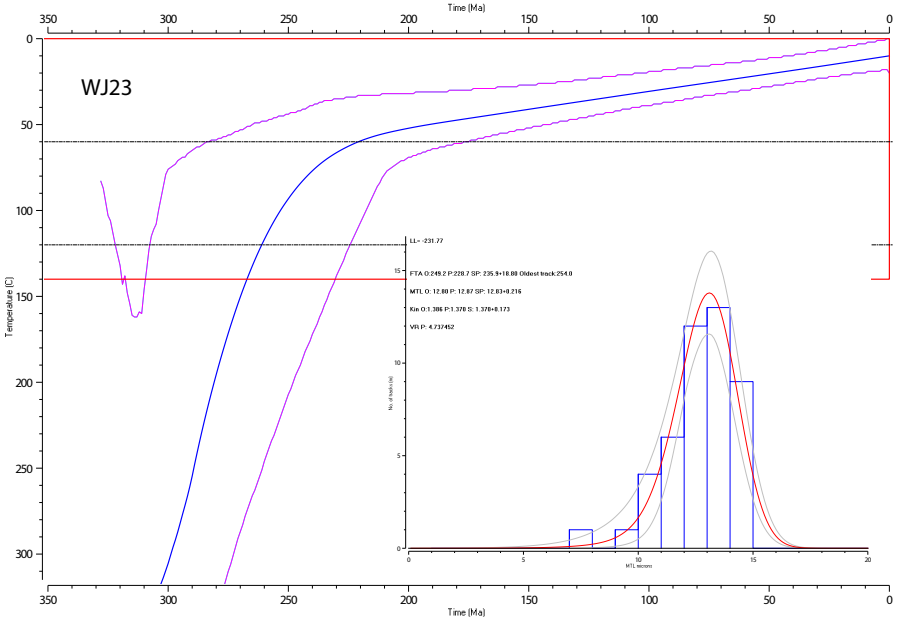

(l) WJ23 modelling report

Appendix D

Late Paleozoic exhumation of the West Junggar Mountains, NW China: Appendix Part 2

The supporting information presented here consists of the tabulated individual grain/confined track length/analytical spot data for this chapter.

D.1 Apatite fission track individual grain data

Table D.1: Apatite fission track individual grain data

Sample	Grain number	^{238}U (ppm)	2σ	N_s	Area (cm^2)	ρ_s (tracks/cm^2)	D_{par} (μm)	Age (Ma)	1σ (Ma)
WJ01_0	1	2.06	0.15	4	2.56E-05	156400	1.18	158.7	80.7
WJ01_1	2	4.46	0.23	13	1.65E-05	790100	0.98	370.3	106.7
WJ01_2	3	13.8	1	19	1.70E-05	1117000	1.03	169.2	41.9
WJ01_3	4	17.8	1.8	28	2.11E-05	1325000	0.61	155.6	34.5
WJ01_4	5	5.4	0.32	7	1.61E-05	434800	1.21	168.3	65.1
WJ01_6	7	145.4	6.5	147	1.27E-05	11560000	1.14	166.2	18.3
WJ01_8	9	5.71	0.27	13	1.61E-05	806500	1.69	295.2	84.8
WJ01_9	10	3.47	0.22	19	6.22E-05	305300	1.4	183.9	45
WJ01_9	10	3.47	0.22	16	2.62E-05	610000	1.4	367.5	97.2
WJ01_11	11	6.03	0.31	21	2.86E-05	734900	1.23	254.7	59
WJ01_13	13	8.47	0.77	12	1.58E-05	757900	1.07	187	57.6
WJ01_14	14	3.42	0.2	3	1.04E-05	289500	1.02	176.9	103.2
WJ01_16	16	7.72	0.37	19	2.44E-05	779400	0.99	211	50.9
WJ01_17	17	3.52	0.19	9	1.72E-05	523700	0.85	311	106.5
WJ01_18	18	6.19	0.62	9	1.13E-05	799500	1.13	270	95.3

Continued on next page

Continued from previous page

Sample	Grain number	^{238}U (ppm)	2σ	N_s	Area (cm^2)	ρ_s (tracks/cm^2)	D_{par} (μm)	Age (Ma)	1σ (Ma)
WJ01_19	19	4.18	0.18	8	1.76E-05	454900	0.99	227.5	82.1
WJ01_20	20	175.8	8.1	135	9.46E-06	14260000	1.27	169.5	19.3
WJ01_21	21	4.35	0.24	16	4.12E-05	388000	1.11	186.4	48.9
WJ01_22	22	2.71	0.21	3	1.18E-05	254900	1	196.6	115.1
WJ01_23	23	1.55	0.12	4	2.12E-05	188800	1.05	254.6	129.7
WJ01_24	24	3.38	0.37	6	1.06E-05	567200	1.1	350.8	149.6
WJ01_25	25	4.12	0.27	11	1.51E-05	727400	1.48	369	115.9
WJ02_0	1	15.76	0.97	17	1.07E-05	1592000	0.92	211.1	54.2
WJ02_1	2	4.19	0.18	7	2.11E-05	331100	0.89	165.1	63.5
WJ02_2	3	15.31	0.84	19	1.76E-05	1079000	1.05	147.3	35.8
WJ02_3	4	11.23	0.75	7	9.72E-06	720000	1.07	134	52
WJ02_4	5	3.14	0.24	9	1.96E-05	459900	0.97	306.1	106.2
WJ02_5	6	3.84	0.18	11	2.91E-05	377700	1.08	205.6	63.8
WJ02_6	7	21.9	1.7	20	1.39E-05	1437000	0.97	137.1	33.4
WJ02_7	8	7.6	1.2	11	1.17E-05	941800	0.99	259	89.4
WJ02_8	9	14.6	0.59	16	1.81E-05	886000	0.9	126.8	32.9
WJ02_9	10	6.48	0.53	10	1.53E-05	653300	0.93	210.7	69.9
WJ02_10	11	3.85	0.21	9	2.10E-05	429200	1.13	233	79.8
WJ02_11	12	12.58	0.85	21	1.98E-05	1062000	1.08	176.4	41.6
WJ02_12	13	2.88	0.12	3	1.65E-05	182200	1.12	132.2	76.9
WJ02_13	14	3.02	0.17	7	1.58E-05	444200	0.86	307.4	118.8
WJ02_14	15	4.02	0.35	4	9.82E-06	407400	1.11	211.8	108.2
WJ02_15	16	7.01	0.48	5	1.10E-05	455800	1.21	135.9	62
WJ02_18	19	19.9	1.8	8	7.71E-06	1038000	1.18	109	40.3
WJ04_0	1	7.41	0.31	28	3.69E-05	758000	0.92	213.8	43.2
WJ04_1	2	1.94	0.12	11	3.87E-05	284600	1.3	306.6	96
WJ04_2	3	5.72	0.34	20	4.05E-05	493700	1.19	180.4	43
WJ04_3	4	1.99	0.097	11	3.66E-05	300200	0.75	315.3	98
WJ04_4	5	1.95	0.13	9	4.71E-05	190900	0.87	204.6	70.5
WJ04_5	6	1.68	0.13	7	3.53E-05	198600	1.07	247.1	96.4
WJ04_6	7	1.74	0.13	7	2.57E-05	272000	1.09	326.8	127.3
WJ04_7	8	1.58	0.11	2	2.04E-05	98210	0.99	129.9	92.6
WJ04_8	9	2.79	0.21	8	5.71E-05	140100	1.49	104.9	38.4
WJ04_9	10	3.42	0.15	23	6.65E-05	345900	1.14	211.4	46.7
WJ04_13	14	1.85	0.13	2	2.26E-05	88620	1.09	100.1	71.4
WJ04_14	15	1.61	0.11	1	2.40E-05	41680	0.94	54.1	54.3
WJ05_0	1	5.97	0.44	28	3.48E-05	804600	1.55	281.7	59.4
WJ05_1	2	10.97	0.56	42	3.32E-05	1266000	1.53	241.2	41.6
WJ05_2	3	5.75	0.27	62	5.24E-05	1184000	1.64	430.4	63.5
WJ05_3	4	8.22	0.44	34	3.35E-05	1014000	1.28	257.8	48.7
WJ05_4	5	8.74	0.78	15	1.04E-05	1448000	1.71	346.3	96.7

Continued on next page

Continued from previous page

Sample	Grain number	^{238}U (ppm)	2σ	N_s	Area (cm^2)	ρ_s (tracks/cm^2)	D_{par} (μm)	Age (Ma)	1σ (Ma)
WJ05_5	6	6.97	0.31	43	3.81E-05	1128000	1.72	338.3	57.2
WJ05_7	8	6.81	0.5	28	3.82E-05	733700	1.52	225.2	47.5
WJ05_8	9	6.61	0.35	18	2.44E-05	738300	1.46	233.5	58
WJ05_9	10	5.64	0.35	45	4.32E-05	1042000	2	386.2	66.3
WJ05_10	11	8.08	0.47	28	2.31E-05	1210000	1.62	313	64.5
WJ05_11	12	11.49	0.58	30	2.37E-05	1265000	1.21	230.1	45.6
WJ05_12	13	8.53	0.43	76	6.40E-05	1187000	1.79	290.9	40.2
WJ05_13	14	7.84	0.33	35	2.80E-05	1252000	1.22	333.8	61.3
WJ05_14	15	8.25	0.85	33	2.19E-05	1506000	1.7	381.6	80.3
WJ05_15	16	7.55	0.49	18	1.68E-05	1074000	1.55	297.3	74.7
WJ05_17	18	2.53	0.11	15	2.74E-05	547500	1.26	452.4	121.3
WJ05_18	19	7.87	0.45	19	1.65E-05	1149000	1.75	305.2	74.3
WJ05_19	20	7.82	0.37	25	2.07E-05	1208000	1.62	322.9	69
WJ05_20	21	8.53	0.47	29	2.60E-05	1114000	1.53	273	55.2
WJ05_21	22	9.6	0.44	57	3.82E-05	1494000	0.96	325.3	49.4
WJ05_22	23	7.3	0.4	28	2.75E-05	1019000	1.46	291.8	59.9
WJ05_23	24	6.73	0.44	38	3.76E-05	1011000	1.63	314	57.9
WJ05_24	25	10.1	0.73	28	2.40E-05	1167000	1.74	241.5	50.8
WJ05_25	26	5.03	0.29	24	2.45E-05	980100	1.82	407.3	89.6
WJ05_26	27	15.8	1.1	30	1.61E-05	1859000	1.5	245.9	50.1
WJ06_0	1	4.12	0.26	28	4.61E-05	608000	2.1	308.5	64
WJ06_1	2	2.38	0.16	9	3.05E-05	295400	1.72	259.4	89.5
WJ06_2	3	4.54	0.22	18	2.11E-05	855000	1.74	393.7	97.5
WJ06_3	4	3.24	0.17	13	4.34E-05	299400	2.28	193.1	55.6
WJ06_4	5	4.88	0.26	25	3.24E-05	771800	1.42	330.6	71.1
WJ06_5	6	4.28	0.25	17	3.75E-05	453500	2.2	221.5	56.7
WJ06_6	7	2.99	0.18	7	1.79E-05	390800	1.83	273.2	105.7
WJ06_7	8	6.24	0.35	16	2.51E-05	636300	1.46	213.1	56
WJ06_8	9	3.15	0.22	13	2.96E-05	439400	2.1	291.6	85.1
WJ06_9	10	2.77	0.18	7	3.12E-05	224100	1.89	169.1	65.6
WJ06_10	11	4.01	0.26	12	1.52E-05	789000	2.14	411.3	124
WJ06_11	12	3.21	0.16	10	2.24E-05	445800	1.9	290.3	94.4
WJ06_13	14	4.72	0.26	23	3.10E-05	742400	2.06	328.8	73.4
WJ06_15	16	15.31	0.6	20	1.23E-05	1632000	2.18	222.8	52.2
WJ06_16	17	7	0.36	35	2.54E-05	1377000	2.11	411.2	76.5
WJ06_17	18	4.17	0.26	20	3.37E-05	594200	2.15	297.8	71.3
WJ06_18	19	5.1	0.35	15	2.26E-05	665300	2	272.7	74.5
WJ06_19	20	4.52	0.24	15	2.57E-05	584100	1.88	270.1	72.9
WJ06_21	22	2.61	0.15	20	4.36E-05	458900	1.79	367.5	87.5
WJ06_22	23	5.46	0.4	18	1.87E-05	963700	1.78	368.9	93.6
WJ06_23	24	3.65	0.21	13	3.34E-05	389100	1.94	222.8	64.4
WJ06_24	25	7.7	0.6	36	2.52E-05	1430000	1.76	388.2	74.9
WJ06_25	26	3.98	0.29	12	2.52E-05	476000	2.06	250	75.8

Continued on next page

Continued from previous page

Sample	Grain number	^{238}U (ppm)	2σ	N_s	Area (cm^2)	ρ_s (tracks/cm^2)	D_{par} (μm)	Age (Ma)	1σ (Ma)
WJ06_26	27	3.1	0.28	12	2.28E-05	526700	1.92	355.1	109.4
WJ06_27	28	4.12	0.19	25	3.16E-05	792000	1.72	401.8	85.7
WJ07_0	1	15.8	1.1	26	1.46E-05	1787000	1.07	236.4	51.1
WJ07_1	2	4.85	0.24	12	1.70E-05	707200	1.08	304.8	91
WJ07_2	3	2.07	0.13	3	2.11E-05	142100	0.93	143.5	83.7
WJ07_3	4	7.47	0.57	23	3.48E-05	660400	1.14	184.8	42.4
WJ07_4	5	5	0.38	12	2.96E-05	406100	1.08	169.7	51.6
WJ07_5	6	5.06	0.23	9	1.68E-05	537400	0.99	222	75.8
WJ07_6	7	5.38	0.39	13	2.75E-05	473600	1.18	184	53.8
WJ07_7	8	4.32	0.26	24	4.81E-05	498500	0.97	241.2	53.2
WJ07_8	9	2.86	0.16	5	2.38E-05	210100	0.88	153.5	69.7
WJ07_9	10	3.99	0.22	8	1.97E-05	406600	1.09	213	77.2
WJ07_10	11	2.95	0.31	7	2.56E-05	273700	1.03	193.9	76.9
WJ07_11	12	6.09	0.42	7	1.41E-05	495900	1.05	170.2	66.1
WJ07_12	13	1.93	0.19	11	3.82E-05	287700	1.03	311.6	100.5
WJ07_13	14	2.81	0.2	12	3.24E-05	370800	0.93	275.8	83.5
WJ07_14	15	5.45	0.32	13	2.28E-05	571200	1.54	219.1	63.4
WJ07_15	16	2.94	0.26	4	2.13E-05	187800	0.9	133.5	68.2
WJ07_16	17	3.41	0.39	17	4.30E-05	394900	1.05	242.1	66.4
WJ07_17	18	4.46	0.34	12	2.17E-05	553000	1.55	259.2	78.8
WJ07_18	19	5.13	0.4	17	3.14E-05	542300	1.28	220.9	57.7
WJ07_19	20	3.47	0.24	12	2.62E-05	457500	1.08	275.6	83.3
WJ07_21	22	4.67	0.21	22	2.80E-05	787000	1.04	352.3	79.4
WJ07_23	24	3.11	0.25	5	2.68E-05	186800	1.16	125.5	57.5
WJ07_24	25	4.65	0.3	15	2.98E-05	502900	0.94	226	61.6
WJ07_26	28	4.66	0.44	10	2.23E-05	447700	0.95	200.8	67.3
WJ07_27	29	4.16	0.49	7	1.17E-05	597100	0.92	300	120
WJ07_28	30	4.88	0.25	18	2.69E-05	668800	1.16	286.5	71.1
WJ07_29	31	2.99	0.16	8	2.60E-05	307200	0.98	214.7	77.8
WJ07_30	32	11.05	0.42	19	1.36E-05	1402000	1.17	265.2	63.6
WJ07_31	33	9.86	0.44	15	1.47E-05	1019000	0.92	216	58
WJ07_33	35	2.42	0.16	6	2.16E-05	277600	1.22	239.8	100.1
WJ07_34	36	4.67	0.48	10	1.21E-05	829800	1.24	371.4	125.4
WJ07_35	37	5.5	0.44	10	1.78E-05	562000	1.18	213.6	70.7
WJ07_36	38	3.07	0.21	7	1.77E-05	396600	0.86	270	104.9
WJ07_37	39	3.04	0.34	7	1.40E-05	501000	1	344.5	137.2
WJ07_38	40	3.37	0.27	8	1.91E-05	417900	1.3	259.2	95.2
WJ08_0	1	5.54	0.29	29	3.35E-05	866000	1.22	326.7	65.8
WJ08_1	2	1.44	0.13	7	2.86E-05	244700	1.15	355.2	139.6
WJ08_2	3	1.81	0.12	13	3.07E-05	423900	0.84	489.6	142.5
WJ08_3	4	2.62	0.12	8	3.61E-05	221700	1.2	176.8	63.9
WJ08_4	5	4.45	0.23	19	2.98E-05	637600	1	299.5	72.5

Continued on next page

Continued from previous page

Sample	Grain number	^{238}U (ppm)	2σ	N_s	Area (cm^2)	ρ_s (tracks/cm^2)	D_{par} (μm)	Age (Ma)	1σ (Ma)
WJ08_5	6	3.61	0.2	16	2.98E-05	537500	1.14	311.2	81.7
WJ08_6	7	4.95	0.25	21	2.92E-05	720500	1.38	304.2	70.4
WJ08_7	8	4.4	0.32	18	2.47E-05	729600	1.35	346.6	87.8
WJ08_8	9	3.2	0.16	15	2.55E-05	587500	1.19	383.8	103.4
WJ08_9	10	6.47	0.36	16	2.77E-05	577600	1.4	186.6	49
WJ08_10	11	2.67	0.21	6	2.29E-05	261800	1.4	204.9	86
WJ08_11	12	1.97	0.11	2	1.11E-05	181100	0.99	192.1	136.7
WJ08_12	13	2.34	0.15	5	1.71E-05	292200	1.33	261	118.9
WJ08_13	14	2.61	0.14	6	2.56E-05	234300	1.18	187.6	78
WJ08_14	15	2.95	0.15	7	1.69E-05	413400	1.18	292.9	113
WJ08_15	16	2.17	0.16	7	2.28E-05	306800	1.05	295.5	115.1
WJ08_16	17	3.39	0.2	5	1.62E-05	308700	0.89	190.3	86.5
WJ08_17	18	1.47	0.15	12	4.45E-05	269400	1.23	383.1	119.4
WJ08_18	19	1.099	0.073	4	1.82E-05	219800	1.54	418.1	212.3
WJ08_19	21	2.82	0.22	6	1.33E-05	452900	1.2	335.7	140.9
WJ08_20	22	1.53	0.1	4	1.54E-05	259700	1.23	354.8	180.1
WJ08_21	24	2.87	0.5	7	1.73E-05	404500	1.2	294.6	123.8
WJ08_22	25	2.19	0.13	4	1.28E-05	312000	1.19	297.8	150.9
WJ08_23	26	2.21	0.14	4	1.51E-05	265100	1.49	250.7	127.2
WJ08_24	27	2.96	0.15	10	2.29E-05	436500	1.3	308.2	100.3
WJ08_25	28	2.94	0.15	8	2.05E-05	390200	1.28	277.4	100.4
WJ08_26	29	2.54	0.19	12	3.06E-05	392100	1.57	322.7	98
WJ08_27	30	2.25	0.15	10	2.54E-05	393500	1.16	365.6	120
WJ08_28	31	4.1	0.28	15	2.02E-05	744500	0.97	379.6	103.7
WJ08_29	32	4.49	0.31	14	2.67E-05	524300	1.21	244.1	68.8
WJ08_30	33	5.11	0.34	8	1.62E-05	494200	1.03	202.1	73.6
WJ08_31	34	3.99	0.21	9	2.26E-05	397500	1.04	208.2	71.3
WJ08_32	35	2.38	0.14	5	1.78E-05	281300	1.22	247	112.3
WJ08_33	36	3.2	0.21	9	3.01E-05	299100	1.13	195.4	67.3
WJ08_34	37	2.27	0.26	9	2.28E-05	394900	1.46	363.6	129.9
WJ08_35	38	3.36	0.26	11	1.88E-05	584300	0.91	363.5	115.1
WJ09_0	1	2.37	0.15	6	1.62E-05	370200	1.53	326.5	136.2
WJ09_1	2	3.7	0.21	4	1.23E-05	325300	1.45	183.7	93.1
WJ09_3	4	2.67	0.17	18	3.87E-05	465600	1.58	364.5	91.5
WJ09_4	5	1.84	0.13	6	2.88E-05	208400	1.03	236.7	99
WJ09_5	6	3.1	0.17	11	2.10E-05	523500	0.96	353	110.1
WJ09_6	7	3.5	0.24	12	3.73E-05	322200	0.96	192.4	58.2
WJ09_7	8	4.99	0.89	8	1.63E-05	492400	1.17	206.2	82.5
WJ09_8	9	4.38	0.26	9	2.04E-05	440500	1.41	210.2	72.2
WJ09_9	10	1.131	0.057	8	4.98E-05	160700	1.38	297	107.5
WJ09_10	11	2.13	0.15	13	4.01E-05	324500	1.33	318.4	93
WJ09_11	12	3.48	0.16	9	2.08E-05	433800	0.98	260.5	89
WJ09_14	15	3.81	0.22	25	3.46E-05	721900	1.25	396.1	85.6

Continued on next page

Continued from previous page

Sample	Grain number	^{238}U (ppm)	2σ	N_s	Area (cm^2)	ρ_s (tracks/cm^2)	D_{par} (μm)	Age (Ma)	1σ (Ma)
WJ09_14	15	3.81	0.22	13	3.69E-05	352600	1.25	193.4	55.9
WJ09_15	16	3.49	0.15	13	3.36E-05	387100	1	231.8	66.4
WJ09_16	17	3.92	0.2	25	3.42E-05	730000	1.31	389.3	83.5
WJ09_17	18	3.45	0.23	3	2.20E-05	136300	1.04	82.5	48.2
WJ09_18	19	3.06	0.15	8	2.52E-05	318100	1.27	217.3	78.6
WJ09_19	20	3.97	0.22	8	2.03E-05	394700	1.44	207.8	75.3
WJ09_20	21	2.38	0.14	8	1.72E-05	464700	1.43	408.1	148.2
WJ09_21	22	1.69	0.12	5	1.32E-05	379200	1.3	469	214.1
WJ09_22	23	3.59	0.17	4	1.33E-05	301700	1.16	175.6	88.8
WJ09_23	24	2.35	0.13	3	3.20E-05	93850	1.25	83.4	48.6
WJ09_24	25	2.03	0.1	9	2.78E-05	324200	1.14	333.8	114.1
WJ09_25	26	2.82	0.16	7	1.16E-05	601200	1.29	445.6	172.3
WJ09_26	27	4.84	0.3	5	1.14E-05	439000	1.37	189.6	86.3
WJ09_27	28	3.82	0.5	10	2.28E-05	438000	1.59	239.7	83.2
WJ09_30	31	1.57	0.1	4	1.41E-05	283900	1.54	378	191.8
WJ10_0	1	3.55	0.18	8	1.56E-05	512400	0.93	301.7	109.2
WJ10_1	2	3.99	0.24	3	1.29E-05	231900	1.22	121.5	70.8
WJ10_2	3	2.39	0.25	6	1.87E-05	320100	1.07	279.9	119.1
WJ10_3	4	3.39	0.41	5	1.20E-05	417300	1.05	257.3	120.1
WJ10_4	5	3.6	0.31	4	1.24E-05	322600	0.94	187.3	95.6
WJ10_5	6	5.56	0.36	6	1.21E-05	497500	1.18	187	78
WJ10_6	7	2.65	0.16	5	1.53E-05	326900	1.2	257.8	117.3
WJ10_7	8	2.11	0.14	8	2.58E-05	310700	1.11	307.8	112.1
WJ10_8	9	3.28	0.2	2	7.40E-06	270200	1.3	172.2	122.6
WJ10_9	10	2.48	0.13	1	8.62E-06	116000	1.17	97.7	98
WJ10_10	11	3.75	0.3	4	1.17E-05	342300	1.34	190.8	97.2
WJ11_0	1	2.55	0.2	8	1.52E-05	524800	0.79	430.2	157.8
WJ11_1	2	3.62	0.19	15	2.24E-05	668600	1.04	386.1	104.2
WJ11_2	3	3.04	0.22	11	2.04E-05	539200	1.05	370.7	117
WJ11_3	4	4.74	0.36	17	2.27E-05	750000	0.95	330.7	86.2
WJ11_4	5	4.12	0.18	8	2.24E-05	356700	0.82	180.9	65.3
WJ11_6	7	2.29	0.2	8	3.44E-05	232700	0.74	212.4	78.3
WJ11_8	9	4.38	0.23	14	2.67E-05	524100	0.81	250.1	69.6
WJ11_9	10	2.86	0.17	5	1.39E-05	360000	1.12	263.1	119.7
WJ11_10	11	3.8	0.22	9	1.54E-05	582900	1.01	320.6	110.1
WJ11_11	13	4.47	0.31	8	1.98E-05	404100	1.18	188.9	68.9
WJ11_12	14	2.12	0.17	4	1.96E-05	204100	1.18	201.2	102.5
WJ11_13	15	4.25	0.24	8	2.07E-05	387100	1.26	190.4	69
WJ11_14	16	2.47	0.29	6	1.02E-05	588000	1.18	497.6	213.4
WJ11_15	17	3.3	0.18	17	3.76E-05	451700	1.06	286.1	73
WJ11_16	18	5.34	0.29	14	2.98E-05	470600	0.76	184.2	51.3
WJ11_17	19	6.96	0.43	31	3.48E-05	890900	0.96	267.5	53.1

Continued on next page

Continued from previous page

Sample	Grain number	^{238}U (ppm)	2σ	N_s	Area (cm^2)	ρ_s (tracks/cm^2)	D_{par} (μm)	Age (Ma)	1σ (Ma)
WJ11_18	20	2.64	0.16	7	1.59E-05	441100	1.03	349.2	135.2
WJ11_19	21	2.61	0.18	14	2.80E-05	500900	0.95	401.2	113.2
WJ11_20	22	2.21	0.12	5	1.85E-05	269700	0.98	255.1	115.9
WJ11_21	23	3.25	0.21	8	3.04E-05	262900	1.18	169.1	61.5
WJ11_22	24	2.79	0.24	5	2.18E-05	229000	1.01	171.5	78.7
WJ11_23	25	3.31	0.17	13	2.39E-05	544200	1.04	343.7	99
WJ11_24	26	3.67	0.2	7	1.42E-05	493100	1.13	280.8	108.5
WJ11_25	27	3.65	0.32	6	2.11E-05	284100	1.08	162.7	68.6
WJ11_26	28	7.43	0.59	17	1.09E-05	1567000	1.04	440.9	115.4
WJ11_27	29	2.56	0.14	2	8.79E-06	227500	1.05	185.7	132.2
WJ11_28	30	3.19	0.21	5	1.80E-05	278000	1.17	182.1	83
WJ11_29	31	3.06	0.15	10	2.57E-05	389900	1	266.3	86.6
WJ11_30	32	3.61	0.19	8	1.72E-05	464300	1.14	268.8	97.3
WJ11_31	33	4.35	0.34	10	1.58E-05	633600	1.03	304.5	100.7
WJ11_32	34	2.44	0.14	1	7.86E-06	127200	1.05	108.9	109.3
WJ11_33	35	3.58	0.22	3	1.23E-05	244000	1.2	142.4	83.1
WJ11_34	36	2.92	0.21	4	1.59E-05	251400	0.93	179.9	91.5
WJ12_0	1	10.82	0.61	42	3.36E-05	1251000	2.81	241.7	42.1
WJ12_1	2	3.09	0.19	18	3.77E-05	477300	2.17	322.9	80.9
WJ12_2	3	14.08	0.65	29	1.93E-05	1499000	2.25	222.5	44.5
WJ12_3	4	6.68	0.34	42	5.91E-05	711000	2.02	222.5	38.4
WJ12_4	5	8.17	0.4	39	3.20E-05	1217000	1.53	311.4	55.2
WJ12_5	6	1.37	0.11	4	2.85E-05	140400	1.15	214.2	109.2
WJ12_6	7	13.51	0.7	46	2.25E-05	2046000	2.52	316.6	52.8
WJ12_7	8	5.81	0.32	9	1.51E-05	596300	3.09	214.5	73.5
WJ12_8	9	3.73	0.19	8	1.83E-05	437300	2.2	245	88.7
WJ12_9	10	4.67	0.25	22	3.92E-05	561000	2.33	251.1	57.1
WJ12_10	11	17.24	0.79	22	1.27E-05	1735000	1.83	210.3	47.5
WJ12_11	12	6.77	0.26	25	2.26E-05	1108000	2.44	342.1	72.5
WJ12_12	13	4.32	0.2	13	2.36E-05	550700	2.11	266.4	76.5
WJ12_13	14	7.02	0.33	20	1.94E-05	1032000	2.38	307.3	72.4
WJ12_14	15	4.56	0.29	8	1.55E-05	517800	2.22	237.3	86.4
WJ12_15	16	5.21	0.32	12	1.89E-05	636200	1.98	255.2	76.8
WJ12_16	17	6.3	0.36	15	2.22E-05	675900	2.25	224.2	60.7
WJ12_17	18	6.98	0.41	11	2.10E-05	523800	1.38	156.8	49
WJ12_18	19	3.11	0.2	13	4.98E-05	260800	1.62	175.3	50.9
WJ12_19	20	3.4	0.21	9	2.06E-05	436000	2.11	268	92.2
WJ12_20	21	3.71	0.23	8	2.53E-05	315800	2.64	177.9	64.7
WJ12_22	23	3.94	0.2	16	1.92E-05	831500	2.24	441.1	115.4
WJ12_23	24	2.07	0.11	6	2.60E-05	231200	2.02	233.4	97
WJ12_24	25	5.39	0.26	8	2.30E-05	348200	2.27	135	48.8
WJ12_25	26	11.69	0.54	35	1.75E-05	1999000	2.47	357.4	66
WJ12_26	27	10.27	0.56	25	1.84E-05	1360000	2.22	276.8	59.6

Continued on next page

Continued from previous page

Sample	Grain number	^{238}U (ppm)	2σ	N_s	Area (cm^2)	ρ_s (tracks/cm^2)	D_{par} (μm)	Age (Ma)	1σ (Ma)
WJ12_27	28	19.6	1.2	20	1.06E-05	1885000	2.18	201	48
WJ12_28	29	7.47	0.42	4	1.09E-05	366900	2.41	102.6	52
WJ12_29	30	5.84	0.28	13	2.30E-05	565900	2.67	202.5	58.2
WJ12_30	31	5.07	0.36	21	2.36E-05	891900	2.22	367.7	87.1
WJ12_31	32	4.3	0.53	6	1.10E-05	545200	2.1	265	114
WJ12_32	33	20.6	1.2	61	2.07E-05	2949000	2.75	299.2	45.6
WJ13_0	1	4.56	0.36	21	4.25E-05	494200	1.2	226.5	54.2
WJ13_1	2	4.58	0.36	19	2.21E-05	860900	0.94	392.9	98
WJ13_2	3	2.52	0.15	17	3.71E-05	457900	1.06	379.8	97.4
WJ13_3	4	5.4	0.42	12	2.32E-05	517000	1.19	200.1	60.9
WJ13_4	5	4.63	0.31	12	1.74E-05	688400	0.85	310.8	93.8
WJ13_5	6	4.63	0.26	11	2.96E-05	372200	1.27	168	52.4
WJ13_6	7	2.99	0.2	15	3.44E-05	435500	1.1	304.4	83.1
WJ13_7	8	3.17	0.25	12	3.76E-05	319000	0.82	210.3	64.1
WJ13_8	9	3.94	0.24	15	4.80E-05	312800	1.13	165.9	45
WJ13_9	10	4.12	0.24	34	6.76E-05	502900	1.3	255.1	48.5
WJ13_10	11	2.93	0.16	13	3.16E-05	412000	1.31	293.9	84.8
WJ13_11	12	3.1	0.14	18	4.34E-05	415100	1.37	279.9	69.1
WJ13_12	13	3.73	0.23	27	3.87E-05	697400	1.2	390.8	82.2
WJ13_13	14	8.67	0.42	16	2.34E-05	683700	0.9	164.8	43
WJ13_14	15	3.55	0.23	19	3.29E-05	578100	1.24	340.4	83.5
WJ13_15	16	3.31	0.18	6	2.10E-05	285600	1.19	180.3	75
WJ13_16	17	2.33	0.13	17	3.38E-05	503200	1.07	451.4	115.4
WJ13_17	18	3.77	0.23	14	3.29E-05	425700	1.07	236	66.1
WJ13_18	19	2.66	0.12	11	3.71E-05	296800	1.08	233.2	72.4
WJ13_19	20	2.16	0.12	12	2.75E-05	437000	1.09	422.9	126.7
WJ13_20	21	3.04	0.27	3	1.81E-05	166100	1.17	114.2	67
WJ13_21	22	4.11	0.17	10	1.85E-05	541700	1.09	275.5	89.3
WJ13_22	23	4.34	0.24	12	1.89E-05	634200	1.23	305.4	91.5
WJ13_23	24	3.19	0.18	9	1.43E-05	629300	1.18	412.4	141.5
WJ13_24	25	2.98	0.13	7	2.62E-05	266900	0.93	187.2	72
WJ13_25	26	4.07	0.24	7	1.49E-05	470700	0.97	241.7	93.5
WJ13_26	27	3.83	0.2	13	1.74E-05	746600	1.18	407.5	117.4
WJ13_27	28	4.31	0.36	26	3.27E-05	795300	1.27	385.7	85.2
WJ13_28	29	3.5	0.25	11	2.48E-05	443600	1.11	264.9	83.5
WJ13_29	30	3.64	0.35	14	3.24E-05	432500	1.17	248.3	72
WJ13_30	31	3.67	0.25	23	4.07E-05	564500	1.4	321.5	73
WJ13_31	32	5.63	0.38	21	1.95E-05	1076000	1.14	399.5	94.2
WJ13_32	33	3.65	0.34	14	2.64E-05	529600	1.06	303.3	87.6
WJ13_33	34	2.98	0.2	8	2.14E-05	374700	1.2	262.8	95.8
WJ13_34	35	2.7	0.15	25	3.74E-05	667900	1.13	517.1	111.5
WJ13_35	36	4.77	0.26	11	1.84E-05	597200	1.22	261.7	81.6
WJ13_36	37	3.42	0.18	8	1.27E-05	629000	1.03	384.4	139.2

Continued on next page

Continued from previous page

Sample	Grain number	^{238}U (ppm)	2σ	N_s	Area (cm^2)	ρ_s (tracks/cm^2)	D_{par} (μm)	Age (Ma)	1σ (Ma)
WJ13_37	38	3.53	0.21	18	4.15E-05	434100	1.11	257	64.2
WJ13_38	39	3.66	0.21	9	2.34E-05	385200	0.94	220	75.5
WJ13_39	40	7.69	0.35	16	2.23E-05	717300	1.08	195	50.8
WJ14_0	1	7.46	0.57	7	1.34E-05	523200	1.19	147	57.7
WJ14_1	2	4.79	0.3	17	6.96E-05	244100	1.1	106.8	27.9
WJ14_2	3	12.4	1.9	9	1.18E-05	766300	1.37	129.5	48.5
WJ14_3	4	96.7	7.9	57	8.14E-06	7007000	1.35	151.9	26.3
WJ14_4	5	10.59	0.7	21	1.44E-05	1460000	1.48	289	69.4
WJ14_5	6	15.7	1.9	28	2.70E-05	1038000	1.2	138.6	32.8
WJ14_6	7	16.9	1.1	26	1.53E-05	1697000	1.18	210.5	46.3
WJ14_7	8	6.05	0.59	15	2.01E-05	746000	1.28	258.5	74
WJ14_8	9	12.4	2	13	1.94E-05	669000	1.56	113.1	37.2
WJ14_11	12	4.42	0.37	7	1.91E-05	366400	1.14	173.8	68.5
WJ14_12	13	8.06	0.64	13	1.08E-05	1209000	1.43	314.4	93.8
WJ14_13	15	11.9	1.1	17	8.39E-06	2027000	1.4	357.1	96.5
WJ14_14	16	13.8	1.1	10	1.21E-05	828300	1.31	125.8	42.1
WJ14_15	17	4.6	0.38	6	1.04E-05	576900	0.96	262.9	111.3
WJ14_16	18	10.47	0.72	17	1.31E-05	1302000	1.39	260.7	68.6
WJ14_17	19	16.3	1.4	18	1.31E-05	1373000	1.36	176.6	46.2
WJ14_18	20	5.59	0.31	12	1.83E-05	657500	1.3	246.6	74.8
WJ14_19	21	47.2	2.9	22	9.37E-06	2349000	1.28	104.3	24.4
WJ14_20	22	12.8	1	9	1.28E-05	703800	1.47	115.2	40.4
WJ14_22	24	10.9	1.2	14	1.46E-05	958400	1.37	184.3	55
WJ14_23	25	51.6	2.6	48	1.29E-05	3729000	1.41	151.5	25.8
WJ14_24	26	8.18	0.54	20	2.64E-05	757500	1.22	194.1	47.6
WJ14_25	27	5.55	0.47	7	1.90E-05	367800	1.74	138.9	54.8
WJ14_26	28	8.54	0.51	15	1.88E-05	798300	1.26	195.9	54
WJ14_27	29	14.41	0.66	16	1.23E-05	1301000	1.31	189.2	50.2
WJ14_28	30	8.68	0.63	13	1.31E-05	991400	1.33	239.4	71
WJ14_29	31	4.24	0.28	6	2.01E-05	297900	1.11	147.3	61.9
WJ14_30	32	10.83	0.43	12	1.55E-05	774800	0.98	149.9	45.1
WJ14_31	33	6.21	0.85	13	1.75E-05	741000	1.01	250.1	79.6
WJ14_32	34	8.92	0.46	10	1.50E-05	668600	1.09	157.1	51.7
WJ14_33	35	19.3	1.9	23	1.70E-05	1353000	1.48	146.9	35.6
WJ14_34	36	7.16	0.37	15	1.65E-05	910200	1.47	266.5	73
WJ14_35	37	6.36	0.48	14	2.12E-05	661400	1.08	218	62.7
WJ14_36	38	11.92	0.89	18	1.55E-05	1162000	1.4	204.3	52.8
WJ14_37	39	4.98	0.28	11	2.19E-05	501500	1.27	211.1	66.7
WJ14_38	40	50.8	4.1	29	8.90E-06	3258000	1.19	134.4	29
WJ15_0	1	25.3	1.3	23	1.32E-05	1745000	1.65	144.6	32.9
WJ15_1	2	10.53	0.56	15	1.78E-05	841900	1.64	167.6	45.9
WJ15_2	3	9.75	0.8	15	1.80E-05	833700	1.48	179.2	50.4

Continued on next page

Continued from previous page

Sample	Grain number	^{238}U (ppm)	2σ	N_s	Area (cm^2)	ρ_s (tracks/cm^2)	D_{par} (μm)	Age (Ma)	1σ (Ma)
WJ15_3	4	11.75	0.54	23	1.74E-05	1321000	1.51	235.7	53.4
WJ15_4	5	38.4	2.1	53	1.35E-05	3915000	1.84	213.7	35.5
WJ15_5	6	37.7	2.2	38	1.28E-05	2965000	1.52	164.8	31
WJ15_6	7	13.36	0.85	22	2.01E-05	1097000	1.69	172.1	40.4
WJ15_7	8	21.2	1.1	33	1.90E-05	1735000	1.4	171.5	33.7
WJ15_8	9	12.76	0.68	18	2.05E-05	876800	1.77	144	36.4
WJ15_9	10	3.84	0.25	6	2.38E-05	252300	1.52	137.7	57.8
WJ15_10	11	22.2	1.7	31	1.35E-05	2303000	1.59	217.5	45.5
WJ15_11	12	7.51	0.31	13	2.13E-05	610500	1.49	170.4	49.5
WJ15_12	13	15.9	1.2	27	2.37E-05	1140000	1.33	150.3	33.1
WJ15_13	14	14.6	0.8	40	1.63E-05	2460000	1.3	353.2	64.9
WJ15_14	15	9.8	0.88	16	1.21E-05	1325000	1.45	283.4	78.3
WJ15_15	16	22	1.4	22	1.30E-05	1696000	1.78	161.6	37.9
WJ15_16	18	20.22	0.98	19	1.25E-05	1518000	1.41	157.4	38.7
WJ15_17	19	19.2	1.1	20	1.27E-05	1580000	1.58	172.5	41.9
WJ15_18	20	39.2	5.5	37	1.03E-05	3609000	1.69	193	44.2
WJ15_19	21	5.69	0.38	12	2.55E-05	470600	1.43	173.4	53
WJ15_20	22	29.1	3.8	22	1.20E-05	1832000	1.54	131.9	34.4
WJ15_21	23	25.4	1.9	27	1.12E-05	2419000	1.64	199.6	43.9
WJ15_22	24	21.6	1.7	11	1.25E-05	882100	1.67	85.6	27.4
WJ15_23	25	25.5	2.4	31	1.54E-05	2014000	1.48	165.5	35.8
WJ15_24	26	17.7	1.1	20	1.54E-05	1301000	1.5	154.1	37.6
WJ15_25	27	20.3	1.4	21	6.00E-06	3502000	1.69	361.6	87.2
WJ15_26	28	34.4	3	29	1.07E-05	2713000	1.4	165.3	36.1
WJ15_27	29	19	1.3	27	1.31E-05	2067000	1.62	228	49.6
WJ15_28	30	31.6	2.3	37	1.05E-05	3540000	1.63	234.8	45.8
WJ15_29	31	8.35	0.39	25	2.02E-05	1235000	1.5	310	67.8
WJ15_30	33	9.9	1.1	13	1.75E-05	743300	1.4	157.4	48.5
WJ15_31	34	52.7	4.6	46	1.20E-05	3830000	1.73	152.3	28.5
WJ15_32	35	18.2	0.98	26	1.20E-05	2165000	1.66	249.4	54.1
WJ16_0	1	13.01	0.86	15	1.45E-05	1037000	0.79	166.6	45.4
WJ16_1	2	17.12	0.78	26	2.26E-05	1150000	0.78	140.4	29.4
WJ16_2	3	17.32	0.79	18	1.08E-05	1675000	0.56	202.1	49.9
WJ16_3	4	16.6	1.2	17	8.56E-06	1987000	0.75	250.2	65
WJ16_5	7	13.05	0.8	16	1.13E-05	1420000	0.96	227.4	60
WJ16_7	10	34.5	3	27	1.23E-05	2200000	0.81	133.3	29.2
WJ16_8	11	24.1	1.7	21	1.23E-05	1711000	0.85	148.4	35.1
WJ16_12	15	20.6	1.2	15	1.03E-05	1464000	0.71	148.5	40.2
WJ16_14	17	20.2	1.2	16	1.11E-05	1437000	0.76	148.7	39.1
WJ16_15	18	19.1	1	16	8.64E-06	1851000	0.76	202.5	53
WJ16_16	19	16.6	1.8	15	1.48E-05	1016000	0.82	127.9	36.6
WJ16_17	20	17.8	2.3	15	9.50E-06	1580000	1.09	185.5	54.6
WJ16_18	21	21.2	1.2	19	1.24E-05	1533000	0.56	151.1	36.8

Continued on next page

Continued from previous page

Sample	Grain number	^{238}U (ppm)	2σ	N_s	Area (cm^2)	ρ_s (tracks/cm^2)	D_{par} (μm)	Age (Ma)	1σ (Ma)
WJ16_19	22	19.5	1.2	12	5.85E-06	2051000	0.55	219.8	66.1
WJ16_20	23	13.32	0.64	11	8.52E-06	1291000	0.71	202.6	62.9
WJ16_21	24	17.8	1.2	11	8.39E-06	1311000	0.87	153.9	48.4
WJ16_22	25	13.45	0.63	6	5.63E-06	1067000	0.75	165.8	68.8
WJ16_23	26	24.9	2.2	11	5.67E-06	1940000	0.84	162.8	52
WJ16_24	27	18.3	2.3	17	1.04E-05	1630000	1.06	186.2	52
WJ16_26	29	24.6	1.4	13	6.36E-06	2045000	0.9	173.7	50.2
WJ16_30	33	16.84	0.97	14	1.38E-05	1014000	0.94	125.8	35.1
WJ16_31	34	14.2	1.1	22	1.53E-05	1442000	0.68	212.2	49.7
WJ16_32	36	22.5	1.3	23	1.22E-05	1881000	1.13	174.7	39.1
WJ16_33	37	15.44	0.69	12	7.43E-06	1615000	1.04	218.6	65.1
WJ17_0	1	3.94	0.22	16	2.21E-05	725200	1.03	384.7	101.1
WJ17_1	2	2.77	0.14	7	2.63E-05	266600	0.78	201.2	77.6
WJ17_2	3	4.46	0.27	20	6.26E-05	319600	1.05	149.8	35.7
WJ17_3	4	5.34	0.3	26	2.52E-05	1031000	1.34	403.6	85.6
WJ17_4	5	12.59	0.65	25	1.42E-05	1764000	1.21	292.9	62.8
WJ17_5	6	2.42	0.13	6	2.43E-05	247400	1.16	213.7	88.8
WJ17_6	7	4.71	0.23	4	1.31E-05	304300	1.61	135	68.3
WJ17_7	8	5.23	0.26	14	1.64E-05	853500	0.87	341.1	94.8
WJ17_8	9	3.42	0.2	13	3.70E-05	351600	1.09	214.9	62.2
WJ17_9	10	2.98	0.19	19	4.16E-05	456400	0.93	320.1	78.5
WJ17_13	14	20.7	1.3	21	1.24E-05	1691000	1.09	170.7	40
WJ17_15	16	5.71	0.35	13	2.18E-05	595600	1.55	218	63.2
WJ17_16	17	23.7	1.3	23	1.60E-05	1435000	1.33	126.5	28.2
WJ17_17	18	5.17	0.33	19	2.35E-05	807100	1.39	326.3	80
WJ17_18	19	3.94	0.29	6	1.31E-05	457400	1.42	242.6	101.6
WJ17_19	20	4.05	0.27	8	1.70E-05	470400	1.01	242.8	88.5
WJ17_20	21	111.9	4.2	68	9.64E-06	7057000	1.49	131.8	18.4
WJ17_21	22	3.24	0.26	4	1.63E-05	245900	1.47	158.6	80.8
WJ17_22	23	75.5	4.2	70	1.02E-05	6880000	1.39	190.5	27.4
WJ17_23	24	5.84	0.37	13	2.84E-05	458400	1.04	164	47.6
WJ18_1	2	3.97	0.16	8	1.48E-05	542400	0.83	285.6	103
WJ18_2	3	4.13	0.22	14	4.49E-05	312000	1.23	157.9	44
WJ18_6	7	4.25	0.33	14	2.12E-05	661600	0.94	325.4	92.5
WJ18_7	8	2.78	0.16	7	1.62E-05	432100	1.04	324.9	125.6
WJ18_8	9	6.21	0.62	6	1.26E-05	474900	1.12	159.8	67.8
WJ18_9	10	8.41	0.36	14	1.48E-05	943300	1.02	234.4	64.9
WJ18_10	11	20.9	1.4	23	1.25E-05	1835000	1.04	183.5	41.6
WJ18_11	12	15.51	0.74	40	1.64E-05	2437000	1.15	328.4	57.5
WJ18_12	13	5.36	0.44	17	1.48E-05	1150000	0.94	448.5	117.8
WJ18_13	14	3.45	0.17	11	1.56E-05	706400	1.17	428	133.1
WJ18_19	20	4.78	0.26	9	1.17E-05	768800	1.34	336.2	115.2

Continued on next page

Continued from previous page

Sample	Grain number	^{238}U (ppm)	2σ	N_s	Area (cm^2)	ρ_s (tracks/cm^2)	D_{par} (μm)	Age (Ma)	1σ (Ma)
WJ18_21	22	4.95	0.3	4	9.35E-06	427800	0.89	180.6	91.6
WJ18_23	24	4.01	0.26	11	3.86E-05	284700	1.2	148.4	46.5
WJ18_24	25	7.65	0.33	19	1.84E-05	1032000	1.18	282	67.8
WJ18_26	27	4.46	0.36	13	2.52E-05	515300	1.06	241.5	71.1
WJ18_28	29	20.38	0.95	34	1.50E-05	2268000	1.25	232.6	43.5
WJ18_29	30	3.95	0.24	15	2.29E-05	654700	1.13	346.5	94.1
WJ18_30	31	3.31	0.2	7	1.57E-05	444900	1.17	280.9	108.8
WJ18_31	32	2.18	0.12	6	1.85E-05	323700	1.23	310.4	129.1
WJ18_32	33	3.63	0.2	10	1.75E-05	570600	1.03	328.6	107.2
WJ18_33	34	16.48	0.55	24	1.94E-05	1237000	1.02	156.9	33.7
WJ19_0	1	8.3	0.44	29	1.97E-05	1472000	2.63	371.8	77.1
WJ19_1	2	11.22	0.68	11	1.30E-05	845500	3.11	157.9	50
WJ19_2	3	24.1	1.3	47	1.35E-05	3473000	2.13	302.1	52.2
WJ19_4	5	5.94	0.35	18	1.80E-05	1001000	2.47	353.3	89.9
WJ19_5	6	7.48	0.43	20	2.02E-05	990600	2.5	277.6	67.4
WJ19_6	7	10.29	0.89	27	1.97E-05	1370000	1.86	279.1	62.5
WJ19_7	8	6.58	0.48	28	2.52E-05	1111000	2.65	354	76.5
WJ19_8	9	7.73	0.48	9	1.17E-05	769300	2.77	208.6	72.4
WJ19_9	10	15.85	0.91	36	1.63E-05	2213000	2.51	292.7	56.1
WJ19_10	11	6.81	0.58	12	1.68E-05	716600	2.54	220.6	68.4
WJ19_11	12	7.89	0.45	24	2.30E-05	1045000	2.65	277.6	62.5
WJ19_12	13	5.57	0.37	18	1.85E-05	970900	2.34	365.4	93.6
WJ19_13	14	23.2	1.2	28	9.71E-06	2884000	2.49	260.6	54.7
WJ19_14	15	32.6	2.5	53	1.59E-05	3342000	2.69	214.9	37.5
WJ19_15	16	11.52	0.82	28	1.67E-05	1678000	2.85	305.3	65.8
WJ19_16	17	9.32	0.62	24	1.51E-05	1593000	2.47	358.3	81.5
WJ19_17	18	11.93	0.82	30	1.44E-05	2080000	3.12	365.5	76.5
WJ21_0	1	6.37	0.28	15	2.25E-05	667100	1.31	219.5	59.8
WJ21_1	2	6.79	0.55	10	1.48E-05	676400	1.52	208.8	69.9
WJ21_2	3	9.72	0.64	14	1.80E-05	777300	1.49	167.6	47.8
WJ21_3	4	18.2	1.1	27	9.97E-06	2708000	1.46	311.9	67.2
WJ21_4	5	10.61	0.88	10	1.37E-05	728200	1.55	143.8	48.2
WJ21_5	6	11.07	0.88	8	1.12E-05	716600	1.44	135.7	50.2
WJ21_6	7	9.95	0.67	12	1.35E-05	887500	1.41	187	57.2
WJ21_7	8	25.3	1.6	18	9.44E-06	1906000	1.65	157.9	40.3
WJ21_8	9	8.17	0.61	15	1.12E-05	1337000	2.08	343.1	95.8
WJ21_9	10	8.42	0.6	7	1.34E-05	524300	1.51	130.5	51.1
WJ21_10	11	49.8	3	26	1.09E-05	2383000	1.53	100.3	21.9
WJ21_11	12	16.7	1	19	1.44E-05	1317000	1.29	165.3	41.1
WJ21_12	13	10.1	0.69	15	1.69E-05	885300	1.58	183.7	51
WJ21_14	15	9.27	0.56	10	1.33E-05	753900	1.48	170.5	56.3
WJ21_15	16	8.39	0.47	8	1.64E-05	487100	1.43	121.7	44.5

Continued on next page

Continued from previous page

Sample	Grain number	^{238}U (ppm)	2σ	N_s	Area (cm^2)	ρ_s (tracks/cm^2)	D_{par} (μm)	Age (Ma)	1σ (Ma)
WJ21_16	17	13	1.9	36	1.45E-05	2480000	1.56	399.9	93.7
WJ21_17	18	6.32	0.33	6	1.07E-05	559100	1.4	185.4	77.6
WJ21_18	19	8.15	0.62	12	1.38E-05	867700	1.59	223.2	68.7
WJ21_19	20	27.9	2.4	12	8.54E-06	1405000	1.39	105.5	32.7
WJ21_20	21	8.45	0.54	12	1.19E-05	1007000	1.35	249.8	76.2
WJ21_21	22	9.27	0.68	14	1.23E-05	1137000	1.27	257.1	73.8
WJ21_22	23	6.75	0.53	18	1.91E-05	942000	1.55	292.5	76
WJ21_23	24	9.36	0.69	10	1.18E-05	850100	1.61	190.4	63.4
WJ21_24	25	9.01	0.56	8	1.50E-05	532200	1.67	123.8	45.4
WJ21_25	26	20.5	1.1	24	1.32E-05	1820000	1.37	186.1	41.7
WJ21_26	27	10.21	0.6	10	1.20E-05	837000	1.54	171.8	56.8
WJ21_27	28	9.06	0.53	16	1.56E-05	1023000	1.5	236.7	63.3
WJ21_28	29	27.4	1.6	22	1.16E-05	1900000	1.51	145.3	33.9
WJ21_29	30	22.5	1.1	19	9.17E-06	2073000	1.39	193.1	47.6
WJ21_30	31	8.6	0.51	11	1.78E-05	619200	1.54	150.9	47.7
WJ21_31	32	9.36	0.66	15	1.69E-05	889300	1.32	199.2	55.4
WJ21_32	33	10.41	0.67	17	1.79E-05	948500	1.72	191	50
WJ21_33	34	37.3	5.1	30	9.01E-06	3329000	1.59	187.1	44.9
WJ21_34	35	5.52	0.44	8	1.48E-05	541900	1.22	205.8	76.2
WJ21_35	36	19.1	2.1	21	1.02E-05	2068000	1.44	227	58
WJ21_36	37	9.3	0.8	11	1.05E-05	1044000	1.29	235.3	75.9
WJ21_37	38	9.85	0.83	15	1.69E-05	890300	1.45	189.5	53.4
WJ21_38	39	8.54	0.64	15	2.20E-05	681100	1.58	167.2	46.7
WJ21_39	40	24.6	1.6	24	1.06E-05	2276000	1.41	193.9	44
WJ22_0	1	8.04	0.73	19	1.55E-05	1225000	1.47	319.4	82.4
WJ22_1	2	15.6	0.96	24	1.33E-05	1804000	1.98	242.4	54.8
WJ22_2	3	7.26	0.54	14	1.18E-05	1187000	1.78	342.7	98.5
WJ22_3	4	19.4	1.5	22	1.49E-05	1478000	1.3	159.7	38.1
WJ22_4	5	13.3	0.79	21	1.32E-05	1593000	1.8	251.1	59.9
WJ22_5	6	7.58	0.42	12	9.48E-06	1266000	1.62	350.1	106.3
WJ22_6	7	42.9	2.4	34	8.01E-06	4246000	1.82	207.5	40.6
WJ22_7	8	16.2	1.3	22	1.07E-05	2050000	1.64	265.3	63.7
WJ22_8	9	11.49	0.94	25	1.12E-05	2231000	1.69	407	93.2
WJ22_9	10	5.99	0.41	16	1.80E-05	891500	1.67	312	84.2
WJ22_10	11	11.12	0.84	15	1.12E-05	1338000	1.57	252.2	70.5
WJ22_11	12	9.08	0.49	21	2.24E-05	936900	1.59	216.3	51.3
WJ22_12	13	9.19	0.49	17	1.31E-05	1302000	1.32	297	77.1
WJ22_13	14	9.34	0.88	12	1.02E-05	1177000	1.68	264.2	82.6
WJ22_14	15	8.28	0.79	15	1.23E-05	1223000	1.43	309.6	88.4
WJ22_15	16	12.36	0.93	19	1.08E-05	1765000	1.55	299.3	75.7
WJ22_16	17	6.95	0.44	13	2.01E-05	648200	1.41	195.5	57.5
WJ22_17	18	13.63	0.77	25	1.60E-05	1564000	1.59	240.5	53.2
WJ22_18	19	9.95	0.57	7	1.02E-05	686200	1.76	144.5	56.3

Continued on next page

Continued from previous page

Sample	Grain number	^{238}U (ppm)	2σ	N_s	Area (cm^2)	ρ_s (tracks/cm^2)	D_{par} (μm)	Age (Ma)	1σ (Ma)
WJ22_19	20	6.38	0.39	10	1.49E-05	670000	1.64	220.1	72.8
WJ22_20	21	10.7	1.1	16	1.42E-05	1129000	1.81	221.2	62.1
WJ22_21	22	15.26	0.73	21	9.81E-06	2140000	1.42	294	69.3
WJ22_22	23	6.5	0.39	15	1.56E-05	961500	1.68	310.1	85.5
WJ22_23	24	10.37	0.63	19	9.87E-06	1925000	1.61	389.1	96.9
WJ22_24	25	7.05	0.46	14	1.34E-05	1044000	1.86	310.4	88.6
WJ22_25	26	8.06	0.78	8	1.14E-05	701100	1.56	182.3	68.2
WJ22_26	27	9.92	0.6	17	1.12E-05	1520000	1.44	321.2	83.9
WJ22_27	28	3.97	0.28	15	1.81E-05	827900	1.37	437.2	121.6
WJ22_28	29	11.08	0.76	11	7.92E-06	1390000	1.24	263	83.7
WJ22_29	30	7.06	0.43	7	1.33E-05	527600	2.05	156.6	61.1
WJ23_0	1	2.94	0.18	4	1.28E-05	312000	1.52	222.4	113.3
WJ23_1	2	1.94	0.32	5	3.69E-05	135600	1.6	146.5	70.7
WJ23_2	3	2.6	0.17	5	2.11E-05	236600	1.1	190.7	87.4
WJ23_3	4	2.91	0.29	9	2.33E-05	386200	1.06	278.2	99
WJ23_4	5	1.289	0.092	4	2.98E-05	134300	1.23	218.4	111.5
WJ23_5	6	2.56	0.14	4	1.54E-05	259900	1.36	212.8	108.2
WJ23_6	7	1.81	0.15	5	1.88E-05	265300	1.11	307.3	141.7
WJ23_8	9	1.29	0.11	4	2.12E-05	188700	1.72	306.6	157.2
WJ23_9	10	2.85	0.22	2	9.71E-06	206000	1.57	151.5	108.4
WJ23_10	11	3.31	0.18	4	1.30E-05	308600	0.84	195.4	99.4
WJ23_11	12	1.77	0.17	3	1.42E-05	211100	1.17	250	147.5
WJ23_12	13	2.64	0.19	5	1.31E-05	382200	1.85	303.5	139.4
WJ23_13	14	2.52	0.21	5	1.16E-05	431600	1.7	359	165.6
WJ23_14	15	2.26	0.16	2	8.92E-06	224300	1.16	208	148.7
WJ23_15	16	0.645	0.065	1	1.63E-05	61240	1.27	199	200.6
WJ23_16	17	8.75	0.95	8	1.08E-05	738900	1.51	177	66.8
WJ23_17	18	2.71	0.22	22	3.96E-05	555200	1.23	429.5	103.2
WJ23_18	19	2.29	0.2	7	1.70E-05	413000	1.31	378.1	149.4
WJ23_19	20	5.85	0.48	9	1.65E-05	544000	1.25	194.9	68.5
WJ23_20	21	2.37	0.2	7	2.35E-05	298200	1.26	263.8	104.1
WJ23_21	22	1.57	0.15	4	1.79E-05	224000	1.63	299.1	153.9
WJ23_22	23	2.69	0.14	3	1.32E-05	226700	1.69	176.6	103.3
WJ23_23	24	2.45	0.17	3	1.24E-05	242000	1.1	207	121.4
WJ23_24	25	4.11	0.32	6	1.27E-05	472000	1.05	240.7	101.7

D.2 Apatite confined track length measurements

Table D.2: Apatite confined track length measurements

Length no.	Confined track length (μm)	Angle to C Axis	Average Dpar (μm)
WJ-02 01	11.01	19.68	1.3
WJ-02 02	14.39	50.32	1
WJ-02 03(1)	12.08	40.23	1.1
WJ-02 03(2)	9.57	80.73	1.1
WJ-02 04	14.21	47.37	1.2
WJ-02 05	10.92	78.51	1
WJ-02 06(1)	13.99	57.84	1.2
WJ-02 06(2)	12.99	64.47	1.2
WJ-02 07	13.63	26.99	1
WJ-02 08(1)	13.12	73.1	1.3
WJ-02 08(2)	11.12	87.04	1.3
WJ-02 08(3)	9.95	59.63	1.3
WJ-02 08(4)	11.14	54.33	1.3
WJ-02 09(1)	13.27	79.44	1.5
WJ-02 09(2)	10.82	52.32	1.5
WJ-02 09(3)	13.53	54.19	1.5
WJ-02 09(4)	13.17	69.15	1.5
WJ-02 10	12.16	77.36	1.1
WJ-02 11	14.47	20.02	1.1
WJ-02 12(1)	12.05	72.1	1.3
WJ-02 12(2)	9.33	43.98	1.3
WJ-02 13	11.59	8.79	1.1
WJ-02 16(1)	13.65	46.17	1.3
WJ-02 16(2)	13.04	5.95	1.3
WJ-02 16(3)	11.87	22.34	1.3
WJ-02 19	9.12	46.93	1.4
WJ-02 20	12.1	87.16	1.2
WJ-02 21	12.36	30.99	1
WJ-02 22	10.2	67.79	1.5
WJ-02 23	13.32	52	1.2
WJ-02 25(1)	12.37	23.65	1.5
WJ-02 25(2)	14.05	19.91	1.5
WJ-02 25(3)	13.33	44.87	1.5
WJ-02 25(4)	12.11	53.16	1.5
WJ-02 26	12.67	81.49	1.2
WJ-02 27	11.9	65.6	1.2
WJ-02 29	12.73	58.82	1.3
WJ-06 01(1)	14.58	78.61	1.9

Continued on next page

Continued from previous page

Length no.	Confined track length (μm)	Angle to C Axis	Average Dpar (μm)
WJ-06 01(2)	13.98	34.39	1.9
WJ-06 01(3)	13.08	70.01	1.9
WJ-06 02(1)	14.83	51.63	2
WJ-06 02(2)	14.1	79.57	2
WJ-06 03(1)	13.67	36.57	1.8
WJ-06 04(1)	12.98	68.81	1.8
WJ-06 04(2)	13.68	52.31	1.8
WJ-06 04(3)	14.9	47.27	1.8
WJ-06 05	13.29	57.39	2.4
WJ-06 06(1)	13.81	19.99	2.2
WJ-06 06(2)	14.12	58.12	2.2
WJ-06 07	12.4	54.53	2.1
WJ-06 08	13.86	45.28	2.3
WJ-06 09(1)	14.3	43.64	1.9
WJ-06 09(2)	12.52	27.07	1.9
WJ-06 09(3)	12.35	67.97	1.9
WJ-06 10	13.84	86.15	2.2
WJ-06 12	15.19	11.25	2.1
WJ-06 13(1)	15.04	67.16	2.4
WJ-06 14(1)	14.89	62.36	1.9
WJ-06 14(2)	13	72.24	1.9
WJ-06 15(1)	14.95	41.24	2.2
WJ-06 15(2)	14.27	71.6	2.2
WJ-06 15(3)	13.25	87.78	2.2
WJ-06 15(4)	14.07	22.71	2.2
WJ-06 16(1)	13.53	83.08	2.1
WJ-06 16(2)	14.11	64.25	2.1
WJ-06 17(1)	14.44	82.36	2.4
WJ-06 18	14.82	33.48	1.7
WJ-06 19(1)	14.17	78.8	2.1
WJ-06 19(2)	15.86	46.89	2.1
WJ-06 01(4)	14.51	37.72	2.1
WJ-06 01(5)	15.9	25.8	2.1
WJ-06 02(3)	14.97	44.53	1.7
WJ-06 02(4)	14.85	42.99	1.7
WJ-06 03(2)	14.36	63.97	1.7
WJ-06 11	12.58	42.93	2.1
WJ-06 13(2)	13.3	78.68	1.9
WJ-06 14(3)	14.63	65.78	2.1
WJ-06 14(4)	15.07	26.86	2.1
WJ-06 15(5)	13.64	65.24	2.1
WJ-06 15(6)	14.11	43.49	2.1
WJ-06 15(7)	14.6	73.79	2.1

Continued on next page

Continued from previous page

Length no.	Confined track length (μm)	Angle to C Axis	Average Dpar (μm)
WJ-06 16(3)	15.69	78.04	2.2
WJ-06 16(4)	13.32	58.51	2.2
WJ-06 16(5)	12.74	83.35	2.2
WJ-06 16(6)	13.64	77.48	2.2
WJ-06 16(7)	13.54	66.21	2.2
WJ-06 16(8)	15.14	41.75	2.2
WJ-06 17(2)	12.18	20.94	2.1
WJ-06 19(3)	14.67	22.59	2
WJ-06 19(4)	13.01	46.83	2
WJ-06 19(5)	15.69	52.52	2
WJ-06 20(1)	12.48	62.27	1.9
WJ-06 20(2)	14.65	76.75	1.9
WJ-06 21	13.78	52.48	2
WJ-06 23	13.52	78.2	1.8
WJ-06 25(1)	11.06	38.8	1.8
WJ-06 25(2)	14.49	8.31	1.8
WJ-06 25(3)	13.33	22.01	1.8
WJ-06 25(4)	14.92	37.93	1.8
WJ-06 25(5)	13.85	66.99	1.8
WJ-06 26	13.42	67.12	2.1
WJ-07 01(1)	13.11	74.38	1.2
WJ-07 01(2)	13.78	43.7	1.2
WJ-07 02	10.85	61.82	1.2
WJ-07 05	15.76	34.91	1.2
WJ-07 07(1)	14.03	39.33	1.3
WJ-07 07(2)	9.04	40.14	1.3
WJ-07 09(1)	11.8	70.87	1.3
WJ-07 09(2)	13.05	74.75	1.3
WJ-07 10	14.05	26.7	1.3
WJ-07 11(1)	12.23	85.45	1.2
WJ-07 11(2)	14.85	45.6	1.2
WJ-07 11(3)	12.85	57.09	1.2
WJ-07 11(4)	12.1	18.89	1.2
WJ-07 12(1)	13.82	18.51	1.3
WJ-07 12(2)	12.99	42.68	1.3
WJ-07 13	12.09	80.86	1.1
WJ-07 14	11.93	68.69	1.2
WJ-07 15	12.81	71.05	1.2
WJ-07 17	11.41	5.33	1.2
WJ-07 18	13.81	37.33	1.2
WJ-07 19	11.42	68.51	1.3
WJ-07 20	14.07	33.36	1.1

Continued on next page

Continued from previous page

Length no.	Confined track length (μm)	Angle to C Axis	Average Dpar (μm)
WJ-07 21(1)	13.95	42.94	1.2
WJ-07 21(2)	13.67	50.83	1.2
WJ-07 22	14.04	53.24	1.1
WJ-07 23	11.27	68.86	1.3
WJ-07 24	12.89	35.69	1
WJ-07 25	12.45	79.53	1.1
WJ-07 26	12.93	18.44	1.3
WJ-07 27	12.07	51.38	1.4
WJ-07 28	10.68	73.11	1.2
WJ-07 29	11.86	69.18	1.3
WJ-07 30(1)	13.65	35.91	1.1
WJ-07 30(2)	11.82	36.38	1.1
WJ-11 01	9.57	75.1	1.1
WJ-11 02	13.14	53.04	1.1
WJ-11 05	11.2	67.95	1.1
WJ-11 06	12.6	74.26	1.1
WJ-11 08	12.8	68.18	1
WJ-11 09	14.28	28.77	1.3
WJ-11 10	11.57	86.61	1.3
WJ-11 11	12.08	56.3	1.3
WJ-11 12	14.26	20.7	1.3
WJ-11 13	13.42	37.07	1.2
WJ-11 14	13.69	75.15	1
WJ-11 15	10.99	40.65	1.4
WJ-11 16	13.74	47.03	1.1
WJ-11 17	12.98	56.83	1.4
WJ-11 18	13.95	46.71	1.2
WJ-11 19	13.28	76.31	1.2
WJ-11 20	12.64	64.96	1.1
WJ-11 23	13.89	64	1.2
WJ-11 25	14.37	60.39	1.4
WJ-11 26	13.42	76.91	1.1
WJ-11 28	13.21	39.89	1.2
WJ-11 29	14.89	74.8	1.3
WJ-11 30(1)	14.43	74.82	1.4
WJ-11 30(2)	12.85	65.85	1.4
WJ-11 31	12.45	21.37	1.4
WJ-11 32(1)	12.29	34.08	1.2
WJ-11 32(2)	13.16	86.26	1.2
WJ-11 32(3)	12.28	45.39	1.2
WJ-11 33(1)	11.24	33.88	1.3
WJ-11 33(2)	13.7	33.62	1.3

Continued on next page

Continued from previous page

Length no.	Confined track length (μm)	Angle to C Axis	Average Dpar (μm)
WJ-11 34	12.48	64.08	1.4
WJ-11 35	14.46	34.88	1.3
WJ-11 36	12.2	48.92	1.4
WJ-11 37	12.41	43.88	1.4
WJ-11 38(1)	12.37	52.74	1.3
WJ-11 38(2)	13.48	53.47	1.3
WJ-11 39	13.8	60.64	1.3
WJ-11 40	13.27	32.81	1.2
WJ-11 41	11.53	74.84	1.2
WJ-11 42	15.22	0	1.2
WJ-11 43	12.22	69.49	1.1
WJ-11 44(1)	13.33	72.57	1.2
WJ-11 44(2)	14.05	56.65	1.2
WJ-11 44(3)	12.74	83.75	1.2
WJ-12 01(1)	13.34	62.55	2.5
WJ-12 01(2)	14.1	13.51	2.5
WJ-12 01(3)	12.37	58.47	2.5
WJ-12 01(4)	14.14	73.6	2.5
WJ-12 01(5)	13.98	64.09	2.5
WJ-12 01(6)	14.95	57.3	2.5
WJ-12 01(7)	14.86	17.78	2.5
WJ-12 01(8)	12.44	75.16	2.5
WJ-12 01(9)	14.35	35.05	2.5
WJ-12 01(10)	14.62	29.64	2.5
WJ-12 01(11)	15.66	45.72	2.5
WJ-12 02(1)	14.52	70.32	2
WJ-12 02(2)	15.63	60.8	2
WJ-12 03	13.28	69.64	2.1
WJ-12 04(1)	14.82	67.41	2.4
WJ-12 05(1)	14.6	62.73	2.2
WJ-12 08(1)	14.56	26.11	2
WJ-12 08(2)	12	76.7	2
WJ-12 09(1)	15.68	17.19	2.1
WJ-12 09(2)	15.69	69.02	2.1
WJ-12 10(1)	10.85	44.41	2.2
WJ-12 11	14.6	23.17	2.2
WJ-12 12	15.2	57.6	1.8
WJ-12 13(1)	14.56	65.01	2.1
WJ-12 13(2)	13.27	81.32	2.1
WJ-12 14(1)	14.07	47.32	2.2
WJ-12 14(2)	14.03	82.44	2.2
WJ-12 14(3)	16.14	87.95	2.2

Continued on next page

Continued from previous page

Length no.	Confined track length (μm)	Angle to C Axis	Average Dpar (μm)
WJ-12 15	14.59	56.08	2
WJ-12 17	14.78	63.83	2.2
WJ-12 18	14.14	39.03	1.9
WJ-12 19	15.47	36.33	2
WJ-12 20	14.93	56.67	1.8
WJ-12 21	12.33	85.49	2.1
WJ-12 24	14.69	69.31	2.3
WJ-12 25(1)	15.99	43.16	2
WJ-12 25(2)	14.63	68.89	2
WJ-12 27	12.26	53.28	2.1
WJ-12 28	13.42	82.3	2
WJ-12 30(1)	14.2	29.07	1.7
WJ-12 30(2)	15.46	22.6	1.7
WJ-12 31	15.07	54.54	2.1
WJ-12 32	14.29	69.62	2.5
WJ-12 33	13.89	77.77	2
WJ-12 34	11.04	57.27	1.4
WJ-12 35	12.6	80.7	2.5
WJ-12 37	16.26	86.18	1.9
WJ-12 38(1)	13.83	81	2
WJ-12 38(2)	16.15	47.03	2
WJ-12 38(3)	13.36	78.09	2
WJ-12 39	13.95	81.72	1.8
WJ-12 40(1)	13.65	63.86	1.9
WJ-12 40(2)	14.15	40.17	1.9
WJ-12 41	13.27	0	1.7
WJ-12 42(1)	12.52	49.22	2
WJ-12 42(2)	14.3	45.34	2
WJ-12 42(3)	13.42	58.28	2
WJ-12 42(4)	12.13	70.59	2
WJ-12 43(1)	14.5	67.03	2.2
WJ-12 43(2)	15.05	71.78	2.2
WJ-12 45(1)	13.35	37.58	1.7
WJ-12 45(2)	12.76	76.77	1.7
WJ-12 46	15.77	46.41	2.3
WJ-12 48(1)	14.17	73.67	1.7
WJ-12 48(2)	13.77	24.42	1.7
WJ-12 48(3)	13.94	46.75	1.7
WJ-12 48(4)	14.41	45.78	1.7
WJ-12 48(5)	13.03	87.98	1.7
WJ-12 48(6)	13.36	65.06	1.7
WJ-12 49	15.33	68.15	1.9
WJ-12 50	15.45	47.66	2.1

Continued on next page

Continued from previous page

Length no.	Confined track length (μm)	Angle to C Axis	Average Dpar (μm)
WJ-12 51	16.04	52.55	2.1
WJ-12 53	15.5	67.29	2.2
WJ-12 54	14.98	55.91	2.3
WJ-12 55(1)	14.13	48.95	1.7
WJ-12 55(2)	13.92	45.73	1.7
WJ-12 04(2)	12.61	59.27	2
WJ-12 05(2)	12.82	88.83	1.5
WJ-12 05(3)	12.78	71.37	1.5
WJ-12 10(2)	15.03	88.48	2.3
WJ-12 22	13.84	56.65	2.7
WJ-12 26(1)	14.03	81.49	2.5
WJ-12 26(2)	14.1	82.92	2.5
WJ-12 26(3)	11.38	81.4	2.5
WJ-12 30(3)	14.32	58.89	2.7
WJ-13 01	11.02	38.47	1.3
WJ-13 02	13.24	61.17	1.4
WJ-13 03(1)	14.74	24.95	1.3
WJ-13 03(2)	12.85	61.46	1.3
WJ-13 04(1)	13.47	72.26	1.2
WJ-13 04(2)	12.46	72.57	1.2
WJ-13 04(3)	12.74	66.66	1.2
WJ-13 05	14.85	36.42	1.4
WJ-13 06	13.91	58.5	1.3
WJ-13 07	13.05	52.7	1.3
WJ-13 08	12.73	67.38	1.2
WJ-13 09	15.67	58.54	1.1
WJ-13 10(1)	13.72	71.52	1.5
WJ-13 10(2)	11.23	38.74	1.5
WJ-13 11(1)	14.86	87.74	1.3
WJ-13 11(2)	13.44	42.76	1.3
WJ-13 11(3)	14.03	52.49	1.3
WJ-13 13(1)	13.44	53.43	1.3
WJ-13 13(2)	15.02	31.59	1.3
WJ-13 14	12.43	68.87	1.2
WJ-13 16(1)	14.37	58.56	1.5
WJ-13 16(2)	14.29	56.3	1.5
WJ-13 17	12.7	67.78	1.4
WJ-13 19	12.5	35.14	1.2
WJ-13 20	12.64	66.28	1.3
WJ-13 21	14.62	63.65	1.3
WJ-13 22	12.12	57.9	1.1
WJ-13 24(1)	13.57	34.67	1.4

Continued on next page

Continued from previous page

Length no.	Confined track length (μm)	Angle to C Axis	Average Dpar (μm)
WJ-13 25(1)	12.14	63.46	1.3
WJ-13 25(2)	13.18	19.39	1.3
WJ-13 25(3)	11.6	54.36	1.3
WJ-13 26	12.23	45.97	1.1
WJ-13 27(1)	14.14	64.63	1.3
WJ-13 27(2)	15.46	76.5	1.3
WJ-13 27(3)	12.33	19.6	1.3
WJ-13 29(1)	10.82	64.66	1.1
WJ-13 29(2)	10.67	48.92	1.1
WJ-13 30(1)	13.27	88.79	1.2
WJ-13 31	13.41	52.81	1.4
WJ-13 32(1)	13.64	50.59	1.4
WJ-13 33(1)	11.69	81.2	1.2
WJ-13 33(2)	12.31	70.23	1.2
WJ-13 34	14.52	76.94	1.2
WJ-13 35	14.34	31.26	1.1
WJ-13 36	14.31	17	1.3
WJ-13 37	12.4	64.08	1.5
WJ-13 38	14.07	71.83	1.3
WJ-13 03(3)	12.04	29.01	1.1
WJ-13 15	14.17	68.45	1.2
WJ-13 24(2)	14.17	60.29	1.2
WJ-13 30(2)	12.19	71.17	1.2
WJ-13 32(2)	12.56	45.85	1.1
WJ-14 01(1)	11.07	71.71	1.6
WJ-14 01(2)	13.55	46	1.6
WJ-14 01(3)	13.04	47.28	1.6
WJ-14 01(4)	8.94	78.58	1.6
WJ-14 01(5)	9.66	68.6	1.6
WJ-14 01(6)	9.28	62.02	1.6
WJ-14 01(7)	11.55	13.13	1.6
WJ-14 01(8)	11.93	79.31	1.6
WJ-14 02	11.32	78.25	1.7
WJ-14 03(1)	12.38	39.17	1.5
WJ-14 03(2)	14.84	82.79	1.5
WJ-14 03(3)	13.29	75.9	1.5
WJ-14 03(4)	11.68	21.83	1.5
WJ-14 03(5)	12.96	26.45	1.5
WJ-14 03(6)	12.56	49.79	1.5
WJ-14 04(1)	12.1	42.28	1.3
WJ-14 04(2)	13.35	37.11	1.3
WJ-14 04(3)	11.81	77.46	1.3

Continued on next page

Continued from previous page

Length no.	Confined track length (μm)	Angle to C Axis	Average Dpar (μm)
WJ-14 04(4)	13.29	31.02	1.3
WJ-14 05	13.49	34.35	1.3
WJ-14 06(1)	13.39	54.91	1.5
WJ-14 06(2)	13.77	59.09	1.5
WJ-14 07	12.78	82.46	1.4
WJ-14 08(1)	13.52	31.55	1.2
WJ-14 08(2)	13.09	36.02	1.2
WJ-14 08(3)	12.56	76.91	1.2
WJ-14 08(4)	9.53	62.16	1.2
WJ-14 09(1)	13.09	51.73	1.2
WJ-14 09(2)	12.82	51.05	1.2
WJ-14 10(1)	13.49	50.37	1.5
WJ-14 10(2)	11.58	89.71	1.5
WJ-14 11	12.92	84.36	1.4
WJ-14 12(1)	12.87	87.34	1.4
WJ-14 12(2)	11.1	42.03	1.4
WJ-14 13	12.32	75.58	1.3
WJ-14 14(1)	12.15	71	1.2
WJ-14 14(2)	14.6	68.58	1.2
WJ-14 14(3)	13.02	86.33	1.2
WJ-14 14(4)	14.24	76.03	1.2
WJ-14 14(5)	10.53	42.77	1.2
WJ-14 14(6)	12.36	70.41	1.2
WJ-14 14(7)	12.15	70.36	1.2
WJ-14 14(8)	11.93	59.02	1.2
WJ-14 15	13.73	78	1.4
WJ-14 16(1)	12.58	79.25	1.4
WJ-14 16(2)	13.37	68.33	1.4
WJ-14 17	12.01	78.84	1.3
WJ-14 18	11.18	64.49	1.3
WJ-14 19	9.37	37.47	1.3
WJ-14 21(1)	9.29	76.47	1.3
WJ-14 21(2)	11.68	63.85	1.3
WJ-14 21(3)	10.23	37.92	1.3
WJ-14 21(4)	9.43	48.63	1.3
WJ-14 22(1)	10.05	74.78	1.3
WJ-14 22(2)	12.05	54.53	1.3
WJ-14 23	12.88	52.45	1.2
WJ-14 24(1)	10.67	63.23	1.5
WJ-14 24(2)	10.08	49.09	1.5
WJ-14 24(3)	9.03	64.46	1.5
WJ-14 25(1)	12.08	71.85	1.2
WJ-14 25(2)	13.55	31.34	1.2

Continued on next page

Continued from previous page

Length no.	Confined track length (μm)	Angle to C Axis	Average Dpar (μm)
WJ-14 26(1)	14.07	60.54	1.3
WJ-14 26(2)	13.72	31.67	1.3
WJ-14 27	11.57	35.08	1.3
WJ-14 28	9.82	44.52	0.9
WJ-14 29(1)	13.77	73.11	1.2
WJ-14 29(2)	8.39	46.15	1.2
WJ-14 29(3)	11.7	71.88	1.2
WJ-14 29(4)	12.08	57.22	1.2
WJ-14 30(1)	10.24	0	1.3
WJ-14 30(2)	12.72	0	1.3
WJ-14 31(1)	13.25	77.94	1.5
WJ-14 31(2)	11.03	72.07	1.5
WJ-14 31(3)	12.46	39.21	1.5
WJ-14 31(4)	12.31	77.06	1.5
WJ-14 31(5)	10.57	87.67	1.5
WJ-14 31(6)	11.9	0.04	1.5
WJ-14 31(7)	12.22	26.11	1.5
WJ-14 32(1)	13.09	71.45	1
WJ-14 32(2)	13.17	64.8	1
WJ-14 33(1)	13.31	51.06	1.6
WJ-14 33(2)	10.59	46.58	1.6
WJ-14 33(3)	8.53	13.73	1.6
WJ-14 34	11.97	83.23	1.3
WJ-14 35(1)	11.85	63.24	0.9
WJ-14 35(2)	10.26	67.48	0.9
WJ-14 37	10.26	65.36	1.3
WJ-14 38	12.87	67.84	1.3
WJ-14 39	10.85	56.6	1.2
WJ-14 40(1)	11.99	46.72	1.4
WJ-14 40(2)	11.61	58.06	1.4
WJ-14 41	10.46	85.63	1.3
WJ-14 42	13.25	58.67	1.4
WJ-14 43(1)	12.01	68.05	1.4
WJ-14 43(2)	11.39	67	1.4
WJ-14 43(3)	12.32	32.8	1.4
WJ-14 43(4)	10.38	74.52	1.4
WJ-14 43(5)	13.98	23.08	1.4
WJ-14 43(6)	11.34	81.3	1.4
WJ-14 44	13.14	61.31	1.4
WJ-15 01(1)	10.37	58.46	1.5
WJ-15 01(2)	11.2	64.99	1.5
WJ-15 01(3)	8.02	48.22	1.5

Continued on next page

Continued from previous page

Length no.	Confined track length (μm)	Angle to C Axis	Average Dpar (μm)
WJ-15 01(4)	13.67	40.14	1.5
WJ-15 01(5)	13.28	71	1.5
WJ-15 01(6)	10.67	74.64	1.5
WJ-15 01(7)	10.92	69.63	1.5
WJ-15 01(8)	12.39	56.11	1.5
WJ-15 01(9)	11.13	77.87	1.5
WJ-15 01(10)	12.16	40.84	1.5
WJ-15 02	13.35	44.49	1.4
WJ-15 03(1)	13.13	80.95	1.4
WJ-15 03(2)	12.75	24.43	1.4
WJ-15 04	10.7	53.68	1.2
WJ-15 05(1)	12.67	82.09	1.5
WJ-15 05(2)	10.96	70.33	1.5
WJ-15 05(3)	12.59	28.71	1.5
WJ-15 06	11.77	65.72	1.5
WJ-15 07(1)	12.72	59.52	1.5
WJ-15 07(2)	12.7	64.31	1.5
WJ-15 08(1)	13.66	46.17	1.7
WJ-15 08(2)	8.97	68.76	1.7
WJ-15 09(1)	12.5	83.04	1.8
WJ-15 09(2)	11.53	82.66	1.8
WJ-15 09(3)	12.69	35	1.8
WJ-15 09(4)	9.57	75.91	1.8
WJ-15 10	12.75	66.14	1.4
WJ-15 11	13.56	61.54	2.1
WJ-15 12(1)	13.41	69.75	1.4
WJ-15 12(2)	13.56	69.48	1.4
WJ-15 13	13.71	63.4	1.4
WJ-15 14(1)	9.98	52.99	1.5
WJ-15 14(2)	11.93	35.79	1.5
WJ-15 15	11.33	83.37	1.5
WJ-15 16	13.16	71.81	1.5
WJ-15 17(1)	13.25	33.95	1.6
WJ-15 17(2)	11.42	35.14	1.6
WJ-15 17(3)	10.84	70.02	1.6
WJ-15 17(4)	13.9	49.48	1.6
WJ-15 17(5)	13.53	64.63	1.6
WJ-15 18(1)	12.31	70.88	1.5
WJ-15 18(2)	13.95	51.87	1.5
WJ-15 19(1)	12.83	62.01	1.5
WJ-15 19(2)	12.83	21	1.5
WJ-15 19(3)	10.3	30.57	1.5
WJ-15 20(1)	10.14	86.54	1.6

Continued on next page

Continued from previous page

Length no.	Confined track length (μm)	Angle to C Axis	Average Dpar (μm)
WJ-15 20(2)	11.48	83.11	1.6
WJ-15 20(3)	13.97	36.93	1.6
WJ-15 21(1)	8.39	71.99	1.5
WJ-15 21(2)	12.29	23.54	1.5
WJ-15 22(1)	11.28	54.46	1.5
WJ-15 22(2)	11.23	52.33	1.5
WJ-15 22(3)	11.52	62.25	1.5
WJ-15 22(4)	10.58	86.74	1.5
WJ-15 23	13.88	70.99	1.5
WJ-15 24(1)	11.46	21.51	1.4
WJ-15 24(2)	13.42	45.4	1.4
WJ-15 25(1)	13.55	55.22	1.7
WJ-15 25(2)	12.77	77.8	1.7
WJ-15 26(1)	12.91	78.47	1.4
WJ-15 26(2)	13.8	78.65	1.4
WJ-15 27(1)	13.11	35.41	1.5
WJ-15 27(2)	13.1	33.41	1.5
WJ-15 27(3)	9.14	30.75	1.5
WJ-15 28(1)	11.52	25.2	1.7
WJ-15 28(2)	12.6	39.74	1.7
WJ-16 01(1)	11.89	79.89	0.7
WJ-16 01(2)	12.98	54.16	0.7
WJ-16 02	12.65	28.46	0.8
WJ-16 03	12.7	52.44	0.8
WJ-16 04	11.33	46.29	0.7
WJ-16 05(1)	12.03	75.79	0.9
WJ-16 05(2)	11.98	43.11	0.9
WJ-16 06	13.17	15.14	1
WJ-16 07	12.13	33.45	1.1
WJ-16 08(1)	11.46	78.8	0.9
WJ-16 08(2)	11.65	47.07	0.9
WJ-16 09	9.49	36.44	0.9
WJ-16 10	13.63	61.49	1.1
WJ-16 11(1)	12.62	64.13	1.3
WJ-16 11(2)	12	35.6	1.3
WJ-16 11(3)	12.61	64.86	1.3
WJ-16 11(4)	11.42	70.75	1.3
WJ-16 11(5)	10.43	65.52	1.3
WJ-16 12	10.07	15.76	1
WJ-16 13	9.77	17.4	1
WJ-16 14	14.43	10.61	0.9
WJ-16 15	9.76	87.78	1

Continued on next page

Continued from previous page

Length no.	Confined track length (μm)	Angle to C Axis	Average Dpar (μm)
WJ-16 16(1)	12.81	72.08	1.1
WJ-16 16(2)	10.72	67.43	1.1
WJ-16 16(3)	13.06	60.93	1.1
WJ-16 17(1)	12.78	16.88	0.9
WJ-16 17(2)	12.56	28.62	0.9
WJ-16 17(3)	13.15	44.62	0.9
WJ-16 18	11.69	48.22	1
WJ-16 20(1)	13.18	88.5	0.8
WJ-16 20(2)	14.57	74.83	0.8
WJ-16 20(3)	12.42	84.26	0.8
WJ-16 20(4)	14.46	86.04	0.8
WJ-16 20(5)	15.58	55.08	0.8
WJ-16 21	14.71	28.59	1.2
WJ-16 23	12.1	20.51	1.1
WJ-16 24(1)	12.08	82.26	1.1
WJ-16 24(2)	12.25	28.9	1.1
WJ-16 25	13.48	28.27	0.9
WJ-16 26(1)	11.84	45.46	1.3
WJ-16 26(2)	14.87	28.97	1.3
WJ-16 27(1)	9.21	19.36	1.1
WJ-16 27(2)	13.46	54.16	1.1
WJ-16 27(3)	13.74	42.89	1.1
WJ-16 27(4)	13.4	36.16	1.1
WJ-16 29	14.55	54.23	0.9
WJ-16 30(1)	14.61	88.42	1
WJ-16 30(2)	11.01	65.02	1
WJ-16 31(1)	10.5	41.17	1
WJ-16 31(2)	10.6	45.29	1
WJ-16 32(1)	14.18	45.71	1.1
WJ-16 32(2)	12.35	53.37	1.1
WJ-16 32(3)	12.19	62.05	1.1
WJ-16 32(4)	9.98	62.35	1.1
WJ-16 33	12.3	58.53	1.1
WJ-16 34	13.73	40.93	1
WJ-16 35	12.62	75.9	1.1
WJ-17 01	11.71	54.91	1.5
WJ-17 02(1)	12.26	16.41	1.8
WJ-17 02(2)	12.55	82.5	1.8
WJ-17 02(3)	12.9	41.28	1.8
WJ-17 02(4)	11.79	62.95	1.8
WJ-17 03(1)	11.36	60.16	1.7
WJ-17 03(2)	12.02	60.96	1.7

Continued on next page

Continued from previous page

Length no.	Confined track length (μm)	Angle to C Axis	Average Dpar (μm)
WJ-17 03(3)	12.52	78.69	1.7
WJ-17 03(4)	12.91	37.4	1.7
WJ-17 04	13.87	59.53	1.6
WJ-17 05(1)	9.8	53.69	1.5
WJ-17 05(2)	9.93	86.43	1.5
WJ-17 06(1)	10.91	83.58	1.7
WJ-17 06(2)	11.59	64.64	1.7
WJ-17 07(1)	11.47	55.57	1.5
WJ-17 07(2)	12.56	78.99	1.5
WJ-17 07(3)	13.5	31.79	1.5
WJ-17 08	14.22	59.07	1.3
WJ-17 09	11.85	64.3	1.7
WJ-17 10(1)	11.67	69.87	1.6
WJ-17 10(2)	13.13	44.11	1.6
WJ-17 11(1)	14.39	36.78	1.3
WJ-17 11(2)	12.88	35.77	1.3
WJ-17 11(3)	12.68	47.97	1.3
WJ-17 11(4)	10	6.58	1.3
WJ-17 11(5)	10.46	88.37	1.3
WJ-17 12(1)	9.67	26.23	1.4
WJ-17 12(2)	13.5	48.54	1.4
WJ-17 12(3)	8.98	52.91	1.4
WJ-17 13	14.41	32.89	1.2
WJ-17 14(1)	8.79	60.84	1.5
WJ-17 14(2)	10.41	69.11	1.5
WJ-17 14(3)	13.01	54.66	1.5
WJ-17 14(4)	13.96	24.52	1.5
WJ-17 14(5)	13.92	45.73	1.5
WJ-17 14(6)	10.13	70.13	1.5
WJ-17 15(1)	13.9	59.83	1.6
WJ-17 15(2)	10.92	72.61	1.6
WJ-17 16(1)	13.56	18.43	1.3
WJ-17 16(2)	11.85	40.91	1.3
WJ-17 16(3)	14.38	48.33	1.3
WJ-17 16(4)	14.46	70.23	1.3
WJ-17 16(5)	14.21	43.18	1.3
WJ-17 16(6)	10.44	84.31	1.3
WJ-17 16(7)	12.13	36.3	1.3
WJ-17 16(8)	10.72	12.11	1.3
WJ-17 16(9)	14.71	17.63	1.3
WJ-18 01(1)	13.84	61.35	1.2
WJ-18 02(1)	8.81	65.17	1

Continued on next page

Continued from previous page

Length no.	Confined track length (μm)	Angle to C Axis	Average Dpar (μm)
WJ-18 02(2)	13.21	27.83	1
WJ-18 03(1)	10.64	37.35	1.3
WJ-18 03(2)	13.07	33.9	1.3
WJ-18 03(3)	13.29	66.11	1.3
WJ-18 04(1)	12.43	76.95	1.4
WJ-18 05(1)	10	56.27	1
WJ-18 06	14.29	38.99	1.1
WJ-18 07	13.88	51.53	1.2
WJ-18 08	9.52	82.43	1.1
WJ-18 09	14.02	85.12	1.2
WJ-18 10(1)	10.57	21.62	1.1
WJ-18 10(2)	11.1	30.09	1.1
WJ-18 10(3)	13.48	67.85	1.1
WJ-18 12(1)	10.04	76.56	1.1
WJ-18 12(2)	12.36	62.72	1.1
WJ-18 12(3)	9.71	58.99	1.1
WJ-18 13	12.74	45.99	1.1
WJ-18 14(1)	14.54	22.91	1.2
WJ-18 14(2)	12.43	69.59	1.2
WJ-18 15	9.12	48.62	0.9
WJ-18 16	11.49	69.94	1.3
WJ-18 17	13.14	20.67	1.1
WJ-18 18(1)	12.07	56.75	1.2
WJ-18 19	13.56	49.71	1.4
WJ-18 23(1)	13.64	79.04	1.2
WJ-18 23(2)	11.46	28.29	1.2
WJ-18 23(3)	11.1	79.38	1.2
WJ-18 24	12.88	55.74	1.2
WJ-18 25(1)	13.78	24.56	1.2
WJ-18 25(2)	10.35	15.95	1.2
WJ-18 26(1)	12.01	58.74	1.1
WJ-18 27	11.83	84.65	1.1
WJ-18 28(1)	13.76	70.64	1.2
WJ-18 29	12.63	27.73	1.2
WJ-18 30	13.47	59.43	1.2
WJ-18 31(1)	11.24	78.28	1.2
WJ-18 31(2)	12.51	81.49	1.2
WJ-18 34(1)	12.89	37.53	1.1
WJ-18 34(2)	8.81	74.41	1.1
WJ-18 35	14.54	65.26	1.1
WJ-18 37	13.9	76.44	1.2
WJ-18 38	10.76	79.51	1.3
WJ-18 39	13.07	66.6	1.1

Continued on next page

Continued from previous page

Length no.	Confined track length (μm)	Angle to C Axis	Average Dpar (μm)
WJ-18 40(1)	14.02	71.26	1.3
WJ-18 40(2)	12.24	84.13	1.3
WJ-18 40(3)	13.93	19.21	1.3
WJ-18 41	11.68	64.69	1.3
WJ-18 42	12.99	62	1.4
WJ-18 43	15.41	40.07	1.1
WJ-18 45	13.08	60.82	1.2
WJ-18 46(1)	8	83.81	1.2
WJ-18 46(2)	15.15	24.51	1.2
WJ-18 47	11.48	37.47	1.3
WJ-18 48(1)	10.79	65.26	1.3
WJ-18 48(2)	13.7	40.13	1.3
WJ-18 49	10.5	49.95	1.1
WJ-18 50(1)	13.88	84.39	1.2
WJ-18 50(2)	13.22	82.22	1.2
WJ-18 51	12.57	64.2	1.2
WJ-18 52	11.02	67.56	1.1
WJ-18 53(1)	14.13	43.72	1.1
WJ-18 53(2)	13.62	64.28	1.1
WJ-18 53(3)	12.63	24.41	1.1
WJ-18 53(4)	11.9	67.49	1.1
WJ-18 54	13.93	53.93	1.3
WJ-18 56	13.75	25.85	1.2
WJ-18 57	14.5	35.35	1.1
WJ-18 58	13.93	57.36	1.2
WJ-18 60	8.63	74.1	0.9
WJ-18 61(1)	14.72	42.81	1.2
WJ-18 61(2)	14.58	45.45	1.2
WJ-18 61(3)	10.68	56.63	1.2
WJ-18 62	13.55	68.61	1
WJ-18 63(1)	13.85	75.5	1.2
WJ-18 63(2)	13.11	64.83	1.2
WJ-18 64	10.43	37.1	1.2
WJ-18 01(2)	12.23	72.69	0.7
WJ-18 01(3)	12.08	44.33	0.7
WJ-18 04(2)	9.88	26.56	0.8
WJ-18 05(2)	13.64	33.22	1.1
WJ-18 18(2)	13.38	57.34	1
WJ-18 26(2)	13.16	77.58	0.8
WJ-18 28(2)	12.43	70.52	0.7
WJ-18 28(3)	11.98	38.32	0.7
WJ-19 01(1)	14.47	60.81	2.8

Continued on next page

Continued from previous page

Length no.	Confined track length (μm)	Angle to C Axis	Average Dpar (μm)
WJ-19 01(2)	13.88	79.91	2.8
WJ-19 01(3)	14.85	78.64	2.8
WJ-19 02(1)	15.05	73.51	2.7
WJ-19 02(2)	14.26	53.23	2.7
WJ-19 02(3)	14.76	52.57	2.7
WJ-19 02(4)	12.94	67.42	2.7
WJ-19 03	15.84	21.74	2.2
WJ-19 04	16.3	51.8	2.7
WJ-19 05(1)	12.45	81.64	2.5
WJ-19 05(2)	15.42	64.21	2.5
WJ-19 07	13.85	45.44	2.5
WJ-19 08	13.84	76.08	2
WJ-19 09(1)	13.98	50.53	2.3
WJ-19 09(2)	14.8	68.73	2.3
WJ-19 10(1)	14.83	44.08	2.6
WJ-19 10(2)	12.19	82.69	2.6
WJ-19 10(3)	14.27	80.07	2.6
WJ-19 11(1)	13.67	65.82	1.9
WJ-19 11(2)	14.53	54.77	1.9
WJ-19 12(1)	12.89	80.19	2
WJ-19 12(2)	15.01	57.83	2
WJ-19 12(3)	10.04	78.64	2
WJ-19 12(4)	13.86	78.63	2
WJ-19 12(5)	13.11	87.81	2
WJ-19 13(1)	14.87	42.39	2.7
WJ-19 13(2)	14.62	21	2.7
WJ-19 13(3)	14.79	55.34	2.7
WJ-19 14(1)	14.47	40.51	2.2
WJ-19 14(2)	13.93	52.88	2.2
WJ-19 14(3)	13.21	56.38	2.2
WJ-19 15(1)	15.6	88.43	2.4
WJ-19 15(2)	14.69	68.85	2.4
WJ-19 15(3)	13.49	84.84	2.4
WJ-19 15(4)	14.17	71.65	2.4
WJ-19 15(5)	13.33	76.85	2.4
WJ-19 16(1)	14.58	87.99	2.3
WJ-19 16(2)	11.99	65.24	2.3
WJ-19 17(1)	13.14	75.37	2.2
WJ-19 17(2)	14.59	88.71	2.2
WJ-19 17(3)	14.05	38.27	2.2
WJ-19 17(4)	13.17	64.88	2.2
WJ-19 17(5)	12.7	69.37	2.2
WJ-19 17(6)	15.18	46.84	2.2

Continued on next page

Continued from previous page

Length no.	Confined track length (μm)	Angle to C Axis	Average Dpar (μm)
WJ-19 17(7)	13.97	44.31	2.2
WJ-19 17(8)	13.12	82.03	2.2
WJ-19 17(9)	14.43	34.24	2.2
WJ-19 17(10)	12.93	76.72	2.2
WJ-19 17(11)	14.15	85.91	2.2
WJ-19 17(12)	15.32	51.21	2.2
WJ-19 17(13)	14.02	79.48	2.2
WJ-19 17(14)	14.45	81.04	2.2
WJ-19 17(15)	13.68	14.15	2.2
WJ-19 17(16)	15.35	48.28	2.2
WJ-19 17(17)	14.51	68.6	2.2
WJ-19 18(1)	13.11	49.75	2.4
WJ-19 18(2)	15.62	61.99	2.4
WJ-19 19(1)	14.28	53.26	2.1
WJ-19 19(2)	14.28	50.1	2.1
WJ-19 20(1)	12.45	79.91	2.4
WJ-19 20(2)	13.39	62.92	2.4
WJ-19 20(3)	13.28	59.4	2.4
WJ-19 21(1)	15.02	58.31	2.3
WJ-19 21(2)	15.86	2.59	2.3
WJ-19 22(1)	13.87	80.31	2.4
WJ-19 22(2)	14.42	66.25	2.4
WJ-19 23(1)	16.15	61.87	2.3
WJ-19 23(2)	15.9	62.12	2.3
WJ-19 23(3)	13.71	12.47	2.3
WJ-19 24(1)	15.5	77.47	2.4
WJ-19 24(2)	13.82	29.84	2.4
WJ-19 24(3)	13.85	88.08	2.4
WJ-19 25(1)	16.26	60.07	2.6
WJ-19 25(2)	16.02	66.67	2.6
WJ-19 26	11.63	84.3	2
WJ-19 28(1)	14.3	63.12	2.4
WJ-19 28(2)	15.32	83.99	2.4
WJ-19 29(1)	13.47	70.66	2.1
WJ-19 29(2)	15.08	88.92	2.1
WJ-19 30(1)	14.87	67.53	2.3
WJ-19 30(2)	13.32	65.71	2.3
WJ-19 30(3)	14.87	88.26	2.3
WJ-19 31	15.06	75.68	2.5
WJ-19 32(1)	13.11	45.69	2.3
WJ-19 32(2)	13.65	70.33	2.3
WJ-19 32(3)	14.48	48.65	2.3
WJ-19 33(1)	14.43	49.94	2.2

Continued on next page

Continued from previous page

Length no.	Confined track length (μm)	Angle to C Axis	Average Dpar (μm)
WJ-19 33(2)	12.98	72.55	2.2
WJ-19 33(3)	12.97	83.72	2.2
WJ-19 34(1)	14.72	79.14	1.7
WJ-19 34(2)	12.57	67	1.7
WJ-19 34(3)	12.76	72.9	1.7
WJ-19 34(4)	13.19	79.93	1.7
WJ-19 34(5)	14.11	80.88	1.7
WJ-19 34(6)	14.65	36.07	1.7
WJ-19 34(7)	12.62	86.15	1.7
WJ-21 01	13.1	44.78	1.5
WJ-21 02	14.31	42.05	1.3
WJ-21 03(1)	12.68	17.21	1.5
WJ-21 03(2)	11.8	59.42	1.5
WJ-21 03(3)	11.97	36.73	1.5
WJ-21 04	13.08	44.41	1.5
WJ-21 05	13.68	39.45	1.4
WJ-21 06(1)	14.42	56.97	1.4
WJ-21 06(2)	11.76	87.75	1.4
WJ-21 07	13.84	28.4	1.5
WJ-21 08	12.76	49.82	1.4
WJ-21 09	13.88	52.28	1.6
WJ-21 10	12.09	53.29	1.6
WJ-21 11	12.98	63.79	1.4
WJ-21 12(1)	11.35	32.05	1.3
WJ-21 12(2)	12.58	58.06	1.3
WJ-21 13(1)	13.42	37.41	1.4
WJ-21 13(2)	10.99	32.8	1.4
WJ-21 14(1)	14.61	54.95	1.5
WJ-21 14(2)	12.73	49.82	1.5
WJ-21 14(3)	10.98	64.82	1.5
WJ-21 14(4)	12.2	47.19	1.5
WJ-21 14(5)	12.66	55.84	1.5
WJ-21 14(6)	11.82	50.61	1.5
WJ-21 14(7)	13.62	53.79	1.5
WJ-21 15	11.34	31.32	1.5
WJ-21 16	13.18	60.05	1.4
WJ-21 18	11.26	74.48	1.5
WJ-21 19(1)	13.77	56.06	1.5
WJ-21 19(2)	11.44	34.31	1.5
WJ-21 19(3)	12.21	51.6	1.5
WJ-21 20	11.17	65.22	1.4
WJ-21 21	9.6	65.91	1.3

Continued on next page

Continued from previous page

Length no.	Confined track length (μm)	Angle to C Axis	Average Dpar (μm)
WJ-21 22	12.07	59.56	1.4
WJ-21 23	14.27	83.2	1.5
WJ-21 24	11.63	49.15	1.5
WJ-21 25	15.32	51.24	1.3
WJ-21 26	11.52	67.3	1.5
WJ-21 27	13.6	28.95	1.5
WJ-21 28	11.06	79.06	1.4
WJ-21 29	13.65	37.07	1.4
WJ-21 30	13.68	56.29	1.3
WJ-21 31	13.25	76.01	1.4
WJ-21 32(1)	11.91	50.27	1.2
WJ-21 32(2)	8.37	71.79	1.2
WJ-21 32(3)	11.04	80.94	1.2
WJ-21 33	12.72	88.45	1.5
WJ-21 34(1)	13.22	34.78	1.2
WJ-21 34(2)	10.68	45.14	1.2
WJ-21 35	13.92	6.54	1.3
WJ-21 36	13.47	28.42	1.5
WJ-21 37	12.92	32.07	1.4
WJ-21 38(1)	12.39	57.35	1.6
WJ-21 38(2)	11.97	60.88	1.6
WJ-21 39(1)	12.54	78.67	1.5
WJ-21 39(2)	13.63	80.18	1.5
WJ-21 39(3)	13.45	77.89	1.5
WJ-21 40(1)	12.2	72.1	1.3
WJ-21 40(2)	13.1	40.32	1.3
WJ-21 41(1)	12.24	61.45	1.4
WJ-21 41(2)	13.03	50.47	1.4
WJ-21 41(3)	13.65	42.67	1.4
WJ-21 41(4)	11.33	47.91	1.4
WJ-21 42	14.94	35.95	1.5
WJ-21 43(1)	12.35	58.6	1.5
WJ-21 43(2)	13.75	74.51	1.5
WJ-22 01(1)	12.88	75.53	1.5
WJ-22 01(2)	12.49	68.49	1.5
WJ-22 02	12.57	52.01	1.4
WJ-22 03	14.41	89	1.5
WJ-22 04(1)	13.22	30.79	1.6
WJ-22 04(2)	10.87	66.58	1.6
WJ-22 04(3)	13.44	73.47	1.6
WJ-22 05	12.92	44.55	1.4
WJ-22 06(1)	12.77	79.79	1.3

Continued on next page

Continued from previous page

Length no.	Confined track length (μm)	Angle to C Axis	Average Dpar (μm)
WJ-22 06(2)	11.56	34.53	1.3
WJ-22 06(3)	10.96	74.79	1.3
WJ-22 07(1)	13	53.27	1.6
WJ-22 07(2)	12.39	67.85	1.6
WJ-22 07(3)	12.44	48.91	1.6
WJ-22 07(4)	14.58	32.03	1.6
WJ-22 07(5)	10.94	79.49	1.6
WJ-22 08(1)	15.45	89.77	1.6
WJ-22 08(2)	10.79	72.1	1.6
WJ-22 09(1)	13.67	51.42	1.8
WJ-22 09(2)	12.59	28.86	1.8
WJ-22 10	12.89	77.99	1.3
WJ-22 11(1)	13.98	84.29	1.7
WJ-22 11(2)	13.08	3.6	1.7
WJ-22 11(3)	14.28	25.71	1.7
WJ-22 12(1)	14.91	55.24	1.5
WJ-22 12(2)	12.69	57.71	1.5
WJ-22 12(3)	11.72	69.9	1.5
WJ-22 12(4)	9.81	49.72	1.5
WJ-22 13(1)	14.29	27.69	1.8
WJ-22 13(2)	14.21	20.43	1.8
WJ-22 13(3)	13.29	89.77	1.8
WJ-22 14(1)	12.48	77.75	1.6
WJ-22 14(2)	13.46	84.79	1.6
WJ-22 14(3)	10.4	71	1.6
WJ-22 15(1)	14.78	52.13	1.7
WJ-22 15(2)	11.33	49.41	1.7
WJ-22 15(3)	10.74	65.96	1.7
WJ-22 15(4)	11.62	79.03	1.7
WJ-22 15(5)	10.38	49.38	1.7
WJ-22 15(6)	13.32	13.47	1.7
WJ-22 15(7)	12.42	55.4	1.7
WJ-22 15(8)	12.77	50.93	1.7
WJ-22 16(1)	13.93	76.65	1.7
WJ-22 16(2)	12.78	62	1.7
WJ-22 17	14.54	57.39	1.7
WJ-22 18	13.63	61.1	1.7
WJ-22 19(1)	12.65	74.56	1.8
WJ-22 19(2)	13.92	81.31	1.8
WJ-22 19(3)	10.99	57.03	1.8
WJ-22 19(4)	12.96	84.92	1.8
WJ-23 01	10.56	13.09	1.4

Continued on next page

Continued from previous page

Length no.	Confined track length (μm)	Angle to C Axis	Average Dpar (μm)
WJ-23 02	12.11	14.16	1.2
WJ-23 05(1)	10.76	82.7	1.3
WJ-23 05(2)	14.04	47.82	1.3
WJ-23 06	14.03	46.37	1.6
WJ-23 08(1)	14.88	37.36	1.6
WJ-23 08(2)	12.98	51.4	1.6
WJ-23 09	11.56	88.21	1.3
WJ-23 10	7.96	73.12	1.6
WJ-23 11	13.79	57.83	1.5
WJ-23 12	13.38	81.43	1.3
WJ-23 13(1)	14.26	74.98	1.3
WJ-23 13(2)	13.81	33.66	1.3
WJ-23 14	13.53	76.1	1.5
WJ-23 15(1)	13.85	47.29	1.3
WJ-23 15(2)	13.86	46.84	1.3
WJ-23 16(1)	12.48	57.09	1.6
WJ-23 16(2)	11.84	79.1	1.6
WJ-23 16(3)	12.92	63.39	1.6
WJ-23 16(4)	10.52	52.76	1.6
WJ-23 16(5)	12.85	88.51	1.6
WJ-23 17	12.58	57.99	1.4
WJ-23 18(1)	13.19	87.47	1.4
WJ-23 18(2)	13.8	50.13	1.4
WJ-23 20	14.37	53.56	1.2
WJ-23 21	13.12	81.83	1.5
WJ-23 22	14.5	84.42	1.4
WJ-23 23	14.67	39.42	1.4
WJ-23 24(1)	9.91	65.65	1.4
WJ-23 24(2)	11.82	71.39	1.4
WJ-23 24(3)	11.98	34.04	1.4
WJ-23 24(4)	13.83	45.47	1.4
WJ-23 24(5)	12.7	46.86	1.4
WJ-23 24(6)	12.18	46.76	1.4
WJ-23 25(1)	14.31	87.65	1.3
WJ-23 25(2)	12.76	61.04	1.3
WJ-23 26(1)	13.57	28.81	1.3
WJ-23 26(2)	12.42	89.15	1.3
WJ-23 26(3)	13.74	75.19	1.3
WJ-23 28	13.74	74.07	1.4
WJ-23 30(1)	12.66	60.87	1.4
WJ-23 30(2)	12.41	55.22	1.4
WJ-23 31(1)	11.91	74.4	1.2
WJ-23 31(2)	10.88	78.94	1.2

Continued on next page

Continued from previous page

Length no.	Confined track length (μm)	Angle to C Axis	Average Dpar (μm)
WJ-23 32	11.43	20.66	1.6
WJ-23 33	14.79	77.96	1.5

D.3 Apatite U–Pb analytical spot data

Table D.3: Apatite U–Pb analytical spot data.

Sample name	Spot no.	$^{238}U/^{206}Pb$	2σ	$^{207}Pb/^{206}Pb$	2σ	ρ
WJ14	1	5.917	0.385	0.623	0.026	0.52
WJ14	2	4.048	0.262	0.693	0.04	0.47
WJ14	4	18.484	0.956	0.1858	0.0087	-0.1
WJ14	5	7.855	0.567	0.544	0.032	0.21
WJ14	6	10.03	0.523	0.467	0.024	0.24
WJ14	7	9.832	0.734	0.489	0.033	0.17
WJ14	11	18.832	1.028	0.1924	0.0087	0.36
WJ14	13	5.624	0.284	0.637	0.031	0.51
WJ14	16	9.372	0.676	0.509	0.033	0.16
WJ14	17	3.861	0.283	0.721	0.038	-0.02
WJ14	18	7.535	0.408	0.576	0.026	0.19
WJ14	19	9.496	0.595	0.489	0.02	0.31
WJ14	20	4.347	0.264	0.662	0.036	0.46
WJ14	21	15.337	0.917	0.273	0.019	0.53
WJ14	22	8.841	0.633	0.536	0.027	0.26
WJ14	25	15.527	0.843	0.269	0.012	0.29
WJ14	26	6.226	0.426	0.592	0.032	0.56
WJ14	27	5.025	0.378	0.718	0.045	0.29
WJ14	28	6.414	0.39	0.652	0.051	0.63
WJ14	29	9.319	0.573	0.498	0.022	0.08
WJ14	30	6.802	0.509	0.622	0.048	0.52
WJ14	31	3.831	0.278	0.709	0.041	0.22
WJ14	32	8.503	0.585	0.555	0.046	0.28
WJ14	34	6.57	0.427	0.587	0.025	0.43
WJ14	35	9	0.623	0.507	0.038	0.42
WJ14	36	5.707	0.358	0.634	0.034	0.34
WJ14	37	4.926	0.339	0.681	0.042	0.56
WJ14	38	7.299	0.639	0.575	0.03	0.03
WJ14	39	4.502	0.243	0.697	0.041	0.38
WJ14	40	15.015	0.811	0.288	0.013	-0.01
WJ15	1	13.717	0.771	0.33	0.015	0.17
WJ15	2	9.233	0.511	0.527	0.031	0.4
WJ15	3	8.976	0.636	0.516	0.026	0.12
WJ15	4	9.532	0.554	0.471	0.022	0.31
WJ15	5	15.06	0.703	0.301	0.011	0.15
WJ15	6	15.847	0.678	0.267	0.015	0.14
WJ15	7	9.794	0.681	0.461	0.033	0.08
WJ15	8	12.919	0.784	0.37	0.018	0.34
WJ15	9	10	0.63	0.465	0.027	0.31
WJ15	10	4.901	0.312	0.665	0.04	0.6

Continued on next page

Continued from previous page

Sample name	Spot no.	$^{238}U/^{206}Pb$	2σ	$^{207}Pb/^{206}Pb$	2σ	ρ
WJ15	11	12.531	0.722	0.36	0.021	-0.06
WJ15	12	6.77	0.398	0.61	0.034	0.65
WJ15	13	10.548	0.623	0.437	0.023	0.42
WJ15	14	10.752	0.589	0.462	0.024	0.3
WJ15	15	8.417	0.524	0.529	0.029	0.05
WJ15	16	12.562	0.631	0.376	0.02	0.19
WJ15	18	12.121	0.661	0.396	0.022	0.05
WJ15	19	11.6	0.619	0.388	0.02	0.32
WJ15	20	13.736	0.83	0.294	0.016	-0.21
WJ15	21	6.079	0.406	0.611	0.041	0.32
WJ15	22	13.55	0.771	0.34	0.017	0.48
WJ15	23	13.123	0.74	0.351	0.017	0.39
WJ15	24	12.345	0.624	0.355	0.018	0.41
WJ15	25	14.409	0.851	0.291	0.015	-0.03
WJ15	26	11.547	0.626	0.393	0.024	0.03
WJ15	27	11.135	0.582	0.374	0.022	0.24
WJ15	28	13.227	0.769	0.323	0.019	0.19
WJ15	29	11.99	0.646	0.414	0.02	0.64
WJ15	30	14.306	0.736	0.291	0.018	0.22
WJ15	31	7.867	0.42	0.559	0.029	0.29
WJ15	33	5.208	0.325	0.641	0.044	0.2
WJ15	34	16.694	0.891	0.249	0.011	0.31
WJ23	1	1.305	0.074	0.792	0.022	0.19
WJ23	3	2.392	0.148	0.777	0.035	0.17
WJ23	4	1.763	0.146	0.788	0.032	0.04
WJ23	5	1.642	0.148	0.826	0.044	0.22
WJ23	6	1.303	0.083	0.786	0.032	0.16
WJ23	7	1.173	0.093	0.782	0.048	0.18
WJ23	8	1.584	0.16	0.755	0.033	0.12
WJ23	9	0.892	0.075	0.794	0.034	0.18
WJ23	10	2.118	0.175	0.767	0.034	-0.01
WJ23	11	1.677	0.143	0.769	0.031	0.42
WJ23	12	2.652	0.232	0.774	0.045	0.08
WJ23	13	1.872	0.126	0.775	0.044	0.26
WJ23	14	1.605	0.097	0.807	0.03	0.15
WJ23	15	1.246	0.113	0.783	0.035	0.14
WJ23	16	0.134	0.011	0.839	0.025	0.01
WJ23	17	4.048	0.426	0.664	0.033	-0.19
WJ23	18	1.763	0.127	0.767	0.031	0.2
WJ23	19	0.502	0.035	0.825	0.037	0.19
WJ23	20	2.801	0.188	0.728	0.029	0.3
WJ23	21	2.242	0.155	0.786	0.046	0.17
WJ23	22	0.852	0.069	0.824	0.032	0.01
WJ23	23	1.798	0.122	0.816	0.042	0.47

Continued on next page

Continued from previous page

Sample name	Spot no.	$^{238}U/^{206}Pb$	2σ	$^{207}Pb/^{206}Pb$	2σ	ρ
WJ23	24	0.887	0.078	0.812	0.042	0.19
WJ23	25	3.891	0.317	0.704	0.038	0.51
WJ22	1	8.25	0.476	0.475	0.035	0.49
WJ22	2	10.869	0.59	0.397	0.024	0.2
WJ22	3	6.816	0.464	0.555	0.044	0.55
WJ22	4	11.454	0.603	0.37	0.019	0.16
WJ22	5	10.373	0.656	0.459	0.026	0.27
WJ22	6	7.898	0.486	0.537	0.03	0.21
WJ22	7	14.326	0.656	0.227	0.012	0.21
WJ22	8	10.672	0.706	0.433	0.034	-0.26
WJ22	9	8.417	0.581	0.5	0.034	0.39
WJ22	10	6.329	0.52	0.595	0.038	0.32
WJ22	11	9.784	0.785	0.452	0.036	0.18
WJ22	12	7.8	0.529	0.528	0.04	0.18
WJ22	13	8.748	0.497	0.483	0.033	0.39
WJ22	14	8.952	0.569	0.496	0.034	0.18
WJ22	15	7.987	0.548	0.509	0.04	0.19
WJ22	16	9.451	0.553	0.435	0.023	0.19
WJ22	17	6.523	0.374	0.543	0.031	0.31
WJ22	18	9.794	0.594	0.443	0.028	0.47
WJ22	19	9.727	0.567	0.474	0.026	0.31
WJ22	20	7.007	0.491	0.564	0.037	0.47
WJ22	21	10.03	0.653	0.444	0.026	0.05
WJ22	22	10.298	0.54	0.406	0.022	0.49
WJ22	23	6.531	0.469	0.58	0.039	0.36
WJ22	24	8.554	0.519	0.493	0.03	0.37
WJ22	25	7.168	0.405	0.584	0.037	0.13
WJ22	26	7.645	0.49	0.55	0.029	0.11
WJ22	27	8.223	0.419	0.493	0.029	0.33
WJ22	28	4.95	0.367	0.64	0.049	0.24
WJ22	29	9.049	0.597	0.434	0.025	0.27
WJ22	30	7.137	0.402	0.581	0.033	0.39
WJ21	1	6.944	0.578	0.602	0.045	0.36
WJ21	2	6.493	0.463	0.609	0.048	0.39
WJ21	3	8.123	0.541	0.493	0.027	0.27
WJ21	4	11.682	0.682	0.385	0.02	0.26
WJ21	5	9.871	0.643	0.444	0.026	0.37
WJ21	6	9.174	0.471	0.435	0.022	0.04
WJ21	7	8.539	0.525	0.513	0.031	0.5
WJ21	8	12.771	0.636	0.308	0.017	0.2
WJ21	9	7.178	0.515	0.547	0.036	0.51
WJ21	10	8.285	0.549	0.481	0.026	0.31
WJ21	11	16.077	0.93	0.187	0.01	0.18
WJ21	12	11.074	0.564	0.38	0.022	0.16

Continued on next page

Continued from previous page

Sample name	Spot no.	$^{238}U/^{206}Pb$	2σ	$^{207}Pb/^{206}Pb$	2σ	ρ
WJ21	13	9.25	0.547	0.478	0.029	0.45
WJ21	14	7.267	0.58	0.527	0.047	0.53
WJ21	15	8.163	0.506	0.508	0.034	0.63
WJ21	16	7.547	0.472	0.555	0.035	0.38
WJ21	17	9.157	0.805	0.402	0.029	-0.31
WJ21	18	6.15	0.31	0.579	0.027	0.26
WJ21	19	7.122	0.385	0.516	0.025	0.29
WJ21	20	13.679	0.729	0.302	0.014	0.26
WJ21	21	7.479	0.408	0.56	0.039	0.37
WJ21	22	8.347	0.466	0.534	0.032	0.27
WJ21	23	6.329	0.48	0.575	0.033	0.5
WJ21	24	7.955	0.462	0.509	0.034	0.52
WJ21	25	7.874	0.508	0.547	0.029	0.21
WJ21	26	12.61	0.747	0.357	0.02	0.41
WJ21	27	8.568	0.587	0.489	0.035	0.62
WJ21	28	8.223	0.52	0.506	0.036	0.39
WJ21	29	13.175	0.659	0.31	0.02	0.38
WJ21	30	12.18	0.548	0.324	0.021	0.22
WJ21	31	7.042	0.456	0.556	0.03	0.24
WJ21	32	8.68	0.467	0.514	0.036	0.22
WJ21	33	8.865	0.558	0.477	0.035	0.46
WJ21	34	14.409	0.872	0.242	0.021	-0.23
WJ21	35	5.747	0.429	0.6	0.038	0.44
WJ21	36	12.886	0.564	0.337	0.019	0.12
WJ21	37	8.403	0.487	0.527	0.027	0.17
WJ21	38	8.673	0.624	0.485	0.032	0.25
WJ21	39	8.169	0.527	0.524	0.036	-0.15
WJ21	40	13.003	0.558	0.31	0.021	0.06
WJ19	1	7.042	0.545	0.464	0.03	0.38
WJ19	2	7.961	0.443	0.436	0.024	0.2
WJ19	3	11.655	0.597	0.239	0.014	0.47
WJ19	4	11.467	0.552	0.243	0.012	0.04
WJ19	5	3.448	0.237	0.675	0.038	0.34
WJ19	6	4.166	0.277	0.622	0.037	0.55
WJ19	7	6.978	0.443	0.445	0.027	0.54
WJ19	8	4.587	0.294	0.621	0.033	0.36
WJ19	9	1.801	0.103	0.741	0.024	0.22
WJ19	10	10.66	0.716	0.339	0.027	0.55
WJ19	11	3.012	0.254	0.655	0.035	0.31
WJ19	12	6.024	0.435	0.537	0.026	0.42
WJ19	13	4.728	0.268	0.582	0.029	0.25
WJ19	14	8.779	0.447	0.384	0.014	0.12
WJ19	15	10.718	0.539	0.28	0.012	0.08
WJ19	16	7.61	0.434	0.474	0.021	0.3

Continued on next page

Continued from previous page

Sample name	Spot no.	$^{238}U/^{206}Pb$	2σ	$^{207}Pb/^{206}Pb$	2σ	ρ
WJ19	18	6.253	0.332	0.519	0.028	0.21
WJ01	1	1.831	0.144	0.836	0.051	0.39
WJ01	2	4.291	0.276	0.732	0.046	0.32
WJ01	3	6.535	0.64	0.569	0.05	0.23
WJ01	4	9.389	0.819	0.452	0.037	0.26
WJ01	5	4.366	0.324	0.737	0.042	0.24
WJ01	6	17.123	0.908	0.195	0.011	0.05
WJ01	7	17.953	0.902	0.1787	0.007	-0.02
WJ01	8	14.492	0.966	0.328	0.022	-0.2
WJ01	9	4.273	0.237	0.683	0.036	0.51
WJ01	10	3.508	0.233	0.731	0.042	0.36
WJ01	11	5.128	0.341	0.635	0.039	0.49
WJ01	12	3.584	0.244	0.761	0.042	0.24
WJ01	13	15.822	1.301	0.277	0.02	0.16
WJ01	14	3.546	0.251	0.764	0.058	0.57
WJ01	16	5.681	0.419	0.632	0.034	0.3
WJ01	17	3.267	0.234	0.703	0.044	0.44
WJ01	19	4.115	0.254	0.777	0.05	0.36
WJ01	20	17.123	0.879	0.151	0.0065	0.31
WJ01	21	3.937	0.263	0.712	0.038	0.44
WJ01	22	1.111	0.172	0.772	0.045	0.01
WJ01	23	1.589	0.131	0.843	0.06	0.29
WJ01	24	6.024	0.508	0.646	0.046	0.11
WJ01	25	3.831	0.293	0.693	0.044	0.55
WJ02	1	11.299	0.829	0.405	0.026	0.18
WJ02	2	5.208	0.406	0.669	0.048	0.48
WJ02	3	12.787	0.817	0.303	0.025	0.35
WJ02	4	10.81	0.771	0.433	0.041	0.48
WJ02	5	4.629	0.364	0.652	0.057	0.4
WJ02	6	6.211	0.462	0.674	0.046	0.49
WJ02	7	14.992	0.809	0.264	0.023	0.01
WJ02	8	20.08	0.967	0.0956	0.0052	0.5
WJ02	9	14.144	0.84	0.294	0.022	0.38
WJ02	10	6.172	0.495	0.534	0.03	0.16
WJ02	11	5.952	0.531	0.665	0.068	-0.09
WJ02	12	13.089	0.873	0.372	0.026	0.34
WJ02	13	2.941	0.224	0.745	0.042	0.44
WJ02	14	5.347	0.486	0.703	0.063	0.46
WJ02	15	6.211	0.578	0.58	0.043	0.05
WJ02	16	8.368	0.455	0.54	0.031	0.44
WJ02	19	13.071	0.922	0.307	0.02	-0.09
WJ04	1	5.885	0.322	0.633	0.037	0.42
WJ04	2	1.564	0.134	0.753	0.048	0.4
WJ04	3	3.802	0.375	0.673	0.051	0.24

Continued on next page

Continued from previous page

Sample name	Spot no.	$^{238}U/^{206}Pb$	2σ	$^{207}Pb/^{206}Pb$	2σ	ρ
WJ04	4	1.766	0.152	0.792	0.058	0.5
WJ04	5	1.683	0.116	0.78	0.039	0.47
WJ04	6	1.631	0.149	0.858	0.048	0.32
WJ04	7	1.76	0.164	0.786	0.046	0.3
WJ04	8	1.23	0.11	0.813	0.047	0.19
WJ04	9	4.048	0.311	0.734	0.049	0.26
WJ04	10	2.824	0.183	0.772	0.046	0.38
WJ04	11	2.518	0.431	0.778	0.08	0.26
WJ04	12	1.834	0.141	0.764	0.034	0.32
WJ04	14	1.692	0.18	0.781	0.054	0.34
WJ04	15	1.321	0.101	0.818	0.048	0.33
WJ05	1	4.566	0.354	0.645	0.052	0.3
WJ05	2	7.745	0.473	0.553	0.032	0.16
WJ05	3	5.221	0.299	0.634	0.028	0.37
WJ05	4	6.25	0.507	0.564	0.032	0.52
WJ05	5	7.501	0.529	0.591	0.037	0.19
WJ05	6	6.038	0.35	0.6	0.031	0.49
WJ05	7	6.25	0.386	0.604	0.035	0.32
WJ05	8	6.369	0.446	0.637	0.036	0.13
WJ05	9	6.48	0.462	0.599	0.039	0.29
WJ05	10	4.366	0.305	0.676	0.041	0.56
WJ05	11	7.132	0.473	0.521	0.038	0.36
WJ05	12	7.173	0.457	0.537	0.038	0.47
WJ05	13	6.329	0.68	0.616	0.074	0.09
WJ05	14	4.385	0.25	0.704	0.031	0.5
WJ05	15	8.244	0.523	0.512	0.038	0.5
WJ05	16	6.134	0.414	0.608	0.043	0.28
WJ05	17	5.701	0.357	0.588	0.04	0.51
WJ05	18	2.597	0.161	0.778	0.049	0.33
WJ05	19	6.381	0.403	0.591	0.035	0.65
WJ05	20	7.012	0.408	0.567	0.043	0.29
WJ05	21	6.211	0.501	0.572	0.041	0.44
WJ05	22	6.587	0.433	0.6	0.048	0.43
WJ05	23	5.882	0.449	0.675	0.044	0.64
WJ05	24	5.181	0.322	0.663	0.04	0.46
WJ05	25	6.944	0.361	0.535	0.029	0.28
WJ05	26	4.651	0.302	0.654	0.041	0.59
WJ05	27	10.131	0.502	0.454	0.023	0.45
WJ06	1	5.376	0.52	0.644	0.064	0.66
WJ06	2	3.508	0.32	0.69	0.057	0.47
WJ06	3	7.501	0.551	0.56	0.044	0.52
WJ06	4	6.711	0.54	0.533	0.051	0.27
WJ06	5	8.583	0.655	0.487	0.039	0.29
WJ06	6	5.998	0.395	0.57	0.043	0.51

Continued on next page

Continued from previous page

Sample name	Spot no.	$^{238}U/^{206}Pb$	2σ	$^{207}Pb/^{206}Pb$	2σ	ρ
WJ06	7	4.629	0.342	0.714	0.059	0.4
WJ06	8	4.566	0.291	0.648	0.04	0.31
WJ06	9	5.494	0.422	0.632	0.046	0.39
WJ06	10	4.444	0.355	0.675	0.053	0.56
WJ06	11	9.033	0.758	0.473	0.046	0.52
WJ06	12	5.128	0.315	0.641	0.051	0.53
WJ06	14	10.373	0.807	0.441	0.058	0.43
WJ06	15	6.527	0.468	0.604	0.049	0.43
WJ06	16	12.61	0.747	0.343	0.022	0.34
WJ06	17	11.198	0.727	0.406	0.032	0.13
WJ06	18	7.042	0.644	0.591	0.051	0.61
WJ06	19	6.896	0.523	0.636	0.057	0.33
WJ06	20	8.064	0.78	0.591	0.076	0.7
WJ06	21	8.403	0.776	0.537	0.056	0.58
WJ06	22	2.785	0.217	0.734	0.051	0.28
WJ06	23	7.331	0.591	0.576	0.051	0.64
WJ06	24	5.524	0.396	0.653	0.045	0.23
WJ06	25	9.842	0.658	0.49	0.036	0.56
WJ06	26	9.066	0.706	0.512	0.051	0.42
WJ06	27	6.493	0.674	0.643	0.07	0.32
WJ06	28	8.038	0.626	0.528	0.07	0.55
WJ07	1	6.024	0.435	0.578	0.029	0.35
WJ07	2	4.016	0.29	0.723	0.06	0.4
WJ07	3	1.522	0.125	0.769	0.045	0.63
WJ07	4	4.629	0.342	0.634	0.057	0.58
WJ07	5	3.663	0.362	0.748	0.061	0.2
WJ07	6	4.291	0.349	0.713	0.044	0.48
WJ07	7	3.584	0.295	0.74	0.045	0.23
WJ07	8	5.747	0.429	0.636	0.051	0.19
WJ07	9	3.03	0.275	0.788	0.037	0.32
WJ07	10	3.787	0.243	0.693	0.05	0.19
WJ07	11	2.5	0.281	0.745	0.073	0.49
WJ07	12	4.31	0.315	0.693	0.05	0.37
WJ07	13	1.855	0.161	0.808	0.047	0.09
WJ07	14	2.331	0.173	0.768	0.051	0.28
WJ07	15	3.968	0.346	0.668	0.055	0.12
WJ07	16	2.898	0.252	0.768	0.055	-0.02
WJ07	17	2.84	0.193	0.754	0.041	0.45
WJ07	18	4.587	0.294	0.695	0.046	0.35
WJ07	19	4.761	0.362	0.649	0.041	0.36
WJ07	20	3.937	0.279	0.643	0.045	0.4
WJ07	22	4.098	0.369	0.739	0.043	0.36
WJ07	24	3.003	0.234	0.771	0.048	0.48
WJ07	25	3.558	0.227	0.671	0.034	0.22

Continued on next page

Continued from previous page

Sample name	Spot no.	$^{238}U/^{206}Pb$	2σ	$^{207}Pb/^{206}Pb$	2σ	ρ
WJ07	27	0.763	0.081	0.854	0.046	0.21
WJ07	28	2.336	0.207	0.715	0.044	0.07
WJ07	29	3.597	0.271	0.751	0.082	0.2
WJ07	30	4.524	0.266	0.668	0.039	0.51
WJ07	31	2.873	0.198	0.788	0.055	0.54
WJ07	32	7.122	0.375	0.597	0.033	0.58
WJ07	33	6.83	0.396	0.584	0.033	0.58
WJ07	35	1.937	0.176	0.757	0.043	0.26
WJ07	36	3.424	0.246	0.74	0.047	0.31
WJ07	37	4.424	0.293	0.718	0.049	0.45
WJ07	38	2.475	0.226	0.741	0.061	0.24
WJ07	39	3.401	0.323	0.778	0.056	0.35
WJ07	40	2.84	0.225	0.775	0.053	0.41
WJ08	1	5.586	0.374	0.696	0.044	0.38
WJ08	2	2.136	0.21	0.745	0.057	0.23
WJ08	3	2.5	0.218	0.814	0.068	0.53
WJ08	4	2.518	0.19	0.815	0.06	0.35
WJ08	5	4.201	0.264	0.735	0.044	0.04
WJ08	6	4.166	0.295	0.696	0.042	0.32
WJ08	7	4.854	0.329	0.664	0.039	0.31
WJ08	8	4.524	0.348	0.625	0.046	0.17
WJ08	9	3.571	0.242	0.759	0.038	0.39
WJ08	10	5.78	0.4	0.64	0.043	0.35
WJ08	11	2.375	0.248	0.801	0.073	0.36
WJ08	12	2.288	0.167	0.784	0.049	0.14
WJ08	13	2.967	0.202	0.767	0.044	0.29
WJ08	14	3.105	0.25	0.715	0.046	0.75
WJ08	15	3.448	0.214	0.729	0.045	0.21
WJ08	16	2.32	0.204	0.8	0.059	0.47
WJ08	17	2.958	0.218	0.716	0.052	0.27
WJ08	18	1.416	0.136	0.785	0.054	0.13
WJ08	19	1.225	0.106	0.785	0.048	0.26
WJ08	21	2.777	0.231	0.771	0.05	0.06
WJ08	22	1.808	0.166	0.8	0.071	0.55
WJ08	24	2.754	0.394	0.74	0.12	0.15
WJ08	25	2.336	0.201	0.719	0.04	0.36
WJ08	26	2.754	0.25	0.79	0.061	0.39
WJ08	27	3.484	0.254	0.747	0.04	0.38
WJ08	28	3.663	0.281	0.724	0.052	0.26
WJ08	29	3.521	0.26	0.717	0.066	0.26
WJ08	30	2.531	0.23	0.772	0.056	0.39
WJ08	31	4.219	0.338	0.702	0.054	0.47
WJ08	32	4.651	0.302	0.657	0.038	0.35
WJ08	33	5.319	0.396	0.654	0.056	0.5

Continued on next page

Continued from previous page

Sample name	Spot no.	$^{238}U/^{206}Pb$	2σ	$^{207}Pb/^{206}Pb$	2σ	ρ
WJ08	34	4.424	0.313	0.692	0.045	0.42
WJ08	35	2.994	0.188	0.728	0.042	0.38
WJ08	36	4.484	0.281	0.671	0.046	0.51
WJ08	37	1.184	0.087	0.808	0.055	0.29
WJ08	38	4.149	0.361	0.774	0.052	0.38
WJ08	39	4.347	0.378	0.707	0.058	0.35
WJ09	1	2.252	0.147	0.782	0.04	0.12
WJ09	2	3.649	0.253	0.747	0.033	0.18
WJ09	3	17.241	0.743	0.236	0.014	-0.22
WJ09	4	2.409	0.156	0.771	0.047	0.52
WJ09	5	1.818	0.132	0.77	0.046	0.1
WJ09	6	2.732	0.216	0.789	0.057	0.45
WJ09	7	3.125	0.224	0.767	0.051	0.46
WJ09	9	4.081	0.249	0.708	0.033	0.39
WJ09	10	1.107	0.095	0.865	0.059	0.48
WJ09	11	1.766	0.146	0.784	0.045	0.38
WJ09	12	2.865	0.205	0.771	0.038	0.27
WJ09	13	16.611	0.993	0.233	0.012	0.2
WJ09	15	3.584	0.192	0.753	0.036	0.52
WJ09	16	3.424	0.246	0.742	0.04	0.38
WJ09	17	3.584	0.231	0.739	0.036	0.63
WJ09	18	3.076	0.198	0.755	0.043	0.35
WJ09	19	2.666	0.149	0.777	0.039	0.2
WJ09	20	3.533	0.224	0.703	0.033	0.47
WJ09	21	2.59	0.154	0.8	0.045	0.54
WJ09	22	1.562	0.109	0.826	0.037	0.22
WJ09	23	3.174	0.211	0.758	0.05	0.38
WJ09	24	2.222	0.148	0.813	0.037	0.35
WJ09	25	1.968	0.131	0.815	0.038	0.61
WJ09	26	2.518	0.164	0.756	0.034	0.22
WJ09	27	3.067	0.244	0.713	0.036	0.42
WJ09	29	2.518	0.133	0.807	0.04	0.03
WJ09	30	2.577	0.225	0.783	0.083	0.48
WJ09	31	1.512	0.107	0.792	0.038	0.31
WJ09	32	2.207	0.151	0.806	0.037	0.19
WJ10	1	2.617	0.157	0.759	0.047	0.46
WJ10	2	4.854	0.329	0.681	0.057	0.43
WJ10	3	1.724	0.139	0.885	0.048	0.45
WJ10	4	2.673	0.185	0.752	0.035	0.17
WJ10	5	2.652	0.182	0.752	0.029	0.21
WJ10	6	2.421	0.181	0.738	0.033	-0.03
WJ10	7	1.706	0.122	0.835	0.042	0.22
WJ10	8	1.584	0.11	0.818	0.045	0.45
WJ10	9	2.386	0.125	0.773	0.038	0.25

Continued on next page

Continued from previous page

Sample name	Spot no.	$^{238}U/^{206}Pb$	2σ	$^{207}Pb/^{206}Pb$	2σ	ρ
WJ10	10	1.988	0.134	0.814	0.044	0.47
WJ10	11	2.724	0.193	0.791	0.055	-0.08
WJ11	1	2.597	0.175	0.806	0.041	0.37
WJ11	2	3.144	0.207	0.734	0.042	0.48
WJ11	3	2.923	0.205	0.746	0.043	0.08
WJ11	4	3.558	0.215	0.725	0.041	0.3
WJ11	5	3.378	0.216	0.732	0.049	0.39
WJ11	7	1.633	0.162	0.797	0.051	0.23
WJ11	8	7.251	0.362	0.523	0.023	0.25
WJ11	9	2.754	0.212	0.734	0.044	0.61
WJ11	10	2.487	0.179	0.789	0.039	0.37
WJ11	11	3.225	0.249	0.747	0.045	0.43
WJ11	12	0.099	0.024	0.85	0.15	0.37
WJ11	13	3.816	0.247	0.756	0.036	0.3
WJ11	14	1.779	0.129	0.764	0.03	0.27
WJ11	15	4.31	0.26	0.72	0.038	0.47
WJ11	16	1.655	0.156	0.747	0.05	-0.18
WJ11	17	2.84	0.201	0.764	0.036	0.41
WJ11	18	4.184	0.262	0.75	0.044	0.53
WJ11	19	5.263	0.304	0.638	0.032	0.67
WJ11	20	2.061	0.157	0.767	0.043	0.42
WJ11	21	2.403	0.19	0.772	0.047	0.27
WJ11	22	1.93	0.119	0.801	0.049	0.28
WJ11	23	2.932	0.18	0.785	0.036	0.47
WJ11	24	2.123	0.18	0.718	0.042	0.49
WJ11	25	2.801	0.204	0.754	0.042	0.59
WJ11	26	2.906	0.202	0.705	0.045	0.51
WJ11	27	3.194	0.183	0.749	0.039	0.24
WJ11	28	4.149	0.223	0.706	0.026	0.26
WJ11	29	2.403	0.15	0.767	0.043	0.48
WJ11	30	2.583	0.173	0.735	0.037	0.04
WJ11	31	2.881	0.166	0.765	0.041	0.15
WJ11	32	3.154	0.208	0.757	0.037	0.4
WJ11	33	3.3	0.261	0.762	0.048	0.32
WJ11	34	2.293	0.163	0.736	0.045	0.44
WJ11	35	2.617	0.171	0.805	0.049	0.29
WJ11	36	2.016	0.113	0.798	0.032	0.38
WJ12	1	6.215	0.32	0.595	0.034	0.61
WJ12	2	2.032	0.185	0.777	0.04	0.48
WJ12	3	8.841	0.445	0.483	0.025	0.46
WJ12	4	4.065	0.297	0.708	0.043	0.71
WJ12	5	7.256	0.405	0.599	0.037	0.48
WJ12	7	8.787	0.54	0.47	0.029	0.47
WJ12	8	4.366	0.228	0.661	0.038	0.35

Continued on next page

Continued from previous page

Sample name	Spot no.	$^{238}U/^{206}Pb$	2σ	$^{207}Pb/^{206}Pb$	2σ	ρ
WJ12	9	3.134	0.206	0.699	0.039	0.31
WJ12	10	3.61	0.221	0.684	0.039	0.19
WJ12	11	11.198	0.564	0.383	0.019	0.32
WJ12	12	5.211	0.298	0.668	0.027	0.19
WJ12	13	3.533	0.224	0.742	0.035	0.37
WJ12	14	5.235	0.328	0.666	0.036	0.3
WJ12	15	3.61	0.273	0.7	0.039	0.33
WJ12	16	4.587	0.315	0.704	0.045	0.16
WJ12	17	4.878	0.285	0.647	0.037	0.2
WJ12	18	5.497	0.259	0.652	0.033	0.43
WJ12	19	5.494	0.603	0.58	0.065	0.48
WJ12	20	2.409	0.168	0.752	0.043	0.21
WJ12	21	2.557	0.202	0.742	0.044	0.42
WJ12	22	3.875	0.315	0.684	0.046	0.24
WJ12	23	3.267	0.192	0.767	0.041	0.17
WJ12	24	6.06	0.514	0.626	0.057	0.59
WJ12	25	4.524	0.266	0.679	0.038	0.16
WJ12	26	8.285	0.439	0.543	0.033	0.48
WJ12	27	7.704	0.415	0.527	0.024	0.39
WJ12	28	10.288	0.497	0.406	0.027	0.57
WJ12	29	5.339	0.313	0.659	0.036	0.29
WJ12	30	4.424	0.254	0.69	0.035	0.51
WJ12	31	3.921	0.246	0.69	0.04	0.41
WJ12	33	9.199	0.541	0.483	0.029	0.44
WJ13	1	4.149	0.361	0.686	0.036	0.51
WJ13	2	4.219	0.284	0.713	0.041	0.48
WJ13	3	2.336	0.158	0.773	0.043	0.42
WJ13	4	3.46	0.335	0.691	0.046	0.42
WJ13	6	4.366	0.286	0.699	0.049	0.41
WJ13	7	3.355	0.315	0.775	0.056	0.53
WJ13	8	2.958	0.227	0.733	0.048	0.34
WJ13	9	4.016	0.241	0.746	0.05	0.09
WJ13	10	4.219	0.302	0.773	0.048	0.43
WJ13	11	3.968	0.251	0.743	0.046	0.38
WJ13	12	3.378	0.228	0.735	0.049	0.62
WJ13	13	3.816	0.262	0.701	0.037	0.33
WJ13	14	7.763	0.566	0.546	0.029	0.26
WJ13	15	3.322	0.231	0.707	0.044	0.35
WJ13	16	3.412	0.198	0.692	0.034	0.5
WJ13	17	2.724	0.193	0.788	0.052	0.45
WJ13	18	3.355	0.247	0.705	0.038	0.57
WJ13	19	3.048	0.213	0.737	0.043	0.57
WJ13	20	2.604	0.176	0.794	0.038	0.07
WJ13	21	3.69	0.245	0.709	0.032	0.38

Continued on next page

Continued from previous page

Sample name	Spot no.	$^{238}U/^{206}Pb$	2σ	$^{207}Pb/^{206}Pb$	2σ	ρ
WJ13	22	4.237	0.269	0.72	0.04	0.39
WJ13	23	4.504	0.284	0.727	0.042	0.47
WJ13	24	3.267	0.245	0.732	0.035	0.22
WJ13	25	3.174	0.211	0.724	0.041	0
WJ13	26	4.032	0.243	0.703	0.034	0.39
WJ13	27	6.949	0.453	0.632	0.044	0.43
WJ13	28	3.968	0.251	0.701	0.041	0.33
WJ13	29	3.759	0.211	0.736	0.042	0.33
WJ13	30	2.816	0.301	0.736	0.066	0.49
WJ13	31	3.717	0.276	0.705	0.045	0.37
WJ13	32	5.319	0.396	0.756	0.053	0.33
WJ13	33	4.149	0.275	0.7	0.034	0.2
WJ13	34	2.525	0.153	0.707	0.041	0.45
WJ13	35	3.205	0.236	0.774	0.051	0.39
WJ13	36	4.504	0.263	0.675	0.039	0.48
WJ13	37	3.436	0.212	0.714	0.038	0.38
WJ13	38	3.875	0.24	0.732	0.046	0.47
WJ13	39	4.166	0.208	0.695	0.036	0.44
WJ13	40	6.172	0.369	0.595	0.042	0.5
WJ16	1	7.587	0.483	0.612	0.06	0.07
WJ16	2	7.818	0.446	0.516	0.021	0.64
WJ16	3	8.896	0.467	0.554	0.031	0.61
WJ16	4	7.53	0.493	0.525	0.022	0.21
WJ16	7	7.501	0.393	0.576	0.026	0.45
WJ16	9	10.706	0.905	0.445	0.036	-0.06
WJ16	10	12.642	0.783	0.364	0.024	0.5
WJ16	11	7.782	0.526	0.539	0.028	0.04
WJ16	18	7.917	0.413	0.545	0.027	0.13
WJ16	19	5.464	0.507	0.59	0.067	0.41
WJ16	21	7.692	0.585	0.522	0.026	0.33
WJ16	22	8.695	0.491	0.517	0.024	0.46
WJ16	23	6.747	0.336	0.571	0.029	0.63
WJ16	24	6.849	0.389	0.522	0.026	0.37
WJ16	25	6.693	0.394	0.588	0.034	0.67
WJ16	26	5.714	0.391	0.564	0.035	0.03
WJ16	29	9.478	0.53	0.462	0.02	0.23
WJ16	33	7.936	0.604	0.526	0.038	0.61
WJ16	34	7.836	0.442	0.587	0.03	0.15
WJ16	36	6.25	0.585	0.589	0.038	0.42
WJ16	37	7.722	0.5	0.528	0.028	0.65
WJ17	1	3.401	0.219	0.717	0.049	0.54
WJ17	2	2.857	0.195	0.758	0.039	0.52
WJ17	3	4	0.272	0.718	0.045	0.59
WJ17	4	4.504	0.304	0.671	0.028	0.26

Continued on next page

Continued from previous page

Sample name	Spot no.	$^{238}U/^{206}Pb$	2σ	$^{207}Pb/^{206}Pb$	2σ	ρ
WJ17	5	7.53	0.43	0.571	0.026	0.3
WJ17	6	2.207	0.146	0.793	0.044	0.42
WJ17	7	3.968	0.22	0.679	0.034	0.58
WJ17	8	4.366	0.286	0.723	0.032	-0.05
WJ17	9	3.311	0.219	0.751	0.04	0.39
WJ17	10	2.557	0.176	0.751	0.04	0.27
WJ17	11	6.944	0.626	0.562	0.057	0.49
WJ17	12	11.976	0.659	0.341	0.016	-0.17
WJ17	14	9.478	0.53	0.512	0.02	0.49
WJ17	15	8.944	0.616	0.5	0.045	0.11
WJ17	16	4.484	0.261	0.673	0.033	0.41
WJ17	17	11.682	0.559	0.44	0.021	0.57
WJ17	18	9.372	0.562	0.543	0.032	0.34
WJ17	19	3.115	0.223	0.745	0.048	0.63
WJ17	20	7.097	0.503	0.528	0.055	0.47
WJ17	21	17.605	0.712	0.198	0.0069	0.25
WJ17	22	3.676	0.283	0.718	0.042	0.12
WJ17	23	16	0.665	0.253	0.012	0.22
WJ17	24	4.237	0.287	0.733	0.056	0.28
WJ18	1	5.291	0.391	0.656	0.034	0.14
WJ18	2	3.46	0.167	0.721	0.029	0.32
WJ18	3	3.571	0.255	0.729	0.055	0.77
WJ18	4	2.132	0.159	0.775	0.046	0.46
WJ18	6	2.865	0.172	0.778	0.032	0.24
WJ18	7	3.521	0.198	0.719	0.032	0.14
WJ18	10	5.76	0.248	0.676	0.028	0.43
WJ18	12	8.561	0.403	0.533	0.032	0.43
WJ18	14	3.086	0.152	0.748	0.038	0.32
WJ18	16	4.484	0.281	0.692	0.029	0.49
WJ18	17	7.616	0.4	0.578	0.032	0.5
WJ18	20	3.436	0.212	0.699	0.033	0.26
WJ18	21	4.081	0.299	0.751	0.039	0.04
WJ18	22	3.623	0.196	0.714	0.033	0.35
WJ18	23	12.771	0.44	0.371	0.02	0.47
WJ18	24	3.597	0.181	0.719	0.04	0.24
WJ18	25	5.094	0.259	0.681	0.034	0.3
WJ18	26	15.576	0.849	0.274	0.017	-0.33
WJ18	27	3.257	0.286	0.763	0.043	0.14
WJ18	29	9.082	0.362	0.51	0.018	0.5
WJ18	30	3.448	0.19	0.742	0.046	0.11
WJ18	31	2.793	0.163	0.723	0.044	0.48
WJ18	32	2.07	0.145	0.772	0.036	0.38
WJ18	33	3.267	0.16	0.714	0.041	0.52
WJ18	34	8.968	0.402	0.562	0.027	0.44

Appendix E

Inherited structure as a control on late Paleozoic and Mesozoic tectonic reactivation in the Tarbagatai Mountains, eastern Kazakhstan: Appendix Part 1

E.1 Introduction

The supporting information presented here is divided into three sections, consisting of the supporting descriptive text, summary data and plots for the apatite fission track analysis, apatite U–Pb dating, and the thermal history modelling. For individual grain/spot analytical data and tables of confined track lengths, see the separate attached supplementary data tables.

E.2 Apatite fission track supplementary information

E.2.1 Data description

Balkhash-Yili

Samples TA-01, TA-07, and TA-27 were sampled from the area immediately to the south-east of the Chingiz-Tabagatai Fault, from the Balkhash-Yili arc. Sample TA-01 produced a central age of 204.5 ± 8.6 Ma, with a dispersion of 12% (n=37) and a P(χ^2) value of 0.14. Confined track length measurement yielded a mean track length (MTL) of 13.6 ± 1.0 μm (n=40). Sample TA-07 produced a central age of 213.4 ± 12.1 Ma, with a dispersion of 6% (n=34) and a P(χ^2) value of 0.29. Confined track length measurement yielded a MTL of 13.1 ± 1.4 μm (n=16). Sample TA-27 produced a central age of 186.6 ± 7.4 Ma, with a dispersion of 0% (n=17) and a P(χ^2) value of 0.65.

Southern Boshchekul-Chingiz

Samples taken from the Boshchekul-Chingiz arc can be divided into two categories based on their geographical location and proximity to NW-SE trending faults. Samples TA-02, TA-04, TA-05, TA-06, TA-10, TA-11, and TA-16 are in the southern section of the sampling area and are generally proximal to NW-SE striking faults. Sample TA-02 produced a central age of 258.7 ± 31.3 Ma, with a dispersion of 29% (n=20) and a P(χ^2) value of 0.13. Sample TA-04 produced a central age of 212.7 ± 20.6 Ma, with a dispersion of 11% (n=25) and a P(χ^2) value of 0.40. Sample TA-05 produced a central age of 156.8 ± 26.5 Ma, with a dispersion of 0% (n=4) and a P(χ^2) value of 0.40. Sample TA-06 produced a central age of 132.5 ± 6.0 Ma, with a dispersion of 7% (n=38) and a P(χ^2) value of 0.65. Confined track length measurement produced a MTL of 13.1 ± 1.1 μm (n=119). Sample TA-10 produced a central age of 168.3 ± 5.7 Ma, with a dispersion of 9% (n=36) and a P(χ^2) value of 0.10. Confined track length measurement produced a MTL of 13.0 ± 1.4 μm (n=100). Sample TA-11 produced a central age of 148.4 ± 8.3 Ma, with a dispersion of 12% (n=27) and a P(χ^2) value of 0.16. Confined track length measurement produced a MTL of 12.1 ± 1.5 μm (n=42). Sample TA-16 produced a central age of 150.0 ± 10.3 Ma, with a dispersion of 21% (n=32) and a P(χ^2) value of 0.02. Confined track length measurement produced a MTL of 13.2 ± 1.4 μm (n=65).

Northern Boshchekul-Chingiz

Samples TA-14, TA-15, TA-17, TA-18, TA-19, and TA-26 lie in the north of the sampled section of the Boshchekul-Chingiz arc. Sample TA-14 produced a central age of 209.7 ± 9.2 Ma, with a dispersion of 0% (n=31) and a P(χ^2) value of 0.84. Confined track length measurement produced a MTL of 13.3 ± 1.1 μm (n=33). Sample TA-15 produced a central age of 197.3 ± 18.8 Ma, with a dispersion of 35% (n=21) and a P(χ^2) value of 0.00. Confined track length measurement produced a MTL of 12.1 ± 1.7 μm (n=32). Sample TA-17 produced a central age of 192.3 ± 9.7 Ma, with a dispersion of 19% (n=34) and a P(χ^2) value of 0.00. Confined track length measurement produced a MTL of 12.1 ± 1.7 μm (n=30). Sample TA-18 produced a central age of 301.1 ± 17.3 Ma, with a dispersion of 21% (n=26) and a P(χ^2) value of 0.00. Confined track length measurement produced a MTL of 12.7 ± 1.4 μm (n=54). Sample TA-19 produced a central age of 184.5 ± 13.5 Ma, with a dispersion of 30% (n=30) and a P(χ^2) value of 0.00. Sample TA-26 produced a central age of

214.1 ± 7.4 Ma, with a dispersion of 11% (n=38) and a P(χ^2) value of 0.07. Confined track length measurement produced a MTL of 13.3 ± 1.2 μm (n=58).

Zharma-Saur

Samples TA-20, TA-22, and TA-23 were taken from the Zharma-Saur arc, to the north-east of the Boshchekul-Chingiz arc. Sample TA-20 produced a central age of 258.4 ± 7.3 Ma, with a dispersion of 0% (n=40) and a P(χ^2) value of 0.90. Confined track length measurement yielded a MTL of 13.6 ± 1.1 μm (n=45). Sample TA-22 produced a central age of 254.3 ± 10.6 Ma, with a dispersion of 10% (n=39) and a P(χ^2) value of 0.21. Confined track length measurement yielded a MTL of 13.8 ± 0.9 μm (n=71). Sample TA-23 produced a central age of 251.4 ± 13.0 Ma, with a dispersion of 23% (n=36) and a P(χ^2) value of 0.00. Confined track length measurement yielded a MTL of 13.3 ± 1.2 μm (n=91).

E.2.2 Figures

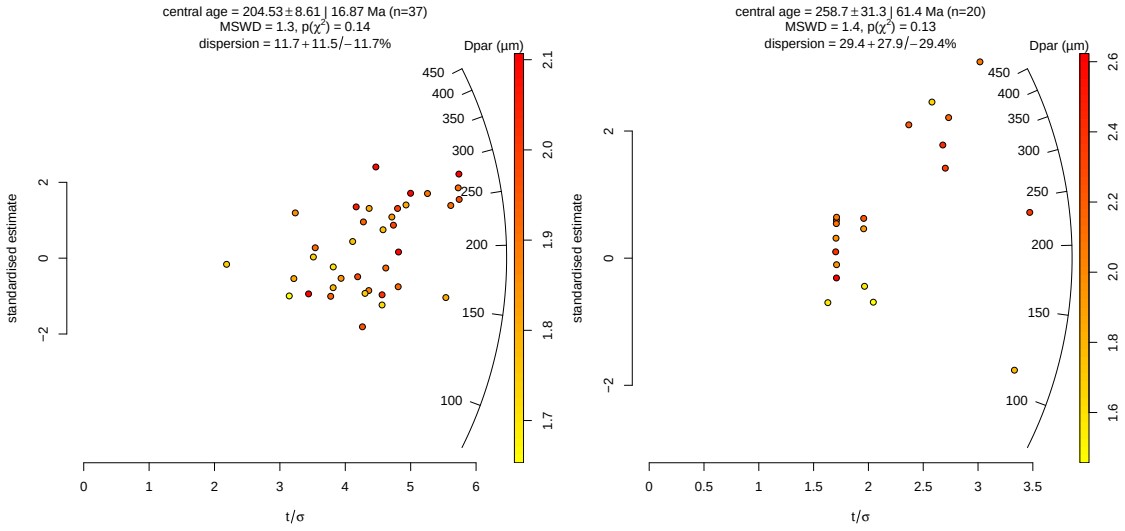

(a) Radial plot for TA01

(b) Radial plot for TA02

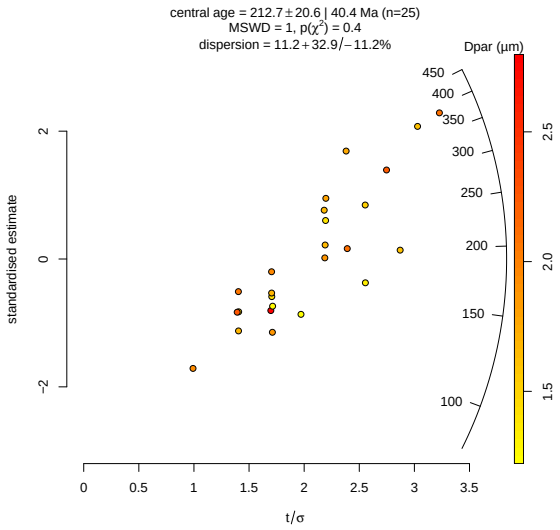

(c) Radial plot for TA04

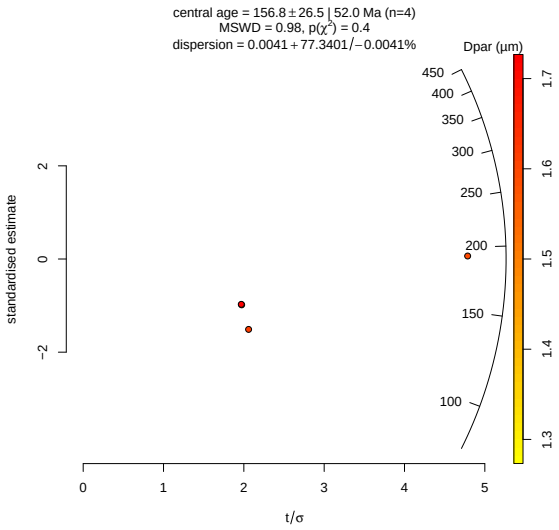

(d) Radial plot for TA05

Figure E.1: Apatite fission track radial plots.

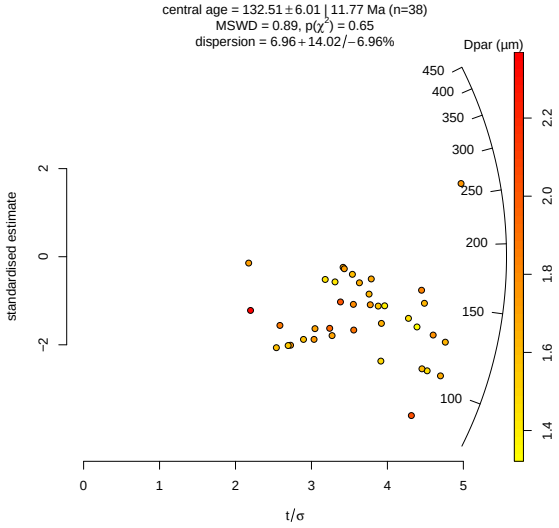

(e) Radial plot for TA06

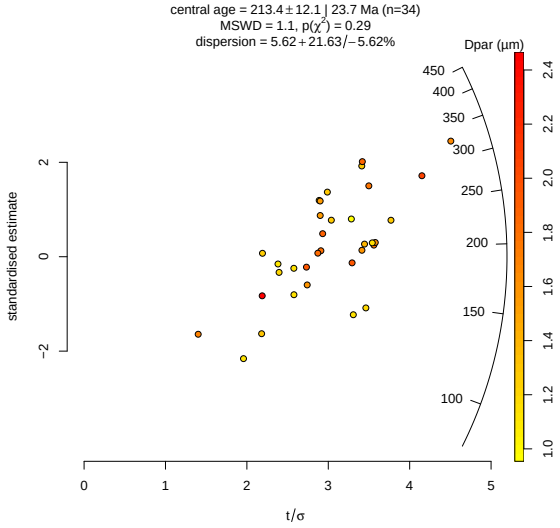

(f) Radial plot for TA07

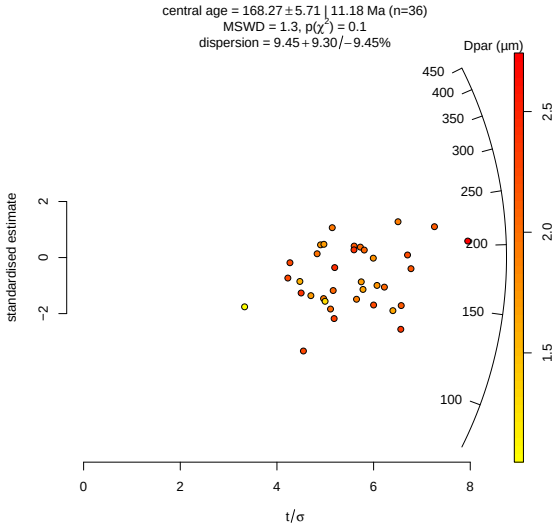

(g) Radial plot for TA10

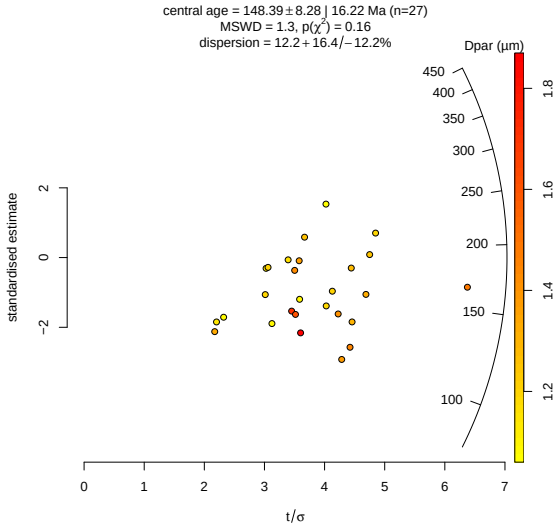

(h) Radial plot for TA11

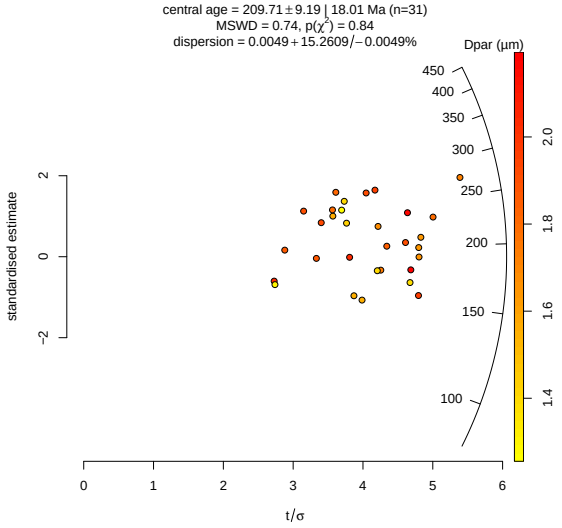

(i) Radial plot for TA14

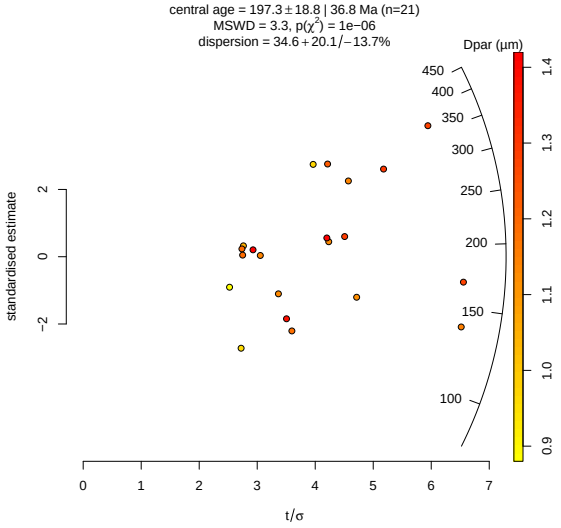

(j) Radial plot for TA15

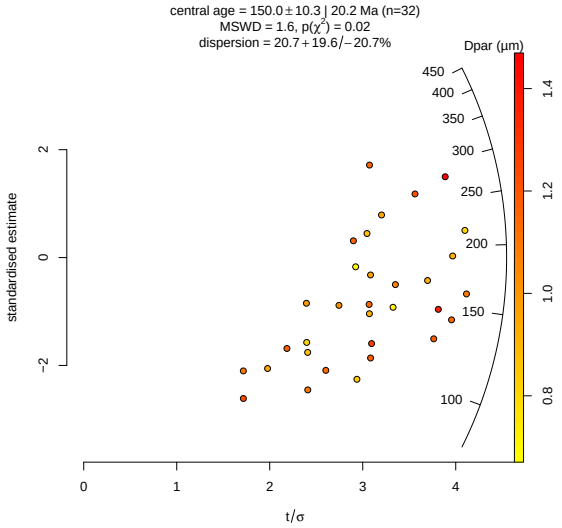

(k) Radial plot for TA16

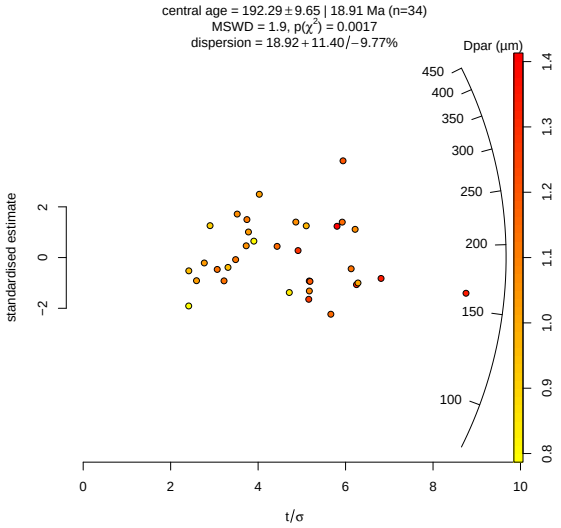

(l) Radial plot for TA17

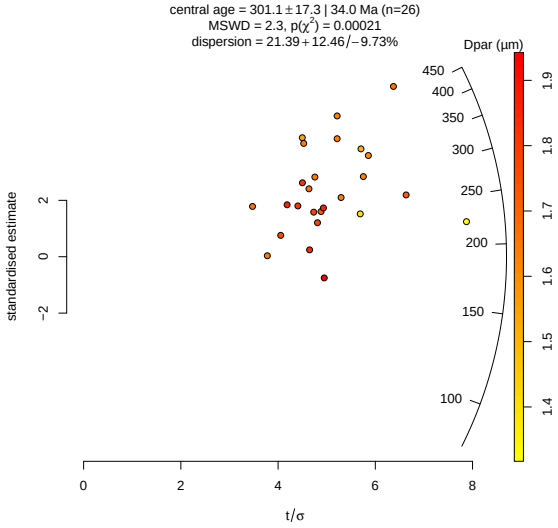

(m) Radial plot for TA18

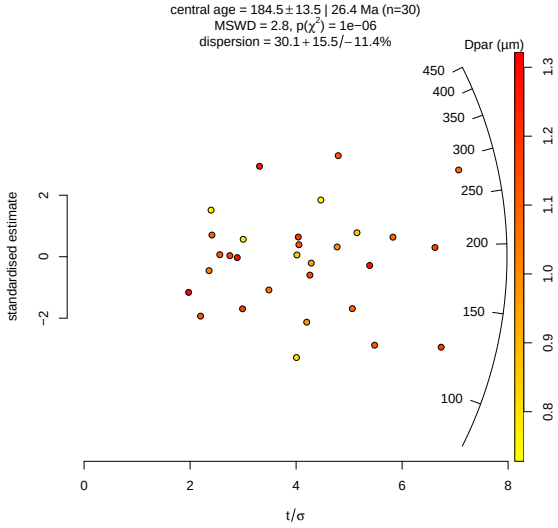

(n) Radial plot for TA19

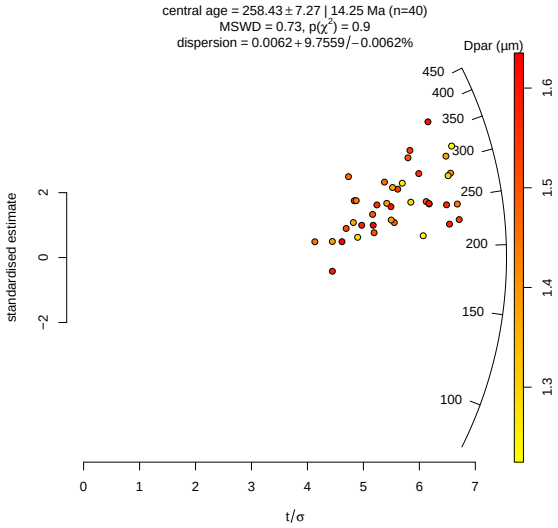

(o) Radial plot for TA20

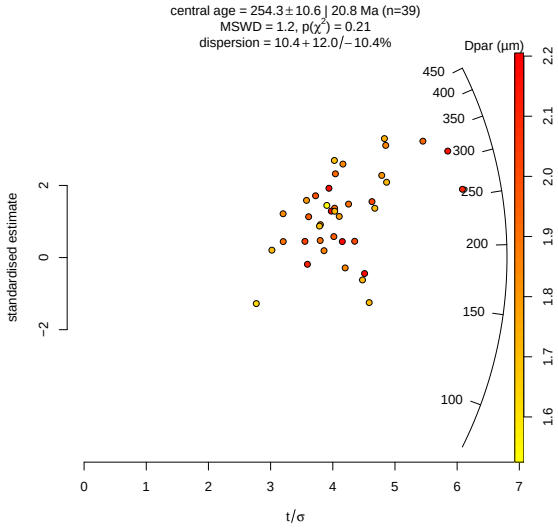

(p) Radial plot for TA22

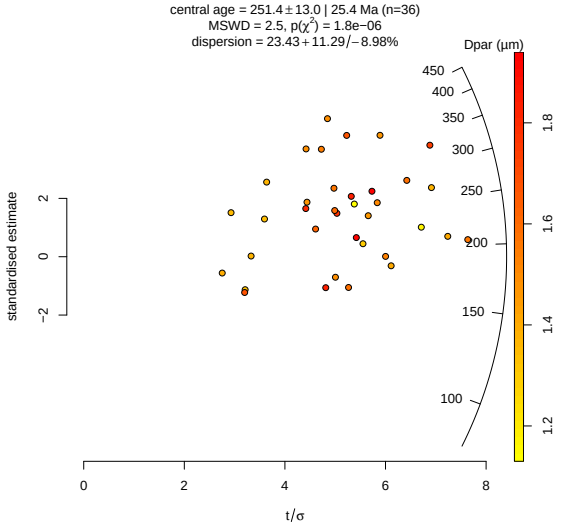

(q) Radial plot for TA23

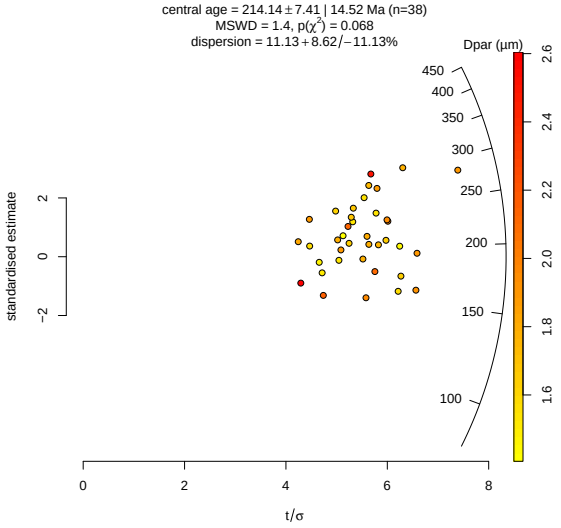

(r) Radial plot for TA26

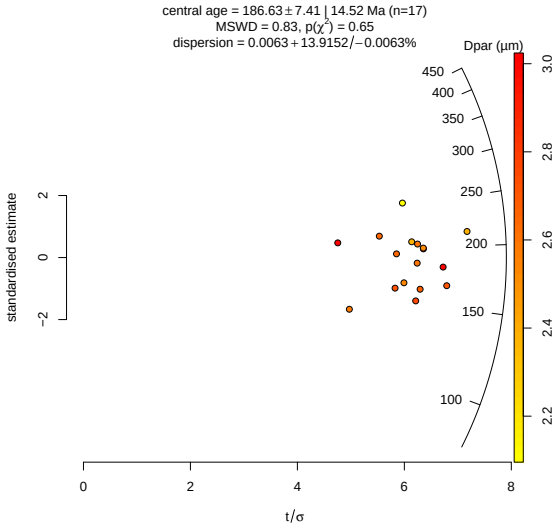

(s) Radial plot for TA27

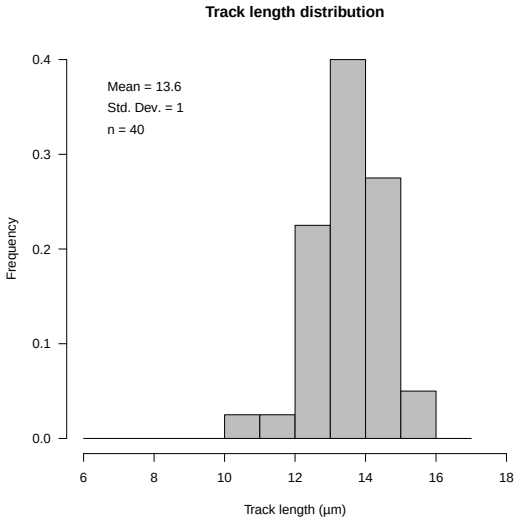

(a) Confined track length histogram for TA01

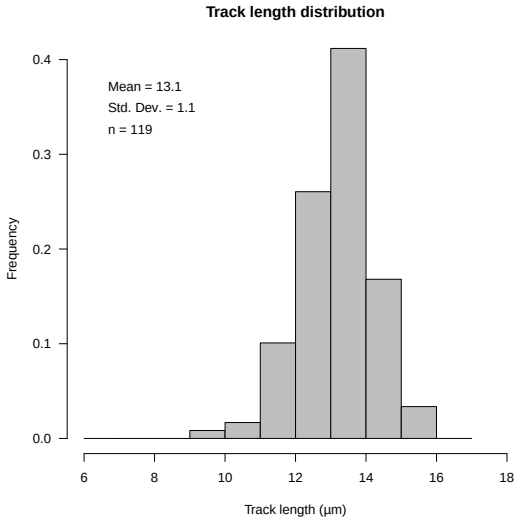

(b) Confined track length histogram for TA06

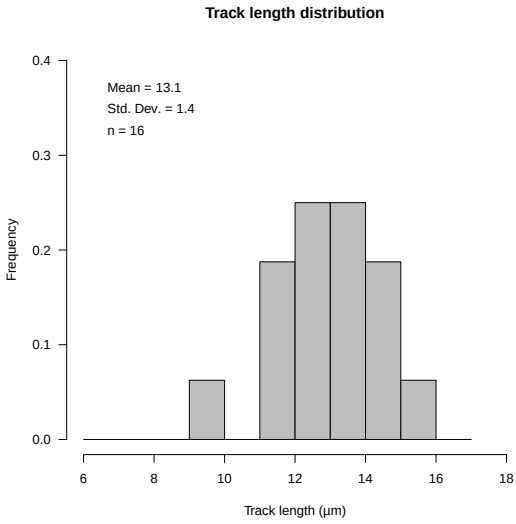

(c) Confined track length histogram for TA07

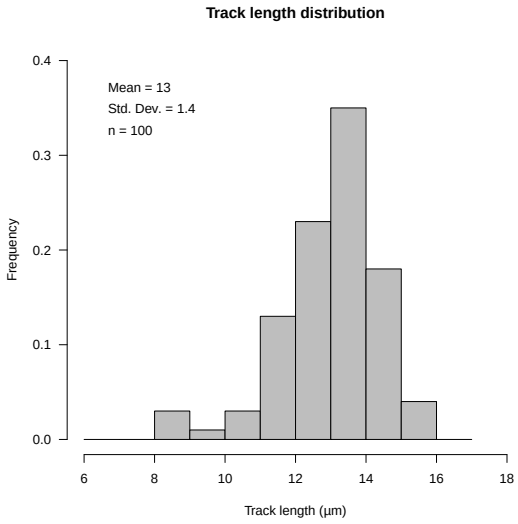

(d) Confined track length histogram for TA10

Figure E.2: Apatite confined track length histograms

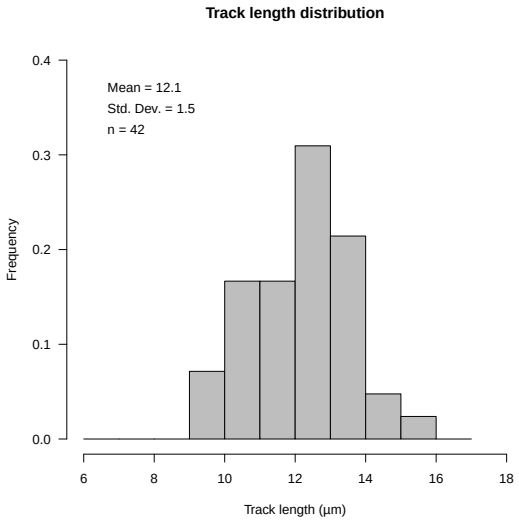

(e) Confined track length histogram for TA11

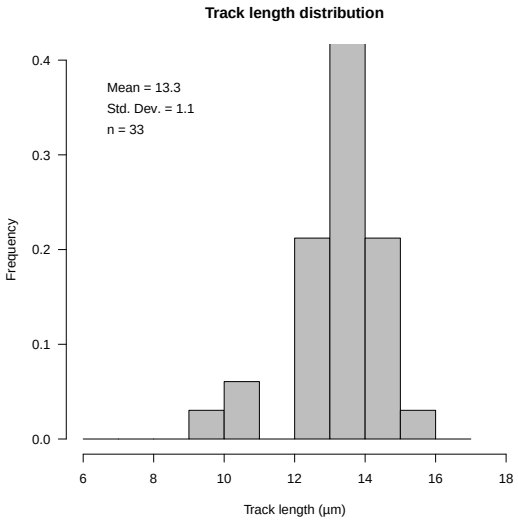

(f) Confined track length histogram for TA14

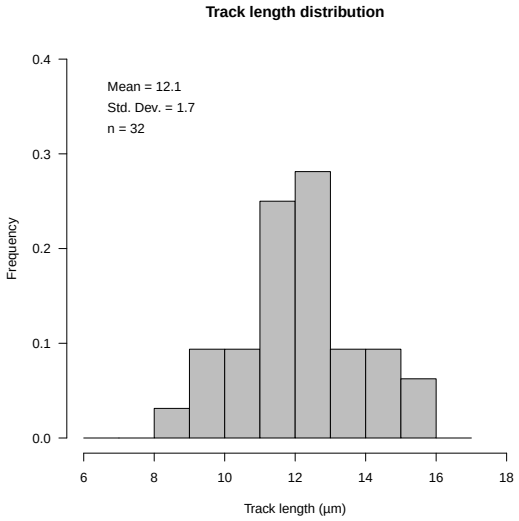

(g) Confined track length histogram for TA15

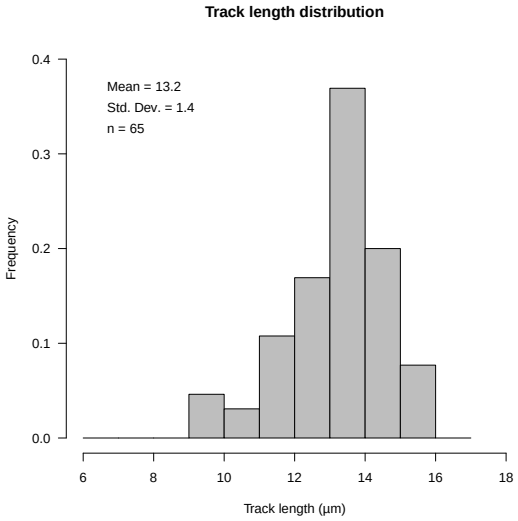

(h) Confined track length histogram for TA16

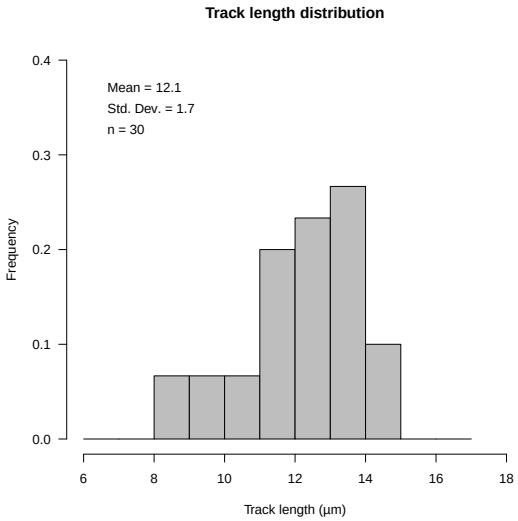

(i) Confined track length histogram for TA17

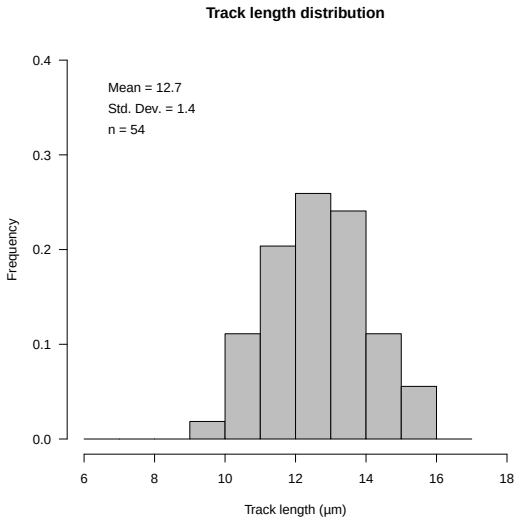

(j) Confined track length histogram for TA18

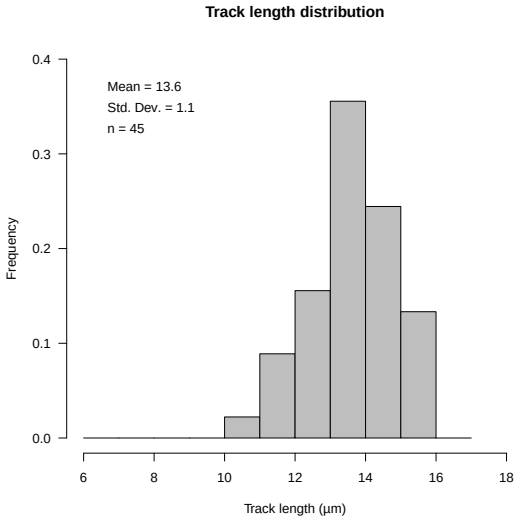

(k) Confined track length histogram for TA20

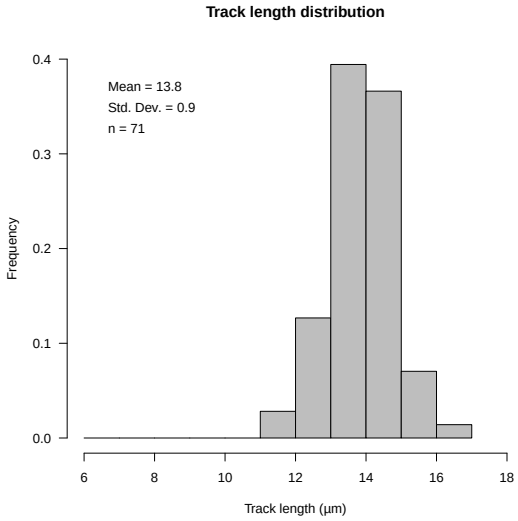

(l) Confined track length histogram for TA22

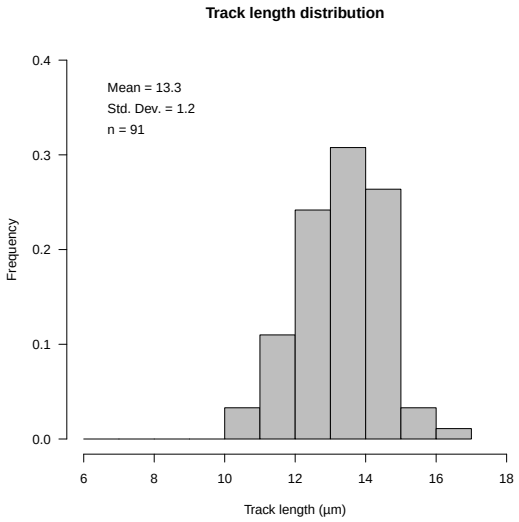

(m) Confined track length histogram for TA23

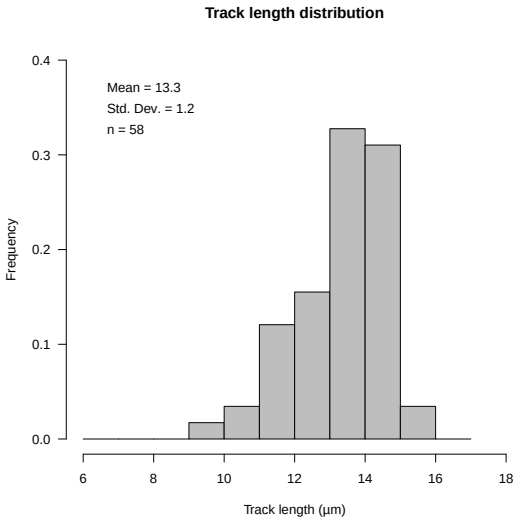

(n) Confined track length histogram for TA26

E.3 Apatite U–Pb data

E.3.1 Method

Apatite U–Pb analysis was conducted at the University of Adelaide using a NewWave UP213 laser ablation unit coupled to an Agilent 7900 mass spectrometer. During analysis the ^{204,206,207,208}Pb, ^{232}Th, and ^{238}U isotopes were measured, with the Madagascar apatite (Thomson et al., 2012) as the primary standard for instrumental drift and downhole fractionation corrections (Chew et al., 2014a). The Mt. McClure apatite (reference age 523.51 ± 2.09 Ma, Schoene and Bowring, 2006, this study, Tera-Wasserburg lower intercept age = 519.3 ± 3.6 Ma, MSWD = 1.2, n = 72) was used as a secondary standard to assess the accuracy of the data. Data reduction was performed in Iolite (Paton et al., 2011) using the "VizualAgeUcomPbine" data reduction scheme (DRS) to account for variable common Pb in the standards (Chew et al., 2014a). The apatite U–Pb dates were calculated using linear regression through a population of analyses in Tera-Wasserburg concordia space (Tera and Wasserburg, 1972), with the lower concordia intercept giving the U–Pb age of the apatite population (e.g. Gibson and Ireland, 1996). For further details on the LA-ICP-MS application of this approach see Chew et al. (2011) and Chew et al. (2014a). Isotopic data were plotted and Tera-Wasserburg lower concordia intercept ages (T-W lower intercept ages) were calculated using the IsoplotR package v.2.3 (Vermeesch, 2018) in R v.3.5.2.

E.3.2 Results

Nineteen samples produced T-W lower intercept ages as the result of apatite U–Pb analysis (Table E.1). The median relative uncertainty was 6%, and sixteen of the samples produced ages with relative uncertainties of <10%. TA04, TA05, and TA20 produced highly uncertain ages and will not be discussed further. Of the sixteen samples that produced high-quality U–Pb data, two produced early Permian ages, ten produced Carboniferous ages, and four produced Devonian ages. These age are interpreted as recording the cooling of the samples through the apatite Pb partial retention zone, usually estimated as being in the range of 370–550 °C (Cochrane et al., 2014). These ages were used to provide a high-temperature constraint during inverse thermal history modelling.

Table E.1: Apatite U–Pb data summary table

Sample	U–Pb age (Ma)	0.95 CI (Ma)	$(^{207}Pb/^{206}Pb)_o$	0.95 CI	MSWD	$P(\chi^2)$	n
TA01	349.4	19.8	0.818	0.042	0.7	0.92	39
TA02	384.6	23.1	0.847	0.023	1.6	0.057	19
TA06	314.6	30.9	0.856	0.04	1.1	0.36	37
TA07	313.5	15.3	0.869	0.032	1.2	0.2	40
TA10	417.2	14.7	0.844	0.073	0.96	0.52	31
TA11	396.6	10.9	0.891	0.031	1.1	0.37	31
TA14	298.6	21.1	0.854	0.032	1.1	0.34	33
TA15	320.5	19.3	0.86	0.035	5.1	0	18
TA16	410.6	18.8	0.897	0.027	1	0.45	36
TA17	282.0	9.7	0.868	0.0093	1.1	0.25	40
TA18	329.9	10.4	0.884	0.02	1.2	0.17	29
TA19	323.4	11.5	0.886	0.011	1.1	0.31	30
TA22	326.8	20.9	0.89	0.016	1.1	0.32	40
TA23	317.5	7.5	0.878	0.013	1.2	0.18	39
TA26	324.7	24.1	0.882	0.033	0.8	0.8	40
TA27	309.9	20.3	0.82	0.104	0.97	0.48	17
Poorly defined							
TA04	*241.6*	*97.5*	*0.744*	*0.047*	*3*	*0*	*17*
TA05	*400.4*	*155.9*	*0.901*	*0.192*	*4*	*0.018*	*4*
TA20	*353.2*	*72.9*	*0.891*	*0.04*	*1.1*	*0.32*	*40*

U–Pb age refers to the lower concordia intercept age calculated by IsoplotR (Vermeesch, 2018). 0.95 CI is the 95% confidence interval of the calculated value. $(^{207}Pb/^{206}Pb)_o$ is the upper (y-axis) intercept of the linear regression through apatite U–Pb analyses.

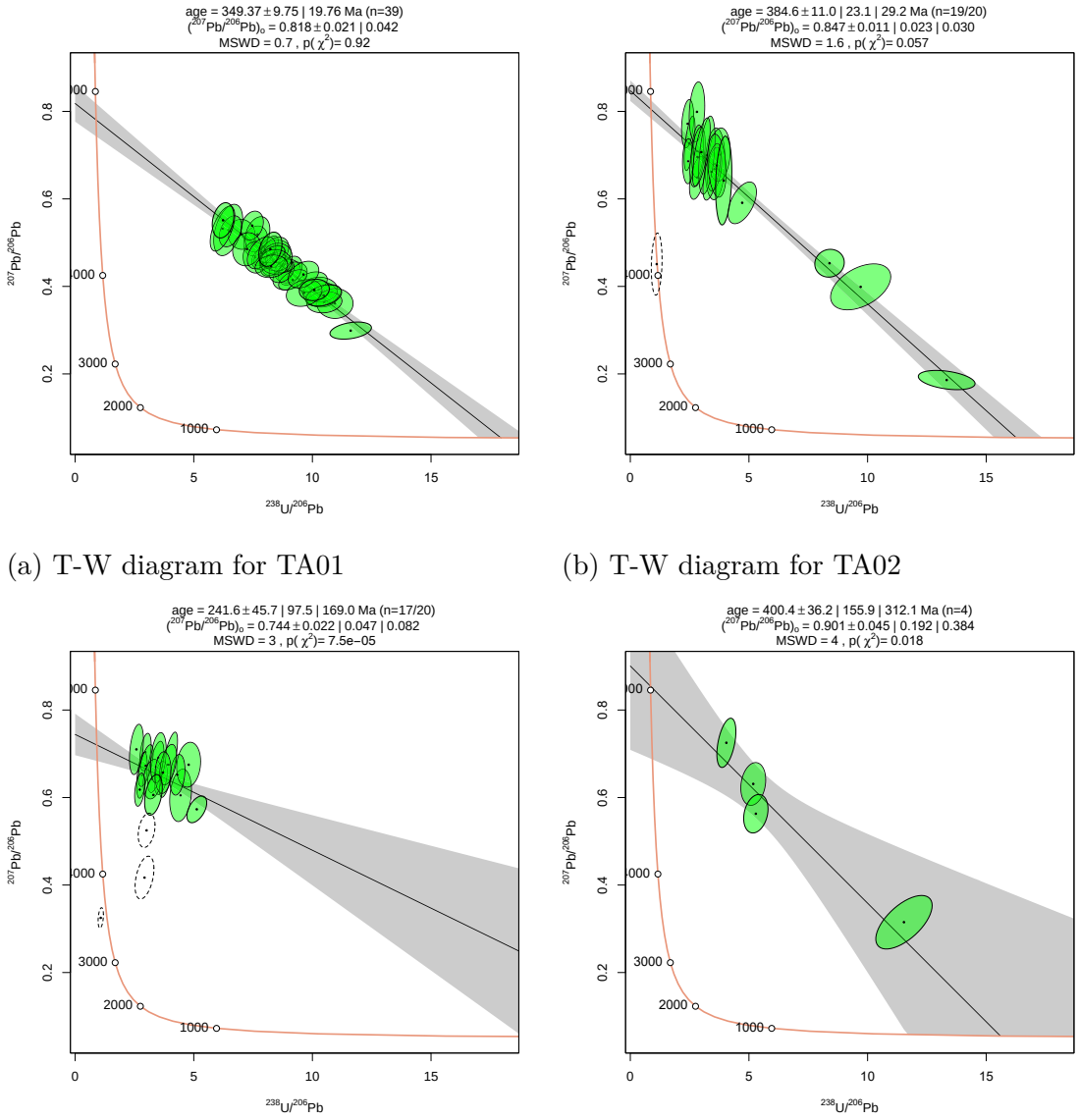

(a) T-W diagram for TA01

(b) T-W diagram for TA02

(c) T-W diagram for TA04

(d) T-W diagram for TA05

Figure E.3: Apatite U–Pb Tera-Wasserburg inverse concordia diagrams. Ellipses are 2σ. Black line is linear regression through apatite U–Pb data. Grey envelope indicates range of 95% confidence interval of linear regression. Dashed ellipses indicate analyses excluded from linear regression.

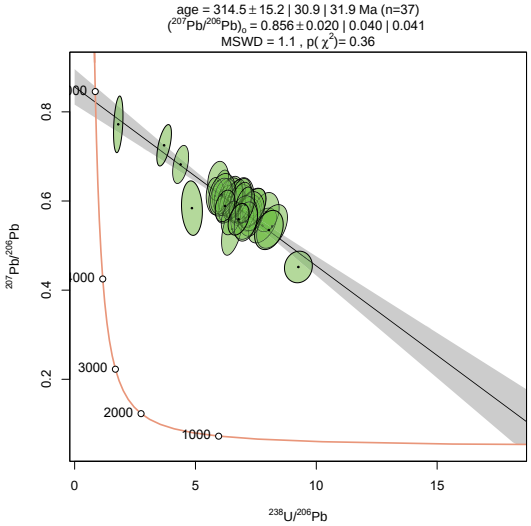

(e) T-W diagram for TA06

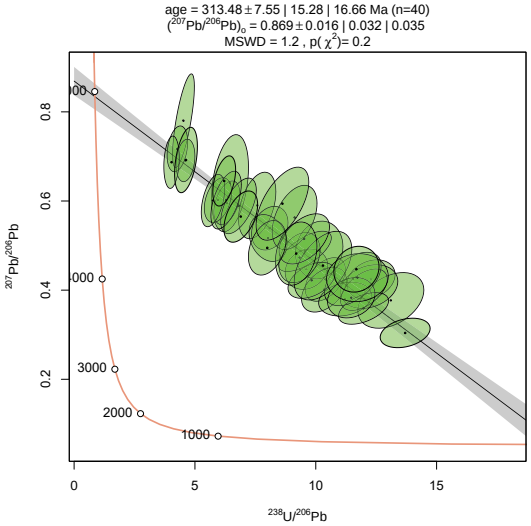

(f) T-W diagram for TA07

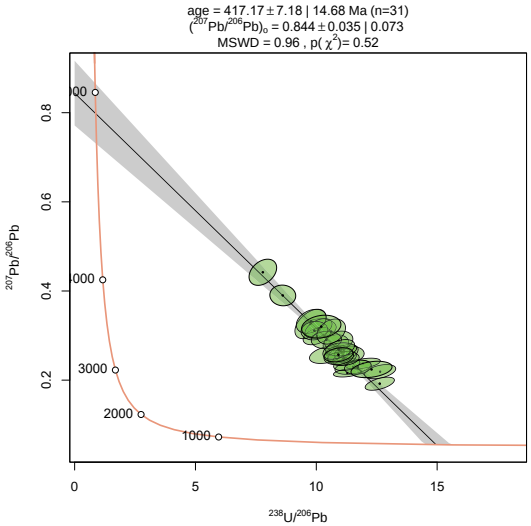

(g) T-W diagram for TA10

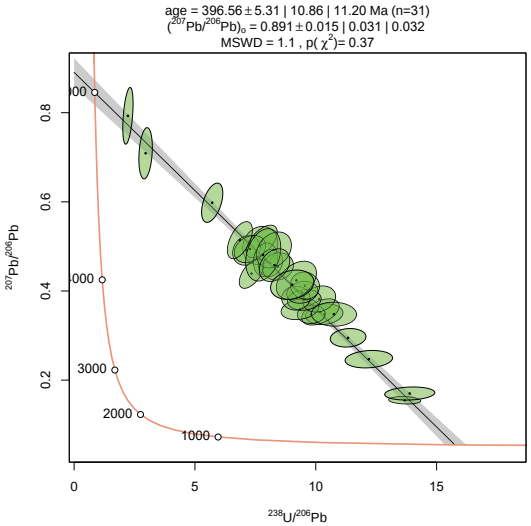

(h) T-W diagram for TA11

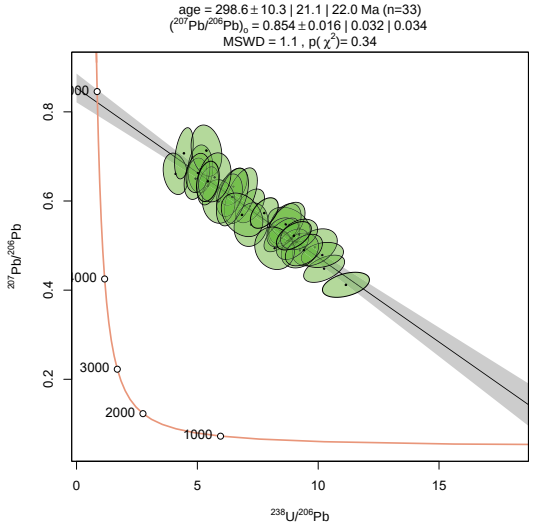

(i) T-W diagram for TA14

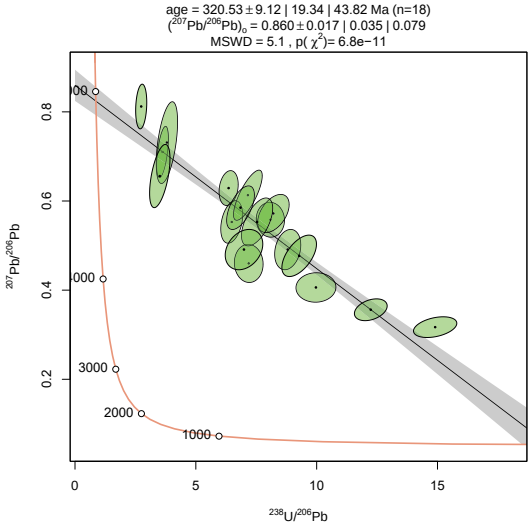

(j) T-W diagram for TA15

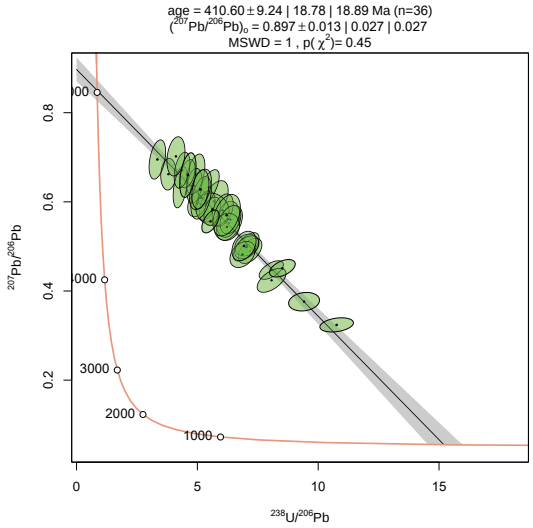

(k) T-W diagram for TA16

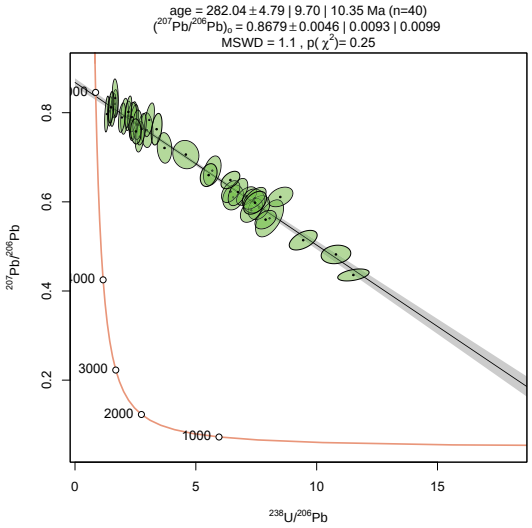

(l) T-W diagram for TA17

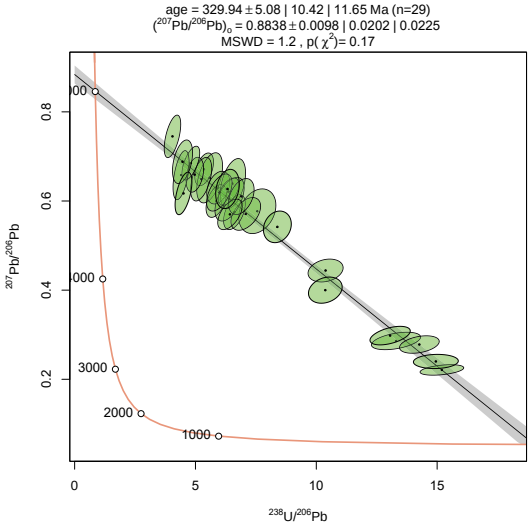

(m) T-W diagram for TA18

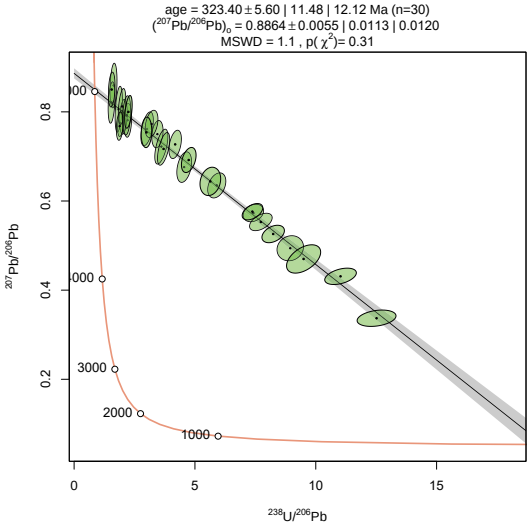

(n) T-W diagram for TA19

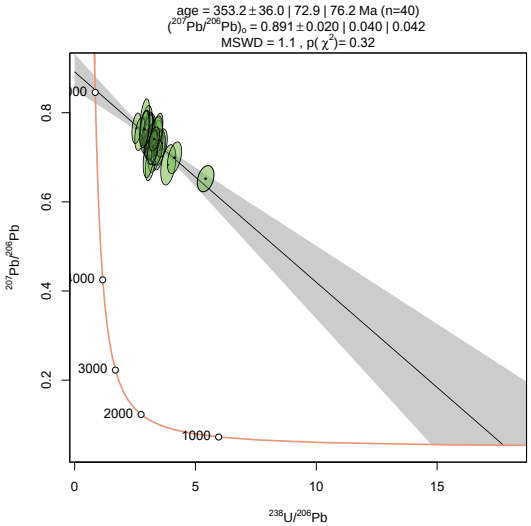

(o) T-W diagram for TA20

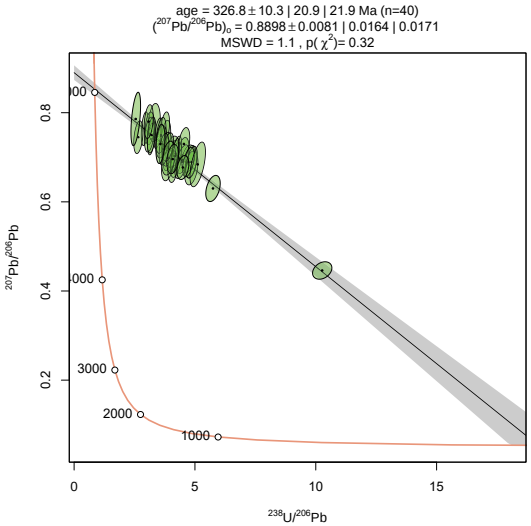

(p) T-W diagram for TA22

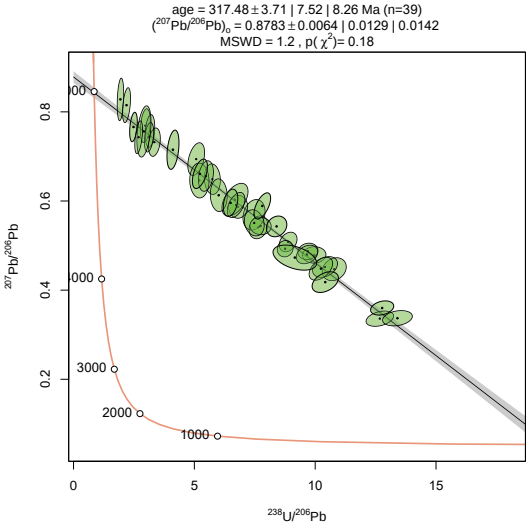

(q) T-W diagram for TA23

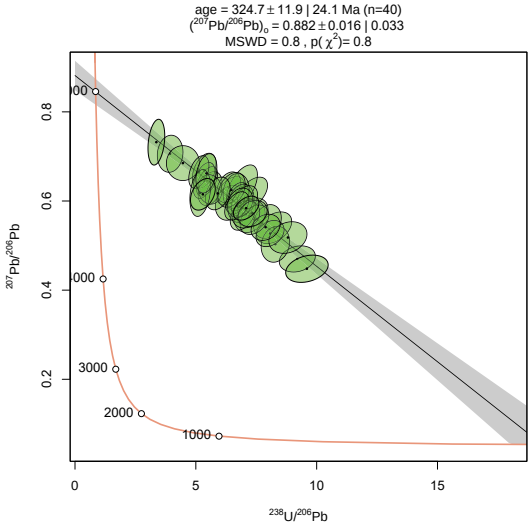

(r) T-W diagram for TA26

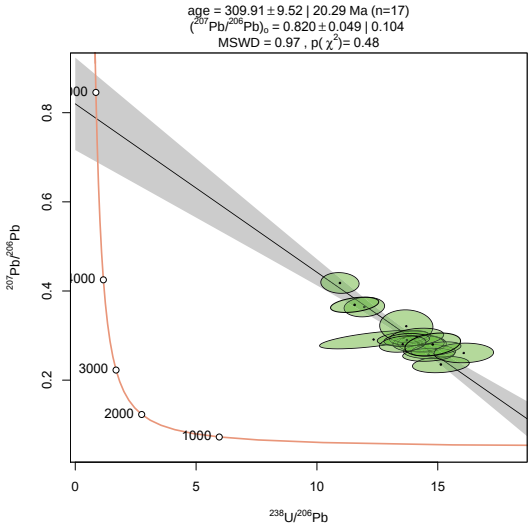

(s) T-W diagram for TA27

E.4 Thermal history modelling

This section contains data and plots that summarize the thermal history modelling carried out as part of this study.

Table E.2: Thermal history modelling inputs, assumptions, and parameters

1. Thermochronological data

Model input data			Data Source	Published data?
Sample Region	AHe	AFT		
Balkhash-Yili				
TA01		x	(1)	Y
TA07		x	(1)	Y
Boshchekul-Chingiz (S)				
TA06	x	x	(1)	Y
TA10	x	x	(1)	Y
TA11		x	(1)	Y
TA16	x	x	(1)	Y
Boshchekul-Chingiz (N)				
TA14		x	(1)	Y
TA15		x	(1)	Y
TA17		x	(1)	Y
TA18		x	(1)	Y
TA26		x	(1)	Y
Zharma-Saur				
TA20		x	(1)	Y
TA22		x	(1)	Y
TA23		x	(1)	Y

Data treatment, uncertainties, and other relevant constraints

He data

Treatment: Each individual analysis input separately into QTQt

Dates (Ma): Uncorrected He date input, α-ejection correction applied in QTQt after (Farley et al., 1996)

Uncertainties (Ma): Analytical uncertainties (1σ) input and resampled with MCMC procedure to account for overdispersion of dates due to sources of uncertainty in He dating that are difficult to quantify

r (μm): Mean equivalent spherical radius of each sample

AFT data

Initial mean track length (μm): 16.3

Track length reduction standard: 0.893

Etchant: 5.0M

Compositional parameter (μm): D_{par}

2. Additional geological information

Assumption	Explanation and data source
Initial high temperature constraints at 400 ± 50 °C at apatite U–Pb age for each sample	Igneous samples. Apatite U–Pb ages from this study
Final constraint at surface conditions, 10 ± 10 °C at 0 Ma	Samples collected from surface

3. System and model specific parameters

AHe radiation damage model: Flowers et al. (2009)
FT annealing model: Ketcham et al. (2007)
FT c-axis projection: no
Modelling code: QTQt 5.7.0 Windows
Iterations: Initial exploratory runs with 10,000 burn-in and 10,000 post burn-in. Final run 100,000 each burn-in and 100,000 post burn-in.
tT path characteristics: Reheating allowed
Acceptance rates: 0.2-0.8. Birth/death: ~1
Fitting criteria: Model specific observed vs. predicted values comparison below
Range of general prior: t=AFT central age ± AFT central age, T = 70 °C ± 70 °C.
Data source:
(1) - this study

E.4.1 Figures

Thermal history modelling outputs - AFT only

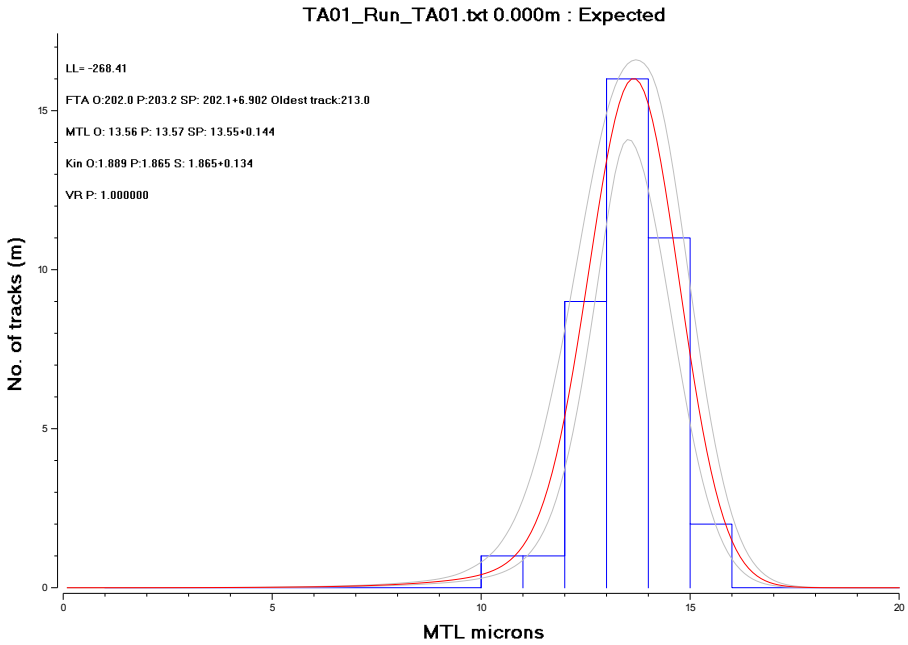

(a) Observed vs predicted values and MTL histogram for TA01

Figure E.4: Inverse thermal history modelling output for samples modelled with AFT data

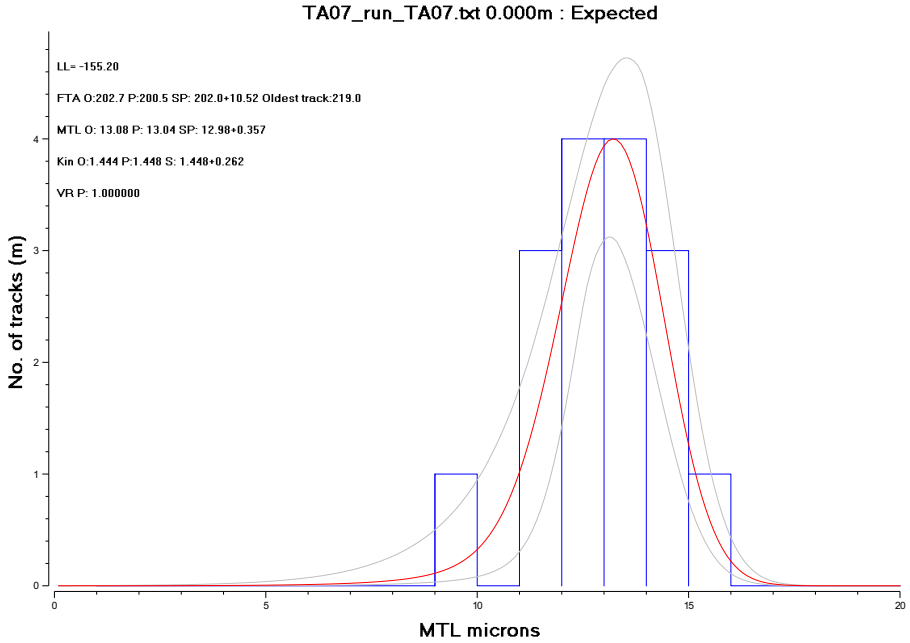

(b) Observed vs predicted values and MTL histogram for TA07

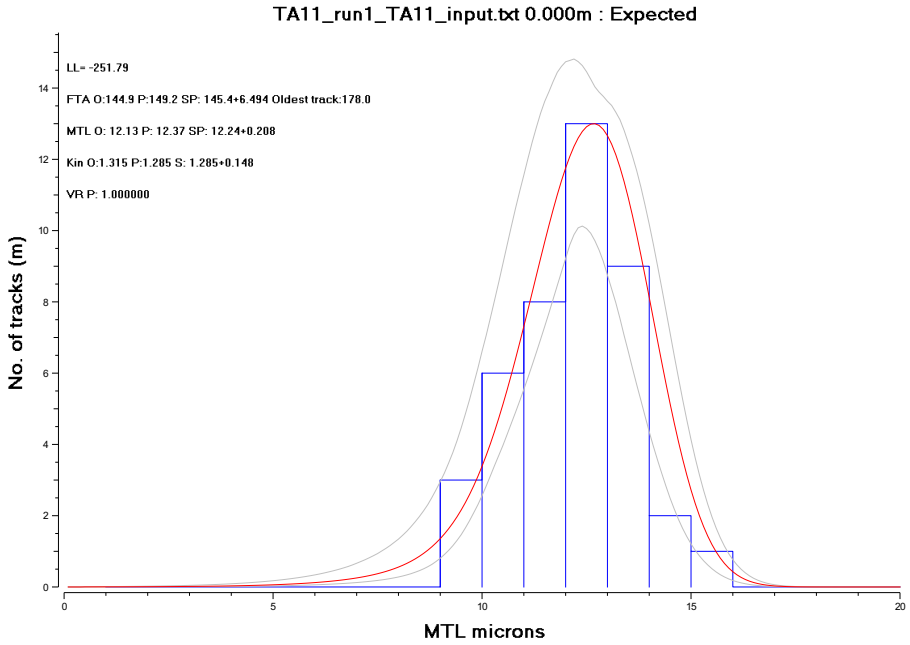

(c) Observed vs predicted values and MTL histogram for TA11

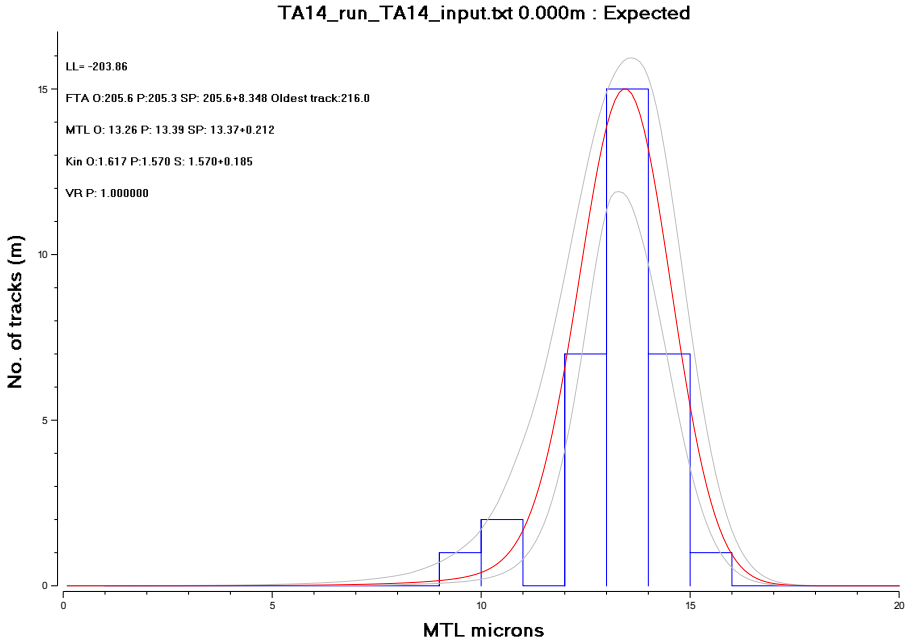

(d) Observed vs predicted values and MTL histogram for TA14

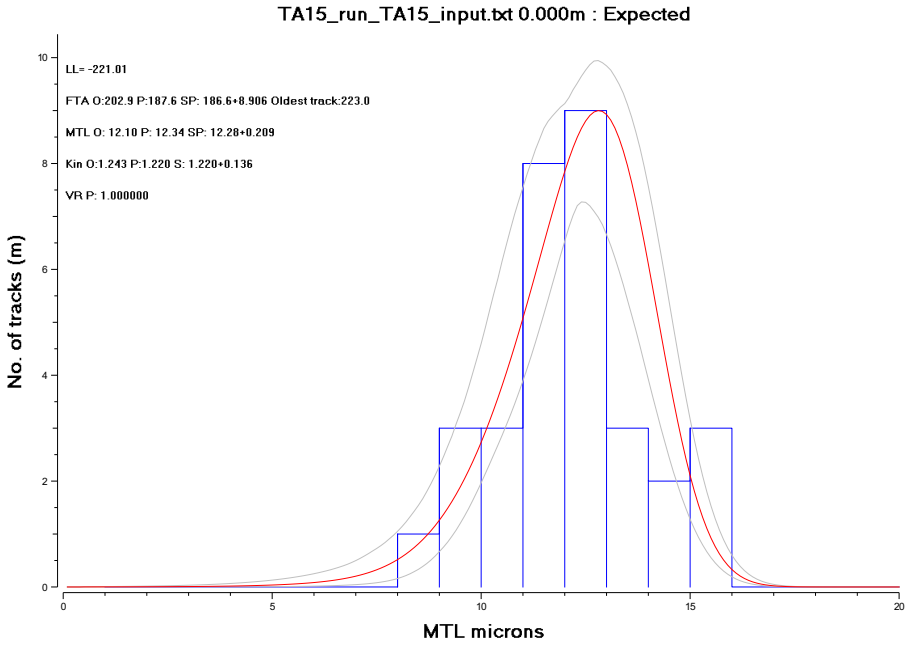

(e) Observed vs predicted values and MTL histogram for TA15

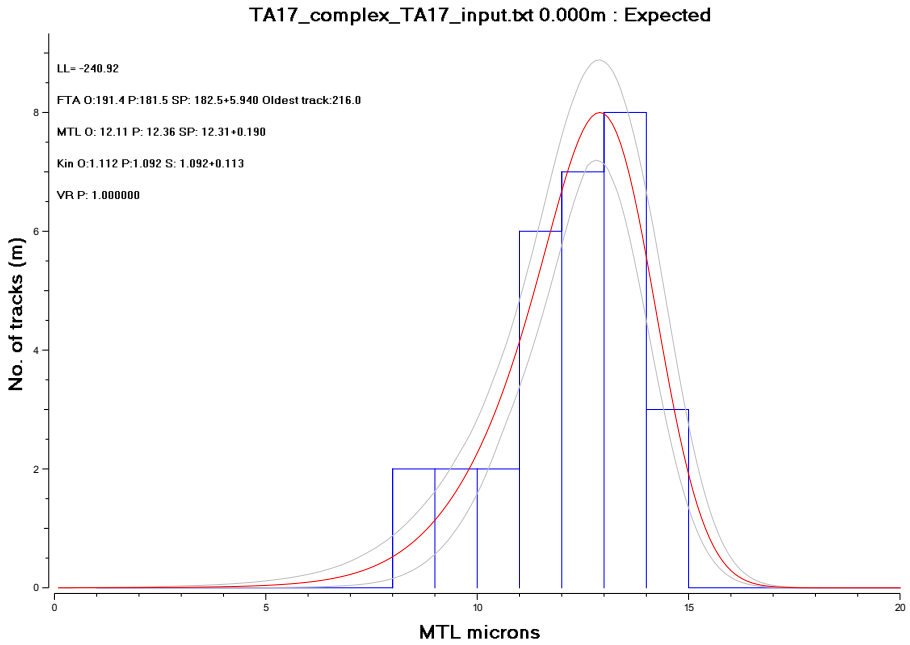

(f) Observed vs predicted values and MTL histogram for TA17

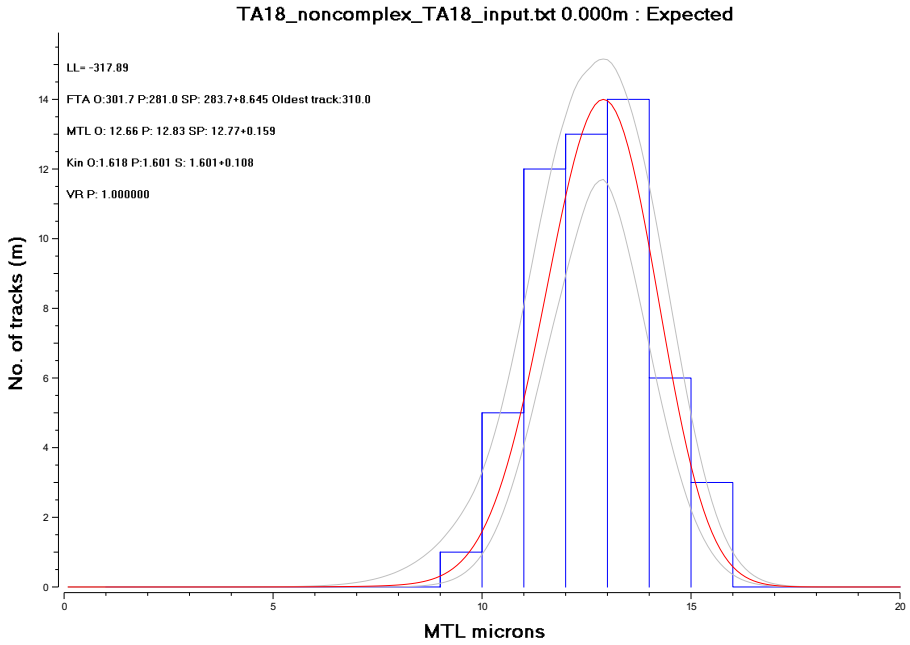

(g) Observed vs predicted values and MTL histogram for TA18

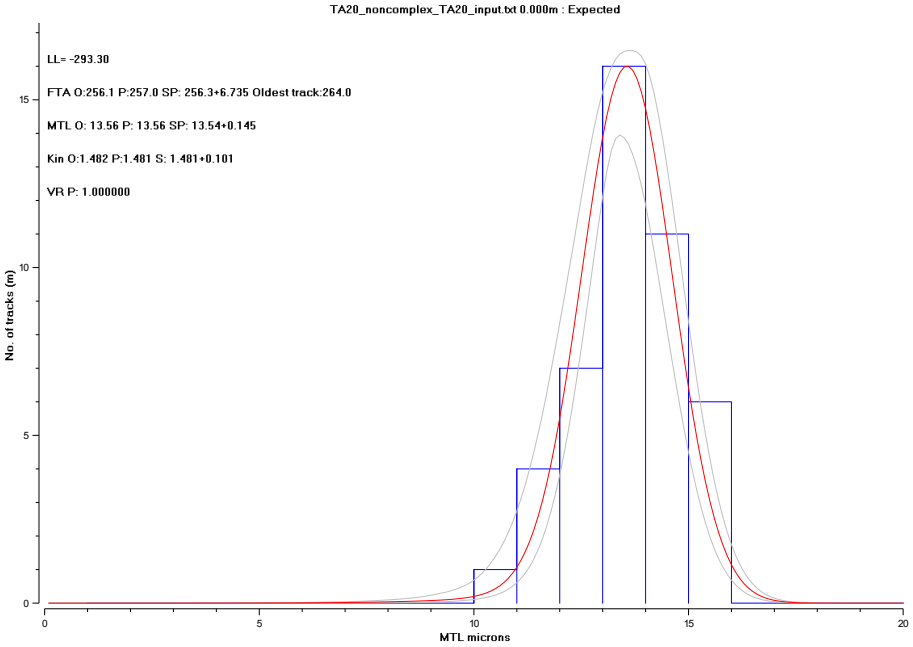

(h) Observed vs predicted values and MTL histogram for TA20

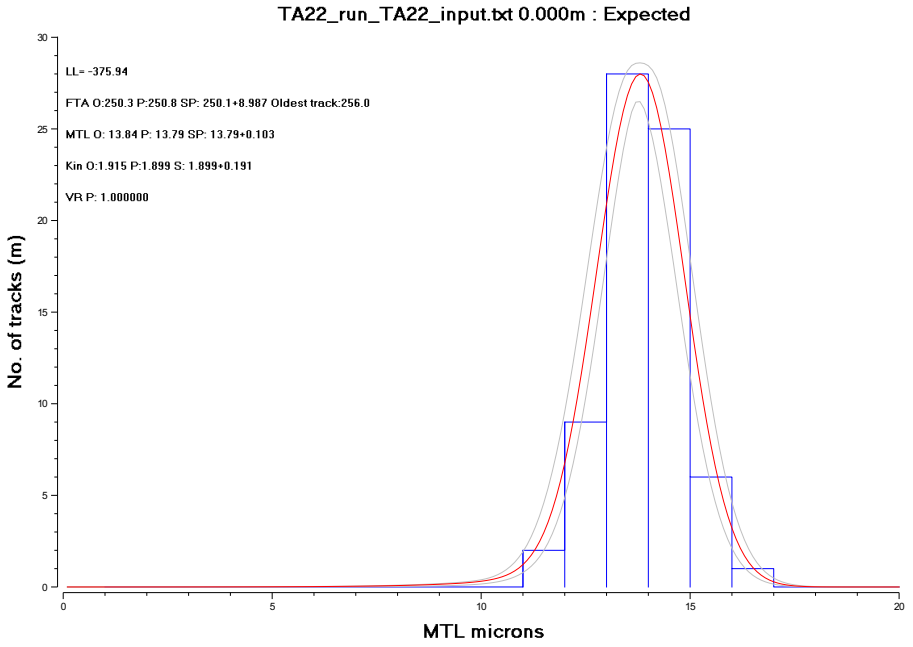

(i) Observed vs predicted values and MTL histogram for TA22

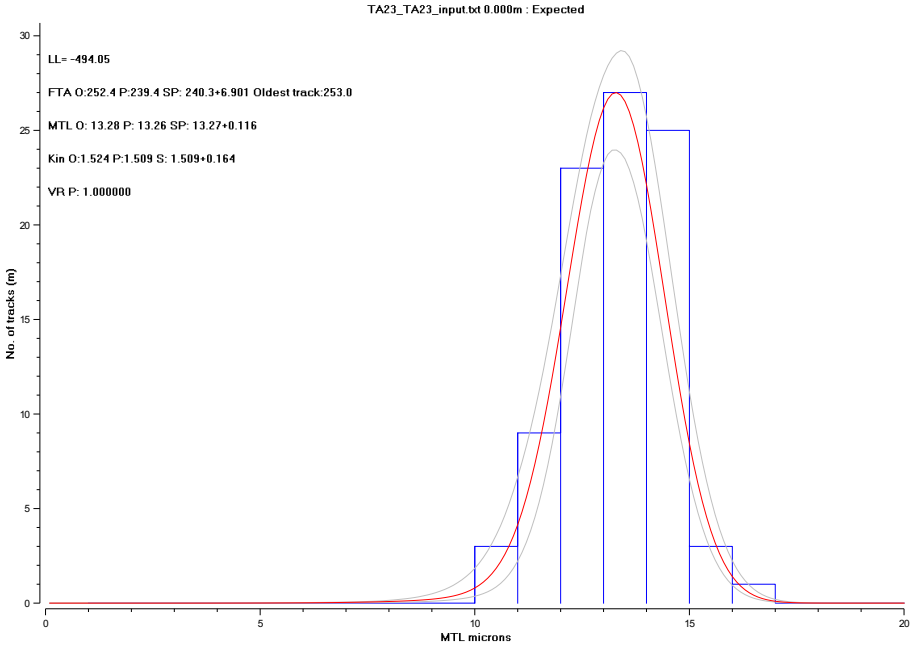

(j) Observed vs predicted values and MTL histogram for TA23

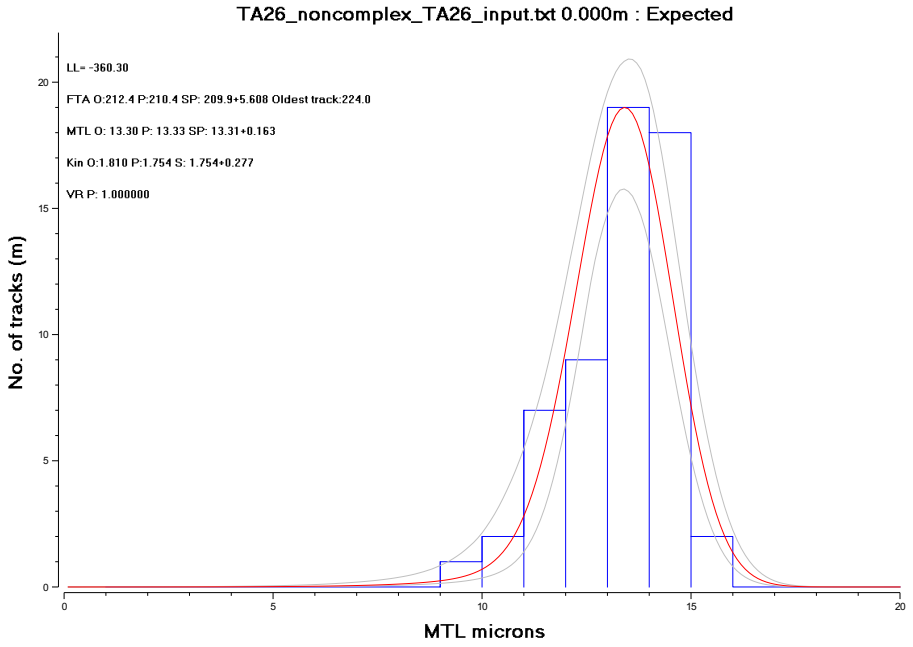

(k) Observed vs predicted values and MTL histogram for TA26

Thermal history modelling output - AFT and AHe

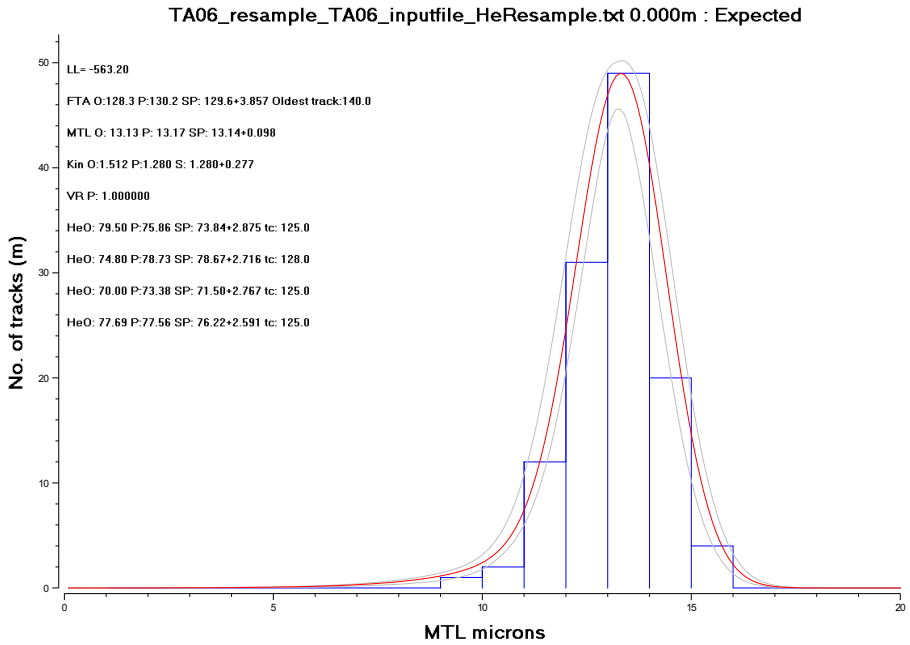

(a) Observed vs predicted values and MTL histogram for TA06

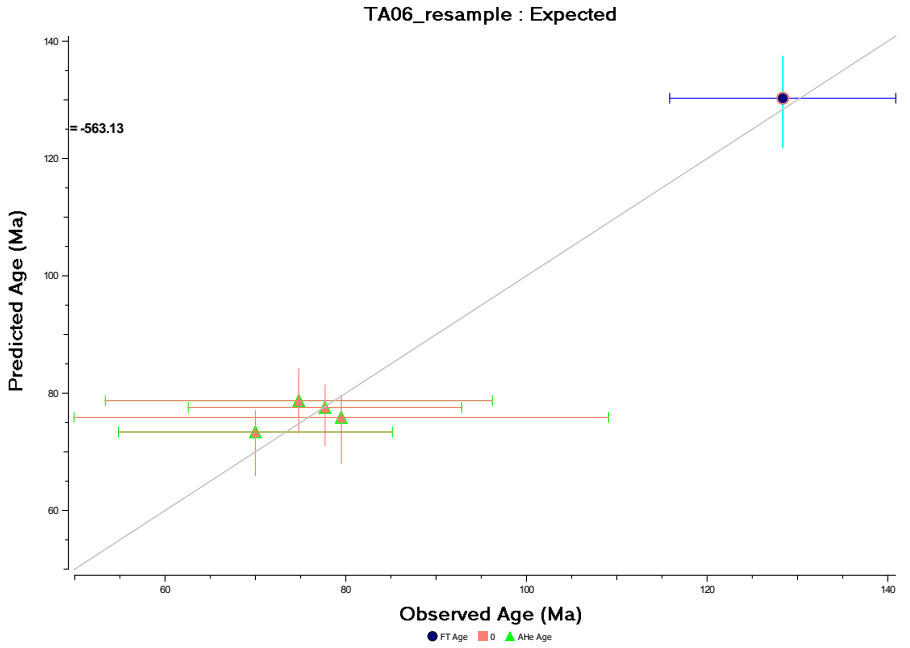

(b) Observed vs predicted values for TA06

Figure E.5: Inverse thermal history modelling output for samples modelled with AFT and AHe data

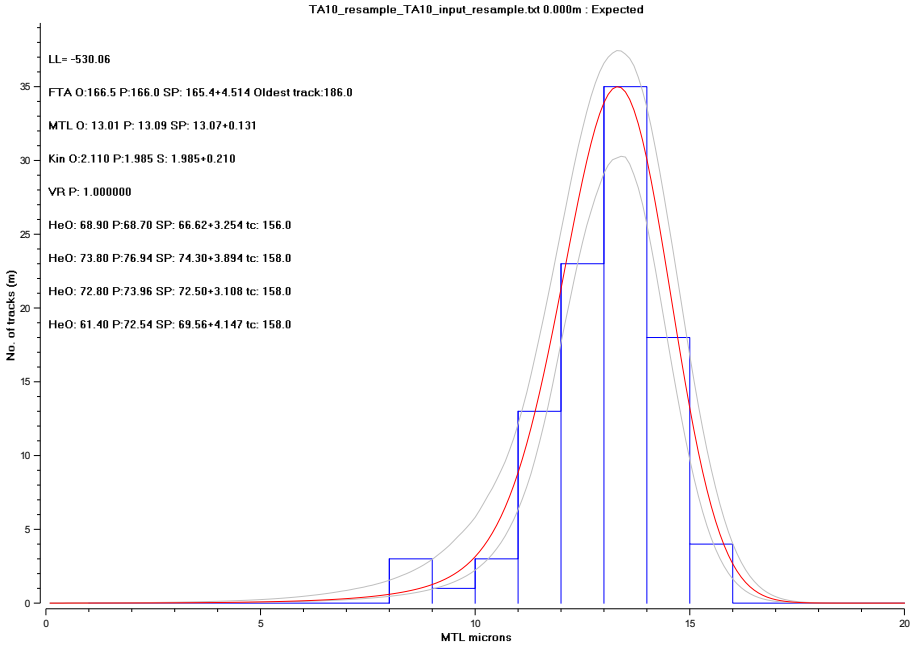

(c) Observed vs predicted values and MTL histogram for TA10

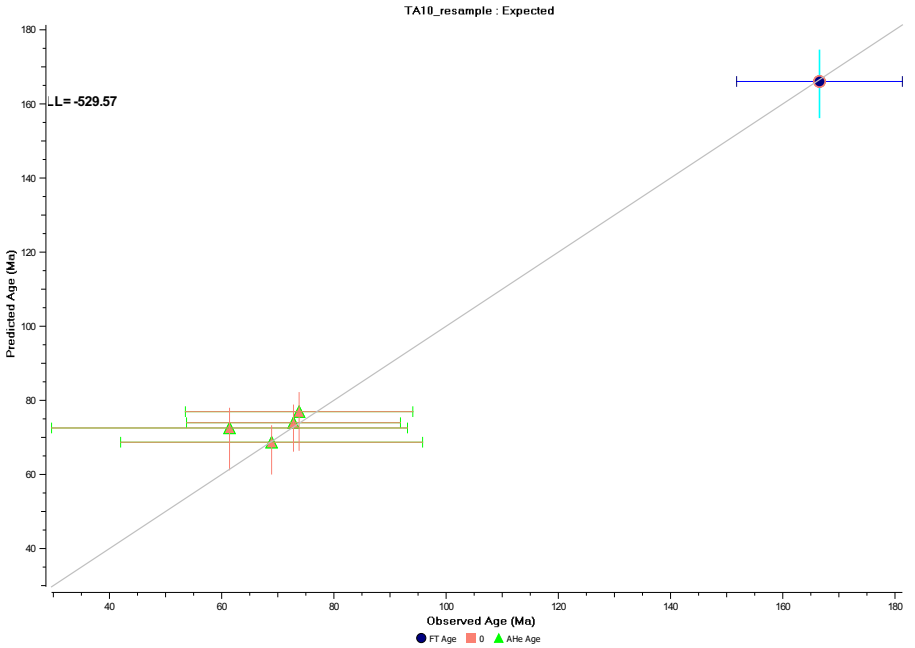

(d) Observed vs predicted values for TA06

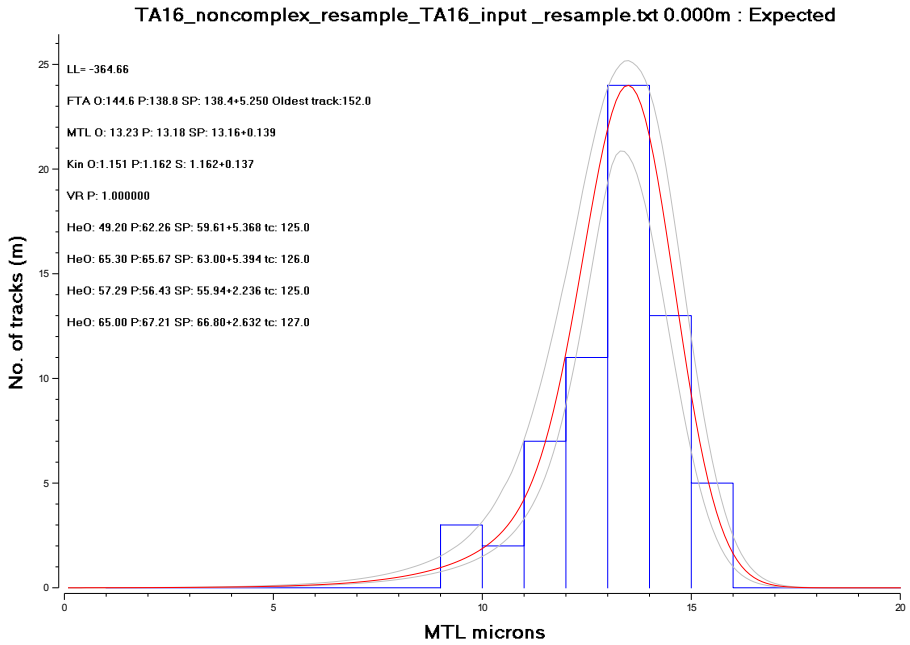

(e) Observed vs predicted values and MTL histogram for TA16

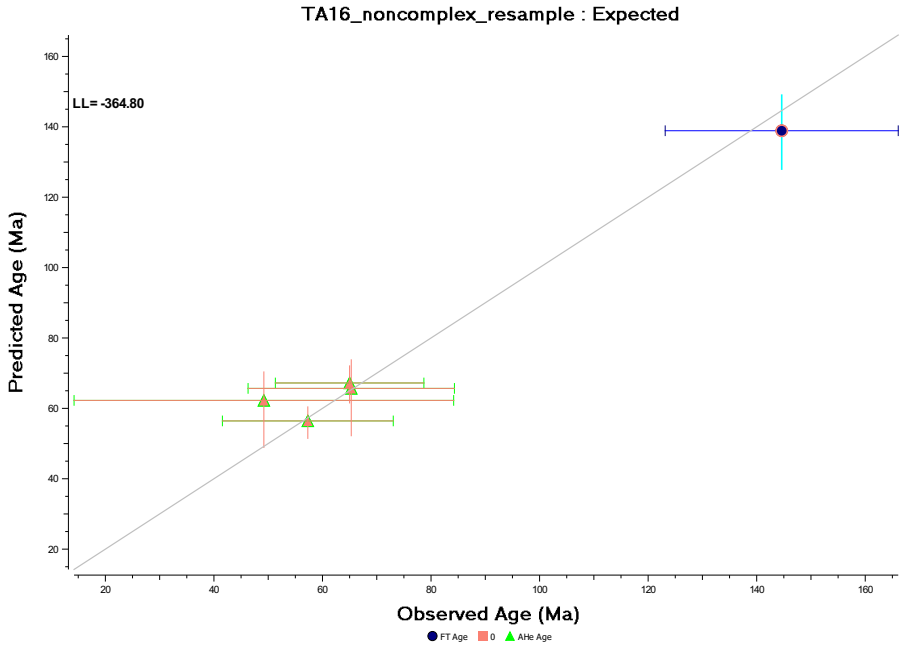

(f) Observed vs predicted values for TA16

Appendix F

Inherited structure as a control on late Paleozoic and Mesozoic tectonic reactivation in the Tarbagatai Mountains, eastern Kazakhstan: Appendix Part 2

The supporting information presented here consists of the tabulated individual grain/confined track length/analytical spot data for this chapter.

F.1 Apatite fission track individual grain data

Table F.1: Apatite fission track individual grain data

Sample name	Grain number	Cl (ppm)	2σ (ppm)	U (ppm)	2σ (ppm)	N_s	Area (cm^2)	ρ_s (tracks/cm^2)	D_{par} (μm)	Age (Ma)	1σ (Ma)
TA01	1	4950	450	12.46	0.99	49	2.90E-05	1687000	2.09	279.3	48.7
TA01	2	5050	520	11.9	1.1	12	7.58E-06	1583000	1.86	274.4	84.8
TA01	3	2260	260	6.68	0.51	5	8.77E-06	570500	1.75	176.2	80.6
TA01	4	4160	420	16.1	2	36	2.57E-05	1400000	1.92	179.4	38.8
TA01	5	4000	390	14.6	1	14	9.65E-06	1451000	1.92	205.0	57.9
TA01	6	2470	340	7.23	0.56	14	2.09E-05	670900	1.75	191.4	54.5
TA01	7	4230	410	13.39	0.96	42	4.12E-05	1021000	1.81	157.3	28.4
TA01	8	3990	520	16.2	1.7	35	2.75E-05	1274000	1.92	162.2	33.7
TA01	9	3140	310	16.1	1.2	47	2.30E-05	2047000	1.91	262.3	45.8
TA01	10	5160	470	11.47	0.61	19	1.62E-05	1174000	1.77	211.1	51.3
TA01	11	4840	410	17.9	1.1	28	1.64E-05	1703000	2.08	196.2	40.8
TA01	12	3530	580	16.5	1.3	38	1.81E-05	2099000	1.9	262.4	49.9
TA01	13	3400	460	28.7	1.9	25	1.24E-05	2014000	1.73	144.7	31.7
TA01	14	4480	320	13.78	0.87	13	1.35E-05	963800	2.09	144.3	42.0
TA01	16	4360	480	11.85	0.69	21	1.54E-05	1363000	1.93	237.2	55.5
TA01	17	4470	380	10.07	0.64	28	2.30E-05	1217000	1.99	249.3	51.9
TA01	18	4500	450	12.03	0.65	26	1.87E-05	1393000	1.84	238.8	50.7
TA01	19	4550	450	14.32	0.87	41	2.43E-05	1687000	1.91	243.0	43.3
TA01	20	4110	430	19.1	1.2	16	1.19E-05	1346000	1.93	145.4	38.5
TA01	21	4710	450	8.39	0.58	24	1.82E-05	1322000	2.08	325.0	72.7
TA01	23	3940	400	17.1	1	43	2.09E-05	2060000	1.97	248.5	43.3
TA01	24	4210	540	11.05	0.87	17	1.78E-05	956600	1.72	178.6	46.8
TA01	25	3570	730	10.3	0.84	11	1.59E-05	690000	1.67	138.2	44.0
TA01	26	4290	390	17.49	0.65	20	1.90E-05	1052000	1.96	124.1	29.1
TA01	27	4990	500	13	1.1	24	1.49E-05	1615000	1.81	256.2	58.7
TA01	28	4980	400	14.92	0.93	27	1.64E-05	1649000	1.98	228.0	48.1
TA01	29	4460	820	13.1	1.3	12	1.18E-05	1019000	1.81	160.4	49.9
TA01	31	4550	480	11.18	0.81	31	2.27E-05	1367000	1.81	252.2	51.2

Continued on next page

Continued from previous page

Sample name	Grain number	Cl (ppm)	2σ (ppm)	U (ppm)	2σ (ppm)	N_s	Area (cm^2)	ρ_s (tracks/cm^2)	D_{par} (μm)	Age (Ma)	1σ (Ma)
TA01	32	4180	430	16.4	1.6	18	1.46E-05	1230000	1.79	154.7	40.6
TA01	33	4880	540	16.7	1.3	33	1.53E-05	2163000	2.08	267.2	53.4
TA01	34	4310	390	12.32	0.71	20	1.98E-05	1008000	1.97	168.8	40.3
TA01	35	4230	380	21.6	1.6	23	1.41E-05	1633000	1.88	155.9	35.8
TA01	36	4290	400	15.6	1.2	26	2.24E-05	1161000	2.01	153.5	33.6
TA01	37	3630	340	13.32	0.85	25	1.73E-05	1443000	1.78	223.5	48.8
TA01	38	3980	360	12.57	0.92	18	1.78E-05	1010000	1.85	165.7	42.1
TA01	39	4650	630	12.7	1.3	23	1.42E-05	1616000	2.05	262.5	63.0
TA01	40	4410	420	11.62	0.61	21	2.44E-05	861300	1.76	152.9	35.5
TA02	1	4180	430	4.06	0.3	4	1.34E-05	298100	1.59	151.4	77.1
TA02	2	2870	380	8.11	0.45	12	2.73E-05	439600	1.8	111.8	33.6
TA02	3	3250	540	4.35	0.82	5	1.75E-05	285200	1.5	135.2	66.1
TA02	5	5060	560	2.13	0.16	3	1.84E-05	163300	2.58	158.1	92.6
TA02	6	4940	550	1.91	0.15	10	2.05E-05	488900	2.07	528.0	175.0
TA02	7	4190	590	1.85	0.14	3	1.24E-05	241200	2.06	268.9	157.4
TA02	8	4610	420	2.83	0.26	3	1.09E-05	276000	2.39	201.2	118.2
TA02	9	5280	360	2.12	0.13	7	1.39E-05	505300	1.68	491.6	190.6
TA02	10	5230	510	1.94	0.14	3	1.15E-05	260100	2.08	276.5	161.8
TA02	11	3600	420	12.29	0.6	13	9.35E-06	1391000	2.35	233.5	67.2
TA02	12	6050	450	2.76	0.24	4	1.24E-05	321500	1.92	240.3	122.8
TA02	13	5350	490	2.13	0.19	6	1.26E-05	475000	2.2	460.0	194.2
TA02	14	3160	660	2.92	0.58	3	1.72E-05	174800	1.59	123.5	75.8
TA02	15	3040	300	2.46	0.18	8	1.57E-05	508400	2.14	426.3	156.1
TA02	16	no value	NaN	2.9	0.3	8	1.54E-05	518400	2.4	368.7	137.6
TA02	17	5180	540	3.32	0.24	3	1.04E-05	287500	1.96	178.6	104.5
TA02	18	6500	580	2.22	0.19	3	1.22E-05	245500	1.98	228.1	133.8
TA02	19	2450	500	2.06	0.16	3	1.15E-05	260500	2.1	260.8	152.8
TA02	20	5800	570	3.39	0.31	8	1.52E-05	526600	2.32	320.4	118.6
TA02	21	5110	790	3.13	0.27	4	1.01E-05	396300	2.22	261.2	133.4

Continued on next page

Continued from previous page

Sample name	Grain number	Cl (ppm)	2σ (ppm)	U (ppm)	2σ (ppm)	N_s	Area (cm^2)	ρ_s (tracks/cm^2)	D_{par} (μm)	Age (Ma)	1σ (Ma)
TA04	1	1170	370	4.73	0.31	3	1.35E-05	222700	1.88	97.1	56.7
TA04	2	1470	340	4.28	0.21	2	9.14E-06	218800	1.5	105.4	75.0
TA04	4	1270	290	3.68	0.22	5	9.59E-06	521500	1.8	292.3	133.1
TA04	5	1280	340	4	0.33	7	1.37E-05	512200	1.55	264.1	103.4
TA04	6	970	320	3.94	0.25	5	1.05E-05	476900	1.43	249.7	113.8
TA04	8	1480	360	4.83	0.39	3	9.53E-06	314700	1.46	134.4	78.8
TA04	9	1030	260	4.94	0.4	9	1.89E-05	476900	1.63	199.1	69.4
TA04	10	1180	300	8.61	0.7	7	1.02E-05	684700	1.38	164.0	64.2
TA04	11	Below LOD	Below LOD	5.88	0.43	10	9.32E-06	1073000	1.63	376.4	124.3
TA04	12	6200	1200	5.6	0.47	3	7.96E-06	377000	1.7	138.9	81.4
TA04	13	1360	280	6.62	0.41	8	7.91E-06	1011000	2.22	315.0	114.7
TA04	14	3180	500	3.83	0.28	5	1.41E-05	355200	1.88	191.3	87.5
TA04	15	8090	590	5.47	0.52	12	1.17E-05	1022000	2.09	385.4	119.4
TA04	16	7100	590	4.11	0.41	3	1.28E-05	235100	2.74	118.0	69.5
TA04	17	3270	360	3.07	0.24	6	1.05E-05	574100	1.77	385.7	162.0
TA04	18	860	340	6.49	0.44	6	9.39E-06	639100	2.1	203.1	85.0
TA04	21	2900	1800	3.92	0.43	2	1.01E-05	198400	2.25	104.4	75.0
TA04	22	1230	390	3.62	0.29	5	1.06E-05	472600	1.68	269.3	123.4
TA04	23	no value	NaN	4.11	0.26	2	7.61E-06	262900	2.06	131.9	94.0
TA04	24	1270	410	4.12	0.35	3	8.90E-06	337200	1.96	168.8	99.0
TA04	26	1250	400	4.8	0.55	1	1.27E-05	78610	1.94	33.8	34.1
TA04	27	1180	410	3.76	0.22	3	1.33E-05	224900	1.31	123.4	72.0
TA04	28	900	310	4.43	0.27	4	1.52E-05	262700	1.28	122.3	62.1
TA04	29	1110	400	4.64	0.27	2	1.04E-05	191600	1.69	85.2	60.6
TA04	30	1110	310	4.2	0.29	5	1.17E-05	427100	1.68	209.8	95.8
TA05	1	1020	590	7.8	1.4	5	1.45E-05	344400	1.61	91.1	44.2
TA05	2	480	320	9.02	0.67	29	3.45E-05	841000	1.59	192.3	40.2
TA05	3	1260	250	6.3	0.36	4	1.14E-05	352000	1.29	115.2	58.4
TA05	4	1950	250	3.56	0.24	4	2.00E-05	199700	1.71	115.7	58.8

Continued on next page

Continued from previous page

Sample name	Grain number	Cl (ppm)	2σ (ppm)	U (ppm)	2σ (ppm)	N_s	Area (cm^2)	ρ_s (tracks/cm^2)	D_{par} (μm)	Age (Ma)	1σ (Ma)
TA06	1	850	290	9.95	0.67	9	1.88E-05	478500	1.6	99.2	34.3
TA06	2	610	300	13.6	2	25	3.66E-05	682800	1.51	103.6	26.5
TA06	3	Below LOD	Below LOD	10.65	0.76	13	1.42E-05	913000	1.71	176.8	51.8
TA06	4	510	230	10.42	0.55	22	3.30E-05	666600	1.36	132.0	30.1
TA06	5	700	240	11.35	0.82	25	4.25E-05	588900	1.48	107.0	23.7
TA06	6	620	420	25.9	3.4	38	2.35E-05	1619000	1.78	128.9	28.0
TA06	8	670	260	8.82	0.6	16	2.47E-05	647400	1.64	151.4	40.3
TA06	9	Below LOD	Below LOD	12.85	0.81	17	1.92E-05	885500	1.58	142.1	36.6
TA06	10	660	270	5.88	0.38	14	3.51E-05	398900	1.8	139.9	39.4
TA06	11	750	310	10.03	0.87	23	3.46E-05	665200	1.48	136.8	32.0
TA06	12	710	410	5.92	0.49	13	3.23E-05	402000	2.01	140.1	41.4
TA06	13	550	250	4.48	0.26	5	2.11E-05	236600	2.33	108.9	49.6
TA06	14	690	320	9.76	0.76	8	1.86E-05	429400	1.75	90.7	33.3
TA06	15	1680	320	10.34	0.7	22	5.33E-05	412400	2.03	82.3	19.1
TA06	16	1260	270	8.06	0.58	24	3.84E-05	624900	1.83	159.9	35.9
TA06	17	490	270	2.12	0.19	5	2.74E-05	182500	1.73	177.6	81.7
TA06	18	570	230	11	1	12	1.96E-05	612600	1.94	114.9	35.5
TA06	19	700	210	9.66	0.63	11	1.46E-05	755400	1.46	161.3	50.7
TA06	20	870	240	10.42	0.68	12	1.49E-05	806500	1.45	159.6	48.2
TA06	21	Below LOD	Below LOD	10.96	0.88	12	2.06E-05	583100	1.71	109.7	33.5
TA06	23	720	360	10.7	0.61	23	4.14E-05	555900	1.63	107.2	24.1
TA06	24	710	300	9.62	0.54	7	1.45E-05	484000	1.87	103.8	40.1
TA06	25	640	480	10.1	1.3	17	2.92E-05	581800	1.89	118.8	33.4
TA06	26	500	270	10.38	0.77	15	1.85E-05	811200	1.67	161.2	44.4
TA06	27	580	250	11.15	0.54	29	2.02E-05	1433000	1.76	265.1	53.3
TA06	28	Below LOD	Below LOD	10.68	0.7	13	1.43E-05	907300	1.73	175.2	51.0
TA06	29	680	280	12.54	0.85	27	4.16E-05	648600	1.68	106.7	22.7
TA06	30	740	250	11.92	0.71	16	1.67E-05	959700	1.69	166.1	43.8
TA06	31	590	280	11.34	0.72	16	2.05E-05	781400	1.75	142.1	37.7
TA06	32	780	280	10.02	0.64	10	1.86E-05	539200	1.71	111.0	36.4
TA06	33	580	240	9.43	0.65	14	1.81E-05	774800	1.61	169.5	47.9

Continued on next page

Continued from previous page

Sample name	Grain number	Cl (ppm)	2σ (ppm)	U (ppm)	2σ (ppm)	N_s	Area (cm^2)	ρ_s (tracks/cm^2)	D_{par} (μm)	Age (Ma)	1σ (Ma)
TA06	34	2900	1400	9.54	0.89	7	1.80E-05	388900	1.6	84.1	33.1
TA06	35	660	220	11.5	0.81	10	1.76E-05	569800	1.74	102.2	33.7
TA06	36	790	380	10	0.96	8	1.84E-05	435000	1.57	89.7	33.3
TA06	37	Below LOD	Below LOD	9.27	0.54	27	4.76E-05	567400	1.65	126.3	26.5
TA06	38	Below LOD	Below LOD	11.53	0.88	18	2.50E-05	720900	1.67	129.0	32.9
TA06	39	870	270	9.16	0.46	23	3.46E-05	665700	1.64	149.9	33.4
TA06	40	Below LOD	Below LOD	8.86	0.59	18	2.93E-05	615200	1.42	143.2	36.1
TA07	1	1550	340	3.42	0.23	5	1.54E-05	325200	1.29	196.1	89.5
TA07	2	910	340	6.26	0.51	14	1.58E-05	884500	1.77	291.4	83.3
TA07	3	1200	280	8.9	0.55	14	1.60E-05	877300	1.74	203.3	57.1
TA07	4	1090	420	5.07	0.41	5	2.27E-05	220800	1.33	89.8	41.2
TA07	5	1870	320	3.26	0.19	9	2.87E-05	313200	1.8	198.2	68.1
TA07	6	990	240	4.95	0.3	13	2.64E-05	492100	1.41	205.1	59.5
TA07	7	1070	330	5.85	0.27	23	2.48E-05	926800	1.66	326.8	72.5
TA07	8	1160	250	3.92	0.27	10	2.15E-05	465300	1.3	244.8	80.6
TA07	9	1100	300	6.79	0.44	16	2.09E-05	766700	1.3	232.9	61.8
TA07	10	990	250	6.32	0.35	14	2.21E-05	632500	1.62	206.4	57.7
TA07	11	2480	410	3.67	0.27	2	1.91E-05	104600	1.69	58.8	41.9
TA07	12	1130	250	5.13	0.39	12	1.99E-05	602000	1.01	242.0	73.7
TA07	13	850	300	5.84	0.4	14	2.40E-05	583700	1.19	206.2	58.2
TA07	15	1580	280	4.79	0.32	8	2.26E-05	354300	1.59	152.6	55.7
TA07	16	1410	290	9.87	0.53	13	1.96E-05	663700	1.22	138.7	40.1
TA07	17	1070	350	5.83	0.49	4	2.25E-05	178100	1.16	63.0	32.2
TA07	18	1370	310	5.41	0.36	12	3.50E-05	343200	1.17	130.9	39.6
TA07	20	1220	250	5.39	0.34	6	1.39E-05	431600	1.23	165.2	69.0
TA07	21	1990	260	3.13	0.2	7	2.67E-05	261800	1.17	172.5	67.0
TA07	22	1350	290	5.17	0.37	9	1.25E-05	718900	1.18	286.8	99.3
TA07	23	920	260	4.13	0.26	7	2.52E-05	278000	1.17	138.8	53.9
TA07	24	1170	310	5.79	0.42	13	2.35E-05	554400	1.59	197.5	57.9
TA07	25	1760	220	2.8	0.18	9	2.33E-05	386900	1.56	285.0	98.3

Continued on next page

Continued from previous page

Sample name	Grain number	Cl (ppm)	2σ (ppm)	U (ppm)	2σ (ppm)	N_s	Area (cm^2)	ρ_s (tracks/cm^2)	D_{par} (μm)	Age (Ma)	1σ (Ma)
TA07	26	1660	460	4.1	0.3	13	1.96E-05	662600	1.32	333.3	97.7
TA07	28	960	250	3.77	0.29	6	1.85E-05	325100	1.14	177.9	74.7
TA07	29	1080	280	3.72	0.3	9	2.56E-05	351300	1.82	194.8	67.8
TA07	31	1200	260	3.91	0.25	9	1.85E-05	486000	1.56	256.4	88.4
TA07	32	970	320	3.25	0.23	13	2.41E-05	539000	1.86	342.1	100.1
TA07	34	1250	300	3.28	0.24	8	2.87E-05	278300	1.93	175.0	64.1
TA07	35	1670	320	4.22	0.28	20	3.41E-05	586900	2.05	286.9	69.1
TA07	36	910	380	2.07	0.15	5	3.83E-05	130400	2.41	129.9	59.4
TA07	37	810	460	3.63	0.41	10	2.54E-05	394400	1.88	224.1	76.5
TA07	38	650	360	5.65	0.41	12	2.40E-05	499600	1.93	182.4	55.4
TA07	40	580	320	3.07	0.28	10	2.24E-05	446500	1.31	300.0	100.4
TA11	1	Below LOD	Below LOD	22.6	1.6	24	1.75E-05	1374000	1.31	125.4	28.1
TA11	2	Below LOD	Below LOD	19.8	1.4	20	1.39E-05	1442000	1.22	150.2	36.4
TA11	3	630	280	24.6	1.1	22	1.74E-05	1265000	1.45	106.1	24.0
TA11	5	Below LOD	Below LOD	9.98	0.9	5	1.45E-05	345400	1.34	71.4	32.9
TA11	6	870	350	9.32	0.69	10	1.29E-05	774300	1.15	171.4	56.6
TA11	7	Below LOD	Below LOD	9.45	0.47	5	1.33E-05	375900	1.16	82.0	37.3
TA11	8	970	330	12.23	0.98	14	1.38E-05	1013000	1.43	170.8	48.8
TA11	9	580	290	18.2	1.5	15	1.63E-05	919000	1.84	104.2	28.9
TA11	11	Below LOD	Below LOD	18.1	1.6	15	9.24E-06	1623000	1.37	185.0	51.7
TA11	14	Below LOD	Below LOD	12.03	0.63	14	1.77E-05	792500	1.11	135.9	37.9
TA11	16	550	260	3.29	0.26	13	4.38E-05	296900	1.18	186.1	54.8
TA11	17	560	360	116	10	74	7.92E-06	9339000	1.48	166.1	26.0
TA11	18	600	280	12.93	0.91	28	2.31E-05	1211000	1.26	193.2	40.7
TA11	19	660	380	20.4	2.1	32	2.14E-05	1498000	1.33	151.5	32.3
TA11	20	Below LOD	Below LOD	16.9	1	23	1.58E-05	1453000	1.29	177.3	39.9
TA11	21	590	340	20.5	1.5	22	2.31E-05	953500	1.38	95.9	22.4
TA11	23	Below LOD	Below LOD	13.21	0.67	18	1.01E-05	1779000	1.09	277.8	69.0
TA11	24	680	310	14.9	1.4	14	1.59E-05	878500	1.7	121.6	35.2
TA11	25	Below LOD	Below LOD	8.71	0.49	10	1.37E-05	730900	1.22	173.1	56.6

Continued on next page

Continued from previous page

Sample name	Grain number	Cl (ppm)	2σ (ppm)	U (ppm)	2σ (ppm)	N_s	Area (cm^2)	ρ_s (tracks/cm^2)	D_{par} (μm)	Age (Ma)	1σ (Ma)
TA11	26	590	250	8.95	0.72	10	1.73E-05	578700	1.21	133.4	44.3
TA11	27	590	270	16.1	1.2	30	1.75E-05	1712000	1.21	219.3	45.2
TA11	28	Below LOD	Below LOD	12.83	0.94	19	2.27E-05	836300	1.2	134.4	33.4
TA11	29	640	340	10.5	1.3	6	1.30E-05	462200	1.1	90.8	39.1
TA11	30	Below LOD	Below LOD	24.1	2	22	1.46E-05	1512000	1.41	129.4	30.6
TA11	31	Below LOD	Below LOD	12.07	0.92	14	2.01E-05	698200	1.6	119.3	33.9
TA11	32	Below LOD	Below LOD	16.9	2.1	12	1.42E-05	848200	1.11	103.5	33.1
TA11	34	Below LOD	Below LOD	7.71	0.49	15	1.80E-05	831900	1.27	222.6	60.7
TA14	1	790	410	12.22	0.86	26	2.14E-05	1213000	1.89	204.7	44.4
TA14	2	1100	420	15.9	1	21	1.55E-05	1353000	1.74	175.5	41.2
TA14	3	940	320	14.37	0.88	37	1.95E-05	1901000	1.72	272.9	50.6
TA14	4	1210	360	7.46	0.46	20	1.97E-05	1018000	1.94	281.5	67.5
TA14	5	Below LOD	Below LOD	5.61	0.31	12	2.35E-05	509700	1.86	187.4	56.2
TA14	6	1330	300	15.5	1.1	32	1.85E-05	1734000	1.79	230.8	46.1
TA14	7	720	320	6.27	0.34	15	1.90E-05	787700	1.29	259.1	70.1
TA14	8	1380	350	15.3	1	17	1.55E-05	1097000	1.56	147.9	38.2
TA14	9	1290	380	16.2	1.3	30	1.92E-05	1562000	1.64	198.9	41.4
TA14	11	820	350	5.01	0.4	15	2.10E-05	716100	1.81	294.8	81.6
TA14	12	Below LOD	Below LOD	9.4	1	14	1.27E-05	1107000	1.91	242.9	71.4
TA14	14	970	390	20.5	1.5	29	1.88E-05	1544000	1.95	155.4	32.4
TA14	15	Below LOD	Below LOD	21	1.6	27	1.11E-05	2442000	2.14	239.9	51.7
TA14	16	1070	380	5.07	0.4	11	1.65E-05	666900	1.89	271.3	86.1
TA14	17	740	400	5.16	0.39	8	2.10E-05	380600	2.02	152.1	55.8
TA14	18	Below LOD	Below LOD	15.8	2.1	21	1.45E-05	1448000	2.02	189.0	49.6
TA14	19	1000	320	13.48	0.79	26	2.25E-05	1157000	2.16	177.0	37.8
TA14	20	730	280	11.95	0.92	23	1.97E-05	1167000	1.84	201.4	46.4
TA14	21	1200	410	6.91	0.48	19	2.03E-05	938000	1.9	280.0	69.2
TA14	22	670	270	4.52	0.34	16	2.67E-05	6.00E+05	1.42	273.8	73.4
TA14	23	1010	380	15.71	0.81	27	1.87E-05	1443000	1.66	189.5	39.4
TA14	24	850	330	9.84	0.94	23	2.13E-05	1081000	1.68	226.6	53.7

Continued on next page

Continued from previous page

Sample name	Grain number	Cl (ppm)	2σ (ppm)	U (ppm)	2σ (ppm)	N_s	Area (cm^2)	ρ_s (tracks/cm^2)	D_{par} (μm)	Age (Ma)	1σ (Ma)
TA14	25	850	290	10.8	1.5	21	1.70E-05	1238000	1.45	236.4	62.8
TA14	26	1110	370	6.64	0.39	14	1.73E-05	809000	1.57	251.3	70.4
TA14	27	940	300	14.88	0.9	26	2.18E-05	1194000	1.4	165.5	35.4
TA14	28	1000	320	13.31	0.81	18	1.92E-05	935800	1.56	145.0	36.4
TA14	29	880	450	5.64	0.43	9	1.64E-05	549000	1.85	200.8	69.7
TA14	30	770	380	14.86	0.8	20	1.59E-05	1259000	1.42	174.8	41.6
TA14	31	Below LOD	Below LOD	5	0.34	8	2.24E-05	357600	1.32	147.5	53.9
TA14	32	810	320	14.34	0.85	28	1.92E-05	1457000	1.64	209.6	43.4
TA14	33	Below LOD	Below LOD	6.1	0.37	14	1.80E-05	776100	1.79	262.4	73.7
TA26	1	Below LOD	Below LOD	11.1	1	55	4.17E-05	1320000	1.57	245.3	42.5
TA26	2	Below LOD	Below LOD	7.43	0.47	26	3.96E-05	656100	1.5	182.1	39.1
TA26	3	Below LOD	Below LOD	7.76	0.53	44	3.76E-05	1172000	2.48	311.5	54.9
TA26	4	Below LOD	Below LOD	15.88	0.98	44	3.29E-05	1338000	2.1	173.8	30.2
TA26	5	610	270	11.96	0.9	72	7.78E-05	925000	1.92	159.5	24.3
TA26	6	Below LOD	Below LOD	7.59	0.58	55	6.44E-05	853500	1.99	231.9	38.6
TA26	7	Below LOD	Below LOD	11.61	0.94	40	2.75E-05	1456000	1.69	258.7	48.5
TA26	8	Below LOD	Below LOD	8.75	0.69	34	4.33E-05	785600	1.56	185.2	36.7
TA26	9	Below LOD	Below LOD	6.08	0.42	24	3.96E-05	606500	1.6	205.8	46.1
TA26	10	Below LOD	Below LOD	8.1	0.42	30	3.59E-05	835000	1.8	212.6	42.4
TA26	11	Below LOD	Below LOD	13.64	0.73	38	3.07E-05	1237000	1.79	187.1	33.9
TA26	12	Below LOD	Below LOD	17	1.3	54	3.15E-05	1717000	1.67	208.3	34.9
TA26	13	Below LOD	Below LOD	9.54	0.79	29	3.71E-05	781100	1.54	168.9	35.8
TA26	14	Below LOD	Below LOD	12.03	0.9	61	5.20E-05	1172000	1.47	200.9	32.2
TA26	15	Below LOD	Below LOD	30.4	2.6	67	2.90E-05	2314000	1.6	157.0	25.3
TA26	17	Below LOD	Below LOD	5.79	0.37	33	5.39E-05	612100	1.45	218.1	42.5
TA26	18	Below LOD	Below LOD	8.63	0.59	37	3.73E-05	992500	1.56	237.2	44.6
TA26	19	780	240	6.76	0.39	30	3.53E-05	849300	1.64	259.1	52.0
TA26	20	930	410	12.06	0.93	37	2.74E-05	1351000	2.12	231.1	44.2
TA26	21	590	270	8.51	0.61	22	3.46E-05	635100	2.56	153.9	35.9
TA26	22	Below LOD	Below LOD	7.63	0.53	47	4.49E-05	1048000	1.88	283.3	48.9

Continued on next page

Continued from previous page

Sample name	Grain number	Cl (ppm)	2σ (ppm)	U (ppm)	2σ (ppm)	N_s	Area (cm^2)	ρ_s (tracks/cm^2)	D_{par} (μm)	Age (Ma)	1σ (Ma)
TA26	23	Below LOD	Below LOD	11.46	0.68	35	2.58E-05	1359000	1.7	244.6	46.2
TA26	25	Below LOD	Below LOD	13.08	0.77	40	4.27E-05	936700	1.96	147.7	26.5
TA26	26	550	330	13.9	0.79	40	2.77E-05	1447000	1.81	214.7	38.3
TA26	27	Below LOD	Below LOD	9.61	0.6	40	3.15E-05	1270000	1.57	272.6	49.2
TA26	28	Below LOD	Below LOD	9.7	0.74	50	5.23E-05	956400	1.77	203.4	34.9
TA26	29	Below LOD	Below LOD	11.88	0.68	34	2.85E-05	1192000	1.66	207.0	39.5
TA26	30	Below LOD	Below LOD	8.61	0.66	64	5.00E-05	1280000	1.79	306.6	48.6
TA26	31	Below LOD	Below LOD	15.9	1.2	73	4.90E-05	1489000	1.9	193.2	29.3
TA26	32	Below LOD	Below LOD	8.29	0.58	24	2.37E-05	1014000	1.89	252.3	56.5
TA26	33	Below LOD	Below LOD	6.27	0.41	21	3.23E-05	650500	1.83	214.0	50.4
TA26	34	Below LOD	Below LOD	10.1	0.64	42	4.20E-05	1001000	1.8	204.4	36.3
TA26	35	Below LOD	Below LOD	10.46	0.65	27	3.71E-05	728800	2.14	143.7	30.3
TA26	36	Below LOD	Below LOD	11.2	0.73	57	6.15E-05	927200	1.66	170.8	27.2
TA26	37	Below LOD	Below LOD	11.1	0.55	82	5.39E-05	1521000	1.9	282.6	38.2
TA26	38	Below LOD	Below LOD	8.63	0.53	32	3.85E-05	830700	1.89	198.5	39.0
TA26	39	Below LOD	Below LOD	13.75	0.74	47	3.02E-05	1559000	1.95	233.9	39.0
TA26	40	Below LOD	Below LOD	6.2	0.42	43	4.90E-05	877000	1.75	291.8	51.8
TA27	1	8510	560	46.6	3	59	1.32E-05	4480000	2.97	198.3	31.2
TA27	2	6610	530	40.8	2.6	46	1.45E-05	3169000	2.71	160.2	27.5
TA27	3	7300	640	42	3.8	48	1.10E-05	4377000	2.64	215.0	38.9
TA27	4	8290	660	28.7	2	28	9.60E-06	2917000	2.99	209.6	44.1
TA27	5	4620	380	45.3	2.4	44	1.04E-05	4253000	2.64	193.7	33.1
TA27	6	5180	590	48.3	2.8	48	1.24E-05	3879000	2.53	165.7	27.6
TA27	7	5790	790	44.9	3.6	66	1.88E-05	3512000	2.67	161.3	25.6
TA27	8	3990	390	51.2	3.5	90	1.70E-05	5296000	2.39	213.4	29.7
TA27	9	7850	910	61.1	4.1	74	1.51E-05	4918000	2.7	166.0	24.4
TA27	10	5390	670	26.8	1.6	57	2.20E-05	2587000	2.52	199.1	31.3
TA27	11	4980	480	44.1	2.7	68	1.75E-05	3876000	2.99	181.3	27.0
TA27	12	4960	510	45.1	3.2	56	1.24E-05	4507000	2.38	206.1	33.6
TA27	13	3780	340	51.2	3.7	52	8.22E-06	6324000	2.13	254.8	42.7

Continued on next page

Continued from previous page

Sample name	Grain number	Cl (ppm)	2σ (ppm)	U (ppm)	2σ (ppm)	N_s	Area (cm^2)	ρ_s (tracks/cm^2)	D_{par} (μm)	Age (Ma)	1σ (Ma)
TA27	14	6240	690	29.7	2	31	1.59E-05	1954000	2.58	135.7	27.3
TA27	15	7900	1300	53.4	4.5	66	1.68E-05	3923000	2.75	151.5	24.4
TA27	16	4600	540	46.8	3	56	1.21E-05	4616000	2.6	203.4	32.6
TA27	17	5730	490	48.4	3	55	1.27E-05	4326000	2.59	184.4	29.5
TA10	1	760	230	29.2	1.8	48	2.35E-05	2043000	2.23	143.1	23.9
TA10	2	no value	NaN	50.6	2.8	59	1.63E-05	3617000	2.13	146.2	22.2
TA10	3	1190	290	27.4	1.3	46	2.13E-05	2158000	1.76	161.1	26.5
TA10	4	960	250	22.7	1	72	2.94E-05	2451000	2.12	220.8	30.4
TA10	5	1680	350	34.9	1.6	31	1.20E-05	2578000	2.06	151.1	29.3
TA10	6	840	270	30.5	1.3	92	3.02E-05	3047000	2.68	204.3	25.7
TA10	7	990	270	43.1	1.7	54	2.00E-05	2707000	2.34	128.5	19.6
TA10	8	780	250	15.2	1.1	21	1.77E-05	1186000	2.23	159.6	37.8
TA10	9	860	370	28	1.2	30	1.66E-05	1813000	2.03	132.4	25.9
TA10	10	1670	310	16.3	1	40	2.46E-05	1627000	2.15	204.2	36.5
TA10	11	1320	300	20	1.2	33	1.91E-05	1732000	2.4	177.1	34.1
TA10	12	1150	320	26.9	1.6	24	2.00E-05	1199000	2.24	91.2	20.0
TA10	14	1090	310	12.98	0.49	27	2.04E-05	1321000	1.75	208.2	42.5
TA10	15	910	380	21.9	1.3	43	2.58E-05	1669000	1.68	155.9	27.0
TA10	16	930	250	39.2	1.4	50	1.85E-05	2705000	1.66	141.1	22.1
TA10	17	1780	310	20.39	0.93	25	1.77E-05	1417000	1.73	142.1	30.2
TA10	18	1300	270	9.83	0.48	31	2.76E-05	1122000	1.95	233.5	45.4
TA10	19	920	300	9.26	0.34	22	3.10E-05	710100	1.59	156.8	35.1
TA10	20	1100	240	28.03	0.83	51	1.61E-05	3165000	1.91	231.0	35.5
TA10	21	1070	320	15.36	0.53	37	3.38E-05	1095000	1.9	145.8	25.8
TA10	22	1560	350	18.48	0.78	37	2.06E-05	1801000	2.37	199.3	35.6
TA10	23	770	280	27.3	1.3	49	2.29E-05	2138000	2.04	160.2	25.7
TA10	24	890	260	17.67	0.91	27	1.60E-05	1686000	1.98	195.2	40.4
TA10	25	1010	300	16.5	2	44	3.86E-05	1140000	1.9	141.3	28.5
TA10	26	1210	240	9.64	0.4	20	2.34E-05	856600	2.24	181.8	42.6
TA10	27	1090	310	18.34	0.89	40	2.20E-05	1816000	2.03	202.5	35.4

Continued on next page

Continued from previous page

Sample name	Grain number	Cl (ppm)	2σ (ppm)	U (ppm)	2σ (ppm)	N_s	Area (cm^2)	ρ_s (tracks/cm^2)	D_{par} (μm)	Age (Ma)	1σ (Ma)
TA10	28	1430	370	19.1	1	23	1.72E-05	1338000	2.37	143.3	31.8
TA10	29	700	300	13.43	0.81	12	1.63E-05	735100	1.11	112.0	33.6
TA10	30	1330	310	20.02	0.8	28	1.37E-05	2043000	1.72	208.7	42.0
TA10	31	720	350	23.95	0.83	28	1.72E-05	1626000	1.32	138.9	27.8
TA10	32	700	260	29.1	1.7	47	1.75E-05	2690000	1.78	189.1	31.5
TA10	33	1240	210	25.4	1.1	58	2.43E-05	2389000	2.21	192.4	28.7
TA10	34	1360	380	24.65	0.96	39	1.98E-05	1967000	1.73	163.2	28.4
TA10	35	1120	290	28.2	1.3	41	1.50E-05	2740000	2.06	198.7	34.2
TA10	36	820	260	34.2	2.1	33	1.58E-05	2085000	2.29	124.7	24.1
TA10	37	790	350	23.9	1.2	62	2.97E-05	2091000	2.15	178.9	26.4
TA15	1	670	320	13.14	0.46	23	1.15E-05	1995000	1.14	310.5	67.9
TA15	2	880	310	10.55	0.43	17	8.69E-06	1956000	0.98	379.2	95.7
TA15	3	820	340	3.74	0.24	10	2.85E-05	351200	1.14	192.1	62.9
TA15	4	1100	390	13.92	0.61	43	1.73E-05	2487000	1.27	365.4	61.5
TA15	5	no value	NaN	6.8	0.37	8	1.13E-05	709100	1.05	213.3	77.2
TA15	6	no value	NaN	13.9	1.2	15	2.15E-05	698400	1.18	102.8	28.6
TA15	7	Below LOD	Below LOD	3.26	0.24	8	2.43E-05	329200	1.19	206.5	75.5
TA15	8	Below LOD	Below LOD	17.4	1.3	21	6.76E-06	3105000	1.22	365.0	86.6
TA15	9	860	300	12.88	0.47	13	1.84E-05	705800	1.37	112.1	32.0
TA15	10	1100	420	11.41	0.59	20	1.70E-05	1176000	1.13	210.8	49.8
TA15	11	1750	460	38.2	1.8	55	2.14E-05	2572000	1.15	137.7	21.1
TA15	12	Below LOD	Below LOD	13.32	0.57	12	1.35E-05	890200	1.13	136.7	40.6
TA15	13	940	360	2.47	0.16	8	3.43E-05	233200	1.19	193.1	70.3
TA15	14	Below LOD	Below LOD	11.85	0.69	26	3.05E-05	851400	1.12	147.0	31.2
TA15	15	Below LOD	Below LOD	12.75	0.65	23	1.70E-05	1351000	1.28	216.7	48.1
TA15	18	1170	470	6.92	0.34	9	1.31E-05	688500	1.4	203.5	69.5
TA15	21	1360	430	12.61	0.97	21	1.57E-05	1336000	1.4	216.7	51.6
TA15	23	Below LOD	Below LOD	27.6	1.9	34	8.03E-06	4235000	1.29	313.8	60.6
TA15	24	Below LOD	Below LOD	57.7	3.1	58	1.22E-05	4770000	1.27	169.1	25.8
TA15	25	Below LOD	Below LOD	9.5	1	7	1.14E-05	615400	0.9	132.5	52.5

Continued on next page

Continued from previous page

Sample name	Grain number	Cl (ppm)	2σ (ppm)	U (ppm)	2σ (ppm)	N_s	Area (cm^2)	ρ_s (tracks/cm^2)	D_{par} (μm)	Age (Ma)	1σ (Ma)
TA15	26	1610	410	18.2	1.5	8	1.29E-05	621700	0.97	69.9	25.7
TA16	1	770	290	6.06	0.34	16	3.66E-05	437000	1.35	147.5	38.7
TA16	2	1160	330	10.4	1.1	17	1.98E-05	859900	0.93	169.1	45.7
TA16	3	980	280	9.01	0.48	10	1.68E-05	595500	0.92	135.2	44.0
TA16	4	690	330	6.36	0.34	3	2.33E-05	128800	1.21	41.4	24.1
TA16	5	1170	280	6.61	0.43	17	1.89E-05	901700	1.44	279.0	71.8
TA16	7	610	250	6.12	0.31	12	2.45E-05	488900	1.06	163.4	48.8
TA16	8	660	230	7.41	0.41	10	1.93E-05	517900	1.14	143.0	46.6
TA16	9	1070	350	10.28	0.67	14	1.06E-05	1328000	1.21	264.2	74.2
TA16	10	no value	NaN	15.9	2	14	1.25E-05	1118000	0.74	143.8	43.2
TA16	11	1300	280	7	0.31	17	3.51E-05	484900	1.14	141.7	35.8
TA16	12	Below LOD	Below LOD	7.13	0.37	9	1.44E-05	623800	0.7	178.9	61.2
TA16	13	Below LOD	Below LOD	5.73	0.3	4	2.13E-05	187800	0.96	67.0	33.9
TA16	14	930	260	4.95	0.26	10	1.25E-05	802400	1.15	331.6	107.9
TA16	15	560	260	5.4	0.24	10	3.65E-05	273900	1.18	103.7	33.6
TA16	16	960	250	15.48	0.63	9	1.35E-05	666000	0.85	88.0	30.0
TA16	18	1110	320	12.89	0.99	20	1.97E-05	1015000	1.08	161.1	39.1
TA16	19	1140	270	4.9	0.27	3	2.25E-05	133600	1.09	55.8	32.5
TA16	20	Below LOD	Below LOD	11.22	0.79	16	2.29E-05	697500	1.17	127.2	33.8
TA16	21	820	320	8.05	0.52	6	1.55E-05	387400	0.82	98.4	41.1
TA16	23	700	290	12.36	0.86	18	1.56E-05	1155000	0.92	191.1	48.2
TA16	25	2260	520	5.8	0.68	11	1.77E-05	622900	0.89	219.7	72.1
TA16	27	570	230	9.18	0.46	6	1.95E-05	307500	1.09	68.5	28.4
TA16	28	510	300	15.97	0.56	10	1.13E-05	885000	1.26	113.3	36.6
TA16	29	600	180	5.6	0.25	10	2.14E-05	467900	0.97	170.9	55.4
TA16	30	500	210	5.42	0.28	6	2.48E-05	242200	0.88	91.4	38.0
TA16	31	Below LOD	Below LOD	5.44	0.37	6	1.69E-05	354200	1	133.2	55.6
TA16	32	Below LOD	Below LOD	4.27	0.34	5	2.73E-05	183100	1.16	87.7	40.1
TA16	34	1120	280	3.9	0.23	11	2.38E-05	463000	0.95	242.8	75.8
TA16	35	820	250	7.18	0.44	19	2.52E-05	753100	0.81	214.5	52.3

Continued on next page

Continued from previous page

Sample name	Grain number	Cl (ppm)	2σ (ppm)	U (ppm)	2σ (ppm)	N_s	Area (cm^2)	ρ_s (tracks/cm^2)	D_{par} (μm)	Age (Ma)	1σ (Ma)
TA16	36	1690	400	4.84	0.33	8	2.46E-05	325100	1.02	137.4	50.1
TA16	38	Below LOD	Below LOD	6.27	0.43	9	1.39E-05	647400	1.16	211.2	72.8
TA16	39	710	210	7.28	0.29	7	2.32E-05	302400	1.13	85.0	32.6
TA17	1	500	260	14.27	0.56	42	2.51E-05	1676000	1.15	240.2	40.6
TA17	2	Below LOD	Below LOD	10.49	0.47	31	3.81E-05	814000	1.35	158.7	30.7
TA17	3	Below LOD	Below LOD	3.71	0.28	16	3.12E-05	513500	1.11	283.1	75.6
TA17	4	Below LOD	Below LOD	1.63	0.11	9	3.86E-05	233300	0.92	292.8	100.9
TA17	5	480	270	17.3	0.96	49	3.28E-05	1493000	1.13	176.5	28.8
TA17	6	790	230	13.61	0.59	48	3.18E-05	1510000	1.07	226.9	36.5
TA17	7	650	250	14.92	0.66	30	1.70E-05	1769000	0.98	242.5	47.5
TA17	8	Below LOD	Below LOD	1.8	0.14	14	5.15E-05	271800	1.07	308.9	87.7
TA17	9	510	200	34.9	1.2	47	1.72E-05	2729000	1.3	159.9	25.6
TA17	10	640	290	11.26	0.66	28	2.01E-05	1393000	1.07	253.0	52.0
TA17	11	630	290	3.78	0.18	22	5.68E-05	387400	1.15	209.6	47.3
TA17	12	Below LOD	Below LOD	12.93	0.56	25	2.79E-05	895300	0.85	141.6	30.1
TA17	13	Below LOD	Below LOD	3.29	0.2	17	4.72E-05	360300	0.82	224.0	57.4
TA17	14	Below LOD	Below LOD	14.79	0.47	37	4.00E-05	924700	1.15	127.9	22.6
TA17	15	760	230	17.72	0.79	31	2.43E-05	1274000	1.09	147.1	28.4
TA17	16	540	260	2.68	0.13	11	5.89E-05	186900	1.13	142.6	44.3
TA17	17	Below LOD	Below LOD	24.8	1.1	126	6.43E-05	1959000	1.33	161.6	18.5
TA17	18	780	220	11.12	0.38	58	6.35E-05	914100	1.33	168.1	24.7
TA17	19	540	250	3.35	0.23	12	4.34E-05	276400	0.96	168.8	51.0
TA17	21	Below LOD	Below LOD	11.63	0.49	31	3.44E-05	9.00E+05	1.19	158.3	30.5
TA17	22	520	220	9.51	0.44	41	3.76E-05	1091000	1.39	234.6	40.4
TA17	23	620	200	13.83	0.7	28	2.06E-05	1357000	1.28	200.7	40.8
TA17	25	460	180	10.98	0.33	47	5.41E-05	868500	1.01	161.8	25.7
TA17	26	550	260	3.61	0.17	13	3.97E-05	327200	1.12	185.4	53.2
TA17	27	670	280	3.78	0.25	16	3.49E-05	457900	1.04	247.8	65.6
TA17	30	850	220	12.05	0.4	30	3.69E-05	812500	1.26	137.9	26.7
TA17	31	550	330	2.42	0.13	7	4.43E-05	157900	1.03	133.5	51.5

Continued on next page

Continued from previous page

Sample name	Grain number	Cl (ppm)	2σ (ppm)	U (ppm)	2σ (ppm)	N_s	Area (cm^2)	ρ_s (tracks/cm^2)	D_{par} (μm)	Age (Ma)	1σ (Ma)
TA17	32	Below LOD	Below LOD	3.68	0.17	15	3.88E-05	386600	1.06	214.9	57.6
TA17	33	Below LOD	Below LOD	9.74	0.36	42	2.45E-05	1717000	1.2	360.6	60.7
TA17	35	Below LOD	Below LOD	3.13	0.17	18	3.34E-05	539600	1.03	352.6	87.6
TA17	36	610	210	4.54	0.2	6	3.14E-05	190900	0.81	86.0	35.6
TA17	37	Below LOD	Below LOD	1.92	0.11	10	6.54E-05	152900	1.13	162.9	53.1
TA17	38	480	250	2.239	0.09	6	3.59E-05	167200	0.96	152.7	63.2
TA17	39	510	200	2.96	0.14	8	3.15E-05	254200	1.04	175.7	63.4
TA18	1	2810	450	6.39	0.42	43	0.00003711	1159000	1.52	371.0	65.0
TA18	2	2740	230	4.85	0.27	34	0.00005083	668800	1.64	282.1	53.3
TA18	3	3170	400	4.91	0.26	23	0.00001975	1164000	1.55	484.9	107.8
TA18	4	1800	270	5.09	0.22	51	0.00004187	1218000	1.66	489.4	76.8
TA18	5	2880	330	6.02	0.28	23	0.00001695	1357000	1.64	461.1	101.8
TA18	6	2950	300	5.24	0.29	28	0.0000415	674700	1.72	263.4	53.9
TA18	7	2940	300	6.11	0.32	23	0.00002266	1015000	1.81	339.8	75.5
TA18	8	2520	350	9.51	0.63	16	0.00001797	890200	1.64	191.5	50.7
TA18	9	2490	430	7.64	0.67	20	0.00002341	854500	1.75	228.8	56.4
TA18	10	3110	460	5.68	0.3	13	0.00001476	880500	1.67	317.1	91.3
TA18	11	2520	310	5.79	0.33	42	0.00004771	880300	1.63	311.0	54.0
TA18	12	2800	280	5.13	0.19	31	0.00002919	1062000	1.63	423.4	81.2
TA18	12	2640	290	5.13	0.19	31	0.00002499	1240000	1.63	494.4	94.8
TA18	13	2300	350	5.12	0.24	42	0.0000479	876700	1.6	350.2	59.8
TA18	16	3150	470	11	1	34	0.00003878	876600	1.92	163.0	32.9
TA18	17	3140	260	4.44	0.17	24	0.0000553	434000	1.83	199.9	43.0
TA18	18	1530	320	28.7	1	85	0.00002726	3118000	1.34	222.2	28.2
TA18	19	2910	290	10.14	0.52	59	0.00004506	1309000	1.71	264.0	39.8
TA18	20	2840	340	4.36	0.24	27	0.00005195	519700	1.77	243.8	50.7
TA18	20	2780	280	4.36	0.24	26	0.00004603	564800	1.77	265.0	56.0
TA18	21	3050	260	4.86	0.23	28	0.00004373	640200	1.84	269.4	54.6
TA18	22	2700	290	6.29	0.32	26	0.00002461	1057000	1.64	343.7	72.3
TA18	23	2300	260	12.48	0.45	19	0.00001057	1798000	1.84	294.7	70.4

Continued on next page

Continued from previous page

Sample name	Grain number	Cl (ppm)	2σ (ppm)	U (ppm)	2σ (ppm)	N_s	Area (cm^2)	ρ_s (tracks/cm^2)	D_{par} (μm)	Age (Ma)	1σ (Ma)
TA18	24	1450	280	24	1.1	39	0.00001341	2908000	1.41	247.8	43.6
TA18	25	3230	320	5.77	0.31	22	0.0000273	805700	1.8	285.6	64.8
TA18	26	2740	390	4.22	0.37	28	0.00004253	658300	1.67	319.1	68.8
TA19	1	730	300	1.73	0.14	7	4.25E-05	164700	1.11	194.7	76.1
TA19	2	600	220	21.81	0.8	57	4.36E-05	1307000	1.18	122.6	18.2
TA19	3	930	290	35.2	2.3	37	1.20E-05	3097000	1.26	180.0	33.4
TA19	4	Below LOD	Below LOD	9.36	0.56	44	4.54E-05	968400	1.09	211.6	36.3
TA19	5	590	300	2.89	0.18	4	2.69E-05	148900	1.3	105.4	53.4
TA19	6	Below LOD	Below LOD	2.78	0.28	6	2.82E-05	212800	1.03	156.6	66.4
TA19	7	Below LOD	Below LOD	1.7	0.15	10	5.25E-05	190500	0.81	229.2	76.3
TA19	8	630	230	6.38	0.3	13	3.00E-05	434000	1.05	139.1	39.9
TA19	9	Below LOD	Below LOD	14.48	0.73	18	1.14E-05	1574000	1.18	222.3	55.0
TA19	10	Below LOD	Below LOD	7.33	0.44	18	6.00E-05	299900	0.82	83.7	20.9
TA19	11	800	440	3.16	0.23	24	5.42E-05	443000	0.75	286.7	64.2
TA19	12	Below LOD	Below LOD	4.82	0.45	10	3.94E-05	253700	1.16	107.7	36.0
TA19	13	1180	380	2.03	0.14	12	2.62E-05	458100	1.25	461.6	139.4
TA19	14	Below LOD	Below LOD	6.02	0.46	22	4.14E-05	532100	0.96	180.8	42.2
TA19	15	560	260	6.76	0.39	32	4.39E-05	729700	0.87	220.8	42.9
TA19	16	590	260	14.3	1.1	21	2.63E-05	799100	0.99	114.3	27.2
TA19	17	540	270	23.17	0.87	29	1.88E-05	1540000	1.08	135.9	26.9
TA19	18	530	280	23.03	0.91	35	2.77E-05	1264000	1.11	112.3	20.5
TA19	19	860	300	9.91	0.57	18	1.93E-05	932500	0.86	192.5	47.9
TA19	20	Below LOD	Below LOD	20.2	0.64	63	2.26E-05	2794000	1.07	282.9	40.0
TA19	21	610	250	9.06	0.4	20	2.74E-05	730400	1.15	164.9	38.7
TA19	22	630	240	33.6	2.2	65	1.99E-05	3261000	1.17	198.5	30.0
TA19	23	830	290	2.67	0.17	8	3.19E-05	250900	1.16	192.2	69.9
TA19	24	680	340	2.56	0.16	5	5.07E-05	98580	1.12	78.8	35.8
TA19	25	Below LOD	Below LOD	7.48	0.53	28	3.78E-05	741600	1	202.8	42.5
TA19	26	480	200	2.6	0.15	27	5.64E-05	478800	1.11	376.7	78.6
TA19	27	870	250	2.84	0.19	6	1.21E-05	496200	0.78	357.4	149.2

Continued on next page

Continued from previous page

Sample name	Grain number	Cl (ppm)	2σ (ppm)	U (ppm)	2σ (ppm)	N_s	Area (cm^2)	ρ_s (tracks/cm^2)	D_{par} (μm)	Age (Ma)	1σ (Ma)
TA19	28	650	300	9.66	0.45	18	1.82E-05	986900	1.12	209.0	51.6
TA19	29	Below LOD	Below LOD	4.97	0.37	9	1.97E-05	456500	1.28	187.9	65.0
TA19	30	700	250	3.06	0.14	6	1.58E-05	380300	1.1	254.2	105.4
TA20	1	960	280	4.3	0.23	27	5.41E-05	499000	1.37	237.4	49.2
TA20	2	1230	300	4.54	0.25	26	3.65E-05	713200	1.46	321.3	67.9
TA20	3	890	370	4.67	0.26	32	5.71E-05	560600	1.49	245.5	47.5
TA20	4	840	230	5.32	0.27	27	3.81E-05	708800	1.5	272.5	56.4
TA20	5	1090	300	4.8	0.19	37	5.71E-05	648200	1.53	276.2	49.2
TA20	6	1270	260	4.45	0.21	41	5.84E-05	701600	1.49	322.5	55.6
TA20	7	1000	240	4.89	0.22	22	4.34E-05	507200	1.38	212.2	47.7
TA20	8	1160	210	3.41	0.18	19	5.34E-05	356000	1.45	213.5	51.7
TA20	9	1120	240	5.83	0.25	53	6.05E-05	876400	1.38	307.5	47.5
TA20	10	920	240	4.1	0.22	35	5.97E-05	586200	1.46	292.4	54.4
TA20	11	1290	310	4.74	0.3	30	5.58E-05	537200	1.57	231.8	46.6
TA20	12	1560	270	4.78	0.26	33	5.46E-05	604300	1.55	258.6	49.3
TA20	13	1610	310	4.69	0.21	22	5.56E-05	395700	1.58	172.6	38.8
TA20	14	880	240	5.25	0.25	37	6.26E-05	591400	1.47	230.4	41.5
TA20	15	1020	340	4.38	0.2	24	5.31E-05	451700	1.62	210.9	45.7
TA20	16	770	290	5.19	0.27	32	5.74E-05	557900	1.5	219.9	42.4
TA20	17	1390	230	4.42	0.21	47	8.65E-05	543600	1.5	251.6	41.1
TA20	18	1040	280	4.49	0.17	35	6.32E-05	554200	1.59	252.5	46.0
TA20	19	960	330	4.77	0.2	53	9.32E-05	568500	1.56	243.8	37.6
TA20	20	1170	280	5	0.22	55	7.97E-05	689700	1.39	282.1	43.0
TA20	21	780	290	4.46	0.22	48	5.88E-05	816600	1.6	374.5	60.9
TA20	22	840	380	5.04	0.24	46	8.81E-05	522400	1.24	212.0	34.9
TA20	23	1110	280	4.81	0.23	25	4.63E-05	540200	1.51	229.7	49.0
TA20	24	1020	270	4.83	0.2	41	6.83E-05	599900	1.3	254.0	43.4
TA20	25	960	260	4.64	0.21	39	6.06E-05	643700	1.27	283.8	49.8
TA20	26	1370	250	5	0.22	31	5.51E-05	562300	1.61	230.0	44.4
TA20	27	1510	320	4.63	0.18	27	5.53E-05	487900	1.28	215.5	44.0

Continued on next page

Continued from previous page

Sample name	Grain number	Cl (ppm)	2σ (ppm)	U (ppm)	2σ (ppm)	N_s	Area (cm^2)	ρ_s (tracks/cm^2)	D_{par} (μm)	Age (Ma)	1σ (Ma)
TA20	28	1190	280	5.19	0.22	55	6.78E-05	811800	1.24	319.9	48.7
TA20	29	1330	240	4.24	0.21	42	6.06E-05	693000	1.53	334.3	57.3
TA20	30	880	200	7.93	0.33	57	6.05E-05	941800	1.44	242.9	36.4
TA20	31	1250	270	4.64	0.18	57	0.0001112	512400	1.53	225.9	33.7
TA20	32	1180	260	4.74	0.23	35	5.85E-05	598600	1.39	258.3	47.7
TA20	33	1140	220	4.35	0.19	54	9.08E-05	594500	1.3	279.5	42.9
TA20	34	910	180	4.85	0.23	48	8.16E-05	587900	1.56	247.9	40.2
TA20	35	1010	250	3.91	0.17	36	6.71E-05	536300	1.37	280.5	50.8
TA20	36	1110	240	4.72	0.22	36	6.66E-05	540500	1.39	234.2	42.6
TA20	37	1250	270	4.69	0.21	44	6.57E-05	670200	1.55	292.3	48.8
TA20	38	1350	230	4.66	0.2	47	8.30E-05	566300	1.59	248.6	40.3
TA20	39	1070	270	4.96	0.22	27	4.09E-05	659500	1.44	272.0	55.8
TA20	40	840	260	4.33	0.18	54	0.0001148	470300	1.57	222.2	34.0
TA22	1	6820	520	5.99	0.3	23	4.57E-05	503700	2.17	172.0	38.1
TA22	2	5780	430	4.78	0.21	19	2.30E-05	826700	1.84	353.7	85.0
TA22	3	5440	450	8.38	0.44	24	4.05E-05	592100	1.72	144.5	31.5
TA22	5	8650	770	5.97	0.44	19	1.93E-05	984000	1.92	337.1	83.4
TA22	6	6610	480	4.12	0.19	20	3.69E-05	541600	1.9	268.9	63.2
TA22	7	5680	520	4.88	0.22	21	4.18E-05	502300	2	210.5	48.4
TA22	8	7170	630	4.56	0.36	20	3.58E-05	558600	1.8	250.6	61.1
TA22	9	7550	730	5.77	0.33	18	2.91E-05	618700	1.94	219.3	54.6
TA22	10	6970	570	6.83	0.37	14	2.33E-05	601600	2.1	180.2	50.2
TA22	11	5980	580	5.96	0.32	18	2.32E-05	776800	1.91	266.6	66.2
TA22	12	6310	570	3.98	0.19	42	6.87E-05	611800	2.14	314.4	53.8
TA22	13	7630	540	4.38	0.2	14	2.52E-05	556000	1.95	259.6	71.9
TA22	14	6020	490	6.03	0.36	20	3.83E-05	522500	1.85	177.2	42.2
TA22	15	5800	450	5.54	0.26	19	3.32E-05	572100	2.17	211.2	50.9
TA22	16	6820	730	5.36	0.37	28	3.50E-05	800300	1.81	305.4	63.8
TA22	17	7780	530	5.2	0.23	35	4.01E-05	872400	1.93	343.2	63.0
TA22	18	5730	560	6.85	0.39	23	4.16E-05	553300	1.73	165.2	36.9

Continued on next page

Continued from previous page

Sample name	Grain number	Cl (ppm)	2σ (ppm)	U (ppm)	2σ (ppm)	N_s	Area (cm^2)	ρ_s (tracks/cm^2)	D_{par} (μm)	Age (Ma)	1σ (Ma)
TA22	19	5420	520	5.33	0.31	28	3.69E-05	759700	1.73	291.5	59.9
TA22	20	5750	540	5.43	0.33	16	2.80E-05	570700	1.9	215.0	56.6
TA22	21	8180	750	5.52	0.33	16	2.46E-05	651300	1.8	241.3	63.5
TA22	22	5730	760	6.29	0.43	14	2.11E-05	662300	2.02	215.4	60.6
TA22	23	5460	530	4.38	0.26	11	1.85E-05	594000	1.84	277.4	86.6
TA22	24	5860	510	3.47	0.19	18	2.86E-05	628500	1.7	370.5	92.0
TA22	25	6010	630	2.99	0.24	10	3.37E-05	296900	1.71	203.1	67.2
TA22	26	4750	440	4.14	0.16	16	3.96E-05	403600	1.86	199.4	51.7
TA22	27	6370	570	5.61	0.27	15	1.82E-05	824800	1.98	300.7	80.8
TA22	28	4040	390	23.23	0.94	45	1.53E-05	2942000	2.09	259.0	42.6
TA22	29	5190	360	6.09	0.26	24	3.04E-05	790000	2.01	265.3	57.3
TA22	30	6400	480	6.17	0.22	17	2.15E-05	791400	2.18	262.4	66.0
TA22	31	4860	580	5	0.32	16	2.74E-05	584200	1.7	239.0	63.1
TA22	32	4570	490	5.8	0.29	17	1.94E-05	876600	2.16	309.1	78.5
TA22	33	4990	430	6.09	0.31	25	3.30E-05	757000	1.71	254.2	54.4
TA22	34	6090	670	5.31	0.37	29	3.10E-05	935500	1.85	360.3	74.3
TA22	35	5260	540	2.82	0.17	17	4.49E-05	379000	1.55	274.9	70.4
TA22	36	4890	470	4.37	0.26	14	2.22E-05	631700	1.8	295.7	82.6
TA22	37	6530	700	5.95	0.43	29	2.65E-05	1093000	1.74	375.7	77.8
TA22	38	6370	630	6.34	0.37	11	1.63E-05	675500	1.9	217.9	68.0
TA22	39	5240	530	4.08	0.19	8	3.35E-05	238800	1.65	119.7	43.2
TA22	40	6310	510	5.82	0.31	18	2.42E-05	742600	1.72	261.0	64.7
TA23	1	1290	730	4	0.22	11	4.22E-05	260900	1.34	133.4	41.6
TA23	2	2850	450	34.2	1.4	32	1.23E-05	2597000	1.58	155.3	29.5
TA23	3	3260	400	14.79	0.71	40	1.97E-05	2030000	1.91	280.7	49.0
TA23	4	1190	430	13.3	0.66	39	2.47E-05	1582000	1.46	243.3	43.0
TA23	5	1150	380	4.7	0.23	27	2.33E-05	1158000	1.49	503.9	104.0
TA23	6	2200	340	34.5	1.4	62	1.38E-05	4509000	1.38	267.3	38.7
TA23	7	1110	220	12.53	0.6	29	2.87E-05	1010000	1.49	164.9	32.9
TA23	8	2110	340	4.19	0.17	25	2.95E-05	847800	1.54	413.9	87.6

Continued on next page

Continued from previous page

Sample name	Grain number	Cl (ppm)	2σ (ppm)	U (ppm)	2σ (ppm)	N_s	Area (cm^2)	ρ_s (tracks/cm^2)	D_{par} (μm)	Age (Ma)	1σ (Ma)
TA23	10	2080	390	17.63	0.76	52	2.12E-05	2458000	1.58	285.2	44.4
TA23	11	2550	310	13.99	0.64	63	2.79E-05	2262000	1.73	330.7	48.1
TA23	12	750	350	4.03	0.47	33	7.19E-05	459300	1.62	233.1	50.6
TA23	13	2000	500	29.6	1.6	62	1.94E-05	3193000	1.19	220.6	32.9
TA23	14	2070	430	4.83	0.33	23	3.53E-05	651200	1.79	275.8	62.5
TA23	15	1290	340	19.04	0.85	34	1.38E-05	2471000	1.16	265.4	49.3
TA23	16	1140	290	4.44	0.19	29	5.24E-05	553500	1.77	255.0	50.7
TA23	17	2240	400	12.44	0.61	42	2.65E-05	1585000	1.51	260.6	44.7
TA23	18	3420	360	18.13	0.72	26	1.93E-05	1349000	1.82	152.2	31.6
TA23	19	3280	490	21.8	1.6	52	2.57E-05	2026000	1.53	190.1	31.7
TA23	20	2260	580	2.8	0.17	8	3.77E-05	212000	1.4	154.9	56.2
TA23	21	2040	430	46.5	2.2	85	1.83E-05	4658000	1.56	204.9	26.8
TA23	22	3920	620	7.6	0.53	35	2.24E-05	1562000	1.66	420.4	80.4
TA23	23	1060	500	3.29	0.25	15	2.43E-05	616700	1.38	383.4	105.4
TA23	24	2680	480	8.93	0.47	29	2.18E-05	1328000	1.56	304.2	61.1
TA23	25	2670	450	2.63	0.14	14	4.01E-05	349600	1.35	271.9	75.6
TA23	27	3270	310	7.17	0.36	29	3.18E-05	913500	1.6	260.6	52.2
TA23	28	1740	340	25.48	0.99	36	1.41E-05	2561000	1.31	205.6	37.0
TA23	29	2050	370	32.1	1.2	45	1.59E-05	2830000	1.41	180.3	29.5
TA23	31	3450	440	6.67	0.4	11	2.61E-05	421800	1.67	129.3	40.4
TA23	32	2360	360	2.11	0.13	12	6.09E-05	197100	1.38	191.1	57.4
TA23	33	3900	480	8.49	0.43	22	1.21E-05	1817000	1.49	437.7	99.0
TA23	35	1790	370	40.6	2	74	1.78E-05	4148000	1.41	209.0	28.9
TA23	36	1210	440	3.03	0.14	22	5.14E-05	428300	1.47	289.1	65.1
TA23	37	3010	430	3.79	0.18	9	1.53E-05	588800	1.36	317.8	108.5
TA23	38	1990	390	9.97	0.43	42	2.24E-05	1875000	1.47	384.7	65.3
TA23	39	4260	380	8.05	0.35	33	3.00E-05	1102000	1.82	280.0	52.6
TA23	40	4800	510	21.5	1.2	36	1.60E-05	2251000	1.9	214.1	39.5

F.2 Apatite confined track length measurements

Table F.2: Apatite confined track length measurements

Length no.	Confined track length (μm)	Angle to C Axis	Average DPar (μm)
TA01			
1	12.99	84.21	1.85
2	12.31	64.37	1.85
3	13.01	24.17	1.85
4	13.66	51.23	1.85
5	13.82	69.99	1.6
6	13.72	69.88	1.83
7	13.43	81.29	2.34
8	14.32	44.39	2.34
9	14.16	85.6	2.17
10	11.64	76.74	1.84
11	14.38	44.46	1.71
12	13.82	74.69	1.9
13	15.4	5.98	1.9
14	13.73	62.49	1.9
15	14.33	20.05	1.59
16	12.58	44.34	1.93
17	14.4	17.05	1.78
18	13.98	19.75	1.78
19	12.13	61.85	2.09
20	12.48	86.9	1.55
21	14.01	76.55	1.97
22	14.79	66.75	1.97
23	15.85	24.48	1.97
24	13.57	60.61	1.97
25	13.58	23.42	1.97
26	14.95	69.27	1.95
27	14.23	28.82	1.95
28	12.92	84.48	1.95
29	13.47	66.54	2.07
30	12.33	73.44	1.68
31	13.71	80.09	1.76
32	12.73	60.71	1.82
33	14.56	60.96	1.82
34	12.56	80.94	1.82
35	14.6	54.03	1.76
36	10.82	79.28	1.68
37	13.36	70.44	1.91
38	13.26	60.28	1.91

Continued on next page

Continued from previous page

Length no.	Confined track length (μm)	Angle to C Axis	Average DPar (μm)
39	13.26	68.93	1.91
40	13.75	84.88	1.91
TA06			
1	11.74	79.46	1.15
2	11.29	66.17	1.29
3	14.22	82.65	0.8
4	13.13	72.18	0.89
5	13.88	28.78	1.16
6	13.45	83.99	1.11
7	13.98	58.62	1.11
8	12.76	79.98	1.11
9	13.44	38.59	1.21
10	14.64	38.9	1.21
11	13.29	86.41	1.22
12	12.97	83.02	1.22
13	14.33	36.48	1.12
14	11.2	67.17	1.29
15	12.56	50.32	1.29
16	13.12	8.18	1.29
17	12.55	23.55	1.57
18	12.22	58.65	1.57
19	14.03	85.22	1.57
20	12.64	45.31	1.43
21	12.25	87.66	1.28
22	12.23	55.46	1.29
23	12.33	53.79	1.29
24	13.7	14.65	1.29
25	12.71	0.03	1.29
26	13.41	86.03	1.33
27	13.23	28.61	1.11
28	14.14	69.61	1.29
29	13.15	49.14	1.29
30	14.03	29.99	1.33
31	12.07	27.24	1.33
32	14.62	63.82	1.33
33	13.68	31.94	1.37
34	13.61	82.63	1.37
35	12.47	66.09	1.33
36	12.3	80.35	1.21
37	12.17	80.64	1.21
38	13.07	68.27	1.24
39	12.68	69.68	1.24

Continued on next page

Continued from previous page

Length no.	Confined track length (μm)	Angle to C Axis	Average DPar (μm)
40	11.23	56.71	1.2
41	13.64	83.64	1.2
42	12.82	78.73	1.2
43	13.23	84.68	1.24
44	13.54	20.77	1.24
45	13.71	44.91	1.25
46	11.8	73.08	1.34
47	12.24	64.71	1.34
48	12.22	66.93	1.34
49	13.28	84.71	1.34
50	11.16	51.26	1.41
51	13.09	68.6	1.34
52	13.85	42.1	1.46
53	13.36	18.35	1.22
54	13.73	83.36	1.22
55	12.66	31.89	1.05
56	15.5	44.74	1.21
57	14.52	27.56	1.21
58	15.26	19.25	1.39
59	13.15	86.26	1.34
60	12.76	75.11	1.34
61	14.36	20.24	1.24
62	13.05	40.52	1.14
63	12.92	80.95	1.24
64	15.38	82.03	1.24
65	11.82	69.73	1.37
66	15.66	53.2	1.32
67	13.25	49.79	1.32
68	14.17	37.84	1.32
69	12.95	33.71	1.33
70	12.07	14.52	1.33
71	13.97	44.44	1.33
72	14.2	23.52	1.3
73	13.48	39.43	1.35
74	11.03	83.92	1.35
75	13.23	21.21	1.35
76	13.26	45.17	1.12
77	13.06	88.76	1.12
78	13.86	42.1	1.12
79	13.48	45.97	1.19
80	14.8	10.87	1.16
81	14.4	68.98	1.29
82	13.48	29.86	1.29

Continued on next page

Continued from previous page

Length no.	Confined track length (μm)	Angle to C Axis	Average DPar (μm)
83	12.34	62.19	1.32
84	14.31	57.18	1.42
85	13.23	56.61	1.34
86	13.68	62.09	1.34
87	13.67	65.2	1.34
88	10.74	72.8	1.72
89	14.16	63.83	1.93
90	12.78	60.75	1.81
91	14.53	59.78	2.08
92	12.9	63.23	2.08
93	11.36	38.96	2.08
94	13.68	44.86	1.95
95	13.84	80.06	1.95
96	14.15	61.52	1.97
97	13.18	23.22	1.91
98	13.3	74.48	2.22
99	13.89	71.67	2.22
100	10.25	83.63	2.15
101	9.37	83.56	2.52
102	14.34	38.8	1.72
103	13.12	73.35	2.26
104	14.06	55.51	2.26
105	12.27	84.22	1.74
106	11.92	30.65	1.74
107	12.02	85.08	1.74
108	13.63	51.7	1.99
109	12.88	69.83	1.84
110	13.6	23.68	2.07
111	13.66	71.32	1.92
112	11.4	85.87	1.92
113	13.58	28.19	1.76
114	11.52	35.96	1.81
115	12.51	67.44	2
116	14.16	79.14	1.75
117	13.2	22.17	1.73
118	13.05	58.09	1.84
119	12.96	38.72	1.82
TA07			
1	12.55	49.56	1.29
2	11.88	51.71	1.18
3	9.78	78.28	1.42
4	13.98	54.62	1.56

Continued on next page

Continued from previous page

Length no.	Confined track length (μm)	Angle to C Axis	Average DPar (μm)
5	12.61	56.62	1.18
6	15.16	70.23	1.55
7	11.64	40.02	1.24
8	12.76	50.93	1.25
9	14.42	32.12	1.25
10	14.94	59.21	1.25
11	11.41	66.66	1.05
12	13.4	19.93	1.26
13	14.34	25.41	1.54
14	13.87	69.91	1.36
15	12.72	53.96	1.23
16	13.92	75.23	1.23
TA10			
1	12.5	15.56	2.23
2	12.77	36.23	2.23
3	13.35	32.69	2.13
4	12.96	9.34	2.13
5	10.96	87.88	2.13
6	13.29	45.11	2.13
7	13.91	39.09	2.13
8	14.85	48.01	2.13
9	14.49	81.21	2.13
10	13.13	84.35	2.13
11	13.38	48.21	2.13
12	14.25	45.1	2.13
13	13.89	47.35	2.13
14	13.42	61.74	2.12
15	12.82	12.33	2.12
16	13.53	79.77	2.12
17	12.94	44.94	2.12
18	14.53	79.41	2.12
19	14.28	54.32	2.12
20	12.11	77.43	2.12
21	13.86	49.2	2.12
22	11.68	77.04	2.12
23	13.12	77.36	2.12
24	14.29	83.78	2.68
25	13.54	42.33	2.68
26	13.68	8.37	2.68
27	13.83	61.85	2.68
28	13.19	83.94	2.68
29	13.45	28.28	2.68

Continued on next page

Continued from previous page

Length no.	Confined track length (μm)	Angle to C Axis	Average DPar (μm)
30	13.16	89.53	2.68
31	14.18	53.31	2.68
32	14.1	20.44	2.34
33	11.55	80.17	2.34
34	11.45	27.75	2.34
35	13.12	63.57	2.34
36	13.53	75.55	2.34
37	11.65	55.01	2.34
38	14.46	72.59	2.34
39	13.46	53.5	2.34
40	12.99	37.17	2.34
41	13.62	58.64	2.23
42	13.74	84.3	2.4
43	13.73	71.22	2.4
44	15.08	31.15	2.4
45	11.02	16.51	2.4
46	11.3	69.46	2.4
47	13.7	49.04	2.4
48	14.28	11.85	2.4
49	12.95	68.46	2.24
50	12.11	76.57	1.71
51	12.51	61.22	1.71
52	12.86	49.27	1.71
53	8.56	81.72	1.71
54	14.02	72.85	1.75
55	13.75	78.05	1.75
56	8.92	62.77	1.66
57	11.76	15.49	1.95
58	11.61	23.36	1.95
59	12.54	82.89	1.95
60	12.53	29.85	1.95
61	11.81	62.59	1.9
62	12.82	64.3	2.37
63	15.86	6.69	2.37
64	11.72	77.04	2.37
65	12.78	24.14	2.04
66	13.7	85.15	2.04
67	12.81	48.38	2.04
68	15.51	56.59	1.9
69	14.34	72.84	2.24
70	11.91	81.2	2.24
71	13.63	53.75	2.24
72	12.53	40.6	2.24

Continued on next page

Continued from previous page

Length no.	Confined track length (μm)	Angle to C Axis	Average DPar (μm)
73	9.71	69.23	2.24
74	13.68	33.43	2.03
75	15.56	13.26	2.03
76	13.23	44.03	2.37
77	14.18	60.28	2.37
78	13.26	3.56	1.32
79	11.01	88.1	1.32
80	13.35	83.56	1.78
81	14.78	6.07	1.78
82	10.88	69.19	1.78
83	13.81	65.36	1.78
84	12.93	81.67	2.21
85	14.45	49.7	2.21
86	13.56	15.69	2.21
87	11.12	54.96	2.21
88	8.39	75.5	2.21
89	12.07	73.46	2.21
90	12.6	67.77	2.21
91	14.95	11.55	1.73
92	13.3	64	1.73
93	14.15	35.11	2.06
94	12.65	18.33	2.06
95	10.9	44.17	2.06
96	12.64	77.35	2.06
97	13.07	86.79	2.06
98	13.13	12.39	2.15
99	14.04	72.31	2.15
100	12.92	51.01	2.15
TA11			
1	12.89	89.92	1.11
2	13.21	70.46	1.47
3	12.69	81.92	1.47
4	13.64	86.8	1.47
5	10.02	23.54	1.47
6	9.38	81.23	1.31
7	14.09	70.22	1.27
8	15.77	67.69	1.34
9	13.94	14.28	1.34
10	11	54.2	1.34
11	14.6	28.3	1.34
12	13.99	46.09	1.31
13	11.62	60.51	1.33

Continued on next page

Continued from previous page

Length no.	Confined track length (μm)	Angle to C Axis	Average DPar (μm)
14	11.21	79.74	1.41
15	11.85	47.39	1.27
16	13.94	69.55	1.26
17	9.29	69.6	1.26
18	12.23	61.64	1.43
19	10.32	52.49	1.43
20	12.66	52.55	1.1
21	12.24	64.98	1.33
22	10.83	65.36	1.33
23	12.29	51.24	1.2
24	11.35	31.88	1.44
25	11.08	62.74	1.44
26	12.3	46.06	0.92
27	12.74	62.75	1.05
28	12.05	31.52	1.05
29	12.12	51.35	1.08
30	12.31	48.47	1.18
31	12.52	79.92	1.18
32	13.49	51.08	1.18
33	13.05	53.9	1.42
34	11.7	34.84	1.42
35	10.15	20.83	1.42
36	11.64	62.02	1.42
37	12.77	67.28	1.42
38	10.15	72.34	1.42
39	9.54	63.53	1.42
40	10.68	72.38	1.42
41	13.14	60.13	1.42
42	13.27	46.96	1.42
TA14			
1	15.23	38.64	1.55
2	12.89	81.24	1.55
3	14.4	35.79	1.57
4	12.9	78.61	1.27
5	12.59	80.09	1.6
6	14.02	79.9	1.7
7	13.91	45.99	1.63
8	14.09	84.31	1.43
9	12.53	45.31	1.43
10	13.72	14.64	1.52
11	14.57	32.89	1.52
12	13.88	48.21	1.68

Continued on next page

Continued from previous page

Length no.	Confined track length (μm)	Angle to C Axis	Average DPar (μm)
13	12.73	71.63	1.56
14	12.75	73.38	1.56
15	13.19	59.41	1.72
16	13.33	62.26	1.79
17	13.67	30.55	1.9
18	10.55	33	1.67
19	13.45	80.68	1.53
20	14.25	88.03	1.67
21	13.52	73.27	1.55
22	14.49	66.27	1.5
23	13.23	40.43	1.5
24	13.8	57.89	1.38
25	12.81	77.33	1.28
26	13.14	31.14	1.28
27	13.98	83.85	1.31
28	13.13	48.66	1.31
29	10.85	87.12	1.16
30	13.28	41.16	1.38
31	13.07	68.61	1.3
32	14.09	46.91	1.36
33	9.73	67.58	1.48
TA15			
1	11.72	76.59	1.14
2	11.12	66.06	1.14
3	11.98	15.29	1.05
4	11.73	22.53	1.37
5	15	43.13	1.37
6	14.07	8.91	1.15
7	11.21	52.84	1.15
8	12.7	47.86	1.13
9	12.8	54.73	1.12
10	13.59	67.13	1.12
11	15.02	78.76	1.28
12	9.25	71.53	1.04
13	12.32	32.05	1.28
14	12.18	86.18	1.28
15	13.52	38.65	1.28
16	12.59	77.06	1.29
17	10.4	61.45	1.27
18	12.89	85.19	1.27
19	12.43	47.96	1.17
20	11.55	46.77	1.17

Continued on next page

Continued from previous page

Length no.	Confined track length (μm)	Angle to C Axis	Average DPar (μm)
21	13.05	57.8	1.54
22	11.97	55.79	1.54
23	9.35	32.7	1.54
24	12.54	51.95	1.54
25	8.62	47.03	1.54
26	10.91	72.17	1.51
27	10.56	62.64	1.1
28	15.08	66.02	1.35
29	9.32	54.15	1.35
30	14.04	45.83	1.35
31	12.5	71.71	1.35
32	11.24	18.74	1.35
TA16			
1	10.19	13.99	1.22
2	13.21	50.35	1.22
3	13.83	84.39	1.11
4	13.02	30.45	1.13
5	14.64	83.52	1.27
6	13.5	48.81	1.21
7	13.88	84.27	1.37
8	14.13	56.1	1.23
9	13.54	59.76	1.15
10	15.25	22.3	1.28
11	10.6	82.69	1.28
12	11.53	84.28	1.24
13	14.96	63.06	1.24
14	13.06	33.48	1.14
15	13.86	48.84	1.14
16	14.1	79.03	1.21
17	14.14	55.27	1.18
18	11.88	69.19	1.18
19	12.93	41.87	1.24
20	12.03	72.17	1.24
21	15.32	41.77	1.18
22	15.35	63.35	1.18
23	13.32	73.98	1.23
24	12.33	53.59	1.18
25	14.02	11.13	1.18
26	14.54	31.05	1.18
27	13.87	40.62	1.18
28	13.85	46.99	1.15
29	12.99	15.4	1.41

Continued on next page

Continued from previous page

Length no.	Confined track length (μm)	Angle to C Axis	Average DPar (μm)
30	13.99	36.02	1.14
31	13.09	88.01	1.14
32	12.91	11.04	1.29
33	13.66	64.62	1.28
34	13.62	71.87	1.24
35	13.24	61.12	1.25
36	15.82	21.58	1.34
37	11.78	68.22	1.24
38	12.4	59.96	1.22
39	11.21	53.25	1.22
40	12.83	30.28	1.13
41	11.16	78.15	1.2
42	9.93	31.55	1.35
43	14.67	54	1.01
44	12.31	54.93	0.87
45	14.77	42.99	0.87
46	9.83	82.05	1.31
47	14.3	61.92	1.29
48	13.39	40.47	1.22
49	13.74	83.67	1.2
50	14.65	65.6	1.56
51	13.14	44.29	1.56
52	12.32	53.69	1.56
53	12.92	85.79	1.3
54	14.79	44.87	1.34
55	13.65	84.79	1.2
56	11.36	22.62	1.24
57	15.55	69.95	1.16
58	13.38	62.56	1.14
59	13.98	30.19	0.96
60	14.91	64.93	0.85
61	13.58	62.91	1.17
62	13.39	38.26	1.08
63	9.63	43.44	1.08
64	12.71	72.62	1.26
65	11.55	48.99	0.83
TA17			
1	11.12	41.58	1.15
2	13.56	76.02	1.15
3	14.06	31.23	1.15
4	9.83	21.75	1.15
5	11.78	40.89	1.15

Continued on next page

Continued from previous page

Length no.	Confined track length (μm)	Angle to C Axis	Average DPar (μm)
6	13.97	70.99	1.15
7	12.82	41.81	1.15
8	11.03	23.28	0.98
9	12.08	65.09	0.98
10	12.79	51.75	1.3
11	13.16	55.28	1.15
12	8.08	72.23	1.09
13	13.92	52.83	1.33
14	13.62	69.3	0.94
15	13.5	62.65	1.07
16	12.27	55.24	1.12
17	8.96	59.38	1.13
18	14.03	63.3	1.04
19	12.14	69.93	1.11
20	12.51	29.11	1.11
21	13.65	79.92	1.12
22	14.19	54.83	1.12
23	13.49	82.82	1.25
24	12.25	75.53	1.25
25	11.29	41.51	1.09
26	11.42	89.35	1.09
27	10.02	78.07	1.09
28	9.45	11.06	1.09
29	10.63	48.24	1.09
30	11.97	71.34	1.09
TA18			
1	10.31	34.3	1.57
2	12.16	12.03	1.57
3	12.37	44.55	1.57
4	13.02	70.83	1.43
5	12.96	84.24	1.5
6	15.31	23.34	1.49
7	14.96	85.12	1.72
8	15.7	46.05	1.69
9	11.18	81.07	1.43
10	12.69	58.6	1.73
11	13.44	36.44	1.73
12	10.98	59.21	1.73
13	12.65	87.01	1.73
14	15.13	48.27	1.73
15	13.33	75.6	1.73
16	12.12	45.24	1.65

Continued on next page

Continued from previous page

Length no.	Confined track length (μm)	Angle to C Axis	Average DPar (μm)
17	14.44	66.98	1.65
18	12.2	74.91	1.65
19	11.34	80.14	1.65
20	13.02	53.71	1.65
21	11	74.96	1.65
22	13.18	30.86	1.65
23	14.38	65.69	1.65
24	11.88	58.69	1.65
25	14.43	80.21	1.65
26	12.07	51.7	1.65
27	14.16	0	
28	11.76	31.51	1.48
29	13.04	61.48	1.37
30	11.25	40.73	1.63
31	11.45	51.82	1.63
32	10.66	71.86	1.63
33	14.16	42.8	1.63
34	11.8	5.38	1.67
35	11.5	23.66	1.67
36	13.99	34.87	1.57
37	13.7	59	1.55
38	12.68	69.12	1.55
39	12.63	65.6	1.55
40	12.79	55.6	1.55
41	12.25	47.55	1.55
42	12.95	62.75	1.4
43	9.89	70.86	1.4
44	13	18.7	1.4
45	13.21	52.37	1.4
46	11.34	59	1.4
47	11.75	21.79	1.67
48	10.72	66.48	1.67
49	13.79	39.52	1.43
50	11.74	60.52	1.5
51	13.6	81.87	1.68
52	13.53	51.8	1.41
53	13.83	79.73	1.68
54	10.56	81.97	1.68
TA20			
1	14.17	49.43	1.49
2	14.28	14.51	1.5
3	13.4	82.78	1.49

Continued on next page

Continued from previous page

Length no.	Confined track length (μm)	Angle to C Axis	Average DPar (μm)
4	14.46	42.92	1.49
5	13.93	36.03	1.46
6	13.5	67.54	1.46
7	13.86	37.76	1.55
8	14.48	63.21	1.55
9	15.24	82.47	1.55
10	13.52	38.36	1.55
11	13.17	45.37	1.58
12	14.01	26.65	1.47
13	12.31	83.93	1.62
14	13.69	61.14	1.5
15	13.19	18.52	1.5
16	12.34	89.95	1.5
17	14.2	83.86	1.5
18	10.38	71.59	1.5
19	13.88	19.55	1.59
20	14.19	52.15	1.59
21	13.36	70.8	1.59
22	15.03	27.85	1.59
23	13.43	69.4	1.59
24	12.37	54.03	1.59
25	11.26	63.9	1.59
26	12.83	64.89	1.59
27	13.68	52.36	1.59
28	15.44	73.69	1.56
29	15.24	47.85	1.39
30	11.73	89.74	1.6
31	14.17	82.85	1.24
32	12.62	50.61	1.51
33	15.14	60.43	1.3
34	13.94	35.63	1.27
35	13.41	83.06	1.61
36	12.91	45.96	1.28
37	13.4	68.79	1.24
38	11.9	73.19	1.24
39	13.69	59.07	1.53
40	14.03	13.53	1.53
41	14.76	34.34	1.56
42	12.86	64.15	1.55
43	14.2	58.92	1.55
44	11.68	84.18	1.44
45	15.11	42.83	1.44

Continued on next page

Continued from previous page

Length no.	Confined track length (μm)	Angle to C Axis	Average DPar (μm)
TA22			
1	12.73	85.04	2.07
2	14.38	49.75	2
3	13.23	52.08	2.35
4	13.46	65.74	2.12
5	14.7	13.75	2.23
6	14.05	22.66	2.1
7	13.86	84.31	2.58
8	14.67	48.78	2.41
9	13.66	66.09	2.25
10	14.91	78.51	2.25
11	12.44	59.9	2.5
12	15.26	63.37	2.5
13	13.3	21.69	2.5
14	13.53	80.49	2.5
15	13.09	87.7	2.08
16	13.93	41.32	2.08
17	14.19	66.25	1.97
18	13.34	34.5	1.67
19	13.08	43.01	1.79
20	15.05	38.41	1.92
21	14.4	58.9	2.12
22	14.28	45.57	1.55
23	14.39	50.11	1.95
24	13.69	31.8	1.63
25	13.22	36.56	1.63
26	15	34.46	1.64
27	13.56	7.33	2.01
28	13.71	77.03	1.72
29	16.24	75.37	1.89
30	13.34	67.4	1.89
31	13.58	85.08	1.89
32	15.67	18.13	1.85
33	14.81	83.11	1.85
34	12.55	53.03	1.87
35	13.38	36.53	1.64
36	13.36	49.74	1.65
37	14.11	74.58	1.71
38	13.71	24.2	1.72
39	14.72	49.51	1.66
40	12.99	51.27	1.48
41	14.79	81.52	1.64
42	14.01	70.23	1.61

Continued on next page

Continued from previous page

Length no.	Confined track length (μm)	Angle to C Axis	Average DPar (μm)
43	13.45	77.7	1.89
44	14.12	76.25	1.89
45	12.59	68.4	1.89
46	11.78	27.32	1.89
47	13.22	65.61	1.89
48	11.82	77.42	1.84
49	14.12	43.87	1.84
50	13.14	56.95	1.84
51	15.19	89.68	1.92
52	14.74	38.34	2.1
53	13.55	75.45	1.95
54	14.29	89.88	1.81
55	14.42	13.77	1.81
56	13.61	73.71	1.81
57	14.09	62.67	1.81
58	15.31	58.75	1.73
59	14.29	13.08	1.73
60	13.96	42.19	1.7
61	13.19	67.78	1.86
62	14.7	57.51	2.09
63	12.66	60.61	2.09
64	12.47	84.25	2.09
65	12.94	16.44	2.09
66	13.06	34.2	2.09
67	14.98	45.16	2.09
68	13.74	83.06	1.71
69	12.6	37.16	1.71
70	14.36	77.91	1.85
71	14.37	60.54	1.72
TA23			
1	12.23	76.08	1.58
2	14.75	79.8	1.58
3	14.38	50.6	1.58
4	12.9	41.02	1.91
5	14.36	70.29	1.91
6	12.77	67.83	1.91
7	15.18	82.4	1.46
8	11.98	76.74	1.46
9	12.29	24.26	1.46
10	13.59	38.28	1.38
11	10.98	89.78	1.38
12	12.04	40.89	1.38

Continued on next page

Continued from previous page

Length no.	Confined track length (μm)	Angle to C Axis	Average DPar (μm)
13	10.58	5.55	1.38
14	13.5	83.57	1.49
15	15.03	75.11	1.54
16	13.61	59.64	1.54
17	13.34	61.29	1.54
18	14.22	66.27	1.54
19	11.92	65.63	1.39
20	11.03	85.06	1.58
21	12.98	56.12	1.58
22	16.12	41.89	1.73
23	14.02	69.69	1.73
24	14.88	9.85	1.73
25	11.57	86.74	1.73
26	13.32	47.77	1.19
27	14.05	78.79	1.19
28	15.11	45.87	1.19
29	12	46.91	1.19
30	11.92	54.81	1.19
31	14.03	47.71	1.19
32	11.74	88.24	1.16
33	12.31	72.36	1.16
34	12.32	69.72	1.77
35	12.48	80.39	1.51
36	12.94	35.39	1.51
37	14.95	35.58	1.51
38	14.33	81.6	1.51
39	13.58	86.5	1.53
40	13.64	82.38	1.53
41	14.41	16.72	1.53
42	12.19	79.29	1.53
43	13.51	44.93	1.53
44	14.47	65.77	1.53
45	12.06	53.28	1.53
46	11.42	64.2	1.53
47	13.49	60.8	1.4
48	13.46	82.64	1.56
49	13.31	53.77	1.56
50	12.48	66.22	1.56
51	12.51	78.62	1.56
52	14	57.85	1.56
53	12.42	55.13	1.56
54	12.13	61.32	1.56
55	13.92	32.09	1.56

Continued on next page

Continued from previous page

Length no.	Confined track length (μm)	Angle to C Axis	Average DPar (μm)
56	14.19	80.55	1.56
57	12.83	73.95	1.56
58	13.5	63.92	1.66
59	13.72	73.06	1.38
60	11.5	72.65	1.46
61	12.56	67.8	1.46
62	12.7	69.83	1.46
63	14.78	13.8	1.41
64	10.09	81.82	1.41
65	13.07	83.68	1.41
66	13.19	56.82	1.41
67	13.74	54.07	1.41
68	14.57	60.97	1.41
69	12.83	37.63	1.41
70	13.12	78.81	1.41
71	13.93	77.36	1.41
72	14.7	64.57	1.5
73	14.43	47.25	1.5
74	14.83	63.35	1.5
75	14.23	70.13	1.67
76	13.09	75.64	1.62
77	14.08	26.38	1.62
78	13.24	80.14	1.62
79	12.38	64.72	1.41
80	13.29	45.78	1.41
81	14.36	30.87	1.41
82	11.08	85.38	1.41
83	12.42	81.68	1.47
84	14.98	32.84	1.47
85	13.43	69.53	1.47
86	13.63	85.09	1.82
87	13.66	58.35	1.9
88	14.2	44.67	1.9
89	13.17	75.02	1.9
90	14.79	63.46	1.9
91	13.7	73.26	1.9
TA26			
1	10.71	79.54	1.63
2	13.71	70.24	2.07
3	13.55	74.19	1.76
4	12.13	78.92	1.6
5	14.65	33.89	1.94

Continued on next page

Continued from previous page

Length no.	Confined track length (μm)	Angle to C Axis	Average DPar (μm)
6	13.16	55.34	1.62
7	12.29	62.66	1.54
8	12.69	81.42	1.54
9	11.73	53.39	1.54
10	14.31	54.25	1.54
11	12.5	77.67	1.54
12	13.74	59.31	1.54
13	11.86	82.97	1.54
14	13.63	70.73	1.61
15	12.53	79.8	1.61
16	14.55	61.28	1.61
17	14.42	42.46	1.61
18	14.21	69.93	1.61
19	11.92	77.12	1.63
20	15.53	47.3	1.58
21	14.49	49.36	1.55
22	13.9	33.9	1.55
23	14.27	32.35	1.82
24	14.53	35.89	1.82
25	11.71	56.28	1.79
26	13.78	60.07	1.79
27	12.65	70.01	2.14
28	11.09	38.52	2.65
29	14.12	27.14	2.19
30	14.01	2.04	2.18
31	14.03	55	2.18
32	11.6	51.97	3.01
33	10.78	38.59	3.01
34	13.92	78.18	2.08
35	13.83	44.23	2.08
36	13.02	39.42	2.08
37	13.69	66.03	1.91
38	13.96	50.27	1.91
39	14.1	67.42	1.91
40	13.81	40.44	1.91
41	14.04	56.85	1.91
42	14.13	80.38	1.61
43	14.12	23.62	1.88
44	14.67	53.41	1.88
45	15.08	63.64	1.88
46	12.9	51.98	1.55
47	13.04	49.82	1.55
48	12.04	67.15	1.67

Continued on next page

Continued from previous page

Length no.	Confined track length (μm)	Angle to C Axis	Average DPar (μm)
49	11.05	68.92	1.49
50	14.75	19.63	1.49
51	9.97	85.69	1.49
52	14.46	43.36	1.33
53	13.97	75.79	1.71
54	13.15	53.37	1.71
55	13.92	30.44	1.71
56	12.05	62.63	1.71
57	13.64	55.53	2.27
58	13.68	38.54	2.27

F.3 Apatite U–Pb analytical spot data

Table F.3: Apatite U–Pb analytical spot data

Sample name	Spot number	$^{238}U/^{206}Pb$	2σ	$^{207}Pb/^{206}Pb$	2σ	ρ
TA01	TA01_1.d	7.604	0.41	0.504	0.028	0.19
TA01	TA01_2.d	7.012	0.467	0.519	0.028	-0.03
TA01	TA01_3.d	6.451	0.499	0.529	0.048	0.41
TA01	TA01_4.d	10.341	0.598	0.382	0.024	-0.03
TA01	TA01_5.d	9.066	0.41	0.436	0.027	0.34
TA01	TA01_6.d	7.686	0.425	0.519	0.033	0.28
TA01	TA01_7.d	8.403	0.564	0.474	0.026	0.19
TA01	TA01_8.d	8.952	0.448	0.435	0.022	0.1
TA01	TA01_9.d	10.298	0.625	0.393	0.023	-0.01
TA01	TA01_10.d	7.462	0.384	0.539	0.027	0.25
TA01	TA01_11.d	9.99	0.518	0.41	0.019	0.27
TA01	TA01_12.d	10.952	0.623	0.361	0.028	0
TA01	TA01_13.d	11.614	0.714	0.299	0.016	0.33
TA01	TA01_14.d	8.375	0.406	0.452	0.022	0.33
TA01	TA01_16.d	8.319	0.436	0.459	0.029	0.38
TA01	TA01_17.d	6.544	0.385	0.526	0.029	0.36
TA01	TA01_18.d	8.045	0.42	0.481	0.028	0.69
TA01	TA01_19.d	7.98	0.439	0.465	0.022	0.28
TA01	TA01_20.d	10.504	0.606	0.364	0.02	0.11
TA01	TA01_21.d	6.211	0.424	0.532	0.042	0.58
TA01	TA01_22.d	10.482	0.593	0.38	0.02	0.35
TA01	TA01_23.d	10.471	0.624	0.379	0.02	0.31
TA01	TA01_24.d	8.382	0.505	0.477	0.029	0.37
TA01	TA01_25.d	9.057	0.59	0.424	0.026	0.31
TA01	TA01_26.d	9.174	0.488	0.415	0.019	0.51
TA01	TA01_27.d	7.587	0.414	0.466	0.029	-0.05
TA01	TA01_28.d	8.703	0.431	0.437	0.023	0.24
TA01	TA01_29.d	8.591	0.464	0.454	0.018	-0.25
TA01	TA01_30.d	6.234	0.373	0.551	0.033	0.24
TA01	TA01_31.d	7.241	0.492	0.485	0.031	0.09
TA01	TA01_32.d	9.652	0.614	0.385	0.025	0.2
TA01	TA01_33.d	9.624	0.528	0.427	0.025	0.33
TA01	TA01_34.d	7.849	0.486	0.477	0.03	0.44
TA01	TA01_35.d	10.08	0.518	0.392	0.02	0.1
TA01	TA01_36.d	8.51	0.521	0.467	0.026	0.06
TA01	TA01_37.d	8.319	0.429	0.473	0.016	0.44
TA01	TA01_38.d	8.445	0.542	0.456	0.023	0
TA01	TA01_39.d	8.271	0.56	0.446	0.021	0.14
TA01	TA01_40.d	8.23	0.399	0.485	0.032	0.3
TA02	TA02_02.d	9.708	1.036	0.399	0.043	0.44

Continued on next page

Continued from previous page

Sample name	Spot number	$^{238}U/^{206}Pb$	2σ	$^{207}Pb/^{206}Pb$	2σ	ρ
TA02	TA02_03.d	3.571	0.344	0.68	0.067	0.11
TA02	TA02_04.d	2.824	0.271	0.648	0.04	0.47
TA02	TA02_05.d	2.415	0.21	0.772	0.045	0.27
TA02	TA02_06.d	2.5	0.187	0.727	0.051	0.58
TA02	TA02_07.d	2.808	0.268	0.799	0.056	0.19
TA02	TA02_08.d	3.759	0.367	0.701	0.05	0.14
TA02	TA02_09.d	2.832	0.208	0.709	0.049	0.23
TA02	TA02_10.d	2.439	0.196	0.686	0.042	0.06
TA02	TA02_11.d	8.396	0.507	0.453	0.026	0.05
TA02	TA02_12.d	3.546	0.251	0.668	0.041	0.36
TA02	TA02_13.d	2.832	0.264	0.696	0.056	0.46
TA02	TA02_14.d	13.333	0.977	0.186	0.018	-0.37
TA02	TA02_15.d	3.225	0.28	0.7	0.073	0.43
TA02	TA02_16.d	1.111	0.185	0.451	0.058	0.14
TA02	TA02_17.d	4.716	0.489	0.591	0.039	0.52
TA02	TA02_18.d	2.994	0.304	0.707	0.064	0.68
TA02	TA02_19.d	3.436	0.307	0.662	0.053	0.61
TA02	TA02_20.d	3.649	0.319	0.676	0.059	-0.21
TA02	TA02_21.d	3.937	0.279	0.642	0.083	0.2
TA04	TA04_01.d	3.61	0.221	0.645	0.031	0.36
TA04	TA04_02.d	3.401	0.277	0.67	0.048	0.59
TA04	TA04_04.d	2.967	0.193	0.704	0.035	0.39
TA04	TA04_05.d	4.444	0.375	0.605	0.049	0.2
TA04	TA04_06.d	3.937	0.31	0.675	0.061	0.73
TA04	TA04_08.d	2.816	0.182	0.651	0.043	0.46
TA04	TA04_09.d	4.784	0.412	0.675	0.042	0.14
TA04	TA04_10.d	5.128	0.341	0.573	0.025	0.49
TA04	TA04_11.d	4.31	0.26	0.652	0.038	0.24
TA04	TA04_14.d	2.976	0.256	0.673	0.039	0.62
TA04	TA04_15.d	3.012	0.29	0.525	0.032	0.29
TA04	TA04_16.d	2.583	0.24	0.71	0.047	0.36
TA04	TA04_17.d	2.923	0.324	0.417	0.04	0.41
TA04	TA04_23.d	1.079	0.09	0.325	0.019	0.29
TA04	TA04_24.d	3.257	0.318	0.642	0.037	0.22
TA04	TA04_26.d	3.508	0.27	0.691	0.047	0.3
TA04	TA04_27.d	2.724	0.178	0.618	0.031	0.38
TA04	TA04_28.d	3.921	0.292	0.675	0.038	0.44
TA04	TA04_29.d	3.703	0.274	0.657	0.039	0.11
TA04	TA04_30.d	3.3	0.304	0.606	0.038	0.37
TA05	TA05_01.d	11.534	0.971	0.315	0.05	0.62
TA05	TA05_02.d	5.181	0.429	0.631	0.04	0.19
TA05	TA05_03.d	5.291	0.419	0.563	0.036	0.24
TA05	TA05_04.d	4.048	0.327	0.725	0.046	0.45
TA06	TA06_1.d	6.644	0.357	0.595	0.027	0.35

Continued on next page

Continued from previous page

Sample name	Spot number	$^{238}U/^{206}Pb$	2σ	$^{207}Pb/^{206}Pb$	2σ	ρ
TA06	TA06_2.d	6.816	0.46	0.594	0.035	0.26
TA06	TA06_3.d	7.199	0.456	0.574	0.034	0.16
TA06	TA06_4.d	6.455	0.404	0.597	0.037	0.46
TA06	TA06_5.d	7.77	0.476	0.545	0.032	0.46
TA06	TA06_6.d	9.259	0.471	0.452	0.029	0.07
TA06	TA06_8.d	6.086	0.314	0.623	0.038	0.35
TA06	TA06_9.d	7.93	0.433	0.575	0.036	0.21
TA06	TA06_10.d	4.385	0.269	0.682	0.035	0.4
TA06	TA06_11.d	5.938	0.352	0.645	0.036	0.17
TA06	TA06_12.d	4.854	0.353	0.584	0.05	-0.11
TA06	TA06_13.d	3.703	0.246	0.725	0.038	0.57
TA06	TA06_14.d	6.273	0.373	0.593	0.035	0.32
TA06	TA06_15.d	7.225	0.391	0.565	0.036	0.06
TA06	TA06_16.d	6.514	0.377	0.609	0.038	0.27
TA06	TA06_17.d	1.805	0.159	0.772	0.052	0.3
TA06	TA06_18.d	6.882	0.44	0.601	0.042	0.22
TA06	TA06_19.d	5.82	0.308	0.611	0.034	0.03
TA06	TA06_20.d	6.523	0.361	0.537	0.048	0.48
TA06	TA06_21.d	6.455	0.416	0.609	0.035	0.22
TA06	TA06_23.d	7.336	0.468	0.586	0.035	0.44
TA06	TA06_24.d	6.226	0.368	0.609	0.034	0.23
TA06	TA06_25.d	7.342	0.474	0.584	0.036	0.48
TA06	TA06_26.d	6.6	0.374	0.603	0.037	0.52
TA06	TA06_27.d	7.32	0.428	0.577	0.036	0.17
TA06	TA06_28.d	6.868	0.382	0.598	0.043	0.32
TA06	TA06_29.d	8.169	0.52	0.543	0.04	0.41
TA06	TA06_30.d	6.858	0.371	0.598	0.036	0.42
TA06	TA06_31.d	7.017	0.453	0.563	0.04	0.15
TA06	TA06_32.d	6.075	0.369	0.611	0.033	0.26
TA06	TA06_33.d	6.097	0.446	0.614	0.039	0.27
TA06	TA06_35.d	6.472	0.33	0.562	0.031	0.33
TA06	TA06_36.d	7.082	0.391	0.554	0.036	0.3
TA06	TA06_37.d	6.222	0.333	0.589	0.029	0.29
TA06	TA06_38.d	8.038	0.484	0.535	0.036	0.28
TA06	TA06_39.d	7.047	0.327	0.591	0.033	0.37
TA06	TA06_40.d	6.784	0.354	0.559	0.029	0.36
TA07	TA07_1.d	6.451	0.624	0.64	0.089	0.32
TA07	TA07_2.d	10.395	0.68	0.424	0.04	0.44
TA07	TA07_3.d	12.285	0.814	0.424	0.036	0.24
TA07	TA07_4.d	9.615	0.721	0.447	0.037	0.16
TA07	TA07_5.d	4.524	0.368	0.78	0.086	0.72
TA07	TA07_6.d	10.141	0.802	0.49	0.053	0.11
TA07	TA07_7.d	13.106	1.116	0.377	0.051	0.37
TA07	TA07_8.d	7.575	0.631	0.59	0.061	0.4

Continued on next page

Continued from previous page

Sample name	Spot number	$^{238}U/^{206}Pb$	2σ	$^{207}Pb/^{206}Pb$	2σ	ρ
TA07	TA07_9.d	12.21	0.969	0.408	0.04	0.24
TA07	TA07_10.d	10.341	0.759	0.401	0.041	0.41
TA07	TA07_11.d	4.273	0.346	0.717	0.042	0.28
TA07	TA07_12.d	9.551	0.893	0.487	0.037	0.67
TA07	TA07_13.d	11.21	0.892	0.38	0.031	0.22
TA07	TA07_14.d	11.99	0.79	0.401	0.038	0.51
TA07	TA07_15.d	6.321	0.439	0.596	0.04	0.42
TA07	TA07_16.d	11.976	0.846	0.359	0.029	0.48
TA07	TA07_17.d	11.534	0.957	0.425	0.049	0.49
TA07	TA07_18.d	9.832	0.802	0.422	0.033	0.42
TA07	TA07_19.d	8.097	0.616	0.539	0.04	0.25
TA07	TA07_20.d	11.467	0.802	0.383	0.037	0.19
TA07	TA07_21.d	4.608	0.318	0.691	0.039	0.2
TA07	TA07_22.d	5.952	0.46	0.602	0.041	0.36
TA07	TA07_23.d	9.328	0.696	0.473	0.046	0.3
TA07	TA07_24.d	8.025	0.644	0.517	0.043	-0.24
TA07	TA07_25.d	4.032	0.26	0.687	0.048	0.16
TA07	TA07_26.d	9.124	0.757	0.563	0.059	0.44
TA07	TA07_27.d	10.298	0.975	0.455	0.063	0.47
TA07	TA07_28.d	9.523	0.852	0.515	0.046	0.47
TA07	TA07_29.d	5.747	0.396	0.601	0.048	0.46
TA07	TA07_30.d	13.698	0.844	0.304	0.027	0.3
TA07	TA07_31.d	9.191	0.701	0.482	0.058	0.23
TA07	TA07_32.d	7.993	0.638	0.495	0.05	0.32
TA07	TA07_33.d	6.802	0.601	0.589	0.051	0.56
TA07	TA07_34.d	6.289	0.514	0.602	0.053	0.53
TA07	TA07_35.d	6.211	0.385	0.645	0.046	0.45
TA07	TA07_36.d	4.629	0.385	0.692	0.06	0.41
TA07	TA07_37.d	8.62	0.891	0.594	0.067	0.58
TA07	TA07_38.d	11.723	1.044	0.428	0.044	0.05
TA07	TA07_39.d	11.682	0.764	0.447	0.042	0.1
TA07	TA07_40.d	6.896	0.57	0.565	0.047	0.47
TA10	TA10_01.d	11.933	0.583	0.2373	0.0098	0.46
TA10	TA10_03.d	11.52	0.61	0.229	0.013	0.36
TA10	TA10_04.d	10.81	0.432	0.281	0.017	0.15
TA10	TA10_05.d	11.286	0.471	0.2164	0.0076	0.37
TA10	TA10_06.d	11.261	0.443	0.235	0.011	0.31
TA10	TA10_07.d	12.642	0.527	0.219	0.013	0.41
TA10	TA10_08.d	10.121	0.573	0.317	0.017	0.08
TA10	TA10_09.d	11.723	0.453	0.229	0.013	0.18
TA10	TA10_10.d	10.02	0.461	0.299	0.016	0.4
TA10	TA10_11.d	9.756	0.523	0.326	0.027	0.48
TA10	TA10_12.d	10.438	0.588	0.257	0.016	0.37
TA10	TA10_13.d	11.363	0.503	0.258	0.015	0.08

Continued on next page

Continued from previous page

Sample name	Spot number	$^{238}U/^{206}Pb$	2σ	$^{207}Pb/^{206}Pb$	2σ	ρ
TA10	TA10_14.d	9.794	0.508	0.332	0.022	0.3
TA10	TA10_15.d	10.869	0.425	0.26	0.014	0.24
TA10	TA10_16.d	12.626	0.494	0.192	0.012	0.54
TA10	TA10_19.d	7.788	0.467	0.442	0.024	0.35
TA10	TA10_20.d	11.173	0.399	0.249	0.013	0.43
TA10	TA10_21.d	8.613	0.437	0.39	0.019	-0.04
TA10	TA10_23.d	11.098	0.517	0.259	0.017	0.46
TA10	TA10_24.d	10.09	0.458	0.316	0.018	0.45
TA10	TA10_25.d	10.928	0.477	0.288	0.018	0.19
TA10	TA10_27.d	9.92	0.452	0.311	0.017	0.1
TA10	TA10_28.d	10.416	0.509	0.29	0.016	0.05
TA10	TA10_29.d	10.615	0.484	0.309	0.023	0.3
TA10	TA10_31.d	11.123	0.532	0.249	0.013	0.11
TA10	TA10_32.d	10.928	0.501	0.253	0.015	0.18
TA10	TA10_33.d	11.025	0.522	0.269	0.012	0.14
TA10	TA10_34.d	10.928	0.537	0.269	0.018	0.44
TA10	TA10_35.d	10.917	0.488	0.257	0.013	0.27
TA10	TA10_36.d	12.285	0.694	0.224	0.015	0.3
TA10	TA10_37.d	10.204	0.666	0.32	0.021	0.19
TA11	TA11_01.d	10.351	0.632	0.348	0.019	0.13
TA11	TA11_02.d	10.193	0.633	0.353	0.024	0.45
TA11	TA11_03.d	9.813	0.471	0.348	0.017	0.05
TA11	TA11_05.d	7.704	0.593	0.502	0.035	0.11
TA11	TA11_06.d	7.132	0.468	0.491	0.027	0.16
TA11	TA11_07.d	7.763	0.524	0.511	0.03	0.57
TA11	TA11_08.d	7.272	0.528	0.494	0.025	0.25
TA11	TA11_09.d	9.345	0.637	0.359	0.019	0.22
TA11	TA11_10.d	2.227	0.173	0.793	0.052	0.42
TA11	TA11_11.d	10.141	0.555	0.382	0.024	0.2
TA11	TA11_12.d	12.195	0.803	0.247	0.016	0.15
TA11	TA11_14.d	7.917	0.407	0.47	0.031	0.13
TA11	TA11_15.d	10.752	0.763	0.348	0.022	-0.02
TA11	TA11_16.d	2.958	0.227	0.709	0.047	0.22
TA11	TA11_17.d	13.679	0.542	0.1548	0.0068	-0.14
TA11	TA11_18.d	8.123	0.409	0.463	0.025	0.12
TA11	TA11_19.d	9.523	0.571	0.38	0.019	0.11
TA11	TA11_20.d	9.174	0.479	0.384	0.022	0.01
TA11	TA11_21.d	9.442	0.526	0.397	0.02	0.16
TA11	TA11_22.d	13.888	0.848	0.17	0.012	0.13
TA11	TA11_23.d	8.431	0.526	0.455	0.025	0.09
TA11	TA11_24.d	9.551	0.492	0.412	0.025	-0.05
TA11	TA11_25.d	7.342	0.415	0.439	0.027	0.57
TA11	TA11_26.d	6.858	0.423	0.514	0.034	0.53
TA11	TA11_27.d	9.199	0.677	0.424	0.035	0.38

Continued on next page

Continued from previous page

Sample name	Spot number	$^{238}U/^{206}Pb$	2σ	$^{207}Pb/^{206}Pb$	2σ	ρ
TA11	TA11_28.d	8.264	0.594	0.492	0.033	0.26
TA11	TA11_29.d	7.824	0.593	0.481	0.048	0.28
TA11	TA11_31.d	8.291	0.515	0.458	0.03	0.29
TA11	TA11_32.d	9.025	0.733	0.414	0.027	0.19
TA11	TA11_33.d	11.337	0.604	0.295	0.017	0.11
TA11	TA11_34.d	5.714	0.359	0.598	0.036	0.48
TA14	TA14_01.d	7.178	0.489	0.589	0.031	0.48
TA14	TA14_02.d	8.795	0.711	0.547	0.032	-0.31
TA14	TA14_03.d	8.628	0.543	0.549	0.037	0.38
TA14	TA14_04.d	6.493	0.463	0.632	0.034	0.43
TA14	TA14_05.d	6.802	0.555	0.612	0.051	0.54
TA14	TA14_06.d	8.583	0.537	0.528	0.028	0.1
TA14	TA14_07.d	6.325	0.44	0.613	0.039	0.29
TA14	TA14_08.d	10.245	0.692	0.448	0.025	0.5
TA14	TA14_09.d	9.861	0.758	0.496	0.034	0.35
TA14	TA14_10.d	4.098	0.419	0.661	0.038	-0.2
TA14	TA14_11.d	5.128	0.42	0.672	0.044	0.07
TA14	TA14_12.d	5.882	0.553	0.599	0.04	-0.03
TA14	TA14_13.d	7.22	0.573	0.547	0.04	0.14
TA14	TA14_14.d	10.172	0.714	0.479	0.023	0.24
TA14	TA14_15.d	11.148	0.795	0.412	0.023	0.39
TA14	TA14_16.d	4.444	0.316	0.707	0.047	0.39
TA14	TA14_17.d	6.451	0.541	0.609	0.053	0.47
TA14	TA14_18.d	9.242	0.632	0.489	0.032	0.24
TA14	TA14_19.d	8.467	0.58	0.524	0.031	0.63
TA14	TA14_20.d	8.665	0.645	0.547	0.041	0.52
TA14	TA14_21.d	4.926	0.388	0.65	0.038	0.26
TA14	TA14_22.d	5.376	0.52	0.713	0.047	-0.19
TA14	TA14_23.d	8.936	0.543	0.503	0.028	0.4
TA14	TA14_24.d	8.196	0.671	0.494	0.039	-0.12
TA14	TA14_25.d	6.849	0.703	0.569	0.04	-0.31
TA14	TA14_26.d	5.443	0.355	0.634	0.035	0.33
TA14	TA14_27.d	9.208	0.627	0.525	0.028	0.32
TA14	TA14_28.d	7.77	0.47	0.573	0.028	0.45
TA14	TA14_29.d	5.025	0.404	0.663	0.036	0.23
TA14	TA14_30.d	9.407	0.628	0.49	0.029	0.42
TA14	TA14_31.d	5.714	0.555	0.653	0.045	0.19
TA14	TA14_32.d	8.992	0.59	0.522	0.026	0.5
TA14	TA14_33.d	5.434	0.383	0.644	0.037	0.26
TA15	TA15_01.d	8.084	0.477	0.558	0.032	-0.03
TA15	TA15_02.d	6.357	0.323	0.629	0.032	0.2
TA15	TA15_03.d	2.739	0.187	0.812	0.041	0.18
TA15	TA15_04.d	8.21	0.532	0.572	0.035	0.46
TA15	TA15_05.d	3.623	0.196	0.71	0.047	0.51

Continued on next page

Continued from previous page

Sample name	Spot number	$^{238}U/^{206}Pb$	2σ	$^{207}Pb/^{206}Pb$	2σ	ρ
TA15	TA15_06.d	7.189	0.485	0.46	0.035	-0.03
TA15	TA15_07.d	3.802	0.361	0.731	0.075	0.5
TA15	TA15_08.d	8.802	0.441	0.491	0.037	0.22
TA15	TA15_09.d	7.535	0.528	0.553	0.044	0.57
TA15	TA15_11.d	12.239	0.554	0.356	0.02	0.34
TA15	TA15_12.d	6.485	0.37	0.553	0.039	0.32
TA15	TA15_14.d	7.153	0.486	0.613	0.046	0.77
TA15	TA15_15.d	6.849	0.469	0.585	0.04	0.58
TA15	TA15_16.d	9.97	0.675	0.406	0.027	0.02
TA15	TA15_18.d	3.508	0.344	0.656	0.058	0.54
TA15	TA15_23.d	9.276	0.585	0.477	0.038	0.56
TA15	TA15_24.d	14.903	0.732	0.317	0.019	0.37
TA15	TA15_26.d	6.993	0.635	0.491	0.037	0.27
TA16	TA16_01.d	4.926	0.315	0.662	0.037	0.42
TA16	TA16_02.d	5.681	0.484	0.601	0.038	0.53
TA16	TA16_03.d	6.325	0.44	0.553	0.032	0.4
TA16	TA16_04.d	5	0.325	0.596	0.024	0.31
TA16	TA16_05.d	5.347	0.314	0.592	0.027	0.32
TA16	TA16_06.d	6.269	0.393	0.561	0.033	0.24
TA16	TA16_07.d	5.464	0.358	0.633	0.032	0.62
TA16	TA16_08.d	7.178	0.401	0.49	0.023	0.48
TA16	TA16_09.d	7.017	0.438	0.499	0.026	0.61
TA16	TA16_11.d	5.614	0.28	0.579	0.026	0.34
TA16	TA16_12.d	6.045	0.358	0.581	0.03	0.4
TA16	TA16_13.d	4.878	0.261	0.636	0.032	0.27
TA16	TA16_14.d	4.291	0.239	0.633	0.038	0.41
TA16	TA16_15.d	3.802	0.26	0.662	0.029	0.09
TA16	TA16_16.d	8.058	0.409	0.447	0.017	0.58
TA16	TA16_17.d	8.071	0.488	0.424	0.022	0.57
TA16	TA16_18.d	7.042	0.401	0.503	0.02	0.2
TA16	TA16_19.d	4.595	0.253	0.663	0.026	0.38
TA16	TA16_20.d	7.047	0.412	0.498	0.021	0.4
TA16	TA16_21.d	5.617	0.568	0.583	0.03	-0.11
TA16	TA16_22.d	10.764	0.567	0.324	0.013	0.28
TA16	TA16_23.d	6.868	0.424	0.482	0.024	0.33
TA16	TA16_26.d	6.93	0.408	0.501	0.027	0.35
TA16	TA16_27.d	6.369	0.352	0.56	0.026	0.3
TA16	TA16_28.d	8.517	0.435	0.451	0.016	0.48
TA16	TA16_29.d	4.366	0.266	0.671	0.033	0.37
TA16	TA16_30.d	5.154	0.345	0.609	0.039	0.41
TA16	TA16_31.d	5.128	0.368	0.628	0.037	0.44
TA16	TA16_32.d	3.344	0.279	0.695	0.036	0.38
TA16	TA16_33.d	6.222	0.425	0.544	0.025	0.11
TA16	TA16_34.d	4.115	0.304	0.702	0.036	0.25

Continued on next page

Continued from previous page

Sample name	Spot number	$^{238}U/^{206}Pb$	2σ	$^{207}Pb/^{206}Pb$	2σ	ρ
TA16	TA16_35.d	5.125	0.288	0.628	0.036	0.28
TA16	TA16_36.d	6.211	0.462	0.57	0.038	0.38
TA16	TA16_37.d	9.416	0.523	0.376	0.017	0.16
TA16	TA16_38.d	4.608	0.276	0.66	0.041	0.39
TA16	TA16_39.d	5.543	0.291	0.556	0.021	0.53
TA17	TA17_01.d	8.051	0.473	0.563	0.034	0.54
TA17	TA17_02.d	6.544	0.351	0.61	0.023	0.19
TA17	TA17_03.d	2.967	0.211	0.761	0.032	-0.07
TA17	TA17_04.d	1.319	0.076	0.797	0.033	0.44
TA17	TA17_05.d	8.496	0.425	0.611	0.018	0.37
TA17	TA17_06.d	7.61	0.364	0.587	0.022	0.3
TA17	TA17_07.d	7.102	0.343	0.613	0.017	0.45
TA17	TA17_08.d	1.449	0.086	0.803	0.027	0.24
TA17	TA17_09.d	11.52	0.53	0.436	0.011	0.41
TA17	TA17_10.d	6.443	0.311	0.623	0.02	0.43
TA17	TA17_11.d	3.076	0.17	0.784	0.031	0.55
TA17	TA17_12.d	7.299	0.372	0.581	0.022	0.43
TA17	TA17_13.d	2.403	0.138	0.783	0.034	0.35
TA17	TA17_14.d	7.886	0.36	0.56	0.017	0.4
TA17	TA17_15.d	9.442	0.472	0.514	0.018	0.5
TA17	TA17_16.d	2.192	0.12	0.793	0.027	0.21
TA17	TA17_17.d	10.799	0.501	0.482	0.017	0.13
TA17	TA17_18.d	6.743	0.331	0.622	0.025	0.5
TA17	TA17_19.d	2.439	0.154	0.778	0.033	0.45
TA17	TA17_20.d	1.655	0.098	0.82	0.026	0.21
TA17	TA17_21.d	7.39	0.382	0.602	0.022	0.07
TA17	TA17_22.d	5.681	0.297	0.67	0.027	0.35
TA17	TA17_23.d	7.434	0.386	0.608	0.02	0.57
TA17	TA17_24.d	1.579	0.097	0.806	0.03	0.43
TA17	TA17_25.d	6.43	0.318	0.649	0.016	0.46
TA17	TA17_26.d	2.673	0.15	0.746	0.028	0.27
TA17	TA17_27.d	2.364	0.15	0.79	0.027	0.21
TA17	TA17_28.d	1.666	0.102	0.833	0.035	-0.11
TA17	TA17_29.d	4.587	0.441	0.706	0.026	-0.08
TA17	TA17_30.d	7.451	0.388	0.598	0.021	0.42
TA17	TA17_31.d	2.049	0.13	0.792	0.033	0.29
TA17	TA17_32.d	2.754	0.159	0.763	0.029	0.47
TA17	TA17_33.d	5.53	0.284	0.66	0.021	0.26
TA17	TA17_34.d	3.703	0.246	0.721	0.028	-0.08
TA17	TA17_35.d	2.583	0.153	0.773	0.027	0.12
TA17	TA17_36.d	3.378	0.182	0.763	0.029	0.34
TA17	TA17_37.d	1.494	0.091	0.812	0.029	0.36
TA17	TA17_38.d	1.941	0.116	0.789	0.027	0.39
TA17	TA17_39.d	2.212	0.112	0.802	0.029	0.53

Continued on next page

Continued from previous page

Sample name	Spot number	$^{238}U/^{206}Pb$	2σ	$^{207}Pb/^{206}Pb$	2σ	ρ
TA17	TA17_40.d	2.518	0.177	0.758	0.023	-0.05
TA18	TA18_01.d	7.558	0.628	0.577	0.041	0.26
TA18	TA18_02.d	5.359	0.315	0.671	0.03	0.45
TA18	TA18_03.d	5.586	0.436	0.652	0.046	0.46
TA18	TA18_04.d	5.235	0.356	0.649	0.04	0.48
TA18	TA18_05.d	5.858	0.343	0.6	0.03	0.45
TA18	TA18_06.d	4.972	0.296	0.659	0.032	0.32
TA18	TA18_07.d	6.613	0.367	0.575	0.032	0.49
TA18	TA18_08.d	7.082	0.501	0.571	0.03	0.46
TA18	TA18_09.d	5.941	0.388	0.63	0.03	0.33
TA18	TA18_10.d	6.548	0.428	0.639	0.046	0.42
TA18	TA18_11.d	6.41	0.493	0.604	0.04	0.52
TA18	TA18_12.d	6.369	0.348	0.621	0.025	0.53
TA18	TA18_12b.d	6.896	0.432	0.61	0.033	0.38
TA18	TA18_13.d	5.988	0.43	0.619	0.034	0.53
TA18	TA18_14.d	13.297	0.831	0.286	0.016	0.44
TA18	TA18_15.d	15.197	0.739	0.221	0.0096	0.4
TA18	TA18_16.d	10.384	0.593	0.444	0.021	0.24
TA18	TA18_17.d	4.807	0.3	0.685	0.031	0.61
TA18	TA18_18.d	14.265	0.671	0.278	0.016	0.35
TA18	TA18_19.d	8.389	0.471	0.542	0.029	0.17
TA18	TA18_20.d	4.048	0.278	0.745	0.039	0.56
TA18	TA18_20b.d	4.405	0.271	0.658	0.045	0.5
TA18	TA18_21.d	4.464	0.338	0.688	0.04	0.41
TA18	TA18_22.d	6.426	0.413	0.57	0.028	0.54
TA18	TA18_23.d	10.373	0.57	0.4	0.024	0.23
TA18	TA18_24.d	13.054	0.681	0.298	0.017	0.49
TA18	TA18_25.d	6.325	0.4	0.627	0.036	0.24
TA18	TA18_26.d	4.504	0.284	0.617	0.039	0.54
TA18	TA18_27.d	14.947	0.759	0.24	0.013	0.07
TA19	TA19_01.d	1.631	0.117	0.859	0.041	0.22
TA19	TA19_02.d	7.418	0.346	0.573	0.016	0.25
TA19	TA19_03.d	12.515	0.657	0.337	0.015	0.28
TA19	TA19_04.d	4.555	0.249	0.676	0.028	0.34
TA19	TA19_05.d	1.848	0.123	0.806	0.042	0.37
TA19	TA19_06.d	2.217	0.132	0.781	0.031	0.13
TA19	TA19_07.d	1.55	0.115	0.821	0.038	0.3
TA19	TA19_08.d	3.448	0.19	0.75	0.025	0.23
TA19	TA19_09.d	5.903	0.306	0.635	0.023	0.33
TA19	TA19_10.d	3.61	0.221	0.722	0.032	0.58
TA19	TA19_11.d	2.04	0.129	0.789	0.032	0.23
TA19	TA19_12.d	3.021	0.209	0.762	0.031	0.5
TA19	TA19_13.d	1.555	0.111	0.85	0.032	0.23
TA19	TA19_14.d	3.205	0.215	0.773	0.025	0.35

Continued on next page

Continued from previous page

Sample name	Spot number	$^{238}U/^{206}Pb$	2σ	$^{207}Pb/^{206}Pb$	2σ	ρ
TA19	TA19_15.d	3.703	0.205	0.717	0.03	0.57
TA19	TA19_16.d	5.636	0.349	0.644	0.026	0.18
TA19	TA19_17.d	7.727	0.382	0.553	0.016	0.49
TA19	TA19_18.d	7.38	0.348	0.576	0.015	0.47
TA19	TA19_19.d	8.944	0.448	0.494	0.023	0.11
TA19	TA19_20.d	8.237	0.379	0.526	0.016	0.38
TA19	TA19_21.d	9.496	0.577	0.47	0.026	0.48
TA19	TA19_22.d	11.025	0.534	0.431	0.015	0.42
TA19	TA19_23.d	1.93	0.104	0.774	0.024	0.37
TA19	TA19_24.d	1.984	0.125	0.812	0.033	0.4
TA19	TA19_25.d	4.182	0.209	0.727	0.026	0.38
TA19	TA19_26.d	1.886	0.113	0.768	0.026	0.23
TA19	TA19_27.d	2.173	0.137	0.792	0.036	0.22
TA19	TA19_28.d	4.743	0.247	0.692	0.023	0.38
TA19	TA19_29.d	2.994	0.179	0.754	0.028	0.09
TA19	TA19_30.d	2.247	0.126	0.8	0.03	0.44
TA20	TA20_01.d	3.205	0.174	0.731	0.028	0.22
TA20	TA20_02.d	3.3	0.174	0.722	0.027	0.62
TA20	TA20_03.d	3.095	0.191	0.738	0.03	0.57
TA20	TA20_04.d	3.875	0.255	0.683	0.037	0.35
TA20	TA20_05.d	2.881	0.149	0.762	0.033	0.45
TA20	TA20_06.d	3.424	0.199	0.733	0.026	0.35
TA20	TA20_07.d	3.3	0.185	0.737	0.026	0.56
TA20	TA20_08.d	2.564	0.157	0.765	0.028	0.29
TA20	TA20_09.d	4.132	0.239	0.699	0.029	0.43
TA20	TA20_10.d	3.003	0.171	0.776	0.033	0.32
TA20	TA20_11.d	3.508	0.209	0.719	0.031	0.43
TA20	TA20_12.d	3.389	0.183	0.723	0.033	0.56
TA20	TA20_13.d	3.322	0.22	0.708	0.034	0.5
TA20	TA20_14.d	3.496	0.195	0.717	0.037	0.47
TA20	TA20_15.d	3.105	0.192	0.759	0.03	0.49
TA20	TA20_16.d	3.174	0.181	0.727	0.036	0.36
TA20	TA20_17.d	3.048	0.185	0.76	0.034	0.37
TA20	TA20_18.d	3.154	0.189	0.694	0.038	0.51
TA20	TA20_19.d	3.289	0.183	0.727	0.029	0.38
TA20	TA20_20.d	3.367	0.204	0.758	0.026	0.28
TA20	TA20_21.d	3.058	0.177	0.759	0.033	0.3
TA20	TA20_22.d	3.225	0.176	0.721	0.03	0.39
TA20	TA20_23.d	2.906	0.16	0.787	0.036	0.4
TA20	TA20_24.d	3.389	0.206	0.743	0.032	0.36
TA20	TA20_25.d	2.923	0.162	0.774	0.026	0.32
TA20	TA20_26.d	3.194	0.204	0.747	0.025	0.38
TA20	TA20_27.d	3.067	0.188	0.701	0.038	0.4
TA20	TA20_28.d	3.436	0.177	0.762	0.03	0.48

Continued on next page

Continued from previous page

Sample name	Spot number	$^{238}U/^{206}Pb$	2σ	$^{207}Pb/^{206}Pb$	2σ	ρ
TA20	TA20_29.d	2.949	0.156	0.741	0.026	0.39
TA20	TA20_30.d	5.42	0.282	0.652	0.024	0.29
TA20	TA20_31.d	3.61	0.182	0.732	0.026	0.3
TA20	TA20_32.d	3.134	0.206	0.734	0.031	0.46
TA20	TA20_33.d	3.164	0.18	0.729	0.029	0.41
TA20	TA20_34.d	3.401	0.196	0.756	0.03	0.35
TA20	TA20_35.d	2.702	0.175	0.752	0.03	0.34
TA20	TA20_36.d	3.012	0.181	0.76	0.029	0.62
TA20	TA20_37.d	3.401	0.185	0.711	0.023	0.4
TA20	TA20_38.d	3.236	0.178	0.722	0.031	0.37
TA20	TA20_39.d	3.3	0.174	0.741	0.022	0.38
TA20	TA20_40.d	2.89	0.158	0.763	0.034	0.36
TA22	TA22_01.d	4.484	0.221	0.704	0.033	0.43
TA22	TA22_02.d	3.802	0.159	0.745	0.031	0.32
TA22	TA22_03.d	5.747	0.244	0.63	0.024	0.39
TA22	TA22_04.d	3.322	0.198	0.778	0.035	0.2
TA22	TA22_05.d	3.759	0.155	0.765	0.03	0.36
TA22	TA22_06.d	2.923	0.119	0.764	0.031	0.37
TA22	TA22_07.d	3.891	0.166	0.704	0.028	0.44
TA22	TA22_08.d	3.125	0.156	0.765	0.03	0.25
TA22	TA22_09.d	4.237	0.175	0.707	0.033	0.55
TA22	TA22_10.d	4.833	0.191	0.69	0.03	0.3
TA22	TA22_11.d	4.115	0.186	0.703	0.029	0.46
TA22	TA22_12.d	3.184	0.121	0.741	0.029	0.38
TA22	TA22_13.d	3.472	0.132	0.754	0.028	0.56
TA22	TA22_14.d	4.728	0.223	0.697	0.025	0.32
TA22	TA22_15.d	4.219	0.195	0.694	0.032	0.46
TA22	TA22_16.d	4.081	0.233	0.712	0.029	0.28
TA22	TA22_17.d	3.61	0.182	0.735	0.03	0.29
TA22	TA22_18.d	4.847	0.227	0.676	0.031	0.33
TA22	TA22_19.d	3.875	0.21	0.684	0.03	0.38
TA22	TA22_20.d	4.079	0.166	0.679	0.029	0.23
TA22	TA22_21.d	3.115	0.164	0.751	0.032	0.35
TA22	TA22_22.d	4.464	0.239	0.69	0.031	0.57
TA22	TA22_23.d	3.205	0.143	0.75	0.033	0.38
TA22	TA22_24.d	3.086	0.152	0.78	0.031	0.3
TA22	TA22_25.d	2.659	0.155	0.745	0.03	0.33
TA22	TA22_26.d	3.597	0.168	0.749	0.033	0.4
TA22	TA22_27.d	3.846	0.177	0.718	0.031	0.22
TA22	TA22_28.d	10.266	0.326	0.446	0.016	0.29
TA22	TA22_29.d	4.861	0.193	0.689	0.029	0.51
TA22	TA22_30.d	4.168	0.144	0.703	0.032	0.64
TA22	TA22_31.d	3.891	0.181	0.723	0.026	0.45
TA22	TA22_32.d	4.543	0.198	0.73	0.03	0.39

Continued on next page

Continued from previous page

Sample name	Spot number	$^{238}U/^{206}Pb$	2σ	$^{207}Pb/^{206}Pb$	2σ	ρ
TA22	TA22_33.d	4.73	0.194	0.689	0.027	0.48
TA22	TA22_34.d	5.115	0.261	0.684	0.041	0.55
TA22	TA22_35.d	2.551	0.162	0.786	0.049	0.49
TA22	TA22_36.d	3.717	0.165	0.718	0.029	0.37
TA22	TA22_37.d	3.906	0.228	0.698	0.031	0.32
TA22	TA22_38.d	4.081	0.199	0.696	0.027	0.26
TA22	TA22_39.d	3.571	0.153	0.73	0.036	0.26
TA22	TA22_40.d	4.5	0.202	0.677	0.022	0.29
TA23	TA23_01.d	2.967	0.167	0.769	0.031	0.3
TA23	TA23_02.d	9.96	0.396	0.479	0.015	0.03
TA23	TA23_03.d	10.787	0.407	0.447	0.021	0.19
TA23	TA23_04.d	7.468	0.373	0.569	0.028	0.21
TA23	TA23_05.d	3.164	0.16	0.757	0.03	0.23
TA23	TA23_06.d	9.699	0.338	0.487	0.015	0.1
TA23	TA23_07.d	6.811	0.32	0.587	0.021	0.02
TA23	TA23_08.d	4.115	0.203	0.715	0.036	0.34
TA23	TA23_09.d	5.743	0.27	0.649	0.028	-0.08
TA23	TA23_10.d	8.88	0.299	0.508	0.018	0.3
TA23	TA23_11.d	7.651	0.316	0.541	0.021	0.19
TA23	TA23_12.d	3.344	0.201	0.732	0.026	0.25
TA23	TA23_13.d	7.739	0.359	0.544	0.016	-0.04
TA23	TA23_14.d	3.125	0.156	0.743	0.027	0.33
TA23	TA23_15.d	8.756	0.268	0.493	0.015	0.08
TA23	TA23_16.d	5.076	0.283	0.694	0.03	0.39
TA23	TA23_17.d	10.405	0.422	0.452	0.019	0.32
TA23	TA23_18.d	10.235	0.398	0.448	0.021	0.47
TA23	TA23_19.d	9.661	0.364	0.48	0.017	0.28
TA23	TA23_20.d	2.915	0.237	0.756	0.047	0.36
TA23	TA23_21.d	12.674	0.465	0.336	0.014	0.34
TA23	TA23_22.d	5.208	0.325	0.646	0.032	-0.02
TA23	TA23_24.d	6.68	0.441	0.603	0.03	0.5
TA23	TA23_25.d	1.941	0.109	0.828	0.039	0.25
TA23	TA23_26.d	13.404	0.503	0.337	0.014	0.25
TA23	TA23_27.d	5.479	0.252	0.656	0.028	0.25
TA23	TA23_28.d	7.479	0.335	0.551	0.024	-0.17
TA23	TA23_29.d	9.157	0.737	0.473	0.023	-0.43
TA23	TA23_30.d	8.403	0.346	0.543	0.019	0.17
TA23	TA23_31.d	5.23	0.254	0.661	0.027	0.5
TA23	TA23_32.d	2.192	0.134	0.815	0.032	0.4
TA23	TA23_33.d	6.009	0.285	0.613	0.03	-0.05
TA23	TA23_34.d	6.724	0.298	0.591	0.023	0.47
TA23	TA23_35.d	12.771	0.391	0.36	0.013	0.27
TA23	TA23_36.d	2.695	0.13	0.743	0.03	0.45
TA23	TA23_37.d	2.481	0.129	0.766	0.027	0.34

Continued on next page

Continued from previous page

Sample name	Spot number	$^{238}U/^{206}Pb$	2σ	$^{207}Pb/^{206}Pb$	2σ	ρ
TA23	TA23_38.d	7.812	0.28	0.589	0.024	0.59
TA23	TA23_39.d	6.497	0.244	0.596	0.025	0.31
TA23	TA23_40.d	10.416	0.444	0.418	0.019	0.39
TA26	TA26_01.d	6.41	0.493	0.596	0.032	0.2
TA26	TA26_02.d	6.43	0.454	0.623	0.026	0.47
TA26	TA26_03.d	5.347	0.4	0.668	0.032	0.41
TA26	TA26_04.d	9.199	0.609	0.47	0.024	0.21
TA26	TA26_05.d	7.342	0.528	0.574	0.027	0.23
TA26	TA26_06.d	5.586	0.405	0.628	0.031	0.33
TA26	TA26_07.d	7.347	0.507	0.618	0.029	0.47
TA26	TA26_08.d	6.906	0.524	0.632	0.04	0.54
TA26	TA26_09.d	3.937	0.434	0.706	0.034	0.08
TA26	TA26_10.d	5.461	0.357	0.644	0.027	0.5
TA26	TA26_11.d	8.237	0.597	0.54	0.029	0.39
TA26	TA26_12.d	7.225	0.522	0.566	0.03	0.19
TA26	TA26_13.d	5.347	0.371	0.646	0.033	0.43
TA26	TA26_14.d	6.357	0.404	0.631	0.028	0.33
TA26	TA26_15.d	9.596	0.718	0.448	0.025	0.27
TA26	TA26_16.d	7.961	0.469	0.554	0.031	0.21
TA26	TA26_17.d	3.367	0.283	0.732	0.042	0.27
TA26	TA26_18.d	6.671	0.445	0.62	0.034	0.1
TA26	TA26_19.d	5.586	0.405	0.626	0.027	-0.08
TA26	TA26_20.d	8.291	0.481	0.503	0.033	0.13
TA26	TA26_21.d	6.706	0.386	0.606	0.029	0.39
TA26	TA26_22.d	6.863	0.447	0.595	0.035	0.21
TA26	TA26_23.d	7.007	0.446	0.6	0.028	0.41
TA26	TA26_24.d	4.464	0.558	0.685	0.032	0
TA26	TA26_25.d	8.071	0.475	0.527	0.024	0.29
TA26	TA26_26.d	7.423	0.485	0.558	0.027	0.32
TA26	TA26_27.d	6.949	0.429	0.57	0.029	0.4
TA26	TA26_28.d	6.476	0.461	0.625	0.032	0.34
TA26	TA26_29.d	7.072	0.47	0.57	0.025	0.14
TA26	TA26_30.d	5.91	0.419	0.617	0.03	0.3
TA26	TA26_31.d	8.81	0.644	0.518	0.029	0.21
TA26	TA26_32.d	5.125	0.341	0.665	0.03	0.39
TA26	TA26_33.d	5.181	0.349	0.618	0.043	0.25
TA26	TA26_34.d	6.83	0.429	0.596	0.027	0.22
TA26	TA26_35.d	7.886	0.491	0.541	0.024	0.22
TA26	TA26_36.d	6.693	0.407	0.589	0.026	0.42
TA26	TA26_37.d	7.347	0.491	0.572	0.024	0.24
TA26	TA26_38.d	5.437	0.354	0.662	0.036	0.3
TA26	TA26_39.d	7.082	0.431	0.584	0.022	0.43
TA26	TA26_40.d	5.291	0.419	0.615	0.029	0.36
TA27	TA27_01.d	12.345	1.828	0.291	0.017	0.66

Continued on next page

Continued from previous page

Sample name	Spot number	$^{238}U/^{206}Pb$	2σ	$^{207}Pb/^{206}Pb$	2σ	ρ
TA27	TA27_02.d	13.605	0.907	0.294	0.013	0.36
TA27	TA27_03.d	15.128	0.961	0.235	0.015	0.19
TA27	TA27_04.d	10.952	0.647	0.418	0.019	-0.06
TA27	TA27_05.d	14.347	0.823	0.282	0.016	0
TA27	TA27_06.d	14.662	0.881	0.264	0.013	0
TA27	TA27_07.d	14.204	0.867	0.282	0.015	0.08
TA27	TA27_08.d	14.619	0.876	0.257	0.012	0.19
TA27	TA27_09.d	14.925	0.846	0.27	0.013	0.43
TA27	TA27_10.d	11.961	0.686	0.364	0.018	0.11
TA27	TA27_11.d	13.698	0.9	0.321	0.03	-0.03
TA27	TA27_12.d	14.124	0.917	0.297	0.016	0.26
TA27	TA27_13.d	16.077	1.008	0.261	0.018	0.05
TA27	TA27_14.d	11.56	0.815	0.369	0.014	0.38
TA27	TA27_15.d	13.717	0.771	0.29	0.012	0.2
TA27	TA27_16.d	13.55	0.789	0.281	0.015	0.25
TA27	TA27_17.d	14.792	0.94	0.28	0.021	0.3

Appendix G

Detrital apatite U–Pb and trace element analysis as a provenance tool: insights from the Yenisey Ridge (Siberia)

G.1 Apatite U–Pb data

Table G.1: Apatite U–Pb individual spot data. ^{207}Pb corr. Age is the ^{207}Pb corrected ^{206}Pb/^{238}U age of the grain. (^{207}Pb/^{206}Pb)$_o$ is the ^{207}Pb/^{206}Pb axis intercept of the regression line used to estimate initial ^{207}Pb/^{206}Pb. E_M is the method used to estimate (^{207}Pb/^{206}Pb)$_o$ where 1 = (^{207}Pb/^{206}Pb)$_o$ determined by regression through apatite U–Pb population and 2 = (^{207}Pb/^{206}Pb)$_o$ calculated using Stacey and Kramers (1975) Pb evolution model for age of zircon U–Pb age peak as described in results section for relevant sample.

Grain	^{207}Pb/ ^{235}U	2σ	^{206}Pb/ ^{238}U	2σ	ρ	^{238}U/ ^{206}Pb	2σ	^{207}Pb/ ^{206}Pb	2σ	ρ	^{207}Pb corr. Age (Ma)	2σ	(^{207}Pb/ ^{206}Pb)$_o$	E_M
YP1_1b	13.6	0.97	0.296	0.021	0.66	3.38	0.24	0.316	0.019	-0.05				
YP1_2b	23.7	1.5	0.339	0.025	0.63	2.95	0.22	0.484	0.021	0.23				
YP1_3b	9.14	0.45	0.2204	0.014	0.60	4.54	0.29	0.287	0.012	0.29				
YP1_4b	19.2	1.4	0.324	0.024	0.69	3.09	0.23	0.407	0.021	0.08				
YP1_5b	4.69	0.23	0.1927	0.012	0.57	5.19	0.32	0.1687	0.0072	0.29				
YP1_6b	7.51	0.42	0.2187	0.014	0.58	4.57	0.29	0.234	0.011	0.21				
YP1_7b	12.4	1.2	0.248	0.019	0.83	4.03	0.31	0.348	0.021	-0.48				
YP1_8b	24.9	2.2	0.399	0.026	0.44	2.51	0.16	0.454	0.027	0.26				
YP1_9b	10.9	0.64	0.233	0.016	0.56	4.29	0.29	0.323	0.016	0.21				
YP1_10b	23.4	1.2	0.345	0.025	0.41	2.90	0.21	0.478	0.026	0.51				
YP1_11b	75.1	8.2	0.8	0.079	0.34	1.25	0.12	0.652	0.057	0.26				
YP1_12b	13.62	0.82	0.309	0.021	0.71	3.24	0.22	0.319	0.015	0.33				
YP1_13b	6	0.39	0.21	0.016	0.43	4.76	0.36	0.200	0.011	0.13				
YP1_14b	18.8	1.8	0.336	0.023	0.65	2.98	0.20	0.397	0.015	-0.13				
YP1_15b	4.72	0.23	0.1983	0.014	0.63	5.04	0.36	0.1690	0.0068	0.27				
YP1_16b	26.1	2.3	0.379	0.033	0.31	2.64	0.23	0.518	0.042	0.32				
YP1_17b	7.08	0.35	0.234	0.016	0.68	4.27	0.29	0.2084	0.0078	0.20				
YP1_18b	35.9	2	0.459	0.036	0.67	2.18	0.17	0.567	0.029	0.39				
YP1_19b	3.95	0.23	0.1782	0.011	0.50	5.61	0.35	0.1528	0.0075	0.10				
YP1_20b	5	0.33	0.1854	0.013	0.69	5.39	0.38	0.1917	0.0096	0.10				
YP1_21b	100	11	0.995	0.1	0.93	1.01	0.10	0.712	0.023	-0.21				
YP1_22b	11.9	0.87	0.251	0.019	0.63	3.98	0.30	0.329	0.019	0.15				
YP1_24b	870	160	6.9	1.1	0.92	0.145	0.023	0.878	0.041	0.20				

Continued on next page

Continued from previous page

Grain	$^{207}Pb/^{235}U$	2σ	$^{206}Pb/^{238}U$	2σ	ρ	$^{238}U/^{206}Pb$	2σ	$^{207}Pb/^{206}Pb$	2σ	ρ	^{207}Pb corr. Age (Ma)	2σ	$(^{207}Pb/^{206}Pb)_o$	E_M
YP1_25b	14.9	1.1	0.278	0.02	0.60	3.60	0.26	0.375	0.022	0.18				
YP1_26b	5.28	0.26	0.1711	0.01	0.46	5.84	0.34	0.2126	0.0092	0.16				
YP1_27b	78	4.4	0.772	0.056	0.68	1.295	0.094	0.706	0.029	0.19				
YP1_28b	25.1	1.9	0.385	0.028	0.82	2.60	0.19	0.475	0.029	-0.06				
YP1_29b	780	150	6.3	1.3	0.97	0.159	0.033	0.888	0.049	-0.08				
YP1_30b	14.89	0.85	0.293	0.018	0.39	3.41	0.21	0.364	0.014	0.42				
YP1_31b	6.02	0.27	0.1842	0.012	0.48	5.43	0.35	0.229	0.009	0.34				
YP1_32b	13.17	0.95	0.258	0.021	0.83	3.88	0.32	0.352	0.015	0.03				
YP1_33b	9.96	0.79	0.243	0.017	0.66	4.12	0.29	0.282	0.017	0.00				
YP1_34b	6.27	0.43	0.1882	0.013	0.52	5.31	0.37	0.2447	0.0097	0.33				
YP1_35b	560	160	6.2	2	0.84	0.161	0.052	0.758	0.070	0.25				
YP1_36b	10.32	0.98	0.236	0.026	0.46	4.24	0.47	0.351	0.025	0.15				
YP1_37b	8.88	0.63	0.213	0.014	0.52	4.69	0.31	0.297	0.014	0.07				
YP1_38b	8.38	0.51	0.2279	0.015	0.64	4.39	0.29	0.254	0.013	0.16				
YP1_39b	3.53	0.17	0.1618	0.0099	0.36	6.18	0.38	0.1572	0.0071	0.25				
YP1_40b	13.64	0.91	0.264	0.019	0.65	3.79	0.27	0.351	0.019	0.30				
YP1_41b	1010	260	8.4	2	0.93	0.119	0.028	0.895	0.047	-0.21				
YP1_42b	12.29	0.77	0.2472	0.016	0.62	4.05	0.26	0.358	0.015	0.15				
YP1_43b	7.81	0.56	0.194	0.015	0.79	5.15	0.40	0.277	0.012	-0.15				
YP1_44b	4.57	0.33	0.1635	0.011	0.47	6.12	0.41	0.193	0.012	0.04				
YP1_45b	9.19	0.79	0.229	0.019	0.27	4.37	0.36	0.289	0.019	0.55				
YP1_46b	2.47	0.13	0.1568	0.0097	0.51	6.38	0.39	0.1147	0.0045	0.24				
YP1_47b	11.81	0.8	0.272	0.025	0.72	3.68	0.34	0.304	0.018	0.52				
YP1_48b	10.71	0.84	0.229	0.019	0.30	4.37	0.36	0.337	0.026	0.35				
YP1_49b	17	1.5	0.299	0.025	0.70	3.34	0.28	0.420	0.022	-0.01				
YP1_50b	7.53	0.39	0.2216	0.015	0.67	4.51	0.31	0.2338	0.0087	0.08				
YP1_51b	10.79	0.71	0.222	0.016	0.63	4.50	0.32	0.33	0.015	0.12				
YP1_52b	22.8	1.6	0.315	0.026	0.70	3.17	0.26	0.501	0.028	0.42				
YP1_53b	5.61	0.32	0.1901	0.012	0.58	5.26	0.33	0.2071	0.0088	0.20				
YP1_54b	5.27	0.32	0.197	0.015	0.65	5.08	0.39	0.191	0.013	-0.01				

Continued on next page

Continued from previous page

Grain	$^{207}Pb/^{235}U$	2σ	$^{206}Pb/^{238}U$	2σ	ρ	$^{238}U/^{206}Pb$	2σ	$^{207}Pb/^{206}Pb$	2σ	ρ	^{207}Pb corr. Age (Ma)	2σ	$(^{207}Pb/^{206}Pb)_o$	E_M
YP1_55b	6.19	0.31	0.2181	0.015	0.69	4.59	0.32	0.1939	0.0073	0.13				
YP1_56b	5.67	0.23	0.2129	0.013	0.32	4.70	0.29	0.1839	0.0075	0.24				
YP1_57b	9.02	0.82	0.25	0.019	0.46	4.00	0.30	0.247	0.015	0.12				
YP1_58b	26.5	2.8	0.425	0.034	0.81	2.35	0.19	0.429	0.028	-0.24				
YP1_59b	5.64	0.28	0.1811	0.012	0.63	5.52	0.37	0.2141	0.0084	0.24				
YP1_60b	13.19	0.85	0.327	0.026	0.63	3.06	0.24	0.279	0.014	0.40				
YP1_61b	25.7	1.9	0.419	0.033	0.76	2.39	0.19	0.450	0.026	0.35				
YP1_62b	37.4	2.6	0.493	0.036	0.66	2.03	0.15	0.544	0.025	0.20				
YP1_63b	36	3.1	0.497	0.039	0.78	2.01	0.16	0.511	0.035	0.17				
YP1_64b	35.4	2.1	0.481	0.037	0.52	2.08	0.16	0.515	0.03	0.38				
YP1_65b	23.1	1.3	0.399	0.031	0.44	2.51	0.19	0.408	0.025	0.59				
YP1_66b	25.5	1.9	0.403	0.032	0.69	2.48	0.20	0.434	0.022	0.02				
YP1_67b	28.4	1.8	0.445	0.031	0.31	2.25	0.16	0.445	0.025	0.41				
YP1_68b	51.4	3	0.662	0.049	0.62	1.51	0.11	0.550	0.028	0.37				
YP1_69b	57.2	3.8	0.723	0.065	0.69	1.38	0.12	0.565	0.028	0.44				
YP1_70b	32.4	1.8	0.437	0.034	0.74	2.29	0.18	0.515	0.02	0.32				
YP1_71b	9.35	0.44	0.229	0.018	0.79	4.37	0.34	0.282	0.013	0.55				
YP1_72b	42.2	3.9	0.574	0.047	0.81	1.74	0.14	0.492	0.025	-0.02				
YP1_73b	4.36	0.31	0.1654	0.012	0.71	6.05	0.44	0.1812	0.0073	0.00				
YP1_74b	3.74	0.19	0.1634	0.01	0.38	6.12	0.37	0.1625	0.0066	0.16				
YP1_75b	171	22	1.79	0.26	0.75	0.559	0.081	0.727	0.042	0.27				
YP1_76b	259	51	2.09	0.32	0.95	0.478	0.073	0.795	0.074	0.01				
YP1_77b	720	110	6.21	1	0.99	0.161	0.026	0.809	0.031	0.22				
YP1_78b	342	45	3.26	0.52	0.96	0.307	0.049	0.753	0.041	0.56				
YP1_79b	3.7	0.18	0.1614	0.011	0.62	6.20	0.42	0.1573	0.0052	0.16				
YP1_80b	18.09	0.91	0.331	0.024	0.43	3.02	0.22	0.38	0.021	0.52				
YP1_1a	12.39	0.55	0.2963	0.0084	0.78	3.37	0.10	0.3049	0.0062	0.57				
YP1_3a	9.99	0.66	0.2306	0.0068	0.77	4.34	0.13	0.3160	0.0089	0.07				
YP1_4a	24.6	3.8	0.365	0.031	0.94	2.74	0.23	0.478	0.028	-0.81				
YP1_5a	23.1	1.7	0.364	0.016	0.82	2.75	0.12	0.466	0.024	-0.53				

Continued on next page

Continued from previous page

Grain	$^{207}Pb/^{235}U$	2σ	$^{206}Pb/^{238}U$	2σ	ρ	$^{238}U/^{206}Pb$	2σ	$^{207}Pb/^{206}Pb$	2σ	ρ	^{207}Pb corr. Age (Ma)	2σ	$(^{207}Pb/^{206}Pb)_o$	E_M
YP1_6a	8.88	0.62	0.22	0.0073	0.81	4.55	0.15	0.2920	0.0076	-0.16				
YP1_7a	26.1	1.3	0.445	0.012	0.59	2.247	0.061	0.428	0.011	0.38				
YP1_8a	6.84	0.38	0.2219	0.0071	0.82	4.51	0.14	0.2239	0.0031	0.60				
YP1_9a	7.49	0.37	0.2195	0.0067	0.88	4.56	0.14	0.2438	0.0060	0.04				
YP1_10a	27	1.4	0.37	0.0094	0.70	2.703	0.069	0.533	0.010	0.34				
YP1_11a	24.12	0.97	0.466	0.011	0.38	2.146	0.051	0.3922	0.0098	0.41				
YP1_13a	25.1	0.93	0.359	0.01	0.07	2.786	0.078	0.533	0.013	0.43				
YP1_14a	2.92	0.11	0.1781	0.0038	0.32	5.61	0.12	0.1239	0.0032	0.34				
YP1_17a	19.52	0.61	0.3419	0.0081	0.47	2.925	0.069	0.416	0.010	0.52				
YP1_18a	28.94	0.85	0.3631	0.0098	0.50	2.754	0.074	0.580	0.017	0.31				
YP1_19a	20.59	0.63	0.3903	0.0091	0.70	2.562	0.060	0.3798	0.0080	0.17				
YP1_20a	5.96	0.25	0.1998	0.004	0.59	5.01	0.10	0.2136	0.0068	-0.09				
YP1_22a	35.7	1.8	0.469	0.015	0.71	2.132	0.068	0.562	0.013	0.12				
YP1_23a	13.96	0.64	0.2994	0.0089	0.58	3.34	0.10	0.3507	0.0088	-0.28				
YP1_24a	24.16	0.62	0.374	0.014	0.53	2.67	0.10	0.487	0.014	-0.18				
YP1_25a	5.71	0.37	0.2131	0.0063	0.79	4.69	0.14	0.1988	0.0054	-0.41				
YP1_26a	9.83	0.28	0.3563	0.0076	0.53	2.807	0.060	0.1988	0.0029	0.49				
YP1_27a	6.72	0.22	0.1992	0.0044	0.57	5.02	0.11	0.2472	0.0071	0.06				
YP1_28a	3.65	0.13	0.1696	0.005	0.58	5.90	0.17	0.1523	0.0044	0.28				
YP1_29a	105	10	1.03	0.1	0.92	0.971	0.094	0.750	0.021	-0.43				
YP1_30a	25.9	1.1	0.4008	0.0093	0.43	2.495	0.058	0.485	0.012	0.49				
YP1_31a	19.7	1	0.2983	0.0094	0.45	3.35	0.11	0.517	0.013	0.20				
YP1_33a	10.18	0.24	0.2672	0.0069	0.45	3.74	0.10	0.2710	0.0073	0.60				
YP1_34a	37.5	1.8	0.508	0.012	0.56	1.969	0.047	0.554	0.013	0.22				
YP1_35a	6.18	0.56	0.1824	0.0056	0.40	5.48	0.17	0.2667	0.0076	0.38				
YP1_36a	22.2	1.6	0.322	0.019	0.82	3.11	0.18	0.502	0.023	-0.79				
YP1_37a	12.98	0.52	0.2315	0.0067	0.76	4.32	0.13	0.386	0.011	-0.09				
YP1_38a	47.9	2.9	0.545	0.021	0.78	1.835	0.071	0.625	0.017	0.12				
YP4_1a	10.9	1.1	0.219	0.012	0.35	4.57	0.32	0.340	0.027	0.03				

Continued on next page

Continued from previous page

Grain	$^{207}Pb/^{235}U$	2σ	$^{206}Pb/^{238}U$	2σ	ρ	$^{238}U/^{206}Pb$	2σ	$^{207}Pb/^{206}Pb$	2σ	ρ	^{207}Pb corr. Age (Ma)	2σ	$(^{207}Pb/^{206}Pb)_o$	E_M
YP4_2a	16.9	1.1	0.279	0.017	0.02	3.58	0.23	0.445	0.042	0.04	927	119	0.912	1
YP4_3a	18.5	1.3	0.412	0.026	0.05	2.43	0.17	0.317	0.025	0.03				
YP4_4a	24	2	0.324	0.025	0.19	3.09	0.27	0.552	0.055	0.06				
YP4_5a	19.80	1.20	0.444	0.026	0.61	2.25	0.15	0.322	0.016	0.02				
YP4_6a	18.7	2.0	0.273	0.018	0.53	3.66	0.28	0.492	0.042	0.04	820	122	0.912	1
YP4_7a	3.03	0.15	0.157	0.007	0.63	6.38	0.29	0.142	0.007	0.01				
YP4_8a	29.2	2.4	0.490	0.044	0.61	2.04	0.23	0.424	0.038	0.04	1788	209	1.014	1
YP4_9a	25.3	2.1	0.306	0.024	0.17	3.27	0.24	0.613	0.062	0.06				
YP4_10a	55.7	4.8	0.689	0.054	0.54	1.45	0.11	0.580	0.038	0.04	1847	274	1.014	1
YP4_11a	17.0	1.0	0.268	0.018	0.16	3.73	0.31	0.468	0.043	0.04	850	120	0.912	1
YP4_12a	29.2	2.0	0.514	0.033	0.58	1.95	0.13	0.424	0.032	0.03				
YP4_13a	31.4	2.1	0.377	0.029	0.21	2.65	0.20	0.618	0.061	0.06				
YP4_14a	3.67	0.24	0.181	0.009	0.64	5.53	0.29	0.147	0.007	0.01	982	49	0.912	1
YP4_15a	11.6	1.1	0.226	0.024	0.44	4.42	0.51	0.357	0.032	0.03				
YP4_16a	28.9	2.1	0.353	0.028	0.54	2.83	0.28	0.596	0.043	0.04	798	173	0.912	1
YP4_17a	17.4	1.7	0.489	0.031	0.69	2.04	0.13	0.258	0.018	0.02	2284	163	1.014	1
YP4_18a	7.96	0.75	0.236	0.014	0.10	4.24	0.26	0.247	0.028	0.03				
YP4_19a	18.3	1.5	0.274	0.025	0.26	3.65	0.35	0.496	0.048	0.05	815	139	0.912	1
YP4_20a	14.18	0.87	0.381	0.018	0.02	2.62	0.13	0.267	0.021	0.02	1760	99	1.014	1
YP4_21a	63.5	6.8	0.792	0.069	0.53	1.26	0.11	0.580	0.051	0.05	2121	371	1.014	1
YP4_22a	21.0	1.9	0.297	0.017	0.56	3.37	0.16	0.507	0.041	0.04				
YP4_23a	27.4	2.4	0.466	0.024	0.35	2.15	0.11	0.415	0.038	0.04	1728	157	1.014	1
YP4_24a	22.7	1.4	0.313	0.025	0.39	3.19	0.27	0.534	0.045	0.05				
YP4_25a	19.9	1.4	0.439	0.025	0.23	2.28	0.13	0.328	0.028	0.03	1860	137	1.014	1
YP4_01c	23.2	1.3	0.449	0.021	0.64	2.227	0.091	0.375	0.015	0.38	1774	111	1.014	1
YP4_02c	6.71	0.3	0.1891	0.0083	0.55	5.29	0.19	0.253	0.01	0.44	888	46	0.912	1
YP4_03c	23	1.8	0.406	0.027	0.54	2.46	0.15	0.406	0.019	0.10	1534	127	1.014	1
YP4_04c	26.6	1.6	0.338	0.021	0.46	2.96	0.18	0.576	0.034	0.48	812	146	0.912	1
YP4_05c	30.2	1.4	0.515	0.028	0.61	1.942	0.078	0.426	0.019	0.47	1870	145	1.014	1
YP4_06c	53.2	4.7	0.649	0.063	0.76	1.54	0.14	0.603	0.038	0.18	1653	274	1.014	1

Continued on next page

Continued from previous page

Grain	$^{207}Pb/^{235}U$	2σ	$^{206}Pb/^{238}U$	2σ	ρ	$^{238}U/^{206}Pb$	2σ	$^{207}Pb/^{206}Pb$	2σ	ρ	^{207}Pb corr. Age (Ma)	2σ	$(^{207}Pb/^{206}Pb)_o$	E_M
YP4_07c	12.15	0.71	0.373	0.02	0.81	2.68	0.13	0.2343	0.0087	0.14	1798	99	1.014	1
YP4_08c	22.5	1	0.457	0.028	0.71	2.2	0.1	0.349	0.015	0.47	1877	133	1.014	1
YP4_09c	14.81	0.92	0.246	0.014	0.38	4.07	0.23	0.439	0.027	0.40	831	88	0.912	1
YP4_10c	24	1.7	0.314	0.019	-0.01	3.18	0.19	0.545	0.035	0.19	824	133	0.912	1
YP4_11c	22.2	1.6	0.31	0.022	0.72	3.23	0.21	0.519	0.026	0.35	869	122	0.912	1
YP4_12c	9.22	0.42	0.362	0.015	0.65	2.8	0.1	0.1832	0.0063	0.14	1858	78	1.014	1
YP4_13c	22.4	1.1	0.306	0.014	0.51	3.27	0.13	0.528	0.023	0.34	839	111	0.912	1
YP4_1b	7.75	0.46	0.188	0.007	0.59	5.31	0.21	0.293	0.015	0.14	833	46	0.912	1
YP4_2b	7.99	0.42	0.193	0.008	0.30	5.17	0.19	0.289	0.015	0.44				
YP4_3b	24.4	2.1	0.466	0.025	0.40	2.15	0.12	0.367	0.031	0.33	1862	146	1.014	1
YP4_4b	23.4	1.7	0.312	0.017	0.46	3.21	0.21	0.527	0.035	0.37	857	128	0.912	1
YP4_5b	27.4	1.7	0.345	0.018	0.45	2.90	0.17	0.559	0.033	0.44	869	143	0.912	1
YP4_6b	16.9	1.0	0.406	0.018	0.57	2.46	0.11	0.296	0.015	0.13	1802	95	1.014	1
YP4_7b	47.4	3.1	0.519	0.036	0.49	1.93	0.12	0.658	0.042	0.45				
YP4_8b	22.3	1.3	0.291	0.013	0.40	3.44	0.15	0.543	0.031	0.39				
YP4_9b	22.5	1.5	0.302	0.018	0.51	3.31	0.19	0.527	0.033	0.36	831	124	0.912	1
YP4_10b	18.0	1.4	0.258	0.016	0.54	3.88	0.27	0.491	0.029	0.19				
YP4_11b	11.97	0.65	0.369	0.015	0.45	2.71	0.11	0.229	0.011	0.35	1791	79	1.014	1
YP4_12b	27.0	1.6	0.338	0.018	0.32	2.96	0.18	0.568	0.031	0.58	831	139	0.912	1
YP4_13b	25.2	1.6	0.329	0.018	0.60	3.04	0.15	0.543	0.026	0.21				
YP4_14b	26.2	1.6	0.332	0.020	0.60	3.01	0.19	0.558	0.032	0.40	840	138	0.912	1
YP4_15b	19.8	1.3	0.292	0.016	0.64	3.42	0.19	0.475	0.026	0.26				
YP4_16b	22.9	1.5	0.419	0.025	0.64	2.39	0.15	0.390	0.021	0.34	1622	125	1.014	1
YP4_17b	41.1	3.0	0.604	0.036	0.75	1.66	0.10	0.489	0.025	0.16	1957	191	1.014	1
YP4_18b	20.5	1.0	0.416	0.016	0.61	2.40	0.10	0.349	0.014	0.16	1713	90	1.014	1
YP4_19b	22.6	1.4	0.306	0.015	0.54	3.27	0.17	0.533	0.031	0.40	829	121	0.912	1
YP4_20b	15	1	0.405	0.015	0.58	2.47	0.09	0.251	0.014	-0.09	1908	83	1.014	1
YP4_21b	9.51	0.95	0.189	0.012	0.65	5.29	0.30	0.347	0.028	-0.10	765	69	0.912	1
YP4_22b	31.0	3.1	0.364	0.023	0.73	2.75	0.18	0.586	0.039	-0.09	847	166	0.912	1
YP4_23b	136	21	1.21	0.16	0.92	0.83	0.10	0.779	0.046	0.03				

Continued on next page

Continued from previous page

Grain	$^{207}Pb/^{235}U$	2σ	$^{206}Pb/^{238}U$	2σ	ρ	$^{238}U/^{206}Pb$	2σ	$^{207}Pb/^{206}Pb$	2σ	ρ	^{207}Pb corr. Age (Ma)	2σ	$(^{207}Pb/^{206}Pb)_o$	E_M
YP4_24b	96	14	0.93	0.13	0.93	1.08	0.17	0.721	0.046	0.13				
YP4_25b	101	14	0.870	0.095	0.76	1.15	0.13	0.746	0.040	0.32				
YP4_26b	28.1	3.9	0.345	0.030	0.76	2.90	0.28	0.528	0.036	-0.27	942	155	0.912	1
YP4_27b	29.3	3.8	0.497	0.037	0.81	2.01	0.14	0.400	0.027	-0.38	1885	177	1.014	1
YP4_28b	10.73	0.67	0.370	0.013	0.62	2.70	0.11	0.201	0.008	0.17				
YP4_29b	12.23	0.79	0.362	0.017	0.72	2.76	0.15	0.240	0.012	0.13	1734	87	1.014	1
YP4_30b	29	2	0.360	0.024	0.36	2.78	0.19	0.586	0.042	0.34				
YP4_31b	31.4	2.3	0.377	0.029	0.58	2.65	0.21	0.607	0.037	0.34	822	175	0.912	1
YP4_32b	4.00	0.27	0.160	0.005	0.35	6.27	0.21	0.179	0.011	0.15	836	32	0.912	1
YP4_33b	26.4	1.8	0.340	0.023	0.61	2.94	0.19	0.555	0.039	0.27	866	153	0.912	1
YP4_34b	21.6	1.5	0.306	0.019	0.54	3.27	0.20	0.519	0.034	0.23	858	126	0.912	1
YP4_35b	20.9	1.5	0.415	0.023	0.60	2.41	0.13	0.378	0.025	0.21				
YP4_36b	14.93	0.73	0.391	0.014	0.31	2.56	0.10	0.274	0.014	0.60	1789	78	1.014	1
YP4_37b	25.9	1.7	0.335	0.025	0.58	2.99	0.22	0.573	0.034	0.51	812	148	0.912	1
YP4_38b	17.8	1.2	0.270	0.017	0.45	3.70	0.23	0.479	0.028	0.35	835	103	0.912	1
YP4_39b	73.40	7.50	0.777	0.076	0.78	1.29	0.14	0.679	0.050	0.32				
YP4_40b	11.7	1.4	0.269	0.016	0.42	3.72	0.25	0.299	0.031	0.04	1164	96	0.912	1
YP6_1a	9.02	0.75	0.357	0.012	0.52	2.80	0.09	0.183	0.011	0.62	1828	67	0.987	2
YP6_2a	37.3	3.3	0.559	0.033	0.37	1.79	0.11	0.475	0.025	0.65	1823	179	0.987	2
YP6_3a	20.1	2.1	0.554	0.036	-0.03	1.81	0.12	0.263	0.028	0.61	2612	214	1.065	2
YP6_4a	13.8	1.2	0.381	0.023	0.73	2.62	0.16	0.234	0.011	0.69	1828	114	0.987	2
YP6_5a	15.2	1.5	0.506	0.025	0.54	1.98	0.10	0.209	0.009	0.42	2539	139	1.065	2
YP6_6a	12.8	1.5	0.355	0.017	0.64	2.82	0.13	0.248	0.010	0.09	1675	86	0.987	2
YP6_7a	10.1	1.2	0.180	0.019	0.01	5.56	0.59	0.432	0.062	0.43				
YP6_8a	21.8	2.0	0.463	0.026	0.30	2.16	0.12	0.333	0.016	0.56	1927	130	0.987	2
YP6_9a	14.9	2.2	0.325	0.027	0.09	3.08	0.26	0.334	0.045	0.46	1365	148	0.987	2
YP6_10a	7.74	0.63	0.315	0.015	0.40	3.17	0.15	0.174	0.007	0.51	1636	78	0.987	2
YP6_11a	17.3	1.7	0.505	0.025	0.62	1.98	0.10	0.227	0.011	0.54	2478	136	1.065	2
YP6_12a	33.9	4.1	0.530	0.036	0.59	1.89	0.13	0.438	0.022	0.46				

Continued on next page

Continued from previous page

Grain	$^{207}Pb/^{235}U$	2σ	$^{206}Pb/^{238}U$	2σ	ρ	$^{238}U/^{206}Pb$	2σ	$^{207}Pb/^{206}Pb$	2σ	ρ	^{207}Pb corr. Age (Ma)	2σ	$(^{207}Pb/^{206}Pb)_o$	E_M
YP6_13a	22.6	2.7	0.546	0.026	0.71	1.83	0.09	0.279	0.011	-0.21	2515	138	1.065	2
YP6_14a	21.9	2.8	0.293	0.020	0.34	3.41	0.23	0.524	0.047	0.55				
YP6_15a	11.4	1.1	0.345	0.012	0.27	2.90	0.10	0.228	0.010	0.18	1672	65	0.987	2
YP6_16a	27.6	2.2	0.452	0.023	0.35	2.21	0.11	0.409	0.018	0.72				
YP6_17a	12.6	1.4	0.331	0.021	-0.14	3.02	0.19	0.268	0.024	0.53	1524	110	0.987	2
YP6_18a	13.1	1.3	0.362	0.020	0.65	2.76	0.15	0.249	0.009	0.49	1706	99	0.987	2
YP6_19a	8.60	0.75	0.311	0.019	0.39	3.22	0.20	0.192	0.008	0.67	1581	96	0.987	2
YP6_20a	2.84	0.55	0.151	0.015	0.18	6.62	0.66	0.134	0.025	0.17	839	85	0.91	1
YP6_21a	14.0	1.3	0.361	0.019	0.51	2.77	0.15	0.262	0.010	0.50	1672	94	0.987	2
YP6_22a	15.8	1.7	0.374	0.041	0.59	2.67	0.29	0.299	0.019	0.23	1644	185	0.987	2
YP6_23a	36.3	3.7	0.540	0.031	0.48	1.85	0.11	0.460	0.029	0.56	1813	177	0.987	2
YP6_24a	12.6	1.5	0.195	0.019	0.54	5.13	0.50	0.444	0.046	0.59				
YP6_25a	14.5	1.4	0.433	0.024	0.65	2.31	0.13	0.213	0.009	0.23				
YP6_26a	8.94	0.87	0.330	0.017	0.37	3.03	0.16	0.185	0.011	0.51	1689	89	0.987	2
YP6_27a	11.7	1.2	0.353	0.022	0.50	2.83	0.18	0.223	0.009	0.49	1721	109	0.987	2
YP6_28a	7.17	0.98	0.291	0.019	0.43	3.44	0.22	0.171	0.019	0.26	1521	102	0.987	2
YP6_29a	25.9	2.4	0.539	0.023	0.47	1.86	0.08	0.325	0.016	0.50				
YP6_30a	11.8	1.3	0.310	0.027	0.07	3.23	0.28	0.283	0.034	0.46	1402	138	0.987	2
YP6_31a	15.0	1.3	0.499	0.022	0.47	2.00	0.09	0.196	0.005	0.52	2543	123	1.065	2
YP6_32a	14.9	1.8	0.333	0.031	0.30	3.00	0.28	0.316	0.042	0.58	1434	160	0.987	2
YP6_33a	8.8	1.1	0.236	0.020	0.25	4.24	0.36	0.250	0.028	0.09	1128	103	0.987	2
YP6_34a	16.4	2.5	0.372	0.035	0.28	2.69	0.25	0.326	0.050	0.20				
YP6_35a	14.6	1.2	0.474	0.019	0.26	2.11	0.08	0.207	0.009	0.48	2375	103	1.065	2
YP6_36a	48.2	3.0	0.695	0.046	0.35	1.44	0.10	0.475	0.034	0.57	2397	250	1.065	2
YP6_37a	12.26	0.95	0.326	0.014	0.41	3.07	0.13	0.243	0.014	0.35	1552	75	0.987	2
YP6_38a	12.1	1.1	0.437	0.019	0.30	2.29	0.10	0.184	0.006	0.50	2247	101	1.065	2
YP6_39a	53	4	0.619	0.045	0.15	1.62	0.12	0.558	0.045	0.73	1695	263	0.987	2
YP6_1b	7.36	0.80	0.154	0.012	0.30	6.50	0.48	0.328	0.033	0.31	638	67	0.885	1
YP6_2b	8.58	0.73	0.164	0.012	0.45	6.08	0.34	0.393	0.034	0.15				
YP6_3b	9.42	0.88	0.174	0.013	0.44	5.75	0.39	0.399	0.033	0.33				

Continued on next page

Continued from previous page

Grain	$^{207}Pb/^{235}U$	2σ	$^{206}Pb/^{238}U$	2σ	ρ	$^{238}U/^{206}Pb$	2σ	$^{207}Pb/^{206}Pb$	2σ	ρ	^{207}Pb corr. Age (Ma)	2σ	$(^{207}Pb/^{206}Pb)_o$	E_M
YP6_4b	12.5	1.0	0.195	0.015	0.56	5.13	0.35	0.460	0.029	0.27				
YP6_5b	11.6	1.3	0.186	0.015	0.57	5.38	0.42	0.414	0.033	0.15	652	82	0.885	1
YP6_6b	23.1	1.5	0.311	0.024	0.71	3.22	0.18	0.552	0.027	0.30				
YP6_7b	22.6	1.8	0.318	0.023	0.69	3.14	0.20	0.512	0.027	0.28	904	127	0.91	1
YP6_8b	26.6	1.3	0.467	0.026	0.62	2.14	0.07	0.400	0.014	0.36				
YP6_9b	25.5	1.2	0.455	0.026	0.66	2.20	0.08	0.391	0.013	0.10				
YP6_10b	27.8	1.2	0.500	0.030	0.72	2.00	0.07	0.403	0.010	0.13	1860	141	0.987	2
YP6_11b	16.0	1.6	0.387	0.036	0.43	2.58	0.23	0.306	0.030	0.43				
YP6_12b	14.4	1.3	0.370	0.030	0.53	2.70	0.20	0.285	0.023	0.26	1659	146	0.987	2
YP6_13b	31.5	1.6	0.547	0.035	0.63	1.83	0.09	0.413	0.018	0.22				
YP6_14b	24.9	1.4	0.495	0.030	0.60	2.02	0.10	0.358	0.014	0.29				
YP6_15b	17.31	0.75	0.413	0.024	0.47	2.42	0.09	0.301	0.011	0.30	1805	116	0.987	2
YP6_16b	22.02	0.93	0.555	0.033	0.68	1.80	0.08	0.284	0.007	0.00				
YP6_17b	17.51	0.84	0.524	0.029	0.66	1.91	0.07	0.243	0.007	0.38	2527	154	1.065	2
YP6_18b	21.8	1.3	0.544	0.035	0.74	1.84	0.09	0.291	0.012	0.18				
YP6_19b	12.31	0.63	0.449	0.025	0.55	2.23	0.09	0.199	0.007	0.20	2270	131	1.065	2
YP6_20b	34.2	2.1	0.630	0.048	0.61	1.59	0.10	0.396	0.022	0.41				
YP6_21b	10.77	0.69	0.334	0.019	0.57	2.99	0.11	0.232	0.012	-0.02				
YP6_22b	11.23	0.68	0.339	0.021	0.41	2.95	0.13	0.242	0.013	0.31				
YP6_23b	11.75	0.94	0.336	0.024	0.61	2.98	0.17	0.245	0.016	0.18	1594	118	0.987	2
YP6_24b	10.51	0.64	0.358	0.020	0.56	2.79	0.11	0.209	0.009	-0.08				
YP6_25b	6.92	0.36	0.330	0.018	0.67	3.03	0.10	0.146	0.005	0.19	1769	95	0.987	2
YP6_26b	9.41	0.56	0.349	0.021	0.55	2.87	0.11	0.191	0.007	0.17				
YP6_27b	12.82	0.66	0.464	0.027	0.75	2.16	0.08	0.197	0.007	0.00	2352	143	1.065	2
YP6_28b	19.1	1.1	0.523	0.031	0.82	1.91	0.08	0.263	0.011	-0.25				
YP6_29b	22.3	1.2	0.531	0.030	0.47	1.88	0.06	0.303	0.014	0.32				
YP6_30b	21.8	1.4	0.574	0.035	0.61	1.74	0.08	0.278	0.016	0.00				
YP6_31b	13.8	0.7	0.482	0.029	0.67	2.07	0.09	0.210	0.008	0.24	2410	154	1.065	2
YP6_32b	10.17	0.56	0.379	0.023	0.50	2.64	0.12	0.189	0.009	0.35	1924	118	0.987	2
YP6_33b	12.02	0.52	0.439	0.023	0.81	2.28	0.07	0.195	0.004	0.20	2228	119	1.065	2

Continued on next page

Continued from previous page

Grain	$^{207}Pb/^{235}U$	2σ	$^{206}Pb/^{238}U$	2σ	ρ	$^{238}U/^{206}Pb$	2σ	$^{207}Pb/^{206}Pb$	2σ	ρ	^{207}Pb corr. Age (Ma)	2σ	$(^{207}Pb/^{206}Pb)_o$	E_M
YP6_34b	6.25	0.23	0.323	0.017	0.49	3.10	0.10	0.140	0.003	0.33	1745	90	0.987	2
YP6_35b	11.07	0.51	0.449	0.027	0.84	2.23	0.10	0.176	0.003	0.45	2331	145	1.065	2
YP6_36b	12.37	0.81	0.361	0.023	0.63	2.77	0.12	0.234	0.010	0.28	1734	113	0.987	2
YP6_37b	8.90	0.46	0.419	0.024	0.86	2.39	0.09	0.151	0.004	-0.29	2234	130	1.065	2
YP6_38b	89	12	1.060	0.150	0.70	0.94	0.15	0.616	0.049	0.29	2826	671	1.065	2
YP6_39b	8.3	1.1	0.312	0.032	0.43	3.21	0.32	0.202	0.025	0.24	1567	164	0.987	2
YP6_40b	24.5	1.3	0.524	0.037	0.59	1.91	0.11	0.331	0.015	0.41	2244	175	1.065	2
YP8_1a	20.5	1.6	0.269	0.021	0.61	3.72	0.29	0.491	0.034	0.52				
YP8_2a	8.13	0.76	0.179	0.011	0.38	5.59	0.34	0.295	0.024	0.31				
YP8_3a	10.58	0.45	0.332	0.020	0.39	3.01	0.18	0.207	0.010	0.73	1650	101	0.966	1
YP8_4a	10.31	0.52	0.324	0.019	0.73	3.09	0.18	0.204	0.010	0.28	1616	96	0.966	1
YP8_5a	14.10	0.85	0.371	0.021	0.39	2.70	0.15	0.238	0.011	0.56	1764	105	0.966	1
YP8_6a	19.0	1.4	0.243	0.022	0.48	4.12	0.37	0.509	0.039	0.67				
YP8_7a	8.3	0.4	0.302	0.017	0.68	3.31	0.19	0.170	0.007	0.58				
YP8_9a	11.19	0.73	0.185	0.009	0.42	5.42	0.28	0.374	0.024	0.34				
YP8_10a	9.41	0.51	0.316	0.015	0.18	3.16	0.15	0.189	0.009	0.42	1608	78	0.966	1
YP8_11a	16.50	0.67	0.430	0.021	0.65	2.33	0.11	0.236	0.009	0.54	2079	106	1.065	2
YP8_12a	20.3	1.9	0.244	0.017	0.18	4.10	0.29	0.531	0.058	0.61				
YP8_13a	11.96	0.56	0.449	0.021	0.79	2.23	0.10	0.185	0.005	0.31				
YP8_14a	7.22	0.32	0.342	0.014	0.60	2.92	0.12	0.148	0.005	0.35	1826	75	0.966	1
YP8_15a	28.8	1.3	0.544	0.026	0.37	1.84	0.09	0.371	0.021	0.70	2202	141	1.065	2
YP8_16a	12.59	0.67	0.378	0.015	0.58	2.65	0.10	0.232	0.010	0.21	1811	80	0.966	1
YP8_17a	12.7	0.5	0.452	0.022	0.62	2.21	0.11	0.201	0.008	0.57	2279	116	1.065	2
YP8_18a	8.34	0.56	0.339	0.017	0.57	2.95	0.15	0.179	0.008	0.29	1744	89	0.966	1
YP8_19a	23.1	1.3	0.308	0.027	0.28	3.25	0.28	0.555	0.048	0.84				
YP8_21a	13.49	0.64	0.448	0.022	0.70	2.23	0.11	0.216	0.008	0.41	2220	114	1.065	2
YP8_22a	9.89	0.68	0.346	0.018	0.53	2.89	0.15	0.208	0.011	0.41	1714	93	0.966	1
YP8_23a	12.00	0.75	0.409	0.024	0.57	2.44	0.14	0.213	0.010	0.54	2033	121	1.065	2
YP8_24a	44.9	2.8	0.732	0.041	0.40	1.37	0.08	0.438	0.025	0.37	2709	241	1.065	2

Continued on next page

Continued from previous page

Grain	$^{207}Pb/^{235}U$	2σ	$^{206}Pb/^{238}U$	2σ	ρ	$^{238}U/^{206}Pb$	2σ	$^{207}Pb/^{206}Pb$	2σ	ρ	^{207}Pb corr. Age (Ma)	2σ	$(^{207}Pb/^{206}Pb)_o$	E_M
YP8_25a	17.10	0.76	0.472	0.028	0.58	2.12	0.13	0.255	0.013	0.61	2231	142	1.065	2
YP8_26a	14.87	0.86	0.437	0.023	0.61	2.29	0.12	0.231	0.012	0.53	2126	118	1.065	2
YP8_27a	26.7	1.7	0.355	0.026	0.49	2.82	0.21	0.523	0.038	0.64				
YP8_28a	13.1	0.9	0.398	0.023	0.59	2.51	0.15	0.228	0.010	0.32	1945	114	1.065	2
YP8_29a	29.1	1.7	0.502	0.036	0.23	1.99	0.14	0.410	0.030	0.69	1822	184	0.966	1
YP8_30a	17.92	0.85	0.387	0.016	0.65	2.58	0.11	0.314	0.013	0.28	1651	88	0.966	1
YP8_31a	12.00	1.40	0.370	0.025	0.55	2.70	0.18	0.232	0.026	-0.17	1774	135	0.966	1
YP8_32a	6.79	0.36	0.293	0.013	0.57	3.41	0.15	0.158	0.005	0.39				
YP8_33a	6.21	0.23	0.283	0.008	0.48	3.54	0.10	0.146	0.005	0.29	1520	44	0.966	1
YP8_34a	12.53	0.92	0.338	0.023	0.42	2.96	0.20	0.256	0.019	0.44	1572	116	0.966	1
YP8_1b	21.3	1.4	0.296	0.021	0.32	3.38	0.18	0.501	0.028	0.34				
YP8_2b	29.6	2.2	0.358	0.031	0.74	2.79	0.23	0.572	0.031	0.41	854	160	0.902	1
YP8_3b	22.4	1.4	0.297	0.022	0.65	3.37	0.19	0.521	0.027	0.34				
YP8_4b	8.20	0.58	0.188	0.012	0.53	5.31	0.23	0.317	0.020	0.22				
YP8_5b	10.4	0.6	0.218	0.014	0.53	4.59	0.24	0.334	0.015	0.25	893	71	0.902	1
YP8_6b	21.6	1.3	0.298	0.020	0.40	3.36	0.18	0.521	0.031	0.43	821	124	0.902	1
YP8_7b	20.5	1.2	0.308	0.023	0.57	3.25	0.19	0.489	0.027	0.39	917	123	0.902	1
YP8_8b	27.0	2.4	0.319	0.026	0.69	3.13	0.23	0.589	0.036	0.17	725	150	0.902	1
YP8_9b	37.2	2.6	0.414	0.032	0.66	2.42	0.16	0.655	0.038	0.27				
YP8_10b	23.9	2.0	0.304	0.024	0.53	3.29	0.25	0.539	0.035	0.42				
YP8_11b	20.0	1.4	0.274	0.018	0.63	3.65	0.22	0.525	0.027	0.11	750	110	0.902	1
YP8_12b	14.33	0.97	0.238	0.017	0.46	4.20	0.22	0.439	0.028	0.24				
YP8_13b	11.34	0.82	0.216	0.014	0.48	4.63	0.22	0.374	0.022	0.29	825	76	0.902	1
YP8_14b	6.80	0.28	0.318	0.017	0.72	3.15	0.10	0.150	0.003	0.18				
YP8_15b	7.63	0.48	0.323	0.021	0.78	3.10	0.15	0.167	0.005	-0.01	1688	108	0.966	1
YP8_16b	19.71	0.81	0.510	0.030	0.64	1.96	0.08	0.271	0.010	0.33				
YP8_17b	16.10	1.70	0.474	0.040	0.88	2.11	0.17	0.245	0.016	-0.30				
YP8_18b	15.47	0.67	0.430	0.024	0.34	2.33	0.08	0.251	0.010	0.45	2042	118	1.065	2
YP8_19b	6.31	0.30	0.313	0.016	0.72	3.20	0.09	0.142	0.004	0.19				
YP8_20b	7.30	0.38	0.327	0.017	0.63	3.06	0.09	0.153	0.005	-0.13	1734	89	0.966	1

Continued on next page

Continued from previous page

Grain	$^{207}Pb/^{235}U$	2σ	$^{206}Pb/^{238}U$	2σ	ρ	$^{238}U/^{206}Pb$	2σ	$^{207}Pb/^{206}Pb$	2σ	ρ	^{207}Pb corr. Age (Ma)	2σ	$(^{207}Pb/^{206}Pb)_o$	E_M
YP8_21b	13.16	0.76	0.469	0.026	0.86	2.13	0.07	0.197	0.006	-0.47	2379	139	1.065	2
YP8_22b	14.1	1.6	0.238	0.020	0.78	4.20	0.32	0.417	0.025	-0.21				
YP8_23b	60.3	5.3	0.605	0.048	0.78	1.65	0.12	0.721	0.037	0.07				
YP8_24b	61.6	5.1	0.601	0.055	0.74	1.66	0.14	0.739	0.038	0.44				
YP8_25b	21.9	1.4	0.305	0.020	0.56	3.28	0.16	0.522	0.027	0.26	838	122	0.902	1
YP8_26b	18.5	1.1	0.494	0.030	0.58	2.02	0.08	0.261	0.011	0.04				
YP8_27b	17.62	0.83	0.437	0.023	0.60	2.29	0.07	0.281	0.009	0.08	1999	111	1.065	2
YP8_28b	14.26	0.68	0.375	0.021	0.58	2.67	0.09	0.268	0.010	0.20				
YP8_29b	12.86	0.51	0.369	0.019	0.52	2.71	0.08	0.245	0.007	0.24				
YP8_30b	15.55	0.70	0.444	0.027	0.79	2.25	0.10	0.243	0.007	0.23				
YP8_31b	12.07	0.50	0.357	0.019	0.45	2.80	0.07	0.231	0.009	0.14				
YP8_36b	8.60	0.54	0.330	0.018	0.62	3.03	0.09	0.179	0.008	-0.16	1697	93	0.966	1
YP8_37b	10.77	0.85	0.364	0.021	0.80	2.75	0.10	0.203	0.009	-0.45	1813	107	0.966	1
YP8_38b	10.48	0.49	0.377	0.023	0.66	2.65	0.11	0.198	0.009	0.21	1890	118	0.966	1
YP8_39b	37.6	2.9	0.562	0.046	0.71	1.78	0.12	0.485	0.025	0.20	1766	210	0.966	1
YP8_40b	22.5	1.3	0.447	0.035	0.67	2.24	0.13	0.354	0.016	0.70	1786	159	0.966	1
YP8_41b	8.70	0.40	0.337	0.019	0.72	2.97	0.11	0.182	0.005	0.24	1726	97	0.966	1
YP8_42b	7.41	0.28	0.338	0.017	0.54	2.96	0.08	0.160	0.004	0.19	1780	89	0.966	1
YP8_43b	9.88	0.37	0.358	0.019	0.68	2.79	0.09	0.200	0.006	0.04	1791	96	0.966	1
YP8_44b	6.48	0.26	0.321	0.018	0.70	3.12	0.11	0.144	0.003	0.38	1724	95	0.966	1
YP8_45b	9.21	0.40	0.379	0.020	0.71	2.64	0.08	0.171	0.004	0.17	1978	103	1.065	2
YP8_46b	8.22	0.41	0.357	0.018	0.62	2.80	0.08	0.164	0.004	0.06	1866	94	0.966	1
YP8_47b	77.7	6.8	0.881	0.088	0.81	1.14	0.10	0.649	0.034	0.40	1823	387	0.966	1
YP8_48b	12.49	0.49	0.461	0.024	0.68	2.17	0.06	0.194	0.005	0.20	2346	127	1.065	2
YP8_49b	16.66	0.79	0.408	0.024	0.53	2.45	0.10	0.289	0.011	0.41				
YP8_50b	26.3	1.6	0.459	0.032	0.78	2.18	0.11	0.397	0.012	0.24				
YP8_51b	23.0	1.2	0.444	0.028	0.50	2.25	0.10	0.370	0.017	0.36	1729	136	0.966	1
YP15_1a	34.9	4.4	0.378	0.036	0.73	2.65	0.25	0.59	0.067	-0.16				
YP15_3a	38.6	4.7	0.424	0.044	0.36	2.36	0.24	0.628	0.066	0.54				

Continued on next page

Continued from previous page

Grain	$^{207}Pb/^{235}U$	2σ	$^{206}Pb/^{238}U$	2σ	ρ	$^{238}U/^{206}Pb$	2σ	$^{207}Pb/^{206}Pb$	2σ	ρ	^{207}Pb corr. Age (Ma)	2σ	$(^{207}Pb/^{206}Pb)_o$	E_M
YP15_5a	17.04	0.86	0.213	0.012	0.29	4.69	0.26	0.525	0.026	0.09	569	87	0.881	1
YP15_6a	45.4	2.3	0.457	0.029	0.25	2.19	0.14	0.667	0.037	0.73				
YP15_7a	32.5	2.5	0.333	0.027	0.57	3.00	0.24	0.627	0.042	0.46				
YP15_8a	26.2	1.8	0.375	0.031	0.36	2.67	0.22	0.464	0.034	0.62				
YP15_9a	10.57	0.55	0.168	0.011	0.57	5.95	0.39	0.405	0.026	0.72	599	65	0.881	1
YP15_10a	30.2	2.3	0.343	0.02	0.52	2.92	0.17	0.594	0.02	0.40	733	144	0.881	1
YP15_11a	36.6	2.9	0.388	0.024	0.38	2.58	0.16	0.642	0.033	0.68				
YP15_12a	40	2.7	0.416	0.029	0.54	2.40	0.17	0.663	0.023	0.15				
YP15_13a	8.51	0.69	0.356	0.02	0.44	2.81	0.16	0.1631	0.0089	0.34	1870	105	1.010	1
YP15_14a	15.1	2.6	0.223	0.041	0.26	4.48	0.82	0.53	0.13	0.63				
YP15_15a	21.5	4.2	0.393	0.05	0.64	2.54	0.32	0.38	0.064	-0.13				
YP15_17a	71.7	4.3	0.672	0.047	0.52	1.49	0.10	0.701	0.046	0.75				
YP15_18a	19.7	1	0.398	0.019	0.45	2.51	0.12	0.327	0.014	0.66	1691	97	1.010	1
YP15_19a	28.5	1.7	0.339	0.028	0.37	2.95	0.24	0.574	0.052	0.70	774	187	0.881	1
YP15_20a	30.6	2.6	0.331	0.027	0.52	3.02	0.25	0.648	0.049	0.46				
YP15_22a	7.38	0.48	0.1601	0.0087	0.08	6.25	0.34	0.32	0.015	0.51	671	49	0.881	1
YP15_23a	22.9	2.2	0.285	0.027	-0.06	3.51	0.33	0.584	0.064	0.68				
YP15_24a	40	12	0.4	0.1	0.87	2.50	0.63	0.635	0.069	-0.47				
YP15_25a	18	1.1	0.23	0.013	0.41	4.35	0.25	0.522	0.031	0.41	618	98	0.881	1
YP15_26a	13.1	1.4	0.366	0.024	0.43	2.73	0.18	0.251	0.019	-0.24	1727	121	1.010	1
YP15_27a	11.75	0.63	0.2201	0.0096	0.31	4.54	0.20	0.36	0.014	0.67	850	62	0.881	1
YP15_28a	4.58	0.32	0.1418	0.0088	0.31	7.05	0.44	0.221	0.015	0.35	698	48	0.881	1
YP15_29a	13.9	1.3	0.245	0.023	0.41	4.08	0.38	0.408	0.036	0.39	859	116	0.881	1
YP15_30a	7.13	0.51	0.167	0.012	0.21	5.99	0.43	0.298	0.026	0.72	725	66	0.881	1
YP15_31a	13.61	0.89	0.368	0.021	0.24	2.72	0.16	0.254	0.016	0.50	1729	106	1.010	1
YP15_32a	18.9	1.1	0.253	0.011	0.02	3.95	0.17	0.515	0.028	0.39	691	100	0.881	1
YP15_33a	5.02	0.43	0.168	0.011	-0.10	5.95	0.39	0.213	0.02	0.06	832	61	0.881	1
YP15_34a	26.1	2	0.312	0.017	0.46	3.21	0.17	0.6	0.026	0.45	655	137	0.881	1
YP15_35a	17	1.2	0.269	0.015	0.03	3.72	0.21	0.445	0.026	0.45	869	99	0.881	1
YP15_37a	5.09	0.51	0.1222	0.009	0.72	8.18	0.60	0.273	0.02	-0.17	558	48	0.881	1

Continued on next page

Continued from previous page

Grain	$^{207}Pb/^{235}U$	2σ	$^{206}Pb/^{238}U$	2σ	ρ	$^{238}U/^{206}Pb$	2σ	$^{207}Pb/^{206}Pb$	2σ	ρ	^{207}Pb corr. Age (Ma)	2σ	$(^{207}Pb/^{206}Pb)_o$	E_M
YP15_39a	19.2	6.4	0.212	0.041	0.91	4.72	0.91	0.537	0.091	-0.52				
YP15_40a	52.4	2.3	0.493	0.023	0.69	2.03	0.09	0.704	0.021	0.45				
YP15_2b	22	1.6	0.307	0.023	0.36	3.26	0.24	0.513	0.034	0.30	838	136	0.881	1
YP15_3b	8.3	0.47	0.1764	0.013	0.38	5.67	0.42	0.337	0.018	0.37	715	66	0.881	1
YP15_4b	8.13	0.52	0.1758	0.013	0.63	5.69	0.42	0.32	0.017	0.20	734	65	0.881	1
YP15_5b	3.69	0.36	0.167	0.013	0.43	5.99	0.47	0.161	0.012	0.18	890	69	0.881	1
YP15_7b	11.73	0.73	0.381	0.027	0.80	2.62	0.19	0.208	0.007	-0.08	1895	134	1.010	1
YP15_8b	31.9	2.7	0.389	0.033	0.78	2.57	0.22	0.577	0.034	0.09	876	183	0.881	1
YP15_9b	8.5	0.66	0.1678	0.013	0.07	5.96	0.46	0.343	0.026	0.52	674	68	0.881	1
YP15_10b	40.9	1.9	0.431	0.029	0.60	2.32	0.16	0.664	0.028	0.48				
YP15_11b	16.7	1	0.427	0.031	0.46	2.34	0.17	0.275	0.015	0.45	1946	149	1.010	1
YP15_12b	26.6	1.5	0.48	0.036	0.61	2.08	0.16	0.384	0.019	0.37	1864	164	1.010	1
YP15_13b	14.11	0.86	0.26	0.02	0.56	3.85	0.30	0.374	0.02	0.35	973	98	0.881	1
YP15_15b	28.1	1.8	0.344	0.029	0.44	2.91	0.25	0.568	0.037	0.49	800	166	0.881	1
YP15_17b	36.4	4.9	0.421	0.049	0.91	2.38	0.28	0.614	0.034	-0.35				
YP15_18b	8.46	0.36	0.35	0.022	0.46	2.86	0.18	0.1683	0.0079	0.39	1829	114	1.010	1
YP15_19b	28.8	1.6	0.335	0.025	0.75	2.99	0.22	0.595	0.025	0.40	714	149	0.881	1
YP15_20b	18.1	1.3	0.451	0.031	0.44	2.22	0.15	0.286	0.018	0.31	2024	153	1.010	1
YP15_21b	105	12	1.0	0.1	0.76	1.03	0.11	0.76	0.062	0.32				
YP15_22b	7.9	0.36	0.343	0.021	0.59	2.92	0.18	0.1622	0.0055	0.05	1806	109	1.010	1
YP15_23b	4.01	0.24	0.1378	0.0091	0.47	7.26	0.48	0.2077	0.0095	0.24	692	48	0.881	1
YP15_25b	46	3.8	0.476	0.041	0.89	2.10	0.18	0.662	0.028	-0.03				
YP15_27b	21.8	2.6	0.301	0.034	0.66	3.32	0.38	0.51	0.048	0.13	828	167	0.881	1
YP15_28b	21.1	2.2	0.293	0.033	0.39	3.41	0.38	0.523	0.053	0.40	780	169	0.881	1
YP15_29b	3.76	0.29	0.1355	0.011	0.43	7.38	0.60	0.201	0.013	0.40	688	57	0.881	1
YP15_30b	10.02	0.45	0.362	0.023	0.56	2.76	0.18	0.191	0.0068	0.24	1840	116	1.010	1
YP15_31b	23.6	2.2	0.299	0.027	0.64	3.34	0.30	0.574	0.034	0.14	685	144	0.881	1
YP15_32b	3.95	0.22	0.1356	0.009	0.41	7.37	0.49	0.2066	0.0085	0.46	683	47	0.881	1
YP15_33b	6.79	0.94	0.167	0.015	0.28	5.99	0.54	0.286	0.037	0.22	740	83	0.881	1
YP15_34b	10.03	0.6	0.1781	0.012	0.28	5.61	0.38	0.404	0.023	0.54	635	67	0.881	1

Continued on next page

Continued from previous page

Grain	$^{207}Pb/^{235}U$	2σ	$^{206}Pb/^{238}U$	2σ	ρ	$^{238}U/^{206}Pb$	2σ	$^{207}Pb/^{206}Pb$	2σ	ρ	^{207}Pb corr. Age (Ma)	2σ	$(^{207}Pb/^{206}Pb)_o$	E_M
YP15_36b	17.8	1.9	0.252	0.023	0.38	3.97	0.36	0.496	0.045	0.34	723	129	0.881	1
YP15_37b	11.84	0.81	0.208	0.015	0.64	4.81	0.35	0.413	0.02	0.14	725	78	0.881	1
YP15_38b	23.4	1.8	0.308	0.03	0.68	3.25	0.32	0.534	0.039	0.54	794	153	0.881	1
YP15_39b	25.5	2.1	0.466	0.038	0.80	2.15	0.17	0.372	0.019	-0.17	1845	170	1.010	1
YP15_40b	60.1	9.9	0.575	0.07	0.80	1.74	0.21	0.697	0.075	0.19				
YP21_01c	5.13	0.45	0.216	0.012	0.25	4.63	0.26	0.170	0.015	0.30	1131	66	0.955	1
YP21_02c	13.4	0.8	0.228	0.013	0.68	4.39	0.25	0.424	0.020	0.16	789	77	0.902	1
YP21_03c	8.97	0.42	0.340	0.013	0.61	2.94	0.11	0.187	0.007	-0.01	1728	69	0.955	1
YP21_04c	10.7	1.1	0.330	0.024	0.55	3.03	0.22	0.235	0.022	0.32	1577	124	0.955	1
YP21_05c	4.19	0.38	0.150	0.012	0.43	6.67	0.53	0.213	0.023	0.12	750	65	0.902	1
YP21_06c	16.29	0.89	0.268	0.013	0.77	3.73	0.18	0.434	0.016	0.03	904	83	0.902	1
YP21_07c	4.68	0.22	0.1681	0.0070	0.68	5.95	0.25	0.196	0.007	0.09	857	38	0.902	1
YP21_08c	17.15	0.75	0.516	0.022	0.52	1.94	0.08	0.236	0.008	0.20	2507	118	1.064	2
YP21_09c	124	13	1.060	0.120	0.74	0.94	0.11	0.822	0.052	0.27				
YP21_10c	26.2	2.2	0.469	0.025	0.17	2.13	0.11	0.395	0.031	0.32	1738	155	0.955	1
YP21_11c	9.22	0.65	0.204	0.011	0.81	4.90	0.26	0.323	0.015	-0.17	853	60	0.902	1
YP21_13c	28.6	1.4	0.484	0.029	0.72	2.07	0.12	0.426	0.016	0.31	1695	146	0.955	1
YP21_14c	10.00	0.82	0.338	0.019	0.76	2.96	0.17	0.211	0.013	-0.24	1666	98	0.955	1
YP21_15c	329	41	2.87	0.41	0.91	0.35	0.05	0.848	0.045	0.35				
YP21_16c	38.5	3.2	0.680	0.054	0.79	1.47	0.12	0.413	0.026	0.25	2605	262	1.064	2
YP21_17c	22.0	1.4	0.462	0.030	-0.12	2.16	0.14	0.343	0.018	0.13	1869	147	0.955	1
YP21_18c	39.3	2.5	0.655	0.033	0.37	1.53	0.08	0.426	0.025	0.07	2448	175	1.064	2
YP21_1a	26.7	0.9	0.471	0.013	0.49	2.12	0.06	0.407	0.013	0.32				
YP21_2a	4.1	0.1	0.1617	0.0054	0.86	6.18	0.21	0.180	0.004	0.16	843	30	0.902	1
YP21_3a	13.02	0.25	0.4560	0.0078	0.65	2.19	0.04	0.206	0.003	0.20				
YP21_4a	30.1	2.0	0.372	0.020	0.73	2.69	0.14	0.582	0.029	0.09				
YP21_5a	8.3	0.8	0.1922	0.0093	0.83	5.20	0.25	0.306	0.020	-0.57				
YP21_6a	26.19	0.67	0.484	0.015	0.68	2.07	0.06	0.392	0.012	0.62	1802	107	0.955	1
YP21_7a	11.12	0.25	0.3571	0.0081	0.70	2.80	0.06	0.224	0.004	0.43	1729	47	0.955	1

Continued on next page

Continued from previous page

Grain	$^{207}Pb/^{235}U$	2σ	$^{206}Pb/^{238}U$	2σ	ρ	$^{238}U/^{206}Pb$	2σ	$^{207}Pb/^{206}Pb$	2σ	ρ	^{207}Pb corr. Age (Ma)	2σ	$(^{207}Pb/^{206}Pb)_o$	E_M
YP21_8a	9.1	0.5	0.2005	0.0063	0.49	4.99	0.16	0.325	0.016	0.09	836	48	0.902	1
YP21_9a	5.67	0.21	0.169	0.005	0.55	5.93	0.17	0.241	0.007	0.21				
YP21_10a	19.82	0.65	0.433	0.018	0.70	2.31	0.10	0.330	0.009	0.63				
YP21_11a	15.57	0.61	0.390	0.011	0.11	2.56	0.07	0.291	0.011	0.56				
YP21_12a	51.4	1.9	0.648	0.026	0.34	1.54	0.06	0.580	0.029	0.65	1611	232	0.955	1
YP21_13a	9.35	0.27	0.356	0.008	0.67	2.81	0.06	0.190	0.005	0.13				
YP21_14a	32.4	1.2	0.625	0.018	0.53	1.60	0.05	0.376	0.012	0.32	2524	102	1.064	2
YP21_15a	18.9	1.7	0.417	0.026	0.86	2.40	0.15	0.333	0.019	-0.41				
YP21_16a	2.91	0.07	0.1515	0.0048	0.26	6.60	0.21	0.139	0.005	0.72	836	27	0.902	1
YP21_17a	9.50	0.54	0.314	0.013	0.23	3.18	0.13	0.219	0.013	0.52				
YP21_1b	10.09	0.65	0.378	0.014	0.70	2.65	0.11	0.186	0.009	-0.03	1922	76	0.955	1
YP21_2b	32.0	2.2	0.350	0.022	0.75	2.86	0.17	0.657	0.029	0.15				
YP21_3b	10.49	0.48	0.367	0.013	0.51	2.72	0.10	0.202	0.009	0.23	1827	70	0.955	1
YP21_6b	1200	320	10.0	1.9	0.94	0.10	0.02	0.916	0.095	-0.53				
YP21_7b	18.7	1.6	0.428	0.019	0.76	2.34	0.10	0.305	0.017	-0.15	1839	106	0.955	1
YP21_8b	7.65	0.99	0.181	0.020	0.36	5.52	0.64	0.311	0.039	0.44	775	101	0.902	1
YP21_9b	8.55	0.38	0.396	0.013	0.59	2.53	0.08	0.155	0.005	-0.10	2102	70	1.064	2
YP21_10b	14.1	1.1	0.229	0.014	0.76	4.37	0.25	0.418	0.019	0.07	802	78	0.902	1
YP21_11b	14.40	0.88	0.400	0.019	0.37	2.50	0.12	0.262	0.013	0.25	1833	99	0.955	1
YP21_12b	85.0	12.0	0.9	0.1	0.91	1.08	0.14	0.648	0.046	-0.25	1887	463	0.955	1
YP21_13b	111	11	1.121	0.094	0.70	0.89	0.09	0.720	0.046	0.24				
YP21_14b	7.6	1.5	0.186	0.017	0.90	5.38	0.64	0.262	0.035	-0.70	860	92	0.902	1
YP21_15b	11.91	0.61	0.229	0.010	0.70	4.37	0.19	0.374	0.013	0.03	873	63	0.902	1
YP21_16b	12.01	0.61	0.2229	0.0088	0.52	4.49	0.17	0.385	0.016	0.38				
YP21_17b	10.59	0.51	0.2227	0.0066	0.60	4.49	0.14	0.345	0.013	0.39	895	52	0.902	1
YP21_19b	18.97	0.71	0.305	0.015	-0.06	3.28	0.17	0.452	0.023	0.80	987	103	0.902	1
YP21_21b	40.9	2.6	0.589	0.034	0.65	1.70	0.10	0.506	0.025	0.31	1750	199	0.955	1
YP21_22b	13.47	0.48	0.468	0.014	0.54	2.14	0.06	0.203	0.005	0.28	2357	75	1.064	2
YP21_23b	31.0	3.1	0.385	0.039	0.72	2.60	0.28	0.607	0.053	0.00				
YP21_24b	8.79	0.83	0.208	0.011	0.83	4.81	0.29	0.297	0.016	-0.43	907	61	0.902	1

Continued on next page

Continued from previous page

Grain	$^{207}Pb/^{235}U$	2σ	$^{206}Pb/^{238}U$	2σ	ρ	$^{238}U/^{206}Pb$	2σ	$^{207}Pb/^{206}Pb$	2σ	ρ	^{207}Pb corr. Age (Ma)	2σ	$(^{207}Pb/^{206}Pb)_o$	E_M
YP21_25b	22.8	1.6	0.470	0.019	0.59	2.13	0.09	0.347	0.018	-0.03	1889	116	0.955	1
YP21_26b	17.97	0.95	0.425	0.016	0.40	2.35	0.09	0.307	0.016	0.26	1821	96	0.955	1
YP21_27b	10.56	0.68	0.367	0.016	0.80	2.72	0.13	0.204	0.007	-0.16	1824	83	0.955	1
YP21_28b	12.37	0.62	0.353	0.014	0.56	2.83	0.11	0.255	0.013	0.16	1638	77	0.955	1
YP21_29b	16.7	1.5	0.382	0.017	0.48	2.62	0.11	0.324	0.026	-0.05	1599	107	0.955	1
YP21_30b	6.80	0.34	0.174	0.005	0.34	5.74	0.18	0.281	0.014	0.27	784	38	0.902	1
YP23_1a	8.23	0.72	0.170	0.010	0.15	5.88	0.34	0.290	0.023	0.41	752	57	0.894	1
YP23_2a	7.03	0.54	0.154	0.008	0.30	6.49	0.32	0.336	0.020	0.44	634	48	0.894	1
YP23_3a	14.66	0.76	0.252	0.015	0.06	3.97	0.24	0.454	0.026	0.55	810	94	0.894	1
YP23_4a	24.7	1.6	0.298	0.015	0.30	3.36	0.17	0.614	0.020	0.22	615	125	0.894	1
YP23_5a	93.6	8.4	0.791	0.068	0.11	1.26	0.11	0.840	0.100	0.73				
YP23_6a	6.20	0.50	0.163	0.011	0.55	6.13	0.41	0.248	0.018	0.24	771	58	0.894	1
YP23_8a	5.62	0.47	0.158	0.011	0.44	6.33	0.44	0.242	0.012	0.37	755	56	0.894	1
YP23_9a	61.60	3.70	0.576	0.055	0.69	1.74	0.17	0.721	0.041	0.61				
YP23_10a	25.8	2.1	0.400	0.027	0.24	2.50	0.17	0.478	0.030	0.53	1199	158	0.894	1
YP23_14a	3.37	0.62	0.141	0.010	-0.02	7.09	0.50	0.163	0.031	0.27	755	61	0.894	1
YP23_15a	16.78	0.91	0.229	0.015	0.13	4.37	0.29	0.526	0.024	0.42	621	92	0.894	1
YP23_17a	8.9	1.1	0.163	0.017	0.74	6.13	0.64	0.402	0.035	0.06	592	82	0.894	1
YP23_18a	5.91	0.57	0.143	0.010	0.30	6.99	0.49	0.308	0.028	0.56	617	56	0.894	1
YP23_21a	51.1	4.8	0.509	0.041	0.70	1.96	0.16	0.760	0.033	0.24				
YP23_22a	19.5	2.0	0.269	0.016	0.59	3.72	0.22	0.505	0.019	0.42	766	99	0.894	1
YP23_23a	8.32	0.66	0.157	0.010	0.26	6.37	0.41	0.381	0.030	0.63	594	61	0.894	1
YP23_24a	45.6	3.8	0.454	0.023	0.75	2.20	0.11	0.716	0.021	0.65				
YP23_28a	13.74	0.87	0.217	0.012	0.22	4.61	0.25	0.431	0.028	0.63	736	80	0.894	1
YP23_30a	15.9	1.1	0.248	0.014	0.47	4.03	0.23	0.471	0.024	0.78	768	91	0.894	1
YP23_32a	17.1	1.6	0.245	0.020	0.47	4.08	0.33	0.522	0.047	0.48	670	125	0.894	1
YP23_33a	24.50	2.30	0.292	0.016	0.24	3.42	0.19	0.606	0.042	0.55	620	144	0.894	1
YP23_01b	15.5	1.2	0.255	0.020	0.46	3.92	0.31	0.439	0.028	0.22	847	104	0.894	1
YP23_02b	29.5	3.3	0.375	0.040	0.80	2.67	0.28	0.574	0.032	-0.26	875	179	0.894	1

Continued on next page

Continued from previous page

Grain	$^{207}Pb/^{235}U$	2σ	$^{206}Pb/^{238}U$	2σ	ρ	$^{238}U/^{206}Pb$	2σ	$^{207}Pb/^{206}Pb$	2σ	ρ	^{207}Pb corr. Age (Ma)	2σ	$(^{207}Pb/^{206}Pb)_o$	E_M
YP23_03b	7.25	0.49	0.188	0.014	0.64	5.32	0.40	0.280	0.013	0.25	842	69	0.894	1
YP23_04b	21.9	1.1	0.295	0.019	0.20	3.39	0.22	0.510	0.029	0.55	827	120	0.894	1
YP23_05b	3.00	0.20	0.140	0.009	0.51	7.13	0.46	0.154	0.007	0.10	760	49	0.894	1
YP23_07b	3.2	0.2	0.160	0.015	0.55	6.25	0.59	0.139	0.008	0.39	881	81	0.894	1
YP23_08b	5.18	0.54	0.178	0.016	0.58	5.62	0.50	0.203	0.018	0.25	896	83	0.894	1
YP23_09b	251	19	2.15	0.18	0.80	0.47	0.04	0.840	0.027	0.09				
YP23_10b	36.6	2.9	0.442	0.036	0.73	2.26	0.18	0.578	0.029	0.09	1013	194	0.894	1
YP23_11b	34.4	1.8	0.413	0.032	0.69	2.42	0.19	0.580	0.025	0.46	943	176	0.894	1
YP23_13b	2.16	0.12	0.127	0.008	0.75	7.87	0.51	0.116	0.004	-0.09	725	46	0.894	1
YP23_14b	18.1	1.0	0.220	0.015	0.55	4.55	0.31	0.573	0.027	0.36	523	96	0.894	1
YP23_15b	13.88	0.69	0.205	0.014	0.37	4.89	0.33	0.475	0.024	0.40	632	80	0.894	1
YP23_16b	52.7	3.7	0.515	0.041	0.58	1.94	0.15	0.738	0.037	0.24				
YP23_17b	17.56	0.88	0.253	0.016	0.54	3.95	0.25	0.504	0.016	0.22	724	93	0.894	1
YP23_19b	29.7	1.8	0.363	0.028	0.54	2.75	0.21	0.590	0.028	0.61	807	160	0.894	1
YP23_20b	24.5	1.6	0.319	0.023	0.72	3.13	0.23	0.534	0.024	0.12	838	129	0.894	1
YP23_21b	160	10	1.363	0.097	0.69	0.73	0.05	0.824	0.032	0.05				
YP23_22b	107	11	1.018	0.094	0.73	0.98	0.09	0.750	0.048	-0.10				
YP23_23b	2.87	0.41	0.139	0.015	0.81	7.19	0.78	0.142	0.011	-0.21	765	81	0.894	1
YP23_24b	8.58	0.41	0.189	0.012	0.50	5.30	0.34	0.328	0.009	0.27	781	60	0.894	1
YP23_25b	27.0	1.4	0.356	0.026	0.57	2.81	0.21	0.547	0.022	0.46	900	143	0.894	1
YP23_26b	11.6	1.2	0.190	0.016	0.90	5.26	0.44	0.468	0.035	-0.25	597	87	0.894	1
YP23_27b	9.58	0.55	0.202	0.016	0.52	4.95	0.39	0.336	0.021	0.45	823	79	0.894	1
YP23_28b	7.73	0.40	0.173	0.012	0.77	5.78	0.40	0.309	0.010	0.23	742	59	0.894	1
YP23_29b	16.47	0.87	0.221	0.015	0.66	4.53	0.31	0.517	0.020	0.21	613	86	0.894	1
YP23_30b	4.01	0.23	0.162	0.010	0.56	6.18	0.38	0.174	0.007	0.15	849	53	0.894	1
YP23_31b	5.86	0.28	0.148	0.009	0.29	6.76	0.42	0.284	0.012	0.54	663	48	0.894	1
YP23_32b	4.30	0.31	0.113	0.009	-0.16	8.88	0.68	0.267	0.021	0.39	523	46	0.894	1
YP23_33b	11.2	1.3	0.200	0.018	0.47	5.00	0.45	0.392	0.042	0.18	736	99	0.894	1
YP23_35b	14.89	0.57	0.220	0.015	0.57	4.55	0.31	0.478	0.020	0.55	673	83	0.894	1
YP23_36b	548	38	4.47	0.40	0.91	0.22	0.02	0.853	0.034	0.14				

Continued on next page

Continued from previous page

Grain	$^{207}Pb/^{235}U$	2σ	$^{206}Pb/^{238}U$	2σ	ρ	$^{238}U/^{206}Pb$	2σ	$^{207}Pb/^{206}Pb$	2σ	ρ	^{207}Pb corr. Age (Ma)	2σ	$(^{207}Pb/^{206}Pb)_o$	E_M
YP23_37b	28.1	2.1	0.326	0.025	0.77	3.07	0.24	0.587	0.024	-0.01	734	140	0.894	1
YP23_38b	19.6	1.9	0.279	0.024	0.61	3.58	0.31	0.488	0.037	0.20	827	128	0.894	1
YP23_39b	5.57	0.22	0.158	0.009	0.36	6.34	0.38	0.252	0.010	0.39	742	49	0.894	1
YP23_40b	18.65	0.94	0.267	0.018	0.46	3.75	0.25	0.493	0.020	0.28	783	101	0.894	1

G.2 Apatite trace element data

Table G.2: Apatite REE element individual spot data part 1. This data is split into three tables for space reasons. **This table** (part 1) contains half the REEs (La, Ce, Pr, Nd, Sm, Eu, and Gd), part 2 contains the other half of the REEs (Tb, Dy, Ho, Er, Tm, Yb, and Lu), and part 3 contains Mn, Sr, Y, Th, and U.

Grain	La (ppm)	La 2SE	Ce (ppm)	Ce 2SE	Pr (ppm)	Pr 2SE	Nd (ppm)	Nd 2SE	Sm (ppm)	Sm 2SE	Eu (ppm)	Eu 2SE	Gd (ppm)	Gd 2SE
YP1_1b	782	38	2870	150	484	25	2315	96	518	28	19.9	1.1	413	22
YP1_2b	141.5	6.7	584	33	100.3	4.6	618	26	208	11	16.21	0.87	298	15
YP1_3b	681	28	2690	170	455	26	2120	100	489	26	22	1.3	416	21
YP1_4b	943	44	3250	230	476	29	2290	110	494	28	20.8	1.7	397	25
YP1_5b	1143	57	4930	370	861	51	4270	230	998	53	45.2	2.8	853	51
YP1_6b	923	43	3810	240	656	43	3520	190	908	55	33	2.2	821	45
YP1_7b	1086	55	4550	320	685	35	3590	160	858	47	41.4	2.5	716	44
YP1_8b	1101	54	3540	190	503	28	2200	110	408	24	13.5	1.1	290	17
YP1_9b	617	29	2380	170	395	24	2070	120	474	38	26.1	1.6	420	26
YP1_10b	537	29	1970	140	302	18	1458	88	318	19	12.78	0.81	256	14
YP1_11b	373	21	1441	92	252	14	1197	67	252	14	9.1	0.75	197	13
YP1_12b	622	29	2500	140	447	22	2500	140	603	28	22.5	1.7	518	32

Continued on next page

Continued from previous page

Grain	La (ppm)	La 2SE	Ce (ppm)	Ce 2SE	Pr (ppm)	Pr 2SE	Nd (ppm)	Nd 2SE	Sm (ppm)	Sm 2SE	Eu (ppm)	Eu 2SE	Gd (ppm)	Gd 2SE
YP1_13b	810	48	3160	150	599	27	3230	150	847	43	42	3.4	765	39
YP1_14b	1545	81	4640	220	669	32	3120	150	596	35	21.1	1.6	455	24
YP1_15b	1173	86	5330	510	867	83	4420	240	1120	120	52.4	6.3	970	100
YP1_16b	1400	110	3740	240	501	40	2260	250	378	28	20.1	1.7	316	28
YP1_17b	868	44	3160	180	524	23	2620	140	577	32	17.02	0.94	475	23
YP1_18b	1165	74	3140	180	396	27	1680	100	306	18	17.7	1.7	256	19
YP1_19b	1278	80	5070	310	865	48	4550	280	1018	60	39.1	2.9	833	45
YP1_20b	1077	77	4450	400	752	59	4050	230	1048	67	50.3	4.7	930	68
YP1_21b	989	42	2820	130	377	21	1670	80	310	14	33.5	1.8	251	15
YP1_22b	487	49	1650	160	285	31	1380	110	336	25	27.5	2.6	362	29
YP1_23b	0.39	0.14	0.94	0.34	0.078	0.047	0.28	0.23	0.02	0.03	0.073	0.054	0.127	0.08
YP1_24b	10.82	0.66	36.2	2.2	6.85	0.49	41.4	3.1	21.1	1.8	2.37	0.28	32.8	2.7
YP1_25b	286	15	1158	63	216	18	1203	80	389	23	22.4	2.1	409	32
YP1_26b	1214	98	4870	440	741	63	3830	300	1022	73	50.2	4.3	972	71
YP1_27b	1453	76	3570	210	443	23	1952	98	371	22	17.7	1.2	298	18
YP1_28b	566	32	1960	110	318	19	1548	95	316	19	12.19	0.72	250	14
YP1_29b	13.1	1.1	43.9	3.4	8.53	0.83	58.5	4	29.1	2.9	3.48	0.48	51.2	5.4
YP1_30b	779	62	2820	220	429	32	2070	150	448	36	13.8	1.2	354	32
YP1_31b	800	39	2990	150	507	29	2660	120	799	43	53.1	2.7	846	38
YP1_32b	720	41	2650	140	433	31	2160	100	481	29	22.4	1.9	402	21
YP1_33b	649	28	2440	120	429	21	2450	140	659	39	28.1	2	598	36
YP1_34b	390	25	1305	93	210	12	1114	67	316	19	29.1	2.4	358	23
YP1_35b	9.66	0.69	31.4	1.8	5.37	0.45	37.8	2.3	15.5	1.5	5.05	0.51	25.8	1.9
YP1_36b	330	35	1460	190	267	31	1560	170	473	57	28.7	3.5	478	62
YP1_37b	654	45	2490	170	442	29	2480	180	757	61	37.7	2.7	774	66
YP1_38b	907	49	3550	250	545	33	2900	150	762	43	35.9	2.4	697	36
YP1_39b	164.4	9.4	627	33	119.9	6.6	784	47	337	18	41.1	2.4	566	31
YP1_40b	601	27	2240	100	386	20	2140	110	539	29	21.8	1.4	451	23
YP1_41b	10.3	0.66	43	3.1	9.68	0.57	71.6	3.9	34.8	2.1	3.98	0.41	53.7	3.2
YP1_42b	494	28	1790	110	297	21	1585	83	430	28	23.1	1.7	443	20
YP1_43b	135.9	9.2	626	49	126.2	8.9	799	54	350	21	25.7	1.9	548	31

Continued on next page

Continued from previous page

Grain	La (ppm)	La 2SE	Ce (ppm)	Ce 2SE	Pr (ppm)	Pr 2SE	Nd (ppm)	Nd 2SE	Sm (ppm)	Sm 2SE	Eu (ppm)	Eu 2SE	Gd (ppm)	Gd 2SE
YP1_44b	372	19	1844	90	349	21	2060	110	565	28	34.1	2.1	535	29
YP1_45b	608	47	2470	270	387	35	1980	170	439	38	19.4	1.9	364	25
YP1_46b	355	28	1720	130	398	39	2800	260	1209	98	86.7	6.3	1490	170
YP1_47b	633	35	2800	200	480	31	2550	150	630	44	22.1	1.4	497	28
YP1_48b	391	24	1595	79	281	14	1650	100	450	27	23.5	1.8	448	27
YP1_49b	683	35	2410	150	368	20	1822	95	394	21	20.1	1.5	309	17
YP1_50b	2310	110	8040	430	1154	55	5590	260	1181	62	40.1	2	952	53
YP1_51b	120.1	7.2	505	30	103	6.1	683	39	280	17	21.4	1.5	412	23
YP1_52b	289	32	910	100	146	15	793	83	247	28	21.1	2.5	298	31
YP1_53b	819	41	3710	210	590	27	3190	160	837	45	41.9	2.3	721	35
YP1_54b	1810	100	6850	440	1146	74	5800	360	1392	72	59.7	4.1	1208	69
YP1_55b	507	23	2510	140	505	23	3140	150	1071	49	32.9	1.9	1055	42
YP1_56b	774	36	2980	170	498	25	2660	130	701	36	34	2	631	37
YP1_57b	610	35	2430	160	408	25	2210	130	562	27	26.1	1.7	510	34
YP1_58b	946	42	3510	190	522	23	2700	150	571	26	20.9	1.4	444	22
YP1_59b	1140	77	4380	290	739	55	3640	280	889	67	41	3.4	747	58
YP1_60b	807	44	2980	180	502	26	2580	150	605	38	22.4	1.5	472	26
YP1_61b	797	55	2750	230	376	23	1880	110	366	23	12.86	0.97	305	16
YP1_62b	637	32	2130	150	301	19	1357	76	282	18	9.49	0.79	209	11
YP1_63b	796	38	2500	170	355	21	1627	82	314	18	8.92	0.7	236	12
YP1_64b	774	47	2620	200	368	23	1644	96	336	19	9.51	0.75	247	14
YP1_65b	1011	51	3490	290	500	31	2290	110	479	29	14.7	1.2	364	19
YP1_66b	910	58	3390	280	494	29	2290	140	501	30	16.3	1	404	29
YP1_67b	833	51	2890	190	428	27	2060	130	441	29	13.4	0.95	336	23
YP1_68b	837	34	2760	160	391	20	1839	88	367	17	9.87	0.85	276	13
YP1_69b	832	39	2730	150	406	26	1758	91	355	19	9.46	0.74	268	14
YP1_70b	756	33	2700	170	407	19	1964	84	442	21	15.6	1.2	360	18
YP1_71b	887	49	3550	220	579	33	2910	160	792	53	32.2	2.3	731	41
YP1_72b	821	39	2800	170	393	22	1784	99	365	19	10.54	0.66	281	16
YP1_73b	712	56	3140	270	592	48	3030	210	895	85	45.2	4.1	820	65
YP1_74b	588	27	2750	140	528	29	2960	140	937	50	53.5	3	964	45

Continued on next page

Continued from previous page

Grain	La (ppm)	La 2SE	Ce (ppm)	Ce 2SE	Pr (ppm)	Pr 2SE	Nd (ppm)	Nd 2SE	Sm (ppm)	Sm 2SE	Eu (ppm)	Eu 2SE	Gd (ppm)	Gd 2SE
YP1_75b	13.8	1.1	64.6	5.3	13.26	0.98	101.3	5.1	50.6	3.4	4.98	0.58	86	5.5
YP1_76b	13.7	1.9	60.4	6.7	11.81	0.82	81.8	6.9	41.7	3.5	3.95	0.41	58.2	4.9
YP1_77b	11.5	1.1	48.7	3.4	9.96	0.69	66.7	5.4	31.9	3.1	3.4	0.57	46.5	3.9
YP1_78b	14.6	1	56	3.6	12.12	0.94	92.1	6.6	49.8	4.2	5.03	0.5	82.1	6
YP1_79b	831	59	3720	350	705	70	3810	320	1121	88	60.3	5	1115	83
YP1_80b	790	58	3120	310	515	43	2540	200	621	46	22	1.4	526	41
YP4_1b	290	11	705	34	77.9	3.6	307	14	38.4	2.5	10.52	0.73	29.8	2.2
YP4_2b	303	14	737	34	83.2	4.8	305	17	39.9	2.6	11.7	0.81	30.8	2.5
YP4_3b	8.06	0.62	25.1	1.6	4.12	0.34	28.7	2.6	10.4	1.4	10.46	0.83	21.6	1.8
YP4_4b	477	20	1180	63	138.7	5.9	563	24	87.2	5.2	20.5	1.3	68.7	3.6
YP4_5b	422	19	1128	70	121.4	5.1	482	24	70.3	4	17.7	1.1	55.7	3
YP4_6b	1332	56	2960	170	370	17	1580	69	309	15	31.8	2.1	285	14
YP4_7b	300	17	718	46	75.8	4.6	272	20	36.7	2.9	12.2	1	29.4	2.5
YP4_8b	472	19	1142	59	123.6	6.3	464	21	61.8	3.2	18.1	1	50.2	2.3
YP4_9b	424	29	1009	66	113.7	7.3	419	28	53.1	4.5	18.9	1.3	45.7	3.3
YP4_10b	516	27	1287	66	138	6.1	513	27	74	4.2	22.1	1.3	55.7	3.9
YP4_11b	1490	68	3690	280	415	19	1815	78	349	17	38.6	2.2	327	16
YP4_12b	491	24	1172	63	136.8	7.7	536	29	75.1	5.8	19.4	1.4	60.1	4.6
YP4_13b	508	22	1219	64	140.1	6.6	555	28	86.6	5.2	18.89	0.98	65.6	3.8
YP4_14b	520	27	1317	69	159.6	9.8	649	35	98.7	6	21.6	1.6	78.8	5.4
YP4_15b	436	26	1064	64	126.3	7.1	484	25	72.8	4.3	17.6	1.1	58.7	3.8
YP4_16b	0.059	0.029	0.294	0.07	0.074	0.027	0.43	0.17	0.26	0.14	0.291	0.082	1.4	0.33
YP4_17b	NA	Below LOD	0.017	0.015	0.0017	0.0035	NA	Below LOD	NA	Below LOD	NA	Below LOD	NA	Below LOD
YP4_18b	0.2	0.059	0.78	0.11	0.103	0.033	0.79	0.25	0.55	0.21	0.353	0.095	1.53	0.33
YP4_19b	553	28	1377	78	170.3	8.6	660	36	107	7.3	23.3	1.4	81.2	5.1
YP4_20b	1514	75	3690	180	452	30	1940	110	371	21	41.3	2.8	348	20
YP4_21b	306	13	727	41	80.2	5.1	295	19	39.3	2.7	16.6	1	32.3	2.2
YP4_22b	431	21	1052	54	119.6	6.8	463	22	69	4.1	17.2	1.2	54.9	3.8
YP4_23b	459	21	1112	64	128.3	7.1	523	30	75.8	5.2	18.3	1.3	60.2	3.6

Continued on next page

Continued from previous page

Grain	La (ppm)	La 2SE	Ce (ppm)	Ce 2SE	Pr (ppm)	Pr 2SE	Nd (ppm)	Nd 2SE	Sm (ppm)	Sm 2SE	Eu (ppm)	Eu 2SE	Gd (ppm)	Gd 2SE
YP4_24b	555	24	1325	74	156.4	7.6	645	39	95.4	6.6	21.6	1.5	76.2	5.1
YP4_25b	559	22	1332	62	155.9	7.9	625	27	93.6	5.5	21.2	1.5	76.1	4
YP4_26b	359	19	837	63	92.5	7	328	18	43.9	3.3	18.8	1.5	33.1	3
YP4_27b	0.71	0.12	2.56	0.25	0.39	0.076	2.17	0.48	0.66	0.32	1.36	0.22	2.25	0.58
YP4_28b	0.99	0.17	3.03	0.4	0.58	0.16	3.38	0.54	2.96	0.75	3.13	0.44	10.7	1.5
YP4_29b	0.346	0.089	0.95	0.15	0.149	0.047	1.27	0.33	0.6	0.24	1.06	0.19	2.94	0.55
YP4_30b	442	23	1129	58	124.9	7.8	502	30	68.2	4.5	17.7	1.1	56.6	3.7
YP4_31b	421	23	982	52	111	5.8	426	23	60	3.9	15.9	1	48.6	3.6
YP4_32b	1000	63	2630	240	292	20	1138	62	184	11	40	2.1	146.1	7.5
YP4_33b	531	29	1263	70	158	11	614	46	92.1	6.4	21	1.5	73.4	5.9
YP4_34b	433	21	1019	56	108.3	5.6	395	17	50.4	3.2	16.9	1.2	40.4	2.8
YP4_35b	0.063	0.033	0.359	0.078	0.059	0.026	0.46	0.2	0.24	0.13	0.349	0.093	0.44	0.19
YP4_36b	1.07	0.15	3.34	0.45	0.57	0.1	2.96	0.59	1.23	0.32	1.79	0.23	2.32	0.43
YP4_37b	211	18	503	51	57.9	5.6	220	18	30.4	2.8	11.7	1.2	25.9	2.9
YP4_38b	410	20	911	39	103.2	5.5	379	14	52.2	2.8	18.5	1.1	44	2.6
YP4_39b	NA	Below LOD	0.069	0.039	NA	Below LOD	0.045	0.063	NA	Below LOD	0.0048	0.0098	0.24	0.15
YP4_40b	1019	41	2510	150	309	16	1199	44	184.2	8.1	52.2	2.1	133.7	6.2
YP8_1b	606	31	1458	74	155.7	7.3	617	26	88.9	4.7	24	1.5	72.6	3.8
YP8_2b	592	25	1472	63	173	11	704	31	106.4	5.7	25.2	1.7	83.2	4.7
YP8_3b	539	27	1266	70	139.5	9	582	34	78.1	5.1	21.3	1.2	62.1	4.1
YP8_4b	561	37	1263	74	131.2	9.6	477	33	60.6	4.4	23.3	1.8	48.5	4.4
YP8_5b	374	17	842	54	80.3	4	291	13	38.1	2.9	17.1	1.2	28.4	1.9
YP8_6b	508	22	1281	71	143.2	6.7	547	25	75.3	4.7	19.7	1.1	60.6	3.6
YP8_7b	580	26	1411	82	159.9	8.2	603	34	87.4	5.6	23.6	1.4	67	4.1
YP8_8b	282	16	631	35	69.2	4.3	258	17	32.8	2.3	11.78	0.94	27.9	2.3
YP8_9b	413	15	971	38	116.6	5.7	462	16	65.1	3.8	15.83	0.88	52.8	2.9
YP8_10b	453	30	1076	84	112.2	8	445	32	59.1	4.5	19.1	1.4	51	4.2
YP8_11b	421	42	1030	110	104	10	407	47	54.6	6.9	17.5	1.8	44.4	5.6
YP8_12b	504	22	1206	64	131.3	6	505	24	67.3	4.3	21.7	1.3	51.6	2.5

Continued on next page

Continued from previous page

Grain	La (ppm)	La 2SE	Ce (ppm)	Ce 2SE	Pr (ppm)	Pr 2SE	Nd (ppm)	Nd 2SE	Sm (ppm)	Sm 2SE	Eu (ppm)	Eu 2SE	Gd (ppm)	Gd 2SE
YP8_13b	479	25	1134	65	127.6	8.1	483	30	66.1	4.5	21.8	1.4	52.8	3.6
YP8_14b	837	51	2320	160	262	17	1029	65	170	11	36.5	2.5	150.2	9.8
YP8_15b	751	50	2020	160	216	12	877	59	128	10	29.5	2.6	108.9	8.2
YP8_16b	1211	55	1630	100	122	6.3	411	23	49.1	3	12.45	0.86	40.4	2.5
YP8_17b	1450	130	1870	180	149	16	493	56	63.2	7.2	15.3	1.6	46.6	5.4
YP8_18b	826	93	1200	140	93.2	8.8	327	27	50.3	6.9	12.7	1.8	44	8.4
YP8_19b	46.8	2.5	303	19	71.6	3.6	507	23	174.3	8.6	42	2	181.3	8.4
YP8_20b	31.6	1.6	215	14	49.8	2.1	374	17	132.1	6.9	33.5	1.7	139.9	6.9
YP8_21b	919	63	2930	240	417	33	1920	150	387	29	65.4	4.9	322	23
YP8_22b	479	27	1078	60	121.4	7.9	463	23	56.9	3.7	20.1	1.2	48.7	3.4
YP8_23b	219	11	490	22	55.1	3.1	201.5	9.8	26.2	1.8	8.59	0.53	20.4	1.8
YP8_24b	215	12	489	23	51.6	2.8	196	11	24.8	1.9	8.45	0.61	21.8	2
YP8_25b	492	19	1154	47	126.9	5.6	473	20	64.7	4.1	19.99	0.8	52	2.6
YP8_26b	254	13	1032	63	180.5	9.4	1021	56	379	21	13.4	1.1	456	26
YP8_27b	140.1	6.6	566	34	99	6.2	581	32	225	13	8.25	0.63	273	13
YP8_28b	72.3	4.1	322	18	61	3.2	401	20	170.8	8.5	7.22	0.46	245	13
YP8_29b	153.4	6.1	640	29	115	5.6	706	30	274	12	9.37	0.65	348	15
YP8_30b	226.5	9.6	911	34	156.7	5.6	931	35	356	16	11.6	0.73	419	17
YP8_31b	133.9	6.2	571	29	106.6	5.9	666	32	274	14	10.64	0.86	341	15
YP8_36b	362	30	807	73	88	6	449	36	92.4	7	53.1	3.5	106.7	9
YP8_37b	1270	140	1780	210	149	17	510	57	81.2	9.6	21.8	2.4	76.6	8.4
YP8_38b	1950	120	4440	260	548	38	2440	140	481	32	47.7	3.6	448	26
YP8_39b	1.37	0.22	4.59	0.48	0.75	0.11	4.98	0.67	2.33	0.46	2.95	0.3	5.64	0.99
YP8_40b	156.7	5.4	700	34	122.9	4.6	733	28	226	11	34.6	1.9	213.8	9.9
YP8_41b	617	21	1351	58	155.2	6.6	664	28	125.1	5.7	42.7	1.9	103.6	4.9
YP8_42b	239	19	970	72	164.2	9.7	924	53	222	13	58.7	3.5	214	13
YP8_43b	500	23	1418	76	226	12	1239	53	348	15	148.4	7.3	356	16
YP8_44b	292	20	782	38	104.3	5.8	521	30	145.7	9.1	37.2	2.2	174.3	9.6
YP8_45b	135.9	5.3	355	19	50.6	2.3	245	13	57	3.5	35.2	1.4	71.8	4
YP8_46b	1289	71	2530	130	244	13	908	45	144.6	8.6	23.7	1.6	127.5	6.8
YP8_47b	102.3	5.2	410	20	70.2	3.5	431	18	166.2	7.4	8.04	0.57	218	12

Continued on next page

Continued from previous page

Grain	La (ppm)	La 2SE	Ce (ppm)	Ce 2SE	Pr (ppm)	Pr 2SE	Nd (ppm)	Nd 2SE	Sm (ppm)	Sm 2SE	Eu (ppm)	Eu 2SE	Gd (ppm)	Gd 2SE
YP8_48b	2064	98	4230	280	414	19	1593	69	238	12	37.7	2	197	10
YP8_49b	132.2	6.7	379	22	54.5	3.1	292	13	73	4.1	20.1	1.1	73.9	4
YP8_50b	45.5	2.6	154.6	8.1	28	1.8	170.2	8.1	50.1	3.9	14.62	0.9	51.7	3.3
YP8_51b	42.9	2.6	151.5	9.1	25.9	1.7	154.4	9.2	42.7	3.1	12.45	0.84	48.8	3.4
YP6_1b	852	31	1880	100	233	11	1030	46	193.4	8.6	41.8	2.1	172.3	8
YP6_2b	761	34	1714	90	207.5	9.6	934	45	174.4	9.2	40.7	2.1	157	7.2
YP6_3b	830	39	1810	110	223	11	1027	50	193.7	9.9	42.9	2.1	169	7.2
YP6_4b	863	29	1925	82	244	14	1058	42	201	11	38.4	1.7	167.3	6.9
YP6_5b	838	33	1820	120	219.4	9.4	996	40	183.5	7.5	36.4	2.2	158.8	8.5
YP6_6b	525	32	1235	69	141	10	548	32	78	5.5	19.8	1.2	62.7	4.5
YP6_7b	488	24	1197	70	133.4	8.9	536	35	79	6.1	21.1	1.5	60.7	4.3
YP6_8b	2370	130	4730	320	487	27	1910	110	258	15	12.47	0.87	153.6	8.6
YP6_9b	2350	100	4860	330	509	26	1850	86	250	12	12.91	0.77	149.3	6.6
YP6_10b	2340	100	4550	210	479	22	1825	69	247	10	11.56	0.66	149.2	7.2
YP6_11b	381	18	935	55	140.5	8.5	669	30	128.1	5.9	40.7	2.6	119	6.5
YP6_12b	418	27	1039	64	137.7	7.5	709	41	144.6	9	41.3	2.9	127.7	7
YP6_13b	29.5	1.8	86.8	6.8	12.68	0.89	70.1	5	17	1.8	4.55	0.58	19.7	2
YP6_14b	32.3	1.8	97.7	5.9	14.65	0.97	75.1	4.6	20.5	1.8	5.83	0.5	21.3	1.9
YP6_15b	42.5	2.2	132	9.2	18.9	1.1	102.4	6.1	28.7	1.8	7.08	0.54	29.4	2.4
YP6_16b	1313	70	3040	150	337	18	1387	69	225	11	28.3	1.5	190.5	9.3
YP6_17b	1303	67	3130	210	349	16	1459	81	232	14	30.1	2	194	11
YP6_18b	1292	67	2800	160	326	20	1287	63	211	11	23.9	1.5	166.2	8.1
YP6_19b	391	18	1090	55	155.5	9.5	701	31	119.5	7	31.5	2.1	101.8	5.3
YP6_20b	43.9	2.8	180	10	30.6	2.2	157.1	9.3	31.7	2.4	6.62	0.67	28.1	2.2
YP6_21b	283	13	958	48	166.1	7.2	1061	56	368	18	11.01	0.86	432	20
YP6_22b	259	12	919	52	162	10	1001	49	347	17	11.16	0.88	404	22
YP6_23b	224	12	773	46	141.2	8.7	855	45	294	17	8.94	0.57	358	19
YP6_24b	114.6	7.9	285	19	35.9	2.8	149	16	20.7	2.7	6.14	0.71	18.2	2.3
YP6_25b	421	41	1042	96	132	12	597	60	94.1	9.9	21.9	2.1	73.6	7.9
YP6_26b	141.4	7.4	391	27	43.2	2.4	191	12	30.6	2.9	7.48	0.64	23.7	2.4

Continued on next page

Continued from previous page

Grain	La (ppm)	La 2SE	Ce (ppm)	Ce 2SE	Pr (ppm)	Pr 2SE	Nd (ppm)	Nd 2SE	Sm (ppm)	Sm 2SE	Eu (ppm)	Eu 2SE	Gd (ppm)	Gd 2SE
YP6_27b	591	46	1430	150	191	16	987	77	234	18	36.7	3.3	199	13
YP6_28b	322	15	677	48	83.9	4.7	414	21	95.7	7.2	22.6	1.3	86.2	5
YP6_29b	279	12	641	35	85.5	4.6	430	23	94.8	5.2	14.47	0.71	81.6	5
YP6_30b	263	24	623	60	80.5	7.4	419	34	92.2	8.4	14.3	1.6	82.4	6.4
YP6_31b	97.9	5.6	494	29	106.2	5.5	687	39	183	11	39.6	2.2	150	8.6
YP6_32b	177	11	795	41	145.2	8.1	838	40	321	14	27.1	1.8	412	18
YP6_33b	1706	70	4590	180	589	30	2508	94	503	19	31.3	1.7	387	18
YP6_34b	3040	160	4330	240	336	17	1114	49	160.3	7.9	43.9	2.8	142.1	7.3
YP6_35b	104.2	6	557	33	117.2	6.1	788	45	248	13	30.4	2.2	238	12
YP6_36b	76.7	5.1	256	15	34.9	2	168	11	29.2	2.5	8.9	0.6	24.6	1.9
YP6_37b	501	21	1808	81	274	14	1289	59	257	12	24.4	1.4	238	12
YP6_38b	10.84	0.61	13.3	1.1	3.32	0.33	24.8	1.7	12.1	1.4	5.53	0.81	14.3	1.4
YP6_39b	282	13	818	55	123	6	699	38	191.6	9.3	41.6	2.4	226	13
YP6_40b	1285	61	1884	93	163	6.5	547	27	64.2	3.3	13.72	0.94	46	2.9
YP15_1b	2.66	0.25	19.8	1.4	6.03	0.38	64.7	4	36.1	2.3	11.64	0.66	54.4	3.2
YP15_2b	3.37	0.31	18	1.5	4.12	0.3	26.3	1.9	13.1	1.4	8.06	0.7	22.7	2.2
YP15_3b	56.6	3.7	215	16	39.1	2.2	222	13	92.7	7.2	26.2	1.9	123	12
YP15_4b	43.3	2	247	15	50.8	2.3	316	15	161.2	8.9	8.23	0.7	230	12
YP15_5b	107.6	7.9	354	23	63	3.9	402	19	144	10	16.2	1.6	185	12
YP15_6b	28.1	1.5	230	11	63.1	3.6	486	19	281	14	163.5	8.2	376	15
YP15_7b	36.8	1.9	303	18	82.4	4	627	35	319	18	10.7	1	370	19
YP15_8b	6.77	0.49	36.9	2.3	8.45	0.56	59.6	3.7	19.2	1.8	5.68	0.55	23.3	1.7
YP15_9b	859	38	2140	110	277	10	1295	58	242	13	25.3	1.4	180.9	7.9
YP15_10b	61.1	3.1	251	15	44.3	2.2	271	12	136.8	6	32.2	1.6	207.2	9.3
YP15_11b	41.6	2.3	164.4	8.8	29.3	1.4	182	12	57.4	3.9	14.1	1.1	77.5	5.4
YP15_12b	93.8	6.2	402	41	65.2	5.2	362	24	105	10	41	3	134.1	9.3
YP15_13b	502	29	1517	96	232	14	1170	68	284	14	5.36	0.53	288	17
YP15_14b	98.5	6.4	169	14	16.5	1.2	74.7	7.1	13.6	1.7	4.07	0.51	13.7	1.4
YP15_15b	56.8	2	177	12	27.1	1.2	155.5	7.3	71.7	4.9	3.33	0.34	153.1	8.7
YP15_16b	34	3.3	201	36	39.7	3.7	237	16	163	16	6.1	1.2	256	20

Continued on next page

Continued from previous page

Grain	La (ppm)	La 2SE	Ce (ppm)	Ce 2SE	Pr (ppm)	Pr 2SE	Nd (ppm)	Nd 2SE	Sm (ppm)	Sm 2SE	Eu (ppm)	Eu 2SE	Gd (ppm)	Gd 2SE
YP15_17b	65.3	3.4	286	14	51.2	2.9	232	11	190	10	2.68	0.44	265	12
YP15_18b	266	21	714	46	88.1	6.8	393	25	64	4.3	28.8	2.5	59.9	4.2
YP15_19b	21.4	1.3	104.4	5.8	22.8	1.3	148.6	9.9	84.2	5	19.6	1.4	149.6	7.9
YP15_20b	77.2	4.1	524	28	122.5	5.9	887	44	270	14	28.6	1.8	294	16
YP15_21b	7.27	0.47	25.2	1.7	4.06	0.36	23.9	1.6	9.71	0.95	3.37	0.28	20.8	1.9
YP15_22b	664	32	1700	110	228	13	996	71	166	13	64.6	5	144	11
YP15_23b	343	31	1120	100	176	13	924	86	303	27	2.99	0.49	378	32
YP15_24b	0.74	0.14	2.27	0.3	0.393	0.072	2.53	0.51	0.66	0.27	0.188	0.077	2.16	0.44
YP15_25b	51.7	3.4	243	15	52.9	2.4	346	15	172.8	8.5	32.6	2.2	275	16
YP15_26b	8.06	0.59	41.3	2.4	10.13	0.59	75.3	4.6	36.3	2.3	8.1	0.64	58.4	3.5
YP15_27b	9.81	0.61	69.4	7	15.81	0.97	124.4	7.5	59.9	4.5	7.3	0.59	71.1	4.7
YP15_28b	10.58	0.73	104.5	7	22.5	1.6	139.9	6.5	25.4	2.2	4.8	0.45	18.2	1.6
YP15_29b	278	17	618	31	81.7	4	402	21	81.3	5.7	21	1.7	69.5	4.7
YP15_30b	5040	310	8250	530	680	41	2190	130	224	15	33	2.3	144	12
YP15_31b	8.58	0.54	29.3	2.1	4.77	0.46	32.8	2.3	16.3	1.3	5.71	0.56	46.3	4.1
YP15_32b	81	3.5	295	15	48.9	2.4	266	12	140.4	7.9	23.3	1.4	229	11
YP15_33b	516	32	1421	95	185	11	939	55	220	14	48.9	3.8	206	15
YP15_34b	455	17	856	44	87.8	4.7	327	16	46.2	3.1	4.89	0.46	34.5	2.4
YP15_35b	10.21	0.61	60.9	3.6	15.9	1.1	123.3	7.1	61	4.1	20.6	1.4	105.9	6.7
YP15_36b	1226	71	2790	190	326	17	1410	100	233	17	24.2	2.4	188	17
YP15_37b	34.3	1.9	102.5	5.4	18.16	0.97	106.2	6.4	48	3.4	13.25	0.94	80.3	5.4
YP15_38b	494	25	1175	67	141.6	9.1	573	37	93	5.8	20.3	1.5	69	4.8
YP15_39b	472	28	1590	110	277	17	1455	79	371	19	104.3	5.8	293	17
YP15_40b	144.8	7.4	543	32	91.9	4.7	471	25	220	12	1.55	0.23	263	16
YP21_1b	198	14	575	41	89.5	6.9	409	17	105.5	6.7	24.2	2.2	114.8	6.8
YP21_2b	619	35	1690	130	219	15	967	58	184	11	22.3	1.3	159.9	8.9
YP21_3b	441	29	1002	69	121.6	7.7	564	36	153	11	49.6	3.2	218	11
YP21_4b	NA	Below LOD	0.07	0.037	NA	Below LOD	0.17	0.11	0.2	0.14	0.87	0.17	0.3	0.15

Continued on next page

Continued from previous page

Grain	La (ppm)	La 2SE	Ce (ppm)	Ce 2SE	Pr (ppm)	Pr 2SE	Nd (ppm)	Nd 2SE	Sm (ppm)	Sm 2SE	Eu (ppm)	Eu 2SE	Gd (ppm)	Gd 2SE
YP21_5b	NA	Below LOD	0.03	0.021	NA	Below LOD	NA	Below LOD	NA	Below LOD	0.268	0.09	0.094	0.091
YP21_6b	86.2	5.2	368	25	66.2	3.5	411	22	188	10	48.9	3.1	310	19
YP21_7b	166.7	8.9	486	30	68.4	5.6	331	24	71.4	6.4	14.9	1.2	64.1	6.3
YP21_8b	611	40	1410	110	180	13	863	69	166	11	42.2	3.2	160	11
YP21_9b	1900	130	3290	210	306	21	999	58	122.7	7.2	20.9	1.4	94.8	6.6
YP21_10b	197	17	698	62	110.9	7.5	640	47	229	17	6.56	0.91	312	21
YP21_11b	24.5	1.1	214	10	61.1	4	460	21	227	11	5.53	0.52	303	14
YP21_12b	28.5	3.1	84.9	8.8	11.4	1.3	57.5	7.2	10.4	1.7	3.24	0.41	11.1	1.4
YP21_13b	20.83	0.96	65.9	2.4	11.05	0.74	63.7	3.9	22.8	1.6	8.08	0.56	27.6	2.5
YP21_14b	175	14	673	50	120.5	7.4	649	51	293	26	7.3	1	380	30
YP21_15b	398	17	1415	73	234	12	1210	61	526	25	7.19	0.56	643	32
YP21_16b	343	18	1263	86	207	13	1107	57	479	28	7.1	0.61	616	37
YP21_17b	657	27	2150	110	314	16	1516	71	567	28	2.97	0.36	674	31
YP21_18b	4.14	0.35	18.3	1.1	3.19	0.3	19.1	1.8	9.4	1.2	5.04	0.47	16.7	1.3
YP21_19b	138.8	8.6	526	34	97.2	6	580	27	236	13	5.86	0.45	275	16
YP21_20b	80.8	4	338	21	60.6	3.9	317	13	143.3	8.5	30.9	1.8	210	10
YP21_21b	115.8	6.7	388	19	69.8	3.7	471	23	234	13	33.9	2	340	16
YP21_22b	868	51	2860	220	414	19	1916	78	396	22	25.3	1.5	314	20
YP21_23b	49	13	182	40	32.9	5.9	201	29	182	14	91	12	463	51
YP21_24b	242	15	831	48	137.5	8.7	719	41	288	21	6.21	0.56	364	25
YP21_25b	1.34	0.16	3.88	0.43	0.61	0.1	3.87	0.68	1.97	0.42	2.48	0.33	6.21	0.86
YP21_26b	430	39	1480	130	235	21	1220	110	393	30	7.28	0.59	461	35
YP21_27b	14.9	1.2	102.9	9.6	24.9	2.1	197	11	86.3	5.9	13.6	1	101	7.1
YP21_28b	34.6	2	163.8	8.2	37.3	2.5	263	16	128.2	6.9	30.1	1.9	178	12
YP21_29b	1.67	0.19	4.52	0.37	0.653	0.082	3.36	0.57	1.36	0.38	2.83	0.32	3.89	0.67
YP21_30b	226	13	723	47	114.5	6.3	669	39	257	14	9.84	0.63	361	21
YP23_01b	29.9	1.9	110.6	6.9	20.8	1.5	145	10	84.6	5.2	34.3	1.8	144.5	8.9
YP23_02b	11.93	0.8	38.4	2.9	8.03	0.77	64.8	4.9	45.4	4.7	7.21	0.84	58.5	4.9
YP23_03b	132.4	7.4	348	23	52.1	2.9	332	21	131.7	8.2	39.2	2.3	241	13

Continued on next page

Continued from previous page

Grain	La (ppm)	La 2SE	Ce (ppm)	Ce 2SE	Pr (ppm)	Pr 2SE	Nd (ppm)	Nd 2SE	Sm (ppm)	Sm 2SE	Eu (ppm)	Eu 2SE	Gd (ppm)	Gd 2SE
YP23_04b	111.1	6.7	425	30	86.3	5.1	579	36	231	16	25	1.6	331	22
YP23_05b	75.9	2.7	310	16	44.5	1.9	201.2	8.6	32.5	1.7	8.01	0.48	27.7	1.9
YP23_06b	0.62	0.1	11.32	0.93	6.15	0.43	106.4	5.9	570	32	195	12	649	39
YP23_07b	187	17	748	74	125	10	677	49	311	29	3.71	0.52	408	40
YP23_08b	13.6	1.1	57.8	3.4	11.94	0.93	84	6.3	46.9	4.6	3.34	0.48	98.2	8.5
YP23_09b	1.29	0.17	5.02	0.42	1.04	0.11	6.76	0.67	4.41	0.49	1.17	0.18	14.8	1.2
YP23_10b	66.4	5.2	258	22	50.9	4	327	22	130	10	40.5	2.9	160.3	9.8
YP23_11b	68.9	4.2	239	17	37.2	2.8	210	18	84.5	6.6	14.8	1.3	137	11
YP23_12b	1.7	0.2	6.45	0.71	1.25	0.15	7.4	1.1	4.31	0.6	1.21	0.21	10.9	1
YP23_13b	456	29	1580	110	251	16	1317	90	542	38	103.1	5.6	773	50
YP23_14b	1229	63	2510	120	303	22	1257	60	203	12	42.8	2.4	138.7	7.9
YP23_15b	92	3.7	272	17	44.7	1.9	255	13	96.6	5.6	4.35	0.44	161.8	7.2
YP23_16b	343	23	1177	92	192	12	1045	62	288	15	34.7	2.3	269	14
YP23_17b	269	14	812	37	131.2	7	706	40	310	18	17.4	1.5	468	24
YP23_18b	55.2	2.7	217	10	40.2	2.1	294	19	142.7	7.6	38.8	2.2	285	21
YP23_19b	130.7	6	403	22	69.3	3.4	403	18	129.5	6.7	4.87	0.39	140.3	7.3
YP23_20b	30.2	1.7	117	10	21.1	1.4	130.2	9	70.1	5.3	13.7	1.1	121	10
YP23_21b	21.5	1.6	78.2	5.9	14.8	1.2	95.9	7.5	47.2	4.5	14.8	1.6	87.3	5.4
YP23_22b	0.214	0.064	1.02	0.17	0.224	0.062	2.14	0.38	1.97	0.57	0.99	0.19	5.9	1.1
YP23_23b	52.3	2.6	211	12	41.7	1.5	284	13	137.5	9.4	6.52	0.47	220.7	9.7
YP23_24b	233.9	8.4	808	44	132.9	6.3	659	30	330	14	7.58	0.52	482	23
YP23_25b	19.1	1.4	75	3.9	13.6	1	76.8	4.9	18.1	1.7	5.27	0.45	20.4	1.9
YP23_26b	40.3	2.2	203	12	39.8	2.6	230	10	95	5.4	15.1	0.96	124.3	5.9
YP23_27b	80.8	3.1	292	18	48.6	1.9	270	12	124.5	5.6	7.54	0.59	189.3	7
YP23_28b	43.1	2.6	196	14	42.1	2.4	336	21	195	11	41.9	2.6	335	19
YP23_29b	12.32	0.63	46.2	2.6	8.37	0.49	49.6	3	19.9	1.7	6.89	0.5	40.1	2.2
YP23_30b	239	18	811	49	135	10	765	62	331	24	79.6	4.3	506	32
YP23_31b	220.6	9.7	786	36	137.1	5.1	805	33	258	12	5.1	0.47	276	13
YP23_32b	1117	46	2260	110	274	14	1146	47	182	9.5	31.3	1.8	136.5	8.3
YP23_33b	1223	52	2740	140	360	19	1643	70	314	17	40.4	2.3	276	16
YP23_34b	3.36	0.25	12.92	0.85	2.39	0.2	14.3	1.3	8.47	0.86	2	0.24	22.1	1.7

Continued on next page

Continued from previous page

Grain	La (ppm)	La 2SE	Ce (ppm)	Ce 2SE	Pr (ppm)	Pr 2SE	Nd (ppm)	Nd 2SE	Sm (ppm)	Sm 2SE	Eu (ppm)	Eu 2SE	Gd (ppm)	Gd 2SE
YP23_35b	105.5	7.5	338	25	57.6	4.1	366	23	156.7	9.2	7.66	0.64	229	15
YP23_36b	82.4	4.3	296	14	47.2	2.6	269	13	106.9	5.5	37	1.9	164.7	7
YP23_37b	132.3	5.8	532	27	95.5	3.9	537	24	231.5	9.3	10.48	0.7	282	12
YP23_38b	19.4	1.4	67.4	4.1	12.57	0.78	86.7	7.2	42.7	3.4	11.9	1.2	81.7	7.1
YP23_39b	179.5	8.4	902	58	224	14	1525	68	623	44	80.2	4.5	793	45
YP23_40b	238	17	904	71	163.5	9.9	1045	65	416	25	6.55	0.74	527	36

Table G.3: Apatite REE element individual spot data part 2. This data is split into three tables for space reasons. Part 1 contains half the REEs (La, Ce, Pr, Nd, Sm, Eu, and Gd), **this table** (part 2) contains the other half of the REEs (Tb, Dy, Ho, Er, Tm, Yb, and Lu), and part 3 contains Mn, Sr, Y, Th, and U.

Grain	Tb (ppm)	Tb 2SE	Dy (ppm)	Dy 2SE	Ho (ppm)	Ho 2SE	Er (ppm)	Er 2SE	Tm (ppm)	Tm 2SE	Yb (ppm)	Yb 2SE	Lu (ppm)	Lu 2SE
YP1_1b	54.6	2.2	297	13	55.5	3.1	142.2	7	19.9	1.1	125.4	6.7	19.01	0.98
YP1_2b	55.6	2.8	386	19	86.6	3.9	257	14	36.4	2	227.3	9.9	36.2	1.7
YP1_3b	56.9	2.9	306	18	60.2	3.3	160.3	9.4	20.5	1.2	137.7	8	22.5	1.3
YP1_4b	53.9	3.2	285	18	54.4	3.6	139.4	8.7	19.2	1.3	119	7.6	20	1.4
YP1_5b	116.1	6.8	666	37	128	7.2	351	23	50.3	3.4	317	21	50.4	3
YP1_6b	121.2	7.5	656	40	130	7.8	345	16	47.2	2.9	285	18	41.3	2.5
YP1_7b	98.6	6.1	547	33	103	6.5	263	17	36	2.3	233	13	35.1	2.5
YP1_8b	38.4	2.4	206	13	39	2.9	94.8	5.8	12.06	0.92	79.4	5.6	12.37	0.89
YP1_9b	61.3	5.5	330	20	69.3	4.9	185	13	24	1.5	154	11	24.8	1.4
YP1_10b	32.7	2.1	182	13	34.4	2.3	84.4	5.3	11.12	0.72	71.7	4.4	11.02	0.7
YP1_11b	24.1	1.4	122.3	7.6	23.3	1.6	56.6	3.7	7.87	0.47	48.6	3.1	6.96	0.55
YP1_12b	69.8	3.7	385	19	78.5	5	190.6	7.5	26.6	1.4	162.9	7.8	24.4	1.7
YP1_13b	108.1	6.6	621	30	120.2	6.7	313	23	41.1	2.2	249	13	38.3	2
YP1_14b	58.8	4	303	17	54.8	2.9	139.8	9.1	18.1	1.2	108.6	7.2	16.5	1.1
YP1_15b	136	13	793	79	150	13	394	30	55.5	6	352	30	54.5	5.7

Continued on next page

Continued from previous page

Grain	Tb (ppm)	Tb 2SE	Dy (ppm)	Dy 2SE	Ho (ppm)	Ho 2SE	Er (ppm)	Er 2SE	Tm (ppm)	Tm 2SE	Yb (ppm)	Yb 2SE	Lu (ppm)	Lu 2SE
YP1_16b	39.3	2.7	202	12	37	3	94.5	6.6	11.54	0.75	70.6	5	10.5	1.1
YP1_17b	61.2	3.4	330	19	62.5	3.2	156.1	7.3	21	1.5	126.7	7.7	18.5	1.2
YP1_18b	32.4	2.4	174	12	32.8	2.2	82.4	5.8	10.62	0.82	67.4	4.1	11.37	0.74
YP1_19b	111.2	5.5	616	33	114.6	7.6	295	17	40.3	2.5	266	13	41.4	2.4
YP1_20b	134.3	7.3	741	52	143	11	394	33	50.3	4.1	336	28	56.6	4.5
YP1_21b	32.8	1.8	176.3	9.4	34	2.1	85.7	6.1	10.53	0.78	68.3	4.4	11.53	0.8
YP1_22b	56.9	4.5	359	28	74.3	6.5	195	18	28.3	2.4	172	17	26.5	2.5
YP1_23b	0.049	0.032	0.35	0.15	0.254	0.081	0.54	0.21	0.042	0.029	0.67	0.29	0.041	0.03
YP1_24b	6.3	0.45	49.1	3.6	11.96	0.92	39.6	2.8	5.63	0.43	34.9	2.6	4.91	0.46
YP1_25b	58.8	4.3	350	25	68.2	5	179	12	23.8	1.7	148	9.9	23	1.8
YP1_26b	149	11	865	57	168	12	473	32	64.2	3.7	434	34	66.9	4.8
YP1_27b	40.1	2.6	208	12	38.9	2.5	96.1	5.8	12.64	0.75	81.3	5.5	13.45	0.9
YP1_28b	30.5	1.6	159.2	8.7	29.8	1.5	73.6	3.8	9.8	0.6	60.6	3.5	9.91	0.67
YP1_29b	9.85	0.81	65	5.6	13.9	1.2	37.4	3.1	4.97	0.39	24.5	2.5	3.59	0.4
YP1_30b	45	3.4	236	19	44.1	3.5	111	11	14.4	1.3	92.6	7.7	14.6	1.1
YP1_31b	128.2	6.1	782	38	156.2	8.4	430	20	59.5	2.9	386	16	63.9	3.2
YP1_32b	53.2	3.4	283	17	53.6	2.9	132.9	8.6	18.1	1.2	112	6.2	17.3	1.1
YP1_33b	86.9	6.1	494	30	97.8	6.4	251	17	34.1	2.2	215	15	32.3	2.3
YP1_34b	57.6	3.6	351	20	76	4.5	200	12	27.9	2.1	174	12	27.5	2.3
YP1_35b	3.36	0.3	17.2	1.7	3.29	0.33	6.71	0.77	0.669	0.096	3.07	0.53	0.53	0.097
YP1_36b	78.7	9.2	416	51	83.4	9.6	223	25	31	4	207	29	32.1	4.3
YP1_37b	113.3	8	629	46	125.2	9.5	318	26	41.1	3	271	20	41.2	3.2
YP1_38b	102.1	6.4	571	36	110	8	289	19	40.2	2.8	263	19	40.4	2.7
YP1_39b	120	6.4	917	48	218	11	666	38	99.5	4.5	655	32	94.1	5.1
YP1_40b	64.5	3.4	354	19	68.6	3.7	178.6	9.3	23.7	1.3	147.7	8.2	23.2	1.4
YP1_41b	7.94	0.55	48.6	2.7	9.9	0.61	25.4	1.4	3.34	0.31	19.7	1.6	3.2	0.3
YP1_42b	70.9	3.8	453	26	100.1	5.6	287	15	42.1	2.1	277	15	44.8	2.3
YP1_43b	104.1	6.6	682	41	151.2	8.5	425	29	56.7	3.5	357	23	54	3.3
YP1_44b	74.1	3.6	421	23	80.7	4.7	206	11	26.7	1.5	170.7	9.5	27.4	1.3
YP1_45b	51.2	3.9	279	15	54.6	4.5	137	9.8	18	1.4	119	10	17.6	1.2
YP1_46b	240	22	1410	120	278	26	744	66	101.2	9.8	607	57	90.4	8.9

Continued on next page

Continued from previous page

Grain	Tb (ppm)	Tb 2SE	Dy (ppm)	Dy 2SE	Ho (ppm)	Ho 2SE	Er (ppm)	Er 2SE	Tm (ppm)	Tm 2SE	Yb (ppm)	Yb 2SE	Lu (ppm)	Lu 2SE
YP1_47b	69.8	4	376	21	71.3	4	184	11	26	1.6	159	11	23.6	1.5
YP1_48b	64.5	3.9	352	22	72.5	4.6	185	14	23.9	1.7	152	10	23	1.4
YP1_49b	41	2.3	220	11	39.4	1.9	99	5.8	11.92	0.74	75.2	4.7	11.7	0.73
YP1_50b	123.3	5.4	670	34	120.9	6.3	303	13	39.4	2.3	248	13	39.6	2.3
YP1_51b	77.5	3.8	550	33	117.5	6.6	341	19	46.5	2.8	308	19	45	2.8
YP1_52b	56.1	5.2	419	41	98.9	9.1	284	24	44.2	5.8	262	19	36.9	2.9
YP1_53b	106.3	5.2	580	34	113	5.5	303	16	41.5	2.3	276	14	43.3	2.3
YP1_54b	169.8	8.5	955	71	194	15	495	30	71.6	4.6	463	31	74.1	4.9
YP1_55b	159.9	7.7	889	42	165.1	6.9	416	18	56.3	3.2	321	16	46	2.4
YP1_56b	88.2	4.5	473	27	89.2	5	215	10	28.9	1.6	183	12	27.9	1.6
YP1_57b	70.8	4.8	384	25	73	5	189	12	25.2	1.8	159	12	24.3	1.8
YP1_58b	58.7	3.4	303	15	56	3.3	142.8	8.3	19.8	1.5	122.1	7.8	19.5	1.3
YP1_59b	106.6	8.5	593	49	115	10	290	22	40.6	2.9	255	17	40.9	3
YP1_60b	65.4	3.8	344	20	63.4	3.8	166.2	9.6	21.8	1.4	140	8.1	20.3	1.1
YP1_61b	36.6	2.1	189	12	35.4	2.2	90.8	6.9	11.55	0.84	72.6	5	10.86	0.78
YP1_62b	27.4	1.6	137.9	7.9	25.1	1.7	62.4	3.2	8.06	0.52	45.5	2.9	7.05	0.5
YP1_63b	29.6	1.8	147.5	7.8	27.1	1.5	62.5	3.6	7.58	0.54	49.1	3.2	7.41	0.52
YP1_64b	31.8	1.7	165.9	8.8	28.7	1.7	67	3.7	9.04	0.56	54.5	3.1	7.91	0.53
YP1_65b	47.6	3.2	237	12	43.8	2.3	106.7	6.3	14.32	0.81	87.8	5.6	13.55	0.91
YP1_66b	53.3	3.3	294	20	54.4	3.3	138.4	8.2	19.6	1.4	126.2	7.2	19.6	1.8
YP1_67b	44.9	2.5	240	16	46.3	3.2	115.6	7.6	15.9	1.2	102.4	6.3	15.8	1.1
YP1_68b	34.8	1.9	180.6	7.9	33	1.8	80.6	4.3	10.66	0.6	67.7	3.5	10.6	0.67
YP1_69b	33.2	1.9	181	11	32.3	1.9	81.1	5	10.47	0.63	68.5	4.1	10.55	0.69
YP1_70b	49.3	2.2	260	11	51.5	2.2	134	6.5	17.8	1.1	117.9	7.1	18.7	1.1
YP1_71b	98.8	6	566	35	110.3	6.8	291	18	40.1	2.2	250	18	38.3	2.5
YP1_72b	34.7	1.8	189	10	35.2	1.8	89.4	5.4	11.44	0.57	75.8	4.6	11.23	0.65
YP1_73b	119.8	8.8	664	49	137	12	365	29	50.1	4.3	330	30	52.3	4.3
YP1_74b	140.7	7.4	827	40	168.2	9.9	438	22	62	3.6	404	23	62.3	3.6
YP1_75b	13.17	0.8	77.2	4.9	15.13	0.83	39.1	2.8	4.58	0.4	26	1.8	3.68	0.29
YP1_76b	9.26	0.62	58.3	3.9	12.58	0.87	32.9	2.6	4.11	0.39	22.3	2.1	3.71	0.41
YP1_77b	7.71	0.6	46	3.9	8.62	0.51	23.5	2	2.88	0.31	17.9	1.6	2.63	0.32

Continued on next page

Continued from previous page

Grain	Tb (ppm)	Tb 2SE	Dy (ppm)	Dy 2SE	Ho (ppm)	Ho 2SE	Er (ppm)	Er 2SE	Tm (ppm)	Tm 2SE	Yb (ppm)	Yb 2SE	Lu (ppm)	Lu 2SE
YP1_78b	12.8	0.72	76.7	4.8	15.75	0.93	38.8	2.5	4.49	0.33	25.8	2.2	3.54	0.29
YP1_79b	163	12	929	69	192	17	525	39	68.2	5	473	43	71.7	5.9
YP1_80b	71.5	5.9	394	34	74.8	6.3	192	18	25.8	2.3	163	12	24.3	1.6
YP4_1b	3.05	0.25	17.5	1.8	3.61	0.29	11.52	0.9	1.67	0.22	12.8	1.1	2.76	0.24
YP4_2b	3.27	0.27	16.3	1.3	3.64	0.29	11.46	0.85	1.71	0.15	14.2	1.2	2.98	0.27
YP4_3b	4.13	0.36	34.1	2.5	8.71	0.58	30.7	2	4.53	0.35	32.6	2.7	5.01	0.35
YP4_4b	7.84	0.44	40.5	2.3	8.71	0.57	22.8	1.5	3.03	0.18	23.7	1.6	3.86	0.23
YP4_5b	6.42	0.47	33.3	2.2	7.27	0.52	20.1	1.3	2.81	0.28	20.4	1.6	3.42	0.28
YP4_6b	37.5	1.7	196.7	8.7	38.6	2.1	89.2	3.8	10.56	0.64	61.4	3.4	7.36	0.46
YP4_7b	3.4	0.31	17.6	1.6	3.79	0.38	11.2	1.1	1.61	0.17	11.5	1.1	2.13	0.19
YP4_8b	5.48	0.37	28.7	1.7	6.38	0.4	18.6	1.1	2.65	0.2	19.1	1.3	3.6	0.3
YP4_9b	4.83	0.5	25.7	2.1	5.57	0.47	16.1	1.4	2.3	0.23	17.2	1.9	3.35	0.31
YP4_10b	6.36	0.47	33.9	2.4	7.54	0.43	22.4	1.5	2.94	0.28	22.6	1.5	4.23	0.33
YP4_11b	42.5	1.9	239	11	44.8	2.3	107.5	4.7	12.34	0.66	73.3	4.8	9	0.49
YP4_12b	6.77	0.54	35.4	2.4	7.51	0.47	21.6	1.5	3.19	0.27	21.7	1.4	3.9	0.25
YP4_13b	7.17	0.48	39.3	2.7	8.23	0.59	22.2	1.5	3.08	0.24	21	1.3	3.79	0.33
YP4_14b	8.97	0.64	47.7	3.3	9.41	0.68	25.8	1.8	3.8	0.3	24.7	1.8	4.18	0.34
YP4_15b	6.59	0.39	35.1	1.9	7.24	0.51	21.5	1.5	2.99	0.23	21.7	1.6	3.91	0.26
YP4_16b	0.416	0.075	3.64	0.47	1.21	0.17	3.75	0.41	0.576	0.076	3.61	0.48	0.76	0.12
YP4_17b	0.018	0.015	0.37	0.14	0.112	0.035	0.57	0.12	0.105	0.032	1.05	0.28	0.181	0.048
YP4_18b	0.368	0.072	3.36	0.39	1.21	0.14	4.69	0.42	0.75	0.1	6.29	0.77	1.13	0.14
YP4_19b	9.61	0.61	49.3	2.8	9.89	0.68	28.1	1.8	4.01	0.3	27.3	1.7	4.31	0.38
YP4_20b	47.1	2.5	258	15	48.5	2.6	110.4	6.2	13.53	0.9	73.7	4.3	9.69	0.62
YP4_21b	3.74	0.26	20.4	1.5	4.4	0.34	12.2	1	1.76	0.17	13.4	1.1	2.94	0.24
YP4_22b	6.41	0.44	32.5	2.1	6.77	0.43	19.2	1.2	2.74	0.23	19.1	1.4	3.3	0.26
YP4_23b	6.4	0.44	34	2.3	7.1	0.52	20.3	1.4	2.82	0.23	20.5	1.3	3.92	0.4
YP4_24b	8.39	0.57	44.6	2.8	9.25	0.66	27.3	1.8	3.69	0.31	24.9	1.8	4.6	0.38
YP4_25b	8.3	0.62	44.8	2.7	9.65	0.53	26.1	2	3.51	0.25	25.7	1.8	4.42	0.33
YP4_26b	3.68	0.27	19.9	1.6	4.46	0.45	12.8	1.1	1.71	0.19	13.1	1.1	2.9	0.31
YP4_27b	0.57	0.1	5.76	0.76	1.63	0.2	5.82	0.63	0.82	0.13	5.73	0.69	1.04	0.15

Continued on next page

Continued from previous page

Grain	Tb (ppm)	Tb 2SE	Dy (ppm)	Dy 2SE	Ho (ppm)	Ho 2SE	Er (ppm)	Er 2SE	Tm (ppm)	Tm 2SE	Yb (ppm)	Yb 2SE	Lu (ppm)	Lu 2SE
YP4_28b	2.4	0.31	20.7	1.9	7.3	0.4	27.2	2.1	4.78	0.42	30.5	2.1	5.19	0.48
YP4_29b	0.76	0.11	7.7	0.84	2.49	0.26	8.92	0.84	1.49	0.19	10.9	1	1.87	0.19
YP4_30b	6.37	0.44	33.2	2.5	7.1	0.48	19.9	1.6	2.88	0.25	19.8	1.4	3.52	0.33
YP4_31b	5.11	0.36	28.5	1.9	5.96	0.47	16.8	1.3	2.29	0.2	17.8	1.2	3.2	0.28
YP4_32b	16.8	1	92.6	5.8	19	1.1	52.1	3.9	7.11	0.51	50.3	3.5	8.72	0.74
YP4_33b	8.39	0.64	44.7	3.4	9.22	0.7	24.9	2.2	3.49	0.35	24.7	2	3.92	0.33
YP4_34b	4.65	0.36	23.2	1.5	5.12	0.35	15.5	1.1	2.42	0.24	19.1	1.4	3.73	0.29
YP4_35b	0.104	0.043	1.13	0.21	0.35	0.074	1.21	0.27	0.229	0.05	1.83	0.34	0.382	0.069
YP4_36b	0.56	0.082	4.63	0.61	1.58	0.19	5.98	0.64	0.97	0.12	6.55	0.69	1.18	0.15
YP4_37b	2.77	0.29	14.4	1.6	3.42	0.36	9.5	1	1.28	0.15	9.1	1.2	1.83	0.2
YP4_38b	4.93	0.31	24.9	1.6	5.46	0.34	15.8	1.1	2.11	0.18	16.2	1.2	3.32	0.28
YP4_39b	0.111	0.042	1.24	0.32	0.478	0.099	1.78	0.28	0.361	0.073	2.7	0.38	0.468	0.091
YP4_40b	14.64	0.67	69.4	3.9	10.37	0.67	21	1.4	2.18	0.18	10.6	1	1.11	0.11
YP8_1b	8.11	0.53	42.5	2.5	9.4	0.56	25.4	1.3	3.68	0.21	26.8	1.7	5.1	0.37
YP8_2b	9.33	0.45	49	2.6	10.69	0.59	28.6	1.3	4.13	0.31	28.4	1.9	4.78	0.35
YP8_3b	6.91	0.52	38.5	2.9	8.12	0.65	21.9	1.6	3.17	0.25	23.1	1.8	4.22	0.35
YP8_4b	4.96	0.36	28.9	2.4	6.15	0.47	19.5	1.6	2.8	0.26	22.2	2.2	4.71	0.4
YP8_5b	3.37	0.26	16.7	1.5	3.46	0.24	11.23	0.96	1.6	0.18	12	1.1	2.67	0.21
YP8_6b	6.72	0.44	34.6	2.2	7.91	0.46	22.3	1.6	3.1	0.28	22	1.6	4.18	0.26
YP8_7b	7.75	0.57	38.6	2.2	8.93	0.52	24.7	1.4	3.65	0.28	26.3	1.9	4.93	0.33
YP8_8b	2.79	0.23	14.6	1.3	3.54	0.27	9.59	0.86	1.44	0.17	10.8	1	2.35	0.21
YP8_9b	6.07	0.3	30.1	1.4	6.3	0.34	18.2	1.2	2.6	0.18	17.4	1.3	3.1	0.24
YP8_10b	5.47	0.51	28.7	2.4	6.93	0.67	17.4	1.4	2.58	0.28	18.8	1.7	3.82	0.34
YP8_11b	4.63	0.59	26.3	3.3	5.45	0.72	17.4	2	2.4	0.3	18.7	2.5	3.51	0.44
YP8_12b	5.8	0.38	30.7	1.5	7	0.5	19.3	1.2	2.98	0.26	22	1.6	4.25	0.31
YP8_13b	5.61	0.46	31.7	2.3	6.83	0.51	19.7	1.4	2.77	0.23	21.9	1.8	4.31	0.33
YP8_14b	21.8	1.6	151	11	37.2	2.7	111	7.6	17.3	1.4	117.1	8	18.6	1.3
YP8_15b	14.4	1.2	94	10	22.8	2.6	67.9	7.6	10.3	1.2	71.7	7.9	11.9	1.5
YP8_16b	4.04	0.3	21	1.3	4.44	0.34	11.6	0.9	1.61	0.16	10.73	0.82	1.97	0.17
YP8_17b	5.1	0.64	26.6	3.1	5.3	0.58	14.1	1.6	1.9	0.25	13.6	1.9	2.4	0.28

Continued on next page

Continued from previous page

Grain	Tb (ppm)	Tb 2SE	Dy (ppm)	Dy 2SE	Ho (ppm)	Ho 2SE	Er (ppm)	Er 2SE	Tm (ppm)	Tm 2SE	Yb (ppm)	Yb 2SE	Lu (ppm)	Lu 2SE
YP8_18b	4.89	0.87	25.1	4.6	4.69	0.41	12.1	1.8	1.69	0.21	10.3	1.1	1.84	0.25
YP8_19b	23	1.1	122.4	5.5	24.1	1.1	59.3	2.7	7.47	0.48	43.8	2.8	6.31	0.35
YP8_20b	17.29	0.77	95.4	3.9	18.41	0.92	45.5	1.6	5.52	0.3	32.7	1.7	4.77	0.31
YP8_21b	43.1	3.2	244	20	50.9	3.9	133	11	17.2	1.5	108.1	9.7	16.9	1.4
YP8_22b	5.37	0.41	28.3	2	6.3	0.42	18.5	1.3	2.52	0.19	19.7	1.5	3.64	0.29
YP8_23b	2.39	0.18	12.4	1.1	2.8	0.21	8.18	0.6	1.25	0.11	8.21	0.81	1.67	0.17
YP8_24b	2.26	0.19	12.3	1.1	2.68	0.29	7.78	0.65	1.15	0.15	8.19	0.7	1.6	0.2
YP8_25b	5.53	0.32	29	1.4	6.75	0.43	18.17	0.94	2.86	0.25	19.4	1.3	3.77	0.26
YP8_26b	67.6	3.7	369	19	69.4	3.9	158.4	8.9	18.1	1.1	91.7	5.3	11.89	0.72
YP8_27b	42.9	2.4	225	13	41.8	2.2	94.8	5.4	10.41	0.63	54.4	3.4	6.93	0.45
YP8_28b	34.8	1.6	192.1	8.6	37.6	2	83.3	3.3	8.97	0.45	45.5	2.5	6.12	0.36
YP8_29b	49.1	2.2	270	11	50.8	2.1	115	5.2	12.19	0.66	62.2	3.3	8.32	0.43
YP8_30b	65.7	2.6	357	15	66.3	2.2	150.8	5.5	16.72	0.78	86.5	3.6	11.23	0.4
YP8_31b	53.1	2.5	280	13	53.3	2.1	119.5	5.7	12.82	0.64	68.7	3.5	8.56	0.47
YP8_36b	14	1	76.9	6.1	16.6	1.1	45.3	3.9	7	0.58	46.6	3.4	8.46	0.6
YP8_37b	8.59	0.9	47.1	6.1	9.4	1.2	25.8	2.9	3.5	0.5	24.4	3.1	4.33	0.48
YP8_38b	62.3	3.8	323	20	63.2	4.2	143.5	8.4	17.2	1.2	98.5	7.1	12.39	0.9
YP8_39b	1.13	0.15	10	1	2.99	0.3	10.3	1	1.51	0.21	11.2	1	1.71	0.17
YP8_40b	26.2	1.4	128.2	6.3	22.9	1.3	49.7	2.7	5.1	0.36	25.5	1.4	3.13	0.24
YP8_41b	13.37	0.67	68.8	3.4	13.56	0.71	36.1	1.7	4.91	0.27	33.5	1.7	5.84	0.4
YP8_42b	25.2	1.6	130.1	8	25.8	1.3	67.2	4	8.19	0.58	54.5	3.8	9.1	0.6
YP8_43b	45.7	2.1	243	12	45.4	2	106.6	4.5	13.06	0.7	68.3	3.5	8.66	0.56
YP8_44b	24.8	1.4	153.8	8.3	31.6	1.7	85.1	4.7	12.07	0.68	81.2	4.4	14	0.62
YP8_45b	10.89	0.71	64.2	3.7	14.86	0.87	45.6	2	6.79	0.47	52.7	2.9	9.92	0.48
YP8_46b	15.76	0.93	80.3	4.4	17.1	1	46.8	3.1	6.39	0.46	42.3	2.5	7.78	0.55
YP8_47b	31.3	1.5	187.6	9	38.3	2	96.4	5.2	12.48	0.81	77.2	5.1	9.95	0.6
YP8_48b	18.9	1.2	91.8	4.3	18.15	0.94	43.3	2.3	4.8	0.34	28.6	1.7	5.11	0.36
YP8_49b	9.45	0.56	50.2	2.6	10.06	0.6	23.7	1.6	3.31	0.25	21.7	1.7	3.81	0.25
YP8_50b	6.58	0.41	34.7	1.9	7.68	0.42	19	1.2	2.32	0.23	16.6	1.2	2.6	0.24
YP8_51b	5.95	0.46	32.8	2.6	6.59	0.39	16.6	1.1	2.15	0.2	13.9	1.2	2.34	0.17

Continued on next page

Continued from previous page

Grain	Tb (ppm)	Tb 2SE	Dy (ppm)	Dy 2SE	Ho (ppm)	Ho 2SE	Er (ppm)	Er 2SE	Tm (ppm)	Tm 2SE	Yb (ppm)	Yb 2SE	Lu (ppm)	Lu 2SE
YP6_1b	20.74	0.99	99.9	4.9	17.8	1.2	39.7	2	4.33	0.3	22.3	1.4	2.94	0.19
YP6_2b	19.1	1.2	89.4	5.1	15.79	0.84	35.8	2.1	3.9	0.31	20.3	1.5	2.62	0.22
YP6_3b	20.1	1.1	99.5	4.9	17.58	0.76	37.8	2	3.98	0.31	21.6	1.5	2.83	0.22
YP6_4b	19.78	0.91	105.7	4.6	18.34	0.99	40.3	2.1	4.73	0.36	24.7	1.6	3.31	0.22
YP6_5b	19.2	0.98	95.2	4.8	17.54	0.99	37.9	2.2	4.46	0.32	24.4	1.7	3.17	0.25
YP6_6b	6.84	0.55	37.9	2.8	8.02	0.53	22	1.5	3.12	0.3	23.2	1.9	4.12	0.28
YP6_7b	6.88	0.53	35.9	2.8	8.23	0.85	22.5	1.8	3.16	0.26	22.8	1.9	4.13	0.31
YP6_8b	15.14	0.97	66.5	4.1	11.52	0.69	25.8	1.7	3.43	0.24	20.3	1.3	2.87	0.21
YP6_9b	14.58	0.85	66.6	3.7	11.19	0.78	26.9	1.6	3.34	0.23	19.9	1.1	2.95	0.26
YP6_10b	14.38	0.66	66.4	3.6	11.37	0.67	25.9	1.6	3.33	0.24	19.4	1.3	2.88	0.21
YP6_11b	13.35	0.68	62	3.5	11.33	0.57	23.9	1.4	2.63	0.22	14.6	1	1.97	0.16
YP6_12b	14.5	1	71	3.9	12.17	0.78	26.9	1.5	2.64	0.3	14.4	1.1	2.02	0.26
YP6_13b	2.17	0.27	10.3	1.2	2.4	0.3	5.7	0.79	0.608	0.079	3.75	0.51	0.92	0.15
YP6_14b	2.48	0.23	12.13	0.96	2.45	0.22	6.13	0.7	0.72	0.11	4.6	0.57	0.88	0.095
YP6_15b	3.22	0.25	17	1.3	3.59	0.31	8.44	0.5	1.08	0.15	7.95	0.8	1.32	0.11
YP6_16b	24.3	1	128.4	6.2	25.6	1.4	64.7	3.2	9.31	0.54	55	3.2	8.08	0.55
YP6_17b	24.4	1.6	143.1	9.7	28	1.8	68.8	4.9	9.18	0.77	58.3	3.7	8.05	0.61
YP6_18b	21.4	1.1	115.4	6.5	23.1	1.2	57.8	3.1	8.08	0.43	48.1	2.7	6.95	0.46
YP6_19b	11.04	0.65	53.2	2.9	10.69	0.64	26.6	1.4	3.1	0.22	19.3	1.4	3.13	0.25
YP6_20b	2.94	0.23	13.6	1.1	2.82	0.27	7.12	0.67	0.7	0.084	4.9	0.63	0.98	0.12
YP6_21b	60.4	3.1	314	14	60.3	2.9	131.1	6.4	13.8	0.92	65.6	4	7.97	0.48
YP6_22b	56.7	2.5	301	14	56	2.9	124.9	5.5	12.74	0.63	61.7	2.7	7.39	0.42
YP6_23b	49.7	2.6	260	13	48.8	2.4	106.3	5.2	11.13	0.69	54.5	3.2	6.38	0.47
YP6_24b	2.14	0.29	9.4	1.7	2.12	0.34	4.75	0.88	0.68	0.13	4.31	0.91	0.89	0.15
YP6_25b	7.58	0.75	34.5	3.4	6.71	0.61	17.1	1.9	2.33	0.29	15.1	1.8	2.79	0.32
YP6_26b	2.36	0.23	11.5	1.1	2.01	0.17	5.3	0.55	0.8	0.11	4.84	0.55	0.93	0.13
YP6_27b	23.3	2	103.2	8.2	18.7	1.4	38.8	3.2	4.42	0.47	21.6	1.9	2.85	0.25
YP6_28b	8.99	0.58	39.1	2.5	6.71	0.45	15.2	1.2	1.51	0.17	8.01	0.84	0.92	0.13
YP6_29b	8.33	0.46	40	2.5	6.99	0.54	14.7	1.2	1.45	0.15	7.62	0.95	1.05	0.13
YP6_30b	8.73	0.96	36.8	3.1	6.99	0.72	14.8	1.3	1.67	0.23	8.7	1.2	0.99	0.17
YP6_31b	15.66	0.7	75.9	4.7	13.08	0.67	29.6	1.7	3.46	0.32	19	1.5	2.59	0.22

Continued on next page

Continued from previous page

Grain	Tb (ppm)	Tb 2SE	Dy (ppm)	Dy 2SE	Ho (ppm)	Ho 2SE	Er (ppm)	Er 2SE	Tm (ppm)	Tm 2SE	Yb (ppm)	Yb 2SE	Lu (ppm)	Lu 2SE
YP6_32b	68.5	3.3	430	22	96.8	4.8	261	12	34.7	1.8	214	10	31.7	1.5
YP6_33b	44.8	1.9	232	10	43.8	2.2	106.7	4.9	14.4	0.77	90	5.1	13.92	0.7
YP6_34b	18.4	1.2	99.1	5.5	20.3	1	57.5	3.1	7.94	0.47	55	3.1	9.41	0.63
YP6_35b	31.3	1.7	162.6	7.8	31.4	1.7	79.3	4.5	10.45	0.55	65.4	3.8	9.99	0.65
YP6_36b	2.54	0.25	13.1	1	2.68	0.23	7.35	0.73	1.05	0.11	8.18	0.88	2.05	0.21
YP6_37b	30.6	1.3	168.1	7.8	35.1	1.9	95.8	5.3	12.95	0.82	87.8	5.7	14.22	0.81
YP6_38b	1.41	0.16	6	0.7	1.04	0.12	2.02	0.31	0.116	0.037	0.31	0.15	0.016	0.013
YP6_39b	30.4	1.5	165.9	9	31.9	1.7	72.4	4.2	8.52	0.5	45.9	2.6	5.71	0.4
YP6_40b	4.96	0.4	22.2	1.9	4.2	0.37	9.8	0.8	1.11	0.11	6.25	0.67	1.02	0.11
YP15_1b	6.31	0.34	31.5	1.9	5.72	0.44	11.33	0.91	1.23	0.12	6.13	0.72	1.08	0.14
YP15_2b	4.34	0.37	30.7	2.1	5.72	0.45	13.4	1.1	1.69	0.17	10.84	0.94	1.38	0.11
YP15_3b	22.3	1.7	140	11	30.7	2.3	80.2	5	11.3	0.84	67.9	5.2	11.3	1
YP15_4b	43.4	2.1	267	13	48.6	2.2	116.8	5.6	14.93	0.84	91.2	6.6	10.13	0.55
YP15_5b	24.9	1.8	145	10	26.9	2.1	64.4	4.8	7.24	0.49	40.8	3.7	5.49	0.46
YP15_6b	42.1	2.7	160.5	9.4	17.9	1	25.7	1.7	1.81	0.17	6.31	0.82	0.419	0.09
YP15_7b	52.9	2.8	286	13	50.2	2.5	115.5	5.4	13.27	0.78	69.5	4	8.96	0.67
YP15_8b	2.89	0.27	15.5	1.5	2.91	0.27	6.44	0.61	0.7	0.12	4.37	0.56	0.67	0.12
YP15_9b	20.4	0.98	107.6	5.6	18.9	1.1	46.1	2.5	5.82	0.38	32.6	1.9	4.39	0.3
YP15_10b	38.8	1.7	222	10	37.4	2.1	85.1	4.5	10.23	0.61	59.5	3.8	7.36	0.44
YP15_11b	11.32	0.79	67.4	4.4	15.2	1	44	3.5	5.76	0.52	37.4	2.3	6.68	0.59
YP15_12b	20	1.5	122.6	9.8	27.1	1.8	73	5.2	9.77	0.78	62.3	3.9	9.53	0.86
YP15_13b	39.9	2.9	229	15	46.9	3.1	128.2	7.9	20.1	1.5	147	11	23	1.8
YP15_14b	2.03	0.27	11.3	1.3	2.15	0.2	6.45	0.83	0.66	0.11	4.76	0.71	0.78	0.11
YP15_15b	34.8	2	291	11	73.8	3.7	241.3	9.7	37.8	1.7	268.6	8.9	36.6	1.5
YP15_16b	53.1	2.8	285	17	42.3	4	88.2	7.4	10.6	1.4	59.6	5.7	6.75	0.88
YP15_17b	59.7	3.1	255	11	27.1	1.3	46	2.2	5.07	0.39	26.6	2	3.1	0.28
YP15_18b	6.36	0.5	35.2	2.8	6.78	0.62	19	1.6	2.77	0.35	18.2	1.7	3.15	0.41
YP15_19b	28.4	1.3	143.6	7.9	18.47	0.85	31.8	2.1	2.59	0.26	10.4	1.1	1.1	0.13
YP15_20b	36.8	1.8	212	9.6	40.8	2.1	97.3	3.5	11.98	0.69	65	3.8	8.67	0.53
YP15_21b	4.5	0.32	34.1	2.2	8.81	0.58	27.1	1.7	4.05	0.35	25.2	2	3.85	0.28

Continued on next page

Continued from previous page

Grain	Tb (ppm)	Tb 2SE	Dy (ppm)	Dy 2SE	Ho (ppm)	Ho 2SE	Er (ppm)	Er 2SE	Tm (ppm)	Tm 2SE	Yb (ppm)	Yb 2SE	Lu (ppm)	Lu 2SE
YP15_22b	13.5	1.2	66.1	6.4	13	1.2	34	3	4.7	0.5	35	3.6	7.16	0.76
YP15_23b	65.5	5.9	409	33	79.7	6.4	179	15	18.4	1.6	92.6	8.5	10.61	0.97
YP15_24b	0.261	0.063	2	0.4	0.495	0.093	1.45	0.27	0.164	0.061	1.5	0.3	0.232	0.054
YP15_25b	50.6	2.3	302	16	49.4	2.2	108.1	6	11.93	0.68	65.5	4.3	8.15	0.57
YP15_26b	9.38	0.5	69.8	3.8	15.42	0.88	46	2.4	6.96	0.46	44.7	2.5	7.22	0.42
YP15_27b	13.53	0.85	99	5.3	20.6	1.3	56.4	3.8	7.21	0.48	42.4	2.9	5.33	0.41
YP15_28b	1.82	0.19	9.3	1	1.67	0.21	3.37	0.39	0.444	0.082	2.84	0.4	0.408	0.083
YP15_29b	7.97	0.49	40	2.5	7.4	0.54	16.2	1.2	1.65	0.2	9.1	1.2	1.26	0.19
YP15_30b	15.2	1.1	74.7	4.6	15.5	1.1	41.9	2.8	5.52	0.46	40.1	2.9	6.66	0.47
YP15_31b	11.76	0.89	117.7	6.3	39.8	2.5	158.2	7.6	29.4	1.5	234	14	37.4	1.7
YP15_32b	47.7	2.9	317	19	58.8	2.7	146	6.5	21.5	1.2	131.7	6.9	16.2	1
YP15_33b	26.3	2	127.8	7.5	23.3	2.2	48	3.4	5.24	0.51	27	2.4	3.45	0.34
YP15_34b	3.94	0.33	18.9	1.3	3.43	0.3	9.02	0.87	0.88	0.11	4.96	0.66	0.87	0.11
YP15_35b	17.3	1.2	106.6	5.8	22	1.4	58.6	3.4	6.57	0.35	37.4	2.5	5.76	0.43
YP15_36b	24	1.7	123.2	8	22	1.7	51.8	4.1	6.05	0.54	31.8	2.4	3.91	0.41
YP15_37b	15.97	0.89	116.1	6	26.5	1.5	77.8	4	12.81	0.85	90.5	5.1	12.09	0.8
YP15_38b	8.01	0.55	42.2	3.2	9.27	0.71	24.4	1.6	3.79	0.34	23.9	2.1	4.09	0.37
YP15_39b	32.4	2.5	146.2	8.7	20.9	1.2	45.5	3.3	4.96	0.54	25.3	2.4	3.19	0.32
YP15_40b	59	3.3	387	18	77.6	3.9	216	10	30.9	1.8	190.7	9.8	26.8	1.4
YP21_1b	15.06	0.91	87.7	4.6	17.7	1.3	49.1	3.2	7.12	0.56	49.5	3.5	8.35	0.69
YP21_2b	21.6	1.3	122.9	6.8	24.2	1.2	61.5	3.9	8.04	0.46	50.6	2.9	7.18	0.48
YP21_3b	37.7	2.1	263	16	61	3	176.4	8.7	25.5	1.6	175	13	28.6	1.9
YP21_4b	0.22	0.055	1.06	0.24	0.19	0.05	0.39	0.14	0.041	0.023	0.34	0.14	0.019	0.015
YP21_5b	0.025	0.016	0.69	0.21	0.184	0.061	0.32	0.11	0.027	0.018	0.181	0.088	0.042	0.024
YP21_6b	52.1	3	269	15	41.1	2.3	67.2	3.7	5.72	0.38	20.6	1.8	1.71	0.21
YP21_7b	8.45	0.9	49.2	4.1	10.51	0.95	28	2.8	4.03	0.36	28.4	3.1	4.67	0.68
YP21_8b	19.6	1.1	100.2	6.2	18.1	1.4	40.7	3.1	4.67	0.41	24	1.8	2.94	0.31
YP21_9b	10.59	0.71	55.5	3.5	10.72	0.78	25.6	1.9	3.12	0.24	19.6	1.8	2.73	0.26
YP21_10b	53.6	3.6	350	28	67.3	4.9	177	14	24.3	2.2	148	12	19.9	1.8
YP21_11b	46.1	2	252	12	45.4	2.1	102.6	5.2	11.59	0.66	56.3	2.9	6.36	0.42

Continued on next page

Continued from previous page

Grain	Tb (ppm)	Tb 2SE	Dy (ppm)	Dy 2SE	Ho (ppm)	Ho 2SE	Er (ppm)	Er 2SE	Tm (ppm)	Tm 2SE	Yb (ppm)	Yb 2SE	Lu (ppm)	Lu 2SE
YP21_12b	1.44	0.22	8.3	1.2	1.79	0.24	5.35	0.72	0.61	0.11	4.58	0.69	0.98	0.14
YP21_13b	3.54	0.3	19.3	1.5	3.55	0.27	8.41	0.72	0.76	0.1	4.63	0.46	0.78	0.11
YP21_14b	79.2	5.7	490	45	78.6	5.6	164	17	17	2.1	81	12	8.16	0.98
YP21_15b	122.5	7.1	724	34	134.6	6.8	331	16	47.8	2.3	297	14	39.7	2
YP21_16b	110.4	6.3	669	39	122.3	6.7	303	17	43.2	2.6	273	15	35.9	2.1
YP21_17b	107.1	4.9	496	23	65.5	3.1	106	4.7	9.36	0.59	41.2	2.9	3.99	0.32
YP21_18b	4.26	0.28	38.4	2.3	11	0.75	39.7	2.5	6.67	0.44	46.6	3.1	5.59	0.42
YP21_19b	40.5	2	246	13	47.4	2.4	121.3	6.8	16.1	1.1	89.7	4.7	11.89	0.67
YP21_20b	35.2	1.7	188.3	9	29.2	1.3	59.8	3.5	7.48	0.52	39.4	2.6	4.08	0.29
YP21_21b	57.9	3	334	12	59	2.9	136.9	6.3	15.89	0.97	89	4.4	10.37	0.58
YP21_22b	34.8	2.1	163.2	9.1	29.1	1.5	66.3	3.1	7.26	0.49	39.6	3.1	5.29	0.46
YP21_23b	60.4	5.2	276	13	45.3	2.9	108.9	8.2	13.8	1.3	82	8.3	10.5	1.2
YP21_24b	60.5	3.9	380	23	72.1	4	183	10	24.6	1.5	169	11	23.7	1.8
YP21_25b	1.2	0.16	10.6	1.2	2.99	0.31	10.2	1.2	1.34	0.18	7.92	0.89	1.48	0.2
YP21_26b	73.3	5.2	432	25	81	4.5	192	11	24.5	1.3	133.7	7.6	17.3	1
YP21_27b	12.79	0.88	75.3	5.5	15.4	0.99	43.5	2.7	5.84	0.43	35.1	2.3	6	0.41
YP21_28b	26.9	1.6	143.4	7	26.7	1.5	66.7	3.5	8.14	0.51	47.8	2.8	7.01	0.53
YP21_29b	0.72	0.1	6.03	0.76	1.66	0.22	5.77	0.5	0.74	0.1	4.86	0.54	0.75	0.1
YP21_30b	64.7	3.4	421	22	83.2	4.4	216	10	27.3	1.4	155	9.2	19.08	0.81
YP23_01b	25	1.6	140.5	8	24.1	1.1	57.5	3.8	7.1	0.5	41.5	2.7	5.09	0.37
YP23_02b	7.95	0.7	39.7	4	6.37	0.63	16.6	2	2.17	0.25	13.4	1.3	2.14	0.34
YP23_03b	42.3	2.7	265	17	51.3	3	129.1	7.8	16.7	1.1	94.8	6	11.54	0.67
YP23_04b	55.8	3.5	369	24	77.4	5.1	208	12	28	1.8	177	11	23.7	1.3
YP23_05b	3.5	0.28	15.7	1.1	2.93	0.25	6.95	0.49	0.837	0.089	4.61	0.43	0.78	0.11
YP23_06b	54.2	3.5	166.8	9.2	19.7	1.4	30.3	1.9	2.89	0.27	13.4	1.1	1.37	0.16
YP23_07b	73	5.3	451	42	81.9	7.7	218	21	29.3	2.2	185	15	25.7	2
YP23_08b	19.5	1.7	132.8	7.8	26.9	2	78.4	6.7	10.5	0.68	70.1	5.1	9.82	0.78
YP23_09b	4.28	0.3	43.4	2.1	15.76	0.7	63.8	3.1	11.02	0.6	78.9	4.2	11.56	0.67
YP23_10b	23.6	1.8	125	8.7	24.7	1.7	63.9	5.7	8.11	0.61	49.7	3.7	7.22	0.68
YP23_11b	21	1.4	116.7	9.3	27.9	2.1	138.2	9.7	28.5	1.9	199	19	23.8	2

Continued on next page

Continued from previous page

Grain	Tb (ppm)	Tb 2SE	Dy (ppm)	Dy 2SE	Ho (ppm)	Ho 2SE	Er (ppm)	Er 2SE	Tm (ppm)	Tm 2SE	Yb (ppm)	Yb 2SE	Lu (ppm)	Lu 2SE
YP23_12b	2.68	0.25	23.3	1.9	6.31	0.54	20.1	1.6	2.73	0.24	15.9	1.2	2.05	0.22
YP23_13b	166	12	1106	69	225	15	570	38	74.8	4.1	440	30	50.8	3.8
YP23_14b	14.94	0.98	70	4.9	11.21	0.86	25.7	2.1	2.77	0.27	14.5	1.2	1.93	0.21
YP23_15b	30.5	1.7	213	11	48.9	2.4	150.9	7.9	24.8	1.4	171.6	9.1	24.1	1.1
YP23_16b	35.7	1.8	195.4	9.7	36.8	1.8	94.7	4.1	13.17	0.77	92	5	12.81	0.8
YP23_17b	83.9	4.9	501	29	83.1	5.3	201	12	24.8	1.5	147.2	9.9	17.9	1.6
YP23_18b	47.2	4.2	270	32	45.8	7.2	83	14	6.7	1.5	26.1	6.8	2.38	0.71
YP23_19b	19.85	0.95	116.4	6.1	21.3	1.1	50.9	2.5	6.36	0.37	36.8	2.2	4.94	0.36
YP23_20b	24.4	1.8	158	12	27.4	2.1	68.6	4.9	10.04	0.83	68.5	5.1	9.17	0.68
YP23_21b	16	1.2	90.6	6.4	16.1	1.4	33.6	2.5	4.42	0.38	23.2	2.4	2.45	0.37
YP23_22b	1.67	0.21	17	0.96	6.34	0.32	29.8	2.1	6.4	0.44	58.9	3.1	10.57	0.58
YP23_23b	45	2.4	284	11	53.4	2.4	128.7	5.2	16.49	0.7	97.5	4.6	12.22	0.82
YP23_24b	97.1	3.7	552	24	92.6	3.7	216.7	8.9	26.4	1.2	154.5	6.6	18.68	0.82
YP23_25b	2.72	0.27	17.1	1.5	3.85	0.36	11.7	1.1	1.7	0.17	11.8	1.1	1.57	0.2
YP23_26b	22.4	1.4	139.9	9.2	26.3	1.3	67.7	4.3	9.06	0.61	49.2	3.2	5.39	0.32
YP23_27b	38.4	1.6	238	11	38.7	1.6	82.7	3.7	9.46	0.54	50.6	3.1	5.57	0.34
YP23_28b	57	3.2	334	20	58.5	2.8	138.8	7.7	18.5	1.1	116.7	7.8	14.94	0.93
YP23_29b	7.78	0.49	55.7	3	14.06	0.81	41.7	2.1	5.95	0.36	38.9	2.4	6.27	0.38
YP23_30b	100.4	6.2	690	45	144	11	355	21	47.1	3.4	286	17	35.6	2.3
YP23_31b	37	1.7	201	10	40.9	1.6	110.1	3.7	12.5	0.59	63.8	3.4	8.5	0.51
YP23_32b	15.23	0.85	77.8	4.3	14.14	0.88	32.2	1.7	3.86	0.29	22.8	1.8	3.23	0.35
YP23_33b	34.2	2.1	167.7	8.7	28.5	1.3	65	3.7	7.9	0.57	40	3.1	5.32	0.38
YP23_34b	5.46	0.34	51.7	3.2	15.03	0.87	56	3.1	8.95	0.47	62.1	3.1	9.46	0.51
YP23_35b	39.4	2.1	258	13	55.9	2.6	151	7	20.1	1.1	134.4	6.5	20.2	1
YP23_36b	34	1.6	221	11	41.4	1.7	100	4	12.82	0.71	71.6	3.5	8.31	0.54
YP23_37b	48.2	2.3	294	14	52.9	2.7	129.1	6.7	15.9	1	83.2	4.7	9.17	0.56
YP23_38b	14.9	1	115.8	8.5	28.5	2.2	91.8	7.8	13.3	1.1	84.4	5.6	11.76	0.99
YP23_39b	126.5	7	735	29	151	12	376	19	49.4	2.8	298	14	40.2	2.1
YP23_40b	87.9	6.2	524	26	102.1	6.9	274	17	36.5	2.2	226	12	28.8	1.9

Table G.4: Apatite REE element individual spot data part 3. This data is split into three tables for space reasons. Part 1 contains half the REEs (La, Ce, Pr, Nd, Sm, Eu, and Gd), part 2 contains the other half of the REEs (Tb, Dy, Ho, Er, Tm, Yb, and Lu), and **this table** (part 3) contains Mn, Sr, Y, Th, and U.

Grain	Mn (ppm)	Mn 2SE	Sr (ppm)	Sr 2SE	Y (ppm)	Y 2SE	Th (ppm)	Th 2SE	U (ppm)	U 2SE
YP1_1b	227	10	151.2	6.1	1627	66	68.1	3.6	14.85	0.71
YP1_2b	223.3	9.9	217	11	2670	120	32.8	1.5	8.19	0.5
YP1_3b	235	12	174.6	9.5	1822	69	84.3	3.7	21.4	1.2
YP1_4b	245	14	160.7	7.3	1698	81	64.6	3.5	11.34	0.68
YP1_5b	258	14	153	11	3940	210	265	17	61.1	4.2
YP1_6b	262	23	163	13	3840	180	171	11	32.6	1.8
YP1_7b	270	13	178	13	3050	170	166.3	9.7	37.7	2.2
YP1_8b	253	14	157	11	1148	61	37.5	2.1	9.15	0.66
YP1_9b	210	11	188.4	7.9	2100	100	70.9	3.6	17.61	0.8
YP1_10b	219	10	160.6	9	1020	50	31.5	1.5	7.36	0.48
YP1_11b	214	13	168	11	675	37	13.56	0.97	2.82	0.2
YP1_12b	252	14	166.9	8.5	2123	78	80.1	4.1	17.3	1
YP1_13b	257	16	151.3	9.7	3500	190	181.3	9.1	48.1	3.2
YP1_14b	249	12	159.7	7.3	1626	88	75.1	4	12.58	0.98
YP1_15b	310	35	174	20	4610	500	287	24	69.2	6
YP1_16b	244	19	165	13	1118	76	49.2	3.7	6.5	0.57
YP1_17b	232	11	148.6	8.6	1813	85	91.4	3.9	40.5	2.3
YP1_18b	270	23	188	14	999	55	43.2	2.5	4.65	0.36
YP1_19b	266	15	158	12	3540	180	332	22	78.8	5.3
YP1_20b	233	19	181	18	4340	260	257	21	57.8	6.2
YP1_21b	241	10	209.5	9.9	1012	54	63.9	3.4	4.67	0.31
YP1_22b	223	27	181	12	2340	150	54.2	5.3	12.2	1
YP1_23b	2.3	1.1	55.9	7.2	20.8	2.2	0.189	0.045	0.068	0.03
YP1_24b	221	13	401	24	386	23	0.038	0.013	0.34	0.052
YP1_25b	205	12	182	15	2180	150	39.5	3.1	9.6	0.68
YP1_26b	266	19	184	12	5210	360	253	19	59.2	5.1
YP1_27b	239	12	238	16	1213	58	20.2	1.1	3.48	0.21
YP1_28b	230	11	165	11	883	43	28.9	1.8	7.18	0.49
YP1_29b	205	16	270	27	417	27	0.168	0.052	0.253	0.05
YP1_30b	220	14	171	13	1345	94	49	3.4	12.65	0.93
YP1_31b	239	14	205	12	5150	250	180.8	7.8	37.6	2
YP1_32b	227	15	157.3	9.7	1634	85	101	12	13.8	1.1
YP1_33b	240	14	172.5	9.1	2860	140	119.1	7.3	23.1	1.6
YP1_34b	236	16	199	11	2250	140	84.7	5.2	30.9	2.2
YP1_35b	188	13	128.9	7.6	99.1	6.4	0.046	0.015	0.175	0.029
YP1_36b	241	23	258	28	2680	340	99	11	22.4	2.5
YP1_37b	233	17	204	18	3980	310	120.2	8.6	27.2	2.1
YP1_38b	280	28	218	13	3370	170	202	16	50.2	4
YP1_39b	220	10	152.2	7.2	6870	370	229	10	57.3	2.9

Continued on next page

Continued from previous page

Grain	Mn (ppm)	Mn 2SE	Sr (ppm)	Sr 2SE	Y (ppm)	Y 2SE	Th (ppm)	Th 2SE	U (ppm)	U 2SE
YP1_40b	243	12	179.9	8.9	2047	94	71.6	3.7	16.08	0.99
YP1_41b	221	13	336	22	325	16	0.066	0.018	0.348	0.046
YP1_42b	233	18	226	13	3220	160	69.8	4.3	17	1.2
YP1_43b	236	15	179	10	4340	250	90.9	6	24.2	1.8
YP1_44b	230	16	194	11	2319	97	183	12	49.3	3.7
YP1_45b	219	17	188	13	1590	110	81.1	5.4	21.3	1.7
YP1_46b	228	16	178	12	7800	560	499	42	146	14
YP1_47b	247	20	144.9	7.6	2030	110	66.8	4.1	18.3	1.5
YP1_48b	236	14	181	12	2040	130	79.7	6.4	19	1.6
YP1_49b	240	12	191	11	1136	55	44.4	2.7	9.6	0.75
YP1_50b	279	16	149.5	7.4	3570	170	229	10	33.8	1.5
YP1_51b	240	11	198	12	3510	180	69.1	3.7	17.8	1.2
YP1_52b	247	22	249	21	2990	290	49.6	3.9	8.88	0.78
YP1_53b	249	13	245	15	3640	190	202.9	8.7	57	3.1
YP1_54b	306	24	183	12	5640	320	471	38	94	10
YP1_55b	259	13	156.7	7.3	4570	160	198.6	7.9	47.3	2.4
YP1_56b	240	10	176	13	2500	130	157.2	9.7	52.2	2.6
YP1_57b	237	11	178	10	2160	120	102.2	6.9	29.8	2.4
YP1_58b	237	12	162.8	8.8	1730	95	66.8	4.4	12.5	0.84
YP1_59b	250	15	178	11	3500	260	193	18	34.1	3.2
YP1_60b	248	17	175	12	1910	100	86.4	5.6	20.9	1.6
YP1_61b	228	14	155	11	1072	60	36.1	2.1	7.43	0.52
YP1_62b	222	13	153.2	8.2	745	39	22.2	1.3	4.79	0.32
YP1_63b	247	12	150.7	9.1	763	33	22.7	1.3	4.56	0.28
YP1_64b	226	14	144.6	6.8	843	39	26.6	1.5	5.51	0.43
YP1_65b	247	12	146.2	8.1	1240	49	47.5	2.7	9.47	0.6
YP1_66b	243	16	173	10	1715	96	50.8	2.9	10.09	0.66
YP1_67b	243	15	182	12	1398	79	40.3	2.7	8.81	0.73
YP1_68b	249.2	9.6	173.8	6.1	1042	50	26.5	1.2	5.5	0.37
YP1_69b	252	13	184	10	987	45	25.4	1.4	4.82	0.31
YP1_70b	238	12	225	15	1575	56	41.4	1.7	8.38	0.55
YP1_71b	243	12	178	11	3340	190	116.5	7.7	27.3	2.2
YP1_72b	247	12	180.9	9.3	1068	53	26.9	1.4	5.69	0.4
YP1_73b	256	23	244	22	4350	300	220	13	81.7	6.7
YP1_74b	236	13	193	12	5150	280	248	12	70.4	3.8
YP1_75b	199	12	218	11	468	27	0.46	0.12	0.82	0.1
YP1_76b	206.4	9.4	295	16	381	21	0.348	0.086	0.62	0.12
YP1_77b	207	10	404	33	274	15	0.298	0.041	0.385	0.068
YP1_78b	211	11	291	13	474	23	0.57	0.11	0.617	0.098
YP1_79b	255	17	211	15	5940	420	369	28	87	6.9
YP1_80b	248	22	199	20	2360	220	73.2	5.9	16.2	1.5
YP4_1b	459	22	485	22	134.8	5.8	18.59	0.8	9.58	0.52
YP4_2b	497	25	494	21	136	6	19.5	1	10.31	0.67

Continued on next page

Continued from previous page

Grain	Mn (ppm)	Mn 2SE	Sr (ppm)	Sr 2SE	Y (ppm)	Y 2SE	Th (ppm)	Th 2SE	U (ppm)	U 2SE
YP4_3b	430	29	341	18	260	15	0.789	0.054	3.97	0.26
YP4_4b	770	31	584	29	262	11	11.44	0.51	3.78	0.26
YP4_5b	775	34	602	44	224	10	10.66	0.53	3.13	0.18
YP4_6b	861	38	306	15	1030	45	27	1.3	10.31	0.54
YP4_7b	694	33	593	35	119.9	7.9	6.87	0.48	1.89	0.16
YP4_8b	783	40	602	36	213.9	9.7	13.06	0.63	3.99	0.23
YP4_9b	726	42	532	26	189	13	14.45	0.76	4.12	0.26
YP4_10b	690	34	551	24	239	12	15.8	0.76	4.82	0.34
YP4_11b	850	42	305	16	1190	47	35.6	1.8	13.86	0.79
YP4_12b	804	41	593	35	243	13	11.29	0.71	3.4	0.25
YP4_13b	783	38	613	36	252	14	11.96	0.64	3.48	0.24
YP4_14b	798	47	600	27	296	15	13.65	0.71	3.46	0.23
YP4_15b	707	43	573	28	247	12	12.22	0.61	3.9	0.24
YP4_16b	511	26	270	17	24.7	1.4	0.076	0.017	4.14	0.28
YP4_17b	566	31	273	15	2.56	0.29	0.092	0.024	2.77	0.2
YP4_18b	445	24	281	15	29.4	1.3	0.106	0.022	6.1	0.36
YP4_19b	818	54	592	31	322	16	14.85	0.78	3.89	0.26
YP4_20b	858	45	316	18	1254	61	39.2	2.3	14.25	0.85
YP4_21b	577	26	537	29	150.3	6.3	20.9	1	13.56	0.77
YP4_22b	747	43	593	34	214	11	10.85	0.57	3.28	0.2
YP4_23b	784	59	582	27	241	10	11.2	0.56	3.84	0.21
YP4_24b	805	37	590	27	295	15	12.55	0.74	5.02	0.36
YP4_25b	776	32	645	36	289	13	12.25	0.66	3.67	0.31
YP4_26b	624	28	532	25	144.4	6.9	21.8	1.3	17.7	1.1
YP4_27b	447	21	294	13	38.3	2.3	1.58	0.54	11.3	0.51
YP4_28b	448	25	291	18	185	12	0.457	0.066	19.6	1.6
YP4_29b	399	20	254	11	62.5	3.4	0.232	0.03	12.9	0.82
YP4_30b	768	43	596	36	224	12	10.22	0.58	3.22	0.23
YP4_31b	806	34	639	32	189.6	8.8	9.39	0.47	2.91	0.21
YP4_32b	737	34	538	33	595	36	14.98	0.94	27.6	2.2
YP4_33b	820	44	587	31	284	20	12.85	0.78	3.29	0.22
YP4_34b	778	31	576	33	183.8	8.2	13.45	0.75	4	0.25
YP4_35b	352	17	252	11	9.51	0.69	0.064	0.02	3.72	0.26
YP4_36b	408	19	274	14	42.4	2.2	0.217	0.038	9.47	0.6
YP4_37b	592	26	528	27	101.9	8	7.18	0.53	2.88	0.21
YP4_38b	680	32	558	30	168.6	7	12.63	0.55	4.87	0.33
YP4_39b	400	17	255	13	10.59	0.6	0.022	0.012	1.035	0.096
YP4_40b	350	13	5440	230	229	10	36.3	1.6	3.07	0.21
YP8_1b	771	34	581	27	293	12	15.31	0.69	4.05	0.18
YP8_2b	880	36	631	32	331	14	14.09	0.68	3.18	0.17
YP8_3b	749	32	582	27	258	15	13.41	0.56	3.65	0.17
YP8_4b	730	37	543	25	219	14	37.8	2.7	10.96	0.78
YP8_5b	652	27	527	25	127.1	5.8	20.3	1.2	8.15	0.5

Continued on next page

Continued from previous page

Grain	Mn (ppm)	Mn 2SE	Sr (ppm)	Sr 2SE	Y (ppm)	Y 2SE	Th (ppm)	Th 2SE	U (ppm)	U 2SE
YP8_6b	820	41	601	23	240	11	13.03	0.6	3.87	0.18
YP8_7b	786	50	584	26	285	14	14.45	0.73	3.73	0.22
YP8_8b	670	35	556	25	116.7	6.1	8.45	0.54	3.51	0.29
YP8_9b	839	35	611	26	203.1	6.9	6.94	0.26	2.3	0.13
YP8_10b	725	30	574	26	206	14	12.09	0.85	3.91	0.29
YP8_11b	692	34	560	34	184	20	13.4	1.2	4.09	0.33
YP8_12b	763	36	574	29	232	9.6	16.29	0.74	5.78	0.37
YP8_13b	675	34	573	31	231	12	19.2	0.96	7.11	0.44
YP8_14b	382	21	302	16	1171	81	138.3	9.3	66.2	4.4
YP8_15b	377	23	303	17	703	75	100.5	9.8	50.3	4.8
YP8_16b	328	14	398	20	131.1	6.6	44.3	2.9	11.93	0.73
YP8_17b	352	27	399	22	175	18	77	12	18.2	3
YP8_18b	280	19	421	23	147	23	70	12	14.6	1.3
YP8_19b	461	19	356	16	665	23	42.1	1.8	69.8	3.4
YP8_20b	444	20	347	15	492	20	31.9	1.4	50.3	2.1
YP8_21b	380	21	206	14	1510	100	85	13	35.2	5.2
YP8_22b	970	100	559	33	213	12	14.33	0.85	6.97	0.84
YP8_23b	691	28	566	31	90.5	4.1	3.31	0.22	1.35	0.12
YP8_24b	674	35	552	29	88.2	4.7	3.36	0.24	1.3	0.13
YP8_25b	749	28	580	23	215.6	7.5	12.16	0.45	3.89	0.2
YP8_26b	331	14	339	15	1751	87	13.2	1.1	21.9	1.3
YP8_27b	262	12	320	17	1073	52	8.78	0.54	15.97	0.84
YP8_28b	252.6	7.3	327	14	937	40	10.46	0.52	17.62	0.8
YP8_29b	276	12	340	19	1285	47	14.84	0.79	23.33	0.99
YP8_30b	301	12	331	16	1662	64	14.6	0.62	25.9	1.2
YP8_31b	274	15	332	19	1312	51	17.3	1.1	26	1.3
YP8_36b	240	11	395	23	518	32	56.1	2.8	24.7	1.2
YP8_37b	375	17	425	20	292	35	108	16	24.8	1.9
YP8_38b	850	33	309	11	1620	100	57.7	5.5	19.3	1.7
YP8_39b	352	16	314	13	77	5.8	0.097	0.024	2.29	0.16
YP8_40b	341	19	256	10	569	24	3.43	0.18	6.09	0.32
YP8_41b	471	17	462	17	382	12	47.1	1.9	47.6	1.9
YP8_42b	496	24	456	22	761	42	34.7	2.9	70.8	4
YP8_43b	621	25	238	12	1273	51	35.9	1.8	34	1.8
YP8_44b	402	20	315	16	965	48	77.3	3.8	75.6	4
YP8_45b	269	10	136.9	6.7	481	19	8.9	0.36	36.4	1.6
YP8_46b	381	18	226.1	9.7	498	24	167.2	8	76.4	3.6
YP8_47b	241	13	467	25	965	40	0.731	0.059	1.32	0.11
YP8_48b	442	22	367	16	518	22	300	11	78.1	3.5
YP8_49b	430	20	702	28	268	12	45.1	1.9	10.88	0.45
YP8_50b	433	25	726	43	203.4	9.1	25.4	1.1	6.41	0.35
YP8_51b	399	20	669	31	181.8	8.2	26.6	1.5	6.45	0.41
YP6_1b	496	21	805	32	454	17	11.96	0.5	3.36	0.21

Continued on next page

Continued from previous page

Grain	Mn (ppm)	Mn 2SE	Sr (ppm)	Sr 2SE	Y (ppm)	Y 2SE	Th (ppm)	Th 2SE	U (ppm)	U 2SE
YP6_2b	519	36	793	39	419	20	9.53	0.41	2.52	0.17
YP6_3b	513	19	835	35	470	20	10.41	0.52	2.74	0.18
YP6_4b	776	30	763	26	485	20	12.33	0.41	3.08	0.17
YP6_5b	795	26	735	32	463	15	12.03	0.68	2.82	0.15
YP6_6b	789	36	617	37	251	11	11.96	0.59	3.57	0.22
YP6_7b	757	38	581	26	251	15	13.27	0.62	3.58	0.22
YP6_8b	308	14	1109	61	335	16	30.4	1.6	13.55	0.78
YP6_9b	307	17	1090	44	331	14	28.1	1.4	13.2	0.77
YP6_10b	314	12	1123	40	328	11	24.9	1	12.06	0.56
YP6_11b	453	21	852	50	299	13	3.75	0.21	1.27	0.1
YP6_12b	454	24	812	48	328	15	4.18	0.35	1.46	0.14
YP6_13b	480	26	374	17	65.4	3.7	0.631	0.07	5.76	0.31
YP6_14b	491	23	379	17	73.4	3.8	0.379	0.061	8.27	0.36
YP6_15b	471	23	364	17	97.2	4	0.968	0.089	12.45	0.66
YP6_16b	433	27	288	14	745	36	28.9	1.3	13.43	0.75
YP6_17b	382	21	265	17	757	30	39.9	2	18.57	0.95
YP6_18b	424	24	276	15	651	29	26.8	1.3	12.11	0.7
YP6_19b	175.7	7.6	355	18	288	15	9.34	0.53	18.8	1.1
YP6_20b	173.9	9.7	427	27	82.7	4.9	0.996	0.097	2.53	0.19
YP6_21b	256	12	187	11	1513	69	0.432	0.047	7.93	0.4
YP6_22b	229	13	186	9.5	1476	66	0.47	0.053	7.79	0.52
YP6_23b	218	11	199.1	9.5	1252	60	0.351	0.041	6.42	0.35
YP6_24b	266	21	723	61	62.6	7	10.6	1.4	20.6	1.5
YP6_25b	264	11	672	37	202	20	73.4	9.1	76	7.1
YP6_26b	256	13	649	34	66	3.9	15.19	0.9	29.1	1.3
YP6_27b	540	26	410	16	486	36	23.9	1.9	43.8	4
YP6_28b	509	20	439	17	182.3	9.1	5.05	0.46	14	1.5
YP6_29b	590	37	441	14	182.7	9.5	3.42	0.19	10.12	0.47
YP6_30b	556	58	436	30	181	15	4.07	0.53	10.4	1.1
YP6_31b	265	11	413	19	352	17	3.99	0.27	16.1	1.1
YP6_32b	385	23	253	15	2780	140	7.63	0.46	26	1.2
YP6_33b	821	39	311	18	1283	52	212.6	7.9	42.2	2
YP6_34b	388	20	426	22	667	31	334	13	125.6	5.5
YP6_35b	259	12	256	14	838	38	24.4	1.2	93.4	4.9
YP6_36b	509	24	406	15	90.1	5.2	2.65	0.39	20.61	0.89
YP6_37b	369	15	311	17	1015	46	91.1	8.5	101	9.1
YP6_38b	4.43	0.66	138.5	9	55.8	2.7	1.56	0.12	0.446	0.043
YP6_39b	675	33	281	16	823	33	3.64	0.23	1.31	0.13
YP6_40b	362	17	383	14	134.7	8.1	31.9	1.7	10.03	0.66
YP15_1b	217.8	9.8	1427	82	143.7	5.4	NA	Below LOD	1.41	0.12
YP15_2b	315	15	175	12	191.9	8.8	0.133	0.035	5.47	0.4
YP15_3b	432	21	225	15	948	57	4.47	0.52	25.6	1.9

Continued on next page

Continued from previous page

Grain	Mn (ppm)	Mn 2SE	Sr (ppm)	Sr 2SE	Y (ppm)	Y 2SE	Th (ppm)	Th 2SE	U (ppm)	U 2SE
YP15_4b	354	17	70.1	3.2	1332	52	3.26	0.23	25.9	1.3
YP15_5b	220	14	592	36	704	45	4.25	0.34	15.9	1
YP15_6b	33.4	1.8	4970	240	460	20	6.51	0.97	NA	NA
YP15_7b	1102	41	203	11	1355	56	0.081	0.029	19.75	0.89
YP15_8b	225.5	9.8	608	30	78.5	4	0.13	0.032	3.83	0.27
YP15_9b	872	26	780	35	520	21	46.8	1.9	13.95	0.75
YP15_10b	649	24	332	13	888	34	0.204	0.045	23.4	1.3
YP15_11b	656	27	220	13	470	26	7.55	0.55	11.28	0.77
YP15_12b	247	12	380	19	727	45	25.3	1.7	7.67	0.57
YP15_13b	467	32	87.5	5.4	1415	77	39.3	2.2	13.96	0.76
YP15_14b	423	26	406	29	60.3	3.4	0.81	0.11	1	0.14
YP15_15b	1105	50	50.4	3.5	2151	83	1.52	0.15	4.09	0.28
YP15_16b	1300	140	125	13	1124	96	0.63	0.19	3.2	0.6
YP15_17b	3860	190	40.5	1.7	990	29	0.6	0.11	7.8	1.1
YP15_18b	440	28	445	28	233	13	60.9	3.7	31.8	2
YP15_19b	456	16	244	11	498	18	0.263	0.041	14.35	0.74
YP15_20b	958	46	441	22	1081	50	4.03	0.26	4.03	0.24
YP15_21b	321	16	143.3	6.6	294	13	0.084	0.02	1.007	0.096
YP15_22b	634	35	412	30	419	22	218	20	48.8	3.3
YP15_23b	3590	430	141.1	9.9	2080	180	2.76	0.29	31.6	2.7
YP15_24b	297	14	338	13	12.77	0.95	0.014	0.011	0.113	0.032
YP15_25b	362	19	225.2	7.9	1144	43	0.071	0.024	12.21	0.76
YP15_26b	420	23	537	25	419	19	0.115	0.028	0.952	0.074
YP15_27b	322	16	285	18	473	18	0.044	0.016	3.02	0.24
YP15_28b	403	20	766	37	43.6	1.9	0.084	0.024	1.38	0.1
YP15_29b	508	26	1487	74	180.2	8.6	39.2	1.9	10.23	0.61
YP15_30b	688	39	309	21	475	24	216	14	26.7	1.9
YP15_31b	548	27	77.1	4.5	1263	51	2.5	0.2	5.83	0.49
YP15_32b	1798	87	137.7	7.9	1288	49	2.88	0.16	29.1	1.7
YP15_33b	545	30	1194	95	557	28	5.76	0.29	2.41	0.19
YP15_34b	374	15	299	14	96.6	3.9	6.7	0.31	11.13	0.5
YP15_35b	392	17	297	13	549	26	0.04	0.015	3.28	0.23
YP15_36b	521	28	450	32	582	35	10.45	0.78	3.46	0.4
YP15_37b	1340	120	140.9	7	695	34	0.682	0.075	12.26	0.86
YP15_38b	739	31	555	26	284	15	13.47	0.82	3.24	0.3
YP15_39b	287	19	491	29	601	28	30.5	1.9	6.3	0.53
YP15_40b	643	30	162.5	9.3	2570	130	3.58	0.22	0.647	0.07
YP21_1b	684	41	571	41	623	42	29.4	1.6	36.7	2.6
YP21_2b	1571	87	234	14	659	33	15.2	1	4.84	0.39
YP21_3b	388	25	315	15	2030	110	91.6	4.9	19.4	1.2
YP21_4b	922	58	139.8	7.8	7.57	0.5	NA	Below LOD	0.073	0.017

Continued on next page

Continued from previous page

Grain	Mn (ppm)	Mn 2SE	Sr (ppm)	Sr 2SE	Y (ppm)	Y 2SE	Th (ppm)	Th 2SE	U (ppm)	U 2SE
YP21_5b	1206	61	151.8	8.6	7.36	0.86	NA	Below LOD	0.119	0.02
YP21_6b	17.4	1.7	1082	60	944	53	0.84	0.11	0.08	0.019
YP21_7b	412	33	230	15	305	20	3.4	0.3	12.3	0.85
YP21_8b	412	31	716	44	484	29	8.45	0.56	1.47	0.13
YP21_9b	486	32	391	25	272	15	104.6	5.8	119.8	7.2
YP21_10b	840	110	187	15	1840	130	5.66	0.55	13.22	0.96
YP21_11b	727	45	222.6	8.8	1030	40	NA	Below LOD	7.3	0.35
YP21_12b	351	15	287	11	50.9	5.6	1.52	0.25	1.68	0.25
YP21_13b	379	18	531	26	93.2	3.5	0.018	0.01	1.08	0.1
YP21_14b	2380	130	118.7	6.1	2230	190	3.88	0.37	25.9	2.1
YP21_15b	3330	160	95.5	4.9	3670	160	20.2	1.3	22.3	1.5
YP21_16b	3270	170	99.5	6.3	3380	140	12.41	0.93	20.5	1.2
YP21_17b	5630	200	66.4	3.1	1968	76	12.54	0.58	22.2	1
YP21_18b	162.2	9.5	1136	62	340	11	0.0153	0.0085	0.029	0.012
YP21_19b	537	26	171.2	9	1360	64	7.51	0.43	8.39	0.46
YP21_20b	916	50	6580	330	646	32	1.366	0.094	0.033	0.013
YP21_21b	1920	79	471	25	1661	71	2.63	0.17	3.18	0.21
YP21_22b	398	27	545	38	766	33	8.07	0.41	38.1	1.7
YP21_23b	650	170	449	61	967	63	51.9	5.1	2.53	0.67
YP21_24b	1910	110	164	10	1980	110	3.88	0.38	18.9	1.4
YP21_25b	423	22	278	10	75.8	6.1	0.172	0.032	6.43	0.47
YP21_26b	1561	82	154.4	7.8	2170	110	0.0102	0.007	7.9	0.57
YP21_27b	518	29	237	13	488	29	1.08	0.45	17.6	1.6
YP21_28b	254	15	375	28	764	41	7.23	0.85	21.3	1.4
YP21_29b	256	17	242	18	44.8	2.9	0.068	0.018	3.09	0.23
YP21_30b	1056	45	143.1	8	2470	110	14.56	0.98	25.2	1.4
YP23_01b	209.4	9.4	244	14	533	31	1.22	0.1	9.85	0.68
YP23_02b	347	30	278	18	182	13	0.63	0.1	6	0.7
YP23_03b	449	23	64	4.1	1274	59	22.9	2.7	7.82	0.56
YP23_04b	2000	100	203	11	2030	120	7.31	0.46	9.03	0.49
YP23_05b	200.8	7.8	218	12	87.9	3.4	0.129	0.029	23.8	1.2
YP23_06b	69	4.7	383	24	343	18	0.373	0.048	0.018	0.01
YP23_07b	735	69	116	12	2180	190	355	91	84.8	6.4
YP23_08b	263	17	149	11	681	34	8.7	1.8	32.4	3.1
YP23_09b	396	18	204	11	474	18	0.021	0.011	1.35	0.1
YP23_10b	428	40	284	16	691	45	5.04	0.41	5.54	0.49
YP23_11b	386	38	254	18	815	53	1.2	0.11	14.7	1.2
YP23_12b	33.2	2.2	416	23	193.7	9	NA	Below LOD	0.027	0.012
YP23_13b	896	47	240	15	5940	390	120.2	8.1	165	12
YP23_14b	304	12	6490	350	314	13	58.5	3.7	11.19	0.8

Continued on next page

Continued from previous page

Grain	Mn (ppm)	Mn 2SE	Sr (ppm)	Sr 2SE	Y (ppm)	Y 2SE	Th (ppm)	Th 2SE	U (ppm)	U 2SE
YP23_15b	630	32	97.4	4.3	1486	42	1.105	0.082	14.03	0.64
YP23_16b	1124	58	501	25	1195	53	13.25	0.79	3.04	0.21
YP23_17b	1583	57	261	16	2154	87	14.1	0.78	40.9	2.8
YP23_18b	22.8	1.8	1082	56	1060	150	0.413	0.057	0.062	0.022
YP23_19b	466	20	348	16	546	19	2.78	0.17	6.89	0.42
YP23_20b	156.5	8.9	134.8	8.6	724	41	0.797	0.076	10.92	0.86
YP23_21b	267	19	513	39	458	26	0.243	0.053	5.83	0.42
YP23_22b	204.7	6.8	81.1	3.2	192.5	5.9	0.059	0.019	1.41	0.12
YP23_23b	944	37	204.3	8.6	1307	53	2.05	0.27	118	21
YP23_24b	6200	260	58.8	2.9	2497	77	2.98	0.17	66.2	3.5
YP23_25b	330	15	156.1	8.6	110.6	5.6	0.22	0.033	8.42	0.55
YP23_26b	312	12	251	17	657	33	0.082	0.024	30.3	3.4
YP23_27b	937	35	68.6	3.6	998	36	1.342	0.085	11.27	0.57
YP23_28b	236	11	97.7	5.9	1260	58	7.23	0.49	43.6	3
YP23_29b	399	16	85	3.3	436	14	0.245	0.038	20.79	0.9
YP23_30b	1371	85	187	16	3230	210	25.9	2.2	49.5	3.9
YP23_31b	358	14	191.5	8.5	931	36	6.43	0.34	29.6	1.1
YP23_32b	656	52	2570	150	391	17	16.23	0.81	12.99	0.74
YP23_33b	606	25	17	1	737	29	16.97	0.76	5.03	0.34
YP23_34b	383	15	235.7	8.9	447	16	0.023	0.012	0.218	0.035
YP23_35b	372	20	191	8.7	1518	69	13.37	0.54	15.52	0.93
YP23_36b	288	14	834	54	1018	42	2.36	0.15	2.41	0.18
YP23_37b	1188	63	67.3	3.1	1493	63	0.446	0.054	5.56	0.32
YP23_38b	398	23	285	16	810	51	0.455	0.079	5.65	0.71
YP23_39b	1620	120	184.7	8	3850	180	26.5	1.6	39.7	2.2
YP23_40b	566	26	141.4	9.1	2710	130	14.7	0.96	16.4	1.2

Bibliography

Abdullin, F., J. Solé, L. Solari, V. Shchepetilnikova, J. J. Meneses-Rocha, N. Pavlinova, and A. Rodríguez-Trejo (2016). "Single-grain apatite geochemistry of Permian–Triassic granitoids and Mesozoic and Eocene sandstones from Chiapas, southeast Mexico: implications for sediment provenance". In: *International Geology Review* 58.9, pp. 1132–1157.

Alexeiev, D., H. Cook, V. Buvtyshkin, and L. Golub (2009). "Structural evolution of the Ural-Tian Shan junction: a view from Karatau ridge, South Kazakhstan". In: *Comptes Rendus Geoscience* 341, pp. 287–297.

Allen, M. B., A. M. C. Şengör, and B. A. Natal'In (1995). "Junggar, Turfan and Alakol basins as Late Permian to ?Early Triassic extensional structures in a sinistral shear zone in the Altaid orogenic collage, Central Asia". In: *Journal of the Geological Society* 152.2, pp. 327–338.

Allen, M., G. Alsop, and V. Zhemchuzhnikov (2001). "Dome and basin refolding and transpressive inversion along the Karatau Fault System, southern Kazakstan". In: *Journal of the Geological Society* 158.1, pp. 83–95.

Allen, M. B., L. Anderson, R. C. Searle, and M. Buslov (2006). "Oblique rift geometry of the West Siberian Basin: tectonic setting for the Siberian flood basalts". In: *Journal of the Geological Society* 163.6, pp. 901–904.

Allen, M. B. and S. J. Vincent (1997). "Fault reactivation in the Junggar region, northwest China: the role of basement structures during Mesozoic-Cenozoic compression". In: *Journal of the Geological Society* 154.1, pp. 151–155.

Andersen, T., M. Kristoffersen, and M. A. Elburg (2016). "How far can we trust provenance and crustal evolution information from detrital zircons? A South African case study". In: *Gondwana Research* 34.Supplement C, pp. 129–148.

Anderson, A. J., K. V. Hodges, and M. C. van Soest (2017). "Empirical constraints on the effects of radiation damage on helium diffusion in zircon". In: *Geochimica et Cosmochimica Acta* 218, pp. 308–322.

Armistead, S. E., A. S. Collins, J. L. Payne, J. D. Foden, B. De Waele, E. Shaji, and M. Santosh (2017). "A re-evaluation of the Kumta Suture in western peninsular India and its extension into Madagascar". In: *Journal of Asian Earth Sciences*.

Ault, A. K. and R. M. Flowers (2012). "Is apatite U–Th zonation information necessary for accurate interpretation of apatite (U–Th)/He thermochronometry data?" In: *Geochimica et Cosmochimica Acta* 79, pp. 60–78.

Avouac, J. P., P. Tapponnier, M. Bai, H. You, and G. Wang (1993). "Active thrusting and folding along the northern Tien Shan and Late Cenozoic rotation of the Tarim relative to Dzungaria and Kazakhstan". In: *Journal of Geophysical Research: Solid Earth* 98.B4, pp. 6755–6804.

Bande, A., E. R. Sobel, A. Mikolaichuk, A. Schmidt, and D. F. Stockli (2017). "Exhumation history of the western Kyrgyz Tien Shan: Implications for intramontane basin formation". In: *Tectonics* 36.1, pp. 163–180.

Barbarand, J., A. Carter, I. Wood, and T. Hurford (2003). "Compositional and structural control of fission-track annealing in apatite". In: *Chemical Geology* 198.1–2 (1-2), pp. 107–137.

Bazhenov, M. L., N. M. Levashova, K. E. Degtyarev, R. Van der Voo, A. V. Abrajevitch, and P. J. A. McCausland (2012). "Unraveling the early–middle Paleozoic paleogeography of Kazakhstan on the basis of Ordovician and Devonian paleomagnetic results". In: *Gondwana Research* 22.3, pp. 974–991.

Bell, E. A., P. Boehnke, T. M. Harrison, and M. M. Wielicki (2018). "Mineral inclusion assemblage and detrital zircon provenance". In: *Chemical Geology* 477, pp. 151–160.

Belousova, E. A., W. L. Griffin, S. Y. O'Reilly, and N. I. Fisher (2002). "Apatite as an indicator mineral for mineral exploration: trace-element compositions and their relationship to host rock type". In: *Journal of Geochemical Exploration* 76.1, pp. 45–69.

Beucher, R., R. W. Brown, S. Roper, F. Stuart, and C. Persano (2013). "Natural age dispersion arising from the analysis of broken crystals: Part II. Practical application to apatite (U–Th)/He thermochronometry". In: *Geochimica et Cosmochimica Acta* 120, pp. 395–416.

Biske, Y. S. and R. Seltmann (2010). "Paleozoic Tian-Shan as a transitional region between the Rheic and Urals-Turkestan oceans". In: *Gondwana Research* 17.2, pp. 602–613.

Blackburn, T., S. A. Bowring, B. Schoene, K. Mahan, and F. Dudas (2011). "U-Pb thermochronology: creating a temporal record of lithosphere thermal evolution". In: *Contributions to Mineralogy and Petrology* 162.3, pp. 479–500.

Briggs, S. M., A. Yin, C. E. Manning, Z.-L. Chen, and X.-F. Wang (2009). "Tectonic development of the southern Chinese Altai Range as determined by structural geology, thermobarometry, 40Ar/39Ar thermochronology, and Th/Pb ionmicroprobe monazite geochronology". In: *Geological Society of America Bulletin* 121.9-10, pp. 1381–1393.

Briggs, S. M., A. Yin, C. E. Manning, Z.-L. Chen, X.-F. Wang, and M. Grove (2007). "Late Paleozoic tectonic history of the Ertix Fault in the Chinese Altai and its implications for the development of the Central Asian Orogenic System". In: *Geological Society of America Bulletin* 119.7-8, pp. 944–960.

Brown, R. W., R. Beucher, S. Roper, C. Persano, F. Stuart, and P. Fitzgerald (2013). "Natural age dispersion arising from the analysis of broken crystals. Part I: Theoretical basis and implications for the apatite (U–Th)/He thermochronometer". In: *Geochimica et Cosmochimica Acta* 122, pp. 478–497.

Bruand, E., M. Fowler, C. Storey, and J. Darling (2017). "Apatite trace element and isotope applications to petrogenesis and provenance". In: *Americal Mineralogist* 102.1, p. 75.

Bruand, E., C. Storey, and M. Fowler (2016). "An apatite for progress: Inclusions in zircon and titanite constrain petrogenesis and provenance". In: *Geology* 44.2, pp. 91–94.

Bruguier, O., J. R. Lancelot, and J. Malavieille (1997). "U–Pb dating on single detrital zircon grains from the Triassic Songpan–Ganze flysch (Central China): provenance and tectonic correlations". In: *Earth and Planetary Science Letters* 152.1, pp. 217–231.

Brunet, M.-F., A. V. Ershov, M. V. Korotaev, V. N. Melikhov, E. Barrier, D. O. Mordvintsev, and I. P. Sidorova (2017). "Late Palaeozoic and Mesozoic evolution of the Amu Darya Basin (Turkmenistan, Uzbekistan)". In: *Geological Society, London, Special Publications* 427.1, pp. 89–144.

Buckman, S. and J. Aitchison (2004). "Tectonic evolution of Palaeozoic terranes in West Junggar, Xinjiang, NW China". In: *Geological Society, London, Special Publications* 226, pp. 101–129.

Bullen, M., D. Burbank, J. Garver, and K. Abdrakhmatov (2001). "Late Cenozoic tectonic evolution of the northwestern Tien Shan: New age estimates for the initiation of mountain building". In: *Geological Society of America Bulletin* 113 (12), pp. 1544–1559.

Burtman, V. (1980). "Faults of Middle Asia". In: *American Journal of Science* 280, pp. 725–744.

Burtner, R. L., A. Nigrini, and R. A. Donelick (1994). "Thermochronology of Lower Cretaceous source rocks in the Idaho-Wyoming thrust belt". In: *AAPG bulletin* 78.10, pp. 1613–1636.

Buslov, M. M. (2011). "Tectonics and geodynamics of the Central Asian Foldbelt: the role of Late Paleozoic large-amplitude strike-slip faults". In: *Russian Geology and Geophysics* 52 (1), pp. 52–71.

Buslov, M. M., Y. Fujiwara, K. Iwata, and N. N. Semakov (2004). "Late Paleozoic-Early Mesozoic Geodynamics of Central Asia". In: *Gondwana Research* 7 (3), pp. 791–808.

Buslov, M. M., I. Y. Saphonova, T. Watanabe, O. T. Obut, Y. Fujiwara, K. Iwata, N. N. Semakov, Y. Sugai, L. V. Smirnova, and A. Y. Kazansky (2001). "Evolution of the Paleo-Asian Ocean (Altai-Sayan Region, Central Asia) and collision of possible Gondwana-derived terranes with the southern marginal part of the Siberian continent". In: *Geosciences Journal* 5.3, pp. 203–224.

Campbell, G., R. Walker, K. Abdrakhmatov, J. Schwenninger, J. Jackson, J. Elliott, and A. Copley (2013). "The Dzhungarian fault: Late Quaternary tectonics and slip rate of a major right-lateral strike-slip fault in the northern Tien Shan region". In: *Journal of Geophysical Research: Solid Earth* 118.10, pp. 5681–5698.

Carlson, W. D., R. A. Donelick, and R. A. Ketcham (1999). "Variability of apatite fission-track annealing kinetics: I. Experimental results". In: *American Mineralogist* 84.9, p. 1213.

Carpena, J., J.-R. Kienast, K. Ouzegane, and C. Jehanno (1988). "Evidence of the contrasted fission-track clock behavior of the apatites from In Ouzzal carbonatites (northwest Hoggar): The low-temperature thermal history of an Archean basement". In: *Geological Society of America Bulletin* 100.8, pp. 1237–1243.

Carpena, J. and J.-L. Lacout (2010). "Thermal annealing of fission tracks in synthetic apatites". In: *Nuclear Instruments and Methods in Physics Research Section B: Beam Interactions with Materials and Atoms* 268.19, pp. 3191–3194.

Carrapa, B., P. DeCelles, P. Reiners, G. Gehrels, and M. Sudo (2009). "Apatite triple dating and white mica 40Ar/39Ar thermochronology of syntectonic detritus in the Central Andes: A multiphase tectonothermal history". In: *Geology* 37.5, pp. 407–410.

Cawood, P. A., A. A. Nemchin, M. Freeman, and K. Sircombe (2003). "Linking source and sedimentary basin: Detrital zircon record of sediment flux along a modern river system and implications for provenance studies". In: *Earth and Planetary Science Letters* 210.1, pp. 259–268.

Charvet, J., L. Shu, S. Laurent-Charvet, B. Wang, M. Faure, D. Cluzel, Y. Chen, and K. De Jong (2011). "Palaeozoic tectonic evolution of the Tianshan belt, NW China". In: *Science China Earth Sciences* 54.2, pp. 166–184.

Chen, J.-F., B.-F. Han, J.-Q. Ji, L. Zhang, Z. Xu, G.-Q. He, and T. Wang (2010). "Zircon U–Pb ages and tectonic implications of Paleozoic plutons in northern West Junggar, North Xinjiang, China". In: *Lithos* 115.1, pp. 137–152.

Cherniak, D. J. (2000). "Rare earth element diffusion in apatite". In: *Geochimica et Cosmochimica Acta* 64.22, pp. 3871–3885.

Cherniak, D. J., W. A. Lanford, and F. J. Ryerson (1991). "Lead diffusion in apatite and zircon using ion implantation and Rutherford Backscattering techniques". In: *Geochimica et Cosmochimica Acta* 55.6, pp. 1663–1673.

Chew, D. M. and R. Donelick (2012). "Chapter 12: Combined apatite fission track and U-Pb dating by LA-ICP-MS and its application in apatite provenance analysis". In: *Mineralogical Association of Canada Short Course 42*.

Chew, D. M., J. A. Petrus, and B. S. Kamber (2014a). "U–Pb LA–ICPMS dating using accessory mineral standards with variable common Pb". In: *Chemical Geology* 363, pp. 185–199.

Chew, D. M., M. G. Babechuk, N. Cogné, C. Mark, G. J. O'Sullivan, I. A. Henrichs, D. Doepke, and C. A. McKenna (2016). "(LA,Q)-ICPMS trace-element analyses of Durango and McClure Mountain apatite and implications for making natural LA-ICPMS mineral standards". In: *Chemical Geology* 435, pp. 35–48.

Chew, D. M., R. A. Donelick, M. B. Donelick, B. S. Kamber, and M. J. Stock (2014b). "Apatite Chlorine Concentration Measurements by LA-ICP-MS". In: *Geostandards and Geoanalytical Research* 38.1, pp. 23–35.

Chew, D. M. and R. A. Spikings (2015). "Geochronology and Thermochronology Using Apatite: Time and Temperature, Lower Crust to Surface". In: *Elements* 11.3, pp. 189–194.

Chew, D. M., P. J. Sylvester, and M. N. Tubrett (2011). "U–Pb and Th–Pb dating of apatite by LA-ICPMS". In: *Chemical Geology* 280.1–2, pp. 200–216.

Choulet, F., Y. Chen, B. Wang, M. Faure, D. Cluzel, J. Charvet, W. Lin, and B. Xu (2011). "Late Paleozoic paleogeographic reconstruction of Western Central Asia based upon paleomagnetic data and its geodynamic implications". In: *Journal of Asian Earth Sciences* 42.5, pp. 867–884.

Choulet, F., M. Faure, D. Cluzel, Y. Chen, W. Lin, and B. Wang (2012a). "From oblique accretion to transpression in the evolution of the Altaid collage: New insights from West Junggar, northwestern China". In: *Gondwana Research* 21.2–3, pp. 530–547.

Choulet, F., M. Faure, D. Cluzel, Y. Chen, W. Lin, B. Wang, and B.-m. Jahn (2012b). "Architecture and evolution of accretionary orogens in the Altaids collage: The early Paleozoic West Junggar (NW China)". In: *American Journal of Science* 312.10, pp. 1098–1145.

Choulet, F., M. Faure, D. Cluzel, Y. Chen, W. Lin, B. Wang, and B. Xu (2016). "Toward a unified model of Altaids geodynamics: Insight from the Palaeozoic polycyclic evolution of West Junggar (NW China)". In: *Science China Earth Sciences* 59.1, pp. 25–57.

Chu, M.-F., K.-L. Wang, W. L. Griffin, S.-L. Chung, S. Y. O'Reilly, N. J. Pearson, and Y. Iizuka (2009). "Apatite Composition: Tracing Petrogenetic Processes in Transhimalayan Granitoids". In: *Journal of Petrology* 50.10, pp. 1829–1855.

Cochrane, R., R. A. Spikings, D. Chew, J.-F. Wotzlaw, M. Chiaradia, S. Tyrrell, U. Schaltegger, and R. Van der Lelij (2014). "High temperature (>350°C) ther-

mochronology and mechanisms of Pb loss in apatite". In: *Geochimica et Cosmochimica Acta* 127, pp. 39–56.

Cunningham, D. (2013). "Mountain building processes in intracontinental oblique deformation belts: Lessons from the Gobi Corridor, Central Asia". In: *Journal of Structural Geology* 46.0, pp. 255–282.

Cunningham, D., L. Owen, L. Snee, and J. Li (2003). "Structural framework of a major intracontinental orogenic termination zone: the easternmost Tien Shan, China". In: *Journal of the Geological Society* 160, pp. 575–590.

Danišík, M., L. Fodor, I. Dunkl, A. Gerdes, J. Csizmeg, M. Hámor-Vidó, and N. J. Evans (2015). "A multi-system geochronology in the Ad-3 borehole, Pannonian Basin (Hungary) with implications for dating volcanic rocks by low-temperature thermochronology and for interpretation of (U–Th)/He data". In: *Terra Nova* 27.4, pp. 258–269.

Danišík, M., J. Kuhlemann, I. Dunkl, N. J. Evans, B. Székely, and W. Frisch (2012a). "Survival of Ancient Landforms in a Collisional Setting as Revealed by Combined Fission Track and (U-Th)/He Thermochronometry: A Case Study from Corsica (France)". In: *The Journal of Geology* 120.2, pp. 155–173.

Danišík, M., P. Shane, A. K. Schmitt, A. Hogg, G. M. Santos, S. Storm, N. J. Evans, L. K. Fifield, and J. M. Lindsay (2012b). "Re-anchoring the late Pleistocene tephrochronology of New Zealand based on concordant radiocarbon ages and combined 238U/230Th disequilibrium and (U–Th)/He zircon ages". In: *Earth and Planetary Science Letters* 349-350, pp. 240–250.

Danišík, M., P. Štěpančíková, and N. J. Evans (2012c). "Constraining long-term denudation and faulting history in intraplate regions by multisystem thermochronology: An example of the Sudetic Marginal Fault (Bohemian Massif, central Europe)". In: *Tectonics* 31.2, n/a–n/a.

Daoudene, Y., D. Gapais, J.-P. Cogné, and G. Ruffet (2017). "Late Jurassic – Early Cretaceous continental extension in northeast Asia – Relationships to plate kinematics". In: *Bull. Soc. géol. Fr.* 188.1-2.

De Grave, J., M. M. Buslov, and P. Van den haute (2007). "Distant effects of India–Eurasia convergence and Mesozoic intracontinental deformation in Central Asia: Constraints from apatite fission-track thermochronology". In: *Journal of Asian Earth Sciences* 29.2–3, pp. 188–204.

De Grave, J., E. De Pelsmaeker, F. I. Zhimulev, S. Glorie, M. M. Buslov, and P. Van den haute (2014). "Meso-Cenozoic building of the northern Central Asian Orogenic Belt: Thermotectonic history of the Tuva region". In: *Tectonophysics* 621, pp. 44–59.

De Grave, J., S. Glorie, M. M. Buslov, A. Izmer, A. Fournier-Carrie, V. Y. Batalev, F. Vanhaecke, M. Elburg, and P. Van den haute (2011a). "The thermo-tectonic history of the Song-Kul plateau, Kyrgyz Tien Shan: Constraints by apatite and

titanite thermochronometry and zircon U/Pb dating". In: *Gondwana Research* 20.4, pp. 745–763.

De Grave, J., S. Glorie, M. M. Buslov, D. F. Stockli, M. O. McWilliams, V. Y. Batalev, and P. Van den haute (2013). "Thermo-tectonic history of the Issyk-Kul basement (Kyrgyz Northern Tien Shan, Central Asia)". In: *Gondwana Research* 23.3, pp. 998–1020.

De Grave, J., S. Glorie, A. Ryabinin, F. Zhimulev, M. M. Buslov, A. Izmer, M. Elburg, F. Vanhaecke, and P. Van den haute (2012). "Late Palaeozoic and Meso-Cenozoic tectonic evolution of the southern Kyrgyz Tien Shan: Constraints from multi-method thermochronology in the Trans-Alai, Turkestan-Alai segment and the southeastern Ferghana Basin". In: *Journal of Asian Earth Sciences* 44, pp. 149–168.

De Grave, J., S. Glorie, F. I. Zhimulev, M. M. Buslov, M. Elburg, F. Vanhaecke, and P. Van den haute (2011b). "Emplacement and exhumation of the Kuznetsk-Alatau basement (Siberia): implications for the tectonic evolution of the Central Asian Orogenic Belt and sediment supply to the Kuznetsk, Minusa and West Siberian Basins". In: *Terra Nova* 23.4, pp. 248–256.

De Pelsmaeker, E., S. Glorie, M. M. Buslov, F. I. Zhimulev, M. Poujol, V. V. Korobkin, F. Vanhaecke, E. V. Vetrov, and J. De Grave (2015). "Late-Paleozoic emplacement and Meso-Cenozoic reactivation of the southern Kazakhstan granitoid basement". In: *Tectonophysics* 662, pp. 416–433.

De Pelsmaeker, E., M. Jolivet, A. Laborde, M. Poujol, C. Robin, F. I. Zhimulev, S. Nachtergaele, S. Glorie, S. De Clercq, V. Y. Batalev, and J. De Grave (2018). "Source-to-sink dynamics in the Kyrgyz Tien Shan from the Jurassic to the Paleogene: Insights from sedimentological and detrital zircon U-Pb analyses". In: *Gondwana Research* 54, pp. 180–204.

Degtyarev, K. E. (2011). "Tectonic evolution of Early Paleozoic island-arc systems and continental crust formation in the Caledonides of Kazakhstan and the North Tien Shan". In: *Geotectonics* 45.1, pp. 23–50.

Degtyarev, K. E., K. N. Shatagin, V. P. Kovach, and A. A. Tretyakov (2015). "The formation processes and isotopic structure of continental crust of the Chingiz Range Caledonides (Eastern Kazakhstan)". In: *Geotectonics* 49.6, pp. 485–514.

Devyatkin, E. (1974). "Structures and formational complexes of the Cenozoic activated stage". In: *Tectonics of the Mongolian People's Republic: Moscow, Nauka* 41, pp. 182–195.

Dickinson, W. R. (2008). "Impact of differential zircon fertility of granitoid basement rocks in North America on age populations of detrital zircons and implications for granite petrogenesis". In: *Earth and Planetary Science Letters* 275.1, pp. 80–92.

Dickinson, W. R. and G. E. Gehrels (2003). "U–Pb ages of detrital zircons from Permian and Jurassic eolian sandstones of the Colorado Plateau, USA: paleogeographic implications". In: *Sedimentary Geology* 163.1, pp. 29–66.

Dill, H. G. (1994). "Can REE patterns and U-Th variations be used as a tool to determine the origin of apatite in clastic rocks?" In: *Sedimentary Geology* 92.3, pp. 175–196.

Dodson, M. H. (1973). "Closure temperature in cooling geochronological and petrological systems". In: *Contributions to Mineralogy and Petrology* 40.3, pp. 259–274.

Donelick, R., P. O'Sullivan, and R. Ketcham (2005). "Apatite Fission-Track Analysis". In: *Reviews in Mineralogy and Geochemistry* 58, pp. 49–94.

Donelick, R. A., R. A. Ketcham, and W. D. Carlson (1999). "Variability of apatite fission-track annealing kinetics; II, Crystallographic orientation effects". In: *American Mineralogist* 84.9, pp. 1224–1234.

Donelick, R. A. and D. S. Miller (1991). "Enhanced tint fission track densities in low spontaneous track density apatites using 252Cf-derived fission fragment tracks: A model and experimental observations". In: *International Journal of Radiation Applications and Instrumentation. Part D. Nuclear Tracks and Radiation Measurements* 18.3, pp. 301–307.

Dumitru, T. A., D. Zhou, E. Z. Chang, S. A. Graham, M. S. Hendrix, E. R. Sobel, and A. R. Carroll (2001). "Uplift, exhumation, and deformation in the Chinese Tian Shan". In: *Geological Society of America Memoirs* 194, pp. 71–99.

Ehlers, T. A. and K. A. Farley (2003). "Apatite (U–Th)/He thermochronometry: methods and applications to problems in tectonic and surface processes". In: *Earth and Planetary Science Letters* 206.1–2, pp. 1–14.

Eizenhöfer, P. R. and G. Zhao (2018). "Solonker Suture in East Asia and its bearing on the final closure of the eastern segment of the Palaeo-Asian Ocean". In: *Earth-Science Reviews* 186, pp. 153–172.

England, P. and P. Molnar (1990). "Surface uplift, uplift of rocks, and exhumation of rocks". In: *Geology* 18.12, pp. 1173–1177.

Evans, N. J., J. P. Byrne, J. T. Keegan, and L. E. Dotter (2005). "Determination of Uranium and Thorium in Zircon, Apatite, and Fluorite: Application to Laser (U-Th)/He Thermochronology". In: *Journal of Analytical Chemistry* 60.12, pp. 1159–1165.

Fan, W.-M., F. Guo, Y.-J. Wang, and G. Lin (2003). "Late Mesozoic calc-alkaline volcanism of post-orogenic extension in the northern Da Hinggan Mountains, northeastern China". In: *Journal of Volcanology and Geothermal Research* 121.1–2, pp. 115–135.

Farley, K. A., R. A. Wolf, and L. T. Silver (1996). "The effects of long alpha-stopping distances on (U-Th)/He ages". In: *Geochimica et Cosmochimica Acta* 60.21, pp. 4223–4229.

Farley, K. (2000). "Helium diffusion from apatite: General behavior as illustrated by Durango fluorapatite". In: *Journal of Geophysical Research: Solid Earth* 105.B2, pp. 2903–2914.

Farley, K. A. (2002). "(U-Th)/He Dating: Techniques, Calibrations, and Applications". In: *Reviews in Mineralogy and Geochemistry* 47.1, pp. 819–844.

Feng, Y., R. G. Coleman, G. Tilton, and X. Xiao (1989). "Tectonic evolution of the West Junggar Region, Xinjiang, China". In: *Tectonics* 8.4, pp. 729–752.

Filippova, I. B., V. A. Bush, and A. N. Didenko (2001). "Middle Paleozoic subduction belts: The leading factor in the formation of the Central Asian fold-and-thrust belt". In: *Russian Journal of Earth Sciences* 3.6.

Fitzgerald, P. G., S. L. Baldwin, L. E. Webb, and P. B. O'Sullivan (2006). "Interpretation of (U–Th)/He single grain ages from slowly cooled crustal terranes: A case study from the Transantarctic Mountains of southern Victoria Land". In: *Chemical Geology* 225.1–2, pp. 91–120.

Fleischer, M. and Z. Altschuler (1986). "The lanthanides and yttrium in minerals of the apatite group - an analysis of the available data". In: *Neues Jahrbuch fuer Mineralogie, Monatshefte* 10, pp. 467–480.

Fleischer, R. L., P. B. Price, and R. M. Walker (1975). *Nuclear tracks in solids: principles and applications*. Univ of California Press.

Flowers, R. M., R. A. Ketcham, D. L. Shuster, and K. A. Farley (2009). "Apatite (U–Th)/He thermochronometry using a radiation damage accumulation and annealing model". In: *Geochimica et Cosmochimica Acta* 73.8, pp. 2347–2365.

Fox, M., J.-G. Dai, and A. Carter (2019). "Badly behaved detrital (U-Th)/He ages: problems with He diffusion models or geological models?" In: *Geochemistry, Geophysics, Geosystems*.

Galbraith, R. F. (1990). "The radial plot: Graphical assessment of spread in ages". In: *International Journal of Radiation Applications and Instrumentation. Part D. Nuclear Tracks and Radiation Measurements* 17.3, pp. 207–214.

Galbraith, R. F., G. M. Laslett, and R. Cox David (1988). "Some calculations relevant to thermal annealing of fission tracks in apatite". In: *Proceedings of the Royal Society of London. A. Mathematical and Physical Sciences* 419.1857, pp. 305–321.

Galbraith, R. (1981). "On statistical models for fission track counting". In: *Journal of the International Association for Mathematical Geology* 12.6, pp. 471–478.

Galbraith, R. (2010). *Statistics for LA-ICPMS fission track dating*. Conference Paper.

Gallagher, K. (2012). "Transdimensional inverse thermal history modeling for quantitative thermochronology". In: *Journal of Geophysical Research: Solid Earth* 117.B2.

Gao, R., L. Xiao, F. Pirajno, G.-c. Wang, X.-x. He, G. Yang, and S.-w. Yan (2014). "Carboniferous–Permian extensive magmatism in the West Junggar, Xinjiang, northwestern China: its geochemistry, geochronology, and petrogenesis". In: *Lithos* 204.

Gautheron, C., L. Tassan-Got, J. Barbarand, and M. Pagel (2009). "Effect of alpha-damage annealing on apatite (U–Th)/He thermochronology". In: *Chemical Geology* 266.3–4, pp. 157–170.

Gautheron, C., L. Tassan-Got, R. A. Ketcham, and K. J. Dobson (2012). "Accounting for long alpha-particle stopping distances in (U–Th–Sm)/He geochronology: 3D modeling of diffusion, zoning, implantation, and abrasion". In: *Geochimica et Cosmochimica Acta* 96, pp. 44–56.

Geng, H., M. Sun, C. Yuan, W. Xiao, W. Xian, G. Zhao, L. Zhang, K. Wong, and F. Wu (2009). "Geochemical, Sr–Nd and zircon U–Pb–Hf isotopic studies of Late Carboniferous magmatism in the West Junggar, Xinjiang: Implications for ridge subduction?" In: *Chemical Geology* 266.3, pp. 364–389.

Gibson, G. and T. Ireland (1996). "Extension of Delamerian (Ross) orogen into western New Zealand: Evidence from zircon ages and implications for crustal growth along the Pacific margin of Gondwana". In: *Geology* 24.12, pp. 1087–1090.

Gillespie, J., S. Glorie, G. Jepson, Z. Y. Zhang, W. J. Xiao, M. Danišík, and A. S. Collins (2017a). "Differential exhumation and crustal tilting in the easternmost Tianshan (Xinjiang, China), revealed by low-temperature thermochronology". In: *Tectonics* 36, pp. 2142–2158.

Gillespie, J., S. Glorie, W. Xiao, Z. Zhang, A. S. Collins, N. Evans, B. McInnes, and J. De Grave (2017b). "Mesozoic reactivation of the Beishan, southern Central Asian Orogenic Belt: Insights from low-temperature thermochronology". In: *Gondwana Research* 43, pp. 107–122.

Gladkochub, D. P., A. M. Stanevich, A. M. Mazukabzov, T. V. Donskaya, S. A. Pisarevsky, G. Nicoll, Z. L. Motova, and T. A. Kornilova (2013). "Early evolution of the Paleoasian ocean: LA-ICP-MS dating of detrital zircon from Late Precambrian sequences of the southern margin of the Siberian craton". In: *Russian Geology and Geophysics* 54.10, pp. 1150–1163.

Gleadow, A. J. W. (1981). "Fission-track dating methods: What are the real alternatives?" In: *Nuclear Tracks* 5.1, pp. 3–14.

Gleadow, A. J. W., I. R. Duddy, P. F. Green, and K. A. Hegarty (1986a). "Fission track lengths in the apatite annealing zone and the interpretation of mixed ages". In: *Earth and Planetary Science Letters* 78.2-3, pp. 245–254.

Gleadow, A. J. W., I. R. Duddy, P. F. Green, and J. F. Lovering (1986b). "Confined fission track lengths in apatite: a diagnostic tool for thermal history analysis". In: *Contributions to Mineralogy and Petrology* 94.4, pp. 405–415.

Gleadow, A. J. W., S. J. Gleadow, D. X. Belton, B. P. Kohn, M. S. Krochmal, and R. W. Brown (2009). "Coincidence mapping - a key strategy for the automatic counting of fission tracks in natural minerals". In: *Geological Society, London, Special Publications* 324.1, pp. 25–36.

Gleadow, A. J. W., B. P. Kohn, D. X. Belton, and R. W. Brown (2002). "Fission Track Dating of Phosphate Minerals and the Thermochronology of Apatite". In: *Reviews in Mineralogy and Geochemistry* 48.1, pp. 579–630.

Gleadow, A., M. Harrison, B. Kohn, R. Lugo-Zazueta, and D. Phillips (2015). "The Fish Canyon Tuff: A new look at an old low-temperature thermochronology standard". In: *Earth and Planetary Science Letters* 424, pp. 95–108.

Glorie, S. and J. De Grave (2016). "Exhuming the Meso-Cenozoic Kyrgyz Tianshan and the Siberian Altai-Sayan: a review based on low-temperature thermochronology". In: *Geoscience Frontiers* 7.2, pp. 155–170.

Glorie, S., J. De Grave, M. M. Buslov, M. A. Elburg, D. F. Stockli, and P. Gerdes A. Van den haute (2010). "Multi-method chronometric constraints on the evolution of the Northern Kyrgyz Tien Shan granitoids (Central Asian Orogenic Belt): From emplacement to exhumation". In: *Journal of Asian Earth Sciences* 38.3-4, pp. 131–146.

Glorie, S., J. De Grave, M. M. Buslov, F. I. Zhimulev, M. A. Elburg, and P. Van den haute (2012a). "Structural control on Meso-Cenozoic tectonic reactivation and denudation in the Siberian Altai: Insights from multi-method thermochronometry". In: *Tectonophysics* 544–545.0, pp. 75–92.

Glorie, S., J. De Grave, M. M. Buslov, F. I. Zhimulev, and I. Y. Safonova (2014). "Detrital zircon provenance of early Palaeozoic sediments at the southwestern margin of the Siberian Craton: Insights from U–Pb geochronology". In: *Journal of Asian Earth Sciences* 82.Supplement C, pp. 115–123.

Glorie, S., J. De Grave, M. M. Buslov, F. I. Zhimulev, D. F. Stockli, V. Y. Batalev, A. Izmer, P. Van den haute, F. Vanhaecke, and M. A. Elburg (2011). "Tectonic history of the Kyrgyz South Tien Shan (Atbashi-Inylchek) suture zone: The role of inherited structures during deformation-propagation". In: *Tectonics* 30.6, TC6016.

Glorie, S., J. De Grave, D. Delvaux, M. M. Buslov, F. I. Zhimulev, F. Vanhaecke, M. A. Elburg, and P. Van den haute (2012b). "Tectonic history of the Irtysh shear zone (NE Kazakhstan): New constraints from zircon U/Pb dating, apatite fission track dating and palaeostress analysis". In: *Journal of Asian Earth Sciences* 45, pp. 138–149.

Glorie, S., I. Alexandrov, A. Nixon, G. Jepson, J. Gillespie, and B.-M. Jahn (2017). "Thermal and exhumation history of Sakhalin Island (Russia) constrained by apatite U-Pb and fission track thermochronology". In: *Journal of Asian Earth Sciences* 143, pp. 326–342.

Glorie, S., A. Otasevic, J. Gillespie, G. Jepson, M. Danišík, F. Zhimulev, D. Gurevich, Z. Zhang, D. Song, and W. Xiao (2019). "Thermo-tectonic history of the Junggar Alatau: insights from integrated apatite U/Pb, fission track and (U-Th)/He thermochronology". In: *Geoscience Frontiers*.

Graham, S., M. Hendrix, C. Johnson, D. Badamgarav, G. Badarch, J. Amory, M. Porter, R. Barsbold, L. Webb, and B. Hacker (2001). "Sedimentary record and tectonic implications of Mesozoic rifting in southeast Mongolia". In: *Geological Society of America Bulletin* 113.12, pp. 1560–1579.

Green, P. F., I. R. Duddy, A. J. W. Gleadow, P. R. Tingate, and G. M. Laslett (1986). "Thermal annealing of fission tracks in apatite: 1. A qualitative description". In: *Chemical Geology: Isotope Geoscience section* 59.0, pp. 237–253.

Green, P. F. (1986). "On the thermo-tectonic evolution of Northern England: evidence from fission track analysis". In: *Geological Magazine* 123.5, pp. 493–506.

Green, P. F., P. V. Crowhurst, I. R. Duddy, P. Japsen, and S. P. Holford (2006). "Conflicting (U–Th)/He and fission track ages in apatite: Enhanced He retention, not anomalous annealing behaviour". In: *Earth and Planetary Science Letters* 250.3, pp. 407–427.

Green, P. and I. Duddy (2018). "Apatite (U-Th-Sm)/He thermochronology on the wrong side of the tracks". In: *Chemical Geology* 488, pp. 21–33.

Guenthner, W. R., P. W. Reiners, R. A. Ketcham, L. Nasdala, and G. Giester (2013). "Helium diffusion in natural zircon: Radiation damage, anisotropy, and the interpretation of zircon (U-Th)/He thermochronology". In: *American Journal of Science* 313.3, pp. 145–198.

Guerit, L., L. Barrier, M. Jolivet, B. Fu, and F. Métivier (2016). "Denudation intensity and control in the Chinese Tian Shan: new constraints from mass balance on catchment-alluvial fan systems". In: *Earth Surface Processes and Landforms* 41.8, pp. 1088–1106.

Guo, Z., Z. Zhang, C. Wu, S. Fang, and R. Zhang (2006). "The Mesozoic and Cenozoic Exhumation History of Tianshan and Comparative Studies to the Junggar and Altai Mountains". In: *Acta Geological Sinica* 80.1, pp. 1–15.

Han, B., J. Ji, B. Song, L. Chen, and L. Zhang (2006). "Late Paleozoic vertical growth of continental crust around the Junggar Basin, Xinjiang, China (Part I): timing of post-collisional plutonism". In: *Acta Petrologica Sinica* 22.5, pp. 1077–1086.

Han, Y. and G. Zhao (2018). "Final amalgamation of the Tianshan and Junggar orogenic collage in the southwestern Central Asian Orogenic Belt: Constraints on the closure of the Paleo-Asian Ocean". In: 186, pp. 129–152.

Hansman, R. J., R. Albert, A. Gerdes, and U. Ring (2018). "Absolute ages of multiple generations of brittle structures by U-Pb dating of calcite". In: *Geology* 46.3, pp. 207–210.

Harlov, D. E. (2015). "Apatite: A Fingerprint for Metasomatic Processes". In: *Elements* 11.3, pp. 171–176.

Hasebe, N., J. Barbarand, K. Jarvis, A. Carter, and A. J. Hurford (2004). "Apatite fission-track chronometry using laser ablation ICP-MS". In: *Chemical Geology* 207.3–4, pp. 135–145.

Hasebe, N., A. Tamura, and S. Arai (2013). "Zeta equivalent fission-track dating using LA-ICP-MS and examples with simultaneous U–Pb dating". In: *Island Arc* 22.3, pp. 280–291.

Heilbronn, G., P. Boulvais, E. Marchand, C. Robin, S. Bourquin, L. Barrier, Y. Jia, B. Fu, and M. Jolivet (2015). "Stable isotope characterization of pedogenic and lacustrine carbonates from the Chinese Tian Shan: Constraints on the Mesozoic–Lower Cenozoic palaeoenvironmental evolution". In: *Chemie der Erde - Geochemistry* 75.1, pp. 133–141.

Hendriks, B. W. H. and T. F. Redfield (2005). "Apatite fission track and (U-Th)/He data from Fennoscandia: An example of underestimation of fission track annealing in apatite". In: *Earth and Planetary Science Letters* 236.1–2, pp. 443–458.

Hendriks, B., P. Andriessen, Y. Huigen, C. Leighton, T. Redfield, G. Murrell, K. Gallagher, and S. B. Nielsen (2007). "A fission track data compilation for Fennoscandia". In: *Norwegian Journal of Geology* 87.1/2, pp. 143–155.

Hendrix, M. S. (2000). "Evolution of Mesozoic Sandstone Compositions, Southern Junggar, Northern Tarim, and Western Turpan Basins, Northwest China: A Detrital Record of the Ancestral Tian Shan". In: *Journal of Sedimentary Research* 70.3, pp. 520–532.

Hendrix, M. S., T. A. Dumitru, and S. A. Graham (1994). "Late Oligocene-early Miocene unroofing in the Chinese Tian Shan: An early effect of the India-Asia collision". In: *Geology* 22.6, pp. 487–490.

Hendrix, M. S., S. A. Graham, A. R. Carroll, E. R. Sobel, C. L. McKnight, B. J. Schulein, and Z. Wang (1992). "Sedimentary record and climatic implications of recurrent deformation in the Tian Shan: Evidence from Mesozoic strata of the north Tarim, south Junggar, and Turpan basins, northwest China". In: *GSA Bulletin* 104.1, pp. 53–79.

Henrichs, I. A., G. O'Sullivan, D. M. Chew, C. Mark, M. G. Babechuk, C. McKenna, and R. Emo (2018). "The trace element and U-Pb systematics of metamorphic apatite". In: *Chemical Geology* 483, pp. 218–238.

Hinton, R. W. (1999). "NIST SRM 610, 611 and SRM 612, 613 Multi-Element Glasses: Constraints from Element Abundance Ratios Measured by Microprobe Techniques". In: *Geostandards Newsletter* 23.2, pp. 197–207.

Holden, N. E. and D. C. Hoffman (2000). "Spontaneous fission half-lives for ground-state nuclide (Technical report)". In: *Pure and Applied Chemistry* 72.8, p. 1525.

Hughes, J. M. and J. F. Rakovan (2015). "Structurally Robust, Chemically Diverse: Apatite and Apatite Supergroup Minerals". In: *Elements* 11.3, pp. 165–170.

Hurford, A. J. and P. F. Green (1983). "The zeta age calibration of fission-track dating". In: *Chemical Geology* 41, pp. 285–317.

Jafarzadeh, M., R. M. Harami, H. Friis, A. Amini, A. Mahboubi, and D. Lenaz (2014). "Provenance of the Oligocene–Miocene Zivah Formation, NW Iran, assessed using heavy mineral assemblage and detrital clinopyroxene and detrital apatite analyses". In: *Journal of African Earth Sciences* 89, pp. 56–71.

Jaffey, A. H., K. F. Flynn, L. E. Glendenin, W. C. Bentley, and A. M. Essling (1971). "Precision Measurement of Half-Lives and Specific Activities of ^{235}U and ^{238}U". In: *Physical Review C* 4.5, pp. 1889–1906.

Jennings, E., H. Marschall, C. Hawkesworth, and C. Storey (2011). "Characterization of magma from inclusions in zircon: Apatite and biotite work well, feldspar less so". In: *Geology* 39.9, pp. 863–866.

Jepson, G. (2018). "The Low-Temperature Tectonic Evolution of the Western Tian Shan (Kazakhstan, Kyrgyzstan, Uzbekistan, Tajikistan)". PhD thesis. School of Physical Sciences, Univesity of Adelaide.

Jepson, G., S. Glorie, D. Konopelko, J. Gillespie, M. Danišík, N. J. Evans, Y. Mamadjanov, and A. S. Collins (2018a). "Thermochronological insights into the structural contact between the Tian Shan and Pamirs, Tajikistan". In: *Terra Nova* 30.2, pp. 95–104.

Jepson, G., S. Glorie, D. Konopelko, J. Gillespie, M. Danišík, R. Mirkamalov, Y. Mamadjanov, and A. S. Collins (2018b). "Low-temperature thermochronology of the Chatkal-Kurama terrane (Uzbekistan-Tajikistan): insights into the Meso-Cenozoic thermal history of the western Tian Shan". In: *Tectonics* 37, pp. 3954–3969.

Jepson, G., S. Glorie, D. Konopelko, R. Mirkamalov, M. Danišík, and A. S. Collins (2018c). "The low-temperature thermo-tectonic evolution of the western Tian Shan, Uzbekistan". In: *Gondwana Research* 64, pp. 122–136.

Johnson, J. E., R. M. Flowers, G. B. Baird, and K. H. Mahan (2017). "Inverted zircon and apatite (U-Th)/He dates from the Front Range, Colorado: High-damage zircon as a low-temperature (<50 °C) thermochronometer". In: *Earth and Planetary Science Letters* 466, pp. 80–90.

Jolivet, M., T. De Boisgrollier, C. Petit, M. Fournier, V. A. Sankov, J. C. Ringenbach, L. Byzov, A. I. Miroshnichenko, S. N. Kovalenko, and S. V. Anisimova

(2009). "How old is the Baikal Rift Zone? Insight from apatite fission track thermochronology". In: *Tectonics* 28.3, TC3008.

Jolivet, M., S. Dominguez, J. Charreau, Y. Chen, Y. Li, and Q. Wang (2010). "Mesozoic and Cenozoic tectonic history of the central Chinese Tian Shan: Reactivated tectonic structures and active deformation". In: *Tectonics* 29.6, TC6019.

Jolivet, M., L. Barrier, O. Dauteuil, A. Laborde, Q. Li, B. Reichenbacher, S.-M. Popescu, J. Sha, and Z. Guo (2018a). "Late Cretaceous–Palaeogene topography of the Chinese Tian Shan: New insights from geomorphology and sedimentology". In: *Earth and Planetary Science Letters* 499, pp. 95–106.

Jolivet, M., P. Boulvais, L. Barrier, C. Robin, G. Heilbronn, J. Ledoyen, Q. Ventroux, Y. Jia, Z. Guo, and E. Bataleva (2018b). "Oxygen and Carbon Stable Isotope Composition of Cretaceous to Pliocene Calcareous Paleosols in the Tian Shan Region (Central Asia): Controlling Factors and Paleogeographic Implications". In: *Geosciences* 8.9, p. 330.

Jolivet, M., S. Bourquin, G. Heilbronn, C. Robin, L. Barrier, M.-P. Dabard, Y. Jia, E. De Pelsmaeker, and B. Fu (2017). "The Upper Jurassic–Lower Cretaceous alluvial-fan deposits of the Kalaza Formation (Central Asia): tectonic pulse or increased aridity?" In: *Geological Society, London, Special Publications* 427.1, p. 491.

Jolivet, M., G. Heilbronn, C. Robin, L. Barrier, S. Bourquin, Z. Guo, Y. Jia, L. Guerit, W. Yang, and B. Fu (2013). "Reconstructing the Late Palaeozoic - Mesozoic topographic evolution of the Chinese Tian Shan: available data and remaining uncertainties". In: *Advances in Geosciences* 37, pp. 7–18.

Jolivet, M., J.-F. Ritz, R. Vassallo, C. Larroque, R. Braucher, M. Todbileg, A. Chauvet, C. Sue, N. Arnaud, R. De Vicente, A. Arzhanikova, and S. Arzhanikov (2007). "Mongolian summits: An uplifted, flat, old but still preserved erosion surface". In: *Geology* 35.10, pp. 871–874.

Jong, K. de, B. Wang, M. Faure, L. Shu, D. Cluzel, J. Charvet, G. Ruffet, and Y. Chen (2009). "New 40Ar/39Ar age constraints on the Late Palaeozoic tectonic evolution of the western Tianshan (Xinjiang, northwestern China), with emphasis on Permian fluid ingress". In: *International Journal of Earth Sciences* 98.6, pp. 1239–1258.

Kapp, P. and P. G. DeCelles (2019). "Mesozoic–Cenozoic geological evolution of the Himalayan-Tibetan orogen and working tectonic hypotheses". In: *American Journal of Science* 319.3, pp. 159–254.

Kapp, P., P. G. DeCelles, G. E. Gehrels, M. Heizler, and L. Ding (2007). "Geological records of the Lhasa-Qiangtang and Indo-Asian collisions in the Nima area of central Tibet". In: *GSA Bulletin* 119.7-8, pp. 917–933.

Käßner, A., L. Ratschbacher, R. Jonckheere, E. Enkelmann, J. Khan, B.-L. Sonntag, R. Gloaguen, M. Gadoev, and I. Oimahmadov (2016a). "Cenozoic intraconti-

nental deformation and exhumation at the northwestern tip of the India-Asia collision—southwestern Tian Shan, Tajikistan, and Kyrgyzstan". In: *Tectonics* 35.9, pp. 2171–2194.

Käßner, A., L. Ratschbacher, J. A. Pfänder, B. R. Hacker, G. Zack, B.-L. Sonntag, J. Khan, K. P. Stanek, M. Gadoev, and I. Oimahmadov (2016b). "Proterozoic-Mesozoic history of the Central Asian orogenic belt in the Tajik and southwestern Kyrgyz Tian Shan: U-Pb, 40Ar/39Ar, and fission-track geochronology and geochemistry of granitoids". In: *Geological Society of America Bulletin* 129.3-4, pp. 281–303.

Ketcham, R. A., P. van der Beek, J. Barbarand, M. Bernet, and C. Gautheron (2018). "Reproducibility of Thermal History Reconstruction From Apatite Fission-Track and (U-Th)/He Data". In: *Geochemistry, Geophysics, Geosystems* 19.8, pp. 2411–2436.

Ketcham, R. A., A. Carter, R. A. Donelick, J. Barbarand, and A. J. Hurford (2007). "Improved modeling of fission-track annealing in apatite". In: *American Mineralogist* 92.5-6, pp. 799–810.

Ketcham, R. A., R. A. Donelick, and W. D. Carlson (1999). "Variability of apatite fission-track annealing kinetics; III, Extrapolation to geological time scales". In: *American Mineralogist* 84.9, pp. 1235–1255.

Kirkland, C. L., C. Yakymchuk, K. Szilas, N. Evans, J. Hollis, B. McDonald, and N. J. Gardiner (2018). "Apatite: a U-Pb thermochronometer or geochronometer?" In: *Lithos* 318-319, pp. 143–157.

Kohn, B. P., M. Lorencak, A. J. W. Gleadow, F. Kohlmann, A. Raza, K. G. Osadetz, and P. Sorjonen-Ward (2009). "A reappraisal of low-temperature thermochronology of the eastern Fennoscandia Shield and radiation-enhanced apatite fission-track annealing". In: *Geological Society Special Publication*. Vol. 324, pp. 193–216.

Krenn, E. and F. Finger (2004). "Metamorphic formation of Sr-apatite and Sr-bearing monazite in a high-pressure rock from the Bohemian Massif". In: *American Mineralogist* 89.8-9, pp. 1323–1329.

Kuzmichev, A. B. and E. V. Sklyarov (2016). "The Precambrian of Transangaria, Yenisei Ridge (Siberia): Neoproterozoic microcontinent, Grenville-age orogen, or reworked margin of the Siberian craton?" In: *Journal of Asian Earth Sciences* 115, pp. 419–441.

Kwon, S. T., G. R. Tilton, R. G. Coleman, and Y. Feng (1989). "Isotopic studies bearing on the tectonics of the West Junggar Region, Xinjiang, China". In: *Tectonics* 8.4.

LaMaskin, T. A. (2012). "Detrital zircon facies of Cordilleran terranes in western North America". In: *GSA Today* 22.3, pp. 4–11.

Laurent-Charvet, S., J. Charvet, P. Monié, and L. Shu (2003). "Late Paleozoic strike-slip shear zones in eastern central Asia (NW China): New structural and geochronological data". In: *Tectonics* 22.2, p. 1009.

Laurent-Charvet, S., J. Charvet, L. Shu, R. Ma, and H. Lu (2002). "Palaeozoic late collisional strike-slip deformations in Tianshan and Altay, Eastern Xinjiang, NW China". In: *Terra Nova* 14.4, pp. 249–256.

Lehmann, J., K. Schulmann, O. Lexa, M. Corsini, A. Kröner, P. Štípská, D. Tomurhuu, and D. Otgonbator (2010). "Structural constraints on the evolution of the Central Asian Orogenic Belt in SW Mongolia". In: *American Journal of Science* 310.7, pp. 575–628.

Levashova, N. M., K. E. Degtyarev, and M. L. Bazhenov (2012). "Oroclinal bending of the Middle and Late Paleozoic volcanic belts in Kazakhstan: Paleomagnetic evidence and geological implications". In: *Geotectonics* 46.4, pp. 285–302.

Levashova, N. M., K. E. Degtyarev, M. L. Bazhenov, A. Q. Collins, and R. Van der Voo (2003a). "Middle Paleozoic paleomagnetism of east Kazakhstan: post-Middle Devonian rotations in a large-scale orocline in the central Ural–Mongol belt". In: *Tectonophysics* 377.3, pp. 249–268.

Levashova, N. M., K. E. Degtyarev, M. L. Bazhenov, A. Q. Collins, and R. van der Voo (2003b). "Permian palaeomagnetism of East Kazakhstan and the amalgamation of Eurasia". In: *Geophysical Journal International* 152.3, pp. 677–687.

Levashova, N. M., R. Van der Voo, A. V. Abrajevitch, and M. L. Bazhenov (2009). "Paleomagnetism of mid-Paleozoic subduction-related volcanics from the Chingiz Range in NE Kazakhstan: The evolving paleogeography of the amalgamating Eurasian composite continentPaleomagnetism of mid-Paleozoic volcanics from Kazakhstan". In: *GSA Bulletin* 121.3-4, pp. 555–573.

Li, D., D. He, Y. Lian, Y. Lu, and Z. Yi (2017a). "Structural evolution and late Carboniferous magmatism of the Zhongguai arc in the western Junggar Basin, Northwest China: implications for tectonic evolution of the Junggar Ocean". In: *International Geology Review* 59.10, pp. 1234–1255.

Li, D., D. He, D. Ma, Y. Tang, Y. Kong, and J. Tang (2015a). "Carboniferous–Permian tectonic framework and its later modifications to the area from eastern Kazakhstan to southern Altai: Insights from the Zaysan–Jimunai Basin evolution". In: *Journal of Asian Earth Sciences* 113, pp. 16–35.

Li, D., D. He, X. Qi, and N. Zhang (2015b). "How was the Carboniferous Balkhash–West Junggar remnant ocean filled and closed? Insights from the Well Tacan-1 strata in the Tacheng Basin, NW China". In: *Gondwana Research* 27.1, pp. 342–362.

Li, G., M. Cao, K. Qin, N. J. Evans, B. I. A. McInnes, and Y. Liu (2014). "Thermal-tectonic history of the Baogutu porphyry Cu deposit, West Junggar as constrained from zircon U–Pb, biotite Ar/Ar and zircon/apatite (U–Th)/He dating". In: *Journal of Asian Earth Sciences* 79, pp. 741–758.

Li, P., M. Sun, G. Rosenbaum, K. Cai, M. Chen, and Y. He (2016a). "Transpressional deformation, strain partitioning and fold superimposition in the southern Chinese Altai, Central Asian Orogenic Belt". In: *Journal of Structural Geology* 87, pp. 64–80.

Li, P., M. Sun, G. Rosenbaum, K. Cai, and Y. Yu (2015c). "Structural evolution of the Irtysh Shear Zone (northwestern China) and implications for the amalgamation of arc systems in the Central Asian Orogenic Belt". In: *Journal of Structural Geology* 80, pp. 142–156.

Li, P., M. Sun, G. Rosenbaum, Y. Jiang, and K. Cai (2016b). "Structural evolution of zonal metamorphic sequences in the southern Chinese Altai and relationships to Permian transpressional tectonics in the Central Asian Orogenic Belt". In: *Tectonophysics* 693, Part B, pp. 277–289.

Li, P., M. Sun, G. Rosenbaum, F. Jourdan, S. Li, and K. Cai (2017b). "Late Paleozoic closure of the Ob-Zaisan Ocean along the Irtysh shear zone (NW China): Implications for arc amalgamation and oroclinal bending in the Central Asian orogenic belt". In: *Geological Society of America Bulletin* 129.5-6, pp. 547–569.

Li, P., M. Sun, G. Rosenbaum, C. Yuan, I. Safonova, K. Cai, Y. Jiang, and Y. Zhang (2018). "Geometry, kinematics and tectonic models of the Kazakhstan Orocline, Central Asian Orogenic Belt". In: *Journal of Asian Earth Sciences* 153, pp. 42–56.

Li, P., C. Yuan, M. Sun, X. Long, and K. Cai (2015d). "Thermochronological constraints on the late Paleozoic tectonic evolution of the southern Chinese Altai". In: *Journal of Asian Earth Sciences* 113, pp. 51–60.

Li, W., J. Hu, and H. Qu (2010). "Fission Track Analysis of Junggar Basin Peripheral Orogen and Its Geological Significance". In: *Acta Geological Sinica* 84.2, pp. 171–182.

Likhanov, I. I., P. S. Kozlov, O. P. Polyansky, N. V. Popov, V. V. Reverdatto, A. V. Travin, and A. E. Vershinin (2007). "Neoproterozoic age of collisional metamorphism in the Transangara region of the Yenisei Ridge (based on 40Ar/39Ar data)". In: *Doklady Earth Sciences* 413.1, pp. 234–237.

Likhanov, I. I., A. D. Nozhkin, V. V. Reverdatto, and P. S. Kozlov (2014). "Grenville tectonic events and evolution of the Yenisei Ridge at the western margin of the Siberian Craton". In: *Geotectonics* 48.5, pp. 371–389.

Likhanov, I. I., V. V. Reverdatto, and P. S. Kozlov (2012). "U-Pb and 40Ar/39Ar evidence for Grenvillian activity in the Yenisey Ridge during formation of the Teya metamorphic complex". In: *Geochemistry International* 50.6, pp. 551–557.

Likhanov, I. I., V. V. Reverdatto, P. S. Kozlov, V. V. Khiller, and V. P. Sukhorukov (2015). "P-T-t constraints on polymetamorphic complexes of the Yenisey Ridge, East Siberia: Implications for Neoproterozoic paleocontinental reconstructions". In: *Journal of Asian Earth Sciences* 113, pp. 391–410.

Likhanov, I. I., V. V. Reverdatto, and A. E. Vershinin (2008). "Fe- and Al-Rich metapelites of the Teiskaya Group, Yenisei Range: Geochemistry, protoliths, and the behavior of their material during metamorphism". In: *Geochemistry International* 46.1, pp. 17–36.

Likhanov, I. I. and M. Santosh (2017). "Neoproterozoic intraplate magmatism along the western margin of the Siberian Craton: Implications for breakup of the Rodinia supercontinent". In: *Precambrian Research* 300.Supplement C, pp. 315–331.

Likhanov, I. I. and V. V. Reverdatto (2007). "Provenance of Precambrian Fe- and Al-rich Metapelites in the Yenisey Ridge and Kuznetsk Alatau, Siberia: Geochemical Signatures". In: *Acta Geologica Sinica - English Edition* 81.3, pp. 409–423.

Lü, H., Y. Chang, W. Wang, and Z. Zhou (2013). "Rapid exhumation of the Tianshan Mountains since the early Miocene: Evidence from combined apatite fission track and (U-Th)/He thermochronology". In: *Science China Earth Sciences* 56.12, pp. 2116–2125.

Ma, Q., L. Shu, and W. Zhu (2006). "Mesozoic-Cenozoic burial, uplift and exhumation: a profile along the Urumqi-Korla highway in the Tianshan Mountains". In: *Xinjiang Geology* 24.2, pp. 99–104.

Ma, X., L. Shu, and J. G. Meert (2015). "Early Permian slab breakoff in the Chinese Tianshan belt inferred from the post-collisional granitoids". In: *Gondwana Research* 27.1, pp. 228–243.

Macaulay, E. A., E. R. Sobel, A. Mikolaichuk, B. Kohn, and F. M. Stuart (2014). "Cenozoic deformation and exhumation history of the Central Kyrgyz Tien Shan". In: *Tectonics* 33.2, 2013TC003376.

Macaulay, E. A., E. R. Sobel, A. Mikolaichuk, A. Landgraf, B. Kohn, and F. Stuart (2013). "Thermochronologic insight into late Cenozoic deformation in the basement-cored Terskey Range, Kyrgyz Tien Shan". In: *Tectonics* 32.3, pp. 487–500.

Malusà, M. G., A. Resentini, and E. Garzanti (2016). "Hydraulic sorting and mineral fertility bias in detrital geochronology". In: *Gondwana Research* 31.Supplement C, pp. 1–19.

Malusà, M. G. and P. G. Fitzgerald, eds. (2019). *Fission-track Thermochronology and Its Application to Geology*. Springer.

Mark, C., N. Cogné, and D. Chew (2016). "Tracking exhumation and drainage divide migration of the Western Alps: A test of the apatite U-Pb thermochronometer as a detrital provenance tool". In: *Geological Society of America Bulletin* 128.9-10, pp. 1439–1460.

McDannell, K. T., D. R. Issler, and P. B. O'Sullivan (2019). "Radiation-enhanced fission track annealing revisited and consequences for apatite thermochronometry". In: *Geochimica et Cosmochimica Acta* 252, pp. 213–239.

McDowell, F. W., W. C. McIntosh, and K. A. Farley (2005). "A precise 40Ar–39Ar reference age for the Durango apatite (U–Th)/He and fission-track dating standard". In: *Chemical Geology* 214.3–4, pp. 249–263.

Mel'nikov, N., M. Yakshin, B. Shishkin, A. Efimov, G. Karlova, L. Kilina, L. Konstantinova, B. Kochnev, B. Kraevsky, P. Mel'nikov, K. Nagovitsin, A. Postnikov, L. Ryabkova, A. Terleev, and E. Khabarov (2005). "The Riphean and Vendian Strata of the Siberian Platform and Its Folded Framing (in Russian)". In: *Stratigraphy of Petroliferous Basins of Siberia*. Ed. by N. Mel'nikov. Novosibirsk: Academic Publishing House Geo, p. 428.

Merdith, A. S., A. S. Collins, S. E. Williams, S. Pisarevsky, J. D. Foden, D. B. Archibald, M. L. Blades, B. L. Alessio, S. Armistead, D. Plavsa, C. Clark, and R. D. Müller (2017). "A full-plate global reconstruction of the Neoproterozoic". In: *Gondwana Research* 50.Supplement C, pp. 84–134.

Metelkin, D. V., I. V. Gordienko, and V. S. Klimuk (2007). "Paleomagnetism of Upper Jurassic basalts from Transbaikalia: new data on the time of closure of the Mongol-Okhotsk Ocean and Mesozoic intraplate tectonics of Central Asia". In: *Russian Geology and Geophysics* 48.10, pp. 825–834.

Metelkin, D. V., V. A. Vernikovsky, A. Y. Kazansky, and M. T. D. Wingate (2010). "Late Mesozoic tectonics of Central Asia based on paleomagnetic evidence". In: *Gondwana Research* 18.2–3, pp. 400–419.

Moecher, D. P. and S. D. Samson (2006). "Differential zircon fertility of source terranes and natural bias in the detrital zircon record: Implications for sedimentary provenance analysis". In: *Earth and Planetary Science Letters* 247.3, pp. 252–266.

Molnar, P. and P. Tapponnier (1975). "Cenozoic Tectonics of Asia: Effects of a Continental Collision: Features of recent continental tectonics in Asia can be interpreted as results of the India-Eurasia collision". In: *Science* 189.4201, pp. 419–426.

Morin, J., M. Jolivet, L. Barrier, A. Laborde, H. Li, and O. Dauteuil (2019). "Planation surfaces of the Tian Shan Range (Central Asia): Insight on several 100 million years of topographic evolution". In: *Journal of Asian Earth Sciences* 177, pp. 52–65.

Morin, J., M. Jolivet, C. Robin, G. Heilbronn, L. Barrier, S. Bourquin, and Y. Jia (2018). "Jurassic paleogeography of the Tian Shan: An evolution driven by far-field tectonics and climate". In: *Earth-Science Reviews*.

Morton, A. C. and C. R. Hallsworth (1999). "Processes controlling the composition of heavy mineral assemblages in sandstones". In: *Sedimentary Geology* 124.1, pp. 3–29.

Morton, A. and G. Yaxley (2007). "Detrital apatite geochemistry and its application in provenance studies". In: *Geological Society of America Special Papers* 420, pp. 319–344.

Nachtergaele, S., E. De Pelsmaeker, S. Glorie, F. Zhimulev, M. Jolivet, M. Danišík, M. M. Buslov, and J. De Grave (2018). "Meso-Cenozoic tectonic evolution of the Talas-Fergana region of the Kyrgyz Tien Shan revealed by low-temperature basement and detrital thermochronology". In: *Geoscience Frontiers* 9.5, pp. 1495–1514.

Nozhkin, A. D., A. S. Borisenko, and P. A. Nevol'ko (2011). "Stages of Late Proterozoic magmatism and periods of Au mineralization in the Yenisei Ridge". In: *Russian Geology and Geophysics* 52.1, pp. 124–143.

Nozhkin, A. D., A. V. Maslov, N. V. Dmitrieva, and Y. L. Ronkin (2012). "Pre-Riphean metapelites of the Yenisei Range: Chemical composition, sources of eroded material, and paleogeodynamics". In: *Geochemistry International* 50.7, pp. 574–610.

Nozhkin, A. D., A. V. Maslov, V. N. Podkovyrov, O. M. Turkina, E. F. Letnikova, Y. L. Ronkin, M. T. Krupenin, N. V. Dmitrieva, E. Z. Gareev, and O. P. Lepikhina (2009). "Geochemistry of Riphean terrigenous rocks in the Southern Urals and Siberia and variations of the continental-crust maturity". In: *Russian Geology and Geophysics* 50.2, pp. 71–86.

Nozhkin, A. D., N. V. Popov, N. V. Dmitrieva, A. A. Storozhenko, and N. F. Vasil'ev (2015). "Neoproterozoic collisional S-type granitoids of the Yenisei Ridge: petrogeochemical composition and U-Pb, Ar-Ar, and Sm-Nd isotope data". In: *Russian Geology and Geophysics* 56.5, pp. 689–695.

Nozhkin, A. D., A. A. Postnikov, K. E. Nagovitsin, A. V. Travin, A. M. Stanevich, and D. S. Yudin (2007). "Neoproterozoic Chingasan Group in the Yenisei Ridge: new data on age and deposition environments". In: *Russian Geology and Geophysics* 48.12, pp. 1015–1025.

Nozhkin, A. D., O. M. Turkina, A. V. Maslov, N. V. Dmitrieva, V. P. Kovach, and Y. L. Ronkin (2008). "Sm-Nd isotopic systematics of precambrian metapelites from the Yenisei range and age variations of their provenances". In: *Doklady Earth Sciences* 423.2, pp. 1495–1500.

Nuriel, P., R. Weinberger, A. Kylander-Clark, B. Hacker, and J. Craddock (2017). "The onset of the Dead Sea transform based on calcite age-strain analyses". In: *Geology* 45.7, pp. 587–590.

O'Sullivan, G. J., D. M. Chew, A. C. Morton, C. Mark, and I. A. Henrichs (2018). "An Integrated Apatite Geochronology and Geochemistry Tool for Sedimentary Provenance Analysis". In: *Geochemistry, Geophysics, Geosystems* 19.4, pp. 1309–1326.

O'Sullivan, P. B. and R. R. Parrish (1995). "The importance of apatite composition and single-grain ages when interpreting fission track data from plutonic rocks: a case study from the Coast Ranges, British Columbia". In: *Earth and Planetary Science Letters* 132.1, pp. 213–224.

Oksanen, J., F. Blanchet, M. Friendly, R. Kindt, P. Legendre, D. McGlinn, P. Minchin, R. B. O'Hara, G. Simpson, P. Solymos, M. Stevens, E. Szoecs, and H. Wagner (2017). *vegan: Community Ecology Package.* Computer Program.

Painter, C. S., B. Carrapa, P. G. DeCelles, G. E. Gehrels, and S. N. Thomson (2014). "Exhumation of the North American Cordillera revealed by multi-dating of Upper Jurassic–Upper Cretaceous foreland basin deposits". In: *Geological Society of America Bulletin* 126.11-12, pp. 1439–1464.

Paton, C., J. Hellstrom, B. Paul, J. Woodhead, and J. Hergt (2011). "Iolite: Freeware for the visualisation and processing of mass spectrometric data". In: *Journal of Analytical Atomic Spectrometry* 26.12, pp. 2508–2518.

Paul, A. N., R. A. Spikings, D. Chew, and J. S. Daly (2019). "The effect of intracrystal uranium zonation on apatite U-Pb thermochronology: A combined ID-TIMS and LA-MC-ICP-MS study". In: *Geochimica et Cosmochimica Acta* 251, pp. 15–35.

Piccoli, P. M. and P. A. Candela (2002). "Apatite in Igneous Systems". In: *Reviews in Mineralogy and Geochemistry* 48.1, pp. 255–292.

Pokrovsky, B. G., M. I. Bujakaite, and O. V. Kokin (2012). "Geochemistry of C, O, and Sr isotopes and chemostratigraphy of neoproterozoic rocks in the northern Yenisei Ridge". In: *Lithology and Mineral Resources* 47.2, pp. 177–199.

Powerman, V., A. Shatsillo, N. Chumakov, I. Kapitonov, and J. Hourigan (2015). "Interaction between the Central Asian Orogenic Belt (CAOB) and the Siberian craton as recorded by detrital zircon suites from Transbaikalia". In: *Precambrian Research* 267.Supplement C, pp. 39–71.

Price, P. B. and R. M. Walker (1963). "Fossil tracks of charged particles in mica and the age of minerals". In: *Journal of Geophysical Research (1896-1977)* 68.16, pp. 4847–4862.

— (1962). "Chemical etching of charged-particle tracks in solids". In: *Journal of applied physics* 33.12, pp. 3407–3412.

Priyatkina, N., A. K. Khudoley, W. J. Collins, N. B. Kuznetsov, and H.-Q. Huang (2016). "Detrital zircon record of Meso- and Neoproterozoic sedimentary basins in northern part of the Siberian Craton: Characterizing buried crust of the basement". In: *Precambrian Research* 285, pp. 21–38.

Qin, M., S. Huang, Z. He, Q. Xu, J. Song, Z. Liu, and Q. Guo (2018). "Evolution of Tectonic Uplift, Hydrocarbon Migration, and Uranium Mineralization in the NW Junggar Basin: An Apatite Fission-Track Thermochronology Study." In: *Acta Geologica Sinica (English Edition)* 92.5, pp. 1901–1916.

Quade, J., D. O. Breecker, M. Daëron, and J. Eiler (2011). "The paleoaltimetry of Tibet: An isotopic perspective". In: *American Journal of Science* 311.2, pp. 77–115.

Roberts, N. M. and R. J. Walker (2016). "U-Pb geochronology of calcite-mineralized faults: Absolute timing of rift-related fault events on the northeast Atlantic margin". In: *Geology* 44.7, pp. 531–534.

Rolland, Y., D. V. Alexeiev, A. Kröner, M. Corsini, C. Loury, and P. Monié (2013). "Late Palaeozoic to Mesozoic kinematic history of the Talas–Ferghana strike-slip fault (Kyrgyz West Tianshan) as revealed by 40Ar/39Ar dating of syn-kinematic white mica". In: *Journal of Asian Earth Sciences* 67-68, pp. 76–92.

Rosen, O. M., K. C. Condie, L. M. Natapov, and A. D. Nozhkin (1994). "Chapter 10 Archean and Early Proterozoic Evolution of the Siberian Craton: A Preliminary Assessment". In: *Developments in Precambrian Geology*. Ed. by K. C. Condie. Vol. 11. Elsevier, pp. 411–459.

Safonova, I., S. Maruyama, T. Hirata, Y. Kon, and S. Rino (2010). "LA ICP MS U–Pb ages of detrital zircons from Russia largest rivers: Implications for major granitoid events in Eurasia and global episodes of supercontinent formation". In: *Journal of Geodynamics* 50.3, pp. 134–153.

Schoene, B. (2014). "4.10 - U–Th–Pb Geochronology A2 - Holland, Heinrich D". In: *Treatise on Geochemistry (Second Edition)*. Ed. by K. K. Turekian. Oxford: Elsevier, pp. 341–378.

Schoene, B. and S. A. Bowring (2006). "U–Pb systematics of the McClure Mountain syenite: thermochronological constraints on the age of the 40Ar/39Ar standard MMhb". In: *Contributions to Mineralogy and Petrology* 151.5, p. 615.

— (2007). "Determining accurate temperature–time paths from U–Pb thermochronology: An example from the Kaapvaal craton, southern Africa". In: *Geochimica et Cosmochimica Acta* 71.1, pp. 165–185.

Schwab, M., L. Ratschbacher, W. Siebel, M. McWilliams, V. Minaev, V. Lutkov, F. Chen, K. Stanek, B. Nelson, W. Frisch, and J. L. Wooden (2004). "Assembly of the Pamirs: Age and origin of magmatic belts from the southern Tien Shan to the southern Pamirs and their relation to Tibet". In: *Tectonics* 23.4, TC4002.

Şengör, A. M. C., B. A. Natal'in, and V. S. Burtman (1993). "Evolution of the Altaid tectonic collage and Palaeozoic crustal growth in Eurasia". In: *Nature* 364.6435, pp. 299–307.

Seward, D., R. Spikings, G. Viola, A. Kounov, G. Ruiz, and N. Naeser (2000). "Etch times and operator variation for spontaneous track length measurements in apatites: an intra-laboratory check". In: *On Track* 10.2, pp. 19–21.

Sha, L.-K. and B. W. Chappell (1999). "Apatite chemical composition, determined by electron microprobe and laser-ablation inductively coupled plasma mass spec-

trometry, as a probe into granite petrogenesis". In: *Geochimica et Cosmochimica Acta* 63.22, pp. 3861–3881.

Shen, C., L. Mei, L. Peng, S. Zhang, L. Liu, and J. Tang (2006). "Fission track evidence for the Mesozoic-Cenozoic tectonic uplift of Mt. Bogda, Xinjiang, northwest China". In: *Chinese Journal of Geochemistry* 25.2, p. 143.

Shen, C., L. Mei, S. Zhang, L. Liu, J. Tang, F. Zhou, S. Yan, and J. Luo (2008). "Fission-track dating evidence on space-time difference of Mesozoic-Cenozoic uplift of the Yilianhabierga Mountain Bogeda Mountain". In: *Journal of Mineralogy and Petrology* 28.2, pp. 63–70.

Shu, L., J. Charvet, L. Guo, H. Lu, and S. Laurent-Charvet (1999). "A Large-Scale Palaeozoic Dextral Ductile Strike-Slip Zone: the Aqqikkudug-Weiya Zone along the Northern Margin of the Central Tianshan Belt, Xinjiang, NW China". In: *Acta Geologica Sinica - English Edition* 73.2, pp. 148–162.

Smye, A. J., J. H. Marsh, P. Vermeesch, J. M. Garber, and D. F. Stockli (2018). "Applications and limitations of U-Pb thermochronology to middle and lower crustal thermal histories". In: *Chemical Geology* 494, pp. 1–18.

Sobel, E. R., J. Chen, and R. V. Heermance (2006a). "Late Oligocene–Early Miocene initiation of shortening in the Southwestern Chinese Tian Shan: Implications for Neogene shortening rate variations". In: *Earth and Planetary Science Letters* 247.1–2, pp. 70–81.

Sobel, E. R. and T. A. Dumitru (1997). "Thrusting and exhumation around the margins of the western Tarim basin during the India-Asia collision". In: *Journal of Geophysical Research: Solid Earth* 102.B3, pp. 5043–5063.

Sobel, E. R., M. Oskin, D. Burbank, and A. Mikolaichuk (2006b). "Exhumation of basement-cored uplifts: Example of the Kyrgyz Range quantified with apatite fission track thermochronology". In: *Tectonics* 25.2, pp. 70–81.

Spear, F. S. and J. M. Pyle (2002). "Apatite, Monazite, and Xenotime in Metamorphic Rocks". In: *Reviews in Mineralogy and Geochemistry* 48.1, pp. 293–335.

Spencer, C., C. Kirkland, and N. Roberts (2018). "Implications of erosion and bedrock composition on zircon fertility; examples from South America and Western Australia". In: *Terra Nova* 30, pp. 289–295.

Stacey, J. S. and J. D. Kramers (1975). "Approximation of terrestrial lead isotope evolution by a two-stage model". In: *Earth and Planetary Science Letters* 26.2, pp. 207–221.

Sun, S.-s. and W. F. McDonough (1989). "Chemical and isotopic systematics of oceanic basalts: implications for mantle composition and processes". In: *Geological Society, London, Special Publications* 42.1, pp. 313–345.

Tagami, T. and P. B. O'Sullivan (2005). "Fundamentals of Fission-Track Thermochronology". In: *Reviews in Mineralogy and Geochemistry* 58, pp. 19–47.

Tang, G.-J., Q. Wang, D. A. Wyman, Z.-X. Li, Y.-G. Xu, and Z.-H. Zhao (2012). "Recycling oceanic crust for continental crustal growth: Sr–Nd–Hf isotope evidence from granitoids in the western Junggar region, NW China". In: *Lithos* 128-131, pp. 73–83.

Tang, W., Z. Zhang, J. Li, K. Li, Z. Luo, and Y. Chen (2015). "Mesozoic and Cenozoic uplift and exhumation of the Bogda Mountain, NW China: Evidence from apatite fission track analysis". In: *Geoscience Frontiers* 6.4, pp. 617–625.

Tapponnier, P. and P. Molnar (1979). "Active faulting and cenozoic tectonics of the Tien Shan, Mongolia, and Baykal Regions". In: *Journal of Geophysical Research: Solid Earth* 84.B7, pp. 3425–3459.

Tera, F. and G. Wasserburg (1972). "U-Th-Pb systematics in three Apollo 14 basalts and the problem of initial Pb in lunar rocks". In: *Earth and Planetary Science Letters* 14.3, pp. 281–304.

Thomson, S. N., G. E. Gehrels, J. Ruiz, and R. Buchwaldt (2012). "Routine low-damage apatite U-Pb dating using laser ablation–multicollector–ICPMS". In: *Geochemistry, Geophysics, Geosystems* 13.2, n/a–n/a.

Tian, Z., W. Xiao, Z. Zhang, and X. Lin (2016). "Fisson-track constrains on superposed folding in the Beishan orogenic belt, southernmost Altaids". In: *Geoscience Frontiers* 7.2, pp. 181–196.

Turkina, O. M., N. G. Berezhnaya, E. N. Lepekhina, and I. N. Kapitonov (2012). "U–Pb (SHRIMP II), Lu–Hf isotope and trace element geochemistry of zircons from high-grade metamorphic rocks of the Irkut terrane, Sharyzhalgay Uplift: Implications for the Neoarchaean evolution of the Siberian Craton". In: *Gondwana Research* 21.4, pp. 801–817.

Turkina, O. M., E. N. Lepekhina, N. G. Berezhnaya, and I. N. Kapitonov (2014). "U-Pb age and Lu-Hf isotope systematics of detrital zircons from paragneiss of the Bulun block (Sharyzhalgai uplift of the Siberian Craton Basement)". In: *Doklady Earth Sciences* 458.2, pp. 1265–1272.

Van der Voo, R., D. J. van Hinsbergen, M. Domeier, W. Spakman, and T. H. Torsvik (2015). "Latest Jurassic–earliest Cretaceous closure of the Mongol-Okhotsk Ocean: A paleomagnetic and seismological-tomographic analysis". In: *Geological Society of America Special Papers* 513, pp. 589–606.

Varganov, A., V. Moskalev, and V. Barmin (2010). *Sheet P-46 (North Yeniseysk)*. Map.

Vassallo, R., M. Jolivet, J. F. Ritz, R. Braucher, C. Larroque, C. Sue, M. Todbileg, and D. Javkhlanbold (2007). "Uplift age and rates of the Gurvan Bogd system (Gobi-Altay) by apatite fission track analysis". In: *Earth and Planetary Science Letters* 259.3–4, pp. 333–346.

Vermeesch, P. (2018). "IsoplotR: a free and open toolbox for geochronology". In: *Geoscience Frontiers* 9, pp. 1479–1493.

Vermeesch, P. (2009). *RadialPlotter: a Java application for fission track, luminescence and other radial plots*. Computer Program.

— (2012). "On the visualisation of detrital age distributions". In: *Chemical Geology* 312–313, pp. 190–194.

— (2013). "Multi-sample comparison of detrital age distributions". In: *Chemical Geology* 341.Supplement C, pp. 140–146.

— (2017). "Statistics for LA-ICP-MS based fission track dating". In: *Chemical Geology* 456, pp. 19–27.

Vermeesch, P., D. Seward, C. Latkoczy, M. Wipf, D. Günther, and H. Baur (2007). "α-Emitting mineral inclusions in apatite, their effect on (U–Th)/He ages, and how to reduce it". In: *Geochimica et Cosmochimica Acta* 71.7, pp. 1737–1746.

Vernikovsky, V. A., D. V. Metelkin, A. E. Vernikovskaya, N. Y. Matushkin, A. Y. Kazansky, P. I. Kadilnikov, I. V. Romanova, M. T. D. Wingate, A. N. Larionov, and N. V. Rodionov (2016). "Neoproterozoic tectonic structure of the Yenisei Ridge and formation of the western margin of the Siberian craton based on new geological, paleomagnetic, and geochronological data". In: *Russian Geology and Geophysics* 57.1, pp. 47–68.

Vernikovsky, V. A., A. E. Vernikovskaya, M. T. D. Wingate, N. V. Popov, and V. P. Kovach (2007). "The 880–864Ma granites of the Yenisey Ridge, western Siberian margin: Geochemistry, SHRIMP geochronology, and tectonic implications". In: *Precambrian Research* 154.3, pp. 175–191.

Vernikovsky, V. A., A. E. Vernikovskaya, A. B. Kotov, E. B. Sal'nikova, and V. P. Kovach (2003). "Neoproterozoic accretionary and collisional events on the western margin of the Siberian craton: new geological and geochronological evidence from the Yenisey Ridge". In: *Tectonophysics* 375.1–4, pp. 147–168.

Vincent, S. J. and M. B. Allen (2001). "Sedimentary record of Mesozoic intracontinental deformation in the eastern Junggar Basin, northwest China: Response to orogeny at the Asian margin". In: *Paleozoic and Mesozoic Tectonic Evolution of Central and Eastern Asia: From Continental Assembly to Intracontinental Deformation*. Ed. by M. S. Hendrix and G. A. Davis. Vol. 194. Geological Society of America.

Volobuev, M. I., S. I. Zykov, N. I. Stupnikova, V. P. Strizhov, and V. L. Myasnikova (1976). "Age of the Basement and Geosynclinal Formations of the Grenvillides in the Yenisei Range (in Russian)". In: *Determination of the Isotopic Age of Ore Deposits*, pp. 39–47.

Wagner, G. A., A. J. W. Gleadow, and P. G. Fitzgerald (1989). "The significance of the partial annealing zone in apatite fission-track analysis: Projected track length measurements and uplift chronology of the transantarctic mountains". In: *Chemical Geology: Isotope Geoscience section* 79.4, pp. 295–305.

Wang, B., Y. Chen, S. Zhan, L. Shu, M. Faure, D. Cluzel, J. Charvet, and S. Laurent-Charvet (2007). "Primary Carboniferous and Permian paleomagnetic results from the Yili Block (NW China) and their implications on the geodynamic evolution of Chinese Tianshan Belt". In: *Earth and Planetary Science Letters* 263.3, pp. 288–308.

Wang, B., D. Cluzel, B. Jahn, L. Shu, Y. Chen, Y. Zhai, Y. Branquet, L. Barbanson, and S. Sizaret (2014). "Late Paleozoic pre- and syn-kinematic plutons of the Kangguer–Huangshan Shear zone: Inference on the tectonic evolution of the eastern Chinese north Tianshan". In: *American Journal of Science* 314.1, pp. 43–79.

Wang, B., D. Cluzel, L. Shu, M. Faure, J. Charvet, Y. Chen, S. Meffre, and K. de Jong (2009a). "Evolution of calc-alkaline to alkaline magmatism through Carboniferous convergence to Permian transcurrent tectonics, western Chinese Tianshan". In: *International Journal of Earth Sciences* 98.6, p. 1275.

Wang, C., L. Gu, Z. Zhang, C. Wu, J. Tang, and X. Tang (2009b). "Petrogenesis and geological implications of the Permian high-K calc-alkaline granites in Harlik Mountains of eastern Tianshan, NW China". In: *Acta Petrologica Sinica* 6, pp. 1499–1511.

Wang, Q., S. Li, and Z. Du (2009c). "Differential uplift of the Chinese Tianshan since the Cretaceous: constraints from sedimentary petrography and apatite fission-track dating". In: *International Journal of Earth Sciences* 98.6, pp. 1341–1363.

Wang, Z., T. Li, J. Zhang, Y. Liu, and Z. Ma (2008). "The uplifting process of the Bogda Mountain during the Cenozoic and its tectonic implication". In: *Science in China Series D: Earth Sciences* 51.4, pp. 579–593.

Webster, J. D. and P. M. Piccoli (2015). "Magmatic Apatite: A Powerful, Yet Deceptive, Mineral". In: *Elements* 11.3, pp. 177–182.

Wildman, M., R. Brown, R. Beucher, C. Persano, F. Stuart, K. Gallagher, J. Schwanethal, and A. Carter (2016). "The chronology and tectonic style of landscape evolution along the elevated Atlantic continental margin of South Africa resolved by joint apatite fission track and (U-Th-Sm)/He thermochronology". In: *Tectonics* 35.3, pp. 511–545.

Windley, B. F., M. B. Allen, C. Zhang, Z. Y. Zhao, and G. R. Wang (1990). "Paleozoic Accretion and Cenozoic Redeformation of the Chinese Tien Shan Range, Central Asia". In: *Geology* 18.2, pp. 128–31.

Windley, B. F., D. Alexeiev, W. Xiao, A. Kröner, and G. Badarch (2007). "Tectonic models for accretion of the Central Asian Orogenic Belt". In: *Journal of the Geological Society* 164.1, pp. 31–47.

Wolf, R. A., K. A. Farley, and D. M. Kass (1998). "Modeling of the temperature sensitivity of the apatite (U–Th)/He thermochronometer". In: *Chemical Geology* 148.1–2, pp. 105–114.

Xiao, W., B. Huang, C. Han, S. Sun, and J. Li (2010). "A review of the western part of the Altaids: A key to understanding the architecture of accretionary orogens". In: *Gondwana Research* 18.2–3, pp. 253–273.

Xiao, W., B. F. Windley, M. B. Allen, and C. Han (2013). "Paleozoic multiple accretionary and collisional tectonics of the Chinese Tianshan orogenic collage". In: *Gondwana Research* 23.4, pp. 1316–1341.

Xiao, W., L. Zhang, K. Qin, S. Sun, and J. Li (2004). "Paleozoic accretionary and collisional tectonics of the eastern Tianshan (China): Implications for the continental growth of central Asia". In: *American Journal of Science* 304.4, pp. 370–395.

Xiao, W., B. Windley, B. Huang, C. Han, C. Yuan, H. Chen, M. Sun, S. Sun, and J. Li (2009). "End-Permian to mid-Triassic termination of the accretionary processes of the southern Altaids: implications for the geodynamic evolution, Phanerozoic continental growth, and metallogeny of Central Asia". In: *International Journal of Earth Sciences* 98.6, pp. 1189–1217.

Xu, X., G. He, H. Li, T. Ding, X. Liu, and S. Mei (2006). "Basic characteristics of the Karamay ophiolitic mélange,Xinjiang,and its zircon SHRIMP dating". In: *Geology in China* 33, pp. 470–475.

Xu, Z., B.-F. Han, R. Ren, Y.-Z. Zhou, L. Zhang, J.-F. Chen, L. Su, X.-H. Li, and D.-Y. Liu (2012). "Ultramafic–mafic mélange, island arc and post-collisional intrusions in the Mayile Mountain, West Junggar, China: Implications for Paleozoic intra-oceanic subduction–accretion process". In: *Lithos* 132-133, pp. 141–161.

Yang, B., T. M. Smith, A. S. Collins, T. J. Munson, B. Schoemaker, D. Nicholls, G. Cox, J. Farkas, and S. Glorie (2018). "Spatial and temporal variation in detrital zircon age provenance of the hydrocarbon-bearing upper Roper Group, Beetaloo Sub-basin, Northern Territory, Australia". In: *Precambrian Research* 304, pp. 140–155.

Yang, G., Y. Li, B. Yang, M. Santosh, B. Zhang, and L. Tong (2013a). "Geochronology and geochemistry of basalts from the Karamay ophiolitic mélange in West Junggar (NW China): Implications for Devonian–Carboniferous intra-oceanic accretionary tectonics of the southern Altaids". In: *GSA Bulletin* 125.3-4, pp. 401–419.

Yang, W., M. Jolivet, G. Dupont-Nivet, Z. Guo, Z. Zhang, and C. Wu (2013b). "Source to sink relations between the Tian Shan and Junggar Basin (northwest China) from Late Palaeozoic to Quaternary: evidence from detrital U-Pb zircon geochronology". In: *Basin Research* 25.2, pp. 219–240.

Yang, Y.-T., C.-C. Song, and S. He (2015). "Jurassic tectonostratigraphic evolution of the Junggar basin, NW China: A record of Mesozoic intraplate deformation in Central Asia". In: *Tectonics* 34, pp. 86–115.

Yin, J., W. Chen, W. Xiao, X. Long, N. Tao, L.-P. Liu, C. Yuan, and M. Sun (2018). "Tracking the multiple-stage exhumation history and magmatic-hydrothermal events of the West Junggar region, NW China: Evidence from 40Ar/39Ar and (U-Th)/He thermochronology". In: *Journal of Asian Earth Sciences* 159, pp. 130–141.

Yin, J., W. Chen, W. Xiao, C. Yuan, M. Sun, G. Tang, S. Yu, X. Long, K. Cai, H. Geng, Y. Zhang, and X. Liu (2015). "Petrogenesis of Early-Permian sanukitoids from West Junggar, Northwest China: Implications for Late Paleozoic crustal growth in Central Asia". In: *Tectonophysics* 662, pp. 385–397.

Yin, J., W. Chen, W. Xiao, C. Yuan, B. F. Windley, S. Yu, and K. Cai (2017). "Late Silurian–early Devonian adakitic granodiorite, A-type and I-type granites in NW Junggar, NW China: Partial melting of mafic lower crust and implications for slab roll-back". In: *Gondwana Research* 43, pp. 55–73.

Yuan, C., M. Sun, S. Wilde, W. Xiao, Y. Xu, X. Long, and G. Zhao (2010). "Post-collisional plutons in the Balikun area, East Chinese Tianshan: Evolving magmatism in response to extension and slab break-off". In: *Lithos* 119.3–4, pp. 269–288.

Yuan, W., A. Carter, J. Dong, Z. Bao, Y. An, and Z. Guo (2006). "Mesozoic–Tertiary exhumation history of the Altai Mountains, northern Xinjiang, China: New constraints from apatite fission track data". In: *Tectonophysics* 412.3–4, pp. 183–193.

Zahirovic, S., K. J. Matthews, N. Flament, R. D. Müller, K. C. Hill, M. Seton, and M. Gurnis (2016). "Tectonic evolution and deep mantle structure of the eastern Tethys since the latest Jurassic". In: *Earth-Science Reviews* 162, pp. 293–337.

Zattin, M., B. Andreucci, S. N. Thomson, P. W. Reiners, and F. M. Talarico (2012). "New constraints on the provenance of the ANDRILL AND-2A succession (western Ross Sea, Antarctica) from apatite triple dating". In: *Geochemistry, Geophysics, Geosystems* 13.10, n/a–n/a.

Zeitler, P. K., A. L. Herczeg, I. McDougall, and M. Honda (1987). "U-Th-He dating of apatite: A potential thermochronometer". In: *Geochimica et Cosmochimica Acta* 51.10, pp. 2865–2868.

Zhai, Q.-G., B.-M. Jahn, R.-Y. Zhang, J. Wang, and L. Su (2011). "Triassic Subduction of the Paleo-Tethys in northern Tibet, China: Evidence from the geochemical and isotopic characteristics of eclogites and blueschists of the Qiangtang Block". In: *Journal of Asian Earth Sciences* 42.6, pp. 1356–1370.

Zhang, C., M. Zhai, B. Allen, A. Saunders, G. Wang, and X. Huang (1993). "Implications of Paleozoic ophiolites from Western Junggar, NW China, for the tectonics of Central Asia". In: *Journal of the Geological Society of London* 150, pp. 551–561.

Zhang, Z., W. Zhu, L. Shu, J. Wan, W. Yang, J. Su, and B. Zheng (2009). "Apatite fission track thermochronology of the Precambrian Aksu blueschist, NW China: Implications for thermo–tectonic evolution of the north Tarim basement". In: *Gondwana Research* 16.2, pp. 182–188.

Zhou, T., F. Yuan, Y. Fan, D. Zhang, D. Cooke, and G. Zhao (2008). "Granites in the Sawuer region of the west Junggar, Xinjiang Province, China: Geochronological and geochemical characteristics and their geodynamic significance". In: *Lithos* 106.3, pp. 191–206.

Zhu, D.-C., S.-M. Li, P. A. Cawood, Q. Wang, Z.-D. Zhao, S.-A. Liu, and L.-Q. Wang (2016). "Assembly of the Lhasa and Qiangtang terranes in central Tibet by divergent double subduction". In: *Lithos* 245, pp. 7–17.

Zorin, Y. A. (1999). "Geodynamics of the western part of the Mongolia–Okhotsk collisional belt, Trans-Baikal region (Russia) and Mongolia". In: *Tectonophysics* 306.1, pp. 33–56.